

DOCTORAL THESIS

Iterative Refinement and Accuracy Validation of Marine Geoid Models

Sander Varbla

TALLINN UNIVERSITY OF TECHNOLOGY
DOCTORAL THESIS
35/2023

Iterative Refinement and Accuracy Validation of Marine Geoid Models

SANDER VARBLA



TALLINN UNIVERSITY OF TECHNOLOGY

School of Engineering

Department of Civil Engineering and Architecture

This dissertation was accepted for the defence of the degree 20/06/2023

Supervisor:

Prof. Artu Ellmann
School of Engineering
Department of Civil Engineering and Architecture
Tallinn University of Technology, Tallinn, Estonia

Pre-reviewer:

Dr. Tarmo Kall
Institute of Forestry and Engineering
Chair of Forest and Land Management and Wood
Processing Technologies
Estonian University of Life Sciences, Tartu, Estonia

Opponents:

Prof. Riccardo Barzaghi
Department of Civil and Environmental Engineering
Politecnico di Milano, Milano, Italy

Prof. Cornelis Slobbe
Faculty of Civil Engineering and Geosciences
Department of Geoscience and Remote Sensing
Delft University of Technology, Delft, The Netherlands

Defence of the thesis: 05/09/2023, Tallinn

Declaration:

Hereby I declare that this doctoral thesis, my original investigation and achievement, submitted for the doctoral degree at Tallinn University of Technology has not been submitted for doctoral or equivalent academic degree.

Sander Varbla

signature



European Union
European Regional
Development Fund



Investing
in your future



Estonian
Research Council

Copyright: Sander Varbla, 2023

ISSN 2585-6898 (publication)

ISBN 978-9916-80-012-6 (publication)

ISSN 2585-6901 (PDF)

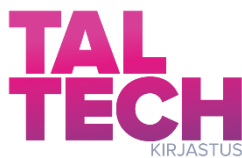
ISBN 978-9916-80-013-3 (PDF)

Printed by Koopia Niini & Rauam

TALLINNA TEHNIKAÜLIKOO
DOKTORITÖÖ
35/2023

Meregeoidi mudelite iteratiivne täpsustamine ja täpsuse valideerimine

SANDER VARBLA



Contents

Contents	5
List of Publications	7
Author’s Contribution to the Publications	8
Introduction	9
Scope and Objectives	11
Limitations	13
Structure	14
Abbreviations	15
Symbols	16
1 Gravimetric Quasigeoid Modelling	20
1.1 Theoretical Principles for Gravity Field Determination	21
1.2 Derivation of Residual Terrain Model Anomalies	23
1.3 Gravity Data Gridding	25
1.4 Bathymetry Influence on the Determined Gravity Field	28
1.5 Quasigeoid Modelling Specifics	29
1.6 Bathymetry Influence on Quasigeoid Modelling	30
2 Derivation of Realistic Dynamic Topography	34
2.1 Theoretical Principles for Dynamic Topography Derivation	34
2.2 Preparation of Dynamic Topography Datasets	37
2.3 Dynamic Topography Computation	39
3 Determination of Offshore Geometric Height Anomalies	42
3.1 Theoretical Principles for Shipborne GNSS Data Processing	42
3.2 Processing of Shipborne GNSS Data	44
3.2.1 GNSS Post-Processing of the Survey Data	45
3.2.2 Reduction of Heights to the Sea Surface	46
3.2.3 Elimination of High-Frequency Attitude and Sea State Effects	47
3.2.4 Derivation of Sailing-Related Corrections	50
3.3 Airborne Laser Scanning Principle	52
3.4 Processing of Airborne Laser Scanning Point Cloud Data	52
3.5 Offshore Geometric Height Anomalies and Sea Surface Heights	53
4 Accuracy Validation of Marine Quasigeoid Models	54
5 Iterative Refinement of Marine Quasigeoid Models	58
5.1 Theoretical Principles for Iterative Data Assimilation	58
5.2 Preparation of Geometric Height Anomalies	61
5.3 Gridding of Geometric Height Anomalies	63
5.4 Iterative Data Assimilation	66
6 Discussion and Concluding Remarks	69
6.1 Gravimetric Quasigeoid Modelling	69
6.2 Accuracy Validation of Marine Quasigeoid Models	70
6.3 Iterative Refinement of Marine Quasigeoid Models	70
List of Figures	72
List of Tables	75

References	76
Acknowledgements.....	84
Abstract.....	85
Lühikokkuvõte.....	87
Appendix 1	89
Appendix 2	121
Appendix 3	135
Appendix 4	161
Appendix 5	185
Appendix 6	217
Appendix 7	245
Curriculum vitae.....	269
Elulookirjeldus.....	273

List of Publications

The thesis has been prepared based on the following peer-reviewed journal articles (indexed by SCOPUS and WOS):

- I **Varbla, S.**, Ellmann, A., & Delpeche-Ellmann, N. (2020). Validation of marine geoid models by utilizing hydrodynamic model and shipborne GNSS profiles. *Marine Geodesy*, 43(2), 134–162. doi:10.1080/01490419.2019.1701153
- II **Varbla, S.**, Ellmann, A., & Delpeche-Ellmann, N. (2021). Applications of airborne laser scanning for determining marine geoid and surface waves properties. *European Journal of Remote Sensing*, 54(1), 558–568. doi:10.1080/22797254.2021.1981156
- III **Varbla, S.**, Ågren, J., Ellmann, A., & Poutanen, M. (2022). Treatment of tide gauge time series and marine GNSS measurements for vertical land motion with relevance to the implementation of the Baltic Sea Chart Datum 2000. *Remote Sensing*, 14(4), #920. doi:10.3390/rs14040920
- IV Liibusk, A., **Varbla, S.**, Ellmann, A., Vahter, K., Uiboupin, R., & Delpeche-Ellmann, N. (2022). Shipborne GNSS acquisition of sea surface heights in the Baltic Sea. *Journal of Geodetic Science*, 12(1), 1–21. doi:10.1515/jogs-2022-0131
- V **Varbla, S.**, Liibusk, A., & Ellmann, A. (2022). Shipborne GNSS-determined sea surface heights using geoid model and realistic dynamic topography. *Remote Sensing*, 14(10), #2368. doi:10.3390/rs14102368
- VI **Varbla, S.** (2022). The influence of bathymetry on regional marine geoid modeling in Northern Europe. *Journal of Marine Science and Engineering*, 10(6), #793. doi:10.3390/jmse10060793
- VII **Varbla, S.**, & Ellmann, A. (2023). Iterative data assimilation approach for the refinement of marine geoid models using sea surface height and dynamic topography datasets. *Journal of Geodesy*, 97(3), #24. doi:10.1007/s00190-023-01711-7

Author's Contribution to the Publications

The author of this thesis contributed to the listed publications by (note that **Publications III, IV, V, and VII** also contain a section detailing authors' contributions):

- I designing and supervising the marine gravity and GNSS survey in the Gulf of Finland; post-processing raw shipborne GNSS data using Trimble Business Center software; developing the methods, which were employed to compute offshore geoid profiles used for validating quasigeoid models; conducting the analysis of the results; drafting the manuscript in cooperation with all the co-authors; visualising the manuscript.
- II conceptualising the study in cooperation with all the co-authors; developing the used methods; processing the provided coordinated point cloud information and conducting the analysis of the results; drafting and visualising the manuscript.
- III conceptualising the study in cooperation with all the co-authors; processing the used data and conducting the analysis of the results; drafting and visualising the manuscript.
- IV conceptualising the study with Prof. Aive Liibusk and Prof. Artu Ellmann; conducting fieldwork in cooperation with all the co-authors; analysing the post-processed shipborne GNSS data; drafting the manuscript with Prof. Aive Liibusk and Prof. Artu Ellmann; visualising the manuscript with Prof. Aive Liibusk.
- V conceptualising the study in cooperation with all the co-authors; developing the used methods; processing the used data and conducting the analysis of the results; drafting and visualising the manuscript.
- VI The research was conducted in its entirety by the author. Before Baltic Sea Chart Datum 2000 quasigeoid computations, the author also revised most Estonian gravity data for better consistency with other Northern Europe gravity observations.
- VII conceptualising the study with Prof. Artu Ellmann; developing the used methods; processing the used data and conducting the analysis of the results; drafting and visualising the manuscript.

Introduction

The geoid is an equipotential surface of the Earth's gravity field that coincides with the undisturbed (neglecting the influence of, e.g., wind and currents) sea level. In geodetic applications, a model of the geoid is adopted as a height reference surface (i.e., the modelled geoid surface represents zero heights), generally for some limited area (e.g., the Baltic Sea region). Such a model is essential for height determination using GNSS (global navigation satellite system) technology, where the measured heights are given relative to the reference ellipsoid (e.g., GRS80; Moritz, 2000). Physically meaningful orthometric heights H (i.e., heights representing the Earth's surface from the geoid along a plumbline) are received by subtracting the modelled geoidal heights N from the measured ellipsoidal heights h (cf. Figure 1):

$$H = h - N. \quad (1)$$

Alternatively, some countries (primarily in Europe) have adopted normal heights H^* and the associated quasigeoid models (described by height anomalies ζ) for defining height systems, historically motivated by the lack of knowledge regarding topographic mass distribution required in accurate geoid determination (i.e., gravity observations need to be downward continued through topography to the geoid for gravity integration). Quasigeoid computation only deals with the Earth's geometry, where integration is conducted on a conceptual telluroid surface that approximates topography; quasigeoid is not an equipotential surface. The height conversion principle, however, remains the same (also refer to Figure 1):

$$H^* = h - \zeta. \quad (2)$$

The differences between the geoid and quasigeoid (or equivalently between orthometric and normal heights) correlate with topographic heights, being a few millimetres to centimetres in areas with low topography and up to a few metres in high mountainous regions (Sjöberg & Bagherbandi, 2012; Foroughi & Tenzer, 2017). In contrast, the differences are negligible offshore, where the quasigeoid practically coincides with the

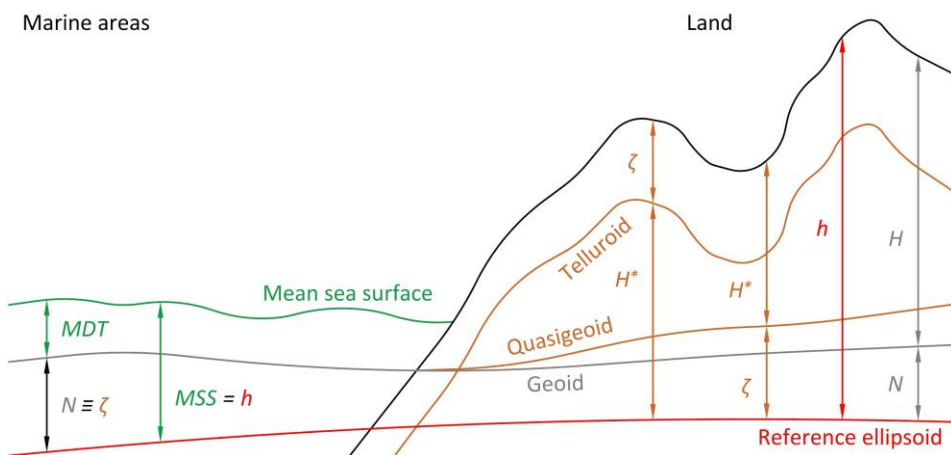


Figure 1. Interrelations between reference surfaces and heights.

geoid (Tenzer & Foroughi, 2018; also see Figure 1). To summarise the above, a (quasi)geoid model is required for height determination using modern satellite techniques.

Such models have various offshore applications. To give some examples, in engineering, accurate (quasi)geoid models provide crucial support for constructing and maintaining offshore structures while staking out structural elements' heights using GNSS measurements (cf. Equations 1 and 2). For safer navigation, a (quasi)geoid model allows real-time GNSS-based monitoring of vessels' under-keel clearance (cf. Figure 2):

$$UKC = h - N - \text{Seabed depth} \quad (3)$$

– Vertical distance between the GNSS antenna and keel,

assuming the availability of bathymetry information, where depths are given relative to the (quasi)geoid model (e.g., Khatun et al., 2020; Schwabe et al., 2020); this is especially important in shallow seas and harbours. The availability of reliable (quasi)geoid models can also facilitate more efficient shipping, where reduction of uncertainties in under-keel clearance management can provide means to load vessels according to the theoretical maximum capacity (heavier load results in an increased draft, which is the measure from the sea surface to the keel). This requires the estimation of a vessel's draft (Catarino, 2021) and accurate water level prognoses relative to a (quasi)geoid model (i.e., dynamic topography DT). The expected under-keel clearance can be determined with these parameters, including (quasi)geoid model referred depth data (cf. Figure 2):

$$UKC = DT - |Draft| - \text{Seabed depth}. \quad (4)$$

From the oceanographic research side, accurate knowledge of the geoid is required to investigate fine-scale currents and other submesoscale marine processes (e.g., Idžanović et al., 2017; Knudsen et al., 2021) – these are represented by the ocean's mean dynamic topography MDT (estimated over some time period), which is defined as a separation between the mean sea surface MSS (estimated over the same period as mean dynamic topography, using, e.g., satellite altimetry measurements) and the geoid (recall that offshore geoidal heights are equivalent to height anomalies):

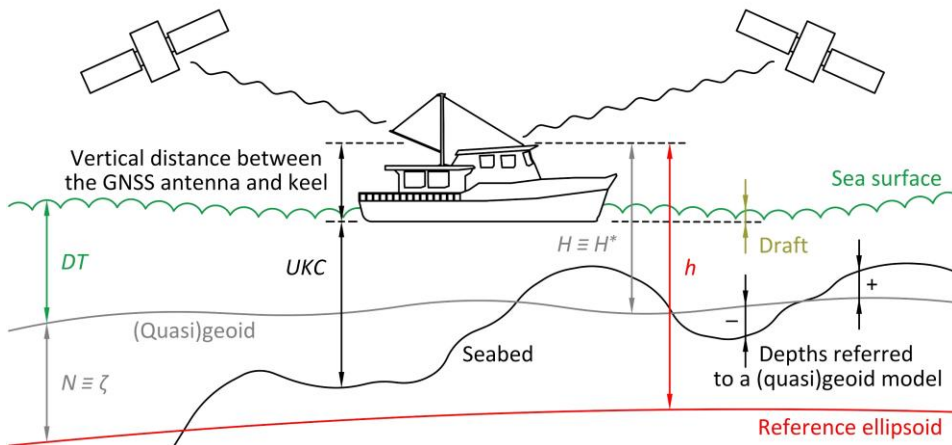


Figure 2. Schematic determination of a vessel's under-keel clearance.

$$MDT = MSS - N \equiv MSS - \zeta; \quad (5)$$

refer to Figure 1. Thus, there is an increasing demand for accurate (quasi)geoid models to benefit from advanced offshore industry technologies and progress marine sciences further.

A remarkable effort has gone toward developing (quasi)geoid modelling theory and approaches that support achieving high accuracy (e.g., see the overview of Wang et al., 2021). On land, the typical accuracy of high-resolution regional (quasi)geoid models can reach a few centimetres, nearing the one-centimetre long-term goal of the geodetic community. For example, this highly demanding task has already been achieved in relatively flat Estonia (Ellmann et al., 2020) and The Netherlands (Slobbe et al., 2019), whereby intensive work toward the goal is ongoing elsewhere, especially in more mountainous regions (e.g., Ågren & Sjöberg, 2014; Foroughi et al., 2023). A particular obstacle to achieving the one-centimetre modelling accuracy is the need for more high-quality gravity observations; offshore regions are one of the most problematic in this regard. The errors of marine (quasi)geoid models are expected to reach up to a few decimetres in the shorter wavelength spectrum due to gravity data void areas and/or inaccurate data (a relevant example is presented by Barzaghi et al., 2018). Since the conventional GNSS-levelling control points used for validating (quasi)geoid modelling solutions cannot be established offshore, the marine (quasi)geoid modelling accuracy estimates are primarily a conjecture. The somewhat questionable performance of marine (quasi)geoid modelling now brings us to the topic of this thesis.

Scope and Objectives

As indicated, problematics related to offshore (quasi)geoid modelling have motivated this thesis' compilation. Already, the currently available (quasi)geoid models may not satisfy the industry and scientific needs, whereas the demand for improved accuracy increases ever further with technological and methodological advancements. As the first order of business, there is a need to associate marine (quasi)geoid modelling solutions with realistic accuracy estimates and identify problematic regions where further improvements are needed. This task requires the development of new (quasi)geoid modelling validation approaches that could be employed offshore.

Various methods exist to measure sea surface heights (SSHs) that approximate the geoid shape. For instance, satellite altimetry records cover most of Earth's marine areas with a reasonable quantification of SSHs (e.g., Vu et al., 2018; Yang et al., 2019; Liibus et al., 2020). However, spatial and temporal resolution characteristics, diminishing reliability in the coastal zone due to approximations in atmospheric, sea state, and geophysical corrections, and waveform distortions caused by coastal inhomogeneities set limitations for using these data (Passaro et al., 2014; Cipollini et al., 2017; Vignudelli et al., 2019). Approaches based on GNSS measurements such as shipborne GNSS surveys (e.g., Jürgenson et al., 2008; Bouin et al., 2009; Lavrov et al., 2017) and airborne laser scanning (ALS; e.g., Cocard et al., 2002; Gruno et al., 2013; Zlinszky et al., 2014) could be helpful in near-coast regions instead by providing increased SSH-determination accuracy. The focus of this thesis is on those latter methods.

Following initial investigations of a shipborne gravity and GNSS campaign in the West Estonian Archipelago (Varbla et al., 2017a), a more elaborate dedicated gravity and GNSS campaign was conducted in the Gulf of Finland (overview of the campaign is given by Varbla et al., 2017b). The results of this campaign are detailed in **Publication I**, which

proves the gravimetric quasigeoid modelling accuracy improvement due to the inclusion of new high-quality marine gravity data. It is essential to emphasise here that the reliability of such validations requires the estimation of dynamic topography (DT) separating the geoid from SSH measurements (refer to Equation 5 principle; also see Figure 2). Admittedly, consideration for DT was neglected in Varbla et al. (2017a) while assessing the performance of quasigeoid modelling solutions. Since then, methodology development for deriving realistic DT has been a continuous process, where **Publication I** describes the first attempt to combine tide gauge (TG) readings with hydrodynamic model (HDM) data. The approach was improved in **Publications II** and **V** and finalised in **Publication VII**, as also adopted in the thesis.

Similarly to DT data, the determined SSHs must be reliable, too. The initial shipborne GNSS data processing methods in **Publication I** were hence further elaborated in **Publication V** to facilitate improved SSH data quality. This elaborated methodology is followed in the thesis for processing shipborne GNSS data. Besides careful data processing, the data gathering procedures must also be rigorous; **Publication IV** focuses on more practical aspects of shipborne GNSS data acquisition. Together, **Publications IV** and **V** describe six additional shipborne GNSS campaigns. Along with these shipborne GNSS-determined SSHs, data from an ALS survey as described in **Publication II** are also employed (additional details can be found in Varbla et al., 2020). **Publication II** also confirms the quasigeoid modelling validation results presented in **Publication I**. Lastly, another crucial consideration is that all data must be used consistently (e.g., common permanent tide concept and uplift epoch); **Publication III** is dedicated to these aspects, with a focus on vertical land motion (VLM).

Problematic (quasi)geoid modelling regions can be identified with the availability of relevant data and methods, as presented in the above papers. For instance, this information could aid in planning and conducting additional dedicated gravity survey campaigns. It is now appropriate to mention that over the past decade, a significant international effort has been dedicated to conducting shipborne gravity surveys (Nordman et al., 2018; Lu et al., 2019; Ince et al., 2020; Saari et al., 2021; Lu et al., 2022) in the Baltic Sea (i.e., the thesis' study area) for developing a high-resolution quasigeoid-based height reference Baltic Sea Chart Datum 2000 (BSCD2000; Schwabe et al., 2020). The above-mentioned gravity surveys described in Varbla et al. (2017a, 2017b) and **Publication I** also contribute toward that goal. Notably, Tallinn University of Technology is one of the BSCD2000 quasigeoid computation centres; aspects of these gravimetric quasigeoid modelling endeavours have been described in **Publication VI**.

Additional gravity data may only sometimes improve (quasi)geoid modelling significantly. Instead, a revised computational approach might be required. With that aim, **Publication VI** explores how the inclusion of bathymetry data in gravimetric quasigeoid modelling could influence the resulting solutions, demonstrating enhanced accuracy as a conclusion. Since (quasi)geoid determination projects that include Northern Europe, such as the more recent EGG2015 (Denker, 2015) and NKG2015 (Ågren et al., 2016), have thus far neglected bathymetry data (not considering the BSCD2000 in this context), these results are essential to encourage the use of bathymetry data in future gravimetric (quasi)geoid modelling efforts.

In principle, **Publication VI** focuses on conventional regional quasigeoid modelling, where the availability of high-quality marine gravity data is crucial. It should be acknowledged that methods for obtaining these data, such as shipborne (see the above references and **Publication I**) and airborne (e.g., Jamil et al., 2017; Wu et al., 2019) gravity

surveys or measurements on ice (e.g., Noréus et al., 1997; Märdla et al., 2015), are usually costly, laborious, and time-consuming. The reliability of historic marine gravity data may also be questionable due to datum inconsistencies (e.g., Denker & Roland, 2005; Featherstone, 2009). Therefore, high-quality marine gravity observations are often distributed sparsely; the data situation in the general Baltic Sea is more of an exception than a rule. As an alternative, **Publication VII** proposes an approach for refining existing gravimetric (quasi)geoid models through iterative data assimilation using SSH and DT datasets (i.e., the same data that can be employed for validation purposes). The high-accuracy gravimetric quasigeoid model computed within the BSCD2000 frames (**Publication VI**) is pivotal here since it allows an independent validation for the developed data assimilation methodology (note that the assimilation case study refines an alternative model with significant errors). Importantly, dedicated campaigns are not necessarily required for high-quality SSH data acquisition. The shipborne GNSS data described in **Publications IV** and **V** were collected autonomously on a research vessel, whereby the **Publication II** ALS measurements represent en route data collected during the routine mapping of offshore islands. In other words, these SSH data were obtained virtually without any (additional) cost or labour.

To summarize the above overview, this thesis has two main objectives, which consist of the following interconnected topical investigations (i.e., sub-objectives for fulfilling the thesis' main objectives):

1. validation of marine (quasi)geoid models;
 - derivation of realistic DT (**Publications I, II, V, and VII**)
 - derivation of SSHs (and geometric height anomalies) from shipborne GNSS measurements (**Publications I, IV, and V**)
 - derivation of SSHs (and geometric height anomalies) from ALS surveyed point clouds (**Publication II**)
 - data consistency-related issues (**Publication III**)
2. improvement of marine (quasi)geoid modelling.
 - impact of new marine gravity observations (**Publications I and II**)
 - influence of bathymetry information (**Publication VI**)
 - potential of DT and SSH datasets in an iterative data assimilation approach (**Publication VII**)

Limitations

There are some limitations in the presented investigations that should be addressed:

1. The investigations are limited to quasigeoid models and modelling; in the following text, quasigeoid-associated terminology is henceforth adopted. However, as already mentioned above, the quasigeoid practically coincides with the geoid offshore (cf. Figure 1). All the investigations and developed approaches thus also apply to geoid models.
2. The Baltic Sea region (i.e., the thesis' study area) is exceptional due to its well-developed geodetic infrastructure, making it a perfect study area for developing novel geodetic approaches. However, the applicability of these approaches remains to be tested in other parts of the world, which can present new challenges due to the specific limitations of the local geodetic infrastructure.

3. The Baltic Sea is an enclosed water body. The developed method for deriving DT benefits from this circumstance since in situ data provides control along the entire coastline. Dynamic topography estimation accuracy would likely degrade significantly due to extrapolation errors with increasing distance from the coast in study areas where the coastline stretches along a single side of a water body.
4. Shipborne GNSS- and ALS-derived SSHs, even if obtained through autonomous means, are generally difficult to obtain; availability of a suitable platform and instrumentation are still required. Furthermore, dedicated campaigns would be costly like marine gravity surveys. It should be noted that most developed principles apply to any arbitrary dataset of SSHs. Satellite altimetry data that are globally available in abundance represent an opportunity in this regard, although coastal regions would remain a challenge.
5. The quasigeoid modelling described in **Publication VI** represents only one component of the final BSCD2000 reference surface. This thesis does not aim to discuss further aspects of the BSCD2000 development and implementation.

Structure

The thesis is divided into sections according to topical investigations, where most sections consist of a theoretical overview and practical implementation of the principles. Only the most essential details and findings are presented to maintain the thesis' conciseness, whereas additional particulars and explanations can be found in the corresponding complementing publications. Minor differences may exist with equations shown in complementing publications for better clarity. In addition, there may exist numerical differences with results in some publications. Such differences are caused by revised methodological approaches and new or improved datasets that have become available (primarily due to recomputations conducted within the frames of **Publication VII**; also refer to the above discussion); furthermore, a few mistakes were corrected (the bias in the results of **Publication V**, see Figures 16 and 17 in the paper, stemmed from permanent tide inconsistencies, as it appeared later). These numerical differences do not affect the conclusions. An exception is the gravimetric quasigeoid modelling solution GQM2022, which was not updated for this thesis, although new gravity data has become available after the completion of **Publication VI**.

The following Section 1 examines the influence of bathymetry on gravimetric quasigeoid modelling. The gravimetric quasigeoid model GQM2022 that results from these investigations is essential for the subsequent topics. In Section 2, the derivation of realistic DT is detailed. Section 3 then reviews the determination of offshore height anomalies (i.e., the geometry of the geoid) using SSHs measured by shipborne GNSS and ALS. Section 4 presents some marine quasigeoid validation results and shows the influence of new gravity data on quasigeoid modelling. Finally, Section 5 demonstrates the iterative data assimilation approach. The main body of the thesis ends with a discussion in Section 6.

Abbreviations

ALS	airborne laser scanning
BHS77	Baltic Height System of 1977
BSCD2000	Baltic Sea Chart Datum 2000
CORS	continuously operating reference stations
d/o	degree and order
DB	dynamic bias
DT	dynamic topography
EVRS	European Vertical Reference System
GGM	global geopotential model
GNSS	global navigation satellite system
HDM	hydrodynamic model
LiDAR	light detection and ranging
LSC	least-squares collocation
LSMSA	least-squares modified Stokes's formula with additive corrections
NAP	Normaal Amsterdams Peil
RTM	residual terrain model
SoAD	sum of absolute differences
SSH	sea surface height
TG	tide gauge
VLM	vertical land motion

Symbols

A, B	denotations for indexes in equations distinguishing two components of a pair
b	breadth of a vessel
BRI_P	bathymetry ruggedness index
C_0	signal variance
C_B	block coefficient
C_{model}	modelled covariance value
\mathbf{C}_{nn}	covariance matrix of observation errors
\mathbf{C}_{st}	cross-covariance matrix of predicted and known signals
\mathbf{C}_{ss}	covariance matrix of predicted signal
\mathbf{C}_{tt}	covariance matrix of known signal
$CORR$	combined sailing-related corrections
d	distance
$d_{A\xi}$	discrepancy between measured and estimated instantaneous sea surface height
d_{LIM}	computation radius
d_{MOD}	modification distance
d_{ZP}	minimum zero padding distance
dh	ellipsoidal height difference between GNSS observation location and continuously operating reference station
\overline{dDB}_B	averaged dynamic bias
DB	dynamic bias
\mathbf{DB}	vector of dynamic bias values
\widehat{DB}	predicted dynamic bias
$\widehat{\mathbf{DB}}$	vector of predicted dynamic bias values
DT	dynamic topography
\widehat{DT}	estimated dynamic topography using the semi-oceanographic method
$\widehat{DT}_{geodetic}$	estimated dynamic topography using the geodetic method
DT_{HDM}	dynamic topography from hydrodynamic model
DT_{RSL}	dynamic topography as represented by relative tide gauge readings
DT_{TG}	dynamic topography as represented by absolute tide gauge readings
\mathbf{E}_{ss}	error covariance matrix of predicted signal
F	low-pass filtering window size
F_{scale}	scale factor
g_P	gravity measurement
G	gravitational constant
GC	geoid change rate
h, h_Q	ellipsoidal height
h_0	ellipsoidal height of continuously operating reference station at the reference epoch

H	orthometric height
H^*, H_p^*	normal height / depth
$\overline{H^*}$	mean depth
H^{ref}, H_p^{ref}	normal height of reference surface in residual terrain model computation
H_{REF}	vertical range from GNSS antenna reference point to sea surface
H_{Tape}^{BM}	tape-measured distance from sea surface to benchmark
H_{TS}^{ARP}	GNSS antenna reference point's height measured by total station
H_{TS}^{BM}	benchmark height measured by total station
$iSSH, iSSH_{A\xi}$	instantaneous sea surface height
$\overline{iSSH}_{A\xi}$	estimated instantaneous sea surface height
$iSSH_{CoM},$	instantaneous sea surface height at vessel's mass centre
$iSSH_{CoM}^\xi$	
i, n	denotations for indexes in equations
I	total number of data (used in different contexts)
J	cost function
k	data assimilation iteration
l	covariance distance
L	modification degree limit
M	upper degree for the use of global geopotential model
MDT	mean dynamic topography
MOD	modification coefficient
MP	modification parameter (data assimilation)
MSS	mean sea surface
N	geoidal height
P	weight
Q_n^L	modified truncation coefficient
r_{CoM}^F	low-pass filtered sea surface height residual
r_{CoM}^{F+C}	low-pass filtered and corrected sea surface height residual
r_{CoM}^{Median}	median value of sea surface height residuals
r_{CoM}^{UF}	unfiltered sea surface height residual
r_{geom}	geometric height anomaly residual
\hat{r}_{geom}	gridded geometric height anomaly residual
R	mean Earth radius
\bar{s}	mean static draft
s_n	modification parameter (LSMSA)
S^L	modified Stokes's function
SSH	sea surface height
t	observation epoch
t_0^{HS}	reference epoch of height reference system
t_0^{RF}	reference epoch of reference frame

T_1	time window for dynamic bias temporal domain uncertainty estimation
T_2	time window for dynamic bias spatial domain uncertainty estimation
UKC	under-keel clearance
v	velocity
$VLM_{geocentric}$	geocentric vertical land motion rate
$VLM_{levelled}$	levelled vertical land motion rate
x, y, z	Cartesian coordinates of moving integration element
$x_1, x_2, y_1, y_2,$	integration limits
z_1, z_2	
x_p, y_p, z_p	Cartesian coordinates of computation point
$X_{1/2}$	correlation length
α	characteristic distance
β	complementary covariance model parameter
γ_0	normal gravity on reference ellipsoid
γ_Q	normal gravity on telluroid
δ_{max}	maximum squat
δg_G^{RTM}	residual terrain model reduction at grid node
δg_P^{RTM}	residual terrain model reduction at arbitrary location
δg_P^T	terrain correction
$\delta \zeta_{ATM}$	combined atmospheric effect
$\delta \zeta_{DWC}$	combined downward continuation effect
$\delta \zeta_{ELL}$	combined ellipsoidal effect
Δg_G^{FAA}	gridded surface free-air gravity anomaly
Δg_P^{FAA}	discrete surface free-air gravity anomaly
Δg_G^{GGM}	gravity anomaly synthesised from global geopotential model at grid node
Δg_n^{GGM}	Laplace harmonic of gravity anomaly derived from global geopotential model
Δg_P^{GGM}	gravity anomaly synthesised from global geopotential model at arbitrary location
Δg_G^{RTMA}	gridded residual terrain model gravity anomaly
$\Delta \mathbf{g}_G^{RTMA}$	vector of gridded residual terrain model gravity anomalies
Δg_P^{RTMA}	discrete residual terrain model gravity anomaly
$\Delta \mathbf{g}_P^{RTMA}$	vector of discrete residual terrain model gravity anomaly
$\Delta H_{MT \Rightarrow ZT}$	height correction for conversion from mean-tide to zero-tide permanent tide concept
$\Delta H_{TF \Rightarrow ZT}$	height correction for conversion from tide-free to zero-tide permanent tide concept
ζ	height anomaly
ζ_{geom}	geometric height anomaly
$\hat{\zeta}_{geom}$	gridded geometric height anomaly
ζ_{model}	modelled height anomaly

$\hat{\zeta}_{model}$	best assimilation estimate of modelled height anomaly
ξ	GNSS antenna number
ρ	density
σ	unit sphere
σ_0	spherical integration cap
σ_{CORR}	uncertainty of combined sailing-related corrections
σ_{db1}	temporal domain uncertainty component of dynamic bias
σ_{db2}	spatial domain uncertainty component of dynamic bias
σ_{DB}	uncertainty of dynamic bias
$\sigma_{\mathcal{DB}}$	uncertainty of predicted dynamic bias
$\sigma_{\mathcal{DT}}$	uncertainty of dynamic topography
σ_{geom}	uncertainty of geometric height anomaly
$\sigma_{\widehat{geom}}$	uncertainty of gridded geometric height anomaly
σ_{GNSS}	uncertainty of GNSS measurements
σ_{model}	uncertainty of modelled height anomaly
$\sigma_{\widehat{model}}$	uncertainty of best assimilation estimate of modelled height anomaly
σ_{MOD}	modified uncertainty of gridded geometric height anomaly
$\sigma_{\hat{r}}$	uncertainty of gridded geometric height anomaly residual
σ_{SSH}	uncertainty of sea surface height
σ_{VLM}	uncertainty of vertical land motion rate
φ, λ	geodetic coordinates / geodetic coordinates of quasigeoid model grid node
$\varphi^{CORS}, \lambda^{CORS}$	geodetic coordinates of continuously operating reference station
$\varphi^{HDM}, \lambda^{HDM}$	geodetic coordinates of hydrodynamic model grid node
$\varphi^{SSH}, \lambda^{SSH}$	geodetic coordinates of sea surface height data point
$\varphi^{TG}, \lambda^{TG}$	geodetic coordinates of tide gauge station
ψ	geocentric angle between computation and integration points
ψ_0	geocentric angle corresponding to integration cap σ_0

1 Gravimetric Quasigeoid Modelling

Due to the advances in satellite gravimetry (e.g., by using data from GRACE and GOCE missions), the quasigeoid can be solved with an accuracy of a few centimetres for longer wavelengths (e.g., Gruber & Willberg, 2019; Brockmann et al., 2021). However, such global geopotential models (GGMs) may be insufficient for regional-scale applications (see the examples in the Introduction) because of omission errors. Regional modelling approaches should be employed instead to determine also the geoid's shorter wavelength signal. For instance, with globally distributed gravity anomalies, gravimetric models can be determined using Stokes's formula (Stokes, 1849). In practice, such an approach is unfeasible due to the limited availability of gravity data, and for that reason, gravity integration is restricted to a smaller spatial domain around the computation points. The resulting truncation error from neglecting the far zone is reduced by modifying Stokes's formula (Molodenskii et al., 1962), allowing terrestrial gravity anomalies to be combined with a suitable GGM.

Stokes's formula can be modified using deterministic or stochastic methods. Deterministic modification methods aim to reduce the truncation error only, whereas stochastic methods also attempt to reduce errors in gravity data through an optimal combination of terrestrial observations with a GGM (e.g., Ellmann, 2005a; Goyal et al., 2022). Here, the unbiased least-squares modified Stokes's formula with additive corrections (LSMSA), which uses a stochastic modification, is employed for gravimetric quasigeoid modelling (Sjöberg, 1991; Sjöberg, 2003a; Sjöberg & Bagherbandi, 2017):

$$\zeta_{model} = \frac{R}{4\pi\gamma_0} \iint_{\sigma_0} S^L(\psi) \Delta g_G^{FAA} d\sigma + \frac{R}{2\gamma_0} \sum_{n=2}^M (s_n + Q_n^L) \Delta g_n^{GGM} \quad (6)$$

$$+ \delta\zeta_{DWC} + \delta\zeta_{ATM} + \delta\zeta_{ELL},$$

where	ζ_{model}	modelled height anomaly;
	R	mean Earth radius;
	γ_0	normal gravity on a reference ellipsoid;
	σ_0	integration cap (with geocentric angle ψ_0) around a computation point;
	S^L	Stokes's function modified up to degree limit L ;
	ψ	geocentric angle between computation and moving integration points;
	Δg_G^{FAA}	gridded surface free-air gravity anomaly;
	σ	unit sphere;
	M	upper degree for the use of a GGM;
	s_n	modification parameter;
	Q_n^L	modified (up to degree limit L) truncation coefficient;
	Δg_n^{GGM}	GGM-derived Laplace harmonic of gravity anomaly;
	$\delta\zeta_{DWC}$	combined downward continuation effect;
	$\delta\zeta_{ATM}$	combined atmospheric effect;
	$\delta\zeta_{ELL}$	combined ellipsoidal effect.

Notice that in the LSMSA approach, the surface free-air gravity anomalies Δg_G^{FAA} are used without any reductions, but these data must be given on a regular grid. Therefore, the quasigeoid modelling accuracy using the LSMSA approach highly depends on prior gravity data processing – how the gravity grid is derived from discrete data (also see Märdla et al.,

2017). The following focuses on deriving a gridded gravity field representation, where the bathymetry contribution to quasigeoid modelling is also introduced. For additional details regarding the other quantities used in gravimetric quasigeoid modelling (cf. Equation 6), please refer to Section 2.2 in **Publication VI**.

1.1 Theoretical Principles for Gravity Field Determination

Gravity measurement g_P on (or above) terrain or sea surface at point P (at a normal height H_P^* relative to the quasigeoid) can be reduced to a surface free-air gravity anomaly:

$$\Delta g_P^{FAA} = g_P - \gamma_Q, \quad (7)$$

where γ_Q is the normal gravity at point Q (at ellipsoidal height $h_Q = H_P^*$ above the reference ellipsoid) on the telluroid (Heiskanen & Moritz, 1967). For quasigeoid modelling using the LSMSA approach, a regular grid must be estimated from such surface free-air gravity anomalies at arbitrary discrete locations. Since the gravity field contains topography and bathymetry correlated high-frequency variability, direct gridding of discrete surface free-air gravity anomalies likely yields unreliable results because it is difficult for interpolation algorithms to predict accurate gravity values at grid nodes. Implementing a band-pass filter that attenuates gravity signals above and below desired frequencies could improve the performance of gravity data gridding.

Surface free-air gravity anomalies can be further reduced to residual terrain model (RTM) anomalies:

$$\Delta g_P^{RTMA} = \Delta g_P^{FAA} - \Delta g_P^{GGM} - \delta g_P^{RTM} \quad (8)$$

by removing the long- (Δg_P^{GGM}) and short-wavelength (δg_P^{RTM}) gravity components. The long-wavelength component can be synthesised from a GGM evaluated up to a suitable degree and order (d/o). For deriving the short-wavelength component (i.e., the RTM reduction), terrain elevation and bathymetric depth data are required (i.e., a digital terrain model is needed). The RTM reduction can be computed as:

$$\delta g_P^{RTM} = 2\pi G\rho(H_P^* - H_P^{ref}) - \left(\delta g_P^T \Big|_{z_1=H_P^*}^{z_2=H^*} - \delta g_P^T \Big|_{z_1=H_P^{ref}}^{z_2=H^{ref}} \right), \quad (9)$$

with terrain correction δg_P^T estimated by summing the attraction of a finite number of rectangular prisms (Forsberg & Tscherning, 1981; Forsberg, 1984):

$$\delta g_P^T = -G \sum_{x_1}^{x_2} \int_{y_1}^{y_2} \int_{z_1}^{z_2} \frac{\rho(z - z_P)}{[(x - x_P)^2 + (y - y_P)^2 + (z - z_P)^2]^{3/2}} dx dy dz, \quad (10)$$

where x_P, y_P, z_P and x, y, z are the local Cartesian coordinates of the computation point P and a moving integration element, respectively; integration limits $x_1, x_2, y_1, y_2, z_1,$ and z_2 define the sizes of prisms. The term G in Equations (9) and (10) denotes the gravitational constant, and ρ is density. Unless topographic density distribution is known, the density can be assumed at 2670 kg/m³ for terrain and 1640 kg/m³ for bathymetric

depths (i.e., the difference between terrain and seawater densities). In Equation (9), terms H_p^* and H^* represent a digital terrain model determined normal heights of the computation point P and a moving integration element, respectively. The corresponding terms H_p^{ref} and H^{ref} denote normal heights of a smooth reference surface, which can be constructed using the same digital terrain model (e.g., by low-pass filtering). Ideally, the reference surface resolution should match the selected d/o of the used GGM (i.e., the Δg_p^{GGM} component); RTM reduction is meant to remove the remaining higher-frequency gravity contribution beyond that d/o.

After proper reductions, the remaining gravity signal of RTM anomalies contains little variability, representing a much smoother alternative compared to the initial surface free-air gravity anomalies. Using least-squares collocation (LSC; Moritz, 1980), gravity values at grid nodes (Δg_G^{RTMA}) can be predicted using the reduced measurements at arbitrary locations (Δg_P^{RTMA}):

$$\Delta \mathbf{g}_G^{RTMA} = \mathbf{C}_{st}(\mathbf{C}_{tt} + \mathbf{C}_{nn})^{-1} \Delta \mathbf{g}_P^{RTMA}, \quad (11)$$

where \mathbf{C}_{st} is the cross-covariance matrix of the predicted (Δg_G^{RTMA}) and known (Δg_P^{RTMA}) signals, and \mathbf{C}_{tt} and \mathbf{C}_{nn} are the covariance matrices of known signal and observation errors, respectively. Ideally, the vector of known signal ($\Delta \mathbf{g}_P^{RTMA}$) should contain centred random variables to ensure prediction accuracy (e.g., the mean signal can be removed before the gridding procedure and later restored on the predicted values). Assuming that the observation errors are uncorrelated, \mathbf{C}_{nn} becomes a diagonal matrix. The \mathbf{C}_{st} and \mathbf{C}_{tt} matrices are derived by fitting a suitable theoretical model to empirical covariance values. For gravity data gridding, the second-order Markov covariance model (Kasper, 1971) can be used:

$$C_{model}(l) = C_0 \left(1 + \frac{l}{\alpha}\right) e^{-l/\alpha}, \quad (12)$$

where C_{model} is the modelled covariance value over the distance l , C_0 is the signal variance, and parameter α is a characteristic distance related to correlation length $X_{1/2}$ as $\alpha \approx 0.596X_{1/2}$ (this relation varies from model to model). The correlation length is defined as a distance where covariance reaches half the value of signal variance.

The prior removed long- and short-wavelength gravity components can be restored on the gridding result to obtain the required gridded surface free-air gravity anomalies:

$$\Delta g_G^{FAA} = \Delta g_G^{RTMA} + \Delta g_G^{GGM} + \delta g_G^{RTM}, \quad (13)$$

where Δg_G^{GGM} and δg_G^{RTM} are now computed at grid node locations (initially removed signals were computed at arbitrary locations P). Since the gravity signal is also restored at the gravity data void areas (i.e., where measurements are unavailable), the described data gridding approach may enhance the gravity field representation. The use of a high-quality digital terrain model (also containing bathymetry information), particularly, can facilitate improved accuracy for subsequent quasigeoid modelling.

1.2 Derivation of Residual Terrain Model Anomalies

The previously described principles were employed first to examine the influence of bathymetry on gravity field estimation from the initial discrete data. To that end, two sets of computations were conducted, where bathymetry information was either neglected or included in RTM reduction. The 3'' \times 3'' NKG-DEM2014 model (some details on its compilation can be found in Ågren et al., 2015) was used in the first set of computations, where the model was averaged to 0.001° \times 0.002° (i.e., 3.6'' \times 7.2'') and 0.01° \times 0.02° grids covering the area from 51°N to 68.5°N and 2.5°E to 37°E. Since NKG-DEM2014 does not contain any bathymetry data (i.e., marine areas have zero heights), an alternative model had to be constructed. The 15'' \times 15'' GEBCO_2021 (GEBCO, 2021) grid was used as the primary bathymetry data source, complemented by the Estonian Maritime Administration obtained multibeam bathymetry dataset in the Estonian marine areas (cf. Figure 3). Primarily, the latter dataset is on a 3.6'' \times 3.6'' grid but also contains some dense scattered points. All these bathymetry data were jointly resampled to a 3'' \times 3'' grid and then subtracted from the initial NKG-DEM2014 grid. For RTM reduction computation, this grid, too, was finally averaged to 0.001° \times 0.002° and 0.01° \times 0.02° grids (the coarse grid can be seen in Figure 3).

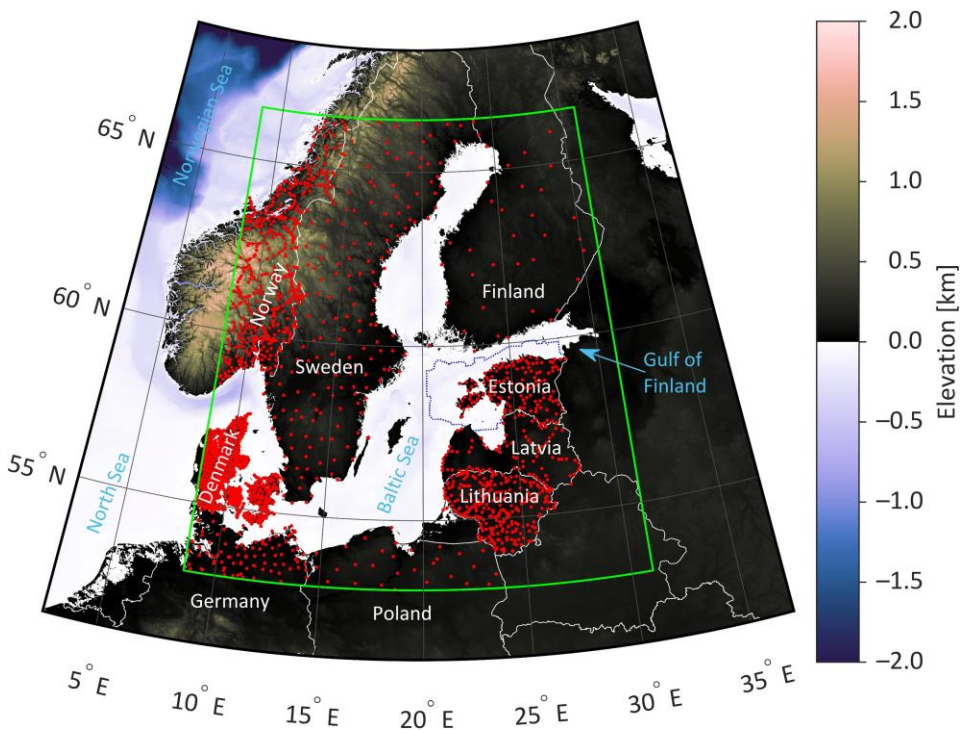
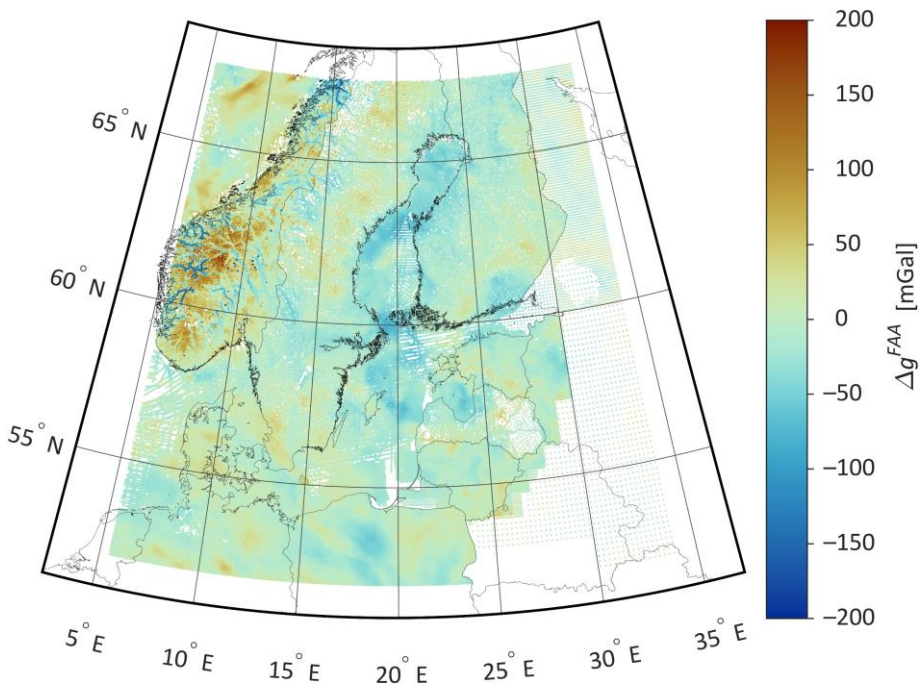


Figure 3. Terrain elevations and bathymetry in the Baltic Sea region. The dashed blue line shows the Estonian Maritime Administration obtained bathymetry data boundaries. Red dots denote locations of GNSS-levelling control points, and the green rectangle borders the quasigeoid modelling target area. [Modified from **Publication VI**]

Gravity data (Figure 4) used in the investigations was provided for preliminary modelling of the BSCD2000 quasigeoid model. These data (final version 3 of the database release) are in the zero-tide permanent tide concept (for more details regarding permanent tide concepts, see, e.g., Ekman, 1989; Poutanen et al., 1996), covering the area from 52°N to 67.5°N and 5.5°E to 34°E. It is clear by comparing Figure 4 to Figure 3 that the surface free-air gravity anomalies are highly correlated with rugged terrain (notice Norway and Sweden) and, therefore, ill-suited for direct gridding. The previously described digital terrain models were hence employed for RTM reduction computations (cf. Equations 9 and 10; sub-program TC of the GRAVSOFIT research software package was used; refer to Forsberg, 1984) to facilitate improved gridding performance through subsequent gravity reductions using these results. Smooth reference surfaces were derived using a spatial moving average low-pass filter on the respective coarse grid models, averaged to the resolution roughly corresponding to degree 300. Integration using the 0.001° × 0.002° grids was performed over a 15 km distance from computation points and over a 200 km distance using the 0.01° × 0.02° grids. Model heights were locally spline interpolated to fit heights of gravity observations in computation points on land (models were left unchanged for marine points).

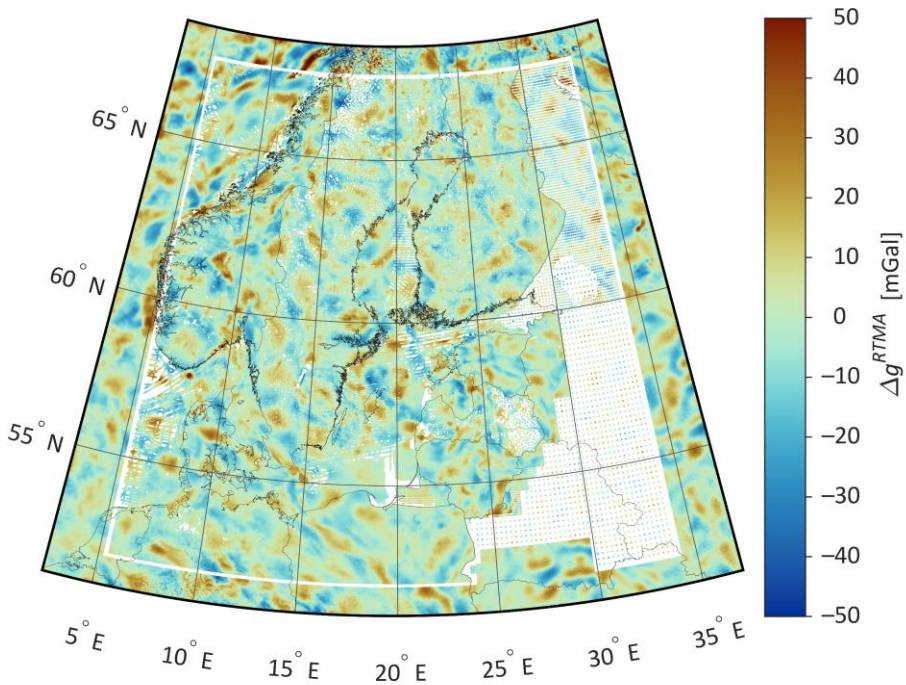


Min = -307.790 mGal Max = 210.460 mGal Mean = -4.957 mGal SD = 19.715 mGal

Figure 4. Surface free-air gravity anomalies (final version 3 of the BSCD2000 gravity database release) and associated descriptive statistics. [Modified from **Publication VI**]

Residual terrain model anomalies were computed by removing RTM reduction and GGM-synthesised gravity components from the initial surface free-air gravity anomalies (cf. Equation 8). The GO_CONS_GCF_2_DIR_R6 GGM (Förste et al., 2019), evaluated to its maximum d/o of 300, was used to account for the latter (i.e., Δg^{GGM} in Equations 8 and 13). A single data point with the smallest a priori error estimate was then retained

in each $0.01^\circ \times 0.02^\circ$ grid cell to improve data processing performance and help reduce aliasing during the gridding procedure. If more than one such point existed, all applicable points were averaged in value and spatially. Additional gravity data were synthesised from the EIGEN-6C4 GGM (Förste et al., 2014) evaluated to its maximum d/o of 2190 on a $0.025^\circ \times 0.05^\circ$ grid (no closer to the existing data than 0.15° and 0.3° in latitude and longitude, respectively) to improve gridding quality at the study area edges. These data, too, were reduced to RTM anomalies, as already described. The resulting dataset of RTM anomalies, where RTM reduction accounted for bathymetry, is presented in Figure 5. Comparison with Figure 4 reveals that these data are much smoother (notice standard deviation estimates and figure scales) and less biased (notice mean values) than the initial surface free-air gravity anomalies.



Min = -60.296 mGal Max = 90.026 mGal Mean = -0.373 mGal SD = 10.298 mGal

Figure 5. The determined RTM anomalies by also considering bathymetry information. [Modified from Publication VI]

1.3 Gravity Data Gridding

Covariance analysis was conducted to estimate the parameters of the second-order Markov covariance model (cf. Equation 12). Empirical autocovariance values of RTM anomalies were computed (after removing the mean signal) in 1 km distance groups. The second-order Markov covariance model was then fitted to the empirical values in the least-squares sense (Figure 6); signal variance was determined from data, not through the fitting procedure. It can be noticed that the inclusion of bathymetry information in the computation of RTM anomalies yields reduced signal variance (106.1 mGal^2 vs 112.6 mGal^2) and smaller covariance values over shorter distances (Figure 6), signifying that the inclusion

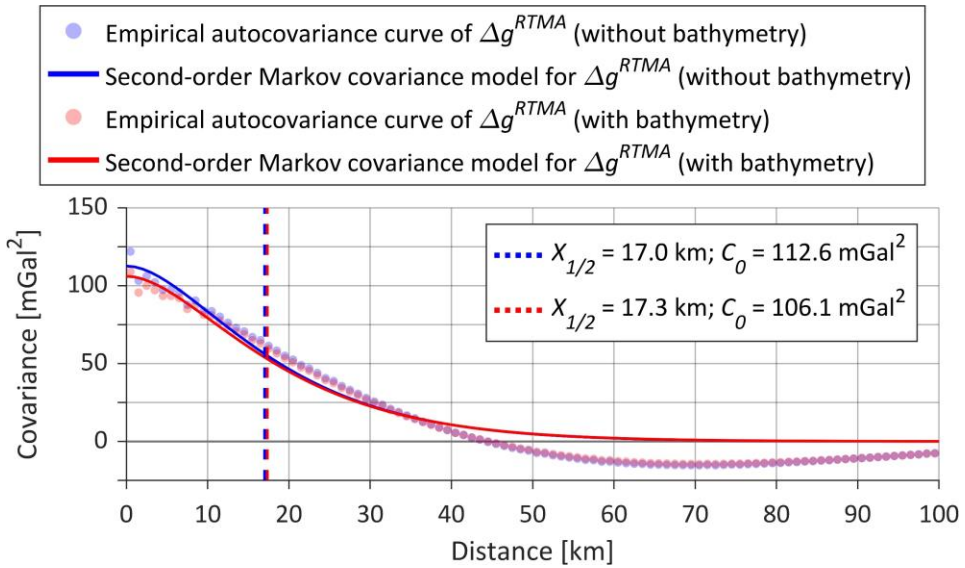
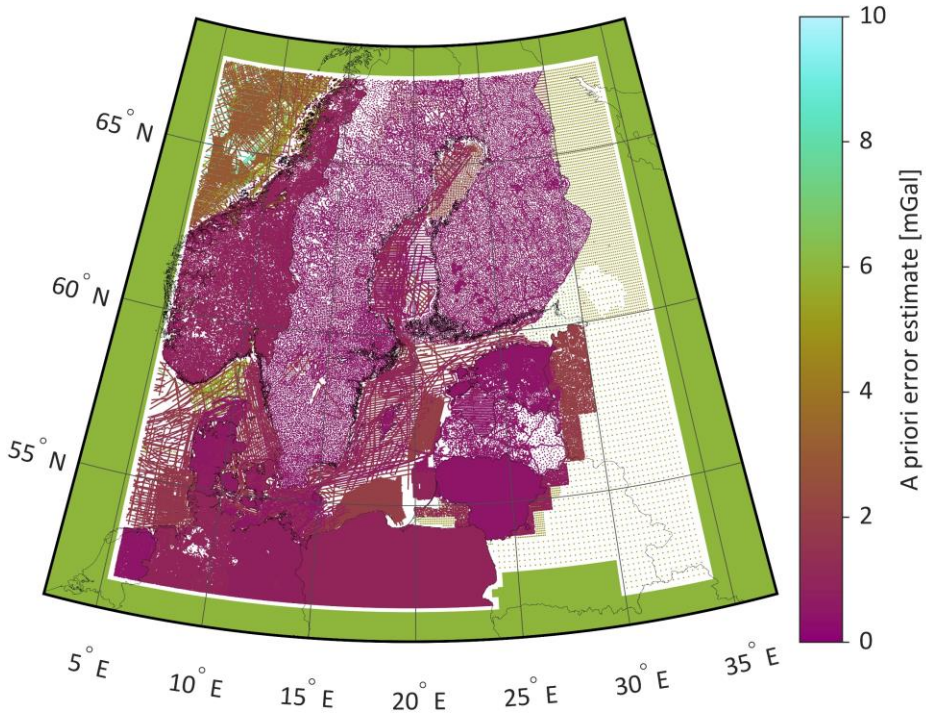


Figure 6. Empirical autocovariance curves of RTM anomalies and the corresponding least-squares fitted second-order Markov covariance models. The associated correlation lengths $X_{1/2}$ are shown with dashed lines; signal variances C_0 are presented in the legend. [Modified from **Publication VI**]

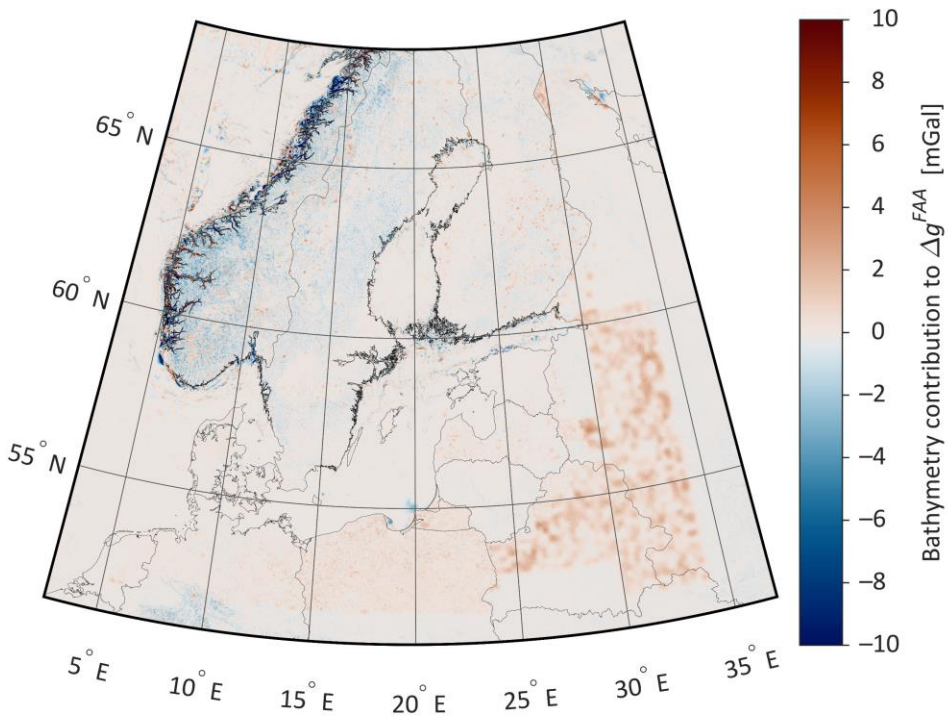


Min = 0.500 mGal Max = 10.000 mGal Mean = 2.382 mGal SD = 2.268 mGal

Figure 7. Gravity data a priori error estimates used in LSC (note that LSC requires variances, i.e., squared values). [Modified from **Publication VI**]

of bathymetry has removed additional gravity signal contained in the initial surface free-air gravity anomalies.

Using the determined parameters (different for the two gridding cases), the second-order Markov covariance model (cf. Figure 6) described the C_{st} and C_{tt} matrices in the LSC prediction (cf. Equation 11). The C_{nn} matrix of errors was constructed using the a priori error estimates of gravity data (Figure 7; errors associated with the Equation 8 reductions were not propagated). A minimum of 0.5 mGal error estimate was defined (i.e., values below that limit were increased to 0.5 mGal). On the other hand, most Norwegian gravity observations were associated with pessimistic estimates of 5 mGal. Since such error estimates may lead to unwanted gravity field smoothing, the Norwegian land data a priori error estimates were reduced to 1 mGal if an estimate exceeded that value (marine data error estimates were left unchanged). For the EIGEN-6C4 synthesised gravity data, a constant 6 mGal a priori error estimate was assumed. The LSC prediction was then set to use the 10 closest data points to the computation point in each quadrant (here, sub-program GEOGRID of GRAVSOFT was used; all further computations in subsequent sections were conducted using self-developed LSC MATLAB implementation). Such data gridding resulted in two RTM anomaly grids ($0.01^\circ \times 0.02^\circ$ spatial resolution) – one where bathymetry information was considered and the second where it was neglected. The previously removed RTM reduction and GGM-synthesised gravity components were restored as the final step to retrieve gridded surface free-air gravity anomalies (cf. Equation 13).



Min = -47.418 mGal Max = 27.557 mGal Mean = -0.063 mGal SD = 1.126 mGal

Figure 8. Bathymetry contribution to gridded surface free-air gravity anomalies. [Modified from Publication VI]

1.4 Bathymetry Influence on the Determined Gravity Field

The influence of bathymetry on gravity field estimation, obtained as the difference between the two surface free-air gravity anomaly grids, is presented in Figure 8. In the Baltic Sea region, the influence of bathymetry generally remains within 2 mGal; similar magnitude differences have also propagated inland. The first cause for these land area differences is the computed RTM reduction, where the used integration radiuses generate bathymetry-induced gravity signal also inland from the coast. The second reason concerns the empirically estimated parameters of the second-order Markov covariance model (cf. Figure 6) that describes the signal properties of the LSC prediction (recall that the model parameters differ for the two gridding cases). The prediction is especially sensitive to these signal differences in sparse data areas (compare Figure 8 to, e.g., Figure 7), where up to 3 mGal differences can be observed between the two surface free-air gravity anomaly grids.

In the Baltic Sea, there are also some sparse locations where consideration for bathymetry has induced up to around 4 mGal differences (Figure 8). Similar magnitude differences between the two grids can also be noticed in the Norwegian Sea. Notably, a significant influence of bathymetry can be seen around Norway's shoreline, where the use of bathymetry information affects the estimated gravity field generally within 20 mGal; however, up to around 40 mGal differences between gridding results can be observed in some locations. The most significant contribution from the bathymetry-generated RTM reduction to gravity data gridding thus occurs in one of the most rugged seabed regions of the study area (i.e., the Norwegian fjords; cf. Figure 8).

For further quantification of bathymetry data consideration-influence on gridding results, the ruggedness of bathymetry should be estimated. The terrain ruggedness index (Riley et al., 1999), which describes elevation differences between adjacent cells of a digital terrain model, was modified for that purpose. The modified index is named the bathymetry ruggedness index and computed as:

$$BRI_P = \frac{1}{I} \sum_{i=1}^I |H_i^* - H_P^*| \cdot \left(1 - \sqrt{d_i/d_{LIM}}\right), \quad (14)$$

where H_P^* is depth at a computation point P , and H^* represents depth at a data point i with distance d from the computation point. Parameter d_{LIM} is the computation radius, where the increasing value yields smoother bathymetry ruggedness index features (i.e., it behaves as a low-pass filter). Term I represents the total number of data points within the computation radius.

The bathymetry ruggedness index (Figure 9) was computed on a $0.01^\circ \times 0.02^\circ$ grid using the jointly resampled $3'' \times 3''$ resolution bathymetry dataset (cf. Section 1.2); computation point depths were determined via bilinear interpolation. The computation radius was set to 10 km since this yielded visually similar signal frequency for the index features compared to the surface free-air gravity anomalies. Although the values of the bathymetry ruggedness index are somewhat arbitrary, the locations of smooth (e.g., the North Sea) and rough bathymetry (e.g., coastal areas of Norway) are easily distinguishable. Comparison with Figure 8 also reveals that the index has rather similar features to the bathymetry contribution on the gridding result of surface free-air gravity anomalies. For example, notice the Norwegian Sea and the central part of the Baltic Sea (for a more detailed comparison, please see Figure 16 in **Publication VI**). The two datasets

are also well correlated, yielding a correlation coefficient of 0.78 (only marine areas in the quasigeoid modelling target area were considered; absolute values of bathymetry contribution to gridded surface free-air gravity anomalies were used). Such an index could hence be valuable for an initial assessment of whether bathymetry should or should not be considered in the gravity field estimation (and consequently in the following quasigeoid determination). Clearly, the impact in the North Sea is negligible (i.e., the index values are near-zero, as is the bathymetry influence on the gridding result). In contrast, significant influence can be expected in more rugged regions, like the Norwegian coast (compare Figure 9 to Figure 8).

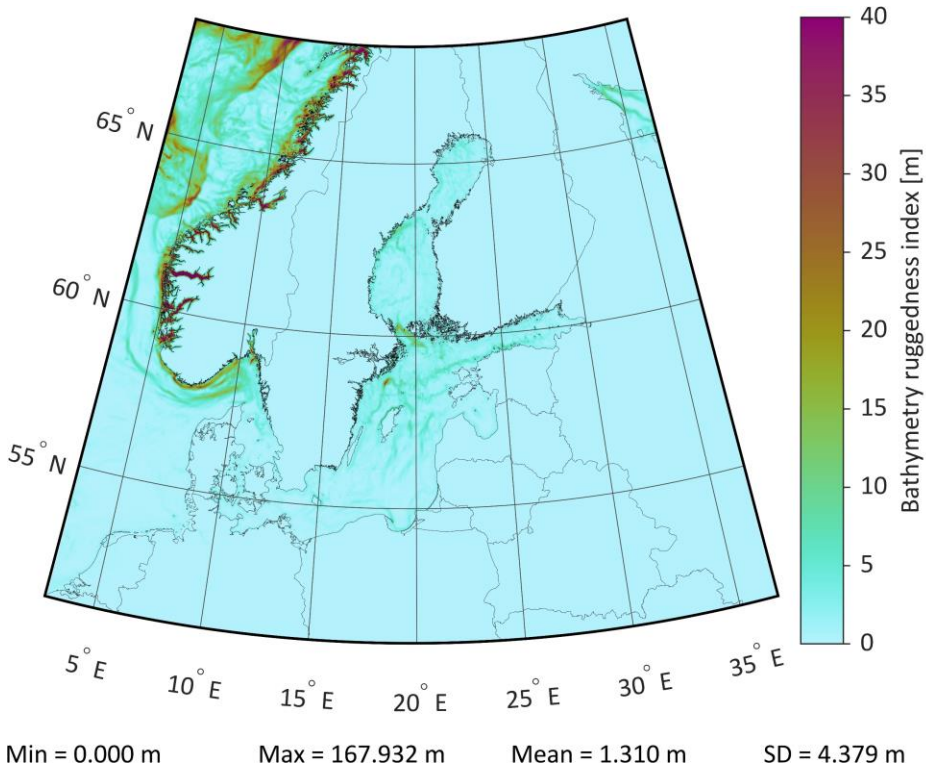


Figure 9. Estimated ruggedness of bathymetry. [Modified from **Publication VI**]

1.5 Quasigeoid Modelling Specifics

The two determined surface free-air gravity anomaly grids were employed in quasigeoid modelling using the unbiased LSMSA approach (cf. Equation 6). GOCO05c (Fecher et al., 2017) was selected as the reference GGM (in the zero-tide permanent tide concept); modification limits L and M were set to degree 200 (in **Publication VI**, other GGMs with varying modification limits were also tested). Modification parameters s_n were determined following Ellmann (2005b, 2012). Since the focus is on marine areas (due to dynamic measuring conditions, gravity data noise is more significant than on land), uncertainties of terrestrial gravity data (i.e., the gridded data) were assumed at 2 mGal in the modification parameters' determination. However, it should be noted that this also slightly reduces the quasigeoid modelling accuracy in regions where data is of better quality (e.g., land).

Importantly, the presented quasigeoid modelling neglects combined atmospheric (Sjöberg, 1999; Sjöberg & Nahavandchi, 2000; Sjöberg, 2001) and ellipsoidal (Sjöberg, 2003b; Ellmann & Sjöberg, 2004; Sjöberg, 2004) effects. This decision stems from the fact that the combined atmospheric effect has more considerable variability in mountainous regions, whereas it is roughly a constant offshore (magnitude of the effect on the quasigeoid model generally remains sub-centimetre in the study area). The magnitude of the combined ellipsoidal effect depends on the integration cap size. In current computations, integration was limited to 2° (i.e., the geocentric angle ψ_0), which would result in only a few millimetres of combined ellipsoidal effect at most. Therefore, these additive corrections were regarded as negligible (some numerical examples can be found in Ellmann, 2005c; Ågren et al., 2009; Märdla et al., 2018). On the other hand, the combined downward continuation effect (Sjöberg, 2003c) has a magnitude of up to a few decimetres in Norway.

1.6 Bathymetry Influence on Quasigeoid Modelling

The influence of bathymetry consideration on quasigeoid modelling (Figure 10) was derived as a difference between the two resulting quasigeoid models – one, where bathymetry information was considered during the gravity data gridding, and the second, where bathymetry was neglected. In the Baltic Sea, most variability due to the use of bathymetry data is generally around a centimetre. Similar magnitude differences between the two quasigeoid modelling solutions also occur inland due to the causes

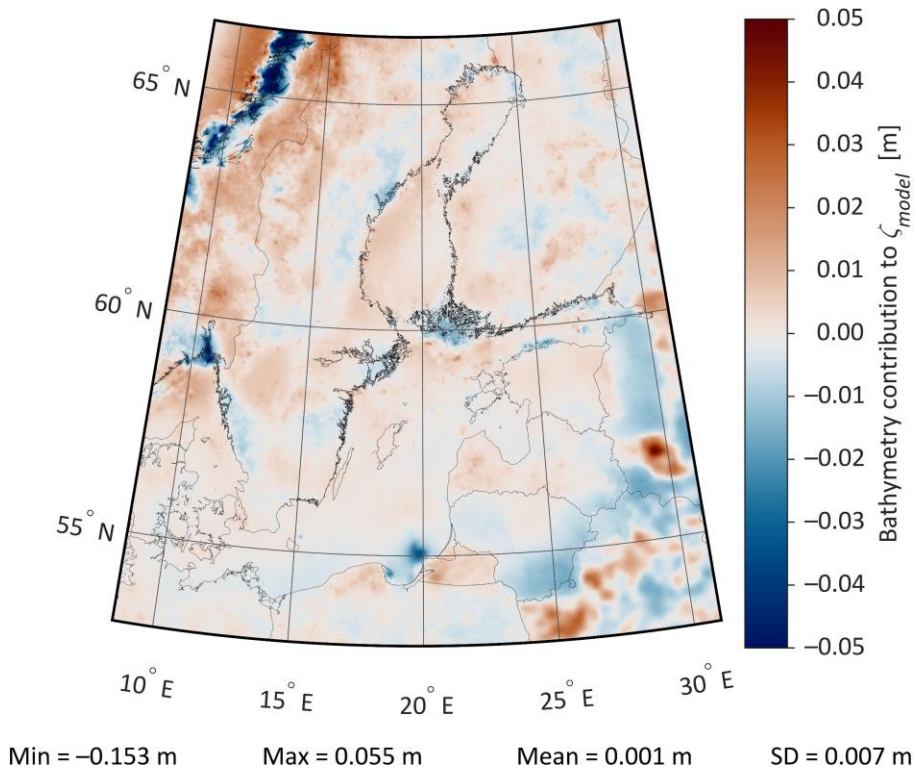


Figure 10. Bathymetry contribution to gravimetric quasigeoid modelling. [Modified from Publication VI]

already described in Section 1.4. More significant inland (also southern Baltic Sea) differences can be seen in regions of sparse gravity data (compare Figure 10 to, e.g., Figure 7), demonstrating the sensitivity of quasigeoid modelling (using the LSMSA approach) to gravity data processing (in this case to the parameters of the second-order Markov covariance model).

Detailed quasigeoid modelling differences up to 3–4 cm can be noticed in the central part of the Baltic Sea and the Gulf of Finland. These locations coincide with the most rugged seabed regions of the Baltic Sea (compare Figure 10 to Figure 9; for a more detailed comparison, please see Figure 16 in **Publication VI**). As with gridding results, the use of bathymetry data has affected the Norwegian coastal areas most also in quasigeoid modelling, where the largest differences reach up to 15 cm. Although quasigeoid modelling differences (cf. Figure 10) are much smoother than the computed bathymetry ruggedness index (cf. Figure 9), the correlation coefficient between the two datasets is 0.65 (all marine areas in the quasigeoid modelling target area were considered; absolute values of quasigeoid modelling differences were used).

Bathymetry data use in quasigeoid modelling can thus improve solutions significantly

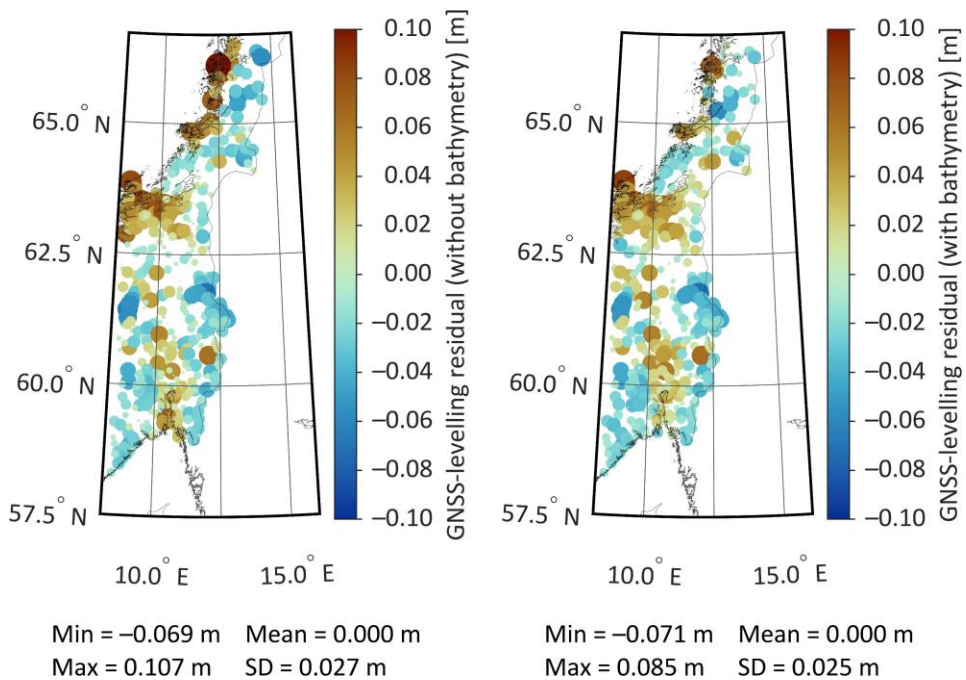


Figure 11. Residuals (mean removed) of gravimetric quasigeoid models relative to the Norwegian GNSS-levelling control points¹. [Modified from **Publication VI**]

¹ Geodetic coordinates and ellipsoidal heights are in the ITRF2008 reference frame and use the zero-tide permanent tide concept. Temporal changes due to the Baltic Sea region's postglacial land uplift are reduced to the epoch 2000.0. Levelled normal heights are in the national (European Vertical Reference System (EVRS) based or compatible) height system realizations and use the zero-tide permanent tide concept with uplift epoch 2000.0. These data also include the Estonian GNSS-levelling control points. In total, there are 1902 GNSS-levelling control points involved within the entire Baltic Sea region.

since this helps to account for the gravity signal variability generated by the Norwegian fjords. These results can be validated using GNSS-levelling control points demonstrating local improvements almost up to a decimetre (Figure 11). Dahl & Forsberg (1998) reached a similar conclusion in the Sognefjord case study (outside the current quasigeoid modelling target area). It can be concluded that using bathymetry information helps refine gravity field determination from the initial discrete data, whereby these refinements (cf. Figure 8) also improve the subsequent quasigeoid modelling. Therefore, it is likely that the detailed differences in the central part of the Baltic Sea and the Gulf of Finland visible in Figure 10 also signify quasigeoid modelling improvements.

The gravimetric quasigeoid model (the model uses the zero-tide permanent tide concept; spatial resolution of the model is $0.01^\circ \times 0.02^\circ$), computed with the inclusion of bathymetry data, is henceforth denoted as GQM2022 and employed in the following investigations. The comparison with 1902 high-precision GNSS-levelling control points¹ in the Baltic Sea region (refer to Figure 3) yields a 3.2 cm agreement (standard deviation)

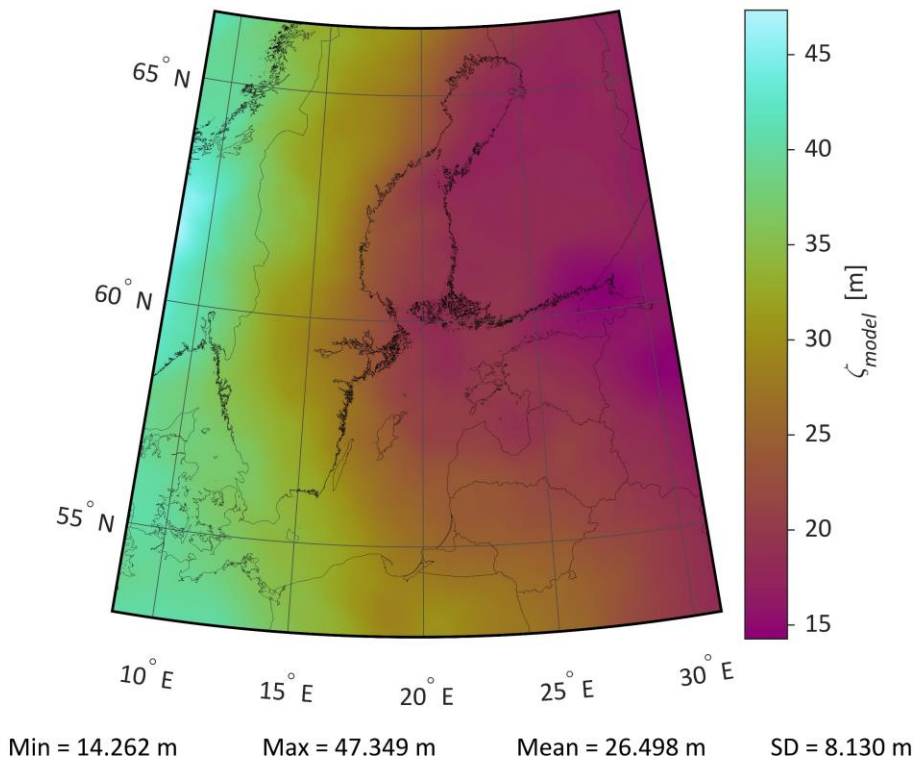


Figure 12. The GQM2022 model, which has also been fitted (using a one-dimensional fit) to the Estonian GNSS-levelling control points². [Modified from **Publication VI**]

² Geodetic coordinates and ellipsoidal heights are in the national ETRS89 realization (EUREF-EST97) and use the zero-tide permanent tide concept. Temporal changes due to the Baltic Sea region's postglacial land uplift are reduced to the epoch 2000.0. Levelled normal heights are in the national European Vertical Reference System (EVRS) realization (EH2000) and use the zero-tide permanent tide concept with uplift epoch 2000.0. These data only include the Estonian GNSS-levelling control points (131 in total).

from a one-dimensional fit and 2.0 cm agreement (standard deviation) after removing individual country mean values from the initial residuals (e.g., the mean residual of Estonian GNSS-levelling control points was removed from all Estonian GNSS-levelling residual values). Since most GNSS data post-processing (see Section 3) was conducted relative only to the Estonian GNSS-CORS (continuously operating reference stations), the GQM2022 was fitted to the Estonian high-precision GNSS-levelling control points² (Rüdja & Varbla, 2022) using a one-dimensional fit. The fitted model is shown in Figure 12, and the fitting residuals are in Figure 13.

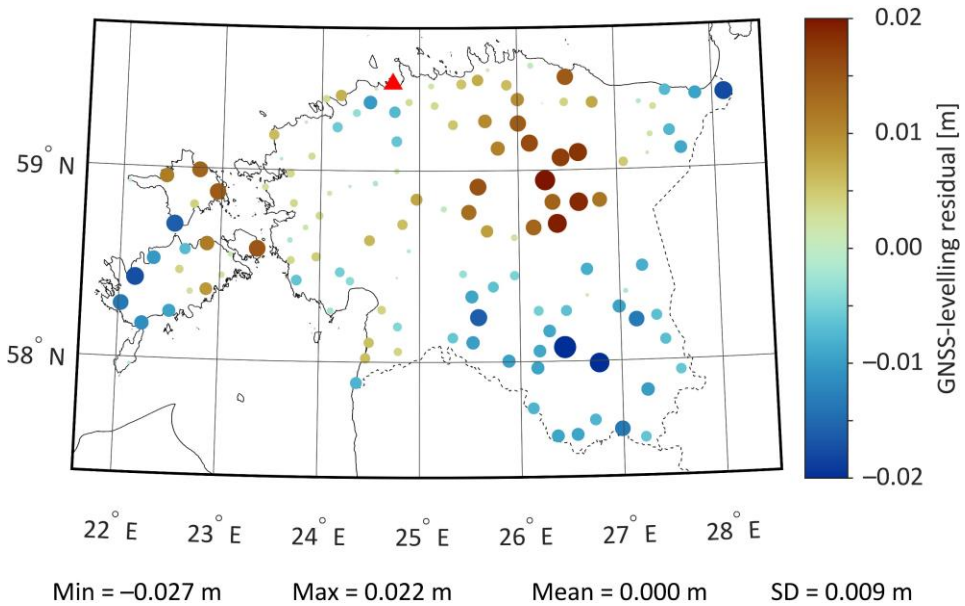


Figure 13. GNSS-levelling fitting residuals of GQM2022 after a one-dimensional fit to the Estonian GNSS-levelling control points². The red triangle denotes the general location of shipborne GNSS campaigns' home harbour (see Section 3.2).

2 Derivation of Realistic Dynamic Topography

Good agreement between GQM2022 and GNSS-levelling control points is a valuable indicator of the solution's acceptable performance. However, such accuracy estimates only represent land areas. The achieved quasigeoid modelling accuracy remains a guess over marine regions because GNSS-levelling control points cannot be established offshore. Instead, various datasets of SSHs that approximate the geoid shape could be employed for validation purposes. These SSHs must be reduced into height anomalies for meaningful validation results by removing the DT. This section reviews the derivation of DT using TG and HDM datasets.

2.1 Theoretical Principles for Dynamic Topography Derivation

High-resolution HDMs are used widely for various practical and research applications, for instance, in unifying vertical datums (e.g., Slobbe et al., 2014; Filmer et al., 2018). Although such models are appealing for sourcing DT data, care should be taken since spatiotemporal biases (i.e., dynamic biases) may exist between HDMs' references and vertical datums (e.g., Slobbe et al., 2013; Rulent et al., 2020). It is becoming common that TG stations are connected to the national height reference systems via precise levelling (e.g., Slobbe et al., 2014; Kollo & Ellmann, 2019; also refer to **Publication III**). With the availability of such TG stations, HDM-contained dynamic bias (DB) can be determined at these TG locations (with coordinates φ^{TG} , λ^{TG} ; also see Figure 14):

$$DB(\varphi^{TG}, \lambda^{TG}, t) = DT_{HDM}(\varphi^{TG}, \lambda^{TG}, t) - DT_{TG}(\varphi^{TG}, \lambda^{TG}, t), \quad (15)$$

where DT_{HDM} and DT_{TG} are HDM- and TG-based DT, respectively, at an observation epoch t . Note that in regions affected by VLM, the relative (to the local solid Earth) TG sea level readings should first be converted to the absolute frame and desired time epoch. In the most common case, where VLM is induced by glacial isostatic adjustment (i.e., VLM is roughly linear in time), the conversion is:

$$DT_{TG}(\varphi^{TG}, \lambda^{TG}, t) = DT_{RSL}(\varphi^{TG}, \lambda^{TG}, t, t_0^{HS}) + VLM_{levelled}(\varphi^{TG}, \lambda^{TG})(t - t_0^{HS}), \quad (16)$$

where DT_{RSL} is TG-based relative DT and $VLM_{levelled}$ is levelled VLM rate (i.e., geoid change rate should not be included) at a TG station. The term t_0^{HS} denotes the reference epoch of a height reference system.

The determined DB has valuable properties that can be employed for estimating its uncertainty; this relies on two assumptions:

1. Although DB changes temporally, it should remain relatively stable over short timeframes (e.g., daily). Erratic behaviour (i.e., sudden jumps in DB values) could, for example, indicate HDM modelling errors, suggest that a TG station is performing poorly, or be caused by extreme weather conditions. The DB temporal domain uncertainty component σ_{db1} can be estimated as a moving standard deviation centred at an observation epoch t :

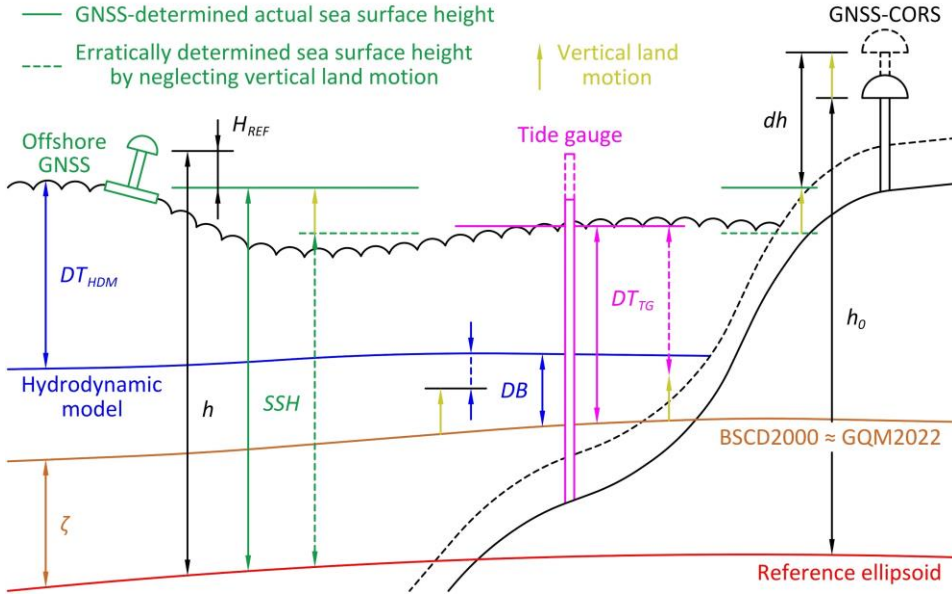


Figure 14. Interrelations between participating datasets. Solid lines denote reference epoch geometry and dashed lines VLM-affected geometry at a GNSS observation epoch. Global sea level rise and geoid change trends are neglected for simplification (i.e., the sea surface is assumed to be unchanged). Notice that the depicted dynamic bias (DB) is negative (cf. Equation 15), as is the height difference dh . [Modified from **Publication V**]

$$\sigma_{ab1}(\varphi^{TG}, \lambda^{TG}, t) = \sqrt{\frac{1}{T_1 - 1} \sum_{i=t-\frac{T_1-1}{2}}^{t+\frac{T_1-1}{2}} \left[DB(\varphi^{TG}, \lambda^{TG}, i) - \frac{1}{T_1} \sum_{i=t-\frac{T_1-1}{2}}^{t+\frac{T_1-1}{2}} DB(\varphi^{TG}, \lambda^{TG}, i) \right]^2}, \quad (17)$$

where T_1 denotes the time window (e.g., the number of sequential hours if DB has hourly temporal resolution) in which DB is assumed to remain stable.

- Dynamic bias is represented by a long-wavelength signal (Lagemaa et al., 2011; Jahanmard et al., 2021). Significant variations in DB values at nearby TG stations may consequently indicate errors in levelling connections to the height reference system or localised phenomena occurring near a TG station. Differences relative to the offshore marine processes may occur as TG stations are generally in sheltered locations (e.g., harbours or river mouths). For the spatial domain uncertainty estimation, averaged differences are first calculated by comparing DB values at TG station A to those at $B = 1, \dots, I$ nearest TG stations:

$$\overline{dDB}_B(\varphi^{TGA}, \lambda^{TGA}, t) = \frac{1}{T_2} \sum_{i=t-\frac{T_2-1}{2}}^{t+\frac{T_2-1}{2}} DB(\varphi^{TGA}, \lambda^{TGA}, i) - \frac{1}{T_2} \sum_{i=t-\frac{T_2-1}{2}}^{t+\frac{T_2-1}{2}} DB(\varphi^{TGB}, \lambda^{TGB}, i), \quad (18)$$

where T_2 denotes the considered time window ($T_2 > T_1$), which is centred at an observation epoch t . Such a moving window is used due to potential progressive sea level changes (e.g., localised phenomena near a TG station). The DB spatial domain uncertainty component σ_{db2} can then be estimated as³:

$$\begin{aligned} & \sigma_{db2}(\varphi^{TG}, \lambda^{TG}, t) \\ &= \sqrt{\frac{1}{I-1} \sum_{B=1}^I \left[\overline{dDB_B}(\varphi^{TG_A}, \lambda^{TG_A}, t) - \frac{1}{I} \sum_{B=1}^I \overline{dDB_B}(\varphi^{TG_A}, \lambda^{TG_A}, t) \right]^2}, \end{aligned} \quad (19)$$

The temporal and spatial domain uncertainty components are assumed to be generally independent. Therefore, the uncertainty propagation law for uncorrelated quantities can be applied to calculate the final DB uncertainty at a TG station:

$$\begin{aligned} & \sigma_{DB}(\varphi^{TG}, \lambda^{TG}, t) \\ &= \sqrt{[\sigma_{db1}(\varphi^{TG}, \lambda^{TG}, t)]^2 + [\sigma_{db2}(\varphi^{TG}, \lambda^{TG}, t)]^2 + [\sigma_{VLM}(\varphi^{TG}, \lambda^{TG})(t - t_0^{HS})]^2}, \end{aligned} \quad (20)$$

where σ_{VLM} is the uncertainty associated with the VLM rate at a TG station. If the VLM is negligible at the TG station site, the last component of Equation (20) can be neglected (similarly, the Equation 16 procedure can be skipped).

Offshore DB can be predicted (computation points should be selected according to the HDM grid nodes with coordinates φ^{HDM} , λ^{HDM}) analogously to Equation (11) using LSC:

$$\widehat{\mathbf{DB}}(t) = \mathbf{C}_{st}(t)[\mathbf{C}_{tt}(t) + \mathbf{C}_{nn}(t)]^{-1}\mathbf{DB}(t), \quad (21)$$

where the \mathbf{C}_{nn} matrix of observation errors is constructed using the estimated uncertainties of DB (σ_{DB} , which should be squared to obtain variance values). Again, the vector of the known signal (\mathbf{DB}) should be centred (e.g., the mean signal can be removed and later restored on the prediction result). For determining the \mathbf{C}_{st} and \mathbf{C}_{tt} matrices, the exponential-cosine covariance model (Vyskočil, 1970) can be used (for reasoning, please refer to Section 3.1 in **Publication VII**):

$$C_{model}(l) = C_0 e^{-l/\alpha} \left[\cos(\beta l) + \left(\frac{\alpha}{\beta} \right) \sin(\beta l) \right], \quad (22)$$

where parameters α and β control the model shape. The model allows negative spatial correlation, which commonly describes DB over some distance.

The DB prediction variance is obtained following Moritz (1980):

$$\mathbf{E}_{ss}(t) = \mathbf{C}_{ss}(t) - \mathbf{C}_{st}(t)[\mathbf{C}_{tt}(t) + \mathbf{C}_{nn}(t)]^{-1}[\mathbf{C}_{st}(t)]^T, \quad (23)$$

³ Future studies should consider using a root mean square estimator instead of standard deviation for spatial domain uncertainty determination since the latter captures only the DB variations but is blind to data biases.

where \mathbf{C}_{ss} is the covariance matrix of the predicted signal (in practical computation, it can be assumed a diagonal matrix constructed using signal variances C_0), \mathbf{E}_{ss} is its error covariance matrix, and \mathbf{T} denotes the transpose operator. The diagonal elements of matrix \mathbf{E}_{ss} are DB prediction variance $[\sigma_{\widehat{DB}}(\varphi^{HDM}, \lambda^{HDM}, t)]^2$ estimates. Since DB uncertainty (Equation 20) describes, in principle, the agreement between HDM and TG data (i.e., the two DT data sources), the DT variance is assumed to be equivalent to the DB prediction variance. The DT uncertainty is hence:

$$\sigma_{\widehat{DT}}(\varphi^{HDM}, \lambda^{HDM}, t) \equiv \sqrt{[\sigma_{\widehat{DB}}(\varphi^{HDM}, \lambda^{HDM}, t)]^2}. \quad (24)$$

The DT itself is obtained by subtracting the predicted DB (Equation 21) from the initial HDM at all the grid nodes $(\varphi^{HDM}, \lambda^{HDM})$:

$$\widehat{DT}(\varphi^{HDM}, \lambda^{HDM}, t) = DT_{HDM}(\varphi^{HDM}, \lambda^{HDM}, t) - \widehat{DB}(\varphi^{HDM}, \lambda^{HDM}, t). \quad (25)$$

If the zeros of TGs coincide with the geoid, the described approach can provide realistic geoid-referred DT estimates. As the final step, the DT and its uncertainty can be determined using bilinear interpolation at SSH data point locations $(\varphi^{SSH}, \lambda^{SSH})$ between the adjacent locations $(\varphi^{HDM}, \lambda^{HDM})$ of corresponding quantities.

2.2 Preparation of Dynamic Topography Datasets

A common NAP (Normaal Amsterdams Peil) referred height reference system BSCD2000 (with reference epoch 2000.0) has been adopted in the Baltic Sea region (for more details, refer to Schwabe et al., 2020). It is realized through GNSS and high-resolution quasigeoid modelling offshore. Onshore, BSCD2000 is compatible with the EVRS-based national height system realizations (e.g., the Estonian EH2000), which approximately refer to the same reference level. Importantly, TG stations in the Baltic Sea region are rigorously connected to the corresponding national height systems via precise levelling. By neglecting measurement errors in levelling connections (also errors in quasigeoid modelling), it can be stated that the zeros of TGs coincide with the BSCD2000 at the reference epoch.

Data (hourly temporal resolution) from 41 TG stations (see Figure 15) were used to derive DT: 15 Estonian⁴, 7 Latvian^{5,6}, 11 Swedish⁷, 7 Finnish⁸, and one Russian⁹. Even though the Estonian, Latvian, Swedish, and Finnish height systems are EVRS-based and heights refer to NAP, some minor across-border discrepancies exist. The pan-continental EVRF2019¹⁰ solution-based height system discrepancies were thus used to improve TG

⁴ <https://www.ilmateenistus.ee/meri/vaatlusandmed/kogu-rannik/kaart/?lang=en> [accessed 7 April 2023]

⁵ <https://www.meteo.lv/hidrologija-datu-meklesana/?nid=466> [accessed 7 April 2023]

⁶ <https://www.meteo.lv/hidrologijas-stacij-u-karte/?nid=465> [accessed 7 April 2023]

⁷ <https://www.smhi.se/data/oceanografi/ladda-ner-oceanografiska-observationer/#param=sealevelrh2000,stations=all> [accessed 7 April 2023]

⁸ <https://en.ilmatieenlaitos.fi/download-observations> [accessed 7 April 2023]

⁹ <https://map.emodnet-physics.eu/platformpage/?platformid=8701&source=cp> [accessed 7 April 2023]

¹⁰ <https://evrs.bkg.bund.de/Subsites/EVRS/EN/Projects/HeightDatumRel/height-datum-rel.html> [accessed 7 April 2023]

data consistency. Because most GNSS data post-processing (see Section 3) was conducted relative only to the Estonian GNSS-CORS (and the GQM2022 was fitted to the Estonian GNSS-levelling control points; recall Section 1.6), the Estonian EH2000 was considered the zero level. Consequently, EVRF2019 yielded a -1 cm correction to the Swedish and Finnish TG readings. On the other hand, Russian TG data refer to the Baltic Height System of 1977 (BHS77), and a $+21$ cm offset had to be added for consistency.

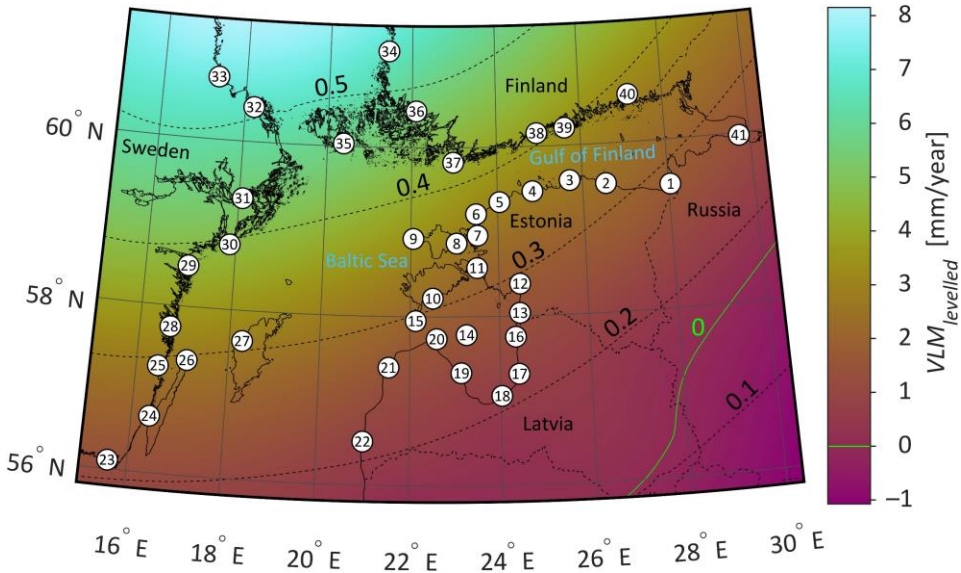


Figure 15. Locations of used TG stations, denoted by numbered circles. In the background is shown the annual levelled VLM rate according to the NKG2016LU model; the accompanying geoid rise rate [mm/year] is shown with dashed isolines.

Besides having a consistent reference level, all data should also use the same permanent tide concept. Whilst Estonian, Latvian, Swedish, and Finnish TG data are given in the zero-tide permanent tide concept, the initial Russian TG data were sourced in the mean-tide concept. These were converted to the zero-tide concept by (Mäkinen, 2008; Ihde et al., 2019):

$$\Delta H_{MT \Rightarrow ZT}(\varphi) = 0.09940 - 0.29541 \sin^2 \varphi - 0.00042 \sin^4 \varphi, \quad (26)$$

where the tide-related height correction $\Delta H_{MT \Rightarrow ZT}$ at a geodetic latitude φ is in meters (the correction should be added to the heights to be corrected). As the final step, all TG data were corrected for VLM according to Equation (16) using the NKG2016LU model (Vestøl et al., 2019); Figure 15 shows the annual levelled VLM rate in the Baltic Sea region.

As for the HDM, the NEMO-Nordic model (Hordoier et al., 2019; Kärnä et al., 2021) was employed for DT derivation (hourly temporal and approximately 1.0 nautical mile spatial resolution). Like Russian TG data, the HDM-obtained DT had to be also converted from the mean-tide permanent tide concept to the zero-tide concept (cf. Equation 26). Regarding ocean tides, then no special treatment was considered, as tides generally remain within a few centimetres at most in the Baltic Sea due to the narrow connection

to the Atlantic Ocean via Danish straits (Medvedev et al., 2013; Medvedev et al., 2016). It should be noted, however, that tides have not been removed from the TG or used SSH data. If a tidal effect is present, then this should cancel out to an extent by subtracting DT from SSH as the modelled DT is tied to TG readings. Minor discrepancies between TG readings and HDM-embedded DT due to different treatments of tides (NEMO-Nordic also contains tides but, in a model, instead of the observed form), if there are any, are considered within the DB.

2.3 Dynamic Topography Computation

NEMO-Nordic DB was estimated (cf. Equation 15) at 41 TG station sites (see Figure 15). Computations were limited to periods when shipborne GNSS campaigns or the ALS survey was conducted (refer to Table 1) to avoid extensive computation times. For the temporal domain uncertainty calculation (cf. Equation 17), parameter T_1 was set to 25 h. A minimum of 12 h of DB data was included in temporal domain uncertainty calculation before or after a campaign's start or end to avoid inconsistencies in the estimation (i.e., shorter than 25 h time windows during a campaign). For calculating the spatial domain uncertainty, Equation (18) was first simplified (because computations were limited to shorter periods) to:

$$\overline{dDB}_B(\varphi^{TG_A}, \lambda^{TG_A}) = \frac{1}{T_2} \sum_{i=1}^{T_2} DB(\varphi^{TG_A}, \lambda^{TG_A}, i) - \frac{1}{T_2} \sum_{i=1}^{T_2} DB(\varphi^{TG_B}, \lambda^{TG_B}, i), \quad (27)$$

where T_2 is the duration over which DT computations were performed (cf. Table 1). Comparisons were conducted with $I = 3$ nearest TG stations to estimate the spatial domain uncertainty (cf. Equation 19). The final DB uncertainty was then calculated according to Equation (20). Figure 16 shows the estimated DB uncertainty during the Salme C1 shipborne GNSS campaign. Notice how around hour 70 (GPS time 117 h), the uncertainty increases at TG₉ and TG₄₁ (also refer to Figure 15); this coincides with the strongest storm winds that occurred during the second half of the Salme C1 campaign (note that the vessel arrived harbour during the beginning of the storm; DT computations

Table 1. Dynamic topography computation time windows.

Campaign (see Section 3)	DT computation time window	Number of HDM grids / DT computation duration [h] (i.e., T_2 ; cf. Equation 27)
Sektor GNSS	02.07.2017 – 07.07.2017	144
ALS	08.05.2018 – 12.05.2018	120
Salme C1 GNSS	06.04.2021 – 10.04.2021	120
Salme C2 GNSS	25.07.2021 – 31.07.2021	168
Salme C3 GNSS	01.08.2021 – 08.08.2021	192
Salme C4 GNSS	24.08.2021 – 27.08.2021	96
Salme C5 GNSS	10.09.2021 – 13.09.2021	96
Salme C6 GNSS	14.09.2021 – 18.09.2021	120

were conducted over extended periods compared to the surveys). It should be mentioned that TG₉ is relatively vulnerable to extreme weather, whereby TG₄₁ is affected by westerly winds that rapidly accumulate water during storms.

Covariance analysis (for each time instance separately) was conducted to estimate the exponential-cosine covariance model parameters (cf. Equation 22). Empirical DB autocovariance values were computed (after removing the mean signal) in 25 km distance groups, whereby groups with less than 15 station pairs (regarding pairs *AB* and *BA* the same, i.e., one) were excluded. The exponential-cosine covariance model was

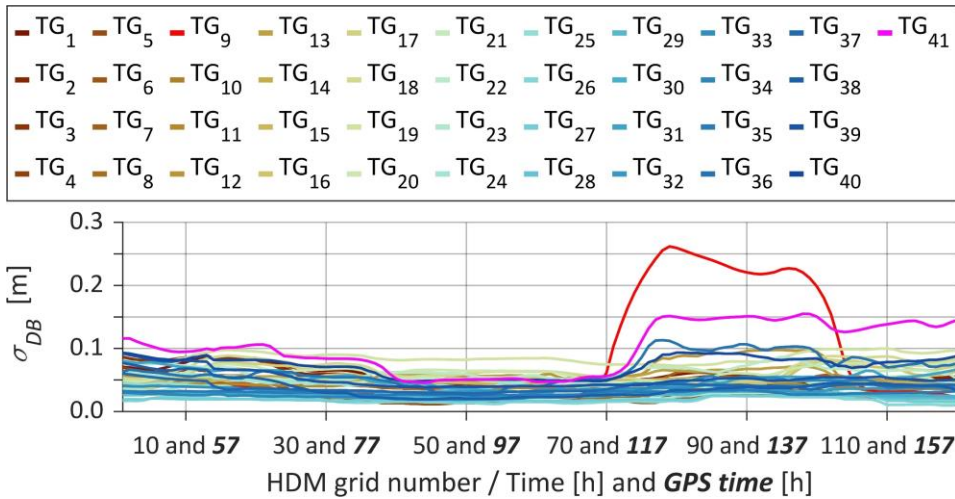


Figure 16. Uncertainty estimates of DB (cf. Equation 20) at each TG station (cf. Figure 15) during the Salme C1 shipborne GNSS campaign (GPS week 2152; see Section 3.2). [Modified from **Publication V**]

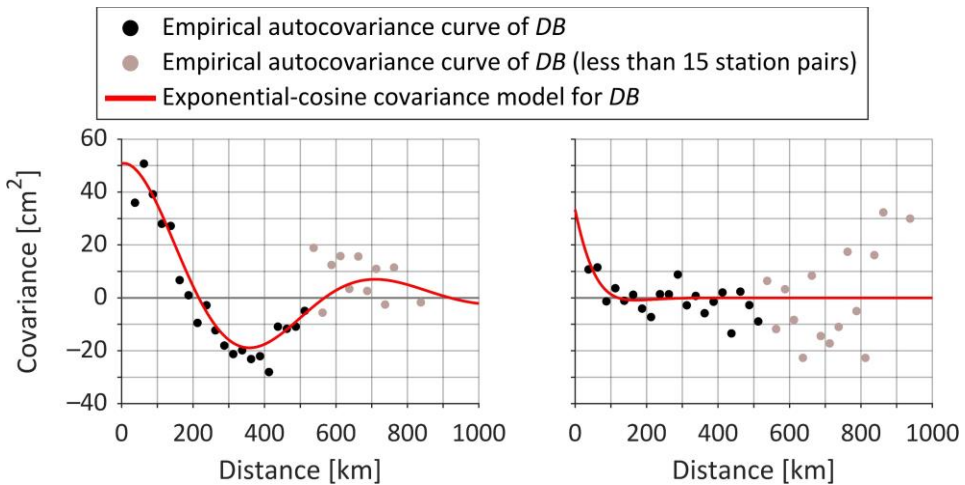


Figure 17. Empirical autocovariance curves of DB corresponding to arbitrary time instances of 04.07.2017 00:00 UTC (left) and 28.07.2021 00:00 UTC (right), and respective least-squares fitted (distance groups with less than 15 station pairs were not considered) exponential-cosine covariance models. [Modified from **Publication VII**]

then fitted to the empirical values using nonlinear least-squares fitting; signal variance was determined from data, not through the fitting procedure. Note that an additional constraint of allowing at most four zero crossings over the first 1000 km distance was introduced to avoid unrealistically oscillating covariance modelling results. Two examples of the modelled covariance at arbitrary time instances can be seen in Figure 17. The figure gives the impression that the spatial correlation of DB can vary significantly due to DB spatiotemporal variations. Consequently, a constant offset is insufficient for reducing HDM-based DT to the required reference level, and DB must be modelled for deriving reliable DT instead.

Using the determined parameters estimated separately for each time instance, the exponential-cosine covariance model described the C_{st} and C_{tt} matrices in Equations (21) and (23). The C_{nn} matrix of errors was constructed using the estimated DB uncertainty (e.g., values shown in Figure 16 for the Salme C1 shipborne GNSS campaign). The resulting DB grids were then subtracted from the initial NEMO-Nordic-based DT estimates (cf. Equation 25), yielding hourly resolution DT grids (recall that both TG and HDM data have hourly temporal resolution). As the final step, DT estimates were determined at SSH measurement locations (see the following Section 3) using bilinear interpolation at SSH observation epochs t (interpolated linearly from the hourly resolution data). Figure 18 presents the estimated DT with its associated uncertainty during the Salme C2 shipborne GNSS campaign. It is also noticeable in Figure 18 that the NEMO-Nordic DB variability during the C2 campaign is around 2 dm, which is rather significant, considering that marine quasigeoid validation requires accurate height anomalies (i.e., the use of HDM data directly for reducing SSHs into height anomalies may provide unreliable results).

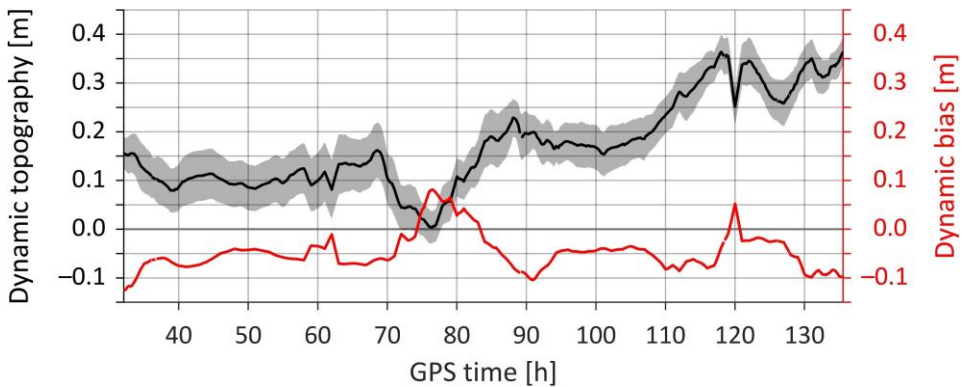


Figure 18. Dynamic topography (cf. Equation 25) and corresponding DB (used in deriving the DT estimates) along the vessel's route during the Salme C2 shipborne GNSS campaign (GPS week 2168). The shaded area shows the DT-associated 1-sigma uncertainty envelope. [Modified from **Publication VII**]

3 Determination of Offshore Geometric Height Anomalies

With the availability of DT estimates, SSHs can be reduced into height anomalies that provide independent validation for marine quasigeoid modelling solutions. Various approaches exist for determining SSHs, such as satellite altimetry (cf. Scope and Objectives), shipborne GNSS measurements (cf. Scope and Objectives) and reflectometry (Roggenbuck & Reinking, 2019), use of GNSS-equipped buoys (e.g., Zhou et al., 2020; Xie et al., 2021) and uncrewed sea vessels/floats (e.g., Penna et al., 2018; Bonnefond et al., 2022), and ALS (cf. Scope and Objectives). Here, the focus is on shipborne GNSS measurements and ALS surveys. In the following, relevant principles will be reviewed.

3.1 Theoretical Principles for Shipborne GNSS Data Processing

The collected shipborne GNSS survey data requires GNSS post-processing relative to a suitable national or global GNSS-CORS network. In the standard post-processing scheme, the GNSS-CORS coordinates are fixed to the reference epoch t_0^{RF} (this may differ from the reference epoch t_0^{HS} of a height system) of the selected national or global reference frame. The actual positions of CORS at a different observation epoch t may deviate from the reference epoch positions, for instance, in elevation due to VLM. Consequently, VLM-generated height change (from epoch t_0^{RF} to epoch t) is propagated to the GNSS observation at epoch t because the height difference dh between the GNSS observation location and GNSS-CORS is referred to the reference epoch t_0^{RF} . This approach facilitates consistency between the height reference and GNSS observations, but only on land. A height discrepancy is introduced to offshore GNSS observations since sea level trends do not follow VLM directly (e.g., geoid change induced by glacial isostatic adjustment still influences sea level trends). Thus, shipborne GNSS survey results may require consideration for VLM occurring at land-located GNSS-CORS in the VLM-affected regions. Assuming that post-processing is conducted relative to a single GNSS-CORS, the VLM-corrected ellipsoidal height is obtained as (also see Figure 14):

$$h(\varphi^{SSH}, \lambda^{SSH}, t, t_0^{HS}) = h_0(\varphi^{CORS}, \lambda^{CORS}, t_0^{RF}) + dh(t) + VLM_{geocentric}(\varphi^{CORS}, \lambda^{CORS})(t - t_0^{RF}) - GC(\varphi^{SSH}, \lambda^{SSH})(t - t_0^{HS}), \quad (28)$$

where h_0 is an ellipsoidal height of a CORS (with coordinates $\varphi^{CORS}, \lambda^{CORS}$) at the reference epoch t_0^{RF} . Terms $VLM_{geocentric}$ and GC denote geocentric VLM and geoid change rate (Figure 15 shows the annual rate of geoid rise in the Baltic Sea region), respectively; also note the following relation:

$$VLM_{geocentric}(\varphi, \lambda) = VLM_{levelled}(\varphi, \lambda) + GC(\varphi, \lambda). \quad (29)$$

It can be noticed in Equation (28) that geoid change is eliminated from the heights of GNSS observations (hence the dependency on reference epoch t_0^{HS}); this is necessary for data consistency. If we assume the existence of a quasigeoid-based height reference surface compatible with a corresponding height system (i.e., the height reference surface represents the reference epoch t_0^{HS}) and that the ellipsoidal heights obtained by Equation (28) represent SSHs, then absolute DT is obtained by subtracting reference surface heights from SSHs (this is the geodetic method for DT determination). The equivalent absolute DT to that was obtained in Section 2 (i.e., via a semi-oceanographic

method; the pure oceanographic approach is usually considered only to use HDM data). In other words, the epochs of quasigeoid models to be validated using height anomalies determined from SSH and DT datasets should ideally match the reference epoch t_0^{HS} of the used height system.

In practice, Equation (28) does not yield SSHs directly, as the reference of a GNSS antenna is unlikely to coincide with the sea surface level. The vertical range (H_{REF}) from the antenna reference to the sea surface (e.g., determined by a total station survey) is required for such a reduction (also refer to Figure 14):

$$iSSH(\varphi^{SSH}, \lambda^{SSH}, t, t_0^{HS}) = h(\varphi^{SSH}, \lambda^{SSH}, t, t_0^{HS}) - H_{REF}, \quad (30)$$

where $iSSH$ represents instantaneous SSH values. These are only an approximation of the actual SSHs, as the measured instantaneous SSHs contain high-frequency attitude changes of the vessel (e.g., pitch and roll motions) and the influence of the sea state (i.e., waves). In addition, the squat effect and change in the static draft (due to fuel consumption) must be accounted for because these cause the vessel to sail with an offset relative to the reference level at which H_{REF} is determined at a harbour (i.e., these are denoted as sailing-related corrections).

High-frequency attitude changes of a vessel can be determined with an inertial measurement unit during GNSS data sampling (Nordman et al., 2018; Saari et al., 2021). As an inertial measurement unit can be costly and require additional dedicated software, an alternative is to install multiple GNSS antennas on the vessel to specify its attitude (Lavrov et al., 2017; Roggenbuck & Reinking, 2019). The shipborne GNSS surveys described later opted for the latter. In the method used, three GNSS antennas form a plane from which more stable attitude-reduced heights can be determined at the position of the vessel's mass centre (i.e., pitch and roll motions occur roughly relative to the mass centre). Such a joint height solution will be denoted $iSSH_{COM}$ (for additional computational details, please refer to Section "Reducing effects from vessel's attitude" in **Publication I** and Section 5.1 in **Publication V**).

The attitude-reduced heights $iSSH_{COM}$ still contain the heave motion of a vessel (i.e., vertical movements) caused by waves. Low-pass filtering can separate the required lower-frequency SSHs from those instantaneous values (Varbla et al., 2017a; Nordman et al., 2018). However, depending on the GNSS data sampling rate, the spatial length of the filtering window can reach several kilometres for obtaining a meaningful filtering effect, which implies that the gradients of geoid and DT may contaminate the low-pass filtering results (especially in steep geoid gradient areas, where the vessel also takes turns). Therefore, a reduction for $iSSH_{COM}$ is first needed:

$$\begin{aligned} r_{COM}^{UF}(\varphi^{SSH}, \lambda^{SSH}, t) &= iSSH_{COM}(\varphi^{SSH}, \lambda^{SSH}, t, t_0^{HS}) - \zeta_{model}(\varphi^{SSH}, \lambda^{SSH}, t_0^{HS}) \\ &- \widehat{DT}(\varphi^{SSH}, \lambda^{SSH}, t) = \widehat{DT}_{geodetic}(\varphi^{SSH}, \lambda^{SSH}, t) - \widehat{DT}(\varphi^{SSH}, \lambda^{SSH}, t), \end{aligned} \quad (31)$$

where r_{COM}^{UF} represents unfiltered SSH residuals. The equation is presented in two steps to illustrate the earlier point regarding quasigeoid-based height reference surface compatibility with a height system (i.e., notice how dependency on reference epoch t_0^{HS} disappears). Term $\widehat{DT}_{geodetic}$ is DT obtained via the geodetic method, and \widehat{DT} is derived as described in Section 2.

The retrieved residual values can be low-pass filtered, for example, using the filtering approach in Varbla et al. (2017a):

$$r_{CoM}^{Median}(\varphi^{SSH}, \lambda^{SSH}, i) = Median \left\{ r_{CoM}^{UF}(\varphi^{SSH}, \lambda^{SSH}, n) \mid i - \frac{F-1}{2} \leq n \leq i + \frac{F-1}{2} \right\}, \quad (32)$$

$$r_{CoM}^F(\varphi^{SSH}, \lambda^{SSH}, i) = \frac{1}{F} \sum_{n=i-\frac{F-1}{2}}^{i+\frac{F-1}{2}} r_{CoM}^{Median}(\varphi^{SSH}, \lambda^{SSH}, n), \quad (33)$$

where F is the filtering window size (i.e., a certain number of GNSS observations), and i represents a specific GNSS observation at epoch t . As the final step, sailing-related corrections should be applied to the filtered SSH residuals:

$$r_{CoM}^{F+C}(\varphi^{SSH}, \lambda^{SSH}, t) = r_{CoM}^F(\varphi^{SSH}, \lambda^{SSH}, t) - CORR(t), \quad (34)$$

where $CORR$ denotes the combined effect of all corrections. The obtained low-pass filtered and corrected SSH residuals describe the sum of all remaining discrepancies between the used datasets. In principle, these residuals can quantify the offshore modelling errors of the quasigeoid model used in Equation (31) reduction, assuming that all other datasets have reasonable accuracy. The initially removed (modelled) height anomalies should be restored on the residual values:

$$\zeta_{geom}(\varphi^{SSH}, \lambda^{SSH}, t, t_0^{HS}) = r_{CoM}^{F+C}(\varphi^{SSH}, \lambda^{SSH}, t) + \zeta_{model}(\varphi^{SSH}, \lambda^{SSH}, t_0^{HS}) \quad (35)$$

to obtain geometric height anomalies that could be used for validating other quasigeoid modelling solutions.

3.2 Processing of Shipborne GNSS Data

In July 2017, a dedicated marine gravity and GNSS campaign (see **Publication I** for more details) was conducted in the Gulf of Finland – this is referred to as the Sektori shipborne GNSS campaign (the route is shown in Figure 19). The campaign aimed to acquire new gravity data for the subsequent quasigeoid modelling tasks, such as the BSCD2000 quasigeoid model development. Most importantly, this survey covered part of a large gravity data void area in the eastern Gulf of Finland (within the extent of the Estonian marine border; the gravity data situation in the Russian waters remains problematic, as is noticeable in Figure 4). Besides the gravimeter, three GNSS devices were installed on the vessel that sampled (15 s sampling rate) its position during the campaign.

Six additional shipborne GNSS campaigns (see **Publications IV** and **V** for more details) were conducted in the spring and summer of 2021 – these are the Salme shipborne GNSS campaigns (the extents of routes are shown in Figure 19), where campaigns are distinguished by denotation C, which is followed by a campaign number. Unlike the dedicated campaign in 2017, these GNSS measurements were conducted autonomously (i.e., no dedicated GNSS operator was on-board), where data were gathered as a by-product of various marine condition monitoring surveys (e.g., water sampling and profiling). Relatedly, it can be noticed in Figure 19 that the routes have no specific design, as is the case with the Sektori shipborne GNSS campaign. Four GNSS devices were installed on the vessel (the sampling rates varied between 15 to 60 s – specifics can be found from **Publication IV**); GNSS receivers were turned on before the vessel left the harbour, and collected data were downloaded upon returning.

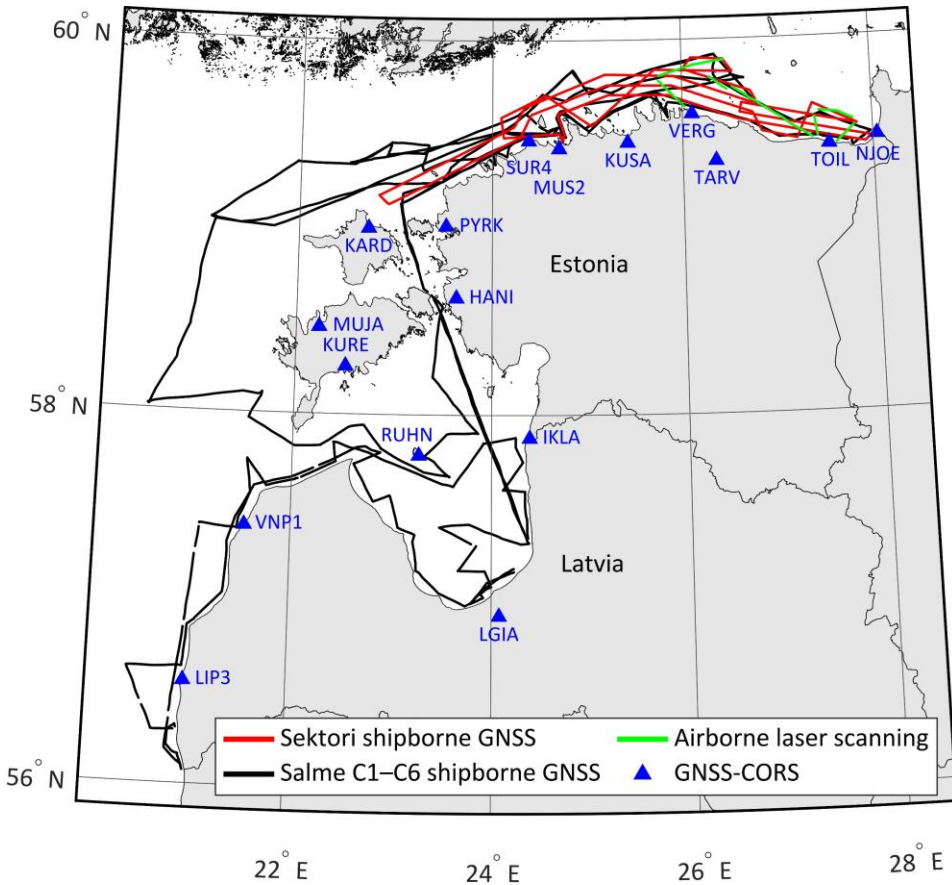


Figure 19. Routes of shipborne GNSS campaigns and ALS survey. Blue triangles denote the locations of GNSS-CORS that were employed for GNSS post-processing.

3.2.1 GNSS Post-Processing of the Survey Data

The collected shipborne GNSS data were post-processed primarily relative to the Estonian GNSS-CORS (Figure 19) using the commercial Trimble Business Center software; post-processing of the Salme C3 GNSS data also included Latvian GNSS-CORS. Since Trimble Business Center allows only one base station at a time for kinematic GNSS post-processing, the closest GNSS-CORS was always used for computing a GNSS data point position. Precise GNSS ephemerides (final orbits) from the International GNSS Service were incorporated into post-processing. As the GNSS-CORS coordinates were fixed to the reference epochs of the national reference frames, the resulting ellipsoidal heights were corrected for VLM according to Equation (28) using the following reference epochs:

- reference epoch t_0^{HS} of the Estonian national EVRS-based height system realization EH2000 is 2000.0;
- reference epoch t_0^{RF} of the Estonian national ETRS89 reference frame realization EUREF-EST97 is 1997.56;
- reference epoch t_0^{HS} of the Latvian national EVRS-based height system realization LAS-2000.5 is 2000.5;

- reference epoch t_0^{RF} of the Latvian national ETRS89 reference frame realization LKS-92 is 1992.75.

The annual VLM and geoid change rates were obtained from the NKG2016LU model (Vestøl et al., 2019; see Figure 15).

During the post-processing and subsequent analysis of the Salme C2 campaign data, it became apparent that the quality of post-processing results had degraded for the most distant route sections from the GNSS-CORS. Previous studies (Roggenbuck et al., 2014; Varbla et al., 2017a; Shih et al., 2021) have demonstrated that the Canadian CSRS-PPP¹¹ online global point positioning service can provide reliable post-processing for remote (from GNSS-CORS) shipborne GNSS measurements. Analysis of post-processed data suggests that the CSRS-PPP ensures relatively consistent accuracy regardless of distance from the coast (i.e., land-located GNSS-CORS) and is thus suitable for replacing poor-performing route sections of Trimble Business Center post-processing results. It is worth mentioning that the CSRS-PPP has shown good performance even for determining shipborne GNSS-based SSHs in a transoceanic scenario (Roggenbuck et al., 2014).

For the Sektori GNSS data post-processing, also another, more sophisticated, commercial software – NovAtel Inertial Explorer – was employed. Unlike Trimble Business Center, the NovAtel software allows including multiple GNSS-CORS (weights are assigned inverse to the distances between GNSS-CORS and a GNSS measurement location) into kinematic GNSS post-processing. As these data were available, a combined height solution from the two software was determined. First, VLM correction was added to the NovAtel post-processing solution according to Equation (28); individual GNSS-CORS-associated correction values were weighted according to the inverse distances between a GNSS data point location and the multiple used CORS (i.e., how post-processing weights are determined in the software). The VLM-corrected post-processing solutions (from Trimble Business Center and NovAtel Inertial Explorer) were then combined by averaging heights at each GNSS observation epoch.

Because GNSS post-processed ellipsoidal heights use the tide-free permanent tide concept, these data had to be converted to the zero-tide concept (Mäkinen, 2008; Ihde et al., 2019):

$$\Delta H_{TF \Rightarrow ZT}(\varphi) = 0.0603 - 0.1790 \sin^2 \varphi - 0.0019 \sin^4 \varphi, \quad (36)$$

where the tide-related height correction $\Delta H_{TF \Rightarrow ZT}$ at a geodetic latitude φ is in meters (the correction should be added to the heights to be corrected). Such a conversion was necessary for consistency with all the other datasets (remember that all the data thus far uses or has been converted to the zero-tide permanent tide concept).

3.2.2 Reduction of Heights to the Sea Surface

It should be admitted that during the Sektori shipborne GNSS campaign, distances between the sea surface and references of GNSS antennas were not measured. This deficiency necessitated the adoption of a different strategy, where the mean $\bar{\gamma}_{CoM}^{UF}$ residual value (cf. Equation 31) was assumed to be zero at the harbour (i.e., the estimated $iSSH = \zeta_{model} + \widehat{DT}$ was assumed errorless; see also Equation 30):

¹¹ <https://webapp.csrscs-nrcan-rncan.gc.ca/geod/tools-outils/ppp.php> [accessed 10 April 2023]

$$H_{REF} = \frac{1}{I} \sum_{i=1}^I [h(\varphi^{SSH}, \lambda^{SSH}, i, t_0^{HS}) - \zeta_{model}(\varphi^{SSH}, \lambda^{SSH}, t_0^{HS}) - \widehat{DT}(\varphi^{SSH}, \lambda^{SSH}, i)], \quad (37)$$

where I is the total number of GNSS observations conducted before the survey when the vessel was moored, and i represents a specific observation at epoch t . In total, 110 to 140 such observations (15 s sampling rate) could be used (different for each antenna because receivers were turned on individually). Regarding the uncertainty of this simplification, then the nearest GNSS-CORS used in those data points' GNSS post-processing is reasonably close (19 km baseline from SUR4; cf. Figure 19), suggesting good quality for the GNSS-determined heights. The height accuracy of temporally averaged (Equation 37) combined solution (cf. Section 3.2.1) is likely around 2 cm. Potential discrepancy due to modelled height anomaly is negligible as the three harbour-surrounding (cf. Figure 13) GNSS-levelling fitting residuals of GQM2022 are only from 1 mm to 3 mm (i.e., it is an excellent agreement; the 1 mm barely visible GNSS-levelling residual is to the left of the red triangle in Figure 13). The most significant discrepancy up to a few centimetres could originate from the estimated DT.

In the case of Salme campaigns, results of a total station survey (notice subscript TS) and tape measurements allowed determining the required range directly:

$$H_{REF} = H_{TS}^{ARP} - H_{TS}^{BM} + H_{Tape}^{BM}, \quad (38)$$

where H_{TS}^{ARP} is the height of an antenna's reference point, H_{TS}^{BM} is the height of a benchmark on the vessel's railing, and H_{Tape}^{BM} is a tape-measured distance between a benchmark and the sea surface. Repeated total station measurements indicated good consistency and around 1 cm accuracy for the determined heights. On the other hand, tape measurements are much more inaccurate – the vessel sways and the sea surface is everchanging, whereby optimal measure of the sea surface is prone to surveyors' subjectivity. It is estimated that an accuracy of around 5 cm could be expected for careful tape measurements, suggesting that the Equation (37) approximation uncertainty is in the same order of magnitude as by measuring H_{REF} directly. The determined vertical distances were used to reduce ellipsoidal heights to the sea surface (cf. Equation 30).

3.2.3 Elimination of High-Frequency Attitude and Sea State Effects

The reduced $iSSH$ values of three GNSS antennas were employed to derive a joint height solution $iSSH_{COM}$ at the vessel's mass centre for the Sektori shipborne GNSS campaign (to see the effect of this calculation, please refer to Figure 9 in **Publication I**). Unfortunately, such a solution was impossible for the Salme C4 campaign as data from only two antennas could be used (due to instrument malfunctioning); the $iSSH$ of two antennas were averaged at each observation epoch t . For the other five Salme campaigns, the availability of four GNSS antennas meant four possible solutions of $iSSH_{COM}^{\xi}$, where $\xi = 1, \dots, 4$ is the number of a solution according to the antenna that was excluded from the computation. Due to data availability, the final solution was determined as:

$$iSSH_{COM}(\varphi^{SSH}, \lambda^{SSH}, t, t_0^{HS}) = \frac{1}{4} \sum_{\xi=1}^4 iSSH_{COM}^{\xi}(\varphi^{SSH}, \lambda^{SSH}, t, t_0^{HS}). \quad (39)$$

Note that using four GNSS antennas can be beneficial. If three GNSS antennas define a plane, then the fourth GNSS antenna should ideally provide a measurement that coincides with that plane (assuming that the height reduction to the sea surface has been successful). In other words, four GNSS antennas form a rigid system that can be validated internally:

$$d_{A\xi}(\varphi^{SSH}, \lambda^{SSH}, t) = \widehat{iSSH}_{A\xi}(\varphi^{SSH}, \lambda^{SSH}, t, t_0^{HS}) - iSSH_{A\xi}(\varphi^{SSH}, \lambda^{SSH}, t, t_0^{HS}), \quad (40)$$

where $d_{A\xi}$ is the discrepancy between measured ($iSSH_{A\xi}$) and estimated ($\widehat{iSSH}_{A\xi}$; i.e., a point on a plane defined by the other three antennas) instantaneous SSH at the location of antenna ξ . Descriptive statistics of these discrepancies are shown in Figure 20, indicating the expected GNSS height determination accuracy offshore. The discrepancy mean values generally remain around a centimetre, suggesting that ellipsoidal heights have been successfully reduced to the sea surface (i.e., all four antennas are approximately on the same plane; also see Equations 30 and 38). Slightly larger values are detected for the Salme C2 campaign, likely due to errors in tape measurements. The weighted (according to campaign distances) mean standard deviation estimate (by averaging Figure 20 values) of 4.1 cm demonstrates overall good performance for height determination. Since Sektori data has been processed similarly (also remember that the height solution is a combined one from two software), comparable accuracy for height determination should be expected.

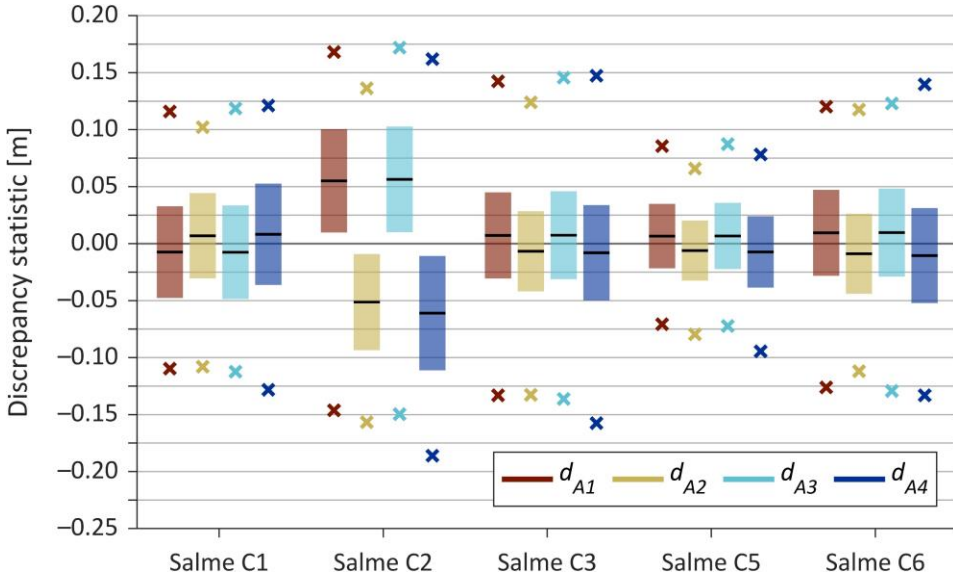


Figure 20. Descriptive statistics of instantaneous SSH discrepancies (cf. Equation 40). Black lines denote mean values, coloured bars standard deviation estimates, and coloured crosses 99th percentile minimum and maximum discrepancies. [Modified from **Publication V**]

The centre of mass instantaneous SSH solutions $iSSH_{CoM}$ were reduced into residual values using Equation (31). Height anomalies were obtained from the GQM2022 model (cf. Section 1.6), and DT estimates were computed as described in Section 2. It is assumed that GQM2022 is compatible (i.e., it corresponds to reference epoch t_0^{HS}) with the

Estonian EH2000 height system after a one-dimensional fit to the Estonian GNSS-levelling control points. The discrepancies due to unaccounted geoid rise (i.e., GQM2022 was not reduced to uplift epoch 2000.0) amount at most 2 mm due to geoid rise variability (refer to Figure 15; the mean geoid rise effect is removed through GNSS-levelling fitting) in the current investigations, which is negligible considering the quasigeoid modelling accuracy, especially offshore.

A sum of absolute differences function (between unfiltered and filtered signals) was compiled for each shipborne GNSS campaign's SSH residuals by low-pass filtering (cf. Equations 32 and 33) unfiltered residuals r_{CoM}^{UF} with varying window sizes (only odd sizes were considered). It can be noticed that the functions are shaped similarly (cf. Figure 21),

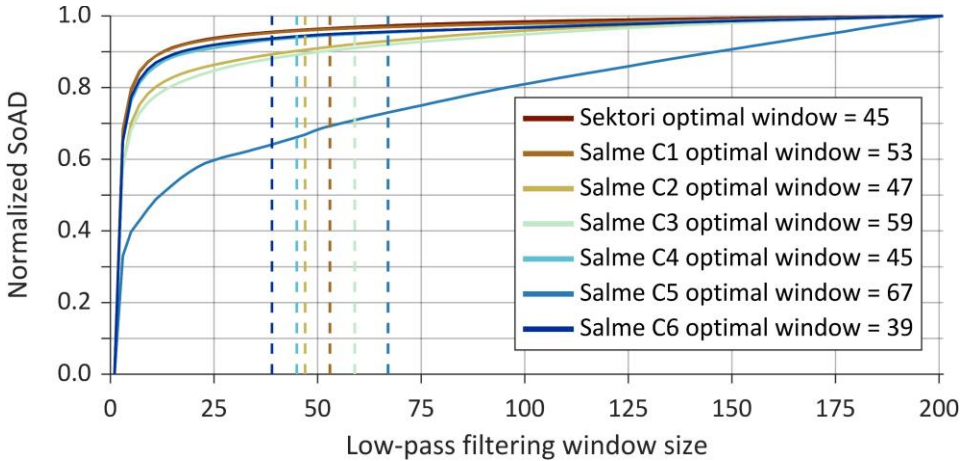


Figure 21. The sum of absolute differences (SoAD) functions for shipborne GNSS campaigns (function associated with the Sektori campaign is hidden behind the Salme C1 function), normalized for comparability according to maximum values. Dashed vertical lines show the optimal filtering window sizes. [Modified from **Publication V**]

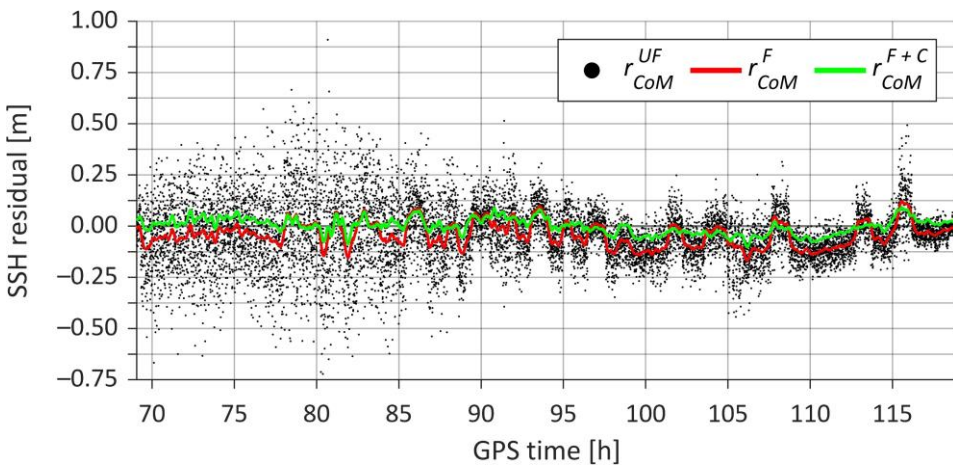


Figure 22. Sea surface height residuals of the Salme C1 shipborne GNSS campaign (GPS week 2152) at various data processing stages.

except the one associated with the Salme C5 campaign, which is much shorter than the rest (i.e., it contains fewer measurements). Optimal filtering window sizes were estimated as points where functions became roughly linear (done separately for each function). Because the estimated window sizes vary (e.g., due to assumed approximations), a weighted (according to campaign distances) mean window size (F) of 51 measurements was determined for consistent low-pass filtering. Figure 22 shows the filtering effect on the initial scattered data (the black dots) of the Salme C1 shipborne GNSS campaign. More significant scattering in the first half is due to windy and wavy conditions (also notice slightly increased DB uncertainties on the left side of Figure 16); the scattering reduces during temporary calmer weather before the start of a storm. The approach used for reducing high-frequency attitude changes of the vessel and low-pass filtering can evidently also handle rough sea measurements. Nevertheless, in the filtered results (the red line in Figure 22), abnormal peaks can be noticed (further discussed in the next section), which, to an extent, can be dealt with by applying sailing-related corrections (in this case, squat correction) to the low-pass filtered SSH residuals.

3.2.4 Derivation of Sailing-Related Corrections

The two sailing-related corrections that should be accounted for are the squat effect and change in the static draft due to fuel consumption. The squat, which causes a vessel to sail deeper than its nominal draft, is a function of a vessel's velocity and dimensions but is also influenced by depth in shallower, more confined waters (Barrass, 2004). Unlike the squat effect, continuous fuel consumption causes a vessel to float gradually higher. The lowest and highest corrections for the static draft are at the time of harbour departure and return, respectively.

Recall that during the Sektori shipborne GNSS campaign, the primary purpose was to collect gravity data. Therefore, a constant velocity of around 8 knots was kept to avoid unnecessary accelerations/decelerations that could degrade gravity data quality. A rough squat correction value was approximated following Barrass (2004):

$$\delta_{max} = \frac{C_B v^{2.08}}{30} \left(\frac{b \bar{s}}{\overline{H^*} b (7.7 + 20(1 - C_B)^2) - b \bar{s}} \right)^{2/3}, \quad (41)$$

where C_B and v are the block coefficient (describes a vessel's shape in the water, where a value of one corresponds to a rectangular block) and velocity of a vessel, respectively, b is a vessel's breadth, \bar{s} is the mean static draft, and $\overline{H^*}$ represents mean water depth. This approximation resulted in a 5.6 cm (maximum) squat, which was applied as a constant offset (because, in general, velocity did not change during the survey) to the low-pass filtered SSH residuals. Any short-term changes in the squat value (e.g., during turns when the vessel slowed down briefly) ought to be eliminated by the median in the low-pass filter (cf. Equation 32).

As mentioned at the end of Section 3.2.3, abnormal peaks appear in low-pass filtered SSH residuals of Salme shipborne GNSS campaigns (refer to Figure 22 – see the red line). These peaks coincide with the occasions of the vessel's stopping (e.g., to take water samples; remember that the primary aim of Salme campaigns was to conduct marine condition monitoring surveys) and are caused by the disappearance of the squat effect. Such stops allowed relating the vessel's velocity to height changes between a moving and static vessel by utilizing low-pass filtered SSH residuals over distances up to 3 km. The determined estimates shown as black dots in Figure 23 represent squat values at

various velocities. As the vessel's dimensions are constant and surveys were conducted in relatively deep waters, the squat effect is approximately a quadratic velocity function (Barrass, 2004; Roggenbuck et al., 2014). Hence, a quadratic function was fitted in the least-squares sense to the empirical data to determine a generalized squat effect function for Salme (see Figure 23). It should be noted here that the shapes and sizes of Sektori and Salme are somewhat similar. Assuming that a comparable squat function also describes Sektori, the proposed 5.6 cm squat value appears slightly underestimated (this might be to do with the fact that Equation 41 is first and foremost meant for shallow waters; in deeper areas, the influence of depth should disappear) compared with an estimate of 7.7 cm (at 8 knots) determined using the function (by neglecting the Y-axis offset term).

Tape measurements (between benchmarks on a railing and the sea surface) were conducted before a vessel sailed off for a survey and after it returned. Differences in these tape-measured values provide means to estimate a correction for the static draft. The Sektori shipborne GNSS campaign relies on a single estimate, whereas the Salme campaigns provided multiple estimates allowing more reliable determination of the correction (notice the spread of estimates shown as red dots in Figure 23, demonstrating inaccuracies in tape measurements). A distance-related least-squares fit of a linear trend was used to derive the corrections for the static draft (see Figure 23).

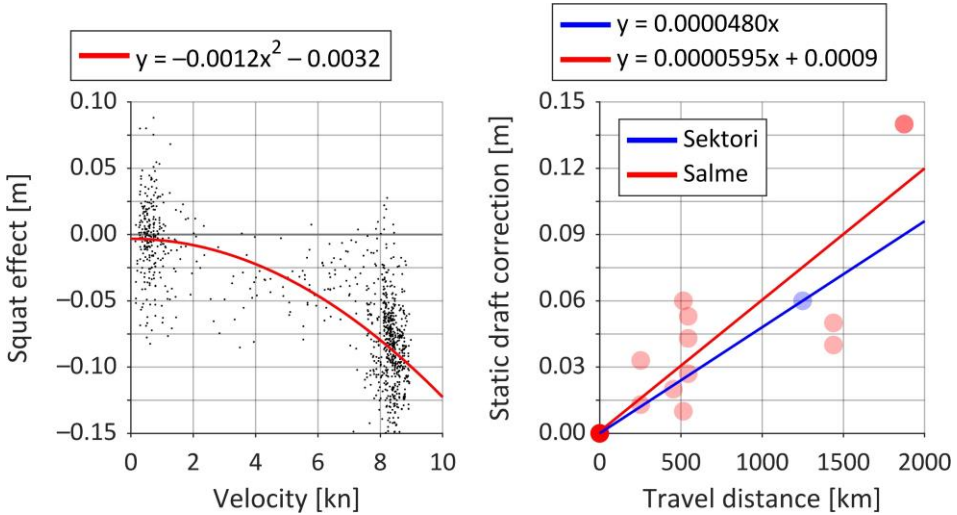


Figure 23. Empirically estimated squat effect for Salme (left) and corrections for the static draft (right). [Modified from **Publication V**]

The combined effect of both corrections (unit is metre; also see Equation 34) can be expressed as:

$$CORR(t) = -0.0560 + 4.80^{-5}d(t), \quad (42)$$

$$CORR(t) = -0.0012[v(t)]^2 + 5.95^{-5}d(t), \quad (43)$$

where v and d are a vessel's velocity (unit is knot) and travelled distance (unit is kilometre), respectively, at a GNSS observation epoch t . Equation (42) is meant for Sektori, and Equation (43) for Salme. The low-pass filtered and corrected SSH residuals r_{CoM}^{F+C} were

determined using Equation (34) by applying those combined corrections (an example of the corrections' effect can be seen in Figure 22 – compare red and green lines). Further investigation of the retrieved residual values is postponed until the treatment of ALS point cloud data is also explained briefly. Then, all the datasets will be jointly free network least-squares adjusted to reduce biases between them.

3.3 Airborne Laser Scanning Principle

Airborne laser scanning is a technique in which an aircraft-mounted LiDAR (light detection and ranging) sensor emits laser pulses and registers reflections from a surface. The range between the sensor and a surface can be determined by measuring the signal return time. The position and orientation of the LiDAR sensor on an aircraft are established with a GNSS device and an inertial measurement unit, allowing derivation of the reflecting surface coordinates using the determined range (also considering the slanted angle of the laser pulse). Such a technique results in an along-route 3D point cloud of the measured surface (e.g., the sea surface).

The conventional use for ALS is dry land topography mapping, where the usual accuracy is estimated to be around 5–15 cm, depending on the measured surface and survey configuration (Huisig & Pereira, 1998; van der Sande et al., 2010). Studies that have examined ALS for marine applications have indicated that similar accuracy can be achieved for mapping the sea surface (e.g., Gruno et al., 2013; Zlinszky et al., 2014; Sutherland et al., 2018; Varbla et al., 2020). However, ALS for such purposes is relatively underutilized compared to dry land applications. Since ALS results in a dense 3D point cloud of SSHs (as opposed to a profile of SSHs using, e.g., shipborne GNSS measurements), the data can also be used for studying marine dynamics (e.g., properties of surface waves – see **Publication II** and also Jahanmard et al., 2022a).

3.4 Processing of Airborne Laser Scanning Point Cloud Data

In May 2018, an ALS survey was performed in the eastern Gulf of Finland within the frames of routine mapping of offshore islands (routes of marine measurements are shown in Figure 19; see **Publication II** for more details). Standard workflow (refer to Gruno et al., 2013; Julge et al., 2014) was used to compute 3D point clouds of instantaneous SSHs; flight trajectory calculations (using GNSS and inertial measurement unit datasets) were conducted relative to the Estonian GNSS-CORS. An operational flight altitude of around 1200 m yielded a 1000–1200 m width for the SSH data corridor.

A 2D moving average low-pass filter was employed to separate the low-frequency SSH signal from instantaneous values (i.e., to remove the effect of waves). The computation step (i.e., the distance between filtering window centres) was set to 62 m, corresponding to the aircraft's average velocity of 62 m/s. The 1116 m length of the filtering window (i.e., windows overlap) was defined according to the $0.01^\circ \times 0.02^\circ$ resolution of regional quasigeoid models. Note that although the width of the SSH data corridor is roughly a kilometre, a systematic upward curve was detected at the edges (effect generally subsides 300–400 m inwards from an edge). A likely cause is the scanner scale error (Kumari et al., 2011). The filtering window width was thus set to 100 m (i.e., 50 m across-track from the nadir position to each side) to be safe in avoiding error propagation to the filtering results. It should be mentioned that the average point cloud density for the centre 100 m of the SSH data corridor is 6.2 p/m^2 . Such filtering windows were centred at the aircraft's nadir and oriented along the trajectory, resulting in 62 m resolution along-nadir SSH profiles.

The obtained SSHs were corrected for VLM similarly to the NovAtel Inertial Explorer post-processed shipborne GNSS measurements (cf. Section 3.2.1) using Equation (28) principle and converted from the tide-free permanent tide concept to the zero-tide concept (cf. Equation 36). Equation (31) principle was then employed to reduce SSHs into residual values. Height anomalies were obtained from the GQM2022 model (cf. Section 1.6), and DT estimates were computed as described in Section 2, as with processing shipborne GNSS data. It can be argued that the reduction should have been conducted before low-pass filtering. However, compared to shipborne GNSS data processing, the filtering window is relatively short (around 1 km for ALS versus up to around 8 km for shipborne GNSS), and the ALS trajectories are generally straight (cf. Figure 19; note that there are 7 different point clouds, which were processed separately), causing the effect of geoid and DT gradient to mostly cancel out in averaging.

3.5 Offshore Geometric Height Anomalies and Sea Surface Heights

All the previously described data processing resulted in 8 datasets of SSH residuals (the Sektori shipborne GNSS campaign, 6 Salme shipborne GNSS campaigns, and the ALS survey). Since there may exist biases between those datasets, for instance, due to errors in tape measurements, all the data were jointly free network least-squares adjusted using mean discrepancies (determined using discrepancies at profile intersections) between individual datasets. The resulting bias estimates were then subtracted from the respective datasets' residual values as constants. For additional details regarding the adjustment approach, please refer to Section 5.4 in **Publication V**. As the final step, Equation (35) was used to retrieve geometric height anomalies that could be used for validating marine quasigeoid modelling solutions. The residuals can also be restored into processed SSHs:

$$SSH(\varphi^{SSH}, \lambda^{SSH}, t) = r_{CoM}^{F+C}(\varphi^{SSH}, \lambda^{SSH}, t) + \zeta_{model}(\varphi^{SSH}, \lambda^{SSH}, t_0^{HS}) + \widehat{DT}(\varphi^{SSH}, \lambda^{SSH}, t) + GC(\varphi^{SSH}, \lambda^{SSH})(t - t_0^{HS}), \quad (44)$$

where the initially removed (cf. Equation 28) geoid change is added back to obtain actual SSHs at an observation epoch t . Note that the propagation of quasigeoid and DT modelling errors into SSHs through low-pass filtering is negligible (refer to Section 6.3 in **Publication V**) if these datasets are reasonably accurate (i.e., do not contain gross errors). Such SSHs could be valuable in validating other SSH datasets, including, for example, satellite altimetry measurements.

4 Accuracy Validation of Marine Quasigeoid Models

This section examines some validation results to demonstrate the use of derived geometric height anomalies. Descriptive statistics of the already determined residual values¹² r_{CoM}^{F+C} after the adjustment (cf. Section 3; i.e., using GQM2022 in the reduction) are shown in Figure 24 for a start. It can be noticed that the standard deviation estimates vary between 1.4 cm (Salme C5 shipborne GNSS campaign) and 4.9 cm (Salme C3 shipborne GNSS campaign), demonstrating the satisfactory performance of the results and overall good consistency between the used and derived datasets. Indeed, there are many potential error sources: the used HDM, VLM, and quasigeoid models; TG, total station, tape, and GNSS/ALS measurements; empirically estimated corrections. Considering that all these datasets contribute to the residuals and that the used GQM2022 quasigeoid model is just one component, it could be safely assumed that marine quasigeoid modelling (cf. Section 1) in the examined study area (cf. Figure 19) is possible with an accuracy better than 5 cm, which is the accuracy that is aimed at in the BSCD2000 quasigeoid modelling offshore (Schwabe et al., 2020).

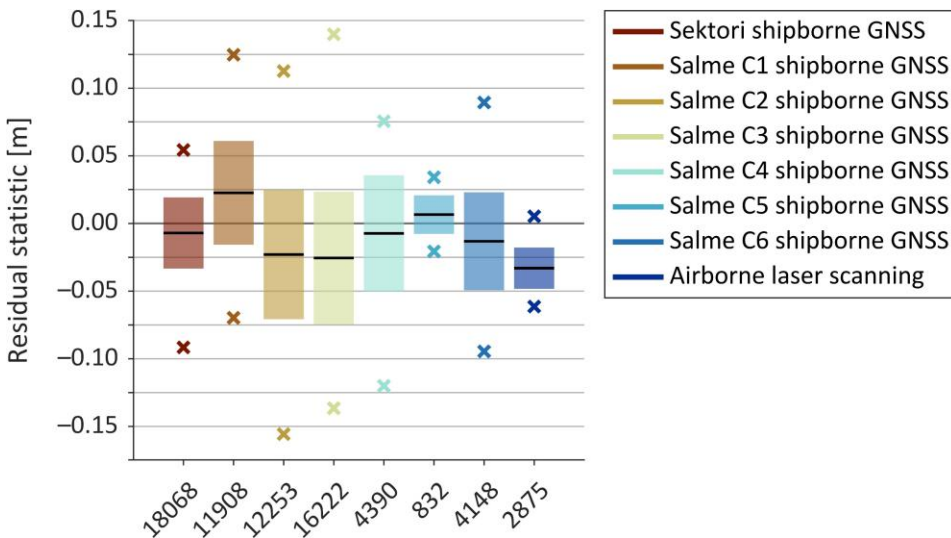


Figure 24. Descriptive statistics of low-pass filtered, corrected, and least-squares adjusted SSH residuals¹² (cf. Section 3; GQM2022 was used in the Equation 31 reduction). Black lines denote mean values, coloured bars standard deviation estimates, and coloured crosses minimum and maximum residuals. The X-axis shows the number of corresponding data points used in calculating the estimates.

Marine gravity data's good quality and dense distribution are essential for achieving high quasigeoid modelling accuracy. Hence, it would be interesting to see how new marine gravity data collected during the Sektori shipborne GNSS campaign has affected the modelling outcome. For a comparison with the GQM2022, the official NKG2015 quasigeoid model (Ågren et al., 2016; reference epoch t_0^{HS} is 2000.0, and spatial resolution of the model is $0.01^\circ \times 0.02^\circ$) was employed (using the zero-tide permanent tide concept).

¹² Geometric height anomalies were subtracted from modelled ones in the Section 4 validations. Therefore, the residuals derived in Section 3 using GQM2022 were multiplied by -1 (i.e., the subtraction order was changed) to be consistent with the other assessments.

Figure 25 shows differences between those two quasigeoid models, substantially caused (there are also dissimilarities in data processing and the used reference GGM) by new shipborne gravity data not included in the NKG2015 development. Locations of data points resulting from the Sektori campaign (refer to **Publication I**) are shown in Figure 25 with red dots. The figure also presents the distribution of another new shipborne marine gravity dataset (see green dots; refer to Saari et al., 2021).

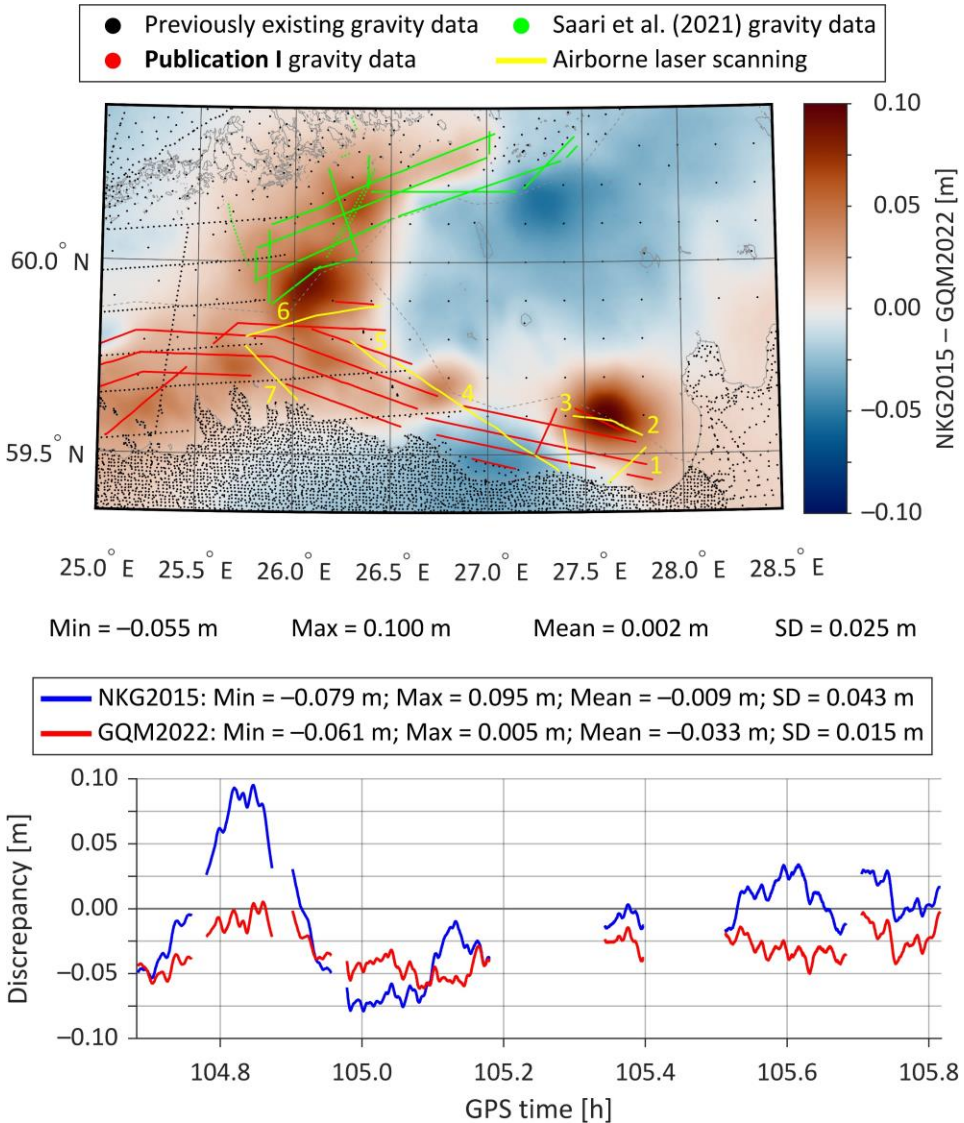


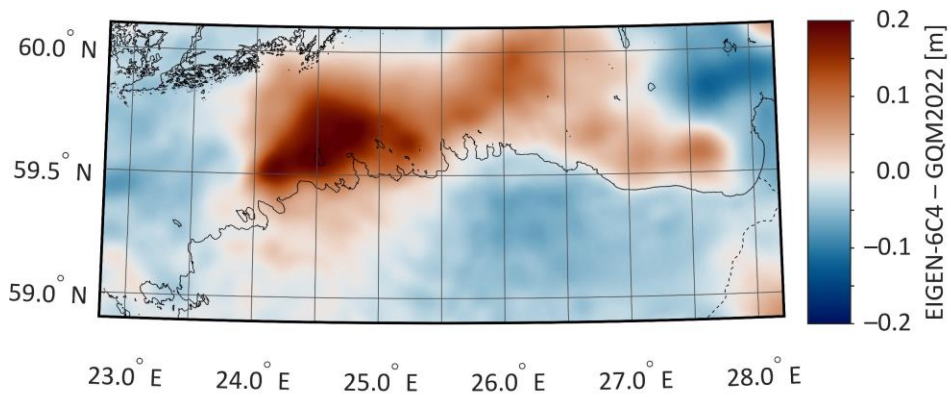
Figure 25. Differences (mainly due to new gravity data – see red and green dots) between the NKG2015 and GQM2022 models' surfaces in the eastern Gulf of Finland (above; notice also the out-of-box descriptive statistics) and discrepancies of those quasigeoid models relative to the ALS-derived geometric height anomalies (below; GPS week 2000). Numbers 1–7 (above) signify the sequence of flight routes (i.e., the order of profile sections in the bottom sub-plot). Descriptive statistics of GQM2022 discrepancies (in the box) are the same as those associated with ALS in Figure 24.

The ALS-derived geometric height anomalies were used to investigate whether the differences in Figure 25 represent enhanced modelling accuracy; resulting discrepancies are shown in the lower sub-plot of Figure 25. These comparisons detect up to 9 cm improvements (similar conclusions are presented in Saari et al., 2021, but with a focus on the northern side of the Gulf of Finland). The most significant increase in modelling accuracy appears in the previously existing gravity data void areas (see the location of profile section 2 and north of profile section 6), where only GGM-synthesised pseudo-observations (regularly spaced gravity data points) could be used during the computation of the NKG2015 model. Notably, the agreement between GQM2022 and ALS-derived height anomalies results in only a 1.5 cm standard deviation (the total length of the profile sections is 184.4 km). Such an excellent agreement signifies that (i) the approach in Section 2 can provide reliable DT estimates; (ii) ALS-measured SSHs are highly accurate; (iii) centimetre-level accuracy could likely be achieved for marine quasigeoid modelling using high-quality shipborne gravity data.

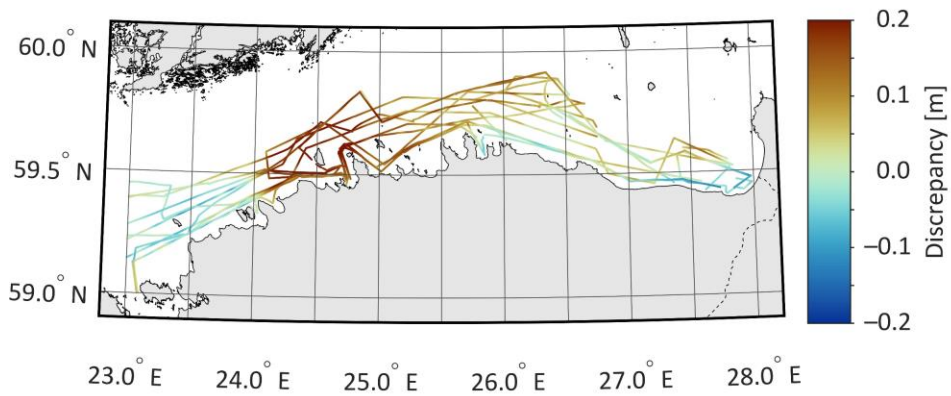
With the next section of the thesis already in mind (i.e., refinement of marine quasigeoid models), the third example involves the high-degree EIGEN-6C4 GGM (Förste et al., 2014). The model was evaluated to its maximum d/o of 2190 (using the zero-tide permanent tide concept), and height anomalies were synthesised on a $0.01^\circ \times 0.02^\circ$ grid. The derived dataset of height anomalies was then fitted to the Estonian high-precision GNSS-levelling control points² (Rüdja & Varbla, 2022) using a one-dimensional fit. It is assumed that after the fit, EIGEN-6C4-derived height anomalies represent reference epoch (t_0^{HS}) 2000.0 (refer to the reasoning regarding the GQM2022 in Section 3.2.3). The resulting GNSS-levelling fitted height anomalies are compared with GQM2022 in Figure 26, which depicts northern Estonia and the Gulf of Finland, where significant differences up to two decimetres are revealed.

For investigating the accuracies of both models, geometric height anomalies derived in Section 3 were extracted within limits from 59°N to 60°N and 23°E to 28°E . These data were then compared with the EIGEN-6C4-derived height anomalies (Figure 26 middle sub-plot) and GQM2022 (Figure 26 bottom sub-plot). It is apparent from those comparisons that the differences between EIGEN-6C4 synthesised height anomalies and GQM2022 (Figure 26 upper sub-plot) are primarily due to EIGEN-6C4 contained errors. The corresponding standard deviation estimates of 7.6 cm (EIGEN-6C4 synthesised height anomalies) and 3.4 cm (GQM2022) demonstrate the considerably better performance of the GQM2022 model. Notice also the 7.0 cm mean value (i.e., systematic bias) associated with the EIGEN-6C4 synthesised height anomalies, compared to the near-zero mean discrepancy of GQM2022.

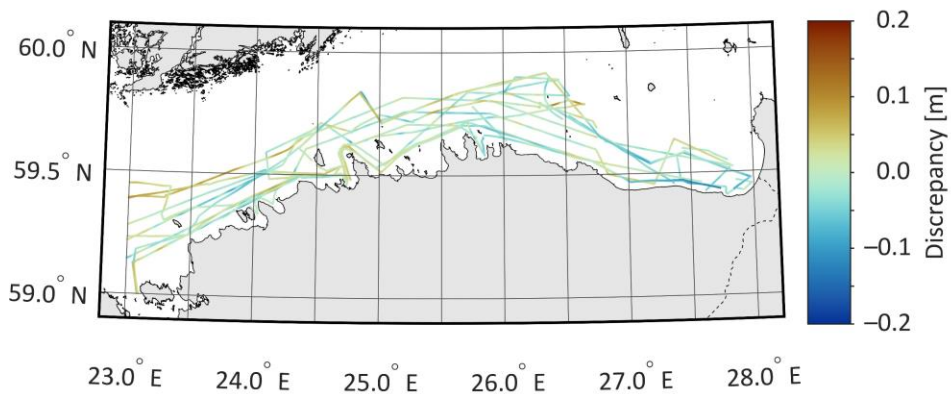
Such errors (especially between meridians 24°E and 25°E) in the GGM appear because EIGEN-6C4 does not sufficiently represent the region's negative anomalous gravity field. Similar errors can be detected (Ellmann et al., 2009) in EGM2008 (Pavlis et al., 2012), the data of which were the basis for compiling higher-degree coefficients of EIGEN-6C4 (Förste et al., 2014). It is evident from Figure 26 assessments that the derived geometric height anomalies are sufficient for quantifying marine quasigeoid modelling errors. Furthermore, this also implies that these data could be potentially used to improve inaccurate modelling solutions (suppose a high-resolution regional quasigeoid model with similar errors exists, or the aim is to substitute a regional solution with high-degree GGM-synthesised height anomalies).



Min = -0.121 m Max = 0.210 m Mean = 0.001 m SD = 0.057 m



Min = -0.121 m Max = 0.250 m Mean = 0.070 m SD = 0.076 m



Min = -0.120 m Max = 0.110 m Mean = -0.004 m SD = 0.034 m

Figure 26. Differences between the EIGEN-6C4 synthesised height anomalies and GQM2022 quasigeoid model in the Gulf of Finland (above), as well as discrepancies of the EIGEN-6C4 synthesised height anomalies (middle) and GQM2022 quasigeoid model (below) relative to the geometric height anomalies derived in Section 3. [Modified from **Publication VII**]

5 Iterative Refinement of Marine Quasigeoid Models

Previous sections of the thesis dealt with gravimetric high-resolution regional quasigeoid modelling (Section 1), derivation of realistic DT estimates (Section 2), and obtaining geometric height anomalies from shipborne GNSS and ALS-measured SSHs using the estimated DT (Section 3). Since the determined geometry information is sufficiently accurate for quantifying significant errors in marine quasigeoid models (Section 4), the potential use of these data for refining modelling errors is now investigated. A relatively straightforward data assimilation approach is employed for improving the accuracy of EIGEN-6C4 synthesised height anomalies. The developed high accuracy (cf. Figure 13 and Section 4) quasigeoid model GQM2022 is then used to validate the outcome. However, first, the relevant principles will be introduced.

5.1 Theoretical Principles for Iterative Data Assimilation

In the following, the dependency on reference epoch t_0^{HS} is omitted for convenience. The modelled and geometric height anomalies are assumed to refer to the same epoch by default. Superscript k is introduced to differentiate data assimilation iterations. The modelled and geometric height anomalies are thus denoted as ζ_{model}^k and ζ_{geom}^k , respectively, where ζ_{model}^1 represents an initial gravimetric quasigeoid model; ζ_{model}^k with $k \geq 2$ are the subsequent combined models. The ζ_{geom}^k with $k \geq 1$ are separate datasets of geometric height anomalies, where the same data points should not be included in more than one of those datasets.

For instance, geometric height anomalies can be determined as already described in Section 3. The uncertainty of those quantities is:

$$\sigma_{geom}^k(\varphi^{SSH}, \lambda^{SSH}, t) = \sqrt{[\sigma_{SSH}^k(\varphi^{SSH}, \lambda^{SSH}, t)]^2 + [\sigma_{DT}^k(\varphi^{SSH}, \lambda^{SSH}, t)]^2}, \quad (45)$$

where σ_{SSH} is the uncertainty associated with SSHs, and σ_{DT} is DT uncertainty derived as described in Section 2.1. The next aim is to develop a continuous grid of geometric height anomalies and associated uncertainties from those discrete data using LSC; these grids are required for adjusting a quasigeoid model between SSH data point locations. Whilst the initial discrete geometric height anomalies are unsuitable for direct gridding, similar principles to gravity field determination (cf. Section 1.1) ought to be adopted. The reduction in the current case is made using a quasigeoid model to be refined:

$$r_{geom}^k(\varphi^{SSH}, \lambda^{SSH}, t) = \zeta_{geom}^k(\varphi^{SSH}, \lambda^{SSH}, t) - \zeta_{model}^k(\varphi^{SSH}, \lambda^{SSH}), \quad (46)$$

where r_{geom}^k are the resulting geometric height anomaly residuals (in principle, these could be the same residuals r_{CoM}^{F+C} as obtained by Equation 34 before Equation 35 signal restoration).

Likely, the available SSH data does not stretch everywhere (e.g., land areas). It is recommended to pad such data void regions with near-zero residual signal to avoid extrapolation errors, where the minimum zero padding distance (i.e., more distant regions are padded) will be denoted d_{ZP} . Residuals of geometric height anomalies and the zero pad are then gridded jointly (computation points should be selected according to quasigeoid model grid nodes with coordinates φ, λ ; for convenience, coordinate

superscript is omitted) analogously to Equation (11) or Equation (21) example, by also following the related principles of LSC. For determining the \mathbf{C}_{st} and \mathbf{C}_{tt} matrices, the exponential covariance model (Shaw et al., 1969) can be used (for reasoning, please refer to Section 3.3 in **Publication VII**):

$$C_{model}(l) = C_0 e^{-l/\alpha}, \quad (47)$$

where parameter α is related to correlation length as $\alpha = (-\ln 0.5)^{-1} X_{1/2} \approx 1.443 X_{1/2}$. Gridded geometric height anomalies are then obtained by restoring the initially removed signal of the quasigeoid model:

$$\hat{\zeta}_{geom}^k(\varphi, \lambda) = \hat{r}_{geom}^k(\varphi, \lambda) + \zeta_{model}^k(\varphi, \lambda). \quad (48)$$

The variance estimates of gridded geometric height anomalies are equivalent to the variances of gridded geometric height anomaly residuals (derived using Equation 23) because the \mathbf{C}_{nn} matrix of observation errors is constructed using the estimated (cf. Equation 45) uncertainties σ_{geom}^k (these should be squared to obtain variance values; errors associated with the Equation 46 reduction are not propagated). Therefore, the uncertainty of gridded geometric height anomalies is:

$$\sigma_{geom}^k(\varphi, \lambda) \equiv \sqrt{[\sigma_{\hat{r}}^k(\varphi, \lambda)]^2}. \quad (49)$$

It can be noticed that time-dependency has disappeared in Equations (48) and (49). Since geometric height anomaly data from various observation epochs are combined during the gridding procedure, the dependency on time is assumed to be eliminated (i.e., gridded geometric height anomalies are a static representation of the geoid).

Note that the uncertainty of gridded geometric height anomalies in SSH data voids depends on the defined uncertainty of the zero pad. This uncertainty should be moderate to avoid geometric height anomaly residuals' signal leakage to the padding regions (i.e., SSH data void areas) during LSC. On the other hand, condition $\sigma_{geom}^k \gg \sigma_{model}^k$, where the latter term is the uncertainty of the quasigeoid model, must be fulfilled in zero pad locations for limiting data assimilation (primarily for determining the uncertainty of the best assimilation estimate) to where SSH data are available using the selected assimilation approach (to be discussed next). The uncertainty of gridded geometric height anomalies is hence artificially increased in padding regions by a location-dependent modification coefficient MOD^k :

$$\sigma_{MOD}^k(\varphi, \lambda) = \sigma_{geom}^k(\varphi, \lambda) MOD^k(\varphi, \lambda), \quad (50)$$

where coefficient values are defined by the function:

$$MOD^k(\varphi, \lambda) = 1 + e^{(\ln 10^{MP}/d_{ZP})[d_{MOD}(\varphi, \lambda) - 3d_{ZP}/4]} - e^{-(\ln 10^{MP}/d_{ZP})[d_{MOD}(\varphi, \lambda) + 3d_{ZP}/4]}. \quad (51)$$

The function depends on the minimum zero padding distance d_{ZP} , modification distance d_{MOD} between a computation point (φ, λ) and the closest data point $(\varphi^{SSH}, \lambda^{SSH})$, and

modification parameter MP that controls the uncertainty increase rate (i.e., the larger the MP value, the higher the σ_{MOD}^k uncertainty compared to the initial uncertainty σ_{geom}^k for distant points). At distance $d_{MOD} = 0$, the function always equals one, and with $MP \geq 1$, the function reaches a value of approximately two at a three-quarters distance of d_{ZP} . The function has been constructed such that σ_{MOD}^k uncertainties are smooth in SSH data and zero pad transition zones, whereas the values increase rapidly thereafter (i.e., in the zero padding regions), fulfilling the condition $\sigma_{MOD}^k \gg \sigma_{model}^k$.

The cost function (modified from Reichle, 2008) of the used assimilation system is defined as:

$$J^k(\varphi, \lambda) = [2 - P^k(\varphi, \lambda)] \frac{[\zeta_{model}^{k+1}(\varphi, \lambda) - \zeta_{model}^k(\varphi, \lambda)]^2}{[\sigma_{model}^k(\varphi, \lambda)]^2} + P^k(\varphi, \lambda) \frac{[\zeta_{model}^{k+1}(\varphi, \lambda) - \hat{\zeta}_{geom}^k(\varphi, \lambda)]^2}{[\sigma_{MOD}^k(\varphi, \lambda)]^2}, \quad (52)$$

where weight P is:

$$P^k(\varphi, \lambda) = \begin{cases} 1, & |\hat{r}_{geom}^k(\varphi, \lambda)| \leq \sigma_{\hat{r}_{SSH}}^k \\ \frac{\sigma_{\hat{r}_{SSH}}^k}{|\hat{r}_{geom}^k(\varphi, \lambda)|}, & |\hat{r}_{geom}^k(\varphi, \lambda)| > \sigma_{\hat{r}_{SSH}}^k \end{cases} \quad (53)$$

$$\sigma_{\hat{r}_{SSH}}^k = \sqrt{\frac{1}{I-1} \sum_{i=1}^I \left[\hat{r}_{geom}^k(\varphi^{SSH}, \lambda^{SSH}, i) - \frac{1}{I} \sum_{i=1}^I \hat{r}_{geom}^k(\varphi^{SSH}, \lambda^{SSH}, i) \right]^2}, \quad (54)$$

with $\sigma_{\hat{r}_{SSH}}^k$ estimated using gridded geometric height anomaly residuals (it is assumed that gridding has eliminated some data noise) at the locations of initial SSH data (i represents a specific SSH observation at epoch t , with I being the total number of SSH data points). Such a weighting scheme is implemented to reduce the risk of propagating significant SSH and DT data errors to the combined quasigeoid model (i.e., regions of most significant discrepancies between modelled and geometric height anomalies are weighted toward the model) – in a practical application, the origin of discrepancies is unknown, whereby uncertainty estimates may not always be reliable.

The cost function J^k should be minimized relative to the refined (i.e., combined) quasigeoid model ζ_{model}^{k+1} to obtain the practical assimilation equation. Thus, solving the differential condition $\partial J^k / \partial \zeta_{model}^{k+1} = 0$ yields:

$$\hat{\zeta}_{model}^{k+1}(\varphi, \lambda) = \frac{P^k(\varphi, \lambda) [\sigma_{model}^k(\varphi, \lambda)]^2 \hat{\zeta}_{geom}^k(\varphi, \lambda) + [2 - P^k(\varphi, \lambda)] [\sigma_{MOD}^k(\varphi, \lambda)]^2 \zeta_{model}^k(\varphi, \lambda)}{P^k(\varphi, \lambda) [\sigma_{model}^k(\varphi, \lambda)]^2 + [2 - P^k(\varphi, \lambda)] [\sigma_{MOD}^k(\varphi, \lambda)]^2}, \quad (55)$$

where $\hat{\zeta}_{model}^{k+1}$ is the best assimilation estimate of ζ_{model}^{k+1} . The uncertainty of the best assimilation estimate is defined:

$$\sigma_{model}^{k+1}(\varphi, \lambda) = \sqrt{\frac{F_{scale}[2 - P^k(\varphi, \lambda)][\sigma_{model}^k(\varphi, \lambda)]^2[\sigma_{MOD}^k(\varphi, \lambda)]^2}{P^k(\varphi, \lambda)[\sigma_{model}^k(\varphi, \lambda)]^2 + F_{scale}[2 - P^k(\varphi, \lambda)][\sigma_{MOD}^k(\varphi, \lambda)]^2}} \quad (56)$$

where $F_{scale} \geq 1$ is the scale factor. Due to the modification of gridded geometric height anomalies' uncertainty (cf. Equation 50), $\sigma_{model}^{k+1} \approx \sigma_{model}^k$ and $\hat{\zeta}_{model}^{k+1} \approx \zeta_{model}^k$ in SSH data void areas where no assimilation occurs because $\sigma_{MOD}^k \gg \sigma_{model}^k$. Note that the latter property can be considered redundant as $\hat{\zeta}_{model}^{k+1} \equiv \zeta_{model}^k \equiv \hat{\zeta}_{geom}^k$ already due to zero padding.

The presented data assimilation system (for a comprehensive flowchart, please refer to Figure 3 in **Publication VII**) is solved iteratively, which allows the introduction of more new information (i.e., refinements) to the final combined model, in contrast to a case where all available data are employed altogether to conduct a single assimilation iteration. In other words, all available data should be separated into sub-datasets ζ_{geom}^k used in consecutive iterations (repeated use of the same data should be avoided). Besides refining inaccuracies of the initial gravimetric quasigeoid model, the approach also allows correcting propagated SSH and DT data errors from earlier assimilation iterations. Note that for the next iteration, $\zeta_{model}^k \equiv \hat{\zeta}_{model}^{k+1}$ and $\sigma_{model}^k \equiv \sigma_{model}^{k+1}$ in Equations (55) and (56). Since $\sigma_{model}^{k+1} < \sigma_{model}^k$ and $\sigma_{model}^{k+1} < \sigma_{MOD}^k \sqrt{F_{scale}}$, the iterative solution converges. The process can be continued until σ_{model}^{k+1} reduces to zero, whereas each consecutive iteration introduces less new information to the combined model. In this regard, $F_{scale} > 1$ can be helpful, allowing extending the assimilation for more iterations by artificially scaling up the uncertainty of geometric height anomalies in determining the uncertainty of the best assimilation estimate. For a meaningful assimilation extension, $\sigma_{MOD}^k \sqrt{F_{scale}} > \sigma_{model}^k$, considering either mean or more minor uncertainties. Note that the iterative solution is always convergent regardless of the scale factor value (because $\sigma_{model}^{k+1} < \sigma_{model}^k$). In the following case study, $F_{scale} = 1$, as only two assimilation iterations could be conducted with the available data.

5.2 Preparation of Geometric Height Anomalies

For refining the errors in EIGEN-6C4 synthesised height anomalies, the same data used in Figure 26 validations were employed. These were divided between two assimilation iterations in a way that the data distribution would be roughly equal. In the first iteration ($k = 1$), Sektori and Salme C4–C6 shipborne GNSS datasets were used, whereas the second iteration ($k = 2$) included Salme C1–C3 shipborne GNSS and ALS datasets. Uncertainty estimates of these data were obtained by first deriving the uncertainty of SSHs, containing several components.

In the case of Salme shipborne GNSS datasets, the uncertainty component associated with GNSS measurements was estimated as:

$$\sigma_{GNSS}(\varphi^{SSH}, \lambda^{SSH}, t) = \frac{1}{4} \sum_{\xi=1}^4 |d_{A\xi}(\varphi^{SSH}, \lambda^{SSH}, t)|, \quad (57)$$

where discrepancies $d_{A\xi}$ (the four estimates are dependent on each other, whereby absolute values generally match closely) were calculated using Equation (40). Recall that

only two GNSS antennas could be used for the Salme C4 shipborne GNSS campaign, making it impossible to estimate location-dependent uncertainties of measurements in such a way (i.e., a rigid system of at least four GNSS antennas is needed). Furthermore, using only two GNSS antennas, the high-frequency attitude changes of the vessel could not be adequately eliminated from instantaneous SSHs (cf. Section 3.2.3), implying poorer data quality compared to the other campaigns. It is also unclear where poor data points might be located (i.e., empirical evidence from Equation 40 requires at least four GNSS antennas). For those reasons, the measurement-related uncertainty of the Salme C4 shipborne GNSS campaign was set three times larger than the mean uncertainty (estimated at 3.3 cm) of the other five campaigns. Since only three antennas were available during the Sektori shipborne GNSS campaign, Equation (40) control calculations could not be conducted either. However, as the data processing was similar to the Salme campaigns (cf. Section 3.2.3), the uncertainty component associated with GNSS measurements was assumed to be equivalent to the Salme campaigns' mean uncertainty of 3.3 cm.

Additional uncertainty components corresponding to VLM (cf. Equation 28; uncertainty was calculated according to the CORS used in Trimble Business Center solutions) and sailing-related corrections were considered. Assuming both the correction for the squat effect and static draft (cf. Section 3.2.4) have an uncertainty of around 2 cm, their combined uncertainty σ_{CORR} comes to approximately 3 cm. The final SSH uncertainty of shipborne GNSS campaigns was then derived as:

$$\sigma_{SSH}(\varphi^{SSH}, \lambda^{SSH}, t) = \sqrt{[\sigma_{GNSS}(\varphi^{SSH}, \lambda^{SSH}, t)]^2 + [\sigma_{VLM}(\varphi^{CORS}, \lambda^{CORS})(t - t_0^{RF})]^2 + \sigma_{CORR}^2}. \quad (58)$$

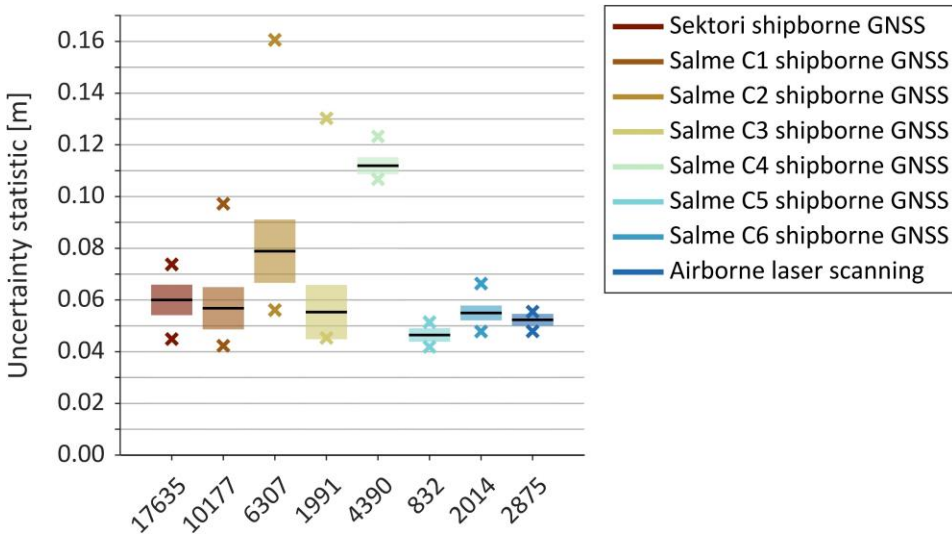


Figure 27. Descriptive statistics of geometric height anomalies' uncertainty estimates (cf. Equation 45). Black lines denote mean values, coloured bars standard deviation estimates, and coloured crosses minimum and maximum uncertainties. The X-axis shows the number of corresponding data points used in calculating the estimates. [Modified from **Publication VII**]

For ALS-derived SSHs, a slightly pessimistic (considering, e.g., Figure 24 results) constant uncertainty of 3 cm was assumed (a separate VLM-related uncertainty was not added to this estimate). It should be mentioned that standard deviation estimates of instantaneous SSHs within low-pass filtering windows (cf. Section 3.4) cannot be used as these grossly overestimate realistic SSH uncertainties, exceeding a decimetre for profile sections 5–7 (cf. Figure 25) due to waves with a significant wave height of around 0.6 m (refer to Jahanmard et al., 2022a) occurring during the survey.

Uncertainty estimates of geometric height anomalies were calculated using Equation (45). Figure 27 shows descriptive statistics of these estimates (considering the data limits from 59°N to 60°N and 23°E to 28°E). Slightly more considerable uncertainties associated with the Salme C2 shipborne GNSS campaign compared to other datasets (excluding the Salme C4 campaign) are caused by biases visible in Figure 20.

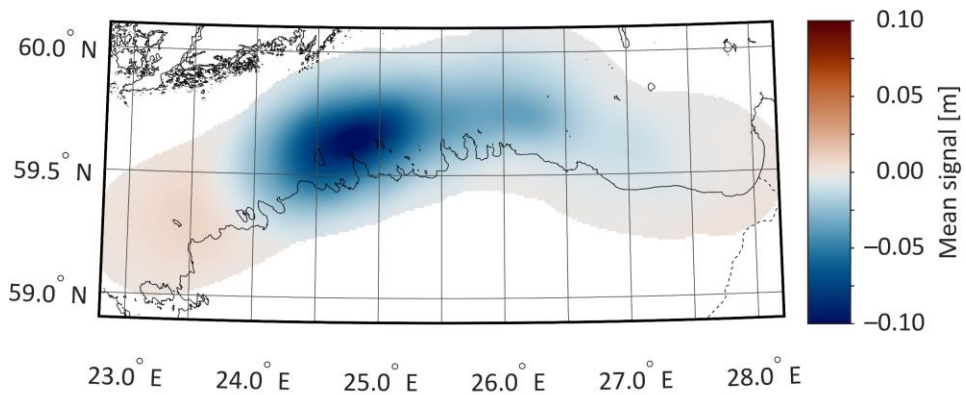
5.3 Gridding of Geometric Height Anomalies

Before further processing, the datasets (first and second iteration) of geometric height anomalies were thinned by averaging all points within each $0.01^\circ \times 0.02^\circ$ grid cell both in value and spatially because these were unnecessarily dense. Such thinning can also reduce data noise and help avoid aliasing during gridding. The first iteration geometric height anomalies were then reduced to residual values r_{geom}^1 (cf. Equation 46) using EIGEN-6C4 synthesised height anomalies. A zero pad was generated on a $0.01^\circ \times 0.02^\circ$ grid (residuals and zero pad can be seen in the upper sub-plot of Figure 29), where the minimum zero padding distance was set to 10 km (i.e., d_{zp} in Equation 51). The zero pad uncertainty was defined as the mean uncertainty of used geometric height anomalies. This definition yielded moderate enough uncertainty to avoid signal leakage to the zero padding region; the uncertainty was also sufficiently high to provide satisfactory gridding results in the SSH data and zero pad transition zones. Note that the padding region was set to be slightly larger than the case study area (an additional 0.5° and 1.0° in the latitudinal and longitudinal direction, respectively). All subsequent computations were conducted considering this larger area to avoid artefacts at edges.

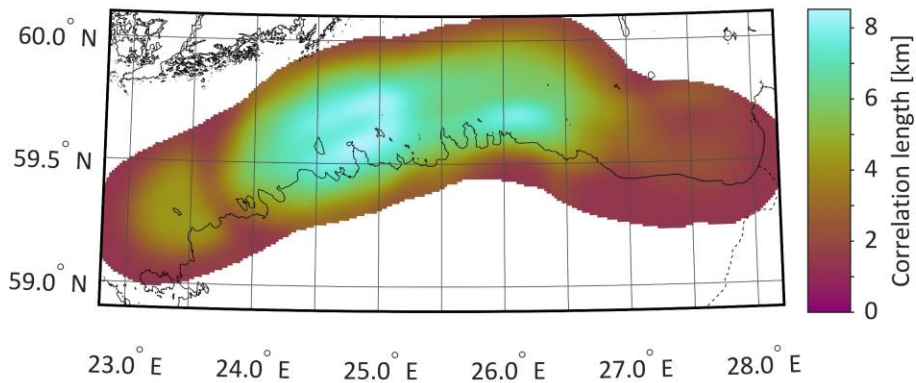
The determined geometric height anomaly residuals represent primarily shorter wavelength spectrum errors associated with EIGEN-6C4 but also contain inaccuracies of geometric height anomalies. This circumstance suggests that the residuals correlate only over a limited area. For enhancing covariance analysis and LSC-based gridding, a moving window with a radius of 30 km from a computation point was used for data selection. The zero pad was treated as a residual signal in covariance analysis and gridding. Computations were only conducted if at least 50 data points (not considering the zero pad) could be found within the 30 km radius (for the first iteration, 17721 computation points were found; locations of these points can be inferred from Figure 28).

Exponential covariance model parameters (cf. Equation 47) were estimated by computing empirical autocovariance values of residuals in 2 km distance groups after a sub-dataset mean signal (the further processed mean signal is shown in the upper sub-plot of Figure 28) had been removed. Groups with less than 50 station pairs (regarding pairs AB and BA the same, i.e., one) were excluded. The exponential covariance model was then fitted to the empirical values in the least-squares sense; signal variance was determined from data, not through the fitting procedure.

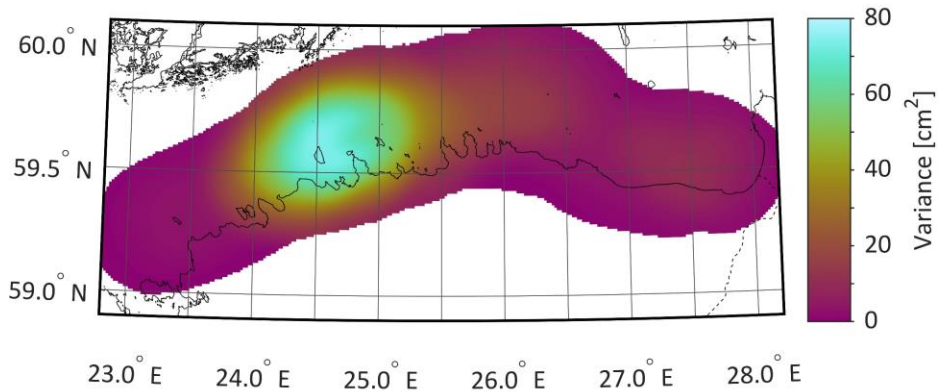
Change in the resulting parameter α and signal variance values was occasionally steep at nearby cells. Therefore, further processing of these parameters using a spatial filter



Min = -0.106 m Max = 0.009 m Mean = -0.015 m SD = 0.021 m

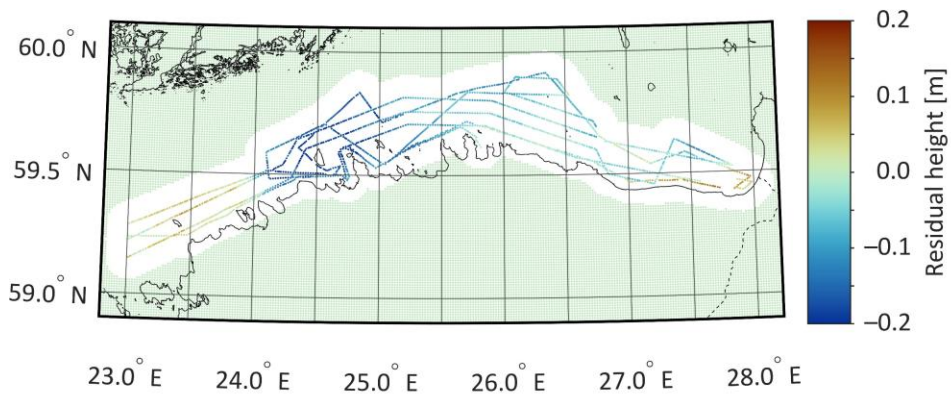


Min = 1.4 km Max = 8.5 km Mean = 3.9 km SD = 2.1 km

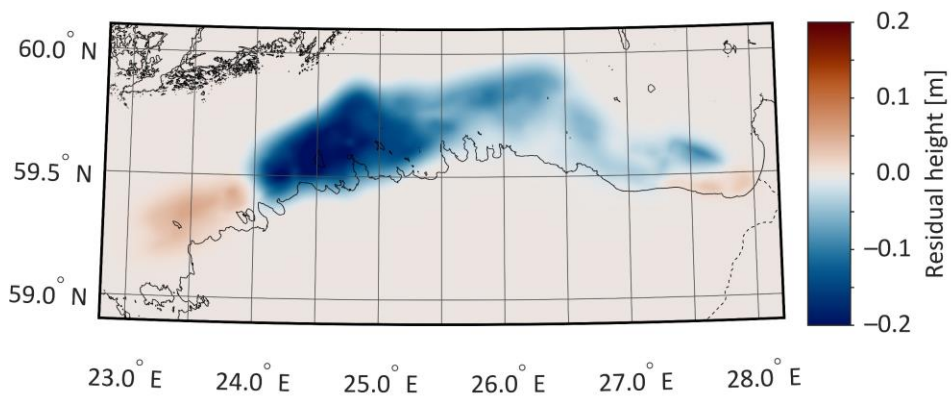


Min = 0.3 cm² Max = 74.3 cm² Mean = 16.1 cm² SD = 19.1 cm²

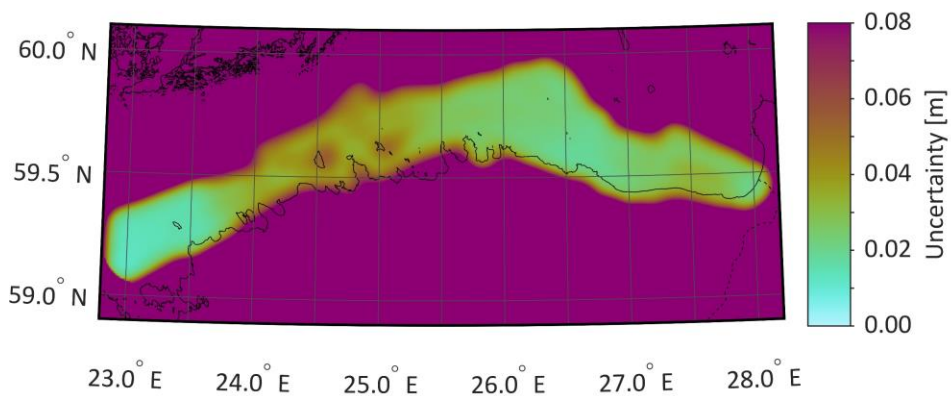
Figure 28. Estimated mean signals (above), correlation lengths (middle), and signal variances (below) used in LSC-based gridding of the first iteration geometric height anomaly residuals r_{geom}^1 . [Modified from **Publication VII**]



Min = -0.247 m Max = 0.121 m Mean = -0.005 m SD = 0.028 m



Min = -0.217 m Max = 0.054 m Mean = -0.013 m SD = 0.038 m



Min = 0.012 m Max = >1 m Mean = >1 m SD = >1 m

Figure 29. Geometric height anomaly residuals (including zero pad) of the first iteration before (i.e., r_{geom}^1 ; above) and after (i.e., \hat{r}_{geom}^1 ; middle) gridding, and the gridding-associated modified uncertainty σ_{MOD}^1 after spatial filtering (below). [Modified from **Publication VII**]

was needed to avoid gridding artefacts. A 3 km radius median filter was used first to eliminate potential gross estimates; these results were smoothed with a 5 km radius averaging filter. The mean signal was filtered similarly for methodological consistency, although this could have been skipped as it only had a negligible influence on the subsequent gridding results. Figure 28 shows the processed location-dependent mean signals (the upper sub-plot), correlation lengths (the middle sub-plot; correlation lengths $X_{1/2}$ are shown as these are more meaningful quantities than the parameter α), and signal variances (the bottom sub-plot). The heterogeneous nature of the geometric height anomaly residuals' signal is quite evident from the figure.

Geometric height anomaly residuals r_{geom}^1 (upper sub-plot of Figure 29) were gridded using LSC, where the input sub-datasets were centred using mean signal values shown in the upper sub-plot of Figure 28. An individual exponential covariance model (cf. Equation 47) described the \mathbf{C}_{st} and \mathbf{C}_{tt} matrices at each computation point, defined by correlation lengths and signal variances shown in Figure 28. The \mathbf{C}_{nn} matrix of errors was constructed using the estimated uncertainty values of geometric height anomalies (cf. Equation 45; also refer to Figure 27). The middle sub-plot of Figure 29 shows the resulting gridded geometric height anomaly residuals \hat{r}_{geom}^1 . Restoring the initially removed signal of EIGEN-6C4 synthesised height anomalies provided gridded geometric height anomalies $\hat{\zeta}_{geom}^1$ (cf. Equation 48).

The computed uncertainty of gridded geometric height anomalies σ_{geom}^1 was modified (cf. Equation 50) by setting the modification parameter $MP = 2$ (cf. Equation 51; for a visualization of the modification function, please refer to Figure 2 in **Publication VII**). Combined with a 10 km zero padding distance (d_{zp} in Equation 51), $MP = 2$ generated smooth transition zones from data to the zero pad regions. Note that the uncertainty of gridded geometric height anomalies is correlated with the distance to SSH data locations, also before the Equation (50) modification. This correlation means that the uncertainty-dependent data assimilation causes profile-wise (refer to, e.g., Figure 29 upper sub-plot) patterns to appear in the combined model. The previously described spatial filtering scheme was hence also used for filtering the modified σ_{MOD}^1 uncertainties to avoid (or at the very least significantly reduce) such patterns in the combined model. The resulting filtered σ_{MOD}^1 uncertainty is shown in the bottom sub-plot of Figure 29. Large values of uncertainty-associated descriptive statistics are due to the modification.

Gridding and associated uncertainty derivation of the second iteration geometric height anomalies were conducted almost precisely as already described. The only exception was that the first iteration assimilation result (i.e., EIGEN-6C4-i1; see the next section) was used for determining residual heights r_{geom}^2 instead of EIGEN-6C4 synthesised height anomalies.

5.4 Iterative Data Assimilation

Gridded geometric height anomalies and associated uncertainties were used to refine EIGEN-6C4 synthesised height anomalies. For that purpose, 8 cm constant uncertainty σ_{model}^1 was defined for the latter according to Figure 26 (the middle sub-plot) validation. Iterative data assimilation then followed Equations (53) to (56). The assimilation results (i.e., combined models) are denoted as EIGEN-6C4-i1 (recall that this model served as an input in the second iteration gridded geometric height anomalies' computation) and EIGEN-6C4-i2 according to the first and second iteration, respectively. The uncertainty of

EIGEN-6C4-i2 is shown in the bottom sub-plot of Figure 30. It can be noticed that the model has maintained its initial 8 cm uncertainty where SSH data were unavailable, which is due to the uncertainty modification (cf. Equations 50 and 51).

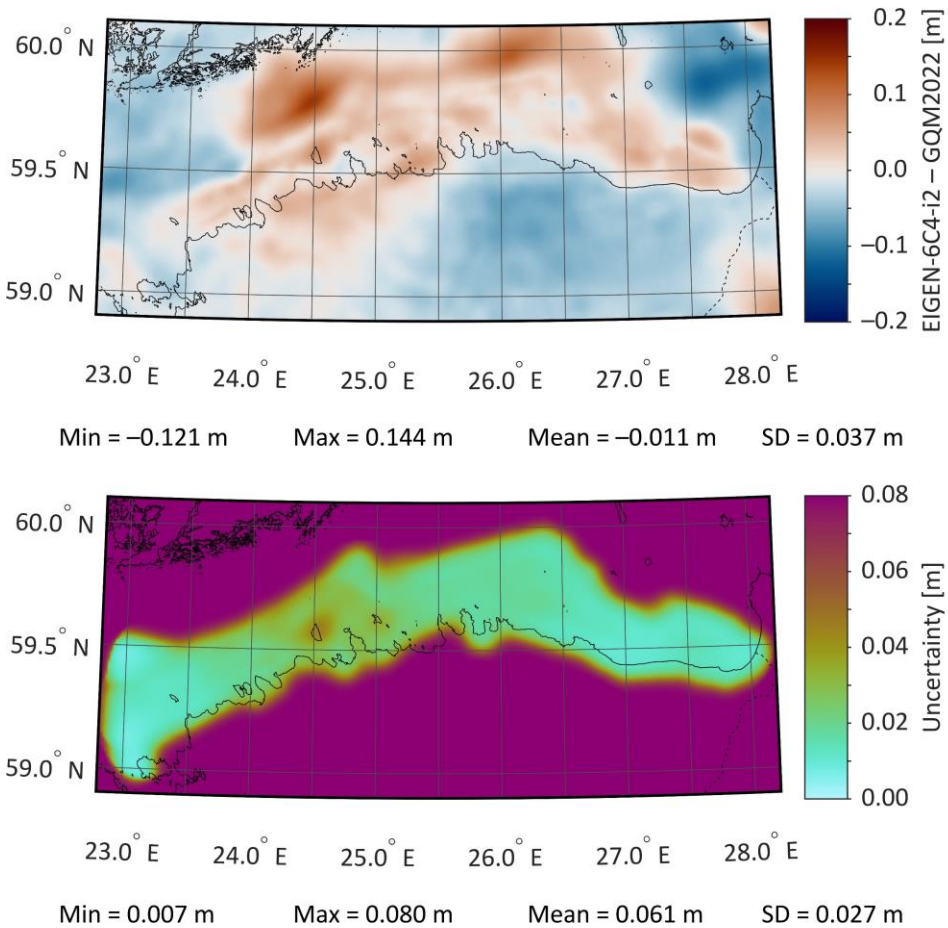


Figure 30. Differences between the EIGEN-6C4-i2 and GQM2022 models' surfaces (above) and EIGEN-6C4-i2-associated uncertainties (below). [Modified from **Publication VII**]

The GQM2022 quasigeoid model was employed to validate the assimilation outcome (cf. Figure 30 upper sub-plot). Compared to the initial differences in Figure 26 (the upper sub-plot), EIGEN-6C4-i2 appears to demonstrate improved modelling accuracy (contributions of both assimilation iterations are shown in Figure 31). By examining Figure 26 and Figure 30 differences along survey routes, the results suggest a reduction in mean difference from 7.4 cm to 1.1 cm and standard deviation estimate from 6.9 cm to 1.9 cm (i.e., a reduction in root mean square error from 10.1 cm to 2.2 cm – a five-fold improvement). These satisfactory results suggest that combined model accuracy in the same order of magnitude as GQM2022 could be achieved in regions of available SSH data by refining EIGEN-6C4 synthesised height anomalies for a few more iterations (this might require $F_{scale} > 1$ in Equation 56). Admittedly, the differences also increased in the case study region's eastern (between meridians 27.5°E and 28°E) and western (between

meridians 23°E and 24°E) extremes, but this relies on the assumption that GQM2022 is correct. According to Figure 13, GQM2022 heights should be slightly elevated in north-eastern Estonia. If this were true, Figure 30 offshore differences in north-eastern Estonia would slightly reduce. Thus, the appearance of those increased differences in Figure 30 compared to Figure 26 could also signify modelling improvements instead of propagated SSH and DT errors, but this remains to be verified.

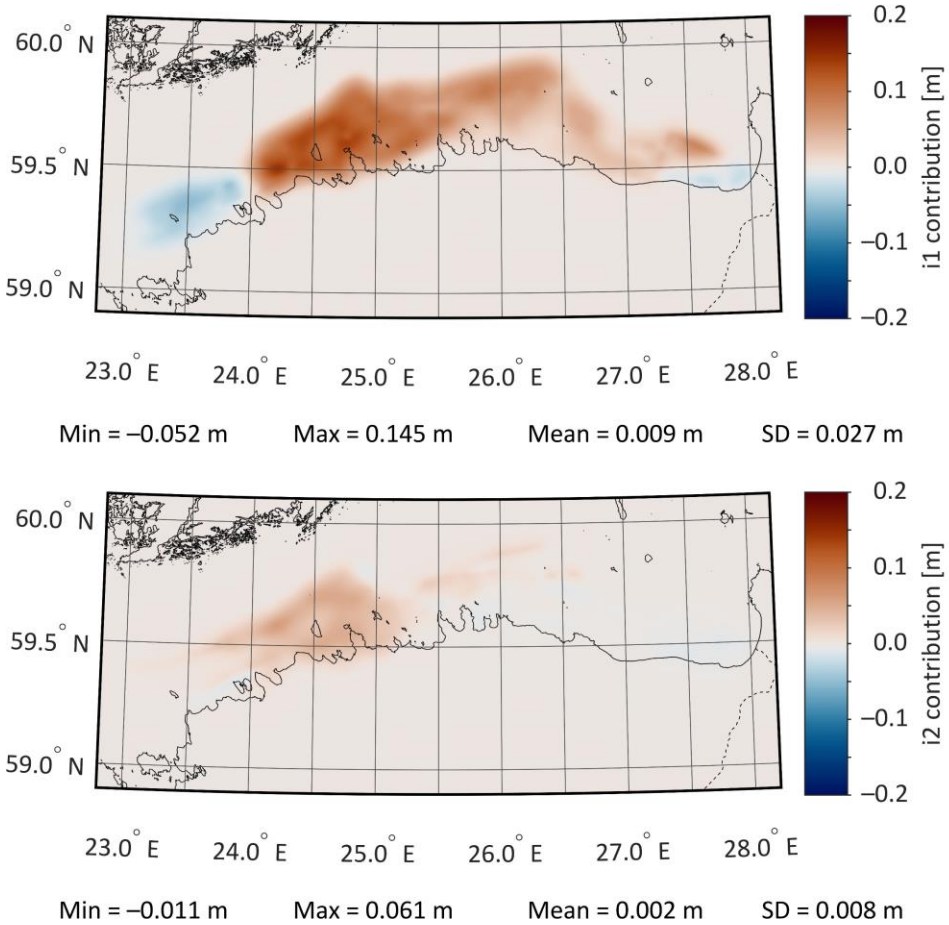


Figure 31. Contributions of the first (i.e., differences between EIGEN-6C4-i1 and EIGEN-6C4; above) and second (i.e., differences between EIGEN-6C4-i2 and EIGEN-6C4-i1; below) assimilation iteration to the final combined model EIGEN-6C4-i2. [Modified from **Publication VII**]

6 Discussion and Concluding Remarks

Technological advances in the offshore industry and applications related to marine sciences requiring ever-increasing data reliability, especially considering the changing climate, have necessitated enhanced development of marine (quasi)geoid models. This thesis has relatedly examined aspects of gravimetric quasigeoid modelling, offshore validation of such models, and the potential to use geoid geometry information in refining gravimetric models in problematic gravity data regions. The following sub-sections highlight the most important conclusions and give some direction for possible future research.

6.1 Gravimetric Quasigeoid Modelling

Section 1 examined one approach (LSMSA) for gravimetric quasigeoid modelling and how including bathymetry data influences the resulting model. It was demonstrated that using bathymetry-based RTM reduction in data processing could help refine gravity field determination from arbitrarily distributed discrete data by retaining valuable high-frequency gravity signal. Such refinements enhance quasigeoid modelling accuracy, where the most significant improvements occur in the rugged seabed regions. Local improvements of almost up to a decimetre were detected in the Norwegian coastal areas using GNSS-levelling control points (Figure 11). The bathymetry ruggedness index (cf. Equation 14 and Figure 9) is the first indicator that could be used for estimating the potential influence of bathymetry on quasigeoid modelling.

During RTM reduction computation, bathymetry-induced gravity signal is also generated inland from the coast (refer to Figure 7 in **Publication VI**). This circumstance implies that a poor-quality bathymetry dataset may diminish the accuracy of gravity field estimation and quasigeoid modelling on land. Although the used 15'' × 15'' GEBCO_2021 grid provided satisfactory outcomes, a higher-resolution and -quality bathymetry dataset could likely further improve the results. Another potential improvement source regards the RTM reduction computation algorithm. Here, the classical approach was used (Forsberg & Tscherning, 1981; Forsberg, 1984; cf. Equations 9 and 10), whereas, in recent years, the theory of RTM computation has advanced (e.g., Yang et al., 2022; Klees et al., 2023). More rigorous forward modelling of the gravity signal is expected to enhance the estimated gravity field and subsequent quasigeoid modelling.

It can be inferred from Section 1.5 that a constant uncertainty is assumed for terrestrial gravity data in determining modification parameters s_n that are required for spectral weighing of GGM and terrestrial data in the LSMSA (quasi)geoid modelling approach (refer to Ellmann, 2005b; Ellmann, 2012). However, the accuracy of terrestrial gravity data is clearly heterogeneous (see Figure 7); this has been one of the criticisms of any (quasi)geoid modelling approach. An interesting experiment would be to implement location-dependent parameterization analogously to the LSC approach used in Section 5.3, all the more as location-dependent gravity field prediction uncertainties can be easily estimated (refer to Equation 23). Uncertainty generalization would then be made within the integration cap σ_0 , not for the whole quasigeoid modelling target area. In that case, each computation point would have its own set of modification parameters s_n . It remains to be examined whether the benefits outweigh the increased computational load.

6.2 Accuracy Validation of Marine Quasigeoid Models

It was demonstrated in Section 4 that marine quasigeoid modelling errors can be successfully quantified using offshore geometric height anomalies. The latter were derived from SSHs measured by shipborne GNSS and ALS (cf. Section 3), with DT estimated according to the method in Section 2. Notably, only a 1.5 cm standard deviation was achieved from a comparison with the GQM2022 quasigeoid model using ALS-based geometric height anomalies (cf. Figure 25), suggesting good accuracy for all the participating datasets (i.e., the quasigeoid model, ALS-measured SSHs, and the estimated DT). The shipborne GNSS-determined geometry provided similarly good consistency. Results in Figure 24 indicate that an accuracy better than 5 cm could be expected for GQM2022 in the examined study area (cf. Figure 19), which is the accuracy aimed at in the BSCD2000 quasigeoid modelling offshore (Schwabe et al., 2020). Importantly, it was shown that the inclusion of new shipborne marine gravity data has significantly improved quasigeoid modelling in the eastern Gulf of Finland, where up to 9 cm improvements were detected (cf. Figure 25).

The developed DT and SSH determination methods could find wider use than only validating marine quasigeoid models. There is potential to use geoid-referred DT for studying marine processes (e.g., using temporally averaged mean DT), whereby highly accurate shipborne GNSS and ALS SSH datasets provide means to validate other sea level data sources, such as satellite altimetry (assuming surveys coincide with the satellite passing at the same time) or HDMs (SSHs can be reduced to DT using a high-resolution regional quasigeoid model). Regarding satellite altimetry: while the accessibility of shipborne GNSS and ALS data might be limited, altimetry data are abundantly available globally. Although coastal regions present a challenge, these data represent an opportunity for accurately determining geoid shape. For example, Jahanmard et al. (2022b) have already proven that satellite altimetry data are sufficiently accurate to quantify errors of the NKG2015 quasigeoid model in the eastern Gulf of Finland (also see Figure 25).

6.3 Iterative Refinement of Marine Quasigeoid Models

The capability of geometric height anomalies to quantify errors in marine quasigeoid modelling solutions implies that these data can also be used for improving the models. A straightforward iterative assimilation scheme was employed in Section 5 to prove that potential. A reduction of EIGEN-6C4 synthesised height anomalies' errors of up to around two decimetres (cf. Figure 26) into sub-decimetre (cf. Figure 30) was shown where SSHs were available. Also, note that the initial differences between EIGEN-6C4 and GQM2022 had a five-fold improvement along survey routes when the combined EIGEN-6C4-i2 model was compared to GQM2022. Hence, there is significant potential in using geometry information to enhance gravimetric quasigeoid models in regions where gravity data has poor quality or is entirely unavailable.

Analogously to GNSS-levelling fitting, such data assimilation could be a follow-on stage to conventional gravimetric quasigeoid modelling. Since the same quasigeoid model should be used over dry land and offshore, a combined seamless solution using GNSS-levelling data and offshore geometric height anomalies would be ideal – this should be further explored. Whilst gravimetric quasigeoid modelling requires previous experience and theoretical knowledge (e.g., physical laws governing the quasigeoid

determination), the proposed assimilation approach might also be a more accessible alternative that uses already existing gravimetric quasigeoid modelling solutions (or a high-degree GGM as in the Section 5 case study) in an easier-to-comprehend formulation.

List of Figures

Figure 1. Interrelations between reference surfaces and heights.	9
Figure 2. Schematic determination of a vessel’s under-keel clearance.	10
Figure 3. Terrain elevations and bathymetry in the Baltic Sea region. The dashed blue line shows the Estonian Maritime Administration obtained bathymetry data boundaries. Red dots denote locations of GNSS-levelling control points, and the green rectangle borders the quasigeoid modelling target area. [Modified from Publication VI]	23
Figure 4. Surface free-air gravity anomalies (final version 3 of the BSCD2000 gravity database release) and associated descriptive statistics. [Modified from Publication VI]...	24
Figure 5. The determined RTM anomalies by also considering bathymetry information. [Modified from Publication VI]	25
Figure 6. Empirical autocovariance curves of RTM anomalies and the corresponding least-squares fitted second-order Markov covariance models. The associated correlation lengths X_{12} are shown with dashed lines; signal variances C_0 are presented in the legend. [Modified from Publication VI]	26
Figure 7. Gravity data a priori error estimates used in LSC (note that LSC requires variances, i.e., squared values). [Modified from Publication VI]	26
Figure 8. Bathymetry contribution to gridded surface free-air gravity anomalies. [Modified from Publication VI]	27
Figure 9. Estimated ruggedness of bathymetry. [Modified from Publication VI]	29
Figure 10. Bathymetry contribution to gravimetric quasigeoid modelling. [Modified from Publication VI]	30
Figure 11. Residuals (mean removed) of gravimetric quasigeoid models relative to the Norwegian GNSS-levelling control points. [Modified from Publication VI]	31
Figure 12. The GQM2022 model, which has also been fitted (using a one-dimensional fit) to the Estonian GNSS-levelling control points. [Modified from Publication VI]	32
Figure 13. GNSS-levelling fitting residuals of GQM2022 after a one-dimensional fit to the Estonian GNSS-levelling control points. The red triangle denotes the general location of shipborne GNSS campaigns’ home harbour (see Section 3.2).	33
Figure 14. Interrelations between participating datasets. Solid lines denote reference epoch geometry and dashed lines VLM-affected geometry at a GNSS observation epoch. Global sea level rise and geoid change trends are neglected for simplification (i.e., the sea surface is assumed to be unchanged). Notice that the depicted dynamic bias (DB) is negative (cf. Equation 15), as is the height difference dh . [Modified from Publication V]	35
Figure 15. Locations of used TG stations, denoted by numbered circles. In the background is shown the annual levelled VLM rate according to the NKG2016LU model; the accompanying geoid rise rate [mm/year] is shown with dashed isolines.	38
Figure 16. Uncertainty estimates of DB (cf. Equation 20) at each TG station (cf. Figure 15) during the Salme C1 shipborne GNSS campaign (GPS week 2152; see Section 3.2). [Modified from Publication V]	40
Figure 17. Empirical autocovariance curves of DB corresponding to arbitrary time instances of 04.07.2017 00:00 UTC (left) and 28.07.2021 00:00 UTC (right), and respective least-squares fitted (distance groups with less than 15 station pairs were not considered) exponential-cosine covariance models. [Modified from Publication VII]	40

Figure 18. Dynamic topography (cf. Equation 25) and corresponding DB (used in deriving the DT estimates) along the vessel’s route during the Salme C2 shipborne GNSS campaign (GPS week 2168). The shaded area shows the DT-associated 1-sigma uncertainty envelope. [Modified from Publication VII]	41
Figure 19. Routes of shipborne GNSS campaigns and ALS survey. Blue triangles denote the locations of GNSS-CORS that were employed for GNSS post-processing	45
Figure 20. Descriptive statistics of instantaneous SSH discrepancies (cf. Equation 40). Black lines denote mean values, coloured bars standard deviation estimates, and coloured crosses 99th percentile minimum and maximum discrepancies. [Modified from Publication V]	48
Figure 21. The sum of absolute differences (SoAD) functions for shipborne GNSS campaigns (function associated with the Sektori campaign is hidden behind the Salme C1 function), normalized for comparability according to maximum values. Dashed vertical lines show the optimal filtering window sizes. [Modified from Publication V]	49
Figure 22. Sea surface height residuals of the Salme C1 shipborne GNSS campaign (GPS week 2152) at various data processing stages	49
Figure 23. Empirically estimated squat effect for Salme (left) and corrections for the static draft (right). [Modified from Publication V]	51
Figure 24. Descriptive statistics of low-pass filtered, corrected, and least-squares adjusted SSH residuals (cf. Section 3; GQM2022 was used in the Equation 31 reduction). Black lines denote mean values, coloured bars standard deviation estimates, and coloured crosses minimum and maximum residuals. The X-axis shows the number of corresponding data points used in calculating the estimates	54
Figure 25. Differences (mainly due to new gravity data – see red and green dots) between the NKG2015 and GQM2022 models’ surfaces in the eastern Gulf of Finland (above; notice also the out-of-box descriptive statistics) and discrepancies of those quasigeoid models relative to the ALS-derived geometric height anomalies (below; GPS week 2000). Numbers 1–7 (above) signify the sequence of flight routes (i.e., the order of profile sections in the bottom sub-plot). Descriptive statistics of GQM2022 discrepancies (in the box) are the same as those associated with ALS in Figure 24	55
Figure 26. Differences between the EIGEN-6C4 synthesised height anomalies and GQM2022 quasigeoid model in the Gulf of Finland (above), as well as discrepancies of the EIGEN-6C4 synthesised height anomalies (middle) and GQM2022 quasigeoid model (below) relative to the geometric height anomalies derived in Section 3. [Modified from Publication VII]	57
Figure 27. Descriptive statistics of geometric height anomalies’ uncertainty estimates (cf. Equation 45). Black lines denote mean values, coloured bars standard deviation estimates, and coloured crosses minimum and maximum uncertainties. The X-axis shows the number of corresponding data points used in calculating the estimates. [Modified from Publication VII]	62
Figure 28. Estimated mean signals (above), correlation lengths (middle), and signal variances (below) used in LSC-based gridding of the first iteration geometric height anomaly residuals <i>rgeom1</i> . [Modified from Publication VII]	64
Figure 29. Geometric height anomaly residuals (including zero pad) of the first iteration before (i.e., <i>rgeom1</i> ; above) and after (i.e., <i>rgeom1</i> ; middle) gridding, and the gridding-	

associated modified uncertainty σ_{MOD1} after spatial filtering (below). [Modified from **Publication VII**] 65

Figure 30. Differences between the EIGEN-6C4-i2 and GQM2022 models' surfaces (above) and EIGEN-6C4-i2-associated uncertainties (below). [Modified from **Publication VII**]..... 67

Figure 31. Contributions of the first (i.e., differences between EIGEN-6C4-i1 and EIGEN-6C4; above) and second (i.e., differences between EIGEN-6C4-i2 and EIGEN-6C4-i1; below) assimilation iteration to the final combined model EIGEN-6C4-i2. [Modified from **Publication VII**] 68

List of Tables

Table 1. Dynamic topography computation time windows.	39
--	----

References

- Ågren, J., & Sjöberg, L. E. (2014). Investigation of gravity data requirements for a 5 mm-quasigeoid model over Sweden. In U. Marti, *Gravity, Geoid and Height Systems* (pp. 143–150). Cham: Springer. doi:10.1007/978-3-319-10837-7_18
- Ågren, J., Sjöberg, L. E., & Kiamehr, R. (2009). The new gravimetric quasigeoid model KTH08 over Sweden. *Journal of Applied Geodesy*, 3(3), 143–153. doi:10.1515/JAG.2009.015
- Ågren, J., Strykowski, G., Bilker-Koivula, M., Omang, O., Mårdla, S., Forsberg, R., . . . Valssson, G. (2016). The NKG2015 gravimetric geoid model for the Nordic-Baltic region. *Proceedings of the International Symposium on Gravity, Geoid and Height Systems 2016*. Thessaloniki, Greece, 19–23 September 2016. doi:10.13140/RG.2.2.20765.20969
- Ågren, J., Strykowski, G., Bilker-Koivula, M., Omang, O., Mårdla, S., Oja, T., . . . Valssson, G. (2015). On the development of the new Nordic gravimetric geoid model NKG2015. *Proceedings of the 26th International Union of Geodesy and Geophysics (IUGG) General Assembly*. Prague, Czech Republic, 22 June–2 July 2015. doi:10.13140/RG.2.2.14121.49761
- Barrass, C. B. (2004). *Ship design and performance for masters and mates*. Oxford: Elsevier.
- Barzaghi, R., Carrion, D., Vergos, G. S., Tziavos, I. N., Grigoriadis, V. N., Natsiopoulos, D. A., . . . Rio, M. H. (2018). GEOMED2: high-resolution geoid of the Mediterranean. In J. T. Freymueller, & L. Sánchez, *International Symposium on Advancing Geodesy in a Changing World* (pp. 43–49). Cham: Springer. doi:10.1007/1345_2018_33
- Bonnefond, P., Laurain, O., Exertier, P., Calzas, M., Guinle, T., Picot, N., & The FOAM Project Team. (2022). Validating a new GNSS-based sea level instrument (CalNaGeo) at Senetosa Cape. *Marine Geodesy*, 45(2), 121–150. doi:10.1080/01490419.2021.2013355
- Bouin, M.-N., Ballu, V., Calmant, S., Boré, J.-M., Folcher, E., & Ammann, J. (2009). A kinematic GPS methodology for sea surface mapping, Vanuatu. *Journal of Geodesy*, 83(12), 1203–1217. doi:10.1007/s00190-009-0338-x
- Brockmann, J. M., Schubert, T., & Schuh, W.-D. (2021). An improved model of the Earth's static gravity field solely derived from reprocessed GOCE data. *Surveys in Geophysics*, 42(2), 277–316. doi:10.1007/s10712-020-09626-0
- Catarino, G. R. (2021). Dynamic draft and under keel clearance: a hydrographic view. *International Hydrographic Review*, 26, 21–37.
- Cipollini, P., Calafat, F. M., Jevrejeva, S., Melet, A., & Prandi, P. (2017). Monitoring sea level in the coastal zone with satellite altimetry and tide gauges. *Surveys in Geophysics*, 38(1), 33–57. doi:10.1007/s10712-016-9392-0
- Cocard, M., Geiger, A., Kahle, H.-G., & Veis, G. (2002). Airborne laser altimetry in the Ionian Sea, Greece. *Global and Planetary Change*, 34(1–2), 87–96. doi:10.1016/S0921-8181(02)00107-8
- Dahl, O. C., & Forsberg, R. (1998). Geoid models around Sognefjord using depth data. *Journal of Geodesy*, 72(9), 547–556. doi:10.1007/s001900050193
- Denker, H. (2015). A new European gravimetric (quasi)geoid EGG2015. *Proceedings of the 26th International Union of Geodesy and Geophysics General Assembly*. Prague, Czech Republic, 22 June–2 July 2015.

- Denker, H., & Roland, M. (2005). Compilation and evaluation of a consistent marine gravity data set surrounding Europe. In F. Sansò, *A Window on the Future of Geodesy* (pp. 248–253). Heidelberg: Springer. doi:10.1007/3-540-27432-4_42
- Ekman, M. (1989). Impacts of geodynamic phenomena on systems for height and gravity. *Bulletin Géodésique*, 63(3), 281–296. doi:10.1007/BF02520477
- Ellmann, A. (2005a). Two deterministic and three stochastic modifications of Stokes's formula: a case study for the Baltic countries. *Journal of Geodesy*, 79(1), 11–23. doi:10.1007/s00190-005-0438-1
- Ellmann, A. (2005b). Computation of three stochastic modifications of Stokes's formula for regional geoid determination. *Computers & Geosciences*, 31(6), 742–755. doi:10.1016/j.cageo.2005.01.008
- Ellmann, A. (2005c). A numerical comparison of different ellipsoidal corrections to Stokes' formula. In F. Sansò, *A Window on the Future of Geodesy* (pp. 409–414). Heidelberg: Springer. doi:10.1007/3-540-27432-4_70
- Ellmann, A. (2012). Using high-resolution spectral models of gravity anomaly for computing stochastic modifications of Stokes's formula. *Computers & Geosciences*, 39, 188–190. doi:10.1016/j.cageo.2011.07.001
- Ellmann, A., & Sjöberg, L. E. (2004). Ellipsoidal correction for the modified Stokes formula. *Bollettino di Geodesia e Scienze Affini*, 63(3), 153–172.
- Ellmann, A., Kaminskis, J., Parseliunas, E., Jürgenson, H., & Oja, T. (2009). Evaluation results of the Earth Gravitational Model EGM08 over the Baltic countries. *Newton's Bulletin*, 4, 110–121.
- Ellmann, A., Märdla, S., & Oja, T. (2020). The 5 mm geoid model for Estonia computed by the least squares modified Stokes's formula. *Survey Review*, 52(373), 352–372. doi:10.1080/00396265.2019.1583848
- Featherstone, W. E. (2009). Only use ship-track gravity data with caution: a case-study around Australia. *Australian Journal of Earth Sciences*, 56(2), 195–199. doi:10.1080/08120090802547025
- Fecher, T., Pail, R., Gruber, T., & The GOCO Consortium. (2017). GOCO05c: a new combined gravity field model based on full normal equations and regionally varying weighting. *Surveys in Geophysics*, 38(3), 571–590. doi:10.1007/s10712-016-9406-y
- Filmer, M. S., Hughes, C. W., Woodworth, P. L., Featherstone, W. E., & Bingham, R. J. (2018). Comparison between geodetic and oceanographic approaches to estimate mean dynamic topography for vertical datum unification: evaluation at Australian tide gauges. *Journal of Geodesy*, 92(12), 1413–1437. doi:10.1007/s00190-018-1131-5
- Foroughi, I., & Tenzer, R. (2017). Comparison of different methods for estimating the geoid-to-quasi-geoid separation. *Geophysical Journal International*, 210(2), 1001–1020. doi:10.1093/gji/ggx221
- Foroughi, I., Goli, M., Pagiatakis, S., Ferguson, S., & Novák, P. (2023). Data requirements for determination of the sub-centimetre geoid. *Earth-Science Reviews*, #104326. doi:10.1016/j.earscirev.2023.104326
- Forsberg, R. (1984). *A study of terrain reductions, density anomalies and geophysical inversion methods in gravity field modelling*. Columbus: Ohio State University.
- Forsberg, R., & Tscherning, C. C. (1981). The use of height data in gravity field approximation by collocation. *Journal of Geophysical Research: Solid Earth*, 86(B9), 7843–7854. doi:10.1029/JB086iB09p07843

- Förste, C., Abrykosov, O., Bruinsma, S., Dahle, C., König, R., & Lemoine, J.-M. (2019). ESA's Release 6 GOCE gravity field model by means of the direct approach based on improved filtering of the reprocessed gradients of the entire mission (GO_CONS_GCF_2_DIR_R6). *GFZ Data Services*. doi:10.5880/ICGEM.2019.004
- Förste, C., Bruinsma, S. L., Abrykosov, O., Lemoine, J.-M., Marty, J. C., Flechtner, F., . . . Biancale, R. (2014). EIGEN-6C4 the latest combined global gravity field model including GOCE data up to degree and order 2190 of GFZ Potsdam and GRGS Toulouse. *GFZ Data Services*. doi:10.5880/icgem.2015.1
- GEBCO Bathymetric Compilation Group 2021. (2021). The GEBCO_2021 grid – a continuous terrain model of the global oceans and land. *NERC EDS British Oceanographic Data Centre NOC*. doi:10.5285/c6612cbe-50b3-0cff-e053-6c86abc09f8f
- Goyal, R., Ågren, J., Featherstone, W. E., Sjöberg, L. E., Dikshit, O., & Balasubramanian, N. (2022). Empirical comparison between stochastic and deterministic modifiers over the French Auvergne geoid computation test-bed. *Survey Review*, 54(382), 57–69. doi:10.1080/00396265.2021.1871821
- Gruber, T., & Willberg, M. (2019). Signal and error assessment of GOCE-based high resolution gravity field models. *Journal of Geodetic Science*, 9(1), 71–86. doi:10.1515/jogs-2019-0008
- Gruno, A., Liibusk, A., Ellmann, A., Oja, T., Vain, A., & Jürgenson, H. (2013). Determining sea surface heights using small footprint airborne laser scanning. In C. R. Bostater, S. P. Mertikas, X. Neyt, & J.-P. Bruyant (Ed.), *Remote Sensing of the Ocean, Sea Ice, Coastal Waters, and Large Water Regions 2013*. Dresden, Germany, 23–26 September 2013: SPIE. doi:10.1117/12.2029189
- Heiskanen, W. A., & Moritz, H. (1967). *Physical geodesy*. San Francisco: W. H. Freeman and Company.
- Hordoir, R., Axell, L., Höglund, A., Dieterich, C., Fransner, F., Gröger, M., . . . Haapala, J. (2019). Nemo-Nordic 1.0: a NEMO-based ocean model for the Baltic and North seas – research and operational applications. *Geoscientific Model Development*, 12(1), 363–386. doi:10.5194/gmd-12-363-2019
- Huising, E. J., & Pereira, L. M. (1998). Errors and accuracy estimates of laser data acquired by various laser scanning systems for topographic applications. *ISPRS Journal of Photogrammetry and Remote Sensing*, 53(5), 245–261. doi:10.1016/S0924-2716(98)00013-6
- Idžanović, M., Ophaug, V., & Andersen, O. B. (2017). The coastal mean dynamic topography in Norway observed by CryoSat-2 and GOCE. *Geophysical Research Letters*, 44(11), 5609–5617. doi:10.1002/2017GL073777
- Ihde, J., Mäkinen, J., & Sacher, M. (2019). *Conventions for the definition and realization of a European Vertical Reference System (EVRS); version 5.2*. Retrieved April 7, 2023, from Federal Agency for Cartography and Geodesy (BKG): https://evrs.bkg.bund.de/SharedDocs/Downloads/EVRS/EN/Publications/EVRFConventions2007.pdf?__blob=publicationFile&v=4
- Ince, E. S., Förste, C., Barthelmes, F., Pflug, H., Li, M., Kaminskis, J., . . . Michalak, G. (2020). Gravity measurements along commercial ferry lines in the Baltic Sea and their use for geodetic purposes. *Marine Geodesy*, 43(6), 573–602. doi:10.1080/01490419.2020.1771486
- Jahanmard, V., Delpeche-Ellmann, N., & Ellmann, A. (2021). Realistic dynamic topography through coupling geoid and hydrodynamic models of the Baltic Sea. *Continental Shelf Research*, 222, #104421. doi:10.1016/j.csr.2021.104421

- Jahanmard, V., Delpeche-Ellmann, N., & Ellmann, A. (2022b). Towards realistic dynamic topography from coast to offshore by incorporating hydrodynamic and geoid models. *Ocean Modelling*, *180*, #102124. doi:10.1016/j.ocemod.2022.102124
- Jahanmard, V., Varbla, S., Delpeche-Ellmann, N., & Ellmann, A. (2022a). Retrieval of directional power spectral density and wave parameters from airborne LiDAR point cloud. *Ocean Engineering*, *266*(1), #112694. doi:10.1016/j.oceaneng.2022.112694
- Jamil, H., Kadir, M., Forsberg, R., Olesen, A., Isa, M. N., Rasidi, S., . . . Aman, S. (2017). Airborne geoid mapping of land and sea areas of East Malaysia. *Journal of Geodetic Science*, *7*(1), 84–93. doi:10.1515/jogs-2017-0010
- Julge, K., Gruno, A., Ellmann, A., Liibus, A., & Oja, T. (2014). Exploring sea surface heights by using airborne laser scanning. *Proceedings of the 2014 IEEE/OES Baltic International Symposium (BALTIC)*. Tallinn, Estonia, 27–29 May 2014: IEEE. doi:10.1109/BALTIC.2014.6887853
- Jürgenson, H., Liibus, A., & Ellmann, A. (2008). Geoid profiles in the Baltic Sea determined using GPS and sea level surface. *Geodesy and Cartography*, *34*(4), 109–115. doi:10.3846/1392-1541.2008.34.109-115
- Kärnä, T., Ljungemyr, P., Falahat, S., Ringgaard, I., Axell, L., Korabel, V., . . . Huess, V. (2021). Nemo-Nordic 2.0: operational marine forecast model for the Baltic Sea. *Geoscientific Model Development*, *14*(9), 5731–5749. doi:10.5194/gmd-14-5731-2021
- Kasper, J. F. (1971). A second-order Markov gravity anomaly model. *Journal of Geophysical Research*, *76*(32), 7844–7849. doi:10.1029/JB076i032p07844
- Khatun, A., Thombre, S., Bhuiyan, M. Z., Bilker-Koivula, M., & Koivula, H. (2020). GNSS-based techniques for accurate height component estimation of vessels in Finnish waterways – a review. In A. Ometov, J. Nurmi, E. S. Lohan, J. Torres-Sospedra, & H. Kuusniemi (Ed.), *Proceedings of the International Conference on Localization and GNSS*. Tampere, Finland, 2–4 June 2020: CEUR.
- Klees, R., Seitz, K., & Slobbe, C. (2023). Exact closed-form expressions for the complete RTM correction. *Journal of Geodesy*, *97*(4), #33. doi:10.1007/s00190-023-01721-5
- Knudsen, P., Andersen, O., & Maximenko, N. (2021). A new ocean mean dynamic topography model, derived from a combination of gravity, altimetry and drifter velocity data. *Advances in Space Research*, *68*(2), 1090–1102. doi:10.1016/j.asr.2019.12.001
- Kollo, K., & Ellmann, A. (2019). Geodetic reconciliation of tide gauge network in Estonia. *Geophysica*, *54*(1), 27–38.
- Kumari, P., Carter, W. E., & Shrestha, R. L. (2011). Adjustment of systematic errors in ALS data through surface matching. *Advances in Space Research*, *47*(10), 1851–1864. doi:10.1016/j.asr.2010.12.015
- Lagemaa, P., Elken, J., & Kõuts, T. (2011). Operational sea level forecasting in Estonia. *Estonian Journal of Engineering*, *17*(4), 301–331. doi:10.3176/eng.2011.4.03
- Lavrov, D., Even-Tzur, G., & Reinking, J. (2017). Expansion and improvement of the Israeli geoid model by shipborne GNSS measurements. *Journal of Surveying Engineering*, *143*(2), #04016022. doi:10.1061/(ASCE)SU.1943-5428.0000204
- Liibus, A., Kall, T., Rikka, S., Uiboupin, R., Suursaar, Ü., & Tseng, K.-H. (2020). Validation of Copernicus sea level altimetry products in the Baltic Sea and Estonian lakes. *Remote Sensing*, *12*(24), #4062. doi:10.3390/rs12244062

- Lu, B., Barthelmes, F., Li, M., Förste, C., Ince, E. S., Petrovic, S., . . . He, K. (2019). Shipborne gravimetry in the Baltic Sea: data processing strategies, crucial findings and preliminary geoid determination tests. *Journal of Geodesy*, *93*(7), 1059–1071. doi:10.1007/s00190-018-01225-7
- Lu, B., Xu, C., Li, J., Zhong, B., & van der Meijde, M. (2022). Marine gravimetry and its improvements to seafloor topography estimation in the southwestern coastal area of the Baltic Sea. *Remote Sensing*, *14*(16), #3921. doi:10.3390/rs14163921
- Mäkinen, J. (2008). *The treatment of the permanent tide in EUREF products*. Retrieved April 7, 2023, from Regional Reference Frame Sub-Commission for Europe (EUREF): http://www.euref.eu/TWG/EUREF%20TWG%20minutes/47-Brussels2008/05-Makinen_tides.pdf
- Märdla, S., Ågren, J., Strykowski, G., Oja, T., Ellmann, A., Forsberg, R., . . . Kaminskis, J. (2017). From discrete gravity survey data to a high-resolution gravity field representation in the Nordic-Baltic region. *Marine Geodesy*, *40*(6), 416–453. doi:10.1080/01490419.2017.1326428
- Märdla, S., Ellmann, A., Ågren, J., & Sjöberg, L. E. (2018). Regional geoid computation by least squares modified Hotine's formula with additive corrections. *Journal of Geodesy*, *92*(3), 253–270. doi:10.1007/s00190-017-1061-7
- Märdla, S., Ellmann, A., Oja, T., & Jürgenson, H. (2015). Improving and validating gravity data over ice-covered marine areas. In C. Rizos, & P. Willis, *IAG 150 Years* (pp. 263–270). Cham: Springer. doi:10.1007/1345_2015_163
- Medvedev, I. P., Rabinovich, A. B., & Kulikov, E. A. (2013). Tidal oscillations in the Baltic Sea. *Oceanology*, *53*(5), 526–538. doi:10.1134/S0001437013050123
- Medvedev, I. P., Rabinovich, A. B., & Kulikov, E. A. (2016). Tides in three enclosed basins: the Baltic, Black, and Caspian seas. *Frontiers in Marine Science*, *3*, #46. doi:10.3389/fmars.2016.00046
- Molodenskii, M. S., Eremeev, V. F., & Yurkina, M. I. (1962). *Methods for study of the external gravitational field and figure of the Earth*. Jerusalem: Israel Program for Scientific Translations.
- Moritz, H. (1980). *Advanced physical geodesy*. Karlsruhe: Wichmann.
- Moritz, H. (2000). Geodetic Reference System 1980. *Journal of Geodesy*, *74*(1), 128–133. doi:10.1007/s001900050278
- Nordman, M., Kuokkanen, J., Bilker-Koivula, M., Koivula, H., Häkli, P., & Lahtinen, S. (2018). Geoid validation on the Baltic Sea using ship-borne GNSS data. *Marine Geodesy*, *41*(5), 457–476. doi:10.1080/01490419.2018.1481160
- Noréus, J. P., Nyborg, M. R., & Hayling, K. L. (1997). The gravity anomaly field in the Gulf of Bothnia spatially characterized from satellite altimetry and in situ measurements. *Journal of Applied Geophysics*, *37*(2), 67–84. doi:10.1016/S0926-9851(97)00007-4
- Passaro, M., Cipollini, P., Vignudelli, S., Quartly, G. D., & Snaith, H. M. (2014). ALES: a multi-mission adaptive subwaveform retracker for coastal and open ocean altimetry. *Remote Sensing of Environment*, *145*, 173–189. doi:10.1016/j.rse.2014.02.008
- Pavlis, N. K., Holmes, S. A., Kenyon, S. C., & Factor, J. K. (2012). The development and evaluation of the Earth Gravitational Model 2008 (EGM2008). *Journal of Geophysical Research: Solid Earth*, *117*(B4), #B04406. doi:10.1029/2011JB008916

- Penna, N. T., Morales Maqueda, M. A., Martin, I., Guo, J., & Foden, P. R. (2018). Sea surface height measurement using a GNSS wave glider. *Geophysical Research Letters*, *45*(11), 5609–5616. doi:10.1029/2018GL077950
- Poutanen, M., Vermeer, M., & Mäkinen, J. (1996). The permanent tide in GPS positioning. *Journal of Geodesy*, *70*(8), 499–504. doi:10.1007/BF00863622
- Reichle, R. H. (2008). Data assimilation methods in the Earth sciences. *Advances in Water Resources*, *31*(11), 1411–1418. doi:10.1016/j.advwatres.2008.01.001
- Riley, S. J., DeGloria, S. D., & Elliot, R. (1999). Index that quantifies topographic heterogeneity. *Intermountain Journal of Sciences*, *5*(1–4), 23–27.
- Roggenbuck, O., & Reinking, J. (2019). Sea surface heights retrieval from ship-based measurements assisted by GNSS signal reflections. *Marine Geodesy*, *42*(1), 1–24. doi:10.1080/01490419.2018.1543220
- Roggenbuck, O., Reinking, J., & Härting, A. (2014). Oceanwide precise determination of sea surface height from in-situ measurements on cargo ships. *Marine Geodesy*, *37*(1), 77–96. doi:10.1080/01490419.2013.868385
- Rüdja, A., & Varbla, S. (2022). Estonian GNSS-leveling dataset with relevance to the implementation of the Baltic Sea Chart Datum 2000. *SEANOE*. doi:10.17882/87718
- Rulent, J., Calafat, F. M., Banks, C. J., Bricheno, L. M., Gommenginger, C., Green, J. A., . . . Martin, A. C. (2020). Comparing water level estimation in coastal and shelf seas from satellite altimetry and numerical models. *Frontiers in Marine Science*, *7*, #549467. doi:10.3389/fmars.2020.549467
- Saari, T., Bilker-Koivula, M., Koivula, H., Nordman, M., Häkli, P., & Lahtinen, S. (2021). Validating geoid models with marine GNSS measurements, sea surface models, and additional gravity observations in the Gulf of Finland. *Marine Geodesy*, *44*(3), 196–214. doi:10.1080/01490419.2021.1889727
- Schwabe, J., Ågren, J., Liebsch, G., Westfeld, P., Hammarklint, T., Mononen, J., & Andersen, O. B. (2020). The Baltic Sea Chart Datum 2000 (BSCD2000) – implementation of a common reference level in the Baltic Sea. *International Hydrographic Review*, *23*, 63–83.
- Shaw, L., Paul, I., & Henrikson, P. (1969). Statistical models for the vertical deflection from gravity-anomaly models. *Journal of Geophysical Research*, *74*(17), 4259–4265. doi:10.1029/JB074i017p04259
- Shih, H.-C., Yeh, T.-K., Du, Y., & He, K. (2021). Accuracy assessment of sea surface height measurement obtained from shipborne PPP positioning. *Journal of Surveying Engineering*, *147*(4), #04021022. doi:10.1061/(ASCE)SU.1943-5428.0000374
- Sjöberg, L. E. (1991). Refined least squares modification of Stokes' formula. *Manuscripta Geodaetica*, *16*(6), 367–375.
- Sjöberg, L. E. (1999). The IAG approach to the atmospheric geoid correction in Stokes' formula and a new strategy. *Journal of Geodesy*, *73*(7), 362–366. doi:10.1007/s001900050254
- Sjöberg, L. E. (2001). Topographic and atmospheric corrections of gravimetric geoid determination with special emphasis on the effects of harmonics of degrees zero and one. *Journal of Geodesy*, *75*(5–6), 283–290. doi:10.1007/s001900100174
- Sjöberg, L. E. (2003a). A computational scheme to model the geoid by the modified Stokes formula without gravity reductions. *Journal of Geodesy*, *77*(7–8), 423–432. doi:10.1007/s00190-003-0338-1

- Sjöberg, L. E. (2003b). Ellipsoidal corrections to order e^2 of geopotential coefficients and Stokes' formula. *Journal of Geodesy*, 77(3–4), 139–147. doi:10.1007/s00190-003-0321-x
- Sjöberg, L. E. (2003c). A solution to the downward continuation effect on the geoid determined by Stokes' formula. *Journal of Geodesy*, 77(1–2), 94–100. doi:10.1007/s00190-002-0306-1
- Sjöberg, L. E. (2004). A spherical harmonic representation of the ellipsoidal correction to the modified Stokes formula. *Journal of Geodesy*, 78(3), 180–186. doi:10.1007/s00190-004-0378-1
- Sjöberg, L. E., & Bagherbandi, M. (2012). Quasigeoid-to-geoid determination by EGM08. *Earth Science Informatics*, 5(2), 87–91. doi:10.1007/s12145-012-0098-7
- Sjöberg, L. E., & Bagherbandi, M. (2017). Applications and comparisons of LSMSA and RCR. In L. E. Sjöberg, & M. Bagherbandi, *Gravity Inversion and Integration* (pp. 181–202). Cham: Springer. doi:10.1007/978-3-319-50298-4_6
- Sjöberg, L. E., & Nahavandchi, H. (2000). The atmospheric geoid effects in Stokes' formula. *Geophysical Journal International*, 140(1), 95–100. doi:10.1046/j.1365-246x.2000.00995.x
- Slobbe, C., Klees, R., Farahani, H. H., Huisman, L., Alberts, B., Voet, P., & De Doncker, F. (2019). The impact of noise in a GRACE/GOCE global gravity model on a local quasi-geoid. *Journal of Geophysical Research: Solid Earth*, 124(3), 3219–3237. doi:10.1029/2018JB016470
- Slobbe, D. C., Klees, R., & Gunter, B. C. (2014). Realization of a consistent set of vertical reference surfaces in coastal areas. *Journal of Geodesy*, 88(6), 601–615. doi:10.1007/s00190-014-0709-9
- Slobbe, D. C., Verlaan, M., Klees, R., & Gerritsen, H. (2013). Obtaining instantaneous water levels relative to a geoid with a 2D storm surge model. *Continental Shelf Research*, 52, 172–189. doi:10.1016/j.csr.2012.10.002
- Stokes, G. G. (1849). On the variation of gravity on the surface of the Earth. *Transactions of the Cambridge Philosophical Society*, 8, 672–695.
- Sutherland, P., Brozena, J., Rogers, W. E., Doble, M., & Wadhams, P. (2018). Airborne remote sensing of wave propagation in the marginal ice zone. *Journal of Geophysical Research: Oceans*, 123(6), 4132–4152. doi:10.1029/2018JC013785
- Tenzer, R., & Foroughi, I. (2018). Effect of the mean dynamic topography on the geoid-to-quasigeoid separation offshore. *Marine Geodesy*, 41(4), 368–381. doi:10.1080/01490419.2018.1452810
- van der Sande, C., Soudarissanane, S., & Khoshelham, K. (2010). Assessment of relative accuracy of AHN-2 laser scanning data using planar features. *Sensors*, 10(9), 8198–8214. doi:10.3390/s100908198
- Varbla, S., Ellmann, A., & Delpeche-Ellmann, N. (2020). Utilizing airborne laser scanning and geoid model for near-coast improvements in sea surface height and marine dynamics. *Journal of Coastal Research*, 95(Sp1), 1339–1343. doi:10.2112/SI95-257.1
- Varbla, S., Ellmann, A., Märdla, S., & Gruno, A. (2017a). Assessment of marine geoid models by ship-borne GNSS profiles. *Geodesy and Cartography*, 43(2), 41–49. doi:10.3846/20296991.2017.1330771
- Varbla, S., Ellmann, A., Metsar, J., & Oja, T. (2017b). Meregravimeetritelised mõõdistused Soome lahel projekti FAMOS raames [The FAMOS marine gravity survey on the Gulf of Finland]. *Geodeet*, 47, 39–43.

- Vestøl, O., Ågren, J., Steffen, H., Kierulf, H., & Tarasov, L. (2019). NKG2016LU: a new land uplift model for Fennoscandia and the Baltic Region. *Journal of Geodesy*, *93*(9), 1759–1779. doi:10.1007/s00190-019-01280-8
- Vignudelli, S., Birol, F., Benveniste, J., Fu, L.-L., Picot, N., Raynal, M., & Roinard, H. (2019). Satellite altimetry measurements of sea level in the coastal zone. *Surveys in Geophysics*, *40*(6), 1319–1349. doi:10.1007/s10712-019-09569-1
- Vu, P. L., Frappart, F., Darrozes, J., Marieu, V., Blarel, F., Ramillien, G., . . . Birol, F. (2018). Multi-satellite altimeter validation along the French Atlantic coast in the southern Bay of Biscay from ERS-2 to SARAL. *Remote Sensing*, *10*(1), #93. doi:10.3390/rs10010093
- Vyskočil, V. (1970). On the covariance and structure functions of the anomalous gravity field. *Studia Geophysica et Geodaetica*, *14*(2), 174–177. doi:10.1007/BF02585616
- Wang, Y. M., Sánchez, L., Ågren, J., Huang, J., Forsberg, R., Abd-Elmotaal, H. A., . . . Zingerle, P. (2021). Colorado geoid computation experiment: overview and summary. *Journal of Geodesy*, *95*(12), #127. doi:10.1007/s00190-021-01567-9
- Wu, Y., Abulaitijiang, A., Featherstone, W. E., McCubbine, J. C., & Andersen, O. B. (2019). Coastal gravity field refinement by combining airborne and ground-based data. *Journal of Geodesy*, *93*(12), 2569–2584. doi:10.1007/s00190-019-01320-3
- Xie, S., Chen, J., Dixon, T. H., Weisberg, R. H., & Zumberge, M. A. (2021). Offshore sea levels measured with an anchored spar-buoy system using GPS interferometric reflectometry. *Journal of Geophysical Research: Oceans*, *126*(11), #e2021JC017734. doi:10.1029/2021JC017734
- Yang, J., Zhang, J., & Wang, C. (2019). Sentinel-3A SRAL global statistical assessment and cross-calibration with Jason-3. *Remote Sensing*, *11*(13), #1573. doi:10.3390/rs11131573
- Yang, M., Hirt, C., Wu, B., Deng, X. L., Tsoulis, D., Feng, W., . . . Zhong, M. (2022). Residual terrain modelling: the harmonic correction for geoid heights. *Surveys in Geophysics*, *43*(4), 1201–1231. doi:10.1007/s10712-022-09694-4
- Zhou, B., Watson, C., Legresy, B., King, M. A., Beardsley, J., & Deane, A. (2020). GNSS/INS-equipped buoys for altimetry validation: lessons learnt and new directions from the Bass Strait validation facility. *Remote Sensing*, *12*(18), #3001. doi:10.3390/rs12183001
- Zlinszky, A., Timár, G., Weber, R., Székely, B., Briese, C., Ressler, C., & Pfeifer, N. (2014). Observation of a local gravity potential isosurface by airborne lidar of Lake Balaton, Hungary. *Solid Earth*, *5*(1), 355–369. doi:10.5194/se-5-355-2014

Acknowledgements

Most of all, I would like to thank my supervisor Artu Ellmann for his time, guidance, and support throughout my studies and for providing valuable opportunities to be involved in academia. Already during my master's studies, he encouraged me to present and publish my research internationally. The success of my doctoral studies can be partially ascribed to these earlier experiences.

My gratitude also goes to the colleagues from the Nordic Geodetic Commission and the Baltic Sea Hydrographic Commission Chart Datum Working Group for their contribution to the employed data for quasigeoid modelling and insights regarding relevant topics to this thesis. I especially want to thank Gabriel Strykowski, Joachim Schwabe, and Jonas Ågren for valuable discussions regarding the presented research. I also want to thank colleagues from the Estonian Land Board, the Estonian University of Life Sciences, and AS Datel. Conversations with Andres Rüdja and Tõnis Oja, among others, have always provided new knowledge and ideas. My thanks also go to colleagues from the Technical University of Munich, especially Thomas Gruber, for welcoming me on my research visit there, which provided valuable insights into geopotential modelling and helped generate new ideas for future research. I am grateful to my co-authors Artu Ellmann, Nicole Delpeche-Ellmann, Jonas Ågren, Markku Poutanen, Aive Liibus, Kaimo Vahter, and Rivo Uiboupin without whom proper completion of the research would have been impossible. Last but not least, I want to thank my family and friends for their support during my doctoral studies.

The research of this thesis was supported by the Estonian Research Council grants "Development of an iterative approach for near-coast marine geoid modelling by using re-tracked satellite altimetry, in-situ and modelled data" [grant number PRG330] and "Development of continuous DYNAmic vertical REference for maritime and offshore engineering by applying machine learning strategies /DYNAREF/" [grant number PRG1785]. Additional funding sources are listed in corresponding sections of **Publications I to VII**.

Abstract

Iterative Refinement and Accuracy Validation of Marine Geoid Models

There is an increasing demand for accurate high-resolution marine (quasi)geoid models for modern offshore engineering, navigation, and research applications. Although the development of highly accurate marine (quasi)geoid models is supported by available (quasi)geoid modelling theory and approaches, there is a significant offshore limitation in the distribution and quality of marine gravity data. Substantially caused by gravity data void areas and/or inaccurate data, marine (quasi)geoid modelling errors are expected to reach up to a few decimetres in the shorter wavelength spectrum. However, since the conventional GNSS-levelling control points are unavailable offshore, marine (quasi)geoid modelling accuracy estimates are primarily a conjecture. This thesis investigates how marine (quasi)geoid modelling could be improved and, importantly, how the errors of resulting models could be quantified. To that end, aspects of gravimetric quasigeoid modelling, realistic dynamic topography derivation, shipborne GNSS and airborne laser scanning surveys, and iterative data assimilation are examined.

An essential component of the thesis was computing a gravimetric high-resolution quasigeoid model GQM2022 of the Baltic Sea region, which was needed to demonstrate the reliability of developed iterative data assimilation and validation approaches. The model computation also considered bathymetry through residual terrain model reduction during the gravity field determination from initial discrete gravity measurements. It was shown that including bathymetry data could help refine the resulting gravity field representation by retaining valuable short-wavelength gravity information. Such refinements can then enhance geoid modelling accuracy, where the most significant improvements should be expected in the rugged seabed regions. The quasigeoid modelling accuracy increased almost up to a decimetre locally in the coastal areas of Norway, where bathymetry contributed the most.

Offshore validation of such gravimetric quasigeoid modelling solutions requires an alternative to the GNSS-levelling control points used on land. Various measurement methods for determining sea surface heights could be employed, where removing dynamic topography from the measured sea surface heights yields geometric height anomalies. These are an independent representation of the marine geoid and are hence suitable for validating gravimetric models. This thesis focuses on determining sea surface heights from shipborne GNSS measurements and airborne laser scanning surveys, whereby dynamic topography is derived by combining hydrodynamic model data with tide gauge readings. The latter allows constraining errors of the two dynamic topography data sources and estimating the uncertainty for the modelled dynamic topography. The determined geometric height anomalies achieve good consistency with the computed gravimetric quasigeoid model GQM2022, suggesting that an accuracy better than 5 cm could be expected for quasigeoid modelling in the examined study area (Estonian and Latvian marine regions). In particular, the airborne laser scanning measured sea surface heights appear highly accurate. Only a 1.5 cm standard deviation was achieved from a comparison with the GQM2022 model in the eastern region of the Gulf of Finland. These comparisons also demonstrated up to 9 cm improvements in modelling accuracy due to new shipborne marine gravity data.

The possibility to reliably quantify marine quasigeoid modelling errors using geometric height anomalies further implies that these data could also be used to refine errors in

gravimetric modelling solutions. An iterative data assimilation scheme was developed to prove that potential. It was shown that errors of the EIGEN-6C4 global geopotential model synthesised height anomalies up to around two decimetres were reduced into sub-decimetre where sea surface heights were available. There is hence significant potential in using geometry information to enhance gravimetric quasigeoid models in regions where gravity data has poor quality or is entirely unavailable. It is proposed that analogously to GNSS-levelling fitting of gravimetric models to height systems on land, such data assimilation could be a follow-on stage to conventional gravimetric quasigeoid modelling offshore.

Lühikokkuvõte

Meregeoidi mudelite iteratiivne täpsustamine ja täpsuse valideerimine

Kaasaegsed inseneeria, navigatsiooni- ja teadusrakendused vajavad meregeoidi täpselt kirjeldavaid mudeleid. Kuigi olemasolevad (kvaasi)geoidi modelleerimise teooria ning meetodid võimaldavad kõrgtäpsete mudelite arvutamist, on üheks olulisimaks takistuseks oodatava täpsuse saavutamisel merealadel gravimeetriliste andmete vähesus ning ebatäpsus. Seetõttu võib eeldada, et meregeoidi mudelite vead ulatuvad kuni mõne detsimeetri suurusjärku gravitatsioonisignaali spektri lühilainepikkuste osas. Kuna aga (kvaasi)geoidi modelleerimise täpsuse valideerimiseks tavapäraselt kasutatavaid GNSS-nivelleerimise kontrollpunkte merele rajada ei saa, siis on meregeoidi modelleerimisel saavutatavad täpsushinnangud reeglina oletuslikud. Eelmainitust tulenevalt on käesoleva väitekirja eesmärkideks uurida, mis moodi oleks võimalik parendada meregeoidi mudelite täpsust, ning kuidas arvutatud mudelitele täpsushinnanguid määrata. Eesmärkide täitmiseks käsitleb töö gravimeetrilist kvaasigeoidi modelleerimist, realistliku dünaamilise meretopograafia arvutamist, laevapõhiseid GNSS ja aerolaserskaneerimise mõõdistusi, ning gravimeetriliste ja geomeetriliste andmete iteratiivset kombineerimist.

Üheks väitekirja olulisimaks osaks oli gravimeetrilise kõrgresolutsioonilise kvaasigeoidi mudeli GQM2022 arvutamine terve Läänemere regiooni kohta. Antud mudeli abil demonstreeriti väljatöötatud andmete kombineerimise ning valideerimise meetodite rakenduslikust. Mudeli loomise gravitatsioonivälja võrgustamise tööfaasi kaasati ka batümeetria andmeid, mille põhjal arvutatud jääkpinnamudeli reduktsiooni (*residual terrain model reduction*) abil taandati esialgsed ebakorrapäraselt paigutatud gravitatsiooniväärtuste punktandmed võrgustamiseks sobilikemaks. Tulemused näitavad, et batümeetria andmete selline kaasamine tagab võrgustatud gravitatsioonivälja suurema täpsuse, kuna nii säilitab modelleeritud väli oma kõrgsagedusliku komponendi. Säärased gravitatsioonivälja täpsustused aitavad omakorda tõsta ka kvaasigeoidi modelleerimise täpsust. Märkimisväärset täpsuse paranemist võib näha kohtades, kus batümeetriat iseloomustavad suured variatsioonid. Nii tõsis kvaasigeoidi modelleerimise täpsus pea detsimeetri võrra Norra rannikualadel, kus batümeetria andmete mõju oli suurim.

Gravimeetriliste kvaasigeoidi mudelite täpsuse valideerimine merealadel vajab uusi meetodeid, kuna maismaal tavapäraselt kasutatavaid GNSS-nivelleerimise kontrollpunkte rakendada ei saa. Eksisteerib erinevaid võimalusi merepinna kõrguse määramiseks referents ellipsoidi suhtes, kusjuures säärased merepinna kõrgused saab taandada geomeetrilisteks kõrgusanomaalia väärtusteks dünaamilise meretopograafia mõju eemaldamisega. Saadud kõrgusanomaaliad kirjeldavad meregeoidi gravimeetrilistest mudelistest sõltumatult, mistõttu on need sobivad gravimeetriliste kvaasigeoidi mudelite valideerimiseks. Antud väitekirjas käsitletakse merepinna kõrguste määramist laevapõhiste GNSS ning aerolaserskaneerimise mõõdistusega. Dünaamiline meretopograafia on aga tuletatud kombineerides sobiva hüdrodünaamika mudeli andmeid veemõõdujaamade lugemitega, mis võimaldab tuvastada mõlema andmestiku vigasid ning hinnata modelleeritud dünaamilise meretopograafia määramatust. Arvutatud geomeetrilised kõrgusanomaaliad ühtivad GQM2022 mudeliga hästi, viidates sellele, et uurimisala piires (Eesti ja Läti merealad) on võimalik kvaasigeoidi modelleerida vähemalt 5 cm täpsusega. Tasub ära märkimist, et eriti häid tulemusi saavutati aerolaserskaneerimise mõõdistusandmetega, kus võrdlus GQM2022 mudeliga Soome lahe idaosas andis

standardhälbe väärtuse vaid 1,5 cm. Need võrdlused demonstreerisid ka seda, et tänu uutele laeval mõõdistatud gravitatsiooniandmetele on kvaasigeoidi modelleerimise täpsus paranenud kuni 9 cm võrra.

Asjaolu, et geomeetriselised kõrgusanomaaliad võimaldavad tuvastada gravimeetriseliste kvaasigeoidi mudelite vigasid merealadel, viitab ka sellele, et neid andmeid saab lisaks rakendada gravimeetriseliste mudelite täpsustamiseks. Selle potentsiaali tõestamiseks töötati välja andmete iteratiivne kombineerimismetoodika. Tulemused näitavad, et EIGEN-6C4 globaalse geopotentsiaalimudeli põhiste kõrgusanomaaliade esialgsed vead kuni paar detsimeetrit vähenevad alla detsimeetri kohtades, kus merepinna kõrguse mõõdistusi läbi viidi. Võib järeldada, et geoidi kuju kirjeldavate geomeetriseliste andmete abil saab täpsustada gravimeetriselisi kvaasigeoidi mudeleid, eriti kohtades, kus gravitatsiooniandmete kvaliteet on kas halb või siis andmed puuduvad üldse. Sarnaselt gravimeetriseliste mudelite sobitamisele kõrgusvõrku GNSS-nivelleerimise punktide järgi maismaal, võiks välja töötatud andmete kombineerimismetoodika olla gravimeetriselise modelleerimise järgseks tööetapiks merealadel.

Appendix 1

Publication I

Varbla, S., Ellmann, A., & Delpêche-Ellmann, N. (2020). Validation of marine geoid models by utilizing hydrodynamic model and shipborne GNSS profiles. *Marine Geodesy*, 43(2), 134–162. doi:10.1080/01490419.2019.1701153



Validation of Marine Geoid Models by Utilizing Hydrodynamic Model and Shipborne GNSS Profiles

Sander Varbla^a, Artu Ellmann^{a,c} , and Nicole Delpêche-Ellmann^b

^aDepartment of Civil Engineering and Architecture, Tallinn University of Technology, Tallinn, Estonia; ^bDepartment of Cybernetics, Tallinn University of Technology, Tallinn, Estonia; ^cEstonian Land Board, Tallinn, Estonia

ABSTRACT

An essential role of the FAMOS international cooperation project is to obtain new marine gravity observations over the Baltic Sea for improving gravimetric geoid modelling. To achieve targeted 5 cm modelling accuracy, it is important to acquire new gravimetric data, as the existing data over some regions are inaccurate and sparse. As the accuracy of contemporary geoid models over marine areas remains unknown, it is important to evaluate geoid modelling outcome by independent data. Thus, this study presents results of a shipborne marine gravity and GNSS campaign for validation of existing geoid models conducted in the eastern section of the Baltic Sea. Challenging aspects for utilizing shipborne GNSS profiles tend to be with quantifying vessel's attitude, processing of noise in the data and referencing to the required datum. Consequently, the novelty of this study is in the development of methodology that considers the above-mentioned challenges. In addition, tide gauge records in conjunction with an operational hydrodynamic model are used to identify offshore sea level dynamics during the marine measurements. The results show improvements in geoid modelling due to new marine gravimetric data. It is concluded that the marine GNSS profiles can potentially provide complementary constraints in problematic geoid modelling areas.

ARTICLE HISTORY

Received 23 September 2019
Accepted 29 November 2019


KEYWORDS

FAMOS; geoid; Gulf of Finland; hydrodynamic model; marine gravimetry; shipborne GNSS

Introduction

An international cooperation project FAMOS (Finalising Surveys for the Baltic Motorways of the Sea) has been initiated to improve the quasigeoid model for the realization of the Baltic Sea Chart Datum 2000 (BSCD2000). This datum is expected to be used as the new common height reference system for the Baltic Sea hydrographic surveying and nautical charts (FAMOS 2019). To accomplish this, one of the primary goals is to improve the accuracy of GNSS (Global Navigation Satellite System) supported

CONTACT Sander Varbla  sander.varbla@taltech.ee 

 Supplemental data for this article can be accessed at <https://doi.org/10.1080/01490419.2020.1701153>.

© 2020 Informa UK Limited, trading as Taylor & Francis Group

bathymetric measurements and navigation by computing a new 5 cm marine geoid model over the entire Baltic Sea.

Unfortunately, the existing gravimetric data over some sections of the Baltic Sea and adjacent regions appear to be spatially insufficient and inaccurate for satisfying the 5 cm geoid modelling requirements (FAMOS 2019). It is estimated that the accuracy of contemporary geoid models over marine areas could often be deficient by 15–20 cm, especially in the gravity data void areas. Therefore, the primary goal of the dedicated marine gravity and GNSS campaign for the Gulf of Finland (the northeastern part of the Baltic Sea) was to fill the large gravity data void areas.

On land, geoid models are customarily validated by using precise GNSS-levelling points; however, such control points cannot be established offshore. Instead, marine geoid models can be assessed by utilizing shipborne GNSS measurements, which have been proven to be effective. For instance, the Nordic Geodetic Commission (NKG) NKG04 gravimetric quasigeoid model (Forsberg, Strykowski, and Solheim 2004) slopes across the Baltic Sea were assessed using GNSS profiles by Jürgenson, Liibus, and Ellmann (2008), whereas the absolute errors of the NKG2015 (Ågren et al. 2016) and the Finnish FIN2005N00 (Bilker-Koivula 2010) quasigeoid models were assessed by Nordman et al. (2018). The NKG2015 model has also been assessed by Varbla et al. (2017). Note that over marine areas, the quasigeoid coincides with the geoid; thus, for brevity the shorter term will be used in the further text.

Thus, different approaches have been employed and one of the key differences highlighted is in determining the attitude of a surveying vessel. For example, in Nordman et al. (2018), an inertial measurement unit (IMU) for specifying vessel's attitude was employed during the GNSS data sampling. In contrast, shipborne GNSS experiments along the Israeli coast between years 2011 and 2015 utilized four GNSS antennas for determining variations in vessel's attitude through the calculation of a spatial rotation between two sets of coordinates (Lavrov, Even-Tzur, and Reinking 2016). Corrections from vessel's attitude were calculated for every GNSS measuring epoch.

The present study utilizes a similar approach to Lavrov, Even-Tzur, and Reinking (2016) by using three GNSS antennae mounted on a surveying vessel. However, instead of calculating the attitude corrections at the locations of each individual GNSS antennae, the combined GNSS height time-series are simply referred to the location of vessel's mass center by a spatial interpolation method (see section 'Reducing effects from vessel's attitude'). We demonstrate that such an approach yields sufficient data quality and most significantly, has promising results during rough sea measurements. Such a method replaces the need for utilizing costly IMU and allows simpler and less time-consuming data processing and analysis.

Another difference in the GNSS approaches utilized is in the methodologies used for filtering noise from the data – sea surface oscillations must be eliminated for rigorous geoid model assessment. For example, Nordman et al. (2018) utilized a moving average low-pass filter. On the contrary, Varbla et al. (2017) developed a double low-pass filtering method that combines a moving median with a moving average. The method is further examined in the present study.

It is important to understand that for marine geoid validation by shipborne GNSS profiles, the dynamic topography (DT) that separates instantaneous sea surface heights (SSH) from geoid needs to be accounted for. Alternatively, due to insufficient marine geoid data, SSH can also be computed by using the SSH anomaly (SSHA) that separates SSH from the mean sea level (MSL). The latter is often utilized due to most data being referenced to MSL (e.g., satellite altimetry products, tide gauges and hydrodynamic models).

Tide gauge (TG) records that refer to a particular vertical datum have been traditionally utilized for estimating DT and SSH. Nevertheless, TGs are usually land bounded; hence, their data are not necessarily representative offshore. For offshore verifications, a few studies have complemented TG records with a regionally adapted hydrodynamic model (HDM). For estimating instantaneous DT corrections, Nordman et al. (2018) used the Baltic Sea Physical Analysis and Forecasting model (Huess 2018), whereas Lavrov, Even-Tzur, and Reinking (2016) used the RIO2007 model (obtained from the European Space Agency developed ‘Archiving, Validation and Interpretation of Satellite Oceanographic data – AVISO’ portal). Alternatively, Slobbe et al. (2018) used two regional high-resolution HDMs, Dutch Continental Shelf model ver. 6 (Zijl, Verlaan, and Gerritsen 2013) and Zuidelijk Noordzee model ver. 4 (Zijl, Sumihar, and Verlaan 2015), to connect TGs of near-coast islands with the national vertical datum.

In this study, a regional HBM-EST model (Estonian implementation of the HIROMB-BOOS model – High Resolution Operational Model for the Baltic Sea-Baltic Operational Oceanographic System) is incorporated for comparing GNSS derived instantaneous SSH (iSSH) with geoidal heights. Also, an empirical method ‘of weights’ is developed that uses a weighted average approximation of TG readings for eliminating a dynamic bias (DB) from the used HDM.

The outline of the paper is as follows. First, theoretical principles of determining iSSH and their use for validating geoid models are outlined. The study area and utilized data are then described. Next, the calculation of the vessel’s attitude effects and filtering of the GNSS data with a double low-pass filtering method are examined. Calculation of the corrections added to the profiles are also discussed. Finally, differences between geoid models and GNSS profiles are presented. A brief summary concludes the paper.

Theoretical principles of marine geoid model validation

Interrelations between sea surface height, geoid surface and mean sea level

MSL is usually calculated from repeated SSH measurements that are averaged over a selected time period. Historically, MSL at selected TG site(s) has also been adopted as the ‘zero’ level of the national/local vertical datum (Kakkuri and Poutanen 1997). Nevertheless, the resulting MSL estimates may vary due to different time spans used. Therefore the ‘static’ geoid appears to be a more appealing reference surface for describing sea level variations. Even though the geoid modelling quality varies globally (mainly depending on the gravity data availability and density), the achievable accuracy of contemporary regional high-resolution geoid models could reach a few cm.

On land, high-precise GNSS-levelling points are customarily used to fit gravimetric geoid models (N^{GG}) to a (MSL-related) national vertical datum; the result could also be called height conversion surface (N). In other words, an appropriate N model extends the national vertical datum to marine areas. Due to a lack of GNSS-levelling control data over marine areas, N can be obtained by cautious extrapolation:

$$N(\varphi, \lambda) = N^{GG}(\varphi, \lambda) - H^{GG}(\varphi, \lambda) \quad (1)$$

where the term H^{GG} denotes a geoid model correction, which is a location dependent value. In case of one-dimensional (1D) bias removal, H^{GG} is a constant. This fitting procedure reduces possible systematic biases in between the geoid model and MSL. Thus, the corrected model N coincides approximately with the zero of the (historical) national vertical datum $MSL(\varphi, \lambda) \approx N(\varphi, \lambda)$ and $SSHA(\varphi, \lambda) \approx DT(\varphi, \lambda)$.

As a result, we show that N can be used instead of MSL as a reference for SSH measurements. This is valid not only to the coastal areas where TGs exist but also in the offshore domain. Accomplishing this signifies that SSHA can now be replaced by DT. In practice, however, there are discrepancies caused by measurement errors, different resolutions and accuracies of reference surface models, e.g., MSL is affected by persistent external forces, such as wind, currents, salinity, etc. (see, e.g., Le Provost 1990). Thus, the assumption $MSL(\varphi, \lambda) \approx N(\varphi, \lambda)$ is only an approximation – to appraise used data and corresponding acquisition technologies/methods. Next, we review interrelations that facilitate the use of GNSS derived SSH for validating a geoid model.

Utilizing shipborne GNSS profiles for geoid model assessment

SSH can be determined from GNSS measurements, which provide heights with respect to geodetic reference ellipsoid, e.g., GRS-80. If the vertical range (R) of the reference point (e.g., vessel’s mass center) with respect to the sea surface is known (a constant value), then $iSSH$ can be computed (Figure 1):

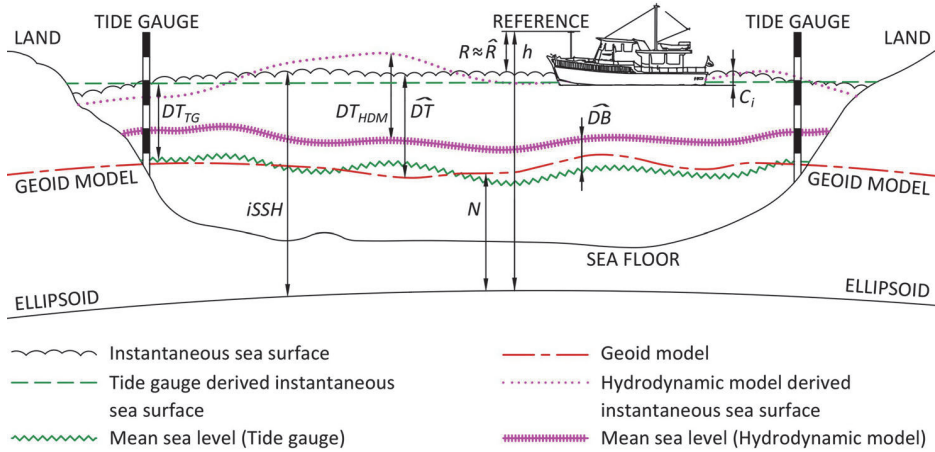


Figure 1. Seaborne derivation of geoid heights with respect to participating reference surfaces. For the used symbols consult the text.

$$iSSH(\varphi_i, \lambda_i) = h(\varphi_i, \lambda_i) - R \quad (2)$$

where h is ellipsoidal height at a location (i.e., vessel's reference point) with geodetic coordinates (φ, λ) and subscript i denotes an i -th time-instant of the measurement.

As $iSSH$ is affected by the wind direction and speed, tidal movement, etc., it can be referred to N by the DT (initially unknown) estimate \widehat{DT} (cf. Figure 1):

$$N(\varphi, \lambda) = iSSH(\varphi_i, \lambda_i) - \widehat{DT}(\varphi_i, \lambda_i) - C_i \quad (3)$$

where C_i marks additional vessel-related corrections at a time-instant i , e.g., correction due to squat (dynamic draft) and static draft (see section 'Accounting for vessel related corrections'). This expression can be used for marine geoid model validation. We postpone the estimation of DT and C_i into the next section and section 'Accounting for vessel related corrections', respectively. Note that $iSSH$ in Eq. 3 can be computed by Eq. 2. However, as direct measuring of R may be inaccurate or complicated, a simpler approach for determining the right-hand side of Eq. 3 can be adopted (preliminarily tested by Varbla et al. 2017). An auxiliary term h^C (that embeds all measurable and model quantities, e.g., DT estimate and corrections due to static draft and squat) is introduced, i.e.,

$$h^C(\varphi_i, \lambda_i) = h(\varphi_i, \lambda_i) - \widehat{DT}(\varphi_i, \lambda_i) - C_i \quad (4)$$

Eq. 3 is thus simplified into:

$$N(\varphi, \lambda) = h^C(\varphi_i, \lambda_i) - R \quad (5)$$

The unknown range R is empirically estimated as an average difference between the computed h^C and geoid model (to be assessed) heights N

at known geoid height location(s):

$$-\hat{R} = \frac{1}{m} * \sum_{n=1}^m [N(\varphi, \lambda) - h^C(\varphi_i, \lambda_i)]_n \quad (6)$$

where subscript i denotes a time-instant of the measurement and m total amount of GNSS measurements; n is the measurement at a time-instant i . The DT and C_i that are embedded in h^C can be temporally and spatially interpolated, see sections ‘Dynamic topography correction for GNSS profiles’ and ‘Accounting for vessel related corrections’. The GNSS measurements can be conducted at the harbor nearby a precise GNSS-levelling point (ideally, one that is also been used for fitting a geoid model to the national vertical datum, i.e., N is precisely known in such a location) before sailing off to a GNSS-profile survey.

Thus, significant deviations from the geoid model along the entire surveying route (locations φ, λ) may now reveal errors in the tested model:

$$[N(\varphi, \lambda) - h^C(\varphi, \lambda)] + \hat{R} = D(\varphi, \lambda) \quad (7)$$

where D is the geoid model deviation (i.e., error) from h^C at a location with geodetic coordinates (φ, λ) . Eq. 7 is essentially the usable approximation of Eq. 3 and thus the main equation to be used for marine geoid validation in the present study. Hence, the method allows determination of deficiencies either in geoid modelling and/or iSSH/DT estimates.

Using hydrodynamic model and tide gauges to determine offshore dynamic topography

Referring to Eq. 3, the left-hand (modelled) and the right-hand side (measured) will not entirely agree with each other. These discrepancies (Eq. 7) manifest as deficiencies in geoid modelling and/or the right-hand side terms of Eq. 3. The DT term can be numerically estimated as follows.

For example, if no usable HDM over the area of interest is available, then DT can be approximated with nearby TG station readings at a time-instant i . If the coastline roughly follows parallels or meridians, the along-shore DT can be spatially interpolated from adjacent TG station readings (cf. Figure 2) as a function of only one coordinate, either longitude or latitude. Note that DT extrapolation from TGs toward open sea may provide poor results.

More reasonably, the DT can also be determined from a suitable HDM by using the vessel’s position $(\varphi_i, \lambda_i, h_i)$ at a time-instant i of interest. However, a modelled sea level may have a bias relative to a geodetic reference system – see, e.g., Allik (2014). This dynamic bias (DB) has a low-frequency component that varies from location to location and is slowly changing in time (Lagemaa, Elken, and Kõuts 2011). Therefore, an HDM

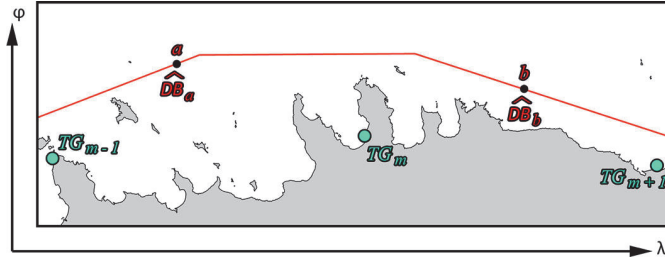


Figure 2. Determination of offshore DB in DT_{HDM} by using TG time series. TG_{m-1} , TG_m and TG_{m+1} are the locations of TG stations, a and b denote individual GNSS profile (red line) points with coordinates φ_i , λ_i , h_i , whereas \widehat{DB}_a and \widehat{DB}_b are the corresponding corrections for DT_{HDM} .

derived MSL can deviate from the historic MSL and consequently from the national vertical datum. Thus, the TG station readings can be used for determining and eliminating such a DB in the HDM (cf. Figure 2).

Hence, in offshore it is recommended to use modelled sea level estimates in conjunction with TG data. For this, the following empirical method ‘of weights’ has been developed in the present study. First, the difference between the HDM induced DT_{HDM} and TG readings DT_{TG} are calculated at locations of individual TG stations:

$$DB(\varphi_j, \lambda_j)_i = DT_{HDM}(\varphi_j, \lambda_j)_i - DT_{TG}(\varphi_j, \lambda_j)_i \quad (8)$$

where $j = 1, \dots, m-1, m, m+1, \dots, n$ denotes a TG station (Figure 2); n is the number of TG stations involved. Subscript i denotes an i -th time-instant.

Then, the weighted correction \widehat{DB} for an offshore point at an i -th time-instant can be calculated. For example, at the location of GNSS profile point a (Figure 2), the correction is:

$$\widehat{DB}_a(\varphi_i, \lambda_i) = \frac{DB(\varphi_1, \lambda_1)_i + \dots + 2*DB(\varphi_{m-1}, \lambda_{m-1})_i + 2*DB(\varphi_m, \lambda_m)_i + \dots + DB(\varphi_n, \lambda_n)_i}{n+2} \quad (9)$$

whereas at the location of GNSS profile point b (Figure 2), the correction is:

$$\widehat{DB}_b(\varphi_i, \lambda_i) = \frac{DB(\varphi_1, \lambda_1)_i + \dots + 2*DB(\varphi_m, \lambda_m)_i + 2*DB(\varphi_{m+1}, \lambda_{m+1})_i + \dots + DB(\varphi_n, \lambda_n)_i}{n+2} \quad (10)$$

Note that the weights of DBs at the locations of TGs depend on the area under inspection (the DB values at two adjacent TG stations, i.e., pairs $m-1/m$ and $m/m+1$, are weighted by the factor two, cf. Eqs. 9 and 10). Such a method is universal and can be used regardless of the locations of TG stations, as opposed to one-coordinate interpolation, which requires the coastline to follow parallels or meridians (more details in section ‘Dynamic topography correction for GNSS profiles’). However, if all the TGs are

situated on the shore following either parallels or meridians, the method only works if: (i) the GNSS profile stays close to the coast and (ii) the geoid surface is not strongly tilting in the direction perpendicular to the coast. Results far from coast can then be improved if the TGs surround the profile (e.g., inclusion of TGs from the opposite coasts of narrow gulfs and bays).

Thus, the initially unknown offshore \widehat{DT} at an i -th time-instant can now be estimated as:

$$\widehat{DT}(\varphi_i, \lambda_i) = DT_{HDM}(\varphi_i, \lambda_i) - \widehat{DB}(\varphi_i, \lambda_i) \quad (11)$$

This expression will be used in section ‘Differences between geoid models and GNSS profiles’ for relating the GNSS profiles to the geoid models to be validated.

Study area and the survey campaign data

The Gulf of Finland, located in the south-eastern section of the Baltic Sea, has an elongated geometry with a length of approximately 400 km and width varying from 48 to 135 km. The mean depth is around 37 m (maximum depth 123 m). This relatively narrow marine area is ideal for a case study to apply the proposed methodology. An interplay of estuarine and wind-driven processes generates a large spatio-temporal variability in salinity and temperature both in the vertical and horizontal directions. For instance, the inflow of saltier water (~ 7 psu) from the western entrance combined with a large amount of fresh-water input from large rivers in the eastern part of the gulf causes an eastward lateral decrease in salinity (down to 0–3 psu), cf. Myrberg and Soomere (2013). A permanent halocline is known to exist in the deeper layers of the western part of the gulf whilst in the eastern section there forms no permanent halocline. The presence of this strong halocline in the western and middle sections of the gulf acts as a barrier to vertical mixing but can also provide a waveguide for the propagation of internal waves into the gulf. It is also the reason that the upper layer circulation dynamics can be detached from the lower layer dynamics.

The FAMOS marine gravity and GNSS campaign was carried out on board of the Estonian Maritime Administration survey vessel ‘MS Sektori’ (hence this particular FAMOS campaign is dubbed Sektori2017 in the further text) between 03.07.2017 and 06.07.2017 (days of the year – DOY 183–187) in the Gulf of Finland, Baltic Sea (Figure 3).

The surveying routes (with the total length of 1249 km or 674 NM) covered the southern part of the Gulf of Finland (cf. Figure 4). Average speed during the experiment was close to 8 knots. Throughout the campaign, westerly winds dominated. Wind speed on DOY 183 and 184 (refer to Figure 4) was between 1–3 m/s and during DOY 185–187



Figure 3. Baltic Sea and the nearby countries. Location of the study area (southern part of the Gulf of Finland) is marked by the red rectangle.

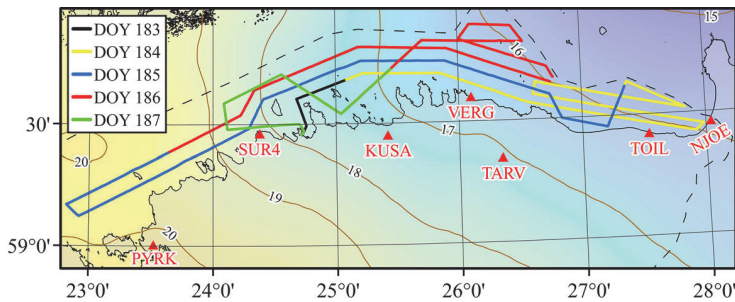


Figure 4. Route of the survey vessel and the used GNSS-CORS stations (denoted by red triangles and 4-letter abbreviations). The yellow-blue background and brown isolines depict the EST-GEOID2017 model height variations with respect to the GRS-80 reference ellipsoid, units in meters. The dashed black line depicts the Estonian border.

generally around 6–9 m/s, reaching up to 11 m/s in the second half of DOY 185. Wave height on DOY 183 and 184 was below 0.5 m, being mainly around 0.2–0.3 m. Hence, calm weather conditions prevailed during DOY 183 and 184, when the Narva Bay gravimetric data void was covered (see Figure 5). However, the last three days of the experiment (DOY 185–187) were carried out on rough sea due to difficult weather conditions. The wave height during DOY 185–187 was generally around 1–1.5 m and even up to 2 m in the second half of DOY 185.

Gravity data acquisition and processing

The main goal of the FAMOS surveying campaign was to acquire new gravity data for subsequent geoid determination. This included also large

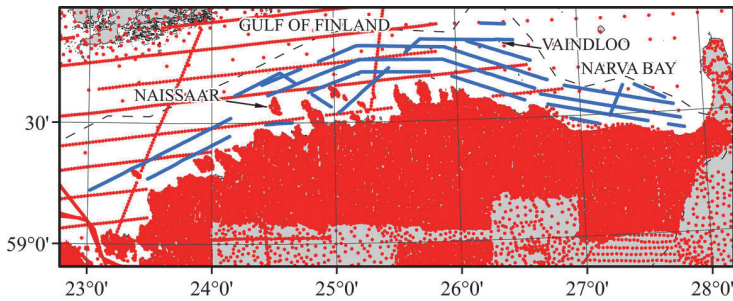


Figure 5. The distribution of previously existing (pre-Sektor2017, colored red) and new (Sektor2017, colored blue) gravimetric data. The dashed black line depicts the Estonian border.

data void areas in the Narva Bay and near Vaindloo island (Figure 5). Gravimetric data were gathered by using a Russian ‘Elektropribor’ manufactured marine gravimeter Chekan-AM that was mounted by the Danish Technical University (DTU) team to the vessel’s cargo bay 70–80 cm below the sea level, near the center of mass of the vessel.

The marine gravity data-set from Chekan-AM measurements was connected to the Estonian gravity network (Oja, Ellmann, and Märdla 2019) before and after the campaign. The marine gravity observations are corrected for the effect of the moving platform (Eötvös correction) and filtered to suppress short wavelength noise. The filter length is approximately 6 min corresponding to less than one NM (at a nominal speed of 8 knots). Remaining noise in the gravity data was subsequently identified and removed. In addition, some gravimetric data over very rough sea and difficult vessel maneuvers (e.g., the sharp turns at beginnings and endings of transit routes) were discarded (the resulting Sektor2017 data gaps are seen in Figure 5). Crossover errors from six identified line crossings amounted to 1.0 mGal, indicating a noise level of 0.7 mGal in the gravity data. The coherent appearance of the anomaly pattern indicates healthy data with only little noise (Olesen 2017).

GNSS data acquisition

In addition to the gravimeter, three GNSS devices were installed on the vessel. Two Topcon PG-A1 GNSS antennas were attached to the vessel’s opposite railings at bow – one to the port (antenna 5260) and the other to the starboard (antenna 5265). The third one, a Javad MarAnt+ GNSS antenna, was attached to the vessel’s railing on top of the captain’s quarters (antenna 5312). Relative locations of the antennas with respect to each other are described in section ‘Reducing effects from vessel’s attitude’.

Three Leica GRX1200 GG PRO GNSS receivers sampled the 3D positions of profile points with a 15 second interval (1/15 Hz) continuously

from the evening of 02.07.2017 to 06.07.2017. The data from seven Estonian GNSS-CORS (see [Figure 4](#), for more details see [Metsar, Kollo, and Ellmann 2018](#)) were used for post-processing the vessel's routes/height profiles. Two commercial software packages were tested for GNSS kinematic data post-processing – Trimble Business Centre™ v4.00 (TBC) and NovAtel Inertial Explorer™ v8.60. The TBC software allows to adopt only one GNSS-CORS (the closest one to a portion of the route was used), whereas the more sophisticated NovAtel software includes multiple GNSS-CORS (their assigned weights are inverse to the distance to each individual route section) for computing the entire route as a single solution. Validation of the two solutions was conducted in [Varbla \(2019\)](#). The final resulting GNSS profile is a combination of two and denoted as the best resulting shipborne GNSS height profile in the further text – for details, see [Varbla \(2019\)](#). The GNSS post-processing was conducted in the EUREF-EST97 coordinate system, which is a national realization of European Terrestrial Reference System ETRS89 in Estonia. It is estimated that the uncertainty of height determination along the entire surveying profile is random and does not exceed 2.6 cm (varies generally within 1.8–2.2 cm).

Height datums and assessed geoid models

The present study validates the quality of different geoid models. A recent international NKG geoid modelling project yielded an improved high-resolution regional geoid model NKG2015 ([Ågren et al. 2016](#)). The project was conducted within 2011–2016 in cooperation between the Nordic-Baltic national mapping agencies and universities. The updated NKG gravity database (containing more than 0.5 million points) was used for the gravity field and geoid modelling computations. The final geoid model was further evaluated by a unified GNSS-levelling dataset (the geodetic and normal heights, which were transformed to a common reference frame and reduced to the epoch 2000.0) of the participating countries. The NKG2015 geoid model has a standard deviation of 3.0 cm from a 1-parameter fit with GNSS-levelling data over the land areas of the Nordic-Baltic region. Fitting results for individual countries vary – for more details see [Ågren et al. \(2016\)](#) and [Märdla et al. \(2017\)](#).

During the recent renovation of the Estonian national levelling network (e.g., see [Kollo and Ellmann 2019](#) for more details), it became evident that the previously used Baltic Height System 1977 (BHS77) had become obsolete due to postglacial land uplift. The annual effect of apparent postglacial land uplift increases from 1.8 mm in the eastern extreme up to 3 mm to the western part of the study area. At the beginning of 2018, Estonia adopted a new EVRS (European Vertical Reference System) based height system

EH2000, in which the values of apparent postglacial land uplift have been taken account for. As a result, this datum change caused the previous heights (belonging to the BHS77) to increase from 14 to 25 cm in a north-westerly direction, i.e., from the periphery of the Fennoscandian postglacial rebound toward its epicenter. Accordingly, such a datum change yields a need for a new national geoid model. Thus, the previous regional geoid model EST-GEOID2011 (Ellmann, Oja, and Jürgenson 2011 and Ellmann et al. 2016) was replaced by EST-GEOID2017 (Ellmann, Märdla, and Oja 2019). This new model is an offspring of the NKG2015 geoid modelling project and that of the FAMOS. Unlike the NKG2015 model, however, the EST-GEOID2017 computations include new marine gravimetric data from the JakobPrei2016 (see Varbla et al. 2017 for more details) and Sektori2017 campaigns. The GNSS-levelling points used for fitting the EST-GEOID2017 model to the new vertical datum belong to the reference epoch 2000.0, whereas a large sub-set of the same Estonian GNSS-levelling points were used for regional fitting of the NKG2015 geoid model. EST-GEOID2017 has been officially imposed by the Estonian Ministry of Environment as a part of the Estonian national geodetic datum. The model is widely used by the surveying industry of Estonia as the official national geoid for converting the GNSS derived heights into normal heights.

All three geoid models were computed by using Least Squares Modification of Stokes' formula with Additive corrections (LSMSA) – see, e.g., Sjöberg (2003) and also a more extended review in Sjöberg and Bagherbandi (2017). To fill a large gravity data void in the easternmost end of the Gulf of Finland (seen in the upper right part of Figure 5), a global geopotential model (GGM) based gravity grid was generated, hitherto referred to as 'GoF patch'. For more details, see Märdla et al. (2017) and Ellmann, Märdla, and Oja (2019). The modelling aspects of the three marine geoid models assessed in the present study are summarized in Table 1.

Differences between the validated geoid models

The inclusion of newly acquired gravimetric data has a significant impact on geoid modelling (Figure 6). Large differences between the previous official Estonia geoid model (EST-GEOID2011) and the new one (EST-GEOID2017) occur in the Narva Bay and near Vaindloo island. These were previously also the areas with large gravimetric data voids (cf. Figure 5).

Similarly, large differences between the NKG2015 and EST-GEOID2017 geoid models can be identified (Figure 7). These are correlated with the areas of new gravimetric data acquisition.

Table 1. Geoid modelling parameters of the three assessed geoid models.

Parameter	NKG2015	EST-GEOID2011	EST-GEOID2017
Background GGM	GO_CONS_ GCF_2_DIR_R5 (Bruinsma et al. 2014)	GO_CONS_ GCF_2_TIM_R2 (Pail et al. 2011)	GOCO05s (Mayer-Gürr et al. 2015)
GGM for GoF patch	DIR-R4 (Bruinsma et al. 2013)	EGM2008 (Pavlis et al. 2012)	DIR-R4
Resolution of GoF patch (arc-deg)	0.1 × 0.2	0.017 × 0.033	0.1 × 0.2
FAMOS gravity data inclusion	No	No	Yes
Gravity data gridding method	R-I-R using LSC. Correlation length 15 km	SBA using kriging with anisotropic variogram model	R-I-R using LSC. Correlation length 23 km
Geoid model computation method	LSMSA	LSMSA	LSMSA
Upper degree of the geopotential model and modified harmonics	300	160	200
Resolution of gravity and geoid model (arc-deg)	0.01 × 0.02	0.017 × 0.033	0.01 × 0.02
Geoid model fitting method	1-parameter fit	6-parameter polynomial fit	Two stage stochastic spatial prediction
Corresponding vertical datum	EVRS, referred to epoch 2000.0	BHS77, epoch unknown	EH2000 (a national realization of EVRS), epoch 2000.0

Used abbreviations: SBA (Simple Bouguer' Anomaly), R-I-R (Remove-Interpolate-Restore), LSC (Least Squares Collocation).

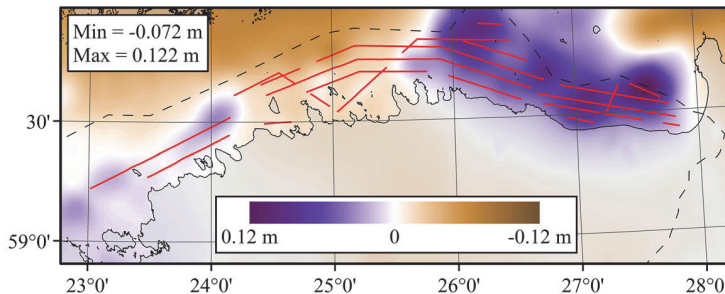


Figure 6. EST-GEOID2011 (refers to BHS77 height system) model differences as compared to EST-GEOID2017 (EH2000 height system), after removal of the general trend of their differences. The latter has been subtracted from the former. Red lines mark the Sektori2017 gravimetric data (also see Figure 5). The dashed black line depicts the Estonian border.

Two aspects can be evaluated by comparing Figures 6 and 7: (i) in general, Figure 7 shows a better agreement in terms of differences and (ii) this may hint that improvements may not only be in the included data, but also in the methodology used in the model computations (cf. Table 1). Thus, the remaining sections of this study demonstrate the intention to identify whether these changes/differences are actual improvements in geoid modelling.

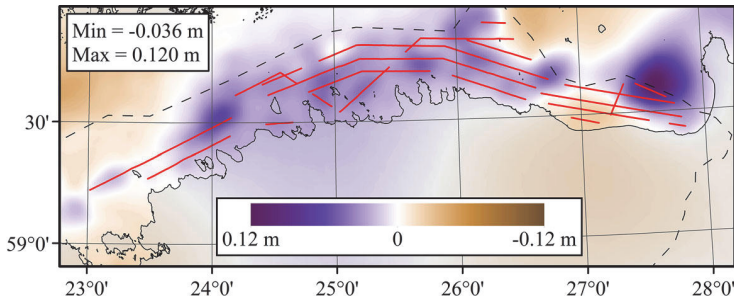


Figure 7. NKG2015 geoid model differences as compared to EST-GEOID2017 (latter has been subtracted from the former). Red lines mark the gravimetric data acquired from Sektori2017 campaign (also see Figure 5), i.e., after the compilation of the NKG model. The dashed black line depicts the Estonian border.

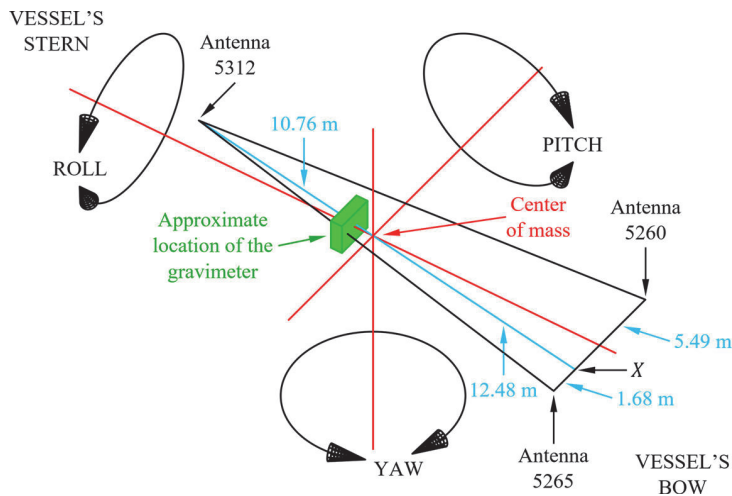


Figure 8. Roll, yaw and pitch motion of a moving vessel and relative locations of the GNSS antennae used. The red lines denote the principal axes of the vessel, whereas the blue line is connecting the stern-mounted antennae to the center of the mass, further extended to the line that connects the two bow-mounted antennae.

GNSS data processing

Reducing effects from vessel's attitude

Determination of SSH requires accurate GNSS profiles. Since the GNSS antennae are attached to a continuously moving platform, it is necessary to consider effects from the vessel's attitude that consists of roll, pitch and yaw motions (Figure 8). The corresponding Figure 9 demonstrates the effect of pitch and roll motions to the GNSS measurements.

In particular, the amplitude of antenna 5312 (close to the vessel's roll axis and thus the most stable out of the three, cf. Figure 8) is smaller than

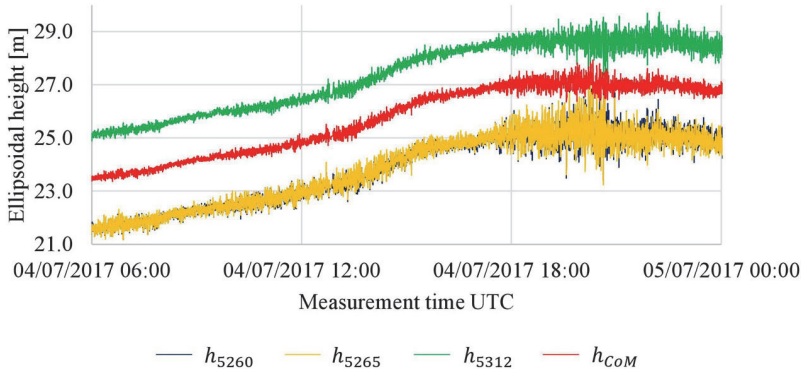


Figure 9. Ellipsoidal heights of the three antennas (h_{5260} , h_{5265} and h_{5312} ; note that h_{5260} and h_{5265} are partially overlapping) and a profile that has its heights calculated to the vessel's mass center (h_{CoM}). Measurements on the left side of the figure are conducted on a rather calm sea, while the right side illustrates measurements on the roughest conditions in which the experiment was carried out. The 18-hour duration corresponds approximately to 265.0 km.

that of antenna 5260 or 5265 (both at the vessel's shaky bow). It can be assumed that during the GNSS profile surveys, the pitch motion of a surveying vessel dominates. As the present study focuses on height determination, yaw motion can be neglected.

As GNSS post-processing resulted in three height profiles (one for each antenna), the vessel's movement at a time-instant needs to be presented as a single reference point. Therefore, the GNSS determined heights are linearly interpolated in two steps above the vessel's mass center as follows (cf. Figure 8):

$$X_i = (h_{5265,i} - h_{5260,i}) \left(\frac{5.49}{5.49 + 1.68} \right) + h_{5260,i} \quad (12)$$

where X is the intersection point of the line from the stern-mounted antenna through the centre of mass and the line that connects the two bow-mounted antennas. Then

$$h_{CoM,i} = (h_{5312,i} - X_i) \left(\frac{12.48}{12.48 + 10.76} \right) + X_i \quad (13)$$

where h_{5260} , h_{5265} and h_{5312} refer correspondingly to the ellipsoidal heights of the used GNSS antennas (cf. Figure 8) at a time-instant i ; h_{CoM} is the ellipsoidal height calculated above the vessel's mass center at the same time-instant i . Note that the constants in Eqs. 12 and 13 stem from the distances in-between the GNSS antennae locations (cf. Figure 8).

Such a calculation reduces significantly the effects of pitch and roll motions and thus replaces the need for IMU. The remaining motions of the artificial h_{CoM} profile are predominantly sea surface oscillations, which

are later eliminated by applying a filtering technique. Thus, the very same profile can be reduced to the vessel's mass center.

Figure 9 shows that the resulting h_{CoM} heights have a smaller vertical amplitude than any of the three GNSS antennas. Comparisons between raw GNSS heights (seen in Figure 9) and their double low-pass filtered (to be discussed shortly in section 'Reducing effects from waves') counterparts yield the following StDev values (along the entire surveying route):

1. Antenna 5260 (h_{5260} in Figure 9) StDev = 0.180 m;
2. Antenna 5265 (h_{5265} in Figure 9) StDev = 0.183 m;
3. Antenna 5312 (h_{5312} in Figure 9) StDev = 0.119 m;
4. Vessel's mass center (h_{CoM} in Figure 9) StDev = 0.088 m.

The h_{CoM} results (option 4) thus yielded the smoothest time series and were therefore used in the further calculations (i.e., after filtering h_{CoM} is the factual h in Eq. 4).

Reducing effects from waves

For reducing the sea surface oscillations in the GNSS data, a double low-pass filter was applied to the h_{CoM} heights. The filtering is continuous through the entire profile (i.e., 1249 km). Considering the average moving speed of the vessel on transit routes, a moving median of 51 measurements (that corresponds to 3160 m in average, at 8 knots and sampling rate of 1/15 Hz) was taken, i.e., the interval from 25 epochs before time-instant i up to 25 epochs after the same time-instant i . Taking a median allows identification and elimination of gross errors in calculations, as well as occasional gross errors in GNSS measurements (i.e., lax a priori error estimates during GNSS post-processing will not affect the final result as the errors are eliminated through filtering). Median also removes short-term changes in squat effect from the measurements (e.g., when the vessel slows down for sharp turns). From that outcome, a moving average of 51 measurements was also taken to further smoothen the GNSS profile. The effect of such filtering on the GNSS height data is shown in Figure 10. Alternative filtering windows were also considered (Figure 10). See Varbla et al. (2017) or Varbla (2019) for more details about the applied filtering methodology.

As seen, shorter (than 51 measurements) filtering windows may retain unwanted short-wavelength vertical fluctuations into the GNSS height profile. On the other hand, larger (than 51) filtering window will not change the result much (the result would be very similar to $h_{Filter51}$). Thus, inclusion of 51 measurements was empirically determined as an optimal length of the filtering window. Note that the resulting signal frequency of the low-pass profile $h_{Filter51}$ is quite similar to that of the assessed geoid models.

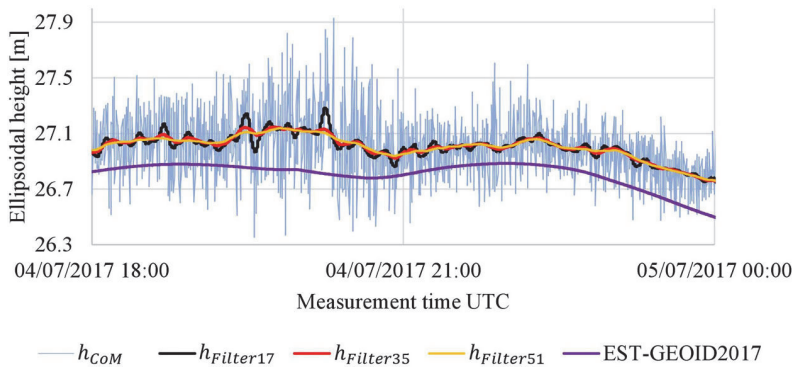


Figure 10. An example of the effect of different double low-pass filtering windows on the raw GNSS profile. h_{CoM} indicates the profile that has its heights calculated to the vessel's mass center. The number in the subscript indicates the size of the double low-pass filtering window (either $8 + 1 + 8 = 17$, $17 + 1 + 17 = 35$ or $25 + 1 + 25 = 51$ measurements). Note that EST-GEOID2017 heights are elevated artificially for the sake of visual comparison. The 6-hour duration corresponds approximately to 87.3 km.

Hydrodynamic processes in the test area and their modelling

Due to numerous archipelagos and shallow areas, the gulf accommodates dynamical features (mesoscale eddies, fronts, specific mixing conditions, etc.) of water circulation (Andrejev et al. 2004a). The spatial scale of these features is influenced by the internal Rossby radius (a horizontal scale describing the effects of the Earth's rotation on fluid motion), which in the gulf has an overall small value ($\sim 2\text{--}4$ km, which has a seasonal variability) compared to open ocean (30–50 km). This scale defines the horizontal scale that marine processes can occur at. It also defines the scale that eddy-permitting and eddy-resolving models are required to reasonably simulate marine processes.

Model simulations (Lehmann, Krauss, and Hinrichsen 2002, Andrejev et al. 2004a) and in-situ surface drifters (Delpeche-Ellmann, Torsvik, and Soomere 2016) have shown that two separate regimes of circulation may exist in the Gulf of Finland. The circulation in the uppermost layer (0–2.5 m) is mainly wind-driven and contains frequent up- and downwelling along the coast (Delpeche-Ellmann, Mingelaité, and Soomere 2017). Typical current velocities in the uppermost layer range from 5 to 10 cm/s (Andrejev, Myrberg, and Lundberg 2004b). Note that all the mentioned factors have an influence on DT modelling, both spatially and temporally.

Several regional models have been developed or adjusted specifically for the Baltic Sea and the Gulf of Finland. Whilst some challenges still exist (mainly with simulating the salinity and temperature vertical profiles), most of the models are capable of reproducing the major hydrodynamic features (Myrberg et al. 2010). Nevertheless, not all of the existing HDMs reflect the DT variations well. The HBM-EST (Lagemaa 2012, 2015) is currently used for most operational sea level forecasting in Estonian waters. The model

is used also in the present study, as it appears to be more reliable than other models over the study area (see, e.g., Varbla 2019).

With the HBM-EST data for every full hour, the DT data (a 24-layer NetCDF file for a single day) were obtained from TalTech Department of Marine Systems database (<http://emis.msi.ttu.ee/allalaadimine/>). The resolution of the model is 0.5 NM (i.e., approximately 0.9 km), which is suitable considering the small Rossby radius in the gulf. The core of the model system is a 3 D baroclinic eddy-resolving circulation model, based on the original BSHcm0d (Kleine 1994) that calculates currents, temperature and salinity in the water column, and sea level. The Estonian implementation of the model has been continuously developed since 2005; for more details see Lagemaas (2012).

The open boundary of the model is at the Danish Straits, where DB is set near zero. Further to the east (i.e., the Gulf of Finland) and north the bias increases. Note that the bias is qualitatively similar in all regional HDMs. Such DB has a low-frequency part that changes in time (Lagemaas, Elken, and Kõuts 2011) and causes the HDM derived DT to deviate from the vertical datum (i.e., EH2000). Origin of the DB is a scientifically unsolved issue. However, it is most likely caused by model inaccuracies, e.g., errors in currents, temperature, salinity and in the parameterization used, which can also induce variability in different HDMs. TG data are thus necessary for validating and correcting HBM-EST (i.e., accounting for DB).

Dynamic topography correction for GNSS profiles

Seven TG stations on the Northern coast of Estonia (Figure 11) are used to determine and eliminate DB from the HBM-EST HDM. These pressure sensor equipped TG stations (see, e.g., Liibus et al. 2013) are included into the recently renovated national high-precise levelling network, whereas their zero values coincide with the geoid surface (see Kollo and Ellmann

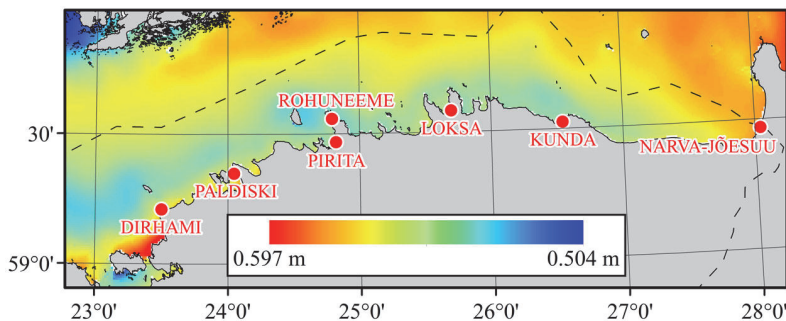


Figure 11. An example of DT from HBM-EST HDM on 05.07.2017 at 14:00 UTC and locations of the TG stations (denoted by red circles) used in the study. DT is given with respect to the HBM-EST internal zero. The dashed black line depicts the Estonian border.

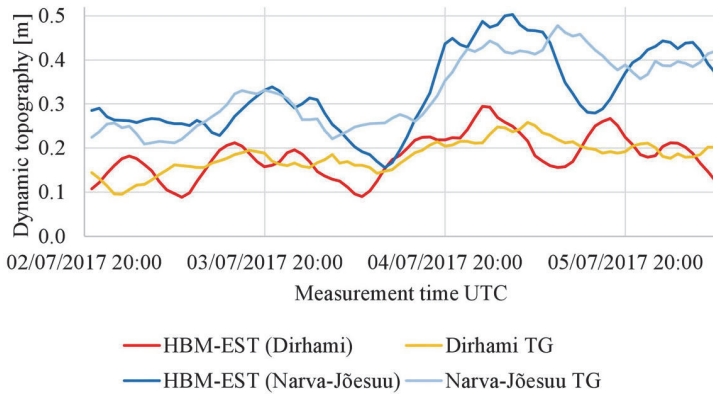


Figure 12. An example of the HBM-EST model derived DT and the Dirhami and Narva-Jõesuu (cf. Figure 11) TG readings during the entire campaign. Note that for the sake of the comparison, the 1 D bias in HBM-EST heights (cf. Table 2, the second column) is removed.

Table 2. Statistics of discrepancies between the raw HDM and the TG control data at the used TG stations (see Figures 11 and 12). Comparison is based on 84 hourly records (the entire timespan of the campaign). Units in meters.

TG station	Average DB* BHS77/EH2000	Min**	Max**	StDev
Dirhami	0.369/0.127	-0.076	0.083	0.042
Paldiski	0.351/0.110	-0.086	0.099	0.041
Rohuneeme	0.370/0.128	-0.073	0.091	0.040
Pirita	0.395/0.158	-0.074	0.089	0.039
Loksa	0.339/0.108	-0.087	0.069	0.041
Kunda	0.337/0.121	-0.112	0.072	0.050
Narva-Jõesuu	0.283/0.091	-0.161	0.088	0.059
StDev:	0.033/0.019			

Notes:

* Average difference between HBM-EST model heights and TG station readings (TG readings are subtracted from HBM-EST heights).

** After removal of the average difference (second column).

2019). Thus, the heights provided by the TGs truly represent the DT and not the SSHA, cf. section ‘Interrelations between sea surface height, geoid surface and mean sea level’. The HBM-EST heights and the Dirhami and Narva-Jõesuu TG station (for their locations see Figure 11) readings are visualized in Figure 12.

Examination of heights derived from the HBM-EST and the TG stations shows somewhat reasonable comparison in that the DT phases appear to be almost similar in many circumstances. Usually HDM tends to overestimate the DT local extremes at TG stations, which is also observed by Izotova (2015). Nevertheless, there appears to be a height difference which can be accounted for as a bias, cf. Table 2. Accordingly, the DT estimate in this study consists of two components – HDM component (DT_{HDM}^T) from HBM-EST (Figure 11) and TG derived bias removal term \widehat{DB} , cf. Eq. 11. Statistics of the discrepancies can be seen in Table 2 (hourly data

from 02.07.2017 21:00 UTC to 06.07.2017 08:00 UTC is considered – the entire timespan of the campaign).

Note that Min, Max and StDev values presented in Table 2 are the same for both height systems. The StDev estimates of average DB at TGs as of 1.9 and 3.3 cm were achieved for the height systems EH2000 and BHS77, respectively. The updated EH2000 associated StDev indicates a better consistency of the new height system. Also note that the differences between the height systems in GNSS assessments are considered within \widehat{DB} due to TG readings being already in corresponding height systems.

As seen from Table 2, the DB at different TG stations is not a constant. Hence, the model DT needs to be corrected by accounting for along-route variable DB. The three methods tested to remove DB from HDM data are as follows:

1. Average bias correction (\widehat{DB}_{TGa}) involving all ($n = 7$) the (equally-weighted) TGs:

$$\begin{aligned}\widehat{DB}_{TGa}(\varphi_i, \lambda_i) &= \\ &= \frac{DB(\varphi_1, \lambda_1)_i + \dots + DB(\varphi_{m-1}, \lambda_{m-1})_i + DB(\varphi_m, \lambda_m)_i + \dots + DB(\varphi_n, \lambda_n)_i}{n}\end{aligned}\quad (14)$$

2. Weighted bias correction (\widehat{DB}_{TGw}), where the two closest TGs are double weighted ($n = 7$) – as explained in section ‘Using hydrodynamic model and tide gauges to determine offshore dynamic topography’:

$$\begin{aligned}\widehat{DB}_{TGw}(\varphi_i, \lambda_i) &= \\ &= \frac{DB(\varphi_1, \lambda_1)_i + \dots + 2*DB(\varphi_{m-1}, \lambda_{m-1})_i + 2*DB(\varphi_m, \lambda_m)_i + \dots + DB(\varphi_n, \lambda_n)_i}{n + 2}\end{aligned}\quad (15)$$

3. Closest bias correction (\widehat{DB}_{TGc}), where only the two closest TGs are involved ($n = 2$):

$$\widehat{DB}_{TGc}(\varphi_i, \lambda_i) = \frac{DB(\varphi_{m-1}, \lambda_{m-1})_i + DB(\varphi_m, \lambda_m)_i}{2}\quad (16)$$

In addition, DT is also linearly east-westwards (i.e., a function of longitude) interpolated (DT_{Inter}) from the TG station readings directly (i.e., without HDM). Differently calculated DT estimates are visualized in Figure 13 and all methods are compared in Table 3. Note that colors in the table represent respective curves of DT in Figure 13.

Note that N in Table 3 refers to the EST-GEOID2017 model; when using the other geoid models, the statistics appeared to be slightly worse. As seen from Table 3, the supplementary TG-based bias correction (either \widehat{DB}_{TGa} ,

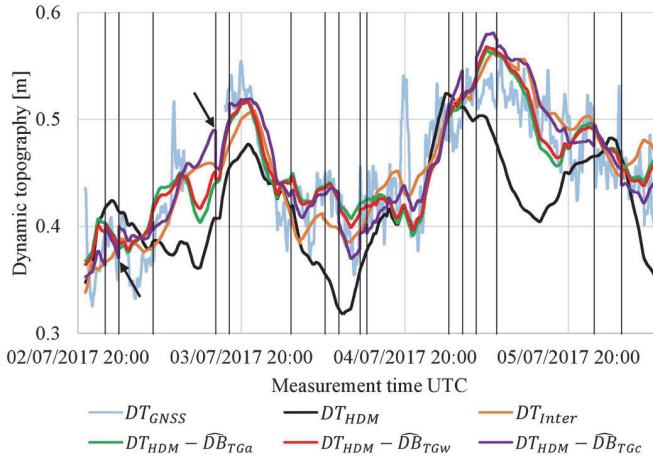


Figure 13. GNSS derived DT (DT_{GNSS}) compared to differently calculated DT estimates (with respect to the geoid) along the entire surveying route. HDM (black line) denotes unaltered HBM-EST model that is lowered by 0.154 m for the sake of visual comparison (average difference from comparison with DT_{GNSS}). Vertical straight lines denote meridians of the along-route TG locations, where input TG stations (and thus corresponding DB value) change in equations, cf. Eq. 15 or 16. The black arrows denote some extreme discrepancies in DT ($DT_{HDM} - \widehat{DB}_{TGc}$) due to the DB change in \widehat{DB}_{TGc} calculation.

Table 3. Discrepancies between the GNSS derived DT (in parentheses; DT_{GNSS} in Figure 13) and differently calculated DT estimates (cf. Figure 13). 18425 GNSS heights are considered in the comparisons. Units in meters.

Estimated discrepancies D (cf. Eq. 7)	Amplitude*	StDev*
$(iSSH - C - N_{SET-GEOID2017}) - DT_{HDM}$	0.210	0.043
$(iSSH - C - N_{EST-GEOID2017}) - DT_{Inter}$	0.189	0.030
$(iSSH - C - N_{EST-GEOID2017}) - (DT_{HDM} - \widehat{DB}_{TGa})$	0.195	0.029
$(iSSH - C - N_{EST-GEOID2017}) - (DT_{HDM} - \widehat{DB}_{TGw})$	0.187	0.028
$(iSSH - C - N_{EST-GEOID2017}) - (DT_{HDM} - \widehat{DB}_{TGc})$	0.170	0.029

Notes: $iSSH$ refers to the best resulting shipborne GNSS height profile (for details, see Varbla 2019); C denotes fuel consumption and squat corrections; DT_{HDM} refers to the HBM-EST model. The preferred data-set is marked in bold font.

*Of discrepancy (D) values, which are calculated at every time-instant (18425 instances in total).

\widehat{DB}_{TGw} or \widehat{DB}_{TGc} method) has a significant impact on the HDM data as any method out of three improves the results (in terms of standard deviation, see Table 3). Good results are also obtained from linear one-coordinate interpolation (DT_{Inter} from TG stations readings). This can be interpreted as a coincidence, as the coastline must stretch either along parallels or meridians for this method to be usable (the current study area is well aligned along the parallels). Thus, it can be utilized rarely. The \widehat{DB}_{TGc} correction method is not preferred, as it leaves sudden height gaps (due to the DB change in Eq. 16 whilst moving along the route) in the DT data. These may reach several cm (e.g., Figure 13 at 03.07 02:01 or 03.07 16:15, marked by arrows) and even up to 3.6 cm at most. Since such

discontinuity is physically unrealistic from the methodological point of view, the optimum (in terms of seamlessness) correction method for HDM can be considered \widehat{DB}_{TGw} . The method performs slightly better than \widehat{DB}_{TGa} , yet minimizes height gaps in DT data, which in the current exercise exceed rarely 5 mm, being 8 mm at most. The \widehat{DB}_{TGw} (as well as \widehat{DB}_{TGa} , but only over a limited area) method is universal and can be used almost everywhere.

Accounting for vessel related corrections

In addition to the vessel's attitude, the squat and static draft effects, which cause a vessel to sail deeper (or higher in the case of static draft) than its nominal draft, must be considered. Squat is a function of water depth, vessel's velocity and its dimensions; it occurs due to a forward motion of a vessel. Squat values can be calculated with a software or obtained manually from a vessel specific squat table – see, e.g., a book by Barrass (2004). Static draft is the linear vertical motion of a vessel, e.g., due to continuous fuel consumption, the vessel would rise upwards.

Tape measurements (between the railing and sea surface) were conducted before and after the experiment (in the harbor). Due to fuel consumption, the railings height had risen approximately 6 cm by the end of the survey. This value is considered as a total fuel consumption correction F . The corresponding correction F_i at time-instance i is obtained by assuming a linear increase along the entire route (as the vessel was moving at an almost constant speed):

$$F_i = F_{i-1} + \frac{F}{n} \quad (17)$$

where n is the total amount of GNSS measurement time instants between the first and last measurements. At the initial time moment, F_1 equals 0 and by the end of the route F_n reaches the maximum (6 cm).

Squat correction was almost a constant, as the vessel was moving with a constant speed, and generally in deep waters. For a short time, the vessel decelerated before taking sharp turns at beginnings and endings of transit routes and accelerated after. However, change in squat effect during turns is eliminated by median in the low-pass filter (as discussed previously).

Differences between geoid models and GNSS profiles

All three geoid models were compared to the best resulting shipborne GNSS height profile (with corrections); all were treated in a similar manner as displayed in Table 3, i.e., the DT correction is derived as $DT_{HDM} - \widehat{DB}_{TGw}$. As seen in Figure 14 (see also Figure 15 for reference), the internal accuracy of the GNSS profile at route intersections is generally rather good

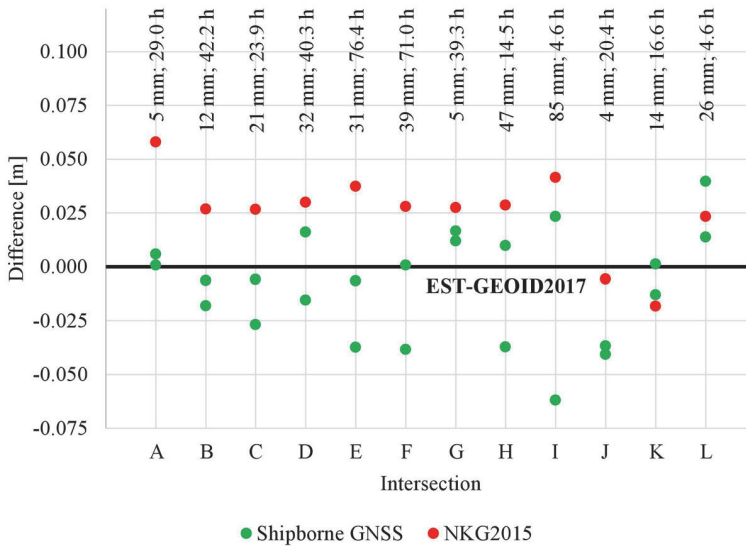


Figure 14. GNSS profile heights (double low-pass filtered after removing \hat{R} , with DT ($DT_{HDM} - \widehat{DB}_{TGW}$), fuel consumption and squat corrections) and NKG2015 geoid model compared to EST-GEOID2017 at profile intersections (Figure 15). Numbers at the upper edge of the figure show height differences of profiles at intersections and time span between crossings.

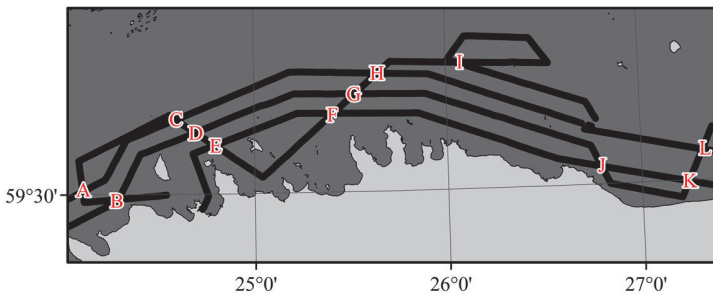


Figure 15. Letter-denoted intersections of the GNSS surveying route.

(average difference at route intersections is 2.7 cm and StDev 2.2 cm). There seems to be no correlation between the time spans and discrepancies at the intersections. For instance, a good 5 mm agreement is achieved at the G intersection after a 39.3 h revisit, whereas the I intersection yields a rather large 85 mm discrepancy only after a 4.6 h revisit. Problematic areas (with differences exceeding 4 cm) appear to be far from the coast (note that without the furthest intersections H and I, the average reduces to 1.9 cm and StDev to 1.2 cm). Such large differences are caused by insufficient DT data, but errors in GNSS raw data are also probable. It is likely that the results far from the coast would improve if Finnish TGs on the opposite coast of the Gulf of Finland were also included in the joint DT estimation.

Table 4. Statistics of differences between the best GNSS profile and geoid models. 18425 profile points are considered in the comparisons. Profile heights have been subtracted from the geoid model heights. Deviations along the entire route are visualized in Figure 16. Units in meters.

Geoid model	Corrections*	Avg**	Min**	Max**	StDev
NKG2015	No	−0.458	−0.590	−0.299	0.065
	Yes	0.029	−0.134	0.095	0.034
EST-GEOID2011	No	−0.226	−0.385	−0.077	0.067
	Yes	0.033	−0.118	0.124	0.040
EST-GEOID2017	No	−0.483	−0.604	−0.327	0.065
	Yes	0.005	−0.128	0.059	0.028

Notes: Best results are highlighted in bold text.

*Marks the use of DT ($DT_{HDM} - DB_{TGW}$), fuel consumption and squat corrections. StDev values (sixth column) of the uncorrected profile are marked red and corrected blue.

**After removal of \hat{R} (see Eqs. 6 and 7 in section ‘Utilizing shipborne GNSS profiles for geoid model assessment’).

Statistics of the GNSS profile compared to the geoid models are presented in Table 4. According to the results, the best agreement was reached with the EST-GEOID2017 model, with a generalized accuracy of approximately 2.8 cm (in terms of standard deviation). However, as Figure 13 and Table 3 suggest, the actual accuracy of the model is likely to be higher, as a portion of error is caused by approximate DT correction. Notice also in Figure 14 how the GNSS measurements converge around the EST-GEOID2017, as opposed to the NKG2015 geoid model, which appears to possess an offset with respect to the GNSS results. This better agreement is a clear indicator of EST-GEOID2017 modelling improvements.

As seen from Table 4, the DT and vessel related corrections have an utmost importance to the assessments. Without these, the results have no significant meaning. Accordingly, the standard deviation estimates are almost the same for all three geoid model assessments (see values denoted by red color).

Comparisons between geoid models and the corrected GNSS profile on the other hand show a good agreement all over the southern side of the Gulf of Finland, e.g., compare Figure 16a or 16b to Figure 16c. Largest improvements appear near Vaindloo island and in the Narva Bay (for location reference see Figure 5) – in areas with the largest geoid model changes due to Sektori2017 gravimetric data. As expected, improvements are larger farther from the coast than those near the coast (Figure 16).

The detected differences reveal problematic geoid and/or HDM modelling areas. It appears that between longitude 26° and 27° and around the island of Naissaar (for location reference see Figure 5), the deviation is systematic (mainly one-signed) in EST-GEOID2017 surface (Figure 16c). Such information should be considered in the following geoid modelling exercises or improvements of HDMs.

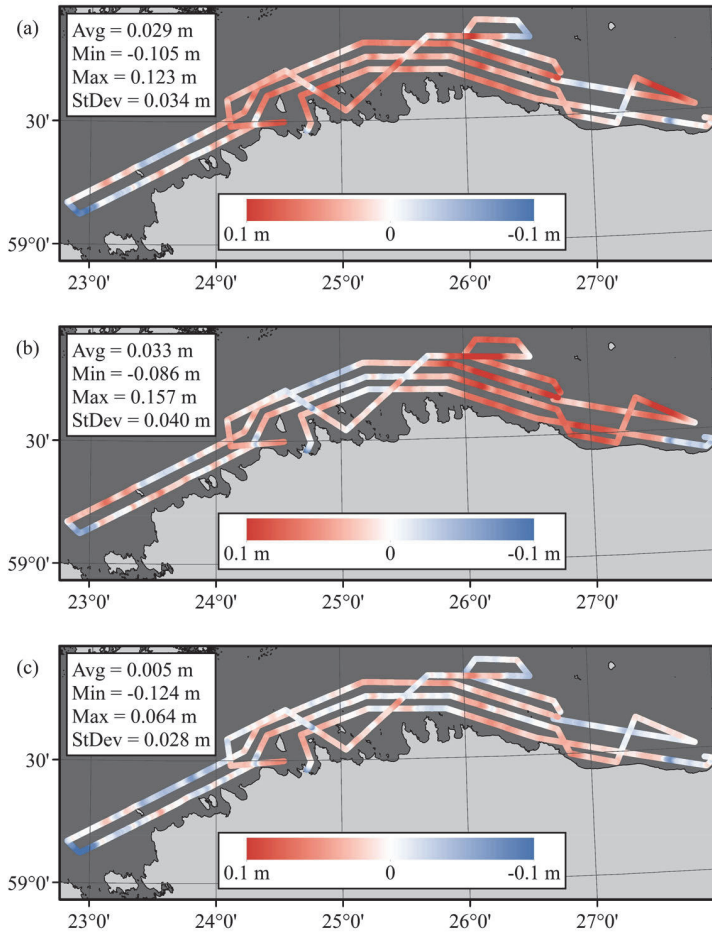


Figure 16. NKG2015 (a), EST-GEOID2011 (b) and EST-GEOID2017 (c) deviations from the GNSS profile (cf. Eq. 7). All models are compared to the double low-pass filtered profile with corrections from DT ($DT_{HDM} - \widehat{DB}_{TGW}$), fuel consumption and squat.

Concluding remarks

The current study has shown that shipborne GNSS profiles are a suitable dataset to evaluate existing geoid models. Applications of appropriate filtering methods to the GNSS data are essential to the assessment. The double low-pass filtering method used in the current study has proven to be suitable. Also, referring GNSS heights to the vessel's center of mass has a significant impact on the results, especially on rough sea measurements. This method is an alternative to using IMU, especially considering the lower price and wider availability of GNSS devices. Corrections from DT, but also from fuel consumption and squat, have an utmost importance to the assessment results. Special care should be devoted to the DB correction computation when using a HDM, as this is the likely source of errors.

The computed shipborne GNSS profiles were used to validate three geoid models in the Gulf of Finland, where newly acquired gravimetric data had a significant impact on geoid modelling. According to the GNSS profiles, the best fitting geoid model over the Gulf of Finland is EST-GEOID2017, which incorporates Sektori2017 marine gravity data. Agreement of the model is 2.8 cm in terms of standard deviation. The standard deviations of NKG2015 and EST-GEOID2011 geoid models (both without the inclusion of Sektori2017 data) are correspondingly 3.4 cm and 4.0 cm.

Note that the marine GNSS datasets have a potential in providing complementary constraints in problematic geoid modelling areas. In addition, methods for GNSS profile-wise fitting (analogous to the usual point-wise GNSS-levelling fitting over dry land) of gravimetric geoid models to the actual height datum over marine areas is a promising venue for further investigations. The shipborne GNSS profiles can be utilized in ways other than the marine geoid model validation. This data can also complement the processing of the marine gravity, e.g., accounting for the vertical acceleration, providing more rigorous marine gravity results. Also, the gravity anomaly gridding methods/results can be assessed by these profiles. The GNSS derived SSH enables further interdisciplinary cooperation with marine and oceanographic scientists for a better understanding of marine dynamics and interpreting the results.

Acknowledgements

The Estonian Maritime Agency and the Estonian Land Board (ELB) are acknowledged for providing resources for carrying out the Sektori2017 marine gravity and GNSS campaign. Gabriel Strykowski and Jens Emil Nielsen from DTU, Jaanus Metsar and Tõnis Oja from the ELB are thanked for field assistance. Anti Gruno and Karin Kollo from the ELB helped with GNSS post-processing. Liisi Kaleva from Estonian Environmental Agency provided the used raw tide gauge data, which were then checked by Karin Kollo. The two anonymous reviewers are thanked for their contribution to the quality of the final manuscript. The figures of this paper have been generated by the ArcMap 10.6, Autodesk AutoCad and Microsoft Excel. Illustrative data for the figures originates from Eurostat and European Environment Agency websites.

Funding

The research is supported by the Estonian Research Council grants PRG330 'Development of an iterative approach for near-coast marine geoid modelling by using re-tracked satellite altimetry, in-situ and modelled data' and IUT33-3 'Wave dynamics for coastal engineering and management'. The fieldwork was conducted within the frames of a Connecting Europe Facility (CEF) project 'FAMOS (Finalising Surveys for the Baltic Motorways of the Sea) Odin' (VEU16013).

ORCID

Artu Ellmann  <http://orcid.org/0000-0002-5512-8461>

References

- Ågren, J., G. Strykowski, M. Bilker-Koivula, O. Omang, S. Mårdla, R. Forsberg, A. Ellmann, T. Oja, I. Liepins, E. Parseliunas, J. Kaminskis, L. E. Sjöberg, and G. Valsson. 2016. The NKG2015 gravimetric geoid model for the Nordic-Baltic region. Presented at the 1st Joint Commission 2 and IGFS Meeting International Symposium on Gravity, Geoid and Height Systems, September 19–23 in Thessaloniki, Greece.
- Allik, A. 2014. Satelliitaltimeetria mõõtmiste integreerimine meretaseme prognoosimudeliga [The integration of satellite altimetry and sea level forecast model]. Bachelor's thesis, Tallinn University of Technology. Accessed April 4, 2019. <https://digi.lib.ttu.ee/i/?7017>.
- Andrejev, O., K. Myrberg, P. Alenius, and P. A. Lundberg. 2004a. Mean circulation and water exchange in the Gulf of Finland – a study based on three-dimensional modelling. *Boreal Environment Research* 9 (1):1–16. Accessed July 18, 2019. <http://www.borenv.net/BER/pdfs/ber9/ber9-001.pdf>.
- Andrejev, O., K. Myrberg, and P. A. Lundberg. 2004b. Age and renewal time of water masses in a semi-enclosed basin – application to the Gulf of Finland. *Tellus A: Dynamic Meteorology and Oceanography* 56 (5):548–58.
- Barrass, C. B. 2004. *Ship design and performance for masters and mates*. Oxford: Elsevier Butterworth-Heinemann.
- Bilker-Koivula, M. 2010. Development of the Finnish Height Conversion Surface FIN2005N00. *Nordic Journal of Surveying and Real Estate Research* 7 (1):76–88.
- Bruinsma, S. L., C. Förste, O. Abrikosov, J.-M. Lemoine, J.-C. Marty, S. Mulet, M.-H. Rio, and S. Bonvalot. 2014. ESA's satellite-only gravity field model via the direct approach based on all GOCE data. *Geophysical Research Letters* 41 (21):7508–14. doi:10.1002/2014GL062045
- Bruinsma, S. L., C. Förste, O. Abrikosov, J.-C. Marty, M.-H. Rio, S. Mulet, and S. Bonvalot. 2013. The new ESA satellite-only gravity field model via the direct approach. *Geophysical Research Letters* 40 (14):3607–12. doi:10.1002/grl.50716
- Delpeche-Ellmann, N., T. Mingelaité, and T. Soomere. 2017. Examining Lagrangian surface transport during a coastal upwelling in the Gulf of Finland, Baltic Sea. *Journal of Marine Systems* 171:21–30. doi:10.1016/j.jmarsys.2016.10.007
- Delpeche-Ellmann, N., T. Torsvik, and T. Soomere. 2016. A comparison of the motions of surface drifters with offshore wind properties in the Gulf of Finland, the Baltic Sea. *Estuarine, Coastal and Shelf Science* 172:154–64. doi:10.1016/j.ecss.2016.02.009
- Ellmann, A., S. Mårdla, and T. Oja. 2019. The 5 mm geoid model for Estonia computed by the least squares modified Stokes's formula. *Survey Review*. doi:10.1080/00396265.2019.1583848
- Ellmann, A., T. Oja, and H. Jürgenson. 2011. Kosmosetehnoloogia rakendused geoidi ja gravitatsioonivälja täpsustamiseks Eesti alal [Application of space technologies to improve geoid and gravity field models over Estonia]. *Geodeet* 41:22–5.
- Ellmann, A., T. Oja, T. All, H. Jürgenson, T. Kall, and A. Liibus. 2016. Raskuskiirenduse anomaalvälja ja geoidi mudelpinna täpsustamine Eestis [Enhanced gravity field and geoid models over Estonia]. *Publicationes Geophysicales Universitatis Tartuensis* 51:152–64. Accessed April 24, 2019. http://www.maaamet.ee/data/files/Ellmann_etal_metobs_150_2016.pdf.

- FAMOS. 2019. Finalising surveys for the Baltic Motorways of the Sea webpage [online]. Accessed May 22, 2019. <https://www.famosproject.eu/famos/>.
- Forsberg, R., G. Strykowski, and D. Solheim. 2004. NKG-2004 geoid of the Nordic and Baltic Area. Presented at the in IAG International Symposium 'Gravity, Geoid and Satellite Gravity Missions', August 30 – September 3, Porto, Portugal. Proceedings on CD-ROM from the International Association of Geodesy.
- Huess, V. 2018. Product User Manual for Baltic Sea Physical Analysis and Forecasting Product BALTICSEA_ANALYSIS_FORECAST_PHY_003_006. Accessed March 26, 2019. <http://cmems-resources.cls.fr/documents/PUM/CMEMS-BAL-PUM-003-006.pdf>.
- Izotova, J. 2015. Operatiivsete meremudelite valideerimine ja võrdlus Läänemere idaosas [Validation of Operational Ocean Models in The Eastern Baltic Sea, thesis in Estonian]. Bachelor's thesis, Tallinn University of Technology. Accessed April 18, 2019. <https://digi.lib.ttu.ee/i/?2677>.
- Jürgenson, H., A. Liibus, and A. Ellmann. 2008. Geoid profiles in the Baltic Sea determined using GPS and sea level surface. *Geodesy and Cartography* 34 (4):109–15. doi:10.3846/1392-1541.2008.34.109-115
- Kakkuri, J., and M. Poutanen. 1997. Geodetic determination of the surface topography of the Baltic Sea. *Marine Geodesy* 20 (4):307–16. doi:10.1080/01490419709388111
- Kleine, E. 1994. Das Operationelle Modell des BSH für Nordsee und Ostsee. Konzeption und Übersicht, Bundesamt für Seeschifffahrt und Hydrographie (manuscript report in German).
- Kollo, K., and A. Ellmann. 2019. Geodetic reconciliation of tide gauge network in Estonia. *Geophysica* 54:27–38.
- Lagemaa, P. 2012. Operational forecasting in Estonian marine waters. PhD thesis, Tallinn University of Technology. Accessed March 25, 2019. <https://digi.lib.ttu.ee/i/?714>.
- Lagemaa, P. 2015. Operatiivne meremudel HBM-EST Tehniline juhend [Technical manual for HBM-EST operational forecasting model]. Accessed March 26, 2019. https://www.kik.ee/sites/default/files/uuringud/operatiivne_meremudel_hbm-est.pdf
- Lagemaa, P., J. Elken, and T. Kõuts. 2011. Operational sea level forecasting in Estonia. *Estonian Journal of Engineering* 17 (4):301–31. doi:10.3176/eng.2011.4.03
- Lavrov, D., G. Even-Tzur, and J. Reinking. 2016. Expansion and improvement of the Israeli geoid model by ship-borne GNSS measurements. *Journal of Surveying Engineering* 143 (2).
- Le Provost, C. 1990. The Geoid and Mean Sea Level. *International Hydrographic Review* 67 (1):171–5. Accessed May 4, 2019. <https://journals.lib.unb.ca/index.php/ihr/article/viewFile/23325/27100>.
- Lehmann, A., W. Krauss, and H.-H. Hinrichsen. 2002. Effects of remote and local atmospheric forcing on circulation and upwelling in the Baltic Sea. *Tellus A: Dynamic Meteorology and Oceanography* 54 (3):299–316. doi:10.1034/j.1600-0870.2002.00289.x
- Liibus, A., A. Ellmann, T. Kõuts, and H. Jürgenson. 2013. Precise hydrodynamic levelling by using pressure gauges. *Marine Geodesy* 36 (2):138–63. doi:10.1080/01490419.2013.771594
- Mayer-Gürr, T., R. Pail, T. Gruber, T. Fecher, M. Rexer, W.-D. Schuh, J. Kusche, J.-M. Brockmann, D. Rieser, N. Zehentner, A. Kvas, B. Klingner, O. Baur, E. Höck, S. Krauss, and A. Jäggi. 2015. The combined satellite gravity field model GOCO05s. In European Geosciences Union General Assembly, 12–17 April 2015, Vienna, Austria. DOI:
- Metsar, J., K. Kollo, and A. Ellmann. 2018. Modernization of the Estonian National GNSS Reference Station Network. *Geodesy and Cartography* 44 (2):55–62. doi:10.3846/gac.2018.2023
- Myrberg, K., and T. Soomere. 2013. The Gulf of Finland, Its Hydrography and Circulation Dynamics. In *Preventive methods for coastal protection*, eds. T. Soomere and E. Quak, 181–222.
- Myrberg, K., V. Ryabchenko, A. Isaev, R. Vankevich, O. Andrejev, J. Bendtsen, A. Erichsen, L. Funkquist, A. Inkala, I. Neelov, K. Rasmus, M. Rodriguez Medina, U. Raudsepp, J. Passenko,

- J. Söderkvist, A. Sokolov, H. Kuosa, T. R. Anderson, A. Lehmann, and M. D. Skogen. 2010. Validation of three-dimensional hydrodynamic models in the Gulf of Finland based on a statistical analysis of a six-model ensemble. *Boreal Environment Research* 15 (5):453–79. Accessed August 10, 2019. <http://www.borenv.net/BER/pdfs/ber15/ber15-453.pdf>.
- Märdla, S., J. Ågren, G. Strykowski, T. Oja, A. Ellmann, R. Forsberg, M. Bilker-Koivula, O. Omang, E. Paršeliūnas, I. Liepinš, and J. Kaminskis. 2017. From discrete gravity survey data to a high-resolution gravity field representation in the Nordic-Baltic region. *Marine Geodesy* 40 (6):416–53. doi:10.1080/01490419.2017.1326428
- Nordman, M., J. Kuokkanen, M. Bilker-Koivula, H. Koivula, P. Häkli, and S. Lahtinen. 2018. Geoid Validation on the Baltic Sea Using Ship-borne GNSS Data. *Marine Geodesy* 41 (5):457–76. doi:10.1080/01490419.2018.1481160
- Oja, T., A. Ellmann, and S. Märdla. 2019. Gravity anomaly field over Estonia. *Estonian Journal of Earth Sciences* 68 (2):55–75. doi:10.3176/earth.2019.06
- Olesen, A. V. 2017. Marine gravity onboard MS Sektoru July 2017, processing report. Danish Technical University (DTU).
- Pail, R., S. Bruinsma, F. Migliaccio, C. Förste, H. Goiginger, W.-D. Schuh, E. Höck, M. Reguzzoni, J. M. Brockmann, O. Abrikosov, M. Veicherts, T. Fecher, R. Mayrhofer, I. Krasbutter, F. Sansò, and C. C. Tscherning. 2011. First GOCE gravity field models derived by three different approaches. *Journal of Geodesy* 85 (11):819–43. doi:10.1007/s00190-011-0467-x
- Pavlis, N. K., S. A. Holmes, S. C. Kenyon, and J. K. Factor. 2012. The development and evaluation of the Earth Gravitational Model 2008 (EGM2008). *Journal of Geophysical Research: Solid Earth* 117 (B4).
- Sjöberg, L. E. 2003. A computational scheme to model the geoid by the modified Stokes formula without gravity reductions. *Journal of Geodesy* 77 (7):423–32. doi:10.1007/s00190-003-0338-1
- Sjöberg, L. E., and M. Bagherbandi. 2017. Applications and Comparisons of LSMSA and RCR. In *Gravity inversion and integration*, eds. L. E. Sjöberg and M. Bagherbandi, 181–202.
- Slobbe, D. C., R. Klees, M. Verlaan, F. Zijl, B. Alberts, and H. H. Farahani. 2018. Height system connection between island and mainland using a hydrodynamic model: A case study connecting the Dutch Wadden islands to the Amsterdam ordnance datum (NAP). *Journal of Geodesy* 92 (12):1439–56. doi:10.1007/s00190-018-1133-3
- Varbla, S. 2019. Assessment of marine geoid models by shipborne GNSS and airborne laser scanning profiles. Master's thesis, Tallinn University of Technology. Accessed June 17, 2019. <https://digi.lib.ttu.ee/i/?12483>.
- Varbla, S., A. Ellmann, S. Märdla, and A. Gruno. 2017. Assessment of marine geoid models by ship-borne GNSS profiles. *Geodesy and Cartography* 43 (2):41–9. doi:10.3846/20296991.2017.1330771
- Zijl, F., M. Verlaan, and H. Gerritsen. 2013. Improved water-level forecasting for the northwest European shelf and North Sea through direct modelling of tide, surge and non-linear interaction. *Ocean Dynamics* 63 (7):823–47. doi:10.1007/s10236-013-0624-2
- Zijl, F., J. Sumihar, and M. Verlaan. 2015. Application of data assimilation for improved operational water level forecasting on the northwest European shelf and North Sea. *Ocean Dynamics* 65 (12):1699–716. doi:10.1007/s10236-015-0898-7

Appendix 2

Publication II

Varbla, S., Ellmann, A., & Delpeche-Ellmann, N. (2021). Applications of airborne laser scanning for determining marine geoid and surface waves properties. *European Journal of Remote Sensing*, 54(1), 558–568. doi:10.1080/22797254.2021.1981156

Applications of airborne laser scanning for determining marine geoid and surface waves properties

Sander Varbla ^a, Artu Ellmann ^a and Nicole Delpêche-Ellmann ^b

^aDepartment of Civil Engineering and Architecture, Tallinn University of Technology, Tallinn, Estonia; ^bDepartment of Cybernetics, Tallinn University of Technology, Tallinn, Estonia

ABSTRACT

Marine and coastal applications require now more than ever accurate and expansive understanding of the marine surface topography in the offshore domain, with the relationship of sea surface heights and geoid (equipotential surface of the Earth) being the key components. This study demonstrates some of the under-utilised and unexplored marine applications of airborne laser scanning (ALS) with respect to geoid heights verification and validation, as well as identification of surface waves properties. A synergistic methodology was developed that combines ALS measurements, hydrodynamic models and tide gauge records in conjunction with geoid models. Examination of the determined discrepancies with respect to the ALS-derived sea surface heights reveals concealed characteristics of the geoid and dynamic topography. A sea surface height accuracy of 1.7 cm in terms of standard deviation was achieved using a high-resolution regional geoid model. Furthermore, ALS point cloud data can be used to retrieve surface wavefield properties (waves heights, wavelengths and directions). In this study a direct method approach is presented. Such a deeper insight into the wave dynamics plays an enormous contribution in the understanding and quantification of coastal processes (erosion and sediment transport), as well as validation and calibration of wave models and relevant sensors.

ARTICLE HISTORY

Received 27 November 2020
Revised 3 August 2021
Accepted 12 September 2021

KEYWORDS

Airborne laser scanner;
dynamic topography; geoid;
hydrogeodesy; sea surface
height; wavefield

Introduction

Although airborne laser scanning (ALS) is conventionally used for dry land topography mapping, it has potentially similar capabilities to provide accurate heights of liquid surfaces (e.g., Gruno et al., 2013; Zlinszky et al., 2014). Unfortunately, ALS' full abilities for determining sea surface heights (SSH) and dynamic topography (DT) have so far been under-utilised and unexplored (except for a few studies, e.g., Varbla et al., 2020a; Vrbancich et al., 2011). This has been partly influenced by the capital-intensive cost of performing ALS surveys (due to fully integrated hardware and aircraft requirements, e.g., Brock et al., 2002), as well as due to insufficient knowledge on the marine geoid. The recent introduction of less costly commercial portable ALS systems may complement the increasing demand for accurate (as good as 5 cm) and reliable SSH estimates from coastal and marine applications (e.g., engineering, navigation, research, climate change).

DT is defined as the SSH deviation from the marine geoid (i.e., $DT = SSH - \text{geoid}$) and represents one of the most useful parameters in terms of marine dynamics. Thus, knowledge of the marine geoid (i.e., the shape of the ocean surface under the influence of the gravity and rotation of the Earth alone) enables

specification and quantification of oceanographic processes (e.g., sea level rise). Currently, many countries (e.g., Canada – Véronneau & Huang, 2016; USA – Li et al., 2016; National Geodetic Survey [NGS], 2013; the Baltic Sea region – Ågren et al., 2016; Ellmann et al., 2020) have implemented a gravity-based height reference datum, where instead of laborious geodetic levelling the redefinition of the national vertical datum is realised through geoid modelling. Such a high-resolution geoid model enables measurements of elevations and depths using existing and emerging global navigation satellite system (GNSS) technologies. We emphasise that these advances are of importance for the utilisation of ALS and its contribution to interdisciplinary research (hydrography, oceanography, geodesy, geophysics, climate research, etc.). Thus, the advances made in ALS technology and geoid modelling signify a necessity for a re-examination of the performance and utilisation of ALS, which may potentially be superior to other methods.

SSH and DT are usually captured by in-situ (GNSS, wave and tide gauges, e.g., Penna et al., 2018; Varbla et al., 2020b; Xu et al., 2016), remote sensing (satellite altimetry, e.g., Archer et al., 2020; Gómez-Enri et al., 2019; Vu et al., 2018) and hydrodynamic models (e.g., Liu & Huang, 2020; Madsen et al., 2019; Slobbe et al., 2013). Whilst most of these techniques represent SSH

and DT adequately, they often suffer from temporal and spatial resolution deficiencies, accuracy uncertainties and most importantly – undisclosed and overlooked variations in their vertical reference datums. For instance, satellite altimetry has coarse spatial and low temporal resolution (orbital cycles of satellite missions vary between 10–35 days). On approaching coastal areas, the satellite altimetry accuracy deteriorates due to approximations in atmospheric, sea state and geophysical corrections, as well as waveform distortions caused by coastal inhomogeneities (e.g., Cipollini et al., 2017; Vignudelli et al., 2019). Whilst modern tide gauges provide good (centimetre-level) accuracy with high temporal resolution (up to seconds), they are restricted spatially to the land bounded coastal locations. Contrarily, hydrodynamic models (HDMs) can derive DT with high spatial and temporal resolution. A major flaw of HDMs, however, is their unknown accuracy due to modelling set-up and associated errors (e.g., boundary conditions, forcings, parameterisations, etc.) and more so due to their arbitrary vertical reference datums (e.g., Jahanmard et al., 2021; Slobbe et al., 2013; Varbla et al., 2020a).

Instead, ALS systems are capable of high spatial resolution SSH monitoring for large areas within a short time frame. Accuracy of an aircraft mounted LiDAR (light detection and ranging) device that emits laser pulses and registers reflections from a land surface is usually estimated to be 5–15 cm (e.g., Huising & Gomes Pereira, 1998; Van der Sande et al., 2010). Less reflective liquid surfaces (e.g., Höfle et al., 2009; Huang et al., 2012) are registered with a similar accuracy (Cocard et al., 2002; Gruno et al., 2013; Julge et al., 2014; Zlinszky et al., 2014) within near-nadir data corridor. The resulting vertical ranges are used to generate along-route 3D point clouds as opposed to SSH profiles provided by other methods (e.g., ship-borne GNSS or satellite altimetry).

The ALS-measured instantaneous SSH can be used indirectly to derive many other datasets. For instance, geoid heights can be reckoned from SSH if DT is known from other sources. Such information is invaluable for the validation of marine geoid models, as conventional precise GNSS-levelling control points cannot be established offshore. This is especially important considering that accurate geoid models are needed to improve coastal mean DT estimates (Huang, 2017) and detect significant mean DT signals on smaller spatial scales that cannot be identified by utilising, e.g., global geopotential models (Idžanović et al., 2017).

Exploiting the advantages of different aforementioned techniques, this study demonstrates a method that combines oceanographic and geodetic approach to determine DT. The tide gauge derived DT is used to validate the HDM embedded DT and estimate the dynamic bias between the HDM and a vertical

datum (see also Jahanmard et al., 2021; Varbla et al., 2020a, 2020b). Thus, the employed methodology allows not only the validation of geoid models, but also the determination of accurate DT and deficiencies in HDMs.

Besides the SSH low-frequency component (geoid and DT), LiDAR also allows the detection of smaller scale marine processes, e.g., surface waves. This has previously been conducted using a fast Fourier transform to obtain the wave number spectrum (e.g., Huang et al., 2012; Hwang et al., 2000) and by direct mapping of the sea surface (Vrbancich et al., 2011). Another direct method to determine sea surface geometry was hinted by Varbla et al. (2020a). Given the vast amount of 3D point cloud data a deeper exploration in terms of methodology and re-analysis is now performed. Such quantification of surface waves properties contributes vitally to the understanding of the coastal processes (e.g., erosion and sediment transport), sea state and extreme events, as well as for the validation of wave models. Currently, many coastal and marine applications still rely on wave data from discrete locations (e.g., wave gauges) that do not reflect the extensive wave dynamics (e.g., waves refraction, coupling, breaking). Thus, a practical case study is conducted to illustrate applicability of the developed method and the obtainable wavefield properties.

This paper thus examines some of the under-utilised and unexplored applications of using portable ALS systems: (i) accurate determination of the low-frequency component of instantaneous SSH that can be used for the validation of geoid models and examination of deficiencies in HDMs, and (ii) investigation of the high-frequency component to quantify the properties of surface waves.

ALS measurements and synergy with hydrodynamic and geoid models

Background theory

The ALS measured SSH (SSH_{ALS}) plays a crucial role in the geoid modelling result verifications, as well as in the HDM derived DT (DT_{HDM}) evaluation with respect to a geoid model. The resulting discrepancies provide useful clues on the performance of HDMs and geoid signals/models in both spatial (for identifying problematic locations) and temporal (not dealt within the scope of this study) contexts. The HDMs, however, may possess a bias relative to a geodetic reference system (Jahanmard et al., 2021; Varbla et al., 2020a, 2020b). This dynamic bias has a low-frequency component that changes temporally and spatially (Lagemaa et al., 2011). The dynamic bias values

$$DB(\varphi_i^{TG}, \lambda_i^{TG}) = DT_{HDM}(\varphi_i^{TG}, \lambda_i^{TG}) - DT_{TG}(\varphi_i^{TG}, \lambda_i^{TG}) \quad (1)$$

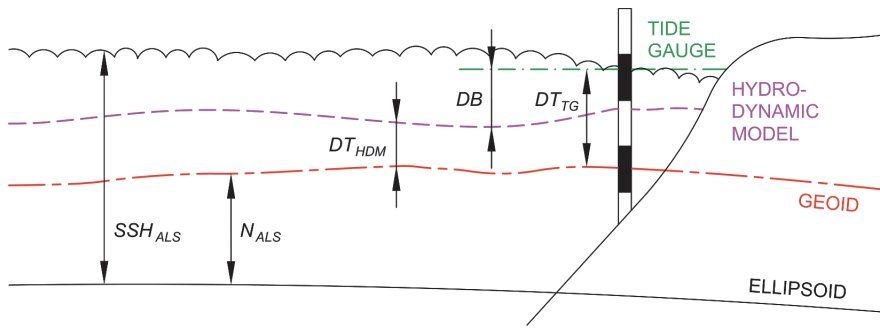


Figure 1. Derivation of the ALS-based geoidal height N_{ALS} . Notice that the depicted dynamic bias is negative (cf. Equation 1).

can be estimated at the locations of tide gauge stations with coordinates $(\varphi_i^{TG}, \lambda_i^{TG})$, where DT_{TG} denotes tide gauge obtained DT and i time-instance of an ALS

measurement. Due to its low-frequency nature, the dynamic bias at other locations (φ, λ_i) can be assumed equal (within limited spatial domain) to the one at tide

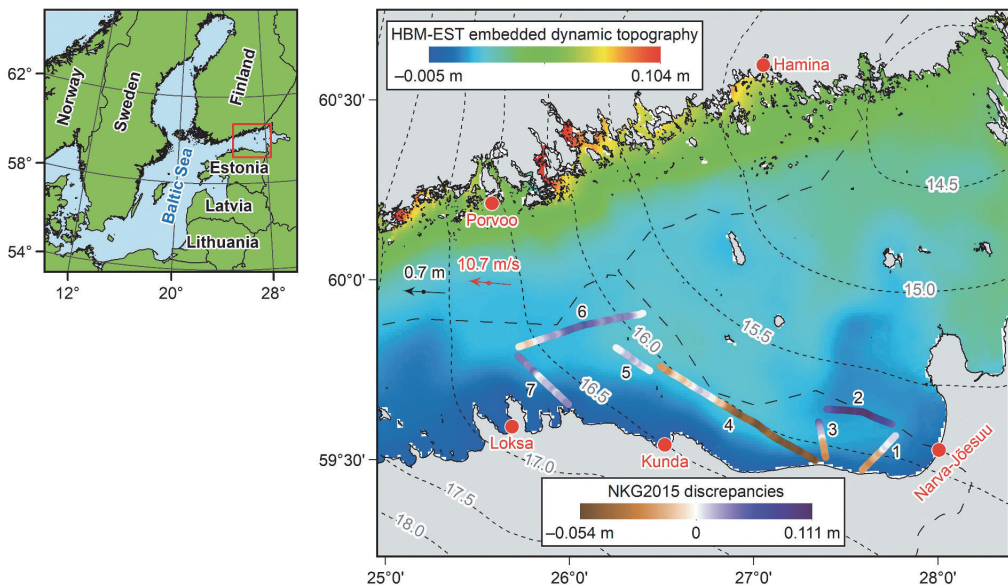


Figure 2. 10.05.2018 ALS campaign (numbers 1–7 signify the sequence of flight routes). Dotted isolines depict the NKG2015 geoid model (units in meters), whereby the bottom colour bar shows its discrepancies with respect to the ALS-based geoidal heights (see also Figure 3(f); the used HDM is HBM-EST). Coloured background shows uncorrected HBM-EST embedded DT (see the top colour bar) at 09:00 UTC. Red circles denote the employed tide gauges. The black and red arrows depict waves (height 0.7 m) and wind (speed 10.7 m/s) directions according to Suomenlahti aaltopöiju wave station and Kalbådgrund meteorological station, respectively (during the 6th profile measurements at 09:30 UTC). Dashed lines depict the country borders.

gauge or estimated using, e.g., linear interpolation. The bias (DB) eliminated DT estimates combined with the SSH_{ALS} provide then the marine geoid heights (N_{ALS} ; cf. Figure 1) as

$$N_{ALS}(\varphi, \lambda) = SSH_{ALS}(\varphi_i, \lambda_i) - [DT_{HDM}(\varphi_i, \lambda_i) - DB(\varphi_i, \lambda_i)]. \quad (2)$$

An intercomparison between N_{ALS} and geoid models (N_{Model}) can now reveal abnormalities that may occur due to underestimated hydrodynamical processes in HDMs and/or geoid model errors as

$$D(\varphi, \lambda) = N_{Model}(\varphi, \lambda) - N_{ALS}(\varphi, \lambda), \quad (3)$$

where D is the discrepancy. As the marine geoid is usually only roughly known compared to on land (where precise GNSS-levelling control points are available and used for fitting gravimetric geoid models

to the national vertical datum), the method allows identification of areas where further exploration may be required.

ALS survey and data processing

A marine ALS survey was performed on 10.05.2018 in the Gulf of Finland (at the eastern section of the Baltic Sea located in the Northern Europe; Figure 2) within the frames of routine mapping of offshore islands. The Estonian Land Board's survey plane Cessna Grand Caravan 208B mounted RIEGL VQ-1560i LiDAR Scanning System (operating at wavelength 1064 nm and pulse repetition rate 1 MHz) was employed. An operational flight altitude of around 1200 m yielded the width of the SSH data corridor ca 1000–1200 m and LiDAR footprint diameter 0.3 m, which is smaller than in most previous studies (e.g., Hwang et al.,

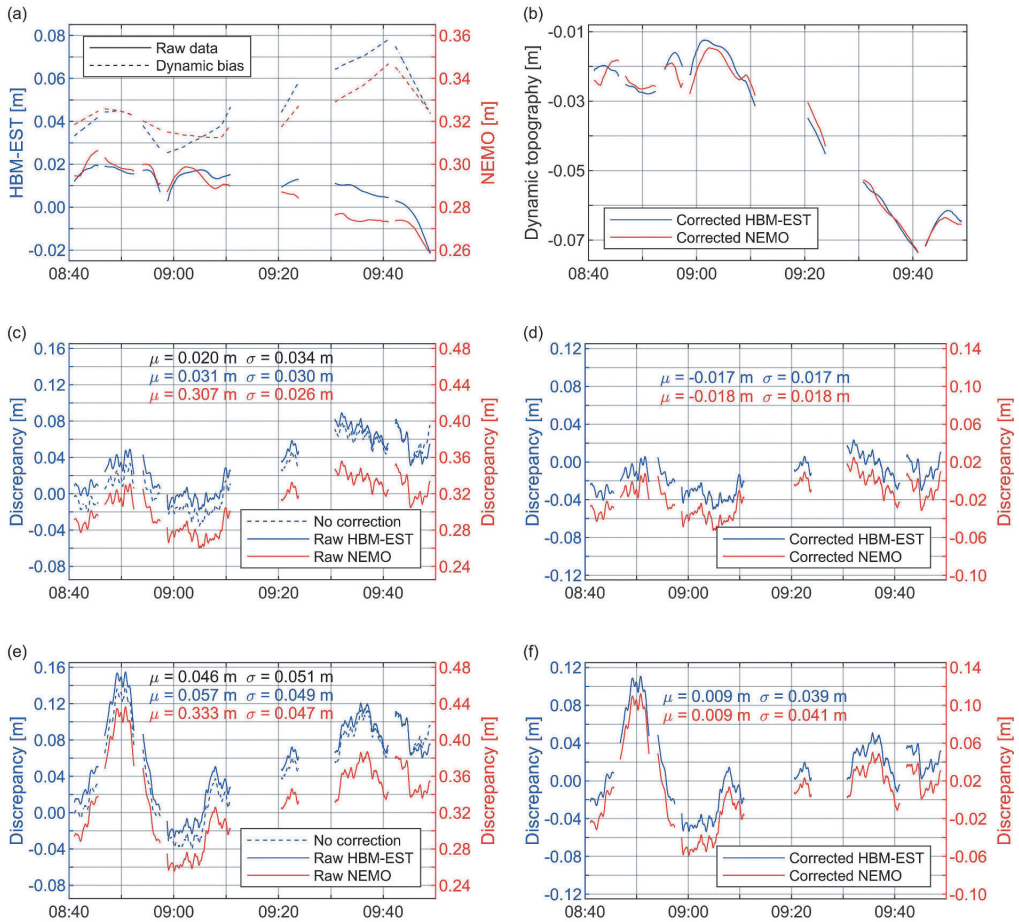


Figure 3. Profile comparisons between (a) raw (uncorrected) HDM embedded $DT_{HDM}(\varphi_i, \lambda_i)$ and the estimated bias values $DB(\varphi_i, \lambda_i)$, (b) corrected HDM data (Equation 2, the term within the square brackets), (c, d) DT-GEOID2017 and (e, f) NKG2015 validation results (Equation 3), whereas legends show the correspondingly applied DT corrections (no correction means that $N_{ALS} = SSH_{ALS}$ in Equation 3). All comparisons consider 2875 data points; time is in UTC on 10.05.2018 (horizontal axes). Average and standard deviations of discrepancies are denoted by μ and σ , respectively.

2000). The ALS measurements were acquired with a total flight time of approximately 1.2 hours that comprised of seven separate profiles (Figure 2).

The airborne GNSS and inertial measurement unit datasets were utilised for flight trajectory calculations with respect to the nearby Estonian national GNSS reference stations (Metsar et al., 2018). The RIEGL RiProcess software and standard workflow (e.g., Gruno et al., 2013) were used to compute 3D coordinated point clouds that depict instantaneous SSH (with respect to the reference ellipsoid GRS-80). This massive point cloud dataset was further processed to obtain the low- and high-frequency (see Section “ALS-derived properties of surface waves”) SSH components. Although data quality is generally uniform, a systematic upward curve in data corridor edges (effect subsides generally inwards 300–400 m from an edge) was detected (Varbla, 2019). A likely cause is the scanner scale error (e.g., Kumari et al., 2011). To avoid error propagation to the results only the mid-corridor ALS data (50 m across-track from the nadir position to each side) was considered in the low-frequency SSH signal determination computations.

To determine the low-frequency component of the ALS-based SSH a 2D moving average low-pass filter was employed (method denoted as M1). The 1116×100 m (along- and across-track directions, respectively) filtering window length was defined to match the regional geoid models’ spatial resolution (0.01×0.02 arc-deg), whereby the filtering step (i.e., the distance between filtering windows centres; the windows overlap) was set 62 m (corresponding to aircraft’s average speed m/s). Filter windows are centred at the plane’s nadir and oriented along the trajectory. The processing resulted in 62 m resolution along-nadir height profiles (SSH_{ALS}), as well as standard deviation values and point cloud densities within the filter windows (the total length of profiles is 184.4 km). The corresponding average point cloud density is 6.2 p/m^2 (for the centre 100 m of the SSH data corridor, i.e., near-nadir point cloud density). If the 1000 m wide SSH data corridor is examined instead, the average point cloud density decreases to 2.9 p/m^2 . This suggests that the pulse energy is reflected away from the LiDAR sensor more often at the SSH data corridor edges. Contrastingly, the expected point cloud density over dry land with the used scanning system is 9.0 p/m^2 when using the same survey parameters.

Dynamic topography data

The utilisation of a HDM plays an imperative role in determining and comparing the offshore DT during the ALS survey. Two regional HDM models, HBM-EST (Estonian implementation of the HIROMB-BOOS model; <http://emis.msi.ttu.ee/download/>) and

assimilated NEMO-Nordic, were employed. Both contain hourly DT data, whereby their spatial resolutions are 0.5 and 1.0 nautical miles, respectively (for details see Hordoier et al., 2019; Lagemaa, 2012). Three nearby Estonian and two Finnish tide gauges (cf. Figure 2) were used to validate the HDMs and estimate dynamic bias between these and the EVRS (European Vertical Reference System) based Estonian national vertical datum EH2000. The Estonian tide gauges are pressure sensor equipped (Liibus et al., 2013) and rigorously connected into recently renovated national high-precise levelling network, whereby their zero values coincide with the geoid surface (Kollo & Ellmann, 2019). The tide gauge-derived DT is thus also referred to the geoid model. To make the Finnish tide gauge readings compatible a height conversion has been applied similarly to Kollo and Ellmann (2019).

Linear interpolation was used to grid (retaining the original HDM resolution) the dynamic bias estimates (Equation 1) over the study area (results are shown in Figure 3(a)). ALS-determined geometric marine geoid heights N_{ALS} were then derived by combining the dynamic bias eliminated DT estimates (cf. Figure 3(b)) with the SSH_{ALS} (Equation 2). The derived N_{ALS} profiles were compared to the shipborne GNSS determined geometric geoid heights profiles presented in Varbla et al. (2020b). Note that DT for both ALS and shipborne GNSS based geoid heights profiles was estimated by using the HBM-EST HDM. The comparisons at 13 intersections yielded a standard deviation estimate of 3.3 cm and an average difference of 1.2 cm (the ALS profiles being higher than the shipborne GNSS-based ones), hence indicating good agreement and reinforcing thus the validity of the ALS data quality (and vice versa).

Comparisons with geoid models

Two regional high-resolution (both 0.01×0.02 arc-deg, i.e., approximately 0.6 nautical miles) quasi-geoid models EST-GEOID2017 (Ellmann et al., 2020) and NKG2015 (Ågren et al., 2016) were validated and used to examine the HDM-derived DT by employing the ALS-determined marine geoid heights (Equation 3; note that over the marine areas the quasigeoid coincides with the geoid). The EST-GEOID2017 is widely used by the Estonian surveying industry as the official national geoid model for converting the GNSS derived ellipsoidal heights into normal heights, whereas NKG2015 is used in the North-Europe countries. A comprehensive review of the models and comparisons between their surfaces are presented in Varbla et al. (2020b). The ALS-based validations (by considering 2875 data points altogether) are shown in

Figure 3 sub-plots (c, d) and (e, f) for EST-GEOID2017 and NKG2015 (see also Figure 2), respectively.

The applied methodology revealed several aspects with respect to the different sources of data, with the ALS results providing the only “true” in-situ source in the offshore domain. Firstly, the validation accuracies (in terms of standard deviation) are 1.7–1.8 cm and 3.9–4.1 cm for EST-GEOID2017 and NKG2015, respectively (Figure 3 sub-plots d and f). This suggests that an accuracy better than 5 cm can be achieved from the developed method. The significantly better performance of EST-GEOID2017 (by a factor of 2) is largely due to the inclusion of new shipborne marine gravity data in the southern half of the Gulf of Finland (acquired during a marine gravity campaign in July 2017) that are not considered in the NKG2015 computation (Varbla et al., 2020b). Roughly 1 dm geoid modelling improvement can be detected (compare Figure 3 sub-plots d and f at 08:50 UTC) in the profile 2 region (cf. Figure 2) where a gravity data void existed previously, thus emphasizing possibilities for better marine geoid modelling. Such ALS analysis can thus reveal poor performance areas of geoid models.

Secondly, the discrepancy comparisons of both quasigeoid models reveal similar negative gradients for profiles 1 and 3 towards shore and in the eastern half of profile 4 (cf. Figure 2, 3(d,f)). EST-GEOID2017 assessment with GNSS-levelling control points by Ellmann et al. (2020, Figure 8) supports this revelation (a control point close to the beginning of profile 1 reveals a -0.8 cm discrepancy). This suggests aggravating impact of gravity data voids, as well as possible errors in the near coast gravity data and that geoid modelling can be further improved in the area. However, note that besides geoid modelling errors, such similar discrepancies between assessments may also indicate problematic areas in the HDMs. Hence, by utilising various geoid models more confident evaluations can be conducted.

Thirdly, the conducted assessments reveal the deficiencies of HDMs. It is obvious from the dynamic bias differences (see Figure 3(a)) that different reference datums are used for the HDMs’ compilation. The 3 dm dynamic bias of NEMO is significantly larger than the one of HBM-EST. Such a bias in offshore must be determined and removed for practical applications. On the contrary, the dynamic bias of NEMO appears to be less varying (significant variations over such a relatively small study area suggest HDM deficiencies) during the survey compared to HBM-EST. The ALS-based validation standard deviation improvements (e.g., 3.4 cm to 3.0 and 2.6 cm for HBM-EST and NEMO, respectively) by considering raw HDM data compared to no correction (i.e., $N_{ALS} = SSH_{ALS}$ in Equation 3) could suggest that NEMO is capable of deriving sea surface dynamics more accurately (cf. Figure 3 sub-plots c and e). However, a likely cause may also be in the

models’ set-up differences. After bias removal (Figure 3(b)) the results are similar (Figure 3 sub-plots d and f). Whilst some identified discrepancies could be due to the geoid modelling, it would also be possible to identify HDM-caused discrepancies with a repeat ALS survey. The discrepancy variations between surveys could then reveal problematic areas that may need a closer look in compilation of future HDMs.

ALS-derived properties of surface waves

From the high-frequency component of raw ALS point cloud data the sea surface waves can be identified. Quantification of their properties has been performed using a 2D fast Fourier transform procedure (e.g., Huang et al., 2012; Hwang et al., 2000) or directly (Vrbancich et al., 2011). In this study a new direct method was developed (denoted as M2) to derive spatial distribution of surface waves properties, which were validated with in-situ wave gauge data (Figure 2). This method first involved a reconstruction of the raw instantaneous SSH as 1×1 m resolution grids using an inverse distance weighted interpolation (a procedure that also reduces potential data noise). Secondly, wavelengths defined as horizontal distances between wave crests (defined as local maxima) were determined and constructed into 1 m resolution along-nadir profiles. Thirdly, wave heights were estimated as differences between along-nadir moving maximum and minimum filters with a 1 m step. The filters’ length (ξ) was defined as

$$\xi(\varphi_i, \lambda_i) = 2\Lambda(\varphi_i, \lambda_i) + 1 + 2\Lambda(\varphi_i, \lambda_i), \quad (4)$$

where Λ denotes the wavelength of the surface waves. The algorithm checks along-nadir SSH in a forward and backward direction two wavelengths each, but also considers that the wave crest or trough may occur to be at the current location with coordinates (φ, λ) – this is denoted by the 1. The ξ was defined to be longer than the detected wavelengths (determined in step two) to avoid unrealistically low wave height estimates due to occasional overlapping waves, which resulted in shorter wavelength estimates as multiple wave crests were detected on a single wave (i.e., if ξ was defined shorter, on such occasions the determination of actual wave crests and troughs may have been unattainable). Although this also means that in other times multiple waves are considered simultaneously (i.e., when wavelengths are estimated correctly), it is assumed that there is no difference between the wave heights within such a short distance (note that the approach determines the highest wave within the filters’ length).

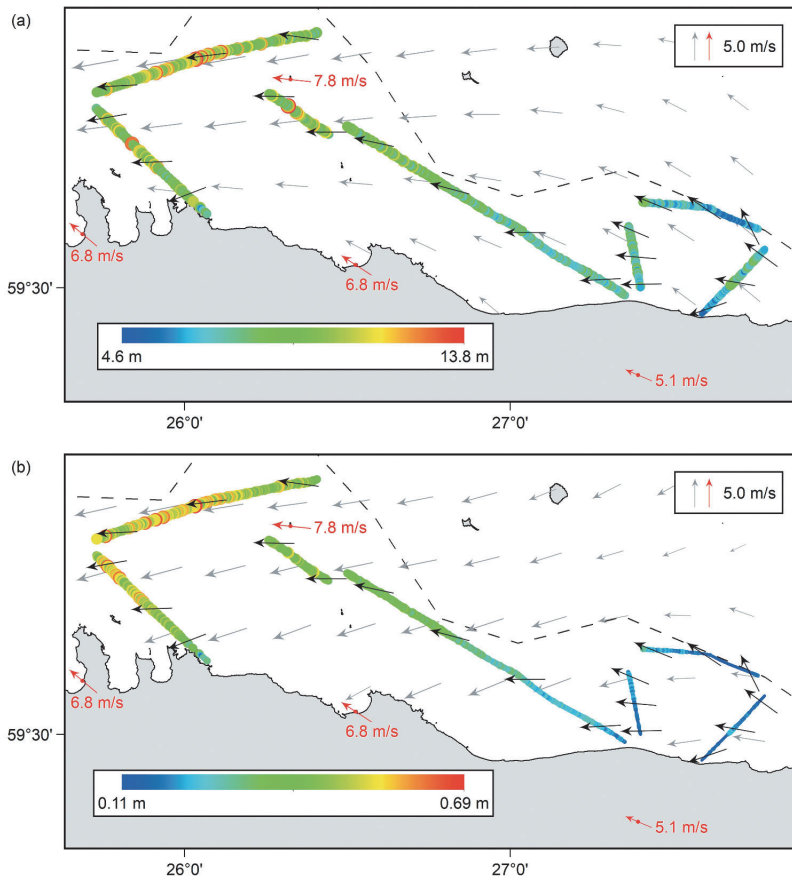


Figure 4. ALS-derived (a) wavelengths and (b) heights of the surface waves. The scaled grey vectors depict (a) HBM-EST and (b) NEMO HDMs embedded wind data (on 10.05.2018 at 09:00 UTC), whereas the scaled red arrows denote the actually measured wind data. The offshore black arrows (non-scaled) show ALS-estimated surface wind waves directions. Dashed black line depicts the Estonian marine border.

Finally, a moving average low-pass filter was applied to generalise the results (e.g., to filter out the estimated shorter wavelengths due to occasional overlapping waves). After removing outliers, a discrete sum of absolute differences function between filtered and reconstructed (step three) signals was first compiled for each profile separately. Maximum test filter length was always set to 2000 m (arbitrary estimate that was determined suitable during the compilation of the filter). Based on the sum of absolute differences function a new function was next compiled by using a three-point centred moving standard deviation. The final filter length was then defined as a value where the new function values reached first time 1/3 of its mean standard deviation. Such filtering resulted in reasonably smoothed wavelength and height profiles without changing the general trends (filter lengths were generally within 150–250 m). The computed wavelengths and heights are shown in Figure 4. High correlation ($r = 0.948$) between M1-derived standard deviation

values and M2-derived wave heights reinforces the assumption of properly reconstructed instantaneous SSH.

During the ALS survey the majority of sea wavelengths varied between 5.9–10.2 m and heights 0.14–0.55 m (Figure 4), whereby higher waves were observed mostly in the NW section of the study area (profiles 5–7; cf. Figure 2). The general trend of these higher wave heights agrees well with the wave buoy (Suomenlahti aaltopoiju) data of 0.7 m (cf. Figure 2). The 1×1 m data grids allowed also to estimate surface wind waves directions (not obtainable from wave gauges). Good agreement with the HDMs-embedded wind directions can be seen in Figure 4, whereas slight differences are expected due to the narrow shape of the Gulf of Finland (Pettersson et al., 2010). Notice that the HBM-EST-embedded wind data (Figure 4(a)) agrees better with both the meteorological stations measured wind and ALS-estimated waves directions than the NEMO model data (Figure 4(b)). As

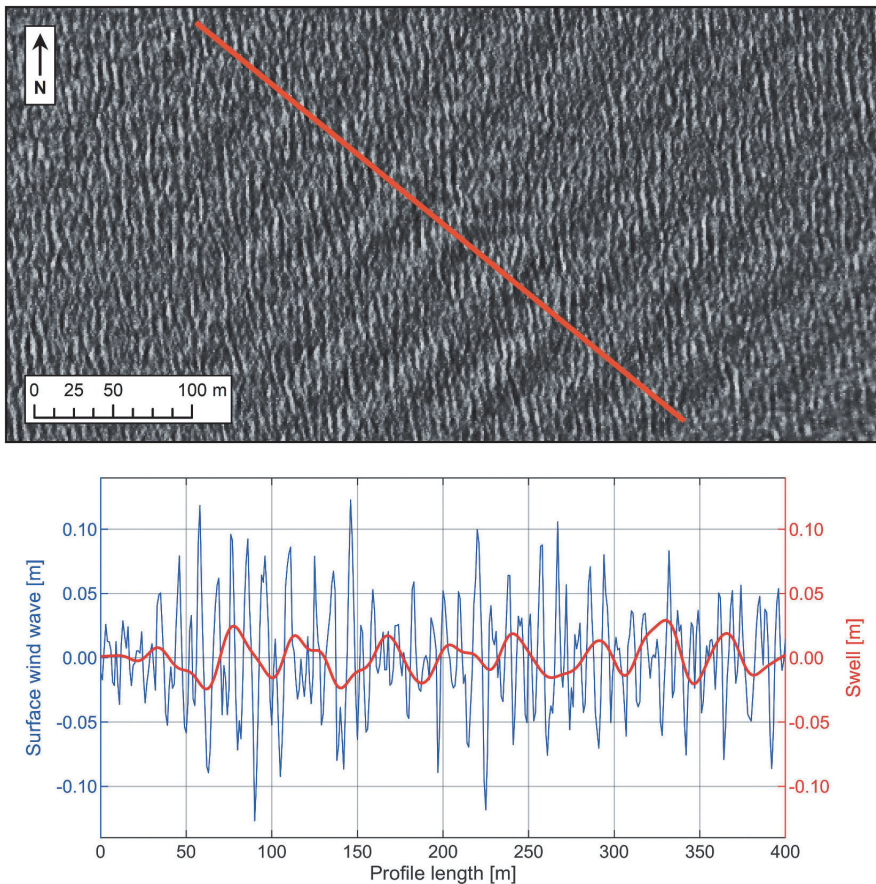


Figure 5. A 1×1 m resolution instantaneous SSH grid (centre section of profile 1, cf. Figure 2) and profiles of surface wind waves and swells (ALS measured signal is the spectral and directional sum of these). Note the two dominating cardinal directions: SE-NW for the swells and E-W for the higher frequency surface wind waves.

expected, Figure 4 also shows waves magnitude dependency on wind speed. Correlation coefficients between ALS-derived wave heights and HDM-embedded wind speeds from HBM-EST and NEMO are 0.846 and 0.795, respectively. Wavelengths, however, are not so well correlated with the HDMs-embedded wind speeds. The respective correlation coefficients are 0.647 and 0.584.

In addition to the wind-generated surface waves the ALS measurements also detected lower frequency swells on the background (Figure 5). A standard MATLAB signal processing low-pass filter was employed to extract the swells features from the ALS-measured sea surface (surface wind waves in Figure 5 were derived by subtracting the determined swell signal from the ALS measured combined signal). The filter's sampling frequency of 62 Hz was defined according to the average speed of the aircraft (62 m/s) and the resolution of the used grids (1×1 m). As the ALS measurements result essentially in a snapshot of the sea surface, it is assumed that the used sampling

frequency is constant in every direction with respect to the trajectory of the aircraft (i.e., the angle between the trajectory and the examined sea surface profile). It was then determined that a passband frequency of 0.5 Hz allows estimation of realistic swells features (this value roughly corresponds also to the estimated average wavelength of swells divided by the average speed of the aircraft). The derived wavelengths of swells agree well (within a few metres) with those measured directly from the computed grids. Also, notice good countability of swell crests (along the profile) from both the 3D sea surface model and the 2D graph in Figure 5. Wavelengths of the detected swells are generally 30–40 m with wave heights of 0.05–0.12 m.

The ALS measurements indicate a rather calm sea, whereby the sea surface was notably smooth in the eastern study area with wave heights mostly around or below 2 dm (Figure 4(b)). Earlier studies (Huang et al., 2012; Julge et al., 2014; Magalhaes et al., 2013; Zlinszky et al., 2014) indicate that such a smooth sea surface degrades the acquired ALS data

in comparison to marine measurements with a more disturbed sea surface and causes significant amount of laser pulses to reflect away from the LiDAR sensor even in the near-nadir zone. According to Julge et al. (2014) sea surface with waves lower than 3–4 dm may already cause significant drop in the ALS data quality and density. The current experiment, however, demonstrates no such relation between the sea state and backscattering (i.e., correlation coefficient between M1-derived near-nadir point cloud densities and M2-derived wave heights is 0.256). Interestingly, the average near-nadir point cloud density with wave heights below 2 dm is 6.4 p/m², which is slightly more than the overall average of 6.2 p/m² for the whole experiment. Hence, high quality data were acquired even with smooth sea surface. Note that Julge et al. (2014), Magalhaes et al. (2013), and Zlinszky et al. (2014) used the previous generation Leica ALS50-II scanning systems. It is thus possible that the specific ALS system used in the previous studies may have been the reason for data quality degradation in smooth sea surface conditions.

Discussion and summary

ALS offers a significant capability for instantaneous and accurate SSH measurements especially in the off-shore domain, which introduces new possibilities for interdisciplinary research. Validation of different marine models (e.g., geoid and hydrodynamic models) and dynamics to identify problematic locations, as well as high-resolution mapping of the wavefield properties can be conducted. For instance, accurate spatio-temporal measurements of the wavefield (e.g., by combining geometry information and wave periods) could be used for the calibration of the wave radars and buoys, sea state parameters and for the calibration and validation of wave models. Given the climate change effects on coastal areas (e.g., extreme events, flooding, coastal erosion) the contribution of ALS is expected to provide new insight and solutions. In addition, simultaneous satellite-derived and ALS-measured SSH and waves properties would allow to assess the satellite data quality.

Remember also that the developed method of this study has potential to reveal problematic areas and naturally occurring phenomena that are poorly described by the used HDM (i.e., discrepancies between the actual and modelled DT manifest as errors in the HDM-based DT). This can be done by conducting repeat ALS surveys, which would reveal both the reoccurring and time-variable discrepancies. Note that the geoid is a comparatively static surface, meaning that the reoccurring discrepancies likely describe the geoid model errors. The DT, on the other hand, varies in time. This suggests that the time-

variable discrepancies could be caused by errors in the HDM that is used to describe the DT during the ALS survey. As certain HDM processes can be over-/under-estimated due to a particular model set-up, the method provides means to identify and quantify such problems. Hence, deeper examination is needed for ALS' utilisation for many other purposes besides determining accurate SSH and surface waves.

Although ALS technology is still relatively expensive compared to some alternative sensors, national authorities are beginning to exploit ALS' capabilities more frequently. A beneficial practice for the research community would hence be the distribution of ALS data over marine areas. Yet currently ALS data is discarded, or the ALS system is turned off entirely over marine areas. The current study is a proof of concept that the research value SSH data can be acquired not only by specially designed ALS equipment but also by using standard ALS mapping routines and portable equipment. For instance, a portable ALS system could be mounted on aircrafts that are used for environmental and marine monitoring, e.g., for oil spills detection that are nowadays conducted regularly by various agencies. Potential future direction (e.g., for coastal monitoring) could also be unmanned aerial vehicle mounted LiDAR devices resulting in cheaper operational costs.

Acknowledgments

The research is supported by the Estonian Research Council grants "Development of an iterative approach for near-coast marine geoid modelling by using re-tracked satellite altimetry, in-situ and modelled data" [grant number PRG330] and "Wave dynamics for coastal engineering and management: the advantages and challenge of the Lagrangian perspective" [grant number PRG1129]. Grünthal, E. from the Estonian Land Board provided the coordinated ALS point clouds. Kaleva, L. from the Estonian Environmental Agency provided the used raw tide gauge data, which were then revised by Kollo, K. from the Estonian Land Board. A special thanks to the Swedish Meteorological and Hydrological Institute (SMHI) for their cooperation in obtaining NEMO-Nordic model data. The three anonymous reviewers are thanked for their contribution to the quality of the manuscript. The processed ALS data used in the study is made available through SEANOE data repository: <https://doi.org/10.17882/76491>.

Funding

This work was supported by the Estonian Research Council [PRG1129, PRG330].

ORCID

Sander Varbla  <http://orcid.org/0000-0003-3031-8645>
Artu Ellmann  <http://orcid.org/0000-0002-5512-8461>

Nicole Delpeche-Ellmann  <http://orcid.org/0000-0002-8481-7960>

References

- Ågren, J., Strykowski, G., Bilker-Koivula, M., Omang, O., Mårdla, S., Forsberg, R., Ellmann, A., Oja, T., Liepins, I., Parseliunas, E., Kaminskis, J., Sjöberg, L. E., & Valsson, G. (2016, September 19–23). *The NKG2015 gravimetric geoid model for the Nordic-Baltic region* [Oral presentation]. 1st joint commission 2 and IGFS meeting international symposium on gravity, geoid and height systems, Thessaloniki, Greece. <https://doi.org/10.13140/RG.2.2.20765.20969>
- Archer, M. R., Li, Z., & Fu, -L.-L. (2020). Increasing the space-time resolution of mapped sea surface height from altimetry. *Journal of Geophysical Research: Oceans*, 125(6), e2019JC015878. <https://doi.org/10.1029/2019JC015878>
- Brock, J. C., Wright, C. W., Sallenger, A. H., Krabill, W. B., & Swift, R. N. (2002). Basis and methods of NASA Airborne Topographic Mapper lidar surveys for coastal studies. *Journal of Coastal Research*, 18(1), 1–13. <https://journals.flvc.org/jcr/article/view/81240>
- Cipollini, P., Calafat, F. M., Jevrejeva, S., Melet, A., & Prandi, P. (2017). Monitoring sea level in the coastal zone with satellite altimetry and tide gauges. *Surveys in Geophysics*, 38(1), 33–57. <https://doi.org/10.1007/s10712-016-9392-0>
- Cocard, M., Geiger, A., Kahle, H.-G., & Veis, G. (2002). Airborne laser altimetry in the Ionian Sea, Greece. *Global and Planetary Change*, 34(1–2), 87–96. [https://doi.org/10.1016/S0921-8181\(02\)00107-8](https://doi.org/10.1016/S0921-8181(02)00107-8)
- Ellmann, A., Mårdla, S., & Oja, T. (2020). The 5 mm geoid model for Estonia computed by the least squares modified Stokes's formula. *Survey Review*, 52(373), 352–372. <https://doi.org/10.1080/00396265.2019.1583848>
- Gómez-Enri, J., González, C. J., Passaro, M., Vignudelli, S., Álvarez, O., Cipollini, P., Mañanes, R., Bruno, M., López-Carmona, M. P., & Izquierdo, A. (2019). Wind-induced cross-strait sea level variability in the Strait of Gibraltar from coastal altimetry and in-situ measurements. *Remote Sensing of Environment*, 221, 596–608. <https://doi.org/10.1016/j.rse.2018.11.042>
- Gruno, A., Liibus, A., Ellmann, A., Oja, T., Vain, A., & Jürgenson, H. (2013, September 23–26). *Determining sea surface heights using small footprint airborne laser scanning* [Paper presentation]. Remote sensing of the ocean, Sea Ice, Coastal Waters, and Large Water Regions 2013, Dresden, Germany. <https://doi.org/10.1117/12.2029189>
- Höfle, B., Vetter, M., Pfeifer, N., Mandlbürger, G., & Stötter, J. (2009). Water surface mapping from airborne laser scanning using signal intensity and elevation data. *Earth Surface Processes and Landforms*, 34(12), 1635–1649. <https://doi.org/10.1002/esp.1853>
- Hordoir, R., Axell, L., Höglund, A., Dieterich, C., Fransner, F., Gröger, M., Liu, Y., Pemberton, P., Schimanke, S., Andersson, H., Ljungemyr, P., Nygren, P., Falahat, S., Nord, A., Jönsson, A., Lake, I., Döös, K., Hieronymus, M., Dietze, H., Löptien, U., ... Haapala, J. (2019). Nemo-Nordic 1.0: A NEMO-based ocean model for the Baltic and North seas – Research and operational applications. *Geoscientific Model Development*, 12(1), 363–386. <https://doi.org/10.5194/gmd-12-363-2019>
- Huang, J. (2017). Determining coastal mean dynamic topography by geodetic methods. *Geophysical Research Letters*, 44(21), 11125–11128. <https://doi.org/10.1002/2017GL076020>
- Huang, Z.-C., Reineman, B. D., Lenain, L., Melville, W. K., & Middleton, J. H. (2012). Airborne lidar measurements of wave energy dissipation in a coral reef lagoon system. *Journal of Geophysical Research*, 117(C3), C03016. <https://doi.org/10.1029/2011JC007203>
- Huising, E. J., & Gomes Pereira, L. M. (1998). Errors and accuracy estimates of laser data acquired by various laser scanning systems for topographic applications. *ISPRS Journal of Photogrammetry and Remote Sensing*, 53(5), 245–261. [https://doi.org/10.1016/S0924-2716\(98\)00013-6](https://doi.org/10.1016/S0924-2716(98)00013-6)
- Hwang, P. A., Krabill, W. B., Wright, W., Swift, R. N., & Walsh, E. J. (2000). Airborne scanning lidar measurement of ocean waves. *Remote Sensing of Environment*, 73(2), 236–246. [https://doi.org/10.1016/S0034-4257\(00\)00098-5](https://doi.org/10.1016/S0034-4257(00)00098-5)
- Idžanović, M., Ophaug, V., & Andersen, O. B. (2017). The coastal mean dynamic topography in Norway observed by CryoSat-2 and GOCE. *Geophysical Research Letters*, 44(11), 5609–5617. <https://doi.org/10.1002/2017GL073777>
- Jahanmard, V., Delpeche-Ellmann, N., & Ellmann, A. (2021). Realistic dynamic topography through coupling geoid and hydrodynamic models of the Baltic Sea. *Continental Shelf Research*, 222, 104421. <https://doi.org/10.1016/j.csr.2021.104421>
- Julge, K., Gruno, A., Ellmann, A., Liibus, A., & Oja, T. (2014, May 26–29). *Exploring sea surface heights by using airborne laser scanning* [Paper presentation]. 2014 IEEE/OES Baltic international symposium, Tallinn, Estonia. <https://doi.org/10.1109/BALTIC.2014.6887853>
- Kollo, K., & Ellmann, A. (2019). Geodetic reconciliation of tide gauge network in Estonia. *Geophysica*, 54(1), 27–38. http://www.geophysica.fi/pdf/geophysica_2019_54_kollo.pdf
- Kumari, P., Carter, W. E., & Shrestha, R. L. (2011). Adjustment of systematic errors in ALS data through surface matching. *Advances in Space Research*, 47(10), 1851–1864. <https://doi.org/10.1016/j.asr.2010.12.015>
- Lagemaa, P. (2012). *Operational forecasting in Estonian marine waters* [Doctoral dissertation]. Tallinn University of Technology. Digital Collection of TalTech Library. <https://digikogu.taltech.ee/en/Item/74037505-e23e-4843-9b9f-8f4dee7f4e7b>
- Lagemaa, P., Elken, J., & Kõuts, T. (2011). Operational sea level forecasting in Estonia. *Estonian Journal of Engineering*, 17(4), 301–331. <https://doi.org/10.3176/eng.2011.4.03>
- Li, X., Crowley, J. W., Holmes, S. A., & Wang, Y.-M. (2016). The contribution of the GRAV-D airborne gravity to geoid determination in the Great Lakes region. *Geophysical Research Letters*, 43(9), 4358–4365. <https://doi.org/10.1002/2016GL068374>
- Liibus, A., Ellmann, A., Kõuts, T., & Jürgenson, H. (2013). Precise hydrodynamic leveling by using pressure gauges. *Marine Geodesy*, 36(2), 138–163. <https://doi.org/10.1080/01490419.2013.771594>
- Liu, W.-C., & Huang, W.-C. (2020). Investigating typhoon-induced storm surge and waves in the coast of Taiwan using an integrally-coupled tide-surge-wave model. *Ocean Engineering*, 212, 107571. <https://doi.org/10.1016/j.oceaneng.2020.107571>
- Madsen, K. S., Høyer, J. L., Suursaar, Ü., She, J., & Knudsen, P. (2019). Sea level trends and variability of the Baltic Sea from 2D statistical reconstruction and altimetry. *Frontiers in Earth Science*, 7, 243. <https://doi.org/10.3389/feart.2019.00243>

- Magalhaes, J. M., Da Silva, J. C. B., Batista, M., Gostiaux, L., Gerkema, T., New, A. L., & Jeans, D. R. G. (2013). On the detectability of internal waves by an imaging lidar. *Geophysical Research Letters*, 40(13), 3429–3434. <https://doi.org/10.1002/grl.50669>
- Metsar, J., Kollo, K., & Ellmann, A. (2018). Modernization of the Estonian national GNSS reference station network. *Geodesy and Cartography*, 44(2), 55–62. <https://doi.org/10.3846/gac.2018.2023>
- National Geodetic Survey. (2013). *The National Geodetic Survey ten-year strategic plan, 2013–2023: Positioning America for the future*.
- Penna, N. T., Morales Maqueda, M. A., Martin, I., Guo, J., & Foden, P. R. (2018). Sea surface height measurement using a GNSS wave glider. *Geophysical Research Letters*, 45(11), 5609–5616. <https://doi.org/10.1029/2018GL077950>
- Pettersson, H., Kahma, K. K., & Tuomi, L. (2010). Wave directions in a narrow bay. *Journal of Physical Oceanography*, 40(1), 155–169. <https://doi.org/10.1175/2009JPO4220.1>
- Slobbe, D. C., Verlaan, M., Klees, R., & Gerritsen, H. (2013). Obtaining instantaneous water levels relative to a geoid with a 2D storm surge model. *Continental Shelf Research*, 52, 172–189. <https://doi.org/10.1016/j.csr.2012.10.002>
- Van der Sande, C., Soudarissanane, S., & Khoshelham, K. (2010). Assessment of relative accuracy of AHN-2 laser scanning data using planar features. *Sensors*, 10(9), 8198–8214. <https://doi.org/10.3390/s100908198>
- Varbla, S. (2019). *Assessment of marine geoid models by shipborne GNSS and airborne laser scanning profiles* [Master's thesis]. Tallinn University of Technology. Digital Collection of TalTech Library. <https://digikogu.taltech.ee/en/item/9b1e0fb0-2739-40ff-8cd9-1868454bbcfb>
- Varbla, S., Ellmann, A., & Delpeche-Ellmann, N. (2020a). Utilizing airborne laser scanning and geoid model for near-coast improvements in sea surface height and marine dynamics. *Journal of Coastal Research*, 95(sp1), 1339–1343. <https://doi.org/10.2112/SI95-257.1>
- Varbla, S., Ellmann, A., & Delpeche-Ellmann, N. (2020b). Validation of marine geoid models by utilizing hydrodynamic model and shipborne GNSS profiles. *Marine Geodesy*, 43(2), 134–162. <https://doi.org/10.1080/01490419.2019.1701153>
- Véronneau, M., & Huang, J. (2016). The Canadian geodetic vertical datum of 2013 (CGVD2013). *Geomatica*, 70(1), 9–19. <https://doi.org/10.5623/cig2016-101>
- Vignudelli, S., Birol, F., Benveniste, J., Fu, -L.-L., Picot, N., Raynal, M., & Roinard, H. (2019). Satellite altimetry measurements of sea level in the coastal zone. *Surveys in Geophysics*, 40(6), 1319–1349. <https://doi.org/10.1007/s10712-019-09569-1>
- Vrbancich, J., Lief, W., & Hacker, J. (2011). Demonstration of two portable scanning LiDAR systems flown at low-altitude for investigating coastal sea surface topography. *Remote Sensing*, 3(9), 1983–2001. <https://doi.org/10.3390/rs3091983>
- Vu, P. L., Frappart, F., Darrozes, J., Marieu, V., Blarel, F., Ramillien, G., Bonnefond, P., & Birol, F. (2018). Multi-satellite altimeter validation along the French Atlantic coast in the southern bay of Biscay from ERS-2 to SARAL. *Remote Sensing*, 10(1), 93. <https://doi.org/10.3390/rs10010093>
- Xu, X.-Y., Xu, K., Shen, H., Liu, Y.-L., & Liu, H.-G. (2016). Sea surface height and significant wave height calibration methodology by a GNSS buoy campaign for HY-2A altimeter. *IEEE Journal of Selected Topics in Applied Earth Observations and Remote Sensing*, 9(11), 5252–5261. <https://doi.org/10.1109/JSTARS.2016.2584626>
- Zlinszky, A., Timár, G., Weber, R., Székely, B., Briese, C., Ressler, C., & Pfeifer, N. (2014). Observation of a local gravity potential isosurface by airborne lidar of Lake Balaton, Hungary. *Solid Earth*, 5(1), 355–369. <https://doi.org/10.5194/se-5-355-2014>

Appendix 3

Publication III

Varbla, S., Ågren, J., Ellmann, A., & Poutanen, M. (2022). Treatment of tide gauge time series and marine GNSS measurements for vertical land motion with relevance to the implementation of the Baltic Sea Chart Datum 2000. *Remote Sensing*, 14(4), #920. doi:10.3390/rs14040920



Article

Treatment of Tide Gauge Time Series and Marine GNSS Measurements for Vertical Land Motion with Relevance to the Implementation of the Baltic Sea Chart Datum 2000

Sander Varbla ^{1,*} , Jonas Ågren ^{2,3}, Artu Ellmann ¹ and Markku Poutanen ⁴

¹ Department of Civil Engineering and Architecture, Tallinn University of Technology, Ehitajate Road 5, 19086 Tallinn, Estonia; artu.ellmann@taltech.ee

² Department of Computer and Geospatial Sciences, University of Gävle, Kungsbäcksvägen 47, 801 76 Gävle, Sweden; jonas.agren@hig.se

³ Department of Geodetic Infrastructure, Lantmäteriet, Lantmäterigatan 2C, 801 82 Gävle, Sweden

⁴ Finnish Geospatial Research Institute FGI, National Land Survey, Geodeetinrinne 2, 02430 Masala, Finland; markku.poutanen@nls.fi

* Correspondence: sander.varbla@taltech.ee

Abstract: Tide gauge (TG) time series and GNSS measurements have become standard datasets for various scientific and practical applications. However, the TG and geodetic networks in the Baltic Sea region are deforming due to vertical land motion (VLM), the primary cause of which is the glacial isostatic adjustment. Consequently, a correction for VLM, either obtained from a suitable VLM model or by utilizing space-geodetic techniques, must be applied to ensure compatibility of various data sources. It is common to consider the VLM rate relative to an arbitrary reference epoch, but this also yields that the resulting datasets may not be directly comparable. The common height reference, Baltic Sea Chart Datum 2000 (BSCD2000), has been initiated to facilitate the effective use of GNSS methods for accurate navigation and offshore surveying. The BSCD2000 agrees with the current national height realizations of the Baltic Sea countries. As TGs managed by national authorities are rigorously connected to the national height systems, the TG data can also be used in a common system. Hence, this contribution aims to review the treatment of TG time series for VLM and outline potential error sources for utilizing TG data relative to a common reference. Similar consideration is given for marine GNSS measurements that likewise require VLM correction for some marine applications (such as validating marine geoid models). The described principles are illustrated by analyzing and discussing numerical examples. These include investigations of TG time series and validation of shipborne GNSS determined sea surface heights. The latter employs a high-resolution geoid model and hydrodynamic model-based dynamic topography, which is linked to the height reference using VLM corrected TG data. Validation of the presented VLM corrected marine GNSS measurements yields a 1.7 cm standard deviation and -2.7 cm mean residual. The estimates are 1.9 cm and -10.2 cm, respectively, by neglecting VLM correction. The inclusion of VLM correction thus demonstrates significant improvement toward data consistency. Although the focus is on the Baltic Sea region, the principles described here are also applicable elsewhere.

Keywords: Baltic Sea; BSCD2000; geoid; glacial isostatic adjustment; GNSS; tide gauge; sea level; vertical land motion



Citation: Varbla, S.; Ågren, J.; Ellmann, A.; Poutanen, M. Treatment of Tide Gauge Time Series and Marine GNSS Measurements for Vertical Land Motion with Relevance to the Implementation of the Baltic Sea Chart Datum 2000. *Remote Sens.* **2022**, *14*, 920. <https://doi.org/10.3390/rs14040920>

Academic Editors: Roland Pail, Pavel Novák, George Vergos and Sergei Badulin

Received: 23 December 2021

Accepted: 12 February 2022

Published: 14 February 2022

Publisher's Note: MDPI stays neutral with regard to jurisdictional claims in published maps and institutional affiliations.



Copyright: © 2022 by the authors. Licensee MDPI, Basel, Switzerland. This article is an open access article distributed under the terms and conditions of the Creative Commons Attribution (CC BY) license (<https://creativecommons.org/licenses/by/4.0/>).

1. Introduction

Tide gauge (TG) time series has become a standard dataset for various scientific and practical applications, whereby the sea level records refer to local solid Earth. The TG records may thus contain both sea level (such as global sea level trend) and solid Earth (such as vertical land motion—VLM) processes. Depending on the application, an independent data source could be required to disentangle these processes in the TG time series. As one of

the primary (scientific) applications of TG data is to study sea level and its variations [1–4], a common approach is to estimate the VLM rate at a TG station, which is then removed from a TG time series before further data utilization. It is essential to acknowledge here that VLM can be separated into non-linear and linear motions.

Causes for non-linear VLM include, for example, earthquakes generated by plate tectonics [5,6], groundwater pumping [7], and natural resources extraction [8]. These non-linear motions typically have relatively short spatial scales, making them difficult to model and consider. It would be impossible to obtain sufficient data without complementary space-geodetic techniques. For instance, non-linear VLM can be estimated from global navigation satellite system (GNSS) station time series [9–11] and interferometric synthetic aperture radar (InSAR) analysis [7,12,13]. Due to the non-linearity of the VLM, however, observed motions cannot be extrapolated to the past or future. In addition, while GNSS stations generally provide reliable and high-accuracy data, it may be difficult to separate the signal of non-linear VLM from data noise (e.g., caused by antenna-related errors or site-dependent effects, such as snow on the antenna radome). There is also currently a partial lack of direct co-location between GNSS and TG stations, which may prevent the utilization of GNSS velocities [9,14]. The impact of non-linear VLM on TG time series may therefore remain unnoticed and is usually neglected.

Glacial isostatic adjustment (GIA) induced VLM is commonly expressed as a spatially dependent linear trend (i.e., constant in time considering the proportionately short time extent of TG time series) due to the long-lasting viscoelastic response of the Earth [15,16]. It is also the primary cause of linear VLM. In addition to the aforementioned space-geodetic techniques, linear VLM can also be estimated by combining TG data with satellite altimetry records [9,17,18]. However, it is necessary to consider that the reliability of altimetry-based results may degrade on approaching coastal areas because of waveform distortions and approximations in atmospheric, sea state, and geophysical corrections [19,20]. Alternatively, VLM rates may be obtained from GIA models [21,22] that generally provide longer-wavelength information instead of localized VLM. Due to the flexural rigidity of the lithosphere, the GIA process results mainly in a smooth deformation. The temporal long-wavelength linear changes of the geoid [23] can also be derived from GIA modeling [16,22]. For applications that require TG-based sea dynamic topography (DT) determined relative to the geoid [3,24,25], the geoid change may need to be removed from the geocentric VLM estimates (e.g., determined by a space-geodetic technique).

The Fennoscandian Shield (including the whole Baltic Sea region) in Northern Europe is an area of a relatively low temporal VLM variability [11]. The primary cause for VLM is GIA [16,26,27], whereas the contribution from seasonal and nonseasonal velocity variability to VLM is typically modest [11]. Furthermore, the estimated current GIA deceleration of 0.002 mm/y^2 can be considered negligible [28]. Several recent studies conducted in the Baltic Sea region [29–32] have relatedly approximated VLM to be linear and employed only the NKG2016LU model [22]. Similarly, non-linear VLM is neglected in this study, although local non-linear VLM, such as subsidence, has been revealed at some TG stations [33]. NKG2016LU is a semi-empirical VLM model that combines geophysical GIA modeling with geodetic observations, implying that the model may also describe other geophysical processes. Tide gauge data have not been included in the model development, thus allowing the use of the model as an independent source of VLM correction for the TG time series.

Although GNSS time series are often used to estimate VLM, for some applications, the GNSS data itself may require consideration for VLM, too. It is a standard approach that the coordinates of continuously operating reference stations (CORS) are fixed to a defining epoch (t_0) of a national or global reference frame, which is usually in the middle of a GNSS campaign used for a frame establishment or some round time-epoch (e.g., 2000.0). The actual positions of the CORS at a different observation time (t) may differ from the positions at the defining epoch (e.g., in elevation due to VLM). As a result, VLM-generated coordinate differences will be introduced to a GNSS measurement at epoch t because a determined height difference $dh(t)$ (between measurement station and GNSS-CORS) is

referred to a reference epoch t_0 . Such an approach facilitates consistency between height reference and results of GNSS measurements. However, this only works for measurements conducted on land. For GNSS-based measurements at sea [24,25], such a standard approach may result in discrepancies because the sea level trends do not follow VLM directly (but they do contain the GIA-induced geoid change). Consequently, an offset is introduced to the marine GNSS measurements relative to a reference (Figure 1). Thus, offshore GNSS measurements may require consideration for VLM occurring at land located GNSS-CORS (and strictly also for the smaller geoid change at sea).

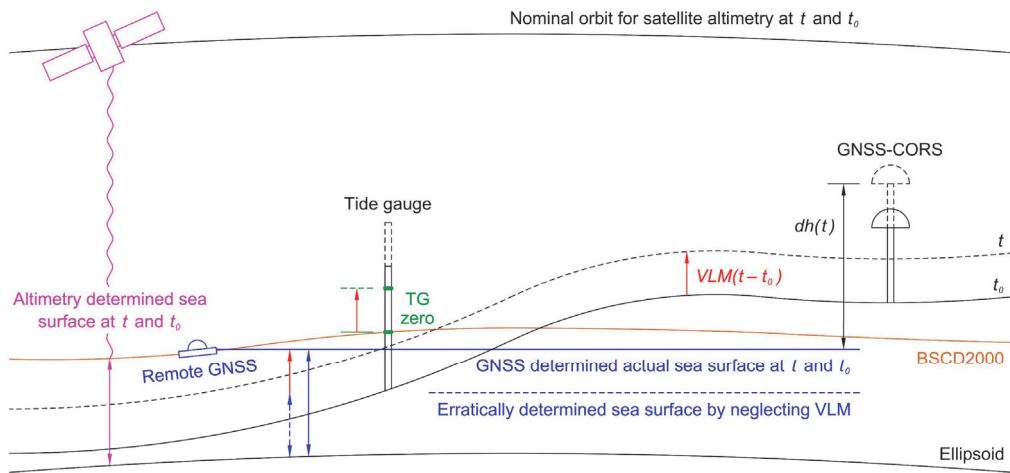


Figure 1. Simplified (assuming that DT and geoid change are negligible) interrelations between VLM (VLM is the uplift rate, as depicted) affected reference surfaces and stations. The solid lines denote geometry at a reference epoch t_0 , whereas the dashed lines are geometry at a time of observation t . Note that BSCD2000 (brown line) coincides with the TG zero and geoid surface (also with sea surface heights in the figure since DT is assumed negligible). Notice that the figure depicts satellite altimetry unaffected by VLM, but in reality, altimetry records do contain GIA-induced geoid change (also refer to Sections 3 and 4).

The common height reference, Baltic Sea Chart Datum 2000 (BSCD2000), has been initiated to facilitate the effective use of GNSS methods for accurate navigation and offshore surveying [34]. Tide gauges of the Baltic Sea region are rigorously connected to the national height systems [33,35] that agree with BSCD2000, which implies that TG readings too, refer to the BSCD2000 (i.e., the zeros of TGs coincide with the BSCD2000 at the reference epoch, neglecting measurement errors in the leveling connections to the height network). Due to the convention, the TG readings at epoch t are initially not transferred for VLM to the epochs of the corresponding height systems (i.e., t_0). Therefore, this contribution aims to review the treatment of the TG time series for VLM. Similarly, the necessity of VLM correction application on marine GNSS measurements is discussed. The underlying principles that allow consistent comparisons between various datasets relative to a common reference and time-epoch (i.e., BSCD2000) are examined, and potential error sources are described. Numerical examples are studied to illustrate the presented principles.

The outline of this paper is as follows. Considering the importance of VLM correction for various TG-related applications, the treatment of TG data in the northern part of the Baltic Sea region is reviewed in Section 2. Specifically, VLM affects the Estonian, Finnish, and Swedish TGs most. The relation between TGs and the BSCD2000 is introduced. The occasional necessity of VLM correction for marine GNSS measurements is explained next, in Section 3. The paper continues with a discussion in Section 4 and ends with a summary in Section 5.

2. Treatment of Tide Gauge Time Series for Vertical Land Motion

Tide gauge stations measure sea level heights relative to the TG zero, which is usually connected to a nearby geodetic benchmark by geodetic precise leveling. These local benchmarks are connected to the national height systems, sometimes as a part of the height reference network, sometimes only with a sloppy connection [35,36]. Besides poor connections, TG records may contain vertical datum shifts also due to, for example, natural disasters, human errors, or insufficient maintenance and documentation [6,37]. Historically, national height systems have been based on one or more TG determined mean sea level estimate(s). The mean sea level is not an equipotential surface due to semi-persistent external forces that affect the mean DT variability (in both temporal and spatial domains). There may thus be discrepancies also between various contemporary national height systems due to different selections of TG stations and epochs for height system realizations [36,38]. For the same reason, there is also a possibility of a national height system distortion [39,40]. These reasons make it difficult to use (historic) TG data in a unified height system (i.e., relative to a common equipotential reference surface), especially over larger areas. A common geodetic height system of high quality is required.

The corrections to a fixed vertical datum are often neglected. For instance, when TG time series is used in oceanographic research, the focus is typically on trends and correlations. Assuming that the VLM trend is linear, such a simplification allows determination of the absolute sea level (ASL) relative to an arbitrary vertical datum:

$$ASL(\varphi, \lambda, t) = RSL(\varphi, \lambda, t, t_0) + VLM(\varphi, \lambda) \cdot (t - t_0), \tag{1}$$

where *RSL* is the relative sea level measured by a TG and *VLM* represents the VLM rate (estimated by a suitable method, cf. Introduction) at a TG location with geodetic coordinates (φ, λ) . Note that *t* represents a TG observation epoch (decimal years) referring to an arbitrary reference epoch t_0 . Depending on the application, VLM in Equation (1) can be expressed relative to different reference surfaces: reference ellipsoid (geocentric or absolute VLM— $VLM_{geocentric}$), geoid (leveled VLM— $VLM_{leveled}$), or mean sea level (apparent VLM— $VLM_{apparent}$). These quantities can be related to each other as:

$$VLM_{geocentric}(\varphi, \lambda) = VLM_{leveled}(\varphi, \lambda) + GC(\varphi, \lambda) = VLM_{apparent}(\varphi, \lambda) + GC(\varphi, \lambda) + SLT(\varphi, \lambda) \tag{2}$$

where *GC* represents geoid change (i.e., geoid rise in the Baltic Sea region) and *SLT* sea level trend. Figure 2 visualizes the rate of $VLM_{leveled}$ and geoid rise in the Baltic Sea region, according to the NKG2016LU model [22].

2.1. Baltic Sea Chart Datum 2000

In the Baltic Sea region, European Vertical Reference System (EVRS) based national height systems have been adopted, where heights are referred to the Normaal Amsterdams Peil (NAP). In Estonia, Finland, and Sweden, the realizations are named as EH2000 [33,35], N2000 [41] and RH 2000 [42,43], respectively (Table 1). Due to the strong influence of GIA, all these realizations have employed the NKG2005LU VLM model [43,44] to reduce leveling observations to the common reference epoch 2000.0 (refer to Figure 3a).

Table 1. National height systems, corresponding t_0 and the number of active TG stations (in 2021) managed by national TG authorities (cf. Figure 2).

Country	Height System	t_0	Number of TG Stations	Managing Authority
Estonia	EH2000	2000.0	15	Estonian Environment Agency (EEA)
Finland	N2000	2000.0	14	Finnish Meteorological Institute (FMI)
Sweden	RH 2000	2000.0	54	Swedish Meteorological and Hydrological Institute (SMHI)

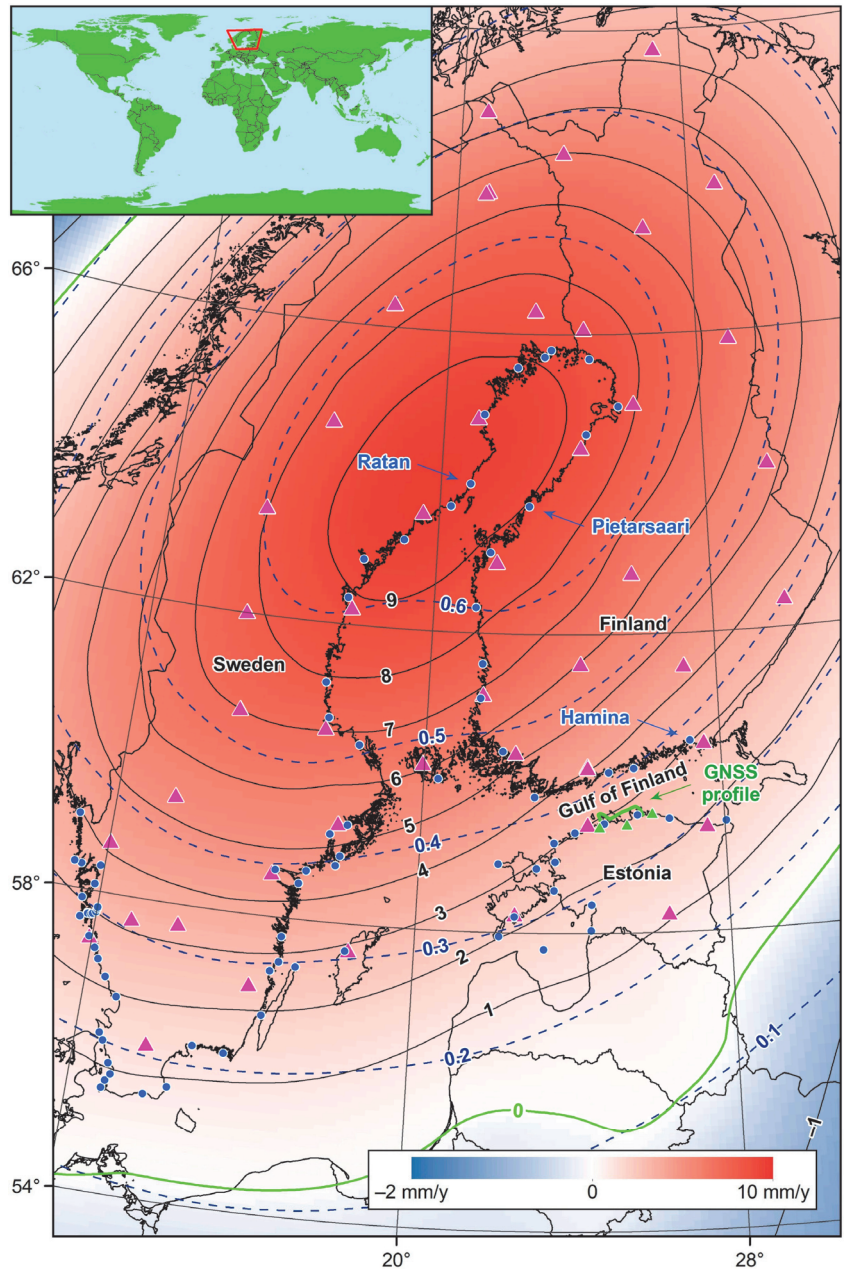


Figure 2. Rate [unit: mm/year] of $VLM_{levelled}$ in the Baltic Sea region according to the NKG2016LU model [22]. The accompanying geoid rise (about an order of magnitude smaller than VLM) is shown with dashed blue isolines. Blue circles denote active Estonian, Finnish, and Swedish TG stations (in 2021) managed by national TG authorities. Magenta triangles show the locations of national GNSS-CORS that also belong to the EUREF Permanent GNSS Network (in 2021). The three green triangles denote Estonian GNSS-CORS employed for the marine GNSS profile computations.

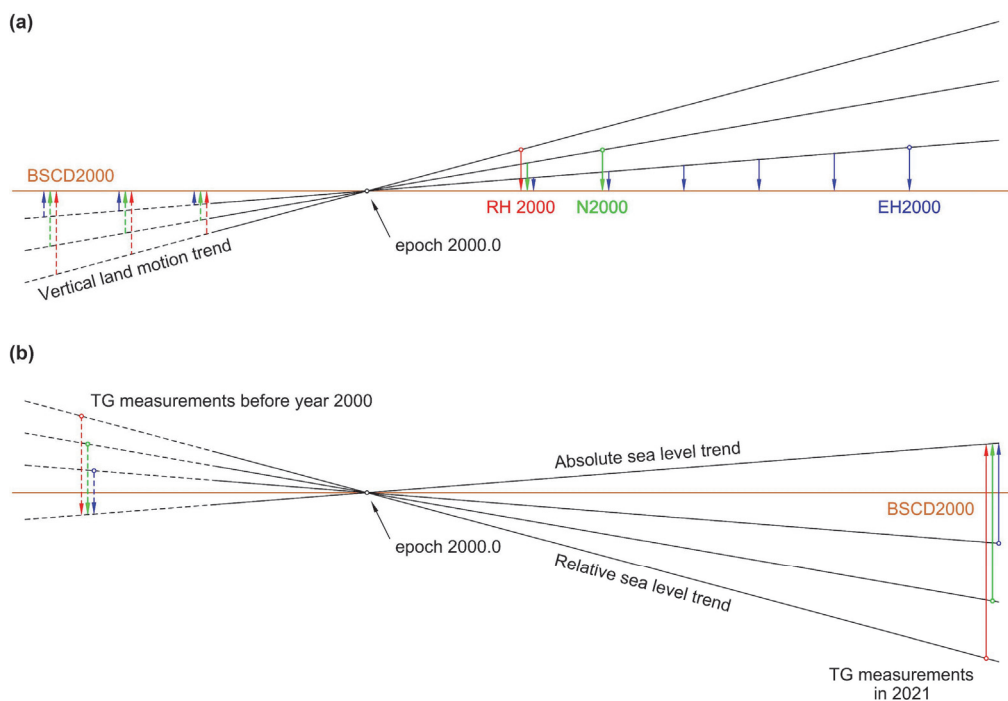


Figure 3. Simplified schematics of (a) reductions of leveling observations to a common uplift reference epoch 2000.0 (the three tilted lines symbolize different VLM rates at different locations) and (b) application of VLM correction to the TG time series (for simplicity, the DT is assumed zero at the time-epoch 2000.0). Note that the separation between BSCD2000 and absolute sea level trend in (b) represents rising sea levels. The dashed lines and arrows denote historical data since the beginning of measurements.

Consequently, these national height systems refer approximately to the same reference level. The difference between N2000 and RH 2000 is a few millimeters [41,45], and the EH2000 reference level appears to be approximately 1 cm higher than those (according to offsets of national height systems relative to EVRF2019 [46]; see also [35]). Such discrepancies can be identified from the common pan-continental adjustment of national leveling networks [47]. However, as all height systems are affected by leveling errors over longer distances, also EVRF2019, it is difficult to say how accurate these system difference estimates are.

Another convincing evidence for accurate knowledge about the national height systems is, for example, the NKG2015 quasigeoid model [48] (over marine areas, the geoid coincides with the quasigeoid, henceforth the shorter term will be used). From a 1-parameter fit (i.e., by removing a vertical offset) to the GNSS-leveling points of the Northern Europe countries, a standard deviation estimate of 2.85 cm was achieved for the model. It is also important to note that the aforementioned height systems are considered static. No further corrections are introduced post-realizations, even though the networks deform due to VLM. The reference epoch for VLM is here 2000.0.

A similar effort has been initiated to adopt BSCD2000, a common NAP referred height reference system with reference epoch 2000.0, for the Baltic Sea hydrographic surveying and engineering, nautical charts and water level information [34,49]. Offshore, BSCD2000 will be realized through GNSS and high-resolution (0.01×0.02 arc-deg) geoid modeling, while onshore, BSCD2000 will be compatible with the national height system realizations of the Baltic Sea countries (e.g., EH2000, N2000, and RH 2000) and will coincide with national geoid models to allow seamless height transitions (this will be achieved through

the blending of the models, developed by different geoid computation centers [50]). For this purpose, the Baltic Sea is being densely covered by ship- and airborne marine gravity data [24,51–55] to allow high-accuracy marine geoid modeling. Note that since the provided discussion is limited to the Estonian, Finnish, and Swedish height system realizations, an interested reader is encouraged to read additional details concerning BSCD2000 and the other Baltic Sea countries from [34,49,50].

Importantly, the described EVRS-based national height systems (EH2000, N2000, and RH 2000), EVRS itself, and BSCD2000 use the zero-tide permanent tide concept [56]. However, the zero-tide concept is not preferred for oceanographic applications as it introduces a latitude-dependent tilt to the sea level. The (normal) heights relative to BSCD2000 should be thus converted to the mean-tide concept instead. According to the EVRS conventions (cf. Section 5 of [57]), the correction for normal heights is:

$$H_{\text{mean-tide}}(\varphi) = H_{\text{zero-tide}}(\varphi) - 0.09940 + 0.29541\sin^2\varphi + 0.00042\sin^4\varphi, \quad (3)$$

where heights are given in meters, and φ is the geodetic latitude of a point of interest (e.g., a TG station). Since BSCD2000 refers to the NAP level, it would be preferred that the conversion is conducted relative to NAP, which is then kept fixed independently of the permanent tide concept. This implies that the following correction should be used instead:

$$H_{\text{mean-tide}}(\varphi) = H_{\text{zero-tide}}(\varphi) + 0.29541(\sin^2\varphi - \sin^2\varphi_{\text{NAP}}) + 0.00042(\sin^4\varphi - \sin^4\varphi_{\text{NAP}}), \quad (4)$$

where φ_{NAP} is the geodetic latitude of NAP (52°22'53" [58] in the European Terrestrial Reference System 1989).

2.2. Tide Gauge Time Series in Relation to the Baltic Sea Chart Datum 2000

A principal component is that the TG stations are rigorously connected to the corresponding national height systems EH2000, N2000, and RH 2000 via precise leveling [33,35]. In addition, regular re-leveling is conducted to verify the stability of TG stations. The determined discrepancies (e.g., due to localized subsidence) are documented and accounted for in the TG time series. Similarly, the TGs are checked for zero drift. The data are adjusted accordingly if TG zero has drifted from its initial position. Such an approach means that the zero values of TGs should approximately coincide with the same equipotential reference surface (i.e., the geoid) at the reference epoch of a height system (e.g., epoch 2000.0 for the Baltic Sea region). This permits the expression of the contemporary TG readings directly as DT relative to the geoid at the system reference epoch, which is primarily needed for studying specific oceanographic processes. The TG determined sea levels are thus referred to the national geoid models, as well as to the BSCD2000. However, it is essential to note that for rigorous applications, these TG data should be checked for datum consistency (i.e., jumps in the data) by the data user, since the data provided by managing authorities may not always be completely reliable.

Considering the above and assuming the VLM trend to be linear allows Equation (1) to be modified as (note that the general formula of Equation (1) is still valid):

$$DT_{\text{ASL}}(\varphi, \lambda, t) = DT_{\text{RSL}}(\varphi, \lambda, t, t_0) + VLM_{\text{levelled}}(\varphi, \lambda) \cdot (t - t_0), \quad (5)$$

where DT_{RSL} is relative DT compiled by the VLM corrupted TG readings, whereas DT_{ASL} is the estimated absolute DT that reflects the actual sea level heights. Since the geoid at the reference epoch t_0 is now chosen as a reference surface, VLM correction should also be referred to the geoid (i.e., VLM_{levelled} is to be used). The geoid change should thus not be included within the VLM correction for DT. Instead of an arbitrary epoch, the system reference epoch t_0 is now used for calculating the VLM correction. On epoch t_0 , the VLM correction is zero (refer to Figure 3b). Table 1 lists t_0 for Estonian, Finnish, and Swedish TG time series (i.e., 2000.0), whereby the accordingly reduced observations by

Equation (5) (i.e., absolute DT) can be used consistently with the other Baltic Sea region geodetic infrastructure.

Note that the relative DT time series can also be transformed to any arbitrary reference epoch t_A :

$$DT_{RSL}(\varphi, \lambda, t, t_A) = DT_{RSL}(\varphi, \lambda, t, t_0) + VLM_{Ilevelled}(\varphi, \lambda) \cdot (t_A - t_0), \quad (6)$$

whereby the following modified Equation (5):

$$DT_{ASL}(\varphi, \lambda, t) = DT_{RSL}(\varphi, \lambda, t, t_A) + VLM_{Ilevelled}(\varphi, \lambda) \cdot (t - t_A), \quad (7)$$

results in the same absolute DT as the initial Equation (5). Derived Equation (7) implies no correct choice for a reference epoch as long as the VLM correction is applied consistently. Such a consistent reference epoch allows practical use of the estimated absolute DT. For example, if the objective is to study mean DT around the Baltic Sea, the resulting absolute mean DT estimates refer to the geoid, thus providing a basis to study and quantify the occurring oceanographic processes (note that Equation (4) should also be considered). Conversely, inconsistent use of reference epoch (e.g., terms $DT_{RSL}(\varphi, \lambda, t, t_0)$ and $VLM_{Ilevelled}(\varphi, \lambda) \cdot (t - t_A)$ are employed together) would produce absolute mean DT estimates that do not refer to the same equipotential reference surface, potentially ensuing in misinterpretation of the results. In case a common reference epoch does not exist, it should be established, but similar use of TG data in a common system also requires that zero values of TGs refer to the same equipotential surface at an established reference epoch (e.g., see [59] for a potential method to connect TG stations to a common system). On the other hand, if the objective is to study sea level trends, adopting a common system may not be beneficial (i.e., consistent use of reference epoch is not mandatory).

2.3. Numerical Examples

The hourly open access TG data from SMHI [60] and FMI [61] (cf. Table 1) are used for presenting the TG time series from 1928 to 2021 for Ratan (Sweden) and Pietarsaari and Hamina (Finland), respectively (refer to Figure 2 for the TG locations). Since FMI currently provides open access TG data only from 1971, the Finnish TG time series are complemented with monthly mean sea level data from the Permanent Service for Mean Sea Level (PSMSL) [62,63] for the period 1928–1970 to examine the most extended common period for all three TGs. Note that the Finnish PSMSL sea level data is also initially sourced from FMI. These monthly mean sea levels were first converted to the N2000 height system (i.e., to relative DT) from the initial PSMSL revised local reference (RLR) system:

$$DT_{RSL}(\varphi, \lambda, t, t_0) = RLR(\varphi, \lambda, t) - C_{PSMSL} + H_{BM}, \quad (8)$$

where C_{PSMSL} is a PSMSL conversion factor associated with the selected TG station (11.025 m and 7.800 m for Pietarsaari and Hamina, respectively) and H_{BM} represents a local benchmark height in N2000 (correspondingly 4.487 m and 1.076 m).

For the sake of compatibility, the hourly SMHI, and FMI TG datasets were also averaged to monthly means. The FMI-based and PSMSL-based relative DT for 1971–2019 (the PSMSL datasets end with 2019) were then compared for validation, yielding -0.3 mm and 0.2 mm average discrepancies for Pietarsaari and Hamina TG time series, respectively. Such minor discrepancies indicate a good datum consistency between the two datasets, which are thus suitable for use together. The corresponding estimated standard deviation values of differences are 3.7 mm and 4.2 mm due to a few outliers that appear as random and would therefore not affect sea level trend estimations. Generally, the differences are within ± 1 mm. Although the datums appear consistent in these examples, it is usually recommended to use metric PSMSL data instead of revised local reference data, since the latter may not always be reliably reduced to a common datum. The metric data is entered into the PSMSL data repository precisely as obtained from the managing authorities. Thus,

the user should check these data themselves for inconsistencies (i.e., jumps in the data) before further data utilization.

The derived monthly averaged DT estimates (SMHI, FMI, and PSMSL obtained data) were next converted from the zero-tide to the mean-tide concept according to Equation (4). A linear trend was then fitted to the monthly averaged TG time series (FMI and PSMSL data are considered together for Finnish TG stations) in the least-squares sense (similarly to [32]) to approximate relative and absolute sea level trends. Importantly, the residuals of monthly averaged DT estimates (after de-trending) are not representing a pure white noise process due to the presence of time-correlated sea level variability (e.g., due to atmospheric and geophysical signals [64]; the residuals are also not normally distributed). Moreover, the sea level rise appears not to be a constant [28,31] (in this study, it is simplified by a linear trend). A more rigorous approach could hence be needed for a more reliable trend estimation (e.g., see [65]). However, the primary aim here is to demonstrate the application of VLM correction, which is a linear process.

The monthly averaged relative sea level (i.e., DT_{RSL}) time series for Ratan TG are presented in Figure 4a. As Ratan is near the epicenter of the Fennoscandian post-glacial uplift (cf. Figure 2; $VLM_{levelled} = 9.5$ mm/y and $\sigma_{VLM} = 0.18$ mm/y according to NKG2016LU), a strong negative trend of -7.5 mm/y dominates. The absolute sea level (i.e., DT_{ASL}) was estimated by Equation (5), revealing an expected rising sea level trend of 2.0 mm/y (Figure 4b). This estimate represents an average annual sea level rise over the examined 94 years. Due to sea level rise acceleration, the current rate estimate is higher (see also [32]). From 1993 to the present, the absolute sea level trend rate was estimated at 4.4 mm/y (Figure 4b), which is more than twice as fast. Yet, due to the shorter period (29 years), this estimate may also contain interdecadal sea level variability (e.g., it has been suggested that the length of TG time series should be at least 60 years for reliable evaluations [1,66]).

Note that all the sea level estimates are given in the Swedish height system RH 2000, which coincides with the BSCD2000 (both using the mean-tide concept). Additionally, notice that at the epoch 2000.0 (i.e., t_0) the relative and absolute sea level estimates (0.264 m according to the trend in Figure 4 sub-plots a and b) coincide. This coinciding value can be considered a mean DT estimate at the Ratan TG in mean-tide BSCD2000 (epoch 2000.0) over the period in question (from 1928 to 2021). However, the mean DT may also include shorter-term (e.g., seasonal or annual) variations (depending on the temporal estimation extent) that are excluded from the presented linear sea level trend. For instance, this is indicated by the variation of monthly averaged DT in Figure 4.

An additional test was conducted where deliberate errors were introduced to the results. The mistakes include (i) use of $VLM_{geocentric}$ (10.2 mm/y at the Ratan TG station; $\sigma_{VLM} = 0.18$ mm/y) instead of $VLM_{levelled}$ to estimate absolute sea levels from the monthly averaged relative sea level time series and (ii) use of an arbitrarily selected epoch 1980.0 instead of epoch 2000.0 as a reference for the VLM correction. The (erroneous) results of this test are shown in Figure 4c. First, it can be noticed that the estimated rising sea level trend of 2.0 mm/y (Figure 4b) increases to 2.7 mm/y (over the examined 94 years) since a significant geoid change signal is now included (notice in Figure 2 that Ratan is near the epicenter of the geoid rise maximum). Such a trend overestimation resulting from the wrong reference surface for the VLM correction (reference ellipsoid instead of geoid) can lead to a severe misinterpretation of the climate-related sea level trend signal. The geoid change signal prominent in the Baltic Sea region is primarily a result of GIA. Secondly, due to the wrong choice of reference epoch, the mean DT estimate at epoch 2000.0 nearly doubles from 0.264 m to 0.467 m. Such a significant increase in the estimate can result in a misconception concerning the occurring oceanographic processes.

Similar to the Ratan TG, the Pietarsaari TG relative sea level time series presents a strong negative trend (Figure 5a). On the other hand, notice how the estimated trend for Hamina, which is the Finnish TG furthest from the uplift epicenter (cf. Figure 2; $VLM_{levelled} = 3.0$ mm/y and $\sigma_{VLM} = 0.18$ mm/y), is -0.8 mm/y (Figure 6a). This suggests that the sea level and solid Earth processes approximately compensate each other over

the examined period. The absolute sea levels for Pietarsaari ($VLM_{levelled} = 8.9$ mm/y and $\sigma_{VLM} = 0.17$ mm/y) and Hamina TGs were estimated similarly to Ratan TG. It can be noticed that the resulting absolute sea level trends of 2.2 mm/y for both (Figures 5b and 6b) are slightly larger than the Ratan estimate of 2.0 mm/y. Errors in the used VLM model could cause such differences, but also note that the sea level rise in the Baltic Sea is not uniform [30]. The estimated standard uncertainties of NKG2016LU are 0.17 to 0.18 mm/y in these locations [22]. Additionally, deliberate errors were also introduced to the Pietarsaari ($VLM_{geocentric} = 9.6$ mm/y and $\sigma_{VLM} = 0.17$ mm/y) and Hamina ($VLM_{geocentric} = 3.4$ mm/y and $\sigma_{VLM} = 0.18$ mm/y) TG data processing, results of which are shown in Figures 5c and 6c, respectively. A similar trend overestimation can be noticed at these two TG stations, as was the case at the Ratan TG station. The overestimation is slightly smaller at the Hamina TG station due to the reduced impact of geoid change (cf. Figure 2).

The comparison between Figures 4b and 6b reveals a slight difference (approximately one centimeter) in the estimated absolute sea level (according to the trend) relative to the mean-tide BSCD2000. For instance, at the epoch 2000.0, the estimates are 0.264 m and 0.272 m for Ratan and Hamina TGs, respectively. Such a small difference may be due to the estimation uncertainty, but spatial variations in the mean DT can also cause the discrepancy. Although the mean DT difference is slight between the examined TG station locations, the mean DT variations in the Baltic Sea exceed a decimeter (e.g., see the example provided in [49]). This illustrates how there can be discrepancies between used height systems if different TGs are employed for different height systems realizations, as was discussed in Section 2. In the present case, however, all the results refer to the same equipotential reference surface and are compatible (i.e., using the mean-tide concept, the monthly averaged absolute sea level estimates of Ratan, Pietarsaari, and Hamina TGs are directly comparable). The monthly averaged absolute sea level estimates are also highly correlated, with the correlation coefficient being 0.994 between the Ratan and Pietarsaari TGs time series. Although Hamina is in a separate basin of the sea (cf. Figure 2), the resulting correlation coefficients are 0.960 and 0.965 when data from Hamina TG are compared to data from Ratan and Pietarsaari TGs, respectively. Note that, according to [64], the sea level oscillates almost synchronously in the Baltic Sea.

On the other hand, by using an arbitrarily selected epoch 1980.0 as a reference for the VLM correction, the mean DT (according to the trend) estimates are 0.467 m (Figure 4c) and 0.341 m (Figure 6c) for Ratan and Hamina TGs, respectively (the estimates are similar even with the correct use of $VLM_{levelled}$ instead of the currently used $VLM_{geocentric}$). Essentially, the wrong choice of the reference epoch has resulted in a significant mean DT tilt since the obtained estimates do not refer to the same equipotential surface. An attempt to interpret such mean DT estimates can lead to results that do not represent the actual oceanographic processes. This example illustrates well why employing the correct reference epoch has utmost importance (as indicated in Section 2.2).

Theoretical Mean Sea Level for Finnish Tide Gauge Data

Notice that in Figures 5a and 6a, a so-called theoretical mean sea level is presented [67]. These are annual estimates (approximated by the Finnish Meteorological Institute) for the long-term expected values of relative sea levels at the Finnish TG stations. In estimating the theoretical mean sea level, the VLM, global sea level trend, and changes in the Baltic Sea water balance are considered according to the most recent knowledge. It appears from Figures 5a and 6a that in 1993 (notice a difference in the trends before and after 1993) the estimation of theoretical mean sea level was improved to keep the estimates synchronized with the true sea level. The trends of theoretical mean sea levels of Pietarsaari and Hamina TGs since 1993 (to present) are correspondingly -4.6 mm/y and 1.4 mm/y and seem to approximately follow the relative sea level trends estimated (as described in Section 2.3) from actual TG data, which are respectively -4.7 mm/y and 1.5 mm/y for the same period (Figures 5a and 6a). The corresponding absolute sea level trends are 4.2 mm/y and 4.5 mm/y (Figures 5b and 6b).

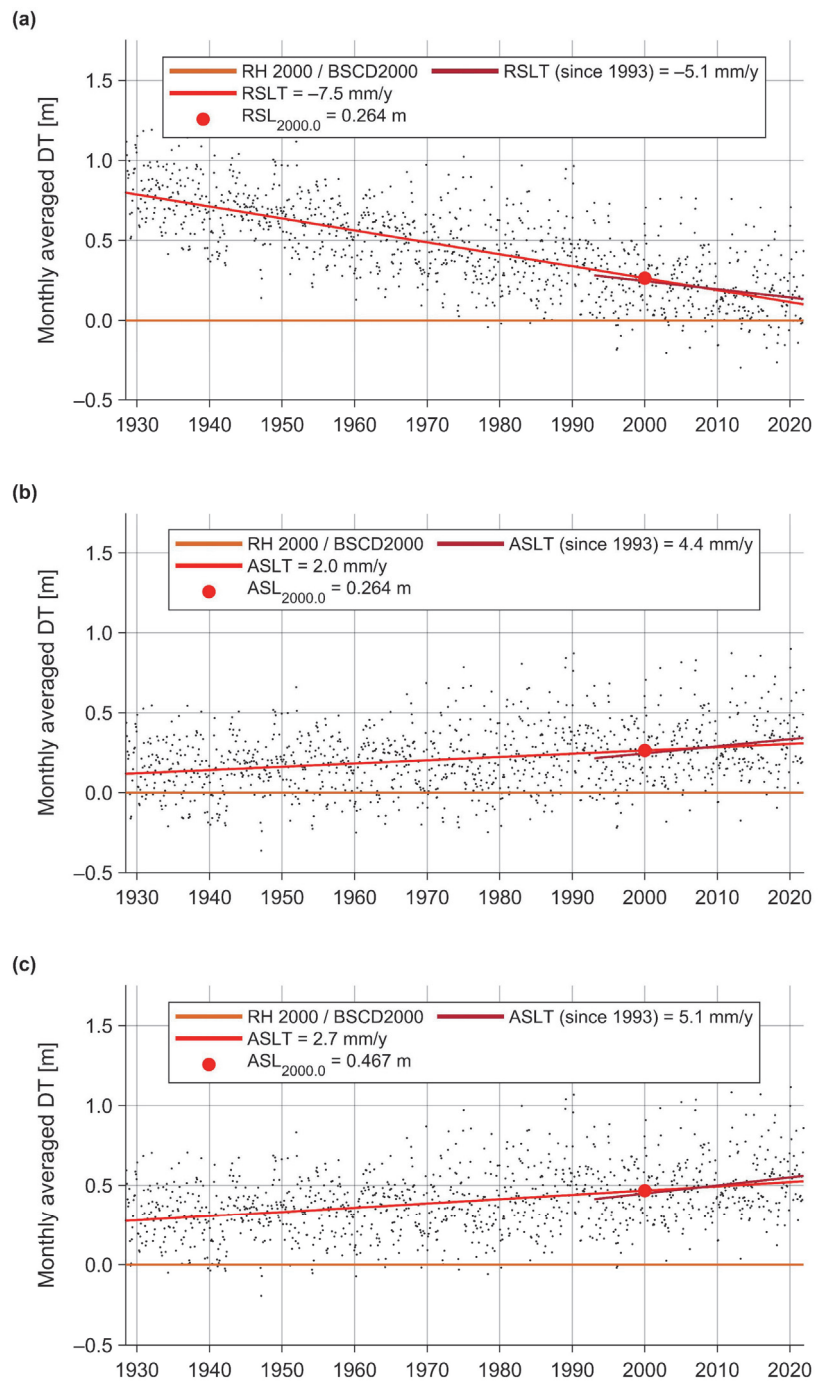


Figure 4. Monthly averaged (a) relative and (b) absolute DT of Ratan TG (cf. Figure 2 for its location) and the estimated sea level trends. In (c) are presented absolute DT and the estimated sea level trends containing purposefully induced errors (i.e., $VLM_{geocentric}$ and an arbitrary reference epoch 1980.0 are used).

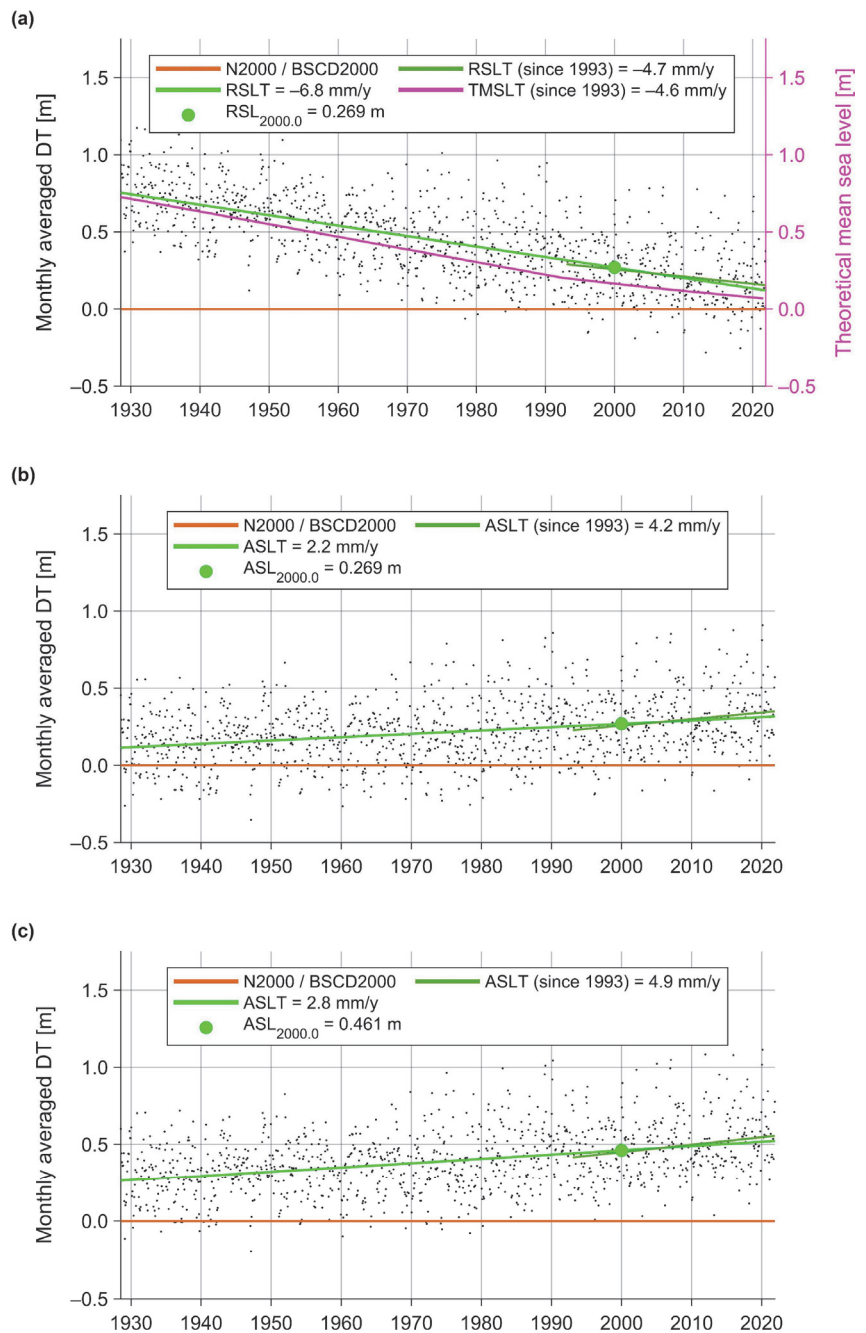


Figure 5. Monthly averaged (a) relative and (b) absolute DT of Pietarsaari TG (cf. Figure 2 for its location) and the estimated sea level trends. In (c) are presented absolute DT and the estimated sea level trends containing purposefully induced errors (i.e., $VLM_{geocentric}$ and an arbitrary reference epoch 1980.0 are used).

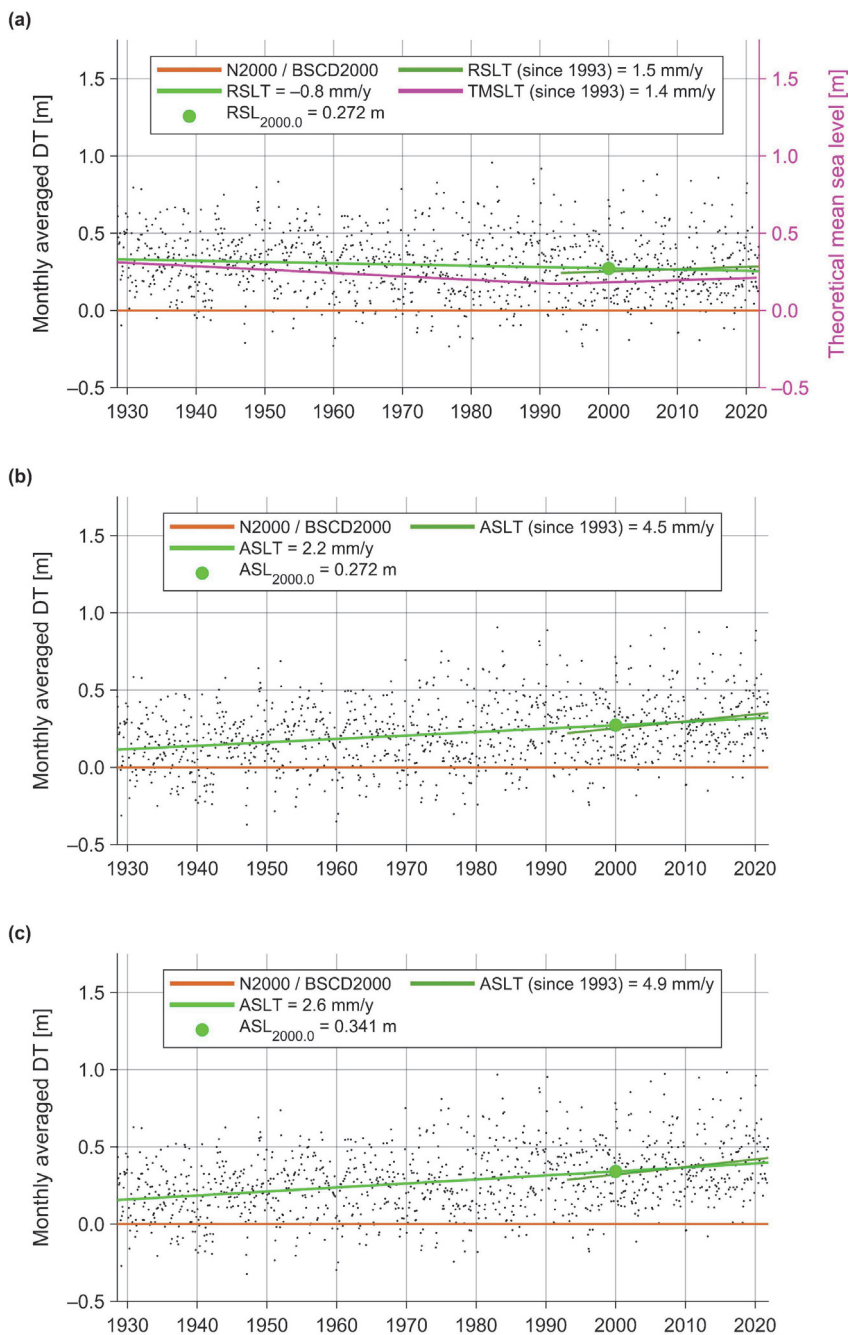


Figure 6. Monthly averaged (a) relative and (b) absolute DT of Hamina TG (cf. Figure 2 for its location) and the estimated sea level trends. In (c) are presented absolute DT and the estimated sea level trends containing purposefully induced errors (i.e., $VLM_{geocentric}$ and an arbitrary reference epoch 1980.0 are used).

Initially, the Finnish TG data shown in Figures 5a and 6a are not given relative to the N2000 height system but to the described theoretical mean sea level estimates instead. Note that such estimates are provided not only for the N2000 but also for older Finnish height systems (e.g., N60). Thus, the TG readings can be transformed into a suitable height system using respective height system associated theoretical mean sea level estimates (Figures 5a and 6a show N2000 associated values [67]).

3. Treatment of Marine GNSS Measurements for Vertical Land Motion

Over the past few decades, a relatively dense network of GNSS-CORS has been established in Northern Europe to monitor deformations in geodetic networks and provide reliable real-time network service for GNSS measurements. For Estonia, Finland, and Sweden, the national GNSS-CORS networks are named ESTPOS [68,69], FinnRef [70,71] and SWEPOS [45,72], respectively (Table 2). Figure 2 shows national GNSS-CORS belonging to the EUREF Permanent GNSS Network [73].

Table 2. National GNSS networks, corresponding t_0 and the number of active GNSS-CORS (in 2021) managed by national surveying authorities (Figure 2 shows GNSS-CORS that also belong to the EUREF Permanent GNSS Network).

Country	GNSS-CORS Network	t_0^1	Number of GNSS Stations	Managing Authority
Estonia	ESTPOS	1997.56	29	Estonian Land Board (ELB)
Finland	FinnRef	1997.0	47	National Land Survey of Finland (NLS)
Sweden	SWEPOS	1999.5	68 + 406 ²	Lantmäteriet

¹ Mean epochs of GNSS measurements for realizing national reference frames. The epochs apply for vertical components only since horizontal coordinates were transferred to the epoch 1989.0 for national implementations of the European Terrestrial Reference System 1989. This implies that the epochs for intraplate deformations are t_0 and for plate tectonics 1989.0. ² Class A + Class B accuracy (1 cm at any given time and at the epoch of reference observations, respectively) national GNSS stations.

As was mentioned in the introduction, the GNSS stations are often used to estimate GNSS velocities, for example, to remove VLM from the relative TG-based sea level time series. The GNSS-CORS that belong to the national networks have relatedly been included in relevant research to estimate GNSS velocities and compile VLM models [22,74–76]. However, as further discussed in the introduction, the GNSS records/measurements may similarly require consideration for VLM in marine applications since the measurements are forced to the reference epoch t_0 (i.e., the coordinates of CORS are fixed to the defining epoch). Although sea level trends contain the GIA-induced geoid change, the general trend of VLM does not influence the sea level (e.g., compare the VLM rate to geoid change in Figure 2). Thus, discrepancies may be introduced by referring GNSS measurements to a reference epoch.

To utilize marine GNSS data, for instance, to validate satellite altimetry determined sea surface heights, the effect of VLM can be included by estimating new CORS coordinates at an observation epoch (considering only the impact of VLM) or by correcting measurements retrospectively for VLM occurring at the CORS. In the latter case, the determination of GNSS-based heights can be expressed in a simplified (assuming ellipsoidal heights and that a single reference station is used) manner as:

$$h_1(\varphi, \lambda, t) = h_0(\varphi_{RS}, \lambda_{RS}, t_0) + dh(t) + VLM_{geocentric}(\varphi_{RS}, \lambda_{RS}) \cdot (t - t_0), \quad (9)$$

where h_0 is an ellipsoidal height of a reference station at a reference epoch t_0 (Table 2 lists t_0 for Estonian, Finnish, and Swedish GNSS-CORS), dh represents an estimated height difference between a reference station and measurement at observation epoch t and VLM denotes the VLM rate at a reference station (also refer to Figure 1). Since satellite altimetry determined sea surface heights and GNSS measurements are given relative to the reference

ellipsoid, $VLM_{geocentric}$ is used. Both satellite altimetry results and GNSS-based ellipsoidal heights h_1 hence, contain the geoid change.

However, ellipsoidal heights h_1 are incompatible with the national height systems and BSCD2000. By following the definition of GNSS reference frames, the VLM correction is:

$$h_2(\varphi, \lambda, t, t_0) = h_0(\varphi_{RS}, \lambda_{RS}, t_0) + dh(t) + [VLM_{geocentric}(\varphi_{RS}, \lambda_{RS}) - VLM_{geocentric}(\varphi, \lambda)] \cdot (t - t_0) \quad (10)$$

where ellipsoidal heights h_2 follow VLM changes of the sea bottom. Equation (10) represents the standard approach where the measurements are forced to the reference epoch t_0 . Therefore, ellipsoidal heights h_2 contain an offset relative to the actual ellipsoidal sea surface heights (cf. dashed blue line in Figure 1) but are useful for navigational purposes. Since depths are given relative to BSCD2000, Equation (10) ensures safe navigation through accurate GNSS-based surveillance of the vessels' under keel clearance (i.e., although sea level trends do not follow VLM directly, sea bottom does).

By subtracting compatible geoid model heights from h_2 , relative DT is obtained, which can be converted to absolute DT by Equation (5). This consideration allows the following modification of Equation (10):

$$h_3(\varphi, \lambda, t, t_0) = h_0(\varphi_{RS}, \lambda_{RS}, t_0) + dh(t) + [VLM_{geocentric}(\varphi_{RS}, \lambda_{RS}) - GC(\varphi, \lambda)] \cdot (t - t_0) \quad (11)$$

where GC represents geoid change. The resulting ellipsoidal heights h_3 represent approximately (i.e., geoid change subtracted) the actual sea surface heights and are consistent with the national height systems and BSCD2000 (cf. solid blue line in Figure 1). By subtracting compatible geoid model heights from h_3 , absolute DT is obtained. Such sea surface heights are suitable for validating marine geoid models following the approaches of [24,25] (a similar approach is also presented in the following numerical example, but sea surface heights are validated instead). Note that similar to the tide gauge data treatment, the correctness of resulting marine GNSS measurements depends too on careful choice of the vertical land motion reference surface and the reference epoch (recall the examples that deliberately introduced errors to the TG data in Section 2.3; cf. Figures 4c, 5c and 6c).

3.1. A Numerical Example

In September 2021, a shipborne GNSS campaign (length of 98 km, cf. Figure 2) was conducted. The first data processing results are now examined to provide a numerical example of marine GNSS surveys. The example presents the derivation and validation of GNSS determined sea surface heights. As the main focus here is on applying the VLM correction, the GNSS data processing and analysis are only described in general terms.

The collected 1/30 Hz shipborne GNSS data was post-processed relative to three EST-POS reference stations (MUS2, KUSA, and VERG, cf. [68] and Figure 2) by employing the commercial Trimble Business Centre software (version 5.52). The standard data processing scheme was utilized, meaning that GNSS-CORS coordinates that refer to the reference epoch (1997.56 for the vertical component, cf. Table 2) were used. Similarly, to [24,51], the closest GNSS-CORS was always employed for a GNSS data point computation (Trimble Business Centre allows only one base station at a time for kinematic data post-processing). Precise GNSS ephemerides were incorporated into post-processing. The resulting data accuracy of such CORS-based post-processing depends heavily on the baseline length (between a GNSS measurement and CORS), which for this campaign remained relatively short, being 20.1 km by average and 29.4 km at most. To an extent, the a priori accuracy estimates for the resulting ellipsoidal heights output by the software can be considered an accuracy indicator. For these ellipsoidal heights, the a priori accuracy was estimated at 2.9 cm by average with a standard deviation of 0.4 cm, indicating relatively stable post-processing performance (high standard deviation can suggest unwanted erratic behavior).

A total station survey was conducted to coordinate the used GNSS antennas (four in total) in the vessel's local system (i.e., locations of GNSS antennas relative to the vessel's railing on both sides). Due to the swaying of the vessel, each point was measured

carefully six times. The standard deviation estimates (based on six measurements) generally remained within a centimeter of the vertical coordinate components. Averages of six measurements were used as the final coordinates. Tape measurements were then used to determine heights from the sea surface to the vessel's railing (from multiple measuring points). Since the sea surface is ever-changing and the vessel swayed during measurements, but the tape measurements are also subjective (surveyor must assess the optimal measure from moving sea surface), these measures likely contain a relatively large error component. The accuracy of tape measurements is expected to remain within 5 cm. Using these total station and tape measurements, the post-processed GNSS antennas' ellipsoidal heights were reduced into instantaneous sea surface heights, which remained relative to the reference ellipsoid.

Note that such shipborne determined instantaneous sea surface heights are rather noisy due to marine conditions (i.e., waves) and vessel's high-frequency attitude changes (e.g., pitch and roll motions). The latter can be estimated and removed from data using three or more GNSS antennas [24,77,78]. Here, the method developed by [24] was employed—the sea surface heights from three antennas were computed jointly to the location of the vessel's stable mass center. Such an approach allows to eliminate (or at the very least significantly reduce) the vessel's high-frequency attitude changes from the joint sea surface height solution. Since 4 antennas were available, a total of 4 different solutions could be computed. As a solution required three antennas (i.e., three points define a plane), the unused fourth one could be used for validation purposes. Based on three used antennas, it was possible to estimate heights (at each GNSS observation epoch t) for the unused fourth antenna (i.e., using the defined plane). The resulting estimates were then compared to the actual measurements of the fourth antenna. Such comparisons resulted in discrepancies that represent height determination accuracy. The 4 (one for each solution) standard deviation estimates of these discrepancies are 2.8, 2.6, 2.9, and 3.1 cm, indicating a good performance of height determination (also notice that these estimates agree well with the mean a priori estimate of 2.9 cm). The average discrepancies for these 4 solutions are 0.7, -0.6 , 0.7, and -0.7 cm, suggesting a successful reduction of post-processed ellipsoidal heights to the sea surface by total station and tape measurements (i.e., all 4 antennas are approximately on the same plane after the reduction). The final instantaneous sea surface heights were then estimated as an average of the 4 solutions at each GNSS observation epoch t .

The obtained instantaneous sea surface heights are presented in Figure 7b as red dots. Notice, however, that the results still contain some noise and require additional corrections (e.g., see the jump in the profile between GPS time 5.59 to 5.64×10^5 s). Furthermore, the validation of the results demands consideration for the ever-changing DT and needs geoidal heights from an independent source (e.g., a suitable geoid model).

3.1.1.1. Derivation of Offshore Dynamic Topography

Although TGs in the Baltic Sea are modern and capable of high measurement accuracy, they are generally sparsely distributed and restricted spatially to land-bound coastal locations (cf. Figure 2). Hydrodynamic models that can provide high spatial and temporal (hourly) resolution for DT are thus appealing alternative data sources. These models, however, usually refer to arbitrary vertical datums (due to free surface assumption), which may result in a bias relative to the used height systems [3,25,30,79,80]. Furthermore, such a dynamic bias changes temporally and spatially, whereby the bias has a long-wavelength nature [3,81]. Due to this, the dynamic bias cannot be eliminated by a simple constant value but must be estimated in both the temporal and spatial domains instead. As the Baltic Sea region TGs are rigorously connected to a unified height system (cf. Section 2.2), they can be used to estimate the dynamic bias contained within a hydrodynamic model.

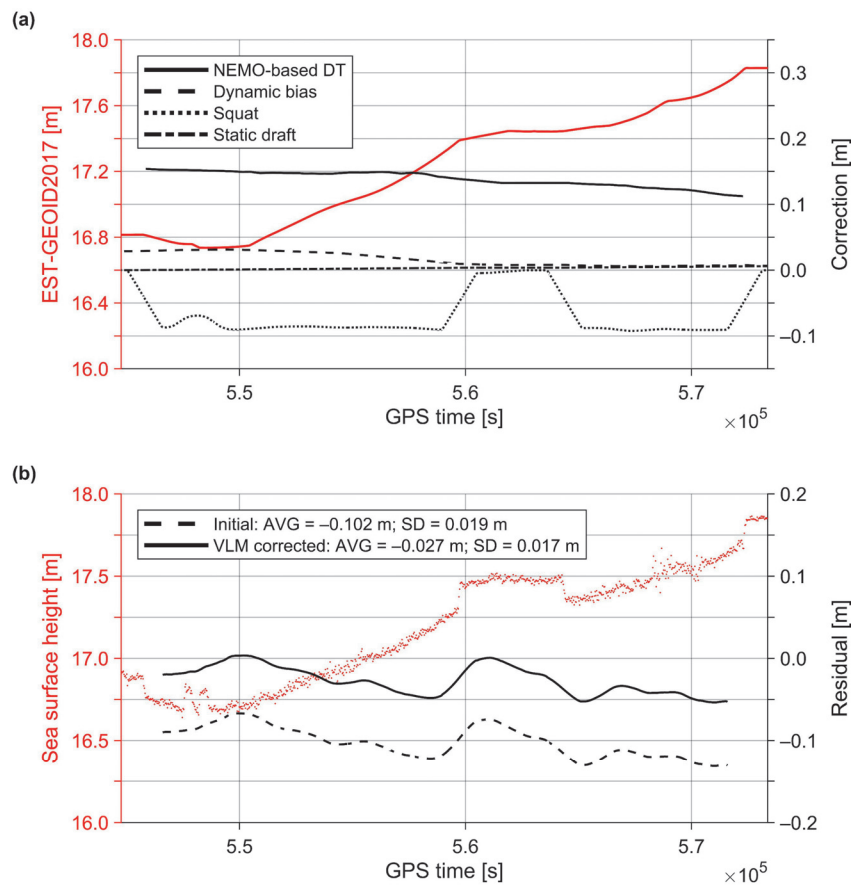


Figure 7. The (a) corrections applied to the GNSS profile and (b) residuals (r_C) of the GNSS profile (after removing geoidal heights and DT, as well as applying the vessel-related corrections), where average and standard deviation of residuals are denoted by AVG and SD, respectively. The red dots in (b) represent instantaneous ellipsoidal sea surface heights.

Thus, the method developed by [3,25] was employed for estimating the dynamic bias of the NEMO-Nordic hydrodynamic model [82,83] that was used for deriving offshore DT (Figure 7a) during the examined shipborne GNSS campaign. Hourly readings from all the Estonian and Finnish TG stations in the Gulf of Finland (cf. Figure 2) were utilized, whereby the 1 cm discrepancy between EH2000 and N2000 (cf. Section 2.1) was subtracted from the readings of Finnish TGs (since all other datasets refer to EH2000). After correcting the TG readings for VLM according to Equation (5) (note that the TG data remains in zero-tide concept), the bias values were estimated at the TG locations for each hour. The difference with the method in [3,25] is that instead of an exact interpolator, the least-squares collocation was used to grid the hourly bias values with the hydrodynamic model resolution. The resulting dynamic bias estimates are shown in Figure 7a.

3.1.2. Determination of Residuals

Since the determined sea surface heights still contain noise (Section 3.1) due to heave motion caused by waves, a low-pass filter needs to be applied. This study employed a low-pass filter that combines moving median and average [51]. The filter window of 51 measurements appraised suitable (i.e., filtered data has a similar signal frequency to

the geoid) by [24] was adopted. However, instead of filtering sea surface heights (*SSH*) directly, the GNSS determined sea surface heights were first reduced by the derived DT from the NEMO-Nordic hydrodynamic model (in Section 3.1.1) and by geoidal heights (*N*):

$$r_{UC}(\varphi, \lambda, t) = SSH(\varphi, \lambda, t) - [DT(\varphi, \lambda, t) - DB(\varphi, \lambda, t)] - N(\varphi, \lambda), \quad (12)$$

where *DT* denotes NEMO-based DT and *DB* is the estimated dynamic bias. Then, the resulting residuals (r_{UC}) were filtered instead. The benefit of such an approach is that the geoid slope (and DT slope) does not contaminate the filtering results (depending on data temporal resolution, the filtering window may be several kilometers long). Here, the Estonian national high-resolution geoid model EST-GEOID2017 [84] was used (Figure 7a).

Finally, vessel-related squat and static draft corrections are needed. For this study, both were estimated empirically from multiple shipborne GNSS campaigns (conducted with the same vessel). The squat effect causes the vessel to sail deeper. In deeper open waters, the squat is a function of the vessel's velocity and dimensions (in shallow waters, the water depth also has an impact) [85]. During some of the GNSS campaigns, the vessel occasionally stopped, which allowed relating the vessel's velocity to the height changes between a stationary and moving vessel (by utilizing filtered residuals (r_{UC}) over distances of up to 3 km). Since squat is approximately a quadratic function of velocity [85,86] (the vessel's dimensions are constants, and the surveys were generally conducted in deep waters at speed around 9 knots), it was estimated as least-squares fit of a second-order polynomial to the empirical data. The squat correction as a function of the vessel's velocity [*squat*(*v*)] is shown in Figure 7a.

Due to fuel consumption, the static draft causes the vessel to float upwards gradually. The lowest/highest estimates of the static draft are correspondingly at the time of harbor departure/arrival. It was thus estimated from differences in tape measurements that were conducted before and after shipborne GNSS campaigns. Since tape measurements may contain errors in the range of static draft itself, all the empirical data was considered altogether. The static draft was then estimated as a distance-related linear trend. The static draft correction as a function of distance [*static draft*(*s*)] is shown in Figure 7a. After estimating the vessel-related corrections, the final corrected residuals (r_C) were calculated as:

$$r_C(\varphi, \lambda, t) = r_{UC}(\varphi, \lambda, t) - squat(v) - static\ draft(s). \quad (13)$$

3.1.3. Correction for Vertical Land Motion

In the land uplift regions, the neglected VLM correction may yield lower than actual sea surface heights (the sea surface heights are artificially suppressed downwards by utilizing CORS coordinates of the reference epoch). It can relatedly be noticed that the final corrected residuals (r_C) contain a -10.2 cm average discrepancy (see the dashed line in Figure 7b). The results were thus corrected for VLM occurring at the ESTPOS reference stations (according to Equation (11)), employed for GNSS post-processing, using the NKG2016LU model. Note that VLM correction is added to GNSS-based heights right after post-processing, and then the afore-described steps are repeated. As a result, the average discrepancy improves to -2.7 cm (see the solid line in Figure 7b). In addition, the standard deviation estimate improves from 1.9 cm to 1.7 cm due to the removal of the VLM-induced slope. Note that at MUS2 (westernmost used ESTPOS station), the VLM rate is 3.2 mm/y ($\sigma_{VLM} = 0.16$ mm/y) and at VERG (easternmost used ESTPOS station) 2.9 mm/y ($\sigma_{VLM} = 0.28$ mm/y), which results in an approximately 6.0 mm west-east directional slope (since epoch 1997.56 to the time of the campaign) in the initial GNSS profile (i.e., the profile without VLM correction).

After correcting for VLM, the remaining residuals shown in Figure 7b originate from several sources. These are errors in the total station, tape, GNSS, and TG measurements, estimated corrections, and deficiencies in the used VLM, hydrodynamic and geoid models. Considering the large variety of different datasets involved, the obtained results (1.7 cm standard deviation and -2.7 cm mean residual) indicate an excellent performance of

the shipborne GNSS measurements. Finally, the geoid and DT signals can be restored on the derived (and VLM corrected) residuals r_C , resulting in sea surface heights that approximately represent the actual sea surface (excluding geoid change) at the time of the shipborne GNSS campaign.

4. Discussion

In the Baltic Sea region, a strong GIA-induced VLM signal deforms the TG and geodetic networks, the effect of which also appears in the TG and GNSS records. Thus, to obtain research appropriate datasets and provide required consistency between them, it is necessary to account for the occurring VLM by utilizing either a suitable VLM model or employing space-geodetic techniques. The current paper has described in Section 2 the use of VLM correction on the TG time series with relevance to the BSCD2000. Additionally, Section 3 explained how marine GNSS measurements might similarly require consideration for VLM. The described principles were illustrated with numerical examples that, among expected results, also presented deliberately erroneous outcomes to demonstrate how mistakes (or neglect in the marine GNSS case) in applying the VLM correction may lead to data misinterpretation.

From the previous discussions and numerical examples, it is evident that, besides introducing significant errors to TG or GNSS datasets through the improper handling of VLM correction, these errors can also propagate to further data applications. Some potential error sources are, for example, the wrong choice of reference surface or epoch for VLM correction. Take, for instance, the TG corrected (i.e., geoid referred) hydrodynamic model-based DT described in Section 3.1.1 (the term within square brackets in Equation (12)), which can be used to study offshore DT. Since DT is defined as a separation between sea surface heights and the geoid, geoid rise in the Baltic Sea region needs to be considered (i.e., VLM_{levelled} must be used for correcting TG data, cf. Equation (5)). Although geoid rise according to NKG2016LU is only in the range of 0.16 mm/y to 0.66 mm/y for the Estonian, Finnish, and Swedish TGs (Figure 2), the changes add up in time. For 2021, the geoid rise would be in the range of 0.3 to 1.4 cm relative to the reference epoch 2000.0. Note, however, that even larger errors could be introduced through inconsistent use of the reference epoch for correcting TG data for VLM (recall the TG data examples in Section 2.3). These errors in the TG data will then propagate similarly to the derived offshore DT. Although the geoid referred hydrodynamic model-based DT can reveal, for instance, mean DT patterns that are not evident by considering the initial hydrodynamic model-based DT [3], the described error sources may lead to a misinterpretation of the results. Importantly, the oceanographic applications also require TG data conversion from the initial zero-tide concept to the mean-tide (cf. Equation (4)) because the zero-tide concept generates a tilt in the DT estimates.

Furthermore, the afore-described geoid referred DT can be used for other applications besides studying the patterns of mean DT. Since conventional precise GNSS-leveling control points cannot be established offshore, the derived DT combined with marine GNSS measurements can be used to validate marine geoid models [24,52,55]. Note that satellite altimetry [87] or airborne laser scanning [25] measurements of sea surface heights can be used similarly. Alternatively, the same datasets may reveal deficiencies in the estimated DT [88]. Such a validation principle is also presented in Section 3.1's numerical example. Yet, in these cases, multiple data sources are used that require consideration for VLM (e.g., by comparing Tables 1 and 2 notice that t_0 can differ for TG and GNSS data). The potential sources of errors are thus twofold.

It should be mentioned, however, that satellite altimetry is an exception. Although the determined sea surface heights contain the GIA-induced geoid change, the general VLM trends do not contaminate these data (cf. Figure 1; also see Figure 2 for a comparison between VLM and geoid change rates). The GIA-induced geoid change can be obtained from a suitable geoid change model that usually accompanies a GIA model (for the Baltic Sea region, the NKG2016LU VLM model provides geoid change). Concerning the current study,

also bear in mind that GNSS-based techniques are a common approach for validating and calibrating satellite altimetry results [89–91]. Hence, consideration of the VLM occurring at the GNSS reference stations is necessary for consistent comparisons (cf. Equation (9)). The validation may otherwise result in a misinterpretation due to neglected VLM that can contaminate the GNSS-based sea surface heights reference data (cf. Section 3.1.3). On the other hand, geoid change corrected satellite altimetry records can also be used for independent validations and inter-comparisons. For instance, to assess TG-based absolute sea level trends (i.e., VLM corrected TG trends, e.g., by GNSS time series). The synergy between various datasets can therefore reveal patterns (e.g., in VLM) that may otherwise remain unnoticed.

5. Conclusions

Implementation of the BSCD2000, a common height reference for the Baltic Sea region, has been initiated to effectively use GNSS methods for accurate navigation and real-time offshore surveying. Offshore, BSCD2000 will be realized through GNSS and geoid modeling, while onshore, BSCD2000 will be compatible with the national height system realizations of the Baltic Sea countries (e.g., EH2000, N2000, and RH 2000) and will coincide with national geoid models to allow seamless height transitions. Another principal component of BSCD2000 is that the TG stations are rigorously connected to the national height systems via precise leveling. Since the zero values of TGs coincide with the BSCD2000, the contemporary TG readings can be expressed directly as DT relative to the geoid at the system reference epoch. Such a common system around the Baltic Sea can provide new geodetic and oceanographic research opportunities. However, it is crucial to consider that the TG and geodetic networks in the Baltic Sea region are deforming due to VLM, the effect of which also appears in the TG and GNSS records.

Thus, this contribution has reviewed the treatment of TG time series for VLM and outlined potential error sources for utilizing TG data relative to a common reference (e.g., BSCD2000 in this study). The described principles were illustrated with numerical examples that, among expected results, also simulated deliberately erroneous outcomes. It was shown that the wrong choice of reference surface for VLM correction (i.e., reference ellipsoid instead of geoid) could lead to a severe misinterpretation of the climate-related sea level trend signal. For instance, instead of the expected sea level rise trend of 2.0 mm/y (an average annual sea level rise over the examined 94 years) at the Ratan TG station (cf. Figure 4b), a trend of 2.7 mm/y (cf. Figure 4c) was obtained instead due to the inclusion of GIA-induced geoid change. Alternatively, by wrongly correcting the TG data relative to an arbitrary reference epoch 1980.0 (instead of 2000.0), the obtained mean DT estimate (at epoch 2000.0 according to the fitted linear trend) at the Pietarsaari TG station was 0.461 m instead of 0.269 m (Figure 5). At the same time, an estimate of 0.341 m was obtained at the Hamina TG instead of the expected 0.272 m (Figure 6). These results demonstrated how inconsistent use of the reference epoch could lead to significant errors in estimating absolute mean DT.

Similar consideration was given to marine GNSS measurements that likewise require VLM correction for some marine applications. A numerical example describing the validation of shipborne GNSS determined sea surface heights was provided to illustrate the described principles. It was shown that the application of VLM correction improves the average residual from -10.2 cm to -2.7 cm (Figure 7). In addition, the standard deviation estimate improved from 1.9 cm to 1.7 cm due to the removal of the VLM-induced slope. Hence, in the VLM-affected regions, the described principles are essential for facilitating consistency between various data sources (e.g., TG, GNSS, and satellite altimetry) and reference surfaces (e.g., BSCD2000).

Author Contributions: Conceptualization, S.V., J.Å., A.E. and M.P.; methodology, S.V.; software, S.V.; validation, S.V.; formal analysis, S.V.; investigation, S.V.; resources, S.V., J.Å., A.E. and M.P.; data curation, S.V., A.E. and M.P.; writing—original draft preparation, S.V.; writing—review and editing, S.V., J.Å., A.E. and M.P.; visualization, S.V.; supervision, A.E.; project administration, A.E.; funding acquisition, A.E. All authors have read and agreed to the published version of the manuscript.

Funding: This research was funded by the Estonian Research Council grant “Development of an iterative approach for near-coast marine geoid modelling by using re-tracked satellite altimetry, in situ and modelled data”, grant number PRG330.

Institutional Review Board Statement: Not applicable.

Informed Consent Statement: Not applicable.

Data Availability Statement: The used hourly Swedish and Finnish TG data can be downloaded from SMHI and FMI webpages [60,61,67]. The monthly mean sea level data for Pietarsaari and Hamina TGs can be downloaded from the PSMSL webpage [62,63]. The employed NKG2016LU VLM model is provided by Lantmäteriet (on behalf of the Nordic Geodetic Commission—NKG): <https://www.lantmateriet.se/en/maps-and-geographic-information/gps-geodesi-och-svepos/Referenssystem/Landhojning/> (accessed on 22 December 2021).

Acknowledgments: Colleagues from the Marine Systems Institute at the Tallinn University of Technology and the crew of the research surveying vessel Salme are thanked for assisting in conducting shipborne GNSS campaigns. A special thanks to OÜ Geosoft, who provided the used GNSS equipment. Aive Liibusk is thanked for post-processing the used shipborne GNSS data. The Estonian Environment Agency provided the used Estonian TG data. A special thanks to the Swedish Meteorological and Hydrological Institute for their cooperation in obtaining NEMO-Nordic model data. The three anonymous reviewers are thanked for their contribution to the quality of the manuscript.

Conflicts of Interest: The authors declare no conflict of interest.

References

- Spada, G.; Galassi, G. New estimates of secular sea level rise from tide gauge data and GIA modelling. *Geophys. J. Int.* **2012**, *191*, 1067–1094. [[CrossRef](#)]
- Breili, K.; Simpson, M.J.R.; Nilsen, J.E.Ø. Observed sea-level changes along the Norwegian coast. *J. Mar. Sci. Eng.* **2017**, *5*, 29. [[CrossRef](#)]
- Jahanmard, V.; Delpêche-Ellmann, N.; Ellmann, A. Realistic dynamic topography through coupling geoid and hydrodynamic models of the Baltic Sea. *Cont. Shelf Res.* **2021**, *222*, 104421. [[CrossRef](#)]
- Watson, C.S.; Legresy, B.; King, M.A. On the uncertainty associated with validating the global mean sea level climate record. *Adv. Space Res.* **2021**, *68*, 487–495. [[CrossRef](#)]
- Klos, A.; Kusche, J.; Fenoglio-Marc, L.; Bos, M.S.; Bogusz, J. Introducing a vertical land motion model for improving estimates of sea level rates derived from tide gauge records affected by earthquakes. *GPS Solut.* **2019**, *23*, 102. [[CrossRef](#)]
- Denys, P.H.; Beavan, R.J.; Hannah, J.; Pearson, C.F.; Palmer, N.; Denham, M.; Hreinsdóttir, S. Sea level rise in New Zealand: The effect of vertical land motion on century-long tide gauge records in a tectonically active region. *J. Geophys. Res. Solid Earth* **2020**, *125*, e2019JB018055. [[CrossRef](#)]
- Raucoules, D.; Le Cozannet, G.; Wöppelmann, G.; de Michele, M.; Gravelle, M.; Daag, A.; Marcos, M. High nonlinear urban ground motion in Manila (Philippines) from 1993 to 2010 observed by DInSAR: Implications for sea-level measurement. *Remote Sens. Environ.* **2013**, *139*, 386–397. [[CrossRef](#)]
- Fokker, P.A.; van Leijen, F.J.; Orlic, B.; van der Marel, H.; Hanssen, R.F. Subsidence in the Dutch Wadden Sea. *Neth. J. Geosci.* **2018**, *97*, 129–181. [[CrossRef](#)]
- Wöppelmann, G.; Marcos, M. Vertical land motion as a key to understanding sea level change and variability. *Rev. Geophys.* **2016**, *54*, 64–92. [[CrossRef](#)]
- Santamaría-Gómez, A.; Gravelle, M.; Dangendorf, S.; Marcos, M.; Spada, G.; Wöppelmann, G. Uncertainty of the 20th century sea-level rise due to vertical land motion errors. *Earth Planet. Sci. Lett.* **2017**, *473*, 24–32. [[CrossRef](#)]
- Hammond, W.C.; Blewitt, G.; Kreemer, C.; Nerem, R.S. GPS imaging of global vertical land motion for studies of sea level rise. *J. Geophys. Res. Solid Earth* **2021**, *126*, e2021JB022355. [[CrossRef](#)]
- Shirzaei, M.; Bürgmann, R. Global climate change and local land subsidence exacerbate inundation risk to the San Francisco Bay area. *Sci. Adv.* **2018**, *4*, eaap9234. [[CrossRef](#)] [[PubMed](#)]
- Grgić, M.; Bender, J.; Bašić, T. Estimating vertical land motion from remote sensing and in-situ observations in the Dubrovnik area (Croatia): A multi-method case study. *Remote Sens.* **2020**, *12*, 3543. [[CrossRef](#)]
- Pfeffer, J.; Allemand, P. The key role of vertical land motions in coastal sea level variations: A global synthesis of multisatellite altimetry, tide gauge data and GPS measurements. *Earth Planet. Sci. Lett.* **2016**, *439*, 39–47. [[CrossRef](#)]

15. Steffen, H.; Wu, P. Glacial isostatic adjustment in Fennoscandia—A review of data and modelling. *J. Geodyn.* **2011**, *52*, 169–204. [[CrossRef](#)]
16. Simpson, M.J.R.; Ravndal, O.R.; Sande, H.; Nilsen, J.E.Ø.; Kierulf, H.P.; Vestøl, O.; Steffen, H. Projected 21st century sea-level changes, observed sea level extremes, and sea level allowances for Norway. *J. Mar. Sci. Eng.* **2017**, *5*, 36. [[CrossRef](#)]
17. Idžanović, M.; Gerlach, C.; Breili, K.; Andersen, O.B. An attempt to observe vertical land motion along the Norwegian coast by CryoSat-2 and tide gauges. *Remote Sens.* **2019**, *11*, 744. [[CrossRef](#)]
18. De Biasio, F.; Baldin, G.; Vignudelli, S. Revisiting vertical land motion and sea level trends in the northeastern Adriatic Sea using satellite altimetry and tide gauge data. *J. Mar. Sci. Eng.* **2020**, *8*, 949. [[CrossRef](#)]
19. Cipollini, P.; Calafat, F.M.; Jevrejeva, S.; Melet, A.; Prandi, P. Monitoring sea level in the coastal zone with satellite altimetry and tide gauges. *Surv. Geophys.* **2017**, *38*, 33–57. [[CrossRef](#)]
20. Vignudelli, S.; Birol, F.; Benveniste, J.; Fu, L.-L.; Picot, N.; Raynal, M.; Roinard, H. Satellite altimetry measurements of sea level in the coastal zone. *Surv. Geophys.* **2019**, *40*, 1319–1349. [[CrossRef](#)]
21. Peltier, W.R.; Argus, D.F.; Drummond, R. Space geodesy constrains ice age terminal deglaciation: The global ICE-6G_C (VM5a) model. *J. Geophys. Res. Solid Earth* **2015**, *120*, 450–487. [[CrossRef](#)]
22. Vestøl, O.; Ågren, J.; Steffen, H.; Kierulf, H.; Tarasov, L. NKG2016LU: A new land uplift model for Fennoscandia and the Baltic region. *J. Geod.* **2019**, *93*, 1759–1779. [[CrossRef](#)]
23. Siegmund, F.; Köhl, A.; Rummel, R.; Stammer, D. Temporal variations of the marine geoid. *J. Geophys. Res. Oceans* **2020**, *125*, e2020JC016433. [[CrossRef](#)]
24. Varbla, S.; Ellmann, A.; Delpeche-Ellmann, N. Validation of marine geoid models by utilizing hydrodynamic model and shipborne GNSS profiles. *Mar. Geod.* **2020**, *43*, 134–162. [[CrossRef](#)]
25. Varbla, S.; Ellmann, A.; Delpeche-Ellmann, N. Applications of airborne laser scanning for determining marine geoid and surface waves properties. *Eur. J. Remote Sens.* **2021**, *54*, 557–567. [[CrossRef](#)]
26. Ludwigen, C.A.; Khan, S.A.; Andersen, O.B.; Marzeion, B. Vertical land motion from present-day deglaciation in the wider Arctic. *Geophys. Res. Lett.* **2020**, *47*, e2020GL088144. [[CrossRef](#)]
27. Simon, K.M.; Riva, R.E.M.; Vermeersen, L.L.A. Constraint of glacial isostatic adjustment in the North Sea with geological relative sea level and GNSS vertical land motion data. *Geophys. J. Int.* **2021**, *227*, 1168–1180. [[CrossRef](#)]
28. Hünicke, B.; Zorita, E. Statistical analysis of the acceleration of Baltic mean sea-level rise, 1900–2012. *Front. Mar. Sci.* **2016**, *3*, 125. [[CrossRef](#)]
29. Gräwe, U.; Klingbeil, K.; Kelln, J.; Dangendorf, S. Decomposing mean sea level rise in a semi-enclosed basin, the Baltic Sea. *J. Clim.* **2019**, *32*, 3089–3108. [[CrossRef](#)]
30. Madsen, K.S.; Høyer, J.L.; Suursaar, Ü.; She, J.; Knudsen, P. Sea level trends and variability of the Baltic Sea from 2D statistical reconstruction and altimetry. *Front. Earth Sci.* **2019**, *7*, 243. [[CrossRef](#)]
31. Agha Karimi, A.; Bagherbandi, M.; Horemuz, M. Multidecadal sea level variability in the Baltic Sea and its impact on acceleration estimations. *Front. Mar. Sci.* **2021**, *8*, 702512. [[CrossRef](#)]
32. Passaro, M.; Müller, F.L.; Oelmann, J.; Rautiainen, L.; Dettmering, D.; Hart-Davis, M.G.; Abulaiti, A.; Andersen, O.B.; Høyer, J.L.; Madsen, K.S.; et al. Absolute Baltic Sea level trends in the satellite altimetry era: A revisit. *Front. Mar. Sci.* **2021**, *8*, 647607. [[CrossRef](#)]
33. Suursaar, Ü.; Kall, T. Decomposition of relative sea level variations at tide gauges using results from four Estonian precise levelings and uplift models. *IEEE J. Sel. Top. Appl. Earth Obs. Remote Sens.* **2018**, *11*, 1966–1974. [[CrossRef](#)]
34. Schwabe, J.; Ågren, J.; Liebsch, G.; Westfeld, P.; Hammarklint, T.; Mononen, J.; Andersen, O.B. The Baltic Sea Chart Datum 2000 (BSCD2000)—Implementation of a common reference level in the Baltic Sea. *Int. Hydrogr. Rev.* **2020**, *23*, 63–83.
35. Kollo, K.; Ellmann, A. Geodetic reconciliation of tide gauge network in Estonia. *Geophysica* **2019**, *54*, 27–38.
36. Woodworth, P.L.; Hughes, C.W.; Bingham, R.J.; Gruber, T. Towards worldwide height system unification using ocean information. *J. Geod. Sci.* **2013**, *2*, 302–318. [[CrossRef](#)]
37. Lan, W.-H.; Kuo, C.-Y.; Kao, H.-C.; Lin, L.-C.; Shum, C.K.; Tseng, K.-H.; Chang, J.-C. Impact of geophysical and datum corrections on absolute sea-level trends from tide gauges around Taiwan, 1993–2015. *Water* **2017**, *9*, 480. [[CrossRef](#)]
38. Amjadiaparvar, B.; Rangelova, E.; Sideris, M.G. The GBVP approach for vertical datum unification: Recent results in North America. *J. Geod.* **2016**, *90*, 45–63. [[CrossRef](#)]
39. Featherstone, W.E.; Filmer, M.S. The north-south tilt in the Australian Height Datum is explained by the ocean’s mean dynamic topography. *J. Geophys. Res. Oceans* **2012**, *117*, C08035. [[CrossRef](#)]
40. Amjadiaparvar, B.; Rangelova, E.V.; Sideris, M.G.; Véronneau, M. North American height datums and their offsets: The effect of GOCE omission errors and systematic levelling effects. *J. Appl. Geod.* **2013**, *7*, 39–50. [[CrossRef](#)]
41. Saaranen, V.; Lehmoskoski, P.; Rouhiainen, P.; Takalo, M.; Mäkinen, J.; Poutanen, M. The new Finnish height reference N2000. In *Geodetic Reference Frames*; Drewes, H., Ed.; International Association of Geodesy Symposia Book Series (IAG SYMPOSIA); Springer: Berlin/Heidelberg, Germany, 2009; Volume 134, pp. 297–302. [[CrossRef](#)]
42. Svensson, R.; Ågren, J.; Olsson, P.-A.; Eriksson, P.-O.; Lilje, M. The new Swedish height system RH 2000 and geoid model SWEN 05LR. In Proceedings of the XXIII International FIG Congress: Shaping the Change, Munich, Germany, 8–13 October 2006.
43. Ågren, J.; Svensson, R. *Postglacial Land Uplift Model and System Definition for the New Swedish Height System RH 2000*; Lantmäteriet: Gävle, Sweden, 2007.

44. Vestøl, O. Determination of postglacial land uplift in Fennoscandia from leveling, tide-gauges and continuous GPS stations using least squares collocation. *J. Geod.* **2006**, *80*, 248–258. [CrossRef]
45. Kempe, C.; Jivall, L.; Lidberg, M.; Lilje, M. On the management of reference frames in Sweden. In Proceedings of the FIG Working Week 2016: Recovery from Disaster, Christchurch, New Zealand, 2–6 May 2016.
46. EVRS Height Datum Relations. Available online: <https://evrs.bkg.bund.de/Subsites/EVRS/EN/Projects/HeightDatumRel/height-datum-rel.html> (accessed on 1 November 2021).
47. EVRF2019. Available online: <https://evrs.bkg.bund.de/Subsites/EVRS/EN/EVRF2019/evrf2019.html> (accessed on 3 November 2021).
48. Ågren, J.; Strykowski, G.; Bilker-Koivula, M.; Omang, O.; Mårdla, S.; Forsberg, R.; Ellmann, A.; Oja, T.; Liepins, I.; Parseliunas, E.; et al. The NKG2015 gravimetric geoid model for the Nordic-Baltic region. In Proceedings of the International Symposium on Gravity, Geoid and Height Systems 2016, Thessaloniki, Greece, 19–23 September 2016. [CrossRef]
49. Ågren, J.; Liesch, G.; Mononen, J. Specification of the Baltic Sea Chart Datum 2000 (BSCD2000). Available online: <http://www.bshc.pro/media/documents/CDWG/CDWG+Specification+of+the+Baltic+Sea+Chart+Datum+2000.pdf> (accessed on 7 December 2021).
50. Schwabe, J.; Strykowski, G.; Ågren, J.; Ellmann, A.; Varbla, S.; Forsberg, R.; Teitsson, H. Status of the “FAMOS Finalization”/BSCD2000 Geoid. Available online: <http://www.bshc.pro/media/documents/CDWG/CDWG13+FAMOS+Finalization+2021-09-07.pdf> (accessed on 20 January 2022).
51. Varbla, S.; Ellmann, A.; Mårdla, S.; Gruno, A. Assessment of marine geoid models by ship-borne GNSS profiles. *Geod. Cartogr.* **2017**, *43*, 41–49. [CrossRef]
52. Nordman, M.; Kuokkanen, J.; Bilker-Koivula, M.; Koivula, H.; Häkli, P.; Lahtinen, S. Geoid validation on the Baltic Sea using ship-borne GNSS data. *Mar. Geod.* **2018**, *41*, 457–476. [CrossRef]
53. Lu, B.; Barthelmes, F.; Li, M.; Förste, C.; Ince, E.S.; Petrovic, S.; Flechtner, F.; Schwabe, J.; Luo, Z.; Zhong, B.; et al. Shipborne gravimetry in the Baltic Sea: Data processing strategies, crucial findings and preliminary geoid determination tests. *J. Geod.* **2019**, *93*, 1059–1071. [CrossRef]
54. Ince, E.S.; Förste, C.; Barthelmes, F.; Pflug, H.; Li, M.; Kaminskis, J.; Neumayer, K.-H.; Michalak, G. Gravity measurements along commercial ferry lines in the Baltic Sea and their use for geodetic purposes. *Mar. Geod.* **2020**, *43*, 573–602. [CrossRef]
55. Saari, T.; Bilker-Koivula, M.; Koivula, H.; Nordman, M.; Häkli, P.; Lahtinen, S. Validating geoid models with marine GNSS measurements, sea surface models, and additional gravity observations in the Gulf of Finland. *Mar. Geod.* **2021**, *44*, 196–214. [CrossRef]
56. Poutanen, M.; Vermeer, M.; Mäkinen, J. The permanent tide in GPS positioning. *J. Geod.* **1996**, *70*, 499–504. [CrossRef]
57. Ihde, J.; Mäkinen, J.; Sacher, M. *Conventions for the Definition and Realization of a European Vertical Reference System (EVRS); Version 5.2*; Federal Agency for Cartography and Geodesy (BKG): Frankfurt, Germany, 2019.
58. Ihde, J.; Augath, W. European Vertical Reference System (EVRS). In Proceedings of the EUREF Symposium 2000, Tromsø, Norway, 22–24 June 2000.
59. Gruber, T.; Ågren, J.; Angermann, D.; Ellmann, A.; Engfeldt, A.; Gisinger, C.; Jaworski, L.; Marila, S.; Nastula, J.; Nilfouroushan, F.; et al. Geodetic SAR for height system unification and sea level research—observation concept and preliminary results in the Baltic Sea. *Remote Sens.* **2020**, *12*, 3747. [CrossRef]
60. SMHI Oceanographic Observations. Available online: <https://www.smhi.se/data/oceanografi/ladda-ner-oceanografiska-observationer/#param=sealevelrh2000,stations=all> (accessed on 4 November 2021).
61. FMI Observations. Available online: <https://en.ilmatietaenlaitos.fi/download-observations#/> (accessed on 4 November 2021).
62. Permanent Service for Mean Sea Level, Pietarsaari. Available online: <https://www.psmsl.org/data/obtaining/stations/194.php> (accessed on 24 November 2021).
63. Permanent Service for Mean Sea Level, Hamina. Available online: <https://www.psmsl.org/data/obtaining/stations/315.php> (accessed on 24 November 2021).
64. Medvedev, I.; Kulikov, E. Low-frequency Baltic Sea level spectrum. *Front. Earth Sci.* **2019**, *7*, 284. [CrossRef]
65. Visser, H.; Dangendorf, S.; Petersen, A.C. A review of trend models applied to sea level data with reference to the “acceleration-deceleration debate”. *J. Geophys. Res. Oceans* **2015**, *120*, 3873–3895. [CrossRef]
66. Douglas, B.C. Global sea rise: A re-determination. *Surv. Geophys.* **1997**, *18*, 279–292. [CrossRef]
67. Theoretical Mean Water and Geodetical Height Systems in Finland. Available online: <https://en.ilmatietaenlaitos.fi/theoretical-mean-sea-level> (accessed on 4 November 2021).
68. Metsar, J.; Kollo, K.; Ellmann, A. Modernization of the Estonian national GNSS reference station network. *Geod. Cartogr.* **2018**, *44*, 55–62. [CrossRef]
69. Metsar, J.; Kollo, K.; Ellmann, A.; Rüdja, A.; Pihlak, P. Multi-epoch GNSS campaigns of the national geodetic network in Estonia. *Geophysica* **2019**, *54*, 51–60.
70. Koivula, H.; Laaksonen, A.; Lahtinen, S.; Kuokkanen, J.; Marila, S. Finnish permanent GNSS network, FinnRef. In Proceedings of the FIG Working Week 2017: Surveying the World of Tomorrow—From Digitalisation to Augmented Reality, Helsinki, Finland, 29 May–2 June 2017.
71. Koivula, H. Finnish Permanent GNSS Network FinnRef. Ph.D. Thesis, Aalto University, Espoo, Finland, 2019.
72. Lilje, M.; Wiklund, P.; Hedling, G. The use of GNSS in Sweden and the national CORS network SWEPOS. In Proceedings of the FIG Congress 2014: Engaging the Challenges—Enhancing the Relevance, Kuala Lumpur, Malaysia, 16–21 June 2014.

73. EUREF Permanent GNSS Network. Available online: https://www.epncb.oma.be/_organisation/about.php (accessed on 4 November 2021).
74. Kall, T.; Oja, T.; Kruusla, K.; Liibusk, A. New 3D velocity model of Estonia from GNSS measurements. *Est. J. Earth Sci.* **2021**, *70*, 107–125. [[CrossRef](#)]
75. Kierulf, H.P.; Steffen, H.; Barletta, V.R.; Lidberg, M.; Johansson, J.; Kristiansen, O.; Tarasov, L. A GNSS velocity field for geophysical applications in Fennoscandia. *J. Geodyn.* **2021**, *146*, 101845. [[CrossRef](#)]
76. Lahtinen, S.; Jivall, L.; Häkli, P.; Nordman, M. Updated GNSS velocity solution in the Nordic and Baltic countries with a semi-automatic offset detection method. *GPS Solut.* **2022**, *26*, 9. [[CrossRef](#)]
77. Lavrov, D.; Even-Tzur, G.; Reinking, J. Expansion and improvement of the Israeli geoid model by shipborne GNSS measurements. *J. Surv. Eng.* **2017**, *143*, 04016022. [[CrossRef](#)]
78. Roggenbuck, O.; Reinking, J. Sea surface heights retrieval from ship-based measurements assisted by GNSS signal reflections. *Mar. Geod.* **2019**, *42*, 1–24. [[CrossRef](#)]
79. Slobbe, D.C.; Verlaan, M.; Klees, R.; Gerritsen, H. Obtaining instantaneous water levels relative to a geoid with a 2D storm surge model. *Cont. Shelf Res.* **2013**, *52*, 172–189. [[CrossRef](#)]
80. Rulent, J.; Calafat, F.M.; Banks, C.J.; Bricheno, L.M.; Gommenginger, C.; Green, J.A.M.; Haigh, I.D.; Lewis, H.; Martin, A.C.H. Comparing water level estimation in coastal and shelf seas from satellite altimetry and numerical models. *Front. Mar. Sci.* **2020**, *7*, 549467. [[CrossRef](#)]
81. Lagemaa, P.; Elken, J.; Kõuts, T. Operational sea level forecasting in Estonia. *Est. J. Eng.* **2011**, *17*, 301–331. [[CrossRef](#)]
82. Hordoir, R.; Axell, L.; Höglund, A.; Dieterich, C.; Fransner, F.; Gröger, M.; Liu, Y.; Pemberton, P.; Schimanke, S.; Andersson, H.; et al. Nemo-Nordic 1.0: A NEMO-based ocean model for the Baltic and North seas—research and operational applications. *Geosci. Model Dev.* **2019**, *12*, 363–386. [[CrossRef](#)]
83. Kärnä, T.; Ljungemyr, P.; Falahat, S.; Ringgaard, I.; Axell, L.; Korabel, V.; Murawski, J.; Maljutenko, I.; Lindenthal, A.; Jandt-Scheelke, S.; et al. Nemo-Nordic 2.0: Operational marine forecast model for the Baltic Sea. *Geosci. Model Dev.* **2021**, *14*, 5731–5749. [[CrossRef](#)]
84. Ellmann, A.; Märdla, S.; Oja, T. The 5 mm geoid model for Estonia computed by the least squares modified Stokes’s formula. *Surv. Rev.* **2020**, *52*, 352–372. [[CrossRef](#)]
85. Barrass, C.B. *Ship Design and Performance for Masters and Mates*; Elsevier: Oxford, UK, 2004.
86. Roggenbuck, O.; Reinking, J.; Härting, A. Oceanwide precise determination of sea surface height from in-situ measurements on cargo ships. *Mar. Geod.* **2014**, *37*, 77–96. [[CrossRef](#)]
87. Mostafavi, M.; Delpeche-Ellmann, N.; Ellmann, A. Accurate sea surface heights from Sentinel-3A and Jason-3 retracers by incorporating high-resolution marine geoid and hydrodynamic models. *J. Geod. Sci.* **2021**, *11*, 58–74. [[CrossRef](#)]
88. Varbla, S.; Ellmann, A.; Delpeche-Ellmann, N. Utilizing airborne laser scanning and geoid model for near-coast improvements in sea surface height and marine dynamics. *J. Coast. Res.* **2020**, *95*, 1339–1343. [[CrossRef](#)]
89. Ardalan, A.A.; Jazireyan, I.; Abdi, N.; Rezvani, M.-H. Evaluation of SARAL/AltiKa performance using GNSS/IMU equipped buoy in Sajafi, Imam Hassan and Kangan Ports. *Adv. Space Res.* **2018**, *61*, 1537–1545. [[CrossRef](#)]
90. Chupin, C.; Ballu, V.; Testut, L.; Tranchant, Y.-T.; Calzas, M.; Poirier, E.; Coulombier, T.; Laurain, O.; Bonnefond, P.; Team FOAM Project. Mapping sea surface height using new concepts of kinematic GNSS instruments. *Remote Sens.* **2020**, *12*, 2656. [[CrossRef](#)]
91. Zhou, B.; Watson, C.; Legresy, B.; King, M.A.; Beardsley, J.; Deane, A. GNSS/INS-equipped buoys for altimetry validation: Lessons learnt and new directions from the Bass Strait validation facility. *Remote Sens.* **2020**, *12*, 3001. [[CrossRef](#)]

Appendix 4

Publication IV

Liibusk, A., Varbla, S., Ellmann, A., Vahter, K., Uiboupin, R., & Delpeche-Ellmann, N. (2022). Shipborne GNSS acquisition of sea surface heights in the Baltic Sea. *Journal of Geodetic Science*, 12(1), 1–21. doi:10.1515/jogs-2022-0131

Research Article

Aive Liibusk*, Sander Varbla, Artu Ellmann, Kaimo Vahter, Rivo Uiboupin, and Nicole Delpeche-Ellmann

Shipborne GNSS acquisition of sea surface heights in the Baltic Sea

<https://doi.org/10.1515/jogs-2022-0131>

received November 28, 2021; accepted May 4, 2022

Abstract: For determining precise sea surface heights, six marine GNSS (global navigation satellite system) survey campaigns were performed in the eastern Baltic Sea in 2021. Four GNSS antennas were installed on the vessel, the coordinates of which were computed relative to GNSS–CORS (continuously operating reference stations). The GNSS–CORS results are compared to the PPP (precise point positioning)-based results. Better accuracy is associated with the GNSS–CORS postprocessed points; however, the PPP approach provided more accurate results for longer than 40 km baselines. For instance, the *a priori* vertical accuracy of the PPP solution is, on average, 0.050 ± 0.006 m and more stable along the entire vessel’s survey route. Conversely, the accuracy of CORS-based solutions decreases significantly when the distances from the GNSS–CORS exceed 40 km, whereas the standard deviation between the CORS and PPP-based solutions is up to 0.075 m in these sections. Note that in the harbor (about 4 km from the nearest GNSS–CORS), the standard deviation of vertical differences between the two solutions remains between 0.013 and 0.024 m. In addition, the GNSS antennas situated in different positions on the vessel indicated different measurement accuracies. It is suggested for further studies that at least one GNSS antenna should be mounted above the mass center of the vessel to reduce the effects of the dominating pitch motion during the surveys.

Keywords: Baltic Sea, Baltic Sea Chart Datum 2000, kinematic GNSS, postprocessing, sea surface height, shipborne GNSS.

* **Corresponding author: Aive Liibusk**, Chair of Forest and Land Management and Wood Processing Technologies, Estonian University of Life Sciences, Tartu, Estonia, e-mail: aive.liibusk@emu.ee

Sander Varbla, Artu Ellmann: Department of Civil Engineering and Architecture, Tallinn University of Technology, Tallinn, Estonia

Kaimo Vahter, Rivo Uiboupin: Department of Marine Systems, Tallinn University of Technology, Tallinn, Estonia

Nicole Delpeche-Ellmann: Department of Cybernetics, Tallinn University of Technology, Tallinn, Estonia

1 Introduction

Sea surface height (SSH) is a key parameter used for understanding the marine environment and is also needed for marine geoid determination, navigation and shipping applications, and climate change research. SSH can be measured or derived from various *in situ* data sources (e.g., tide gauges [TGs] and global navigation satellite system [GNSS]), satellite altimetry (SA), and hydrodynamic models (HDMs) (Madsen et al., 2015). Although SA provides reasonable quantification of SSH, the method is often limited by spatial and temporal resolution characteristics and reliability that tend to diminish on approaching coastal areas due to land contamination, coastal process, etc. (Passaro et al., 2014; Mostafavi et al., 2021). Contrarily, HDMs are efficient in deriving SSH at appropriate spatial and temporal resolutions. However, HDMs are based on mathematical models and approximations that influence their accuracy. Most critically, the vertical reference data of HDMs are often undisclosed (Jahanmard et al., 2021; Varbla et al., 2021), which makes it challenging to combine HDMs with other sources of sea-level information.

As a result, *in situ* measurements provide an alternate solution that links and verifies SSH and HDM data. TGs have been most commonly and reliably utilized to validate other data sources (Cipollini et al., 2017; Hunter et al., 2017). However, TGs are often land bound and only representative of sea level within a particular domain around their location. Hence, there is a need for more *in situ* SSH measurements in the coastal and offshore areas. Thus, the GNSS technology has become favored for SSH data acquisition (Xu et al., 2016; Penna et al., 2018). The GNSS measurements can be performed at almost any marine location of interest (for instance, complex coastal areas) at a very high spatial and temporal resolution (Tranchant et al., 2021). Shipborne GNSS measurements especially are invaluable for numerous applications, such as the calibration and validation of remote sensing data (Liibusk et al., 2020; Crétaux et al., 2011), bathymetry mapping (Guo et al., 2016; Foster et al., 2009), validation of sea-level forecast

models (Liibusk *et al.*, 2020), and marine geoid models (Varbla *et al.*, 2020; Saari *et al.*, 2021; Jürgenson *et al.*, 2008; Nordman *et al.*, 2018). The accuracy of shipborne-derived SSH generally remains within 5 cm (Saari *et al.*, 2021; Varbla *et al.*, 2020). Although SSH with an accuracy of only a few centimeters can be determined by airborne laser scanning (Varbla *et al.*, 2021), shipborne GNSS measurements allow significantly lower equipment and operational costs. Conversely, the accuracy of the shipborne GNSS method exceeds roughly twice that of SA (Liibusk *et al.*, 2020; Mostafavi *et al.*, 2021).

Due to the necessity and urgency for connecting the vertical references of the different sea level sources, the validation of marine geoid models especially is an essential contribution to the connection of height systems, specifically for obtaining a unified chart datum and for more precise GNSS-based navigation and hydrographic surveying in the future. For example, the nine countries surrounding the Baltic Sea have agreed on a unified chart datum BSCD2000 (Baltic Sea Chart Datum 2000) that is based on the definitions of the European Vertical Reference System (EVRS) (BSHC 2021). The zero level of the BSCD2000 is referred to the Normaal Amsterdams Peil (NAP), whereby the height reference surface of BSCD2000 is the equipotential surface of the Earth's gravity field, i.e., a marine geoid model (Schwabe *et al.*, 2020). Thus, the BSCD2000 significantly contributes to the consistency and accuracy of the Baltic Sea hydrographic surveying, marine engineering, and nautical chart publications.

Previous studies have presented the use of shipborne GNSS as a reliable and accurate technique for determining SSH (Saari *et al.*, 2021; Varbla *et al.*, 2020). This contribution now takes a more realistic approach to describing and explaining the different techniques and approaches that can be implemented when performing shipborne GNSS surveys in the dynamically varying sea conditions. The primary focus is on utilizing the local continuously operating reference stations (CORSS) versus global precise point positioning (PPP)-based GNSS postprocessing approaches. However, the location and the type of a GNSS antenna and the distance of the antenna's reference point (ARP) from the instantaneous sea surface also have crucial roles in the accurate SSH determination. Therefore, these aspects are also covered in more detail. Note that the article concentrates solely on height determination, and the discussion on the horizontal coordinate components has been neglected here. Since marine conditions and geoid slope do not vary significantly over short distances, a coordinate determination accuracy of a few meters would be acceptable.

The study was conducted in the complex coastal area of the Eastern Baltic Sea during the spring and summer months of 2021. The research expeditions required

collaboration between the Estonian and Latvian authorities and scientists from various institutes and backgrounds (geodesy, oceanography, hydrography, and environmental studies). Such campaigns are usually time consuming. Thus, it is valuable to implement autonomous monitoring/surveying systems that can record environmental data independently (Liblik *et al.*, 2016; Toming *et al.*, 2017). A similar approach was adopted in the current study, where GNSS-based SSH measurements were conducted as a by-product of various research expeditions.

This article first presents a brief overview of the interdisciplinary marine campaigns in the Baltic Sea. Next, a more detailed description of the shipborne GNSS measurements and kinematic GNSS data postprocessing is provided. In addition, the problems that may occur with such measurements and data postprocessing are emphasized. The article ends with a short discussion and conclusions.

2 Study area

The Baltic Sea is a shallow, semi-enclosed estuarine water body in northern Europe with nine countries surrounding it (see inset in Figure 1). The primary source of freshwater originates from the continental rivers, and salty water infiltrates from the North Sea via the narrow Danish Straits. In addition, the sea level dynamics in various spatial and temporal scales in the Baltic Sea are influenced by a number of processes: large-scale atmospheric circulation, meteorological conditions, North Atlantic mean sea-level changes, storm surges, seiches, etc. (Weisse *et al.*, 2021). The average water depth of the Baltic Sea is approximately 52 m. The dominant wind direction in the Baltic Sea is southwest. The winter and autumn seasons tend to have the strongest winds and highest waves (Jakimavičius *et al.*, 2018). Hence, the summer months are the most favorable for conducting shipborne GNSS surveys.

The Baltic Sea is divided into several subsections that vary in geomorphology and depth. The expeditions were conducted in the subbasins of the eastern Baltic Sea: Gulf of Riga (including Väinameri), Gulf of Finland, and Eastern Baltic Proper (cf. Figure 1). Most of the GNSS survey campaigns were performed in the southern half of the Gulf of Finland. The mean water depth in the Gulf of Finland is around 37 m (the maximum depth is 123 m). The short-term sea-level dynamics (e.g., yearly, seasonal, daily) in the Gulf of Finland are affected by changes in the water balance that are mostly driven by atmospheric conditions (e.g., wind forcing), river runoff, and the presence of sea ice (Post and Kõuts, 2014; Lagemaa *et al.*, 2011; Soosaar *et al.*, 2016). Localized events (storm surges, coastal upwellings, etc.; see, e.g., Delpêche-Ellmann and Soomere, 2017)

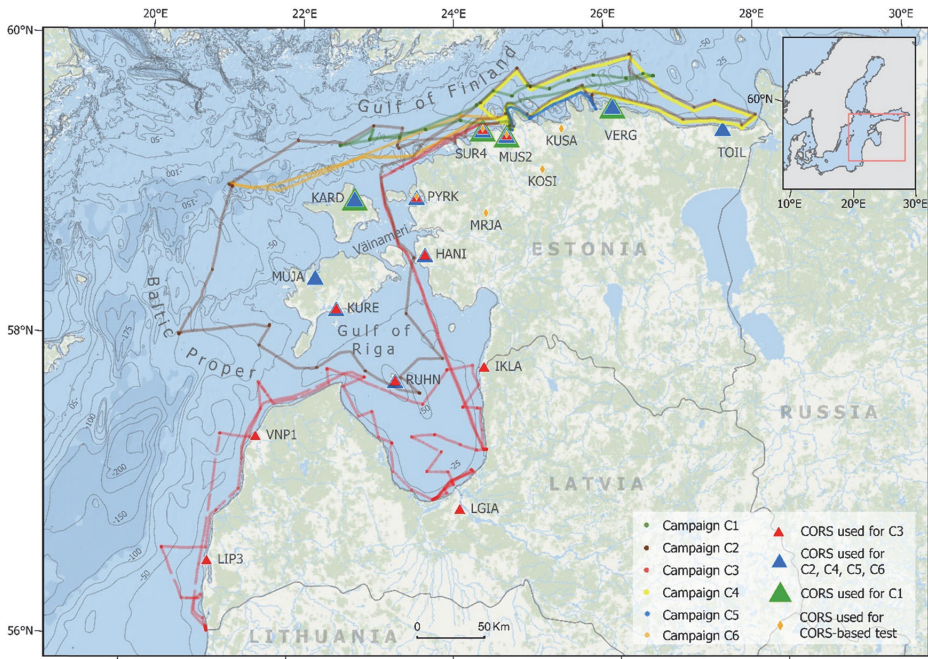


Figure 1: Six marine expeditions conducted in the Baltic Sea in spring and summer 2021, supervised by the Marine Systems Institute from the Tallinn University of Technology. Note that the dots in ship routes denote stops for conducting various marine experiments. The bathymetry data are from the Baltic Sea Bathymetry Database (data.bshc.pro).

also affect the short-term and seasonal variability. Due to the prevailing southwest wind direction, storminess, and river discharge (including the Neva River), a higher mean sea level and extreme water levels tend to occur on the eastern coasts of the Baltic Sea.

The Baltic Proper, located in the central section of the Baltic Sea, has an average depth of 62 m. It connects the Baltic Sea western sections with its northern and eastern sections (cf. Figure 1). The Gulf of Riga and Vainameri (between the West Estonian Archipelago and the Estonian mainland) are semi-enclosed water bodies with an area of around $140 \text{ km} \times 150 \text{ km}$ and $50 \text{ km} \times 50 \text{ km}$, respectively. The average water depth is 23 m in the Gulf of Riga and 4.7 m in the Vainameri. The water bodies are connected to each other and to the Baltic Proper by four narrow straits. Therefore, the sea-level variations in the Gulf of Riga and Vainameri are affected by local wind and sea-level events in the Baltic Proper.

The Baltic Sea is also extraordinary compared to other sea areas as it is strongly affected by vertical land motion due to the postglacial isostatic adjustment, where the land uplift increases from near zero in the southern section of the Baltic Sea to about 10 mm/year in the northern part (Vestøl et al., 2019). Understanding sea-level variations in the Baltic

Sea is vital due to their impact on the region's human activities, economy, and coastal safety. The Baltic Sea region is fortunate since it hosts an extensive long-term multinational network of TGs and high-quality geodetic infrastructure. The most prolonged continuous sea-level observations have been conducted in Stockholm, starting in 1774 (Ekman, 2009). The region also has a high-resolution and accurate quasigeoid model NKG2015 (Ågren et al., 2016). Such conditions around one sea are unique worldwide since it also consists of many archipelagos and dynamic ocean processes that make it challenging to capture accurate sea level data from the various data sources (e.g., SA and HDMs). Thus, the Baltic Sea makes an ideal test site to conduct shipborne GNSS studies.

3 Materials and methods

3.1 Research surveying vessel Salme as a platform for sea-level measurements

The multifunctional research surveying vessel R/V Salme (Figure 2) was used for the expeditions. In general, the

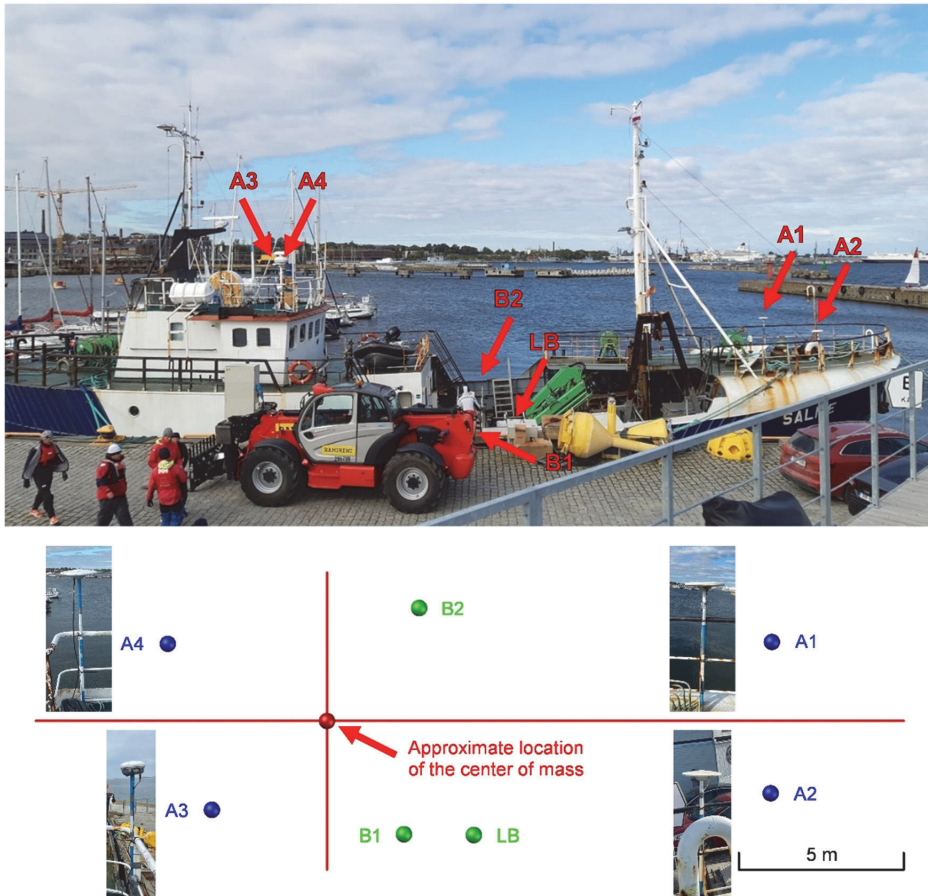


Figure 2: Research surveying vessel Salme and installed GNSS antennas (A1, A2, A3, and A4) on the board. Water measurements were conducted relative to the benchmarks on the vessel's railing (points B1, B2, and LB; note that B1 is behind the loader). The red lines in the scheme denote the vessel's principal axes.

vessel is unusually small (length 31.3 m and breadth 7.2 m; see Table 1 for more details), considering the variety of challenging oceanographic conditions. The vessel's small size also affects its stability (and thus also SSH measurements), especially during strong winds and high waves. It is impractical to use this vessel for marine surveys with wind speeds and wave heights more than 15 m/s and 2 m, respectively. However, in the case of a moderate sea state, the vessel is feasible for various research campaigns and for performing national marine environmental monitoring programs in Estonia and Latvia. The R/V Salme usually conducts oceanographic surveys (e.g., vertical profiling of marine physical parameters, marine biology, chemistry, geology). In addition, the vessel can be

Table 1: Technical parameters of the research surveying vessel R/V Salme

Parameter	Value
Displacement tonnage	249 t
Length	31.3 m
Breadth	7.2 m
Ship draft	3.2 m
Gross tonnage	223 t
Summer deadweight tonnage	262 t
Fuel tank(s)	11 m ³ + 14 m ³
Freshwater tank(s)	12 m ³ + 5 m ³
Wastewater tank	13 m ³
Maximum speed	9 knots

used as a platform for offshore GNSS-based SSH measurements, which is the focus of the current study.

There are two engines on the R/V Salme. The main engine is located almost at the vessel's center, whereas the auxiliary engine is a bit closer to the starboard. This causes the vessel to tilt slightly to the right. Note that the influence of engine vibrations on the SSH measurement results was not detected due to the relatively low (sub-Hz) GNSS data sampling frequency. In addition, there are two freshwater tanks on the vessel – one (12 m³) in the center at the bow and the second (5 m³) in the port at the stern. The wastewater tank (13 m³) is located in front of the freshwater tank at the bow. Thus, freshwater and wastewater do not significantly influence the vessel's tilt during the GNSS campaigns.

3.2 Survey campaigns

Six offshore survey campaigns were conducted in the Eastern Baltic Sea in spring and summer 2021 (Figure 1). Relevant to this study, some of the stops (from 15 to 150 min) on the ship routes for various marine experiments are partly overlapping, thus allowing the repeatability analysis of the GNSS-based SSH that can enable adequate quality assurance of the results. Note that the bold dots in the tracks of campaigns C1–C3 in Figure 1 indicate the stations where the vessel stopped for collecting water samples (e.g., chlorophyll, turbidity, nutrients, phytoplankton) and measuring the vertical profiles of water properties (e.g., temperature, salinity, oxygen, light attenuation).

Each cruise had a primary objective related to different projects carried out by the Tallinn University of Technology (TalTech). The times and purposes of the campaigns are listed in Table 2. During the campaigns, the GNSS receivers were deployed in an autonomous piggyback mode (thus not using specially designated GNSS profile routes). Note that the total length of the GNSS profiles reached almost 5,000 km.

3.3 On-board locations of GNSS instruments and parameters for data recording

Concurrently with all the other experiments described earlier (Table 2), the shipborne GNSS measurements were also conducted to determine SSH. At least three GNSS antennas need to be used for estimating and removing the vessel's high-frequency attitude changes (pitch and roll motions, as well as heave) from the measurement data

Table 2: Marine survey campaigns in the coastal waters of Estonia and Latvia in 2021

Campaign	Date	Length of the route (km)	Maximum wind speed (m/s)	Purpose of the campaign
C1	06.04.2021–08.04.2021	544	18	TalTech basic research – to map the extent of oxygen deficiency in the bottom layer of the Baltic Sea
C2	26.07.2021–30.07.2021	1,439	12	Estonian marine monitoring program – to collect data for assessing the ecological status of the sea
C3	01.08.2021–07.08.2021	1,874	12	Latvian marine monitoring program – to assess the ecological impact of different anthropogenic and natural factors on the Latvian marine environment on the long-term basis
C4	24.08.2021–26.08.2021	515	13	Estonian marine monitoring program (Eastern Gulf of Finland) – to collect data for assessing the ecological status of the sea
C5	09.09.2021–11.09.2021	510 [†]	12	TalTech basic research – coastal monitoring in the southern coast of the Gulf of Finland
C6	15.09.2021–17.09.2021	454	13	TalTech basic research – servicing the monitoring station in the Baltic Proper

[†]GNSS profiles were measured over a 98 km (cf. C5 in Figure 1).

(Roggenbuck and Reinking, 2019; Varbla *et al.*, 2020). Consideration of the vessel's attitude allows increasing the reliability of the determined SSH. This study used four multifrequency GNSS receivers on the R/V Salme to guarantee GNSS data from at least three receivers. Such an approach would leave one spare receiver, data of which could be employed if something unfortunate happened (e.g., gaps in data records or loss of power for one of the receivers). Two GNSS antennas were mounted to the vessel's bow (A1 and A2 installed to the port and starboard, respectively) and the other two on top of the wheelhouse (A3 and A4 installed to the starboard and port, respectively; Figure 2). A detailed overview of the used GNSS instruments and their technical parameters are listed in Tables 3 and 4, respectively.

Note in Table 4 that the internal memory of three GNSS receivers is relatively small (~55 MB). The first campaign (C1) data logging interval was set to 15 s for all the receivers (Table 3) since a trained crew member could download observation data during the campaign. This was not possible for subsequent expeditions. Thus, for subsequent campaigns, the logging interval was increased to 30 s for the Trimble NetR5 receivers (A1 and A2; note in Table 3 that the Trimble R4 Model 2 was replaced with a Trimble NetR5 receiver) and to 60 s for the Trimble R8s system (A3). This allowed for conducting several campaigns without the risk of running out of internal memory storage. The Trimble NetR9 receiver (A4) was continued to be operated with a data logging interval of 15 s (Table 3). All receivers created a new file every 12 h, which is the optimal file size for postprocessing of data later on.

It was possible to use Trimble GA830 antennas (A1 and A2) in connection with Trimble NetR9 and Trimble NetR5 (Table 3) during the first campaign (C1). These antennas have been specifically designed for marine applications and are convenient to use on the vessel due to their smaller dimensions (14.9 cm diameter × 9.9 cm height). For subsequent campaigns, the bow-mounted GNSS antennas were replaced with Trimble Zephyr Geodetic antennas (34.3 cm diameter × 7.6 cm height). Both types of antennas have been designed to support centimeter-level accuracy and support GNSS signals, including GPS L2C and L5, GLO-NASS, and even Galileo.





3.4 Height determination of GNSS antennas relative to the sea surface

One of the primary tasks in shipborne GNSS measurements is determining the heights of GNSS ARPs relative

Table 3: Instruments used during the R/V Salme GNSS campaigns in 2021: A1, A2, A3, and A4 denote the GNSS antennas on the board of R/V Salme (cf. Figure 2)

Campaign	A1 (at the port bow)	A2 (at the starboard bow)	A3 (at the starboard on top of the wheelhouse)	A4 (at the port on top of the wheelhouse)
C1	Trimble NetR9 receiver + Trimble GA830 antenna	Trimble NetR5 receiver + Trimble GA830 antenna	Trimble R8s GNSS system	Trimble R4-2 GNSS system
Data logging [s]	15	15	15	15
C2–C6	Trimble NetR5 receiver + Trimble Zephyr Geodetic antenna	Trimble NetR5 receiver + Trimble Zephyr Geodetic Model 2 antenna	Trimble R8s GNSS system	Trimble NetR9 receiver + Trimble Zephyr Geodetic Model 2 antenna
Data logging [s]	30	30	60	15

Table 4: Technical parameters of the used instruments

	Trimble NetR9	Trimble NetR5	Trimble R8s	Trimble R4-2
Receiver				
GNSS supported	GPS, GLONASS, Galileo	GPS, GLONASS	GPS, GLONASS, Galileo, BeiDou	GPS, GLONASS
GNSS accuracy	H: ± 8 mm + 1 ppm V: ± 15 mm + 1 ppm	H: ± 10 mm + 1 ppm V: ± 20 mm + 1 ppm	H: ± 8 mm + 1 ppm V: ± 15 mm + 1 ppm	H: ± 8 mm + 1 ppm V: ± 15 mm + 1 ppm
Internal memory (Hours showed based on the measurements ¹)	4 GB (~5,000 h) of raw data observables based on recording data from 24 ² satellites at 15 s epoch intervals	55 MB (~500 h) of raw data observables based on recording data from 15 ² satellites at 15 s epoch intervals	56 MB (~960 h) of raw data observables based on recording data from 15 satellites at 15 s epoch intervals	57 MB (~450 h) of raw data observables based on recording data from 15 satellites at 15 s epoch intervals

¹Note that the observation time for different receivers varies and could be caused by the used software version (varies between receivers). Trimble data saving format *.t02 was used during all campaigns.

²Different number of average satellites is caused by the number of supported satellite systems. Trimble NetR9 logged GPS, GLONASS, and Galileo data. Only GPS and GLONASS data were logged by other receivers.

to the instantaneous sea surface to achieve accurate SSH. Therefore, all ARPs and selected locations (i.e., benchmarks) on the railing (B1, B2, and LB) were coordinated by total station measurements before the first campaign (C1)

(Figure 3). Due to the slight movements of the vessel, six measurements were carefully made for determining the coordinates of every point. The measurements were then averaged (the averaged coordinates are presented in Table 5).



Figure 3: Total station survey for coordinating the ARPs (A2) and benchmarks on the vessel's railing (B1, B2, and LB; note that B1 is behind the car).

Table 5: Local (in an arbitrary reference frame) coordinates of the vessel's center of mass (CoM), GNSS ARPs (A1, A2, A3, and A4), and benchmarks (B1, B2, and LB) on the vessel's railing, as well as heights of these points above sea surface before the campaigns

Point	X	Y	Z	Height from sea surface before a campaign					
				C1	C2	C3	C4	C5	C6
B1	-8.626	-1.490	-1.402	2.297	2.360	NA	2.400	2.340	2.360
B2	-13.411	-6.424	-1.014	2.673	2.590	2.580	2.590	2.660	2.620
LB	-7.191	-3.048	-1.192	2.497	2.570	2.520	2.540	2.560	2.560
A1	-5.484	-13.679	1.635	5.326	5.344	5.288	5.348	5.358	5.351
A2	-2.100	-10.582	1.549	5.240	5.258	5.202	5.262	5.272	5.265
A3	-13.072	2.342	3.441	7.132	7.150	7.094	7.153	7.163	7.157
A4	-17.708	-0.033	3.562	7.254	7.271	7.215	7.275	7.285	7.278
CoM	-12.735	-2.053	NA	NA	NA	NA	NA	NA	NA

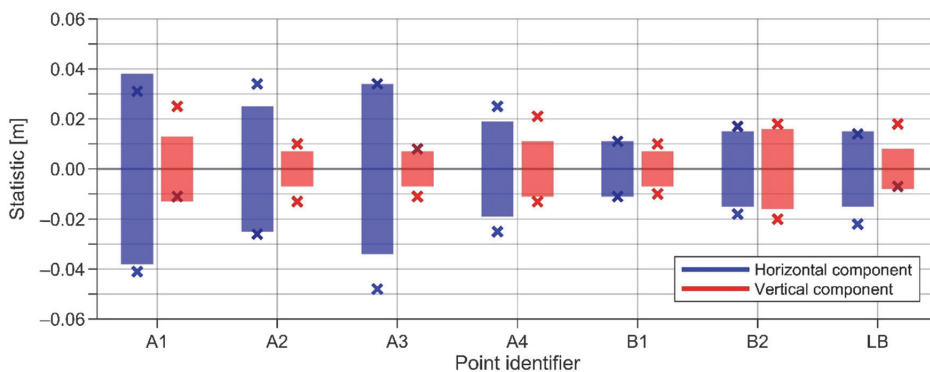
Units are in meters.

Statistics of these six measurements are shown in Figure 4. Relevantly to height determination, it can be noted that the variability (in terms of standard deviation) of the vertical coordinate components is generally around 1 cm, thus suggesting good height determination accuracy. Note that the approximate location of the vessel's mass center was also measured during the survey (cf. Figure 2 and Table 5), which can help estimate the vessel's attitude from the GNSS measurement data (the vessel swings around its mass center axis). Also, the total station was set up on the pier during the survey. Such an approach is recommended only during calm weather in sheltered harbors, which was the case in this study. Otherwise, the total station should be set up on board the vessel to eliminate problems caused by the vessel's movements during the survey (Stępień *et al.*, 2019).

In addition, all benchmark heights were referred to the instantaneous sea surface. The heights between the sea

surface and points B1, LB (starboard side), and B2 (port side) were determined by conducting tape measurements (a solid rod was used to determine the distance, which was then measured) in the harbor every time before the sail off for each campaign (cf. Table 5). Since the sea surface is ever changing and the vessel sways during such measurements, but the measurements are also subjective (the surveyor must assess the optimal measure from the moving sea surface), these distance measures likely contain a relatively large error component. It is estimated that the accuracy of these distance measurements is within 5 cm.

During the first campaign (C1), tape measurements were also conducted randomly during the survey at sea (at stops). These measurements indicated that the general attitude of the vessel does not change significantly and that the vessel is always slightly tilted to the right (i.e., starboard side – notice that point B1 is always lower than point B2) due to the position of the auxiliary engine

**Figure 4:** Statistical properties (with respect to mean values) of the total station measured coordinate components. The colored bars denote standard deviation estimates, whereby minimum and maximum coordinate component differences are shown with crosses.

(see the survey vessel characteristics mentioned earlier). In addition, the tape measurements were also conducted after the campaigns (Table 6). The difference (compare values in Table 5 to those in Table 6) in railing's height before and after a campaign can later help estimate the vessel's total static draft (due to fuel consumption).

The heights of the ARPs above the sea surface (H_{ARP}) were estimated as follows:

$$H_{\text{ARP}} = H_{\text{ARP}}^{\text{TS}} - H_{\text{Railing}}^{\text{TS}} + H_{\text{Railing}}^{\text{Tape}}, \quad (1)$$

where $H_{\text{ARP}}^{\text{TS}}$ and $H_{\text{Railing}}^{\text{TS}}$ denote total station measured heights of ARP and benchmarks on the vessel's railing, respectively, and $H_{\text{Railing}}^{\text{Tape}}$ are the corresponding tape measurements (cf. Table 5). Each ARP was determined relative to each benchmark on the railing. For instance, the antenna A1 associated values for the C1 campaign are 5.334 m (using benchmark B1), 5.322 m (using benchmark B2), and 5.324 m (using benchmark LB). These values indicate that the distances between sea surface and benchmarks on the railing have been determined accurately. The final ARP height was then estimated as an average of those (for each antenna and campaign separately). The final ARP heights above the sea surface are presented in Table 5 for all the campaigns.

By examining the heights of points B1, B2, and LB in Table 5, it can be noted that after the first campaign (C1), a slight change in the vessel's general attitude occurs – the starboard points B1 and LB rise, whereas the port point B2 decreases. For subsequent campaigns (C2–C6), however, no further significant change occurs. Note that after the first campaign (C1), the vessel had to be maintained due to engine failure, which may have caused the change in the vessel's general attitude. Ideally, total station measurements should thus have been repeated before the second campaign (C2). Yet, Table 5 also reveals that the differences between the four ARPs above sea surface remain relatively unchanged despite the change in

vessel's attitude, which is due to considering all points on the railing during the estimation of ARPs (the averaging more or less eliminates the attitude change).

3.5 Configuration of GNSS receivers

GNSS measurements were configured to work autonomously. The GNSS receivers were turned on a few hours before the vessel left the harbor (or even a day before the departure). The receivers logged data during the campaigns, and the data were downloaded upon arrival at the harbor. Due to technical problems caused by the data logging of Trimble R8s (the automatic compression of files was unsuccessful due to software error), this routine was not followed during the C1 campaign, and Trimble R8s data were downloaded every 12 h into the field computer. For the subsequent campaigns, the technical problem was eliminated, which enabled data logging into the receiver's internal memory, similar to other instruments. Note that there were also problems (due to loss of power) with antenna A1 during the first half of the C2 campaign and antennas A3 and A4 during the C4 campaign. These power-related issues caused a loss of data as the instruments were not logging during the campaigns.

Trimble NetR5 and NetR9 are designed for base stations, and therefore, it is easy to configure these receivers through Ethernet cable. Conversely, Trimble Configuration Toolbox had to be used to set up Trimble R8s for the campaigns. This software enables to configure the interval of logging and the duration of every compiled file. Due to the configuration, the GNSS receiver starts to log data automatically when it is turned on. This is advantageous since after restoring power following a sudden power failure, the GNSS receiver continues its operation (although during the C4 campaign, power failure of Trimble R8s and NetR9 was unfortunately permanent).

Table 6: Dynamic topography (DT) measured at the harbor and at the Pirita automatic TG station (roughly 5 km away), as well as heights of benchmarks (B1, B2, and LB) above sea surface after the GNSS campaigns

Point	C1	C2	C3	C4	C5	C6
	DT before/after a GNSS campaign					
Measured DT at the port with respect to geoid ¹	0.408/NA	0.154/0.324	0.424/0.174	0.525/0.355	0.235/NA	NA/0.045
DT at the Pirita TG	0.391/0.689	0.242/0.401	0.502/0.222	0.526/0.367	0.244/0.136	0.149/0.059
	Height from the instantaneous sea surface after a GNSS campaign					
B1	2.340	NA	NA	2.390	NA	2.330
B2	2.700	2.640	2.720	2.600	NA	2.640
LB	2.550	2.610	2.660	2.600	NA	2.530

Units are in meters.

¹DT was measured before and after a campaign from the benchmark on the pier.

3.6 The used GNSS–CORS networks

Estonian and Latvian GNSS–CORS were used as the reference for kinematic data postprocessing. The stations belong to Estonian and Latvian national GNSS–CORS networks named ESTPOS (managed by Estonian Land Board) and LATPOS (managed by Latvian Geospatial Information Agency), respectively. Four Estonian and two Latvian CORS are also incorporated into the EUREF Permanent GNSS Network (EPN). The primary goal for EPN is to implement the European Terrestrial Reference System ETRS89 across the continent. In addition, GNSS–CORS have importance for monitoring the national geodetic reference systems and their components. Nowadays, GNSS–CORS are widely used for different types of kinematic applications as well, for instance, to determine not only airborne and mobile laser scanning trajectories but also shipborne trajectories, and for real-time network (RTN) measurements by surveyors. Currently, 29 GNSS–CORS equipped with Leica GR25 receivers and Leica AR25 Choke Ring antennas are working in ESTPOS (Metsar *et al.*, 2018). Raw data (GPS, GLONASS, and Galileo) with logging intervals of 1 s in RINEX ver 3.02 format are available on the ESTPOS system Spider Business Center (gnss-rtk.maaamet.ee).

In total, 27 GNSS–CORS are working in LATPOS in 2021, mainly equipped with Leica GR30 and LEIAR20 LEIM Choke Ring Antennas (Maciuk *et al.*, 2020). Raw data (GPS, GLONASS, Galileo, and BeiDou) in RINEX ver 3.04 format (including BeiDou data) are available on the LATPOS system Spider Business Center (latpos.l-gia.gov.lv). The locations of coastal GNSS–CORS used for the GNSS postprocessing are shown in Figure 1.

4 Data processing

4.1 GNSS data postprocessing

All the collected GNSS kinematic data were postprocessed using the commercial Trimble Business Center (TBC) software ver 5.52. Precise ephemerides (final orbits) by IGS (International GNSS Service) were incorporated into all GNSS data postprocessing. GPS and GLONASS data with an elevation mask of 10° were used. These two GNSS were incorporated into data postprocessing because two onboard receivers (A2 and A4) supported only GPS and GLONASS. Data from Estonian and Latvian national GNSS–CORS networks were used as base stations, whereby

the closest GNSS–CORS was always chosen for postprocessing of a route portion (cf. Figure 1; note that TBC allows only selecting one base station at a time for kinematic data postprocessing). All used GNSS–CORS coordinates were corrected for vertical land motion using the NKG2016LU model (Vestøl *et al.*, 2019) to obtain the actual SSHs at the contemporary measurement epochs (not the artificial BSCD2000 at epoch 2000.0).

For most survey routes, the baselines between the measured points and the GNSS–CORS generally remained under 40 km, the exception being route C2 with longer baselines. The change from one GNSS–CORS to another caused changes in the baseline lengths (e.g., from 40 to 15 km), but no significant jumps in the resulting heights were detected. By overlapping profiles postprocessed relative to the two GNSS–CORS, the mean height differences (representing jumps) generally remained around 2 cm, decreasing with shorter baselines. Note that for the C2 expedition (mainly in the Baltic Proper), the baselines from the GNSS–CORS to the measured points reached up to 120 km. Since TBC does not allow estimation of atmospheric parameters for kinematic postprocessing, such lengthy baselines may result in unreliable postprocessing results. Previous studies (Varbla *et al.*, 2017; Shih *et al.*, 2021) have shown that the Canadian Spatial Reference System Precise Point Positioning (CSRS-PPP) online service (webapp.geod.nrcan.gc.ca) can provide reliable postprocessing results for shipborne GNSS measurements far from shore. Thus, due to the long baselines for the C2 expedition, the remote data postprocessing utilizing the CSRS-PPP solution was employed. Note that only fixed TBC and CSRS-PPP solutions for every baseline are considered valid data for further analysis. A detailed overview of the online PPP technique can be found in the studies by Mireault *et al.* (2008) and Banville *et al.* (2021).

As the data files postprocessed by using CSRS-PPP online service contain no GPS seconds, the GPS seconds were first calculated by using the available decimal day of the year data. It then became evident (due to the mismatch of coordinates and height variations between subsequent measurements) that the timestamps given by CSRS-PPP have a +30 s offset for antennas A1, A2, and A4 and a +60 s offset for antenna A3 with respect to the timestamps given by TBC (likely due to GPS “leap seconds”). Thus, the following time corrections were introduced to the CSRS-PPP-based GPS seconds: –30 s for antennas A1, A2, and A4 and –60 s for antenna A3. To compare the results of the two software, all the TBC and CSRS-PPP results were then matched by using the GPS seconds.

4.2 Comparisons between the GNSS postprocessing height solutions

Figure 5b shows that the TBC postprocessed data degrade significantly westward from 22°E meridian (antennas A2 and A4 show similar tendencies in data quality degradation, whereby the performance, in general, is slightly better than the one of antenna A3 presented in Figure 5b), whereas CSRS-PPP appears to provide more or less consistent results along the whole route (Figure 5a and b; also compare the presented standard deviation estimates of TBC and CSRS-PPP *a priori* vertical accuracies). Note also in Figure 6 how the discrepancies between CSRS-PPP and TBC solutions become significantly larger from GPS time 45–70 h, which roughly corresponds to data westward from 22°E meridian (largest differences can be seen for antenna A3). These data are the measurements furthest from the used coastal GNSS–CORS.

The differences in Figure 6 were further plotted in relation to the TBC solution-associated baseline lengths (Figure 7a; note that antenna A1 was excluded since there are no data associated with extensive baselines – refer to Figure 5a). It appears that the differences between CSRS-PPP and TBC solutions remain relatively similar up to CORS reckoned baseline lengths around 40–50 km. After that threshold, however, the scattering of differences

increases. To further examine the performance of these differences, functions of standard deviation estimates were compiled for each antenna (except antenna A1). The differences between CSRS-PPP and TBC solutions were divided into sets according to the TBC solution-associated baseline lengths. Each set represents an increase of 1 km in the baseline length (for instance, a set representing baselines from 23 to 24 km). A standard deviation estimate was then calculated for each set. The results presented in Figure 7b confirm the previous assumption – the differences between the two solutions become noisier with TBC solution baseline lengths more than 40–50 km.

An additional independent test was also conducted by using the GNSS time series of CORS. Data from five Estonian CORS (SUR4, KOSI, KUSA, MRJA, and PYRK; cf. Figure 1) were postprocessed in the kinematic mode (postprocessing parameters remained as described earlier) using both TBC and CSRS-PPP. The used time series was 24 h long with a logging interval of 15 s (i.e., 5,761 data samples were examined). The Estonian CORS denoted as MUS2 was chosen as the base station for TBC-based postprocessing. The resulting TBC and CSRS-PPP height solutions were then compared to the official heights. Statistics of these comparisons are presented in Figure 8a. It appears that the TBC-associated statistics remain relatively similar up to baseline lengths of 41 km. With a baseline length of

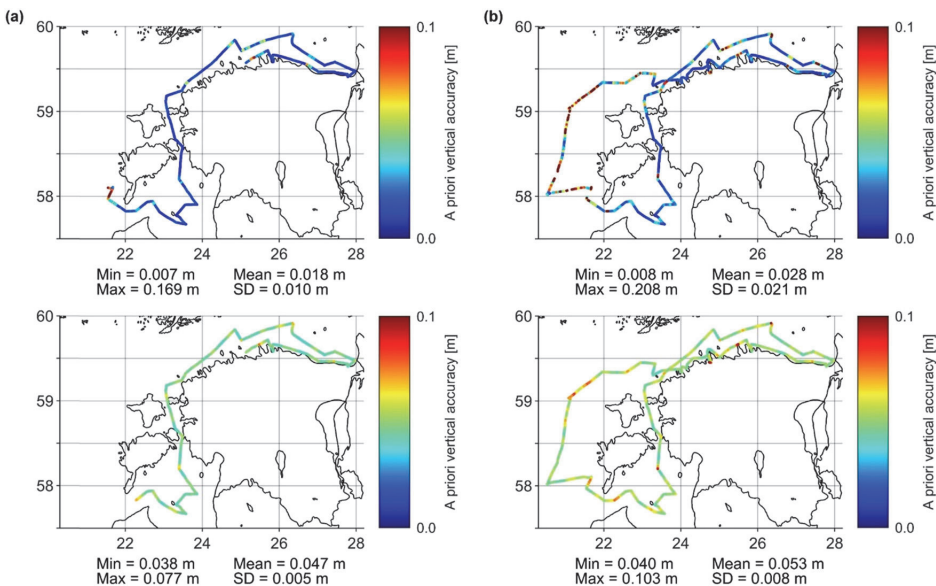


Figure 5: *A priori* vertical accuracies of the bow-mounted antenna A1 (a) and the top-mounted A3 (b) during the C2 campaign, estimated by TBC (top) and CSRS-PPP (bottom).

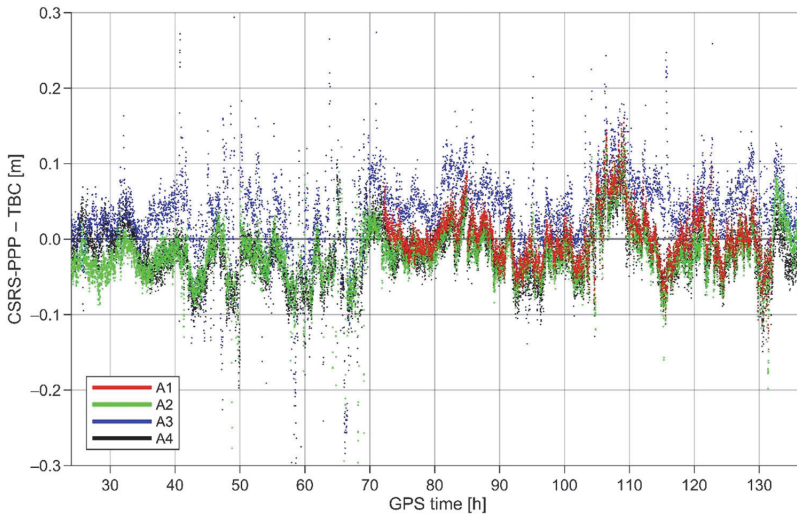


Figure 6: Differences between the CSRS-PPP and TBC SSH solutions for the whole C2 campaign.

61 km, a 2 cm bias appears, and with a baseline length of 81 km, the bias increases further, as does the standard deviation estimate. Note that such biases can also appear in TBC marine data solutions when changing from one GNSS-CORS to another. Conversely, the CSRS-PPP-associated statistics remain relatively similar at all times.

Figure 8b shows statistics of these postprocessing solutions' formal accuracies. Compared to the determined errors in Figure 8a, the *a priori* estimates appear overestimated, especially for the CSRS-PPP solutions (different software use different algorithms). Although TBC-related *a priori* estimates (generally around 3 cm) are

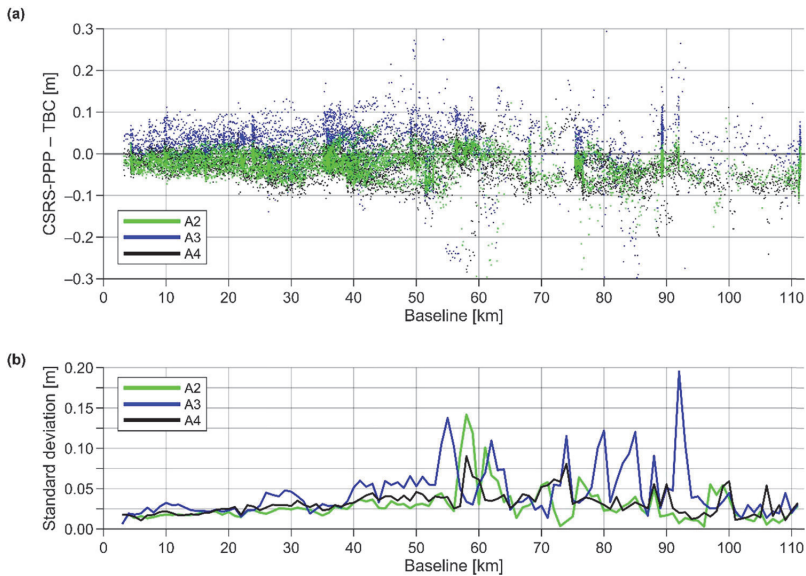


Figure 7: Differences between the CSRS-PPP and TBC SSH solutions (cf. Figure 6) in relation to TBC-associated baseline lengths (a) and differences as a function of standard deviation (b).

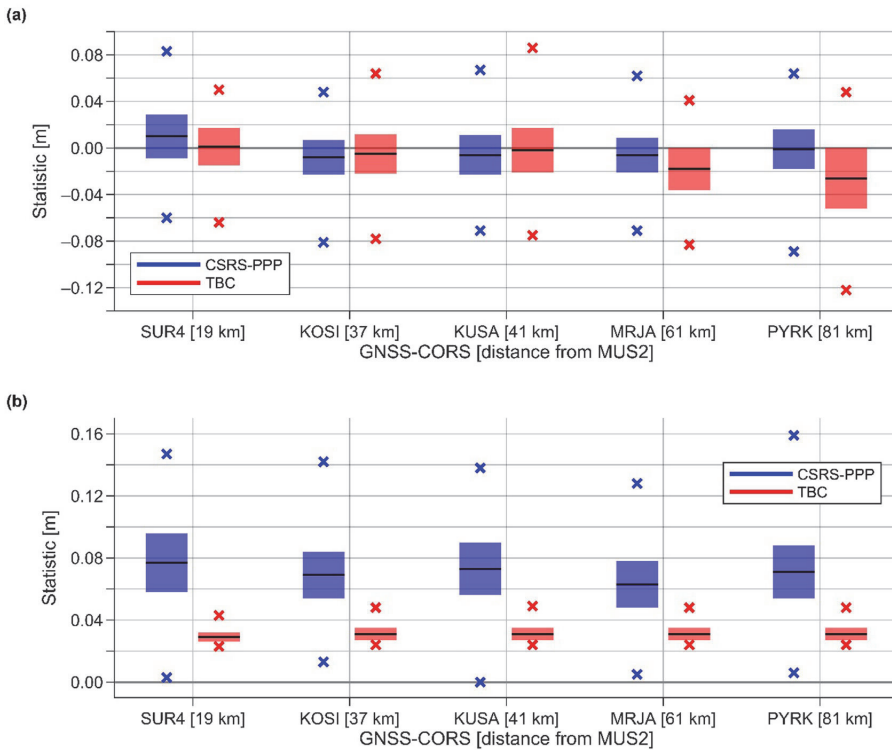


Figure 8: Statistical properties of (a) height differences between the official CORS heights and the CSRS-PPP and TBC height solutions postprocessed in the kinematic mode, and (b) the *a priori* accuracies of these postprocessing solutions. The black lines are mean values, and colored bars denote standard deviation estimates. Crosses denote minimum and maximum values.

more similar to the actual errors, the actual data quality degradation with the increased baseline lengths is not as apparent. According to Figure 8b, the best formal accuracy is obtained for the shortest baseline, whereas the estimates remain similar for the other four tests. Thus, the *a priori* estimates output by the software may not be reliable in estimating the absolute data errors (but could be helpful in relative comparisons as discussed at the beginning of Section 4.2). The comparisons and tests described earlier suggest that the maximum baselines should be kept under 40 km in CORS-based postprocessing. Since the TBC postprocessed data performance degrades westward 22°E, which also represents longer baselines, these data should be replaced by more reliable CSRS-PPP results.

Besides erratic behavior between TBC and CSRS-PPP height solution differences at longer TBC-associated baselines, it appears from Figure 6 that the differences may also contain a systematic component. Therefore, the differences were further investigated in five separate cases for all four antennas. Statistics of these investigations are

presented in Figure 9 (note that antenna A1 has data available for only one of these cases). Although all the antenna types and ARPs were defined in the raw data before GNSS postprocessing using TBC and CSRS-PPP, the comparisons show that the systematic component differs slightly between the antennas (Figures 6 and 9). For instance, the systematic difference (considering all data) for antennas A2 and A4 is around -2 cm, but for antenna A3, it is around 4 cm. It can also be noted that the systematic component is not a constant during the whole campaign and tends to change a few centimeters (notice variability in Figure 6). However, note that according to Figure 8a, a bias may appear in TBC-based solutions with longer baselines. The mean differences representing data westward from 22°E may therefore not be suitable for use since these represent primarily long baselines. Thus, the offsets (i.e., the systematic components under discussion) computed by considering all data (mean differences associated with blue bars in Figure 9) were applied to the CSRS-PPP postprocessed data (it appears that the variability of the systematic component in Figure 6 is random). It is

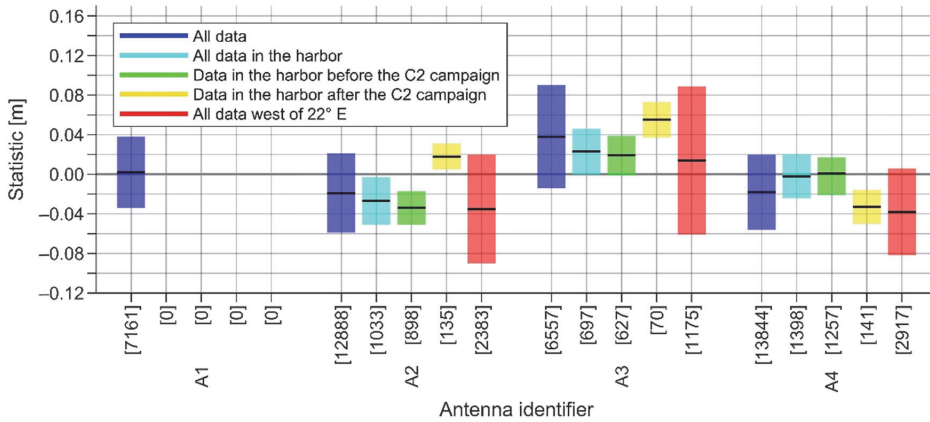


Figure 9: Statistical properties of differences between CSRS-PPP and TBC height solutions in five cases (see the legend). The black lines are mean differences, and colored bars denote standard deviation estimates. The total number of data points considered in comparisons can be found in square brackets.

assumed that the residual differences in all the investigated cases act as random errors (i.e., the presented standard deviation estimates in Figure 9 are not considered while choosing the suitable offsets). A meridian of 22°E was next chosen as a cut-off limit (according to the previous discussion), meaning that all TBC postprocessed data westward the limit were replaced by CSRS-PPP postprocessed data (with the applied offsets). No data were replaced for antenna A1 since the CSRS-PPP data do not extend westward from 22°E (Figure 5a).

Figure 9 also shows relatively good consistency (in terms of standard deviation) between the TBC and CSRS-PPP height solutions: 0.013–0.024 m when the vessel was static at the harbor (TBC-associated baselines are around 4 km) and 0.036–0.052 m for the whole dataset. Slightly larger estimates of 0.044–0.075 m (in terms of standard deviation) by considering only the replaced route sections could be due to the poorer performance of the TBC postprocessed data, as the performance of CSRS-PPP appears to be more or less consistent along the whole route of the vessel (see the bottom subpanels of Figure 5). These results suggest that CSRS-PPP data are suitable to complement the TBC postprocessed data in the poorer performing areas (e.g., at distant locations from GNSS-CORS).

Figure 10 presents *a priori* vertical accuracies for all the antennas during all the GNSS campaigns. It appears from these figures that antenna A3 (Figure 10c) shows the worst performance, whereas antenna A4 (Figure 10d) seems to perform the best (compare the mean and standard deviation estimates presented in figures). However, the statistical properties of antenna A3 with respect to the other antennas are at the millimeter level, which can be

considered negligible considering the application. Therefore, both the external Trimble Zephyr Geodetic antennas and Trimble R8s receiver with an internal GNSS antenna are suitable for shipborne GNSS measurements. The choice depends more on the ease of use for such expeditions.

4.3 Determination of SSHs

After GNSS postprocessing, the computed ellipsoidal heights (h_{ARP}) of the ARPs can be reduced into SSH by subtracting the previously determined ARPs above the sea surface (H_{ARP} ; cf. equation (1) and Table 5):

$$\text{SSH} = h_{\text{ARP}} - H_{\text{ARP}}. \quad (2)$$

An example of the determined SSH during the second campaign (C2) is presented in Figure 11. First, it can be seen how the SSH follows roughly the height of the NKG2015 quasigeoid model (Ågren *et al.*, 2016) but contains a significant amount of noise (primarily due to the heave motion of the vessel caused by the waves). It appears that the noise is more prominent during the last portion of the campaign, suggesting slightly rougher sea conditions in comparison to the beginning of the campaign. However, the determined SSH should ideally follow a similar line to the geoid, meaning that a low-pass filter needs to be applied to the data (see, e.g., Varbla *et al.*, 2017). Also, note that at the beginning of the campaign, the NKG2015 model appears higher than the determined SSH, but the opposite is true at the end of the campaign. This could be due to ever-changing dynamic topography (DT), travel distance-dependent linear static

draft, or both (cf. Tables 5 and 6). For instance, if the aim is to validate the NKG2015 quasigeoid model, DT and static draft corrections must be added to the determined SSH (see, e.g., Varbla et al., 2020). According to Jahanmard et al. (2021), the study area mean DT in the summer season (during which most of the campaigns were conducted) ranges from 0.10 to 0.35 m, suggesting the expected DT. However, it is essential to emphasize that instantaneous DT can vary significantly. For example, in the study by Varbla et al. (2021), the DT was only a few centimeters, whereas in the study by Varbla et al. (2020), the maximum DT reached almost 0.6 m (both studies were conducted in the same area as this one). Importantly, since the Baltic Sea is connected to the Atlantic Ocean via narrow Danish straits, the tides are minimal, remaining within a few centimeters. Considering geoid modeling, DT estimation, and height determination accuracies, the influence of tides in the study

area can be regarded as negligible. Thus, these are not considered.

Figure 11 also suggests that the SSH of antenna A2 (at the vessel's bow) is more scattered than the one of antenna A4 (on top of the wheelhouse). This becomes evident if the measured SSH is compared to the NKG2015 model, which yields standard deviation estimates of 0.224 and 0.162 m for antennas A2 and A4, respectively. The more significant differences for antenna A2 are due to dominating pitch motion of the vessel, which is more prominent at the bow of the vessel compared to the wheelhouse, which is near its more stable center (cf. Figure 2). These results indicate that the high-frequency attitude changes of the vessel need to be considered as well, for instance, by determining SSH at the more or less stable mass center of the vessel by combining data from at least three GNSS antennas (see, e.g., Varbla et al., 2020).

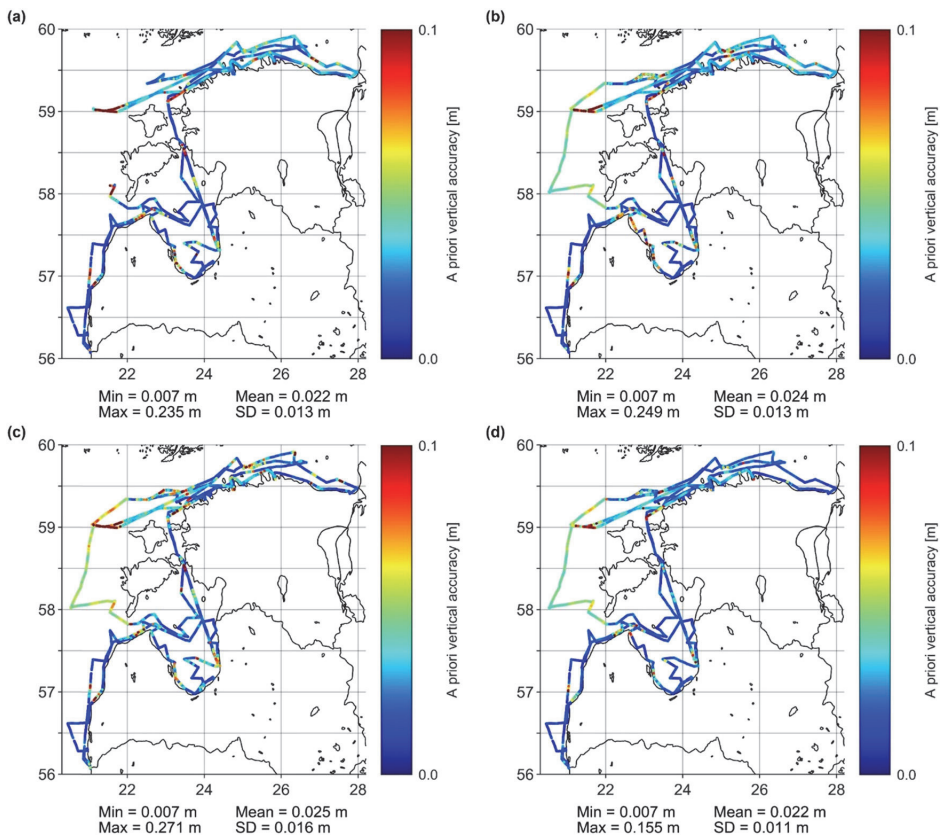


Figure 10: *A priori* vertical accuracies of antenna A1 (a), A2 (b), A3 (c), and A4 (d) during all the campaigns. Note that the estimates westward 22°E meridian of C2 campaign (cf. Figure 1) represent the CSRS-PPP.

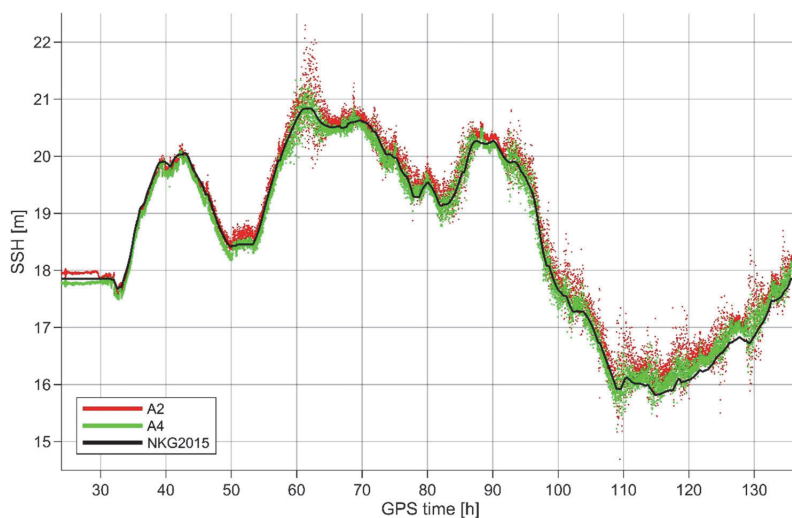


Figure 11: SSH determined by antennas A2 and A4 during the second campaign (C2). No static draft nor DT corrections are included at this stage of analysis. The black line represents the heights of the NKG2015 quasigeoid model. Note that the time span of 10 h corresponds roughly to 160 km (~90 nautical miles).

To further assess the performance of the determined SSH, the SSH of the same or different campaigns can be compared at intersections. However, Figure 11 suggests that the data scattering may dominate such a comparison. Thus, a low-pass filter (a combination of moving median and average) developed by Varbla *et al.* (2017) and successfully employed by Varbla *et al.* (2020) was used to filter SSH (i.e., to reduce the impact of the vessel's attitude and waves on comparisons). The filter window was set to 51 measurements, as was appraised suitable by Varbla *et al.* (2020). Two criteria were then defined to search intersections between filtered SSH of different campaigns: (i) distance between points less than 250 m and (ii) time between intersections (also consecutive points) more than 30 min. The resulting statistical properties are presented in Figure 12. It can be noted that the results differ slightly, for example, if campaign C2 is compared to C4 and vice versa. Since the algorithm searches intersections by moving along the validated campaign, the two tests may yield different points for comparisons (i.e., the algorithm moves along different routes for the two validation cases).

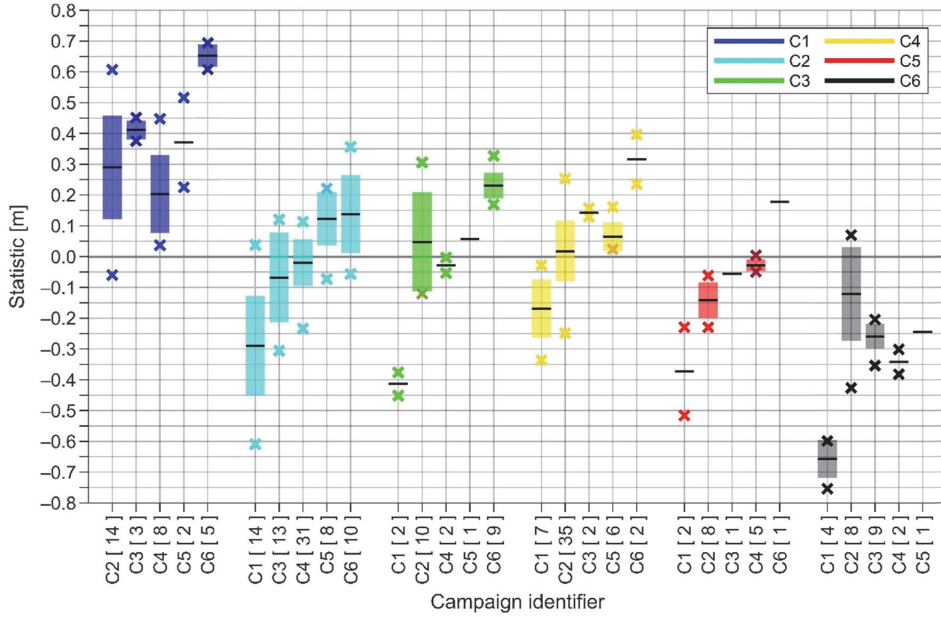
The statistics presented in Figure 12 show relatively good agreement, especially considering that the compared SSH contains ever-changing DT and is not corrected for the static draft. For instance, the mean differences suggest that DT was highest during the C1 campaign and lowest during the C6 campaign. The DT measurements in

Table 6 seem to confirm this result. Table 6 also shows that up to 30 cm change in DT can be expected during a campaign. Such a large variability can contribute significantly to the standard deviation estimates. Therefore, the estimates in Figure 12, which mainly vary between 5 and 15 cm, indicate high accuracy of the determined SSH. Also, note that the antenna A4 (Figure 12b)-associated standard deviation estimates are generally lower than those of antenna A2 (Figure 12a), demonstrating again a better performance of the near mass center-mounted antenna.

Since DT appears to affect the intersection assessments between various campaigns, the two criteria described earlier were employed to also search for campaign-internal intersections. It is assumed that the DT change may have a reduced effect on the assessment results during a single campaign. Statistics of the detected campaign-internal intersections are presented in Figure 13.

Indeed, the standard deviation estimates are reduced compared to the results shown in Figure 12. The highest estimate of around 11 cm is associated with the A2 antenna during the C2 campaign (Figure 13a). Note also how the larger estimates are associated with longer campaigns (cf. Table 2). This result again indicates the impact of DT and also static draft (since fuel consumption increases with travel distance). In addition, the mean differences are less biased, being generally within 5 cm. It can also be seen that antenna A4 results (Figure 13b) indicate slightly

(a)



(b)

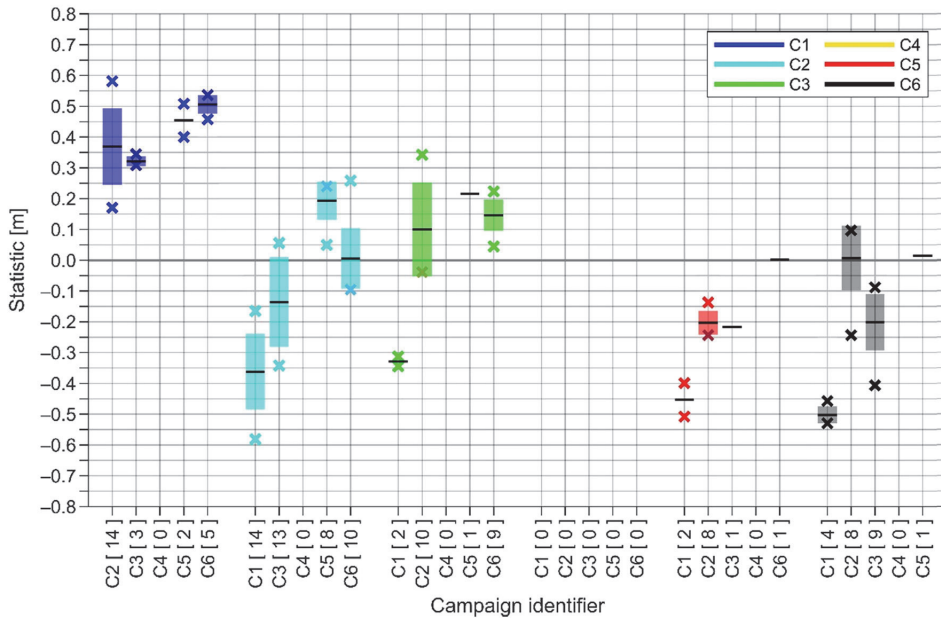


Figure 12: Statistical properties of differences between low-pass filtered SSH of antennas A2 (a) and A4 (b) at intersections between campaigns. The black lines are mean differences, and colored bars denote standard deviation estimates of differences. Crosses denote minimum and maximum differences. Note that color shows the validated campaign and the X-axis validation dataset. In square brackets are the total number of detected intersections for each comparison.

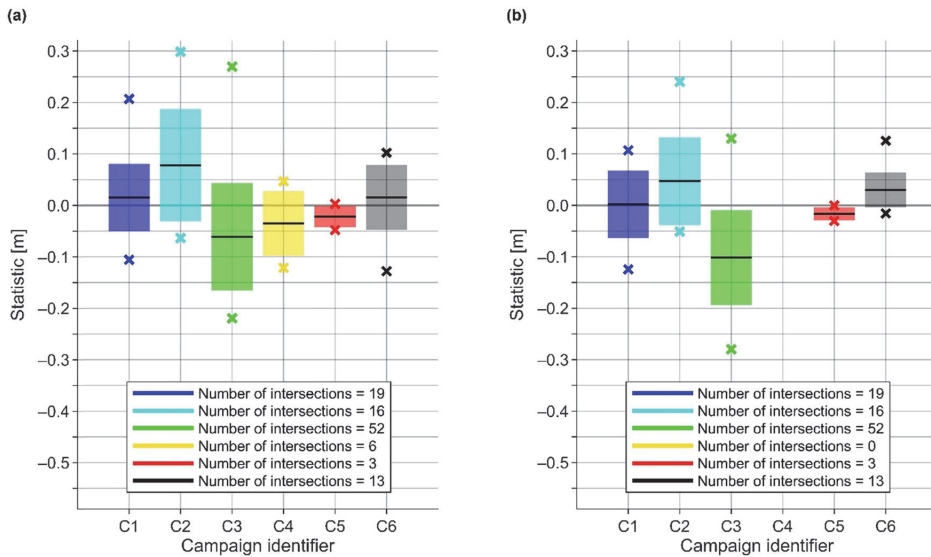


Figure 13: Statistical properties of differences between low-pass filtered SSH of antennas A2 (a) and A4 (b) at campaign-internal intersections. The black lines are mean differences, and colored bars denote standard deviation estimates of differences. Crosses denote minimum and maximum differences.

superior performance in comparison to antenna A2 (Figure 13a), which is consistent with the previous assessments.

5 Discussion

Results of six shipborne GNSS survey campaigns performed in the Baltic Sea demonstrated that it is possible to obtain reasonable quantification of SSHs in the coastal and offshore areas. Such surveys, however, are often challenged by other unexpected circumstances. For example, during the campaigns, some of the main problems/challenges encountered were caused by: (i) the GNSS receiver's software error. The problem was not detected before the campaign. Therefore, the Trimble R8s GNSS system could not produce correctly compressed data files, and the system's internal memory became full at sea; (ii) the hardware and logistical issues. Most of the GNSS equipment were rented in this study, and the GNSS receivers and antennas had to be changed between the C1 and C2 campaigns (cf. Table 3). This required meticulous checks of GNSS receivers' settings and the type of GNSS antennas; (iii) the GNSS kinematic data postprocessing. Two different data processing software were used due to the distance of some of the GNSS measurements from the coast. The

GNSS-CORS-based (by using TBC) and CSRS-PPP-based (for more distant GNSS profiles) results were combined to achieve the best height accuracy for nearshore and offshore data points; (iv) the vessel's high-frequency attitude changes and marine conditions.

The derived SSH can be applied for various applications, such as the validation of geoid models, HDM fields, and altimetry products. However, further data processing needs to be conducted. For instance, the high-frequency attitude changes must be eliminated from measurements data, and vessel-related corrections must be implemented. However, such data processing is out of the scope of the current contribution that focuses on designing the marine GNSS surveys and on potential problems (and solutions to these) that may arise during these campaigns. Details of further data processing are reported in Varbla *et al.* (2022).

The procedures used in this study for obtaining SSH via shipborne GNSS can also be implemented for other marine regions. However, it is essential to be aware that (i) the position of GNSS antenna on the vessel affects the results; (ii) reliable GNSS results can still be achieved with long baselines (e.g., by using CSRS-PPP); (iii) mounting of GNSS equipment should be carefully considered; and (iv) unexpected events may occur during shipborne GNSS measurements (e.g., unfavorable weather conditions, equipment, and software malfunctioning).

6 Concluding remarks

This article describes the technical procedures for acquiring shipborne GNSS data, with the primary focus on equipping the designated survey vessel and processing the GNSS data. A case study was performed in the eastern section of the Baltic Sea during the spring and summer of 2021. These surveys consisted of six different campaigns (with a total length of nearly 5,000 km), where the GNSS–CORS network stations of Estonia and Latvia served as base stations for the postprocessing of GNSS kinematic data.

It is expected that the distances from the GNSS–CORS vary during shipborne GNSS surveys. Thus, two different processing methods were employed. These were GNSS–CORS-based and CSRS-PPP-based kinematic postprocessing approaches. Results demonstrate that for long baselines (i.e., 40–120 km between a GNSS–CORS and a measurement), better results were obtained using the CSRS-PPP, while for shorter baselines (i.e., 4–40 km), the GNSS–CORS-based kinematic postprocessing is preferred. Therefore, CSRS-PPP is the recommended method for offshore surveys with significant distances from the coast (and thus also from GNSS–CORS).

Different GNSS antennas (cf. Table 3) were utilized in this study, and a slight difference was observed in their performance. The resulting accuracy is related to the antenna's location on the vessel (due to high-frequency attitude changes) and to some technical aspects (external antennas appear to have more accurate results). Also, to obtain accurate SSH, the computed GNSS ellipsoidal heights must be corrected for ARP. Once this was performed, a comparison between computed SSH and the NKG2015 geoid model yielded standard deviation estimates of 0.224 and 0.162 m for the antenna at the vessel's bow and on top of the wheelhouse, respectively. This emphasizes that the position choice of the GNSS antenna influences the resulting SSH.

Performing shipborne GNSS surveys can be challenging at sea due to potential equipment and software failure, unpredictable weather conditions, vessel limitations, etc. All these factors can affect the data quality and results. For the results to be successful, careful consideration needs to be given to the mounting of the GNSS equipment, vessel's parameters and appropriateness, and processing methods of the GNSS data. Although shipborne GNSS surveys can be expensive, they can be incorporated with other expeditions (a piggyback approach). The resulting SSH datasets can provide an alternate source of accurate sea level data, especially in challenging coastal locations that are not surveyed by other sensors (e.g., SA, TGs). Such SSH can

also assist in improving marine geoid and hydrodynamic modeling.

Acknowledgments: The authors are grateful to the crew of R/V Salme, who all were very professional and helpful. The three anonymous reviewers are thanked for their contribution to the quality of the manuscript. Special thanks to OÜ Geosoft, who provided the used GNSS equipment. In addition, our thanks to the Estonian Land Board and Latvian Geospatial Information Agency for GNSS–CORS data. This research was partly supported by the grant P200188MIGX: “A 3D model of intraplate deformations combining remote sensing and *in-situ* measurements with an application to implement a semi-dynamic reference frame in Estonia,” and by the Estonian Research Council grant PRG330: “Development of an iterative approach for near-coast marine geoid modelling by using re-tracked satellite altimetry, *in-situ* and modelled data.”

Author contributions: A. Liibus, S. Varbla, and A. Ellmann designed the research concept and drafted the manuscript. A. Liibus and S. Varbla conducted data processing and visualized the manuscript. All authors contributed to data collection, discussion, review, and editing and approved the final manuscript.

Conflict of interest: The authors declare that they have no conflict of interest.

References

- Ågren, J., G. Strykowski, M. Bilker-Koivula, O. Omang, S. Mårdla, R. Forsberg, et al. 2016. “The NKG2015 gravimetric geoid model for the Nordic-Baltic region.” *1st Joint Commission 2 and IGFS Meeting International Symposium on Gravity, Geoid and Height Systems*. Thessaloniki. doi: 10.13140/RG.2.2.20765.20969.
- Banville, S., E. Hassen, P. Lamothe, J. Farinaccio, B. Donahu, Y. Mireault, et al. 2021. “Enabling ambiguity resolution in CSRS-PPP.” *Navigation—Journal of the Institute of Navigation* 68(2), 433–51. doi: 10.1002/navi.423.
- BSHC. Baltic Sea Hydrographic Commission. Retrieved from BSHC Chart Datum Working Group, 2021 <http://www.bshc.pro/working-groups/cdwg/>
- Cipollini, P., F. Calafat, S. Jevrejeva, A. Melet, and P. Prandi. 2017. “Monitoring sea level in the coastal zone with Satellite Altimetry and Tide Gauges.” *Surveys in Geophysics* 38, 33–57. doi: 10.1007/s10712-016-9392-0.
- Crétau, J. F., S. Calmant, V. Romanovski, F. Perosanz, S. Tashbaeva, P. Bonnefond, et al. 2011. “Absolute calibration of Jason radar altimeters from GPS kinematic campaigns over lake Issykkul.”

- Marine Geodesy* 34(3–4), 218–91. doi: 10.1080/01490419.2011.585110.
- Delpeche-Ellmann, N. and T. Soomere. 2017. “Examining Lagrangian surface transport during a coastal upwelling in the Gulf of Finland, Baltic Sea.” *Journal of Marine Systems* 171, 21–30. doi: 10.1016/j.jmarsys.2016.10.007.
- Ekman, M. 2009. *The changing level of the Baltic Sea during 300 years: A clue to understanding the Earth*. Summer Inst. for Historical Geophysics.
- Foster, J., G. Carter, and M. Merrifield. 2009. “Ship-based measurements of sea surface topography.” *Geophysical Research Letters* 36(11), L11605. doi: 10.1029/2009GL038324.
- Guo, J., Z. Dong, Z. Tan, X. Liu, C. Chen, and C. Hwang. 2016. “A crossover adjustment for improving sea surface height mapping from *in-situ* high rate ship-borne GNSS data using PPP technique.” *Continental Shelf Research* 125, 54–60. doi: 10.1016/j.csr.2016.07.002.
- Hunter, J., P. Woodworth, T. Wahl, and R. Nicholls. 2017. “Using global tide gauge data to validate and improve the representation of extreme sea levels in flood impact studies.” *Global and Planetary Change* 156, 34–45. doi: 10.1016/j.gloplacha.2017.06.007.
- Jahanmard, V., N. Delpeche-Ellmann, and A. Ellmann. 2021. “Realistic dynamic topography through coupling geoid and hydrodynamic models of the Baltic Sea.” *Continental Shelf Research* 222, 104421. doi: 10.1016/j.csr.2021.104421.
- Jakimavičius, D., J. Kriaučiūnienė, and D. Šarauskienė. 2018. “Assessment of wave climate and energy resources in the Baltic Sea nearshore (Lithuanian territorial water).” *Oceanologia* 60(2), 207–18. doi: 10.1016/j.oceano.2017.10.004.
- Jürgenson, H., A. Liibusk, and A. Ellmann. 2008. “Geoid profiles in the baltic sea determined using GPS and sea level surface.” *Geodesy and Cartography* 34(4), 109–15. doi: 10.3846/1392-1541.2008.34.109-115.
- Lagemaa, P., J. Elken, and T. Kõuts. 2011. “Operational sea level forecasting in Estonia.” *Estonian Journal of Engineering* 17(4), 301. doi: 10.3176/eng.2011.4.03.
- Liblik, T., M. Skudra, and U. Lips. 2016. “On the buoyant sub-surface salinity maxima in the Gulf of Riga,” *Oceanologia* 59(2), 113–128. doi: 10.1016/j.oceano.2016.10.001.
- Liibusk, A., T. Kall, S. Rikka, R. Uiboupin, U. Suursaar, and K. Tseng. 2020. “Validation of copernicus sea level altimetry products in the Baltic Sea and Estonian Lakes.” *Remote Sensing* 12(24), 4062. doi: 10.3390/rs12244062.
- Maciuk, K., I. Värna, and C. Xu. 2020. “Characteristics of seasonal variations and noises of the daily double-difference and PPP solutions.” *Journal of Applied Geodesy* 15(1), 61–73. doi: 10.1515/jag-2020-0042.
- Madsen, K., J. Hoyer, W. Fu, and C. Donlon. 2015. “Blending of satellite and tide gauge sea level observations and its assimilation in a storm surge model of the North Sea and Baltic Sea.” *Journal of Geophysical Research: Oceans* 120(9), 6405–18. doi: 10.1002/2015JC011070.
- Metsar, J., K. Kollo, and A. Ellmann. 2018. “Modernization of the Estonian National GNSS reference station network.” *Geodesy and Cartography* 44(2), 55–62. doi: 10.3846/gac.2018.2023.
- Mireault, Y., P. Tétrault, F. Lahaye, P. Héroux, and J. Kouba. 2008. “Online precise point positioning: A new, timely service from natural resources Canada.” *GPS World* 19(9), 59–64.
- Mostafavi, M., N. Delpeche-Ellmann, and A. Ellmann. 2021. “Accurate sea surface heights from Sentinel-3A and Jason-3 retracers by incorporating high-resolution marine geoid and hydrodynamic models.” *Journal of Geodetic Science* 11(1), 58–74. doi: 10.1515/jogs-2020-0120.
- Nordman, M., J. Kuokkanen, M. Bilker-Koivula, H. Koivula, P. Häkli, and S. Lahtinen. 2018. “Geoid validation on the Baltic sea using ship-borne GNSS data.” *Marine Geodesy* 41(5), 457–76. doi: 10.1080/01490419.2018.1481160.
- Passaro, M., P. Cipollini, S. Vignudelli, G. Quartly, and H. Snaith. 2014. “ALES: A multi-mission adaptive subwave form retracker for coastal and open ocean altimetry.” *Remote Sensing of Environment* 145, 173–189. doi: 10.1016/j.rse.2014.02.008.
- Penna, N., M. Morales Maqueda, I. Martin, J. Guo, and P. Foden. 2018. “Sea surface height measurement using a GNSS wave glider.” *Geophysical Research Letters* 45(11), 5609–16. doi: 10.1029/2018GL077950.
- Post, P. and T. Kõuts. 2014. “Characteristics of cyclones causing extreme sea levels in the northern Baltic Sea.” *Oceanologia* 56(2), 241–58. doi: 10.5697/oc.56-2.241.
- Roggenbuck, O. and J. Reinking. 2019. “Sea surface heights retrieval from ship-based measurements assisted by GNSS signal reflections.” *Marine Geodesy* 42(1), 1–24. doi: 10.1080/01490419.2018.1543220.
- Saari, T., M. Bilker-Koivula, H. Koivula, M. Nordman, P. Häkli, and S. Lahtinen. 2021. “Validating geoid models with marine GNSS measurements, sea surface models, and additional gravity observations in the gulf of Finland.” *Marine Geodesy* 44(2), 196–214. doi: 10.1080/01490419.2021.1889727.
- Schwabe, J., J. Ågren, G. Liebsch, P. Westfeld, T. Hammarklint, J. Mononen, and et al. 2020. “The Baltic Sea Chart Datum 2000 (BSCD2000) – Implementation of a common reference level in the Baltic Sea.” *International Hydrographic Review* 23, 63–83.
- Shih, H-C, T-K Yeh, Y. Du, and K. He. 2021. “Accuracy assessment of sea surface height measurement obtained from shipborne PPP positioning.” *Journal of Surveying Measurements* 147(4), 04021022. doi: 10.1061/(ASCE)SU.1943-5428.0000374.
- Soosaar, E., I. Maljutenko, R. Uiboupin, M. Skudra, and U. Raudsepp. 2016. “River bulge evolution and dynamics in a non-tidal sea – Daugava River plume in the Gulf of Riga, Baltic Sea.” *Ocean Science* 12(2), 417–32. doi: 10.5194/os-12-417-2016.
- Stępień, G., A. Tomczak, and T. Ziębka. 2019. “Application of total free station method (TFS) for offshore surveying in oblique coordinate system.” *International Journal of Advances in Science Engineering and Technology* 7(2), 32–7.
- Toming, K., T. Kutser, R. Uiboupin, A. Arikas, K. Vahter, and B. Paavel. 2017. “Mapping water quality parameters with Sentinel-3 ocean and land colour instrument imagery in the Baltic Sea.” *Remote Sensing* 9(10), 1070. doi: 10.3390/rs9101070.
- Tranchant, Y-T, L. Testut, C. Chupin, V. Ballu, and P. Bonnefond. 2021. “Near-coast tide model validation using GNSS unmanned surface vehicle (USV), a case study in the pertuis charentais (France).” *Remote Sensing* 13(15), 2886. doi: 10.3390/rs13152886.
- Varbla, S., A. Ellmann, and N. Delpeche-Ellmann. 2021. “Applications of airborne laser scanning for determining marine geoid and surface waves properties.” *European Journal of Remote Sensing* 54(1), 557–67. doi: 10.1080/22797254.2021.1981156.

- Varbla, S., A. Ellmann, and N. Delpeche-Ellmann. 2020. "Validation of marine geoid models by utilizing hydrodynamic model and shipborne GNSS profiles." *Marine Geodesy* 43(2), 134–62. doi: 10.1080/01490419.2019.1701153.
- Varbla, S., A. Ellmann, S. Märdla, and A. Gruno. 2017. "Assessment of marine geoid models by ship-borne GNSS profiles." *Geodesy and Cartography* 43(2), 41–9. doi: 10.3846/20296991.2017.1330771.
- Varbla, S., A. Liibus, and A. Ellmann. 2022. "Shipborne GNSS-determined sea surface heights using geoid model and realistic dynamic topography." *Remote Sensing* 14(10), 2368. doi: 10.3390/rs14102368.
- Vestøl, O., J. Ågren, H. Steffen, H. Kierulf, and L. Tarasov. 2019. "NKG2016LU: a new land uplift model for Fennoscandia and the Baltic Region." *Journal of Geodesy* 93, 1759–79. doi: 10.1007/s00190-019-01280-8.
- Weisse, R., I. Dailidienė, B. Hünicke, K. Kahma, K. Madsen, A. Omstedt, et al. 2021. "Sea level dynamics and coastal." *Earth System Dynamics* 12(3), 871–98. doi: 10.5194/esd-12-871-2021.
- Xu, X., K. Xu, H. Shen, Y. Liu, and H-G Liu. 2016. "Sea surface height and significant wave height calibration methodology by a GNSS Buoy campaign for HY-2A altimeter." *IEEE Journal of Selected Topics in Applied Earth Observations and Remote Sensing* 9, 5252–61. doi: 10.1109/JSTARS.2016.2584626.

Appendix 5

Publication V

Varbla, S., Liibus, A., & Ellmann, A. (2022). Shipborne GNSS-determined sea surface heights using geoid model and realistic dynamic topography. *Remote Sensing*, *14*(10), #2368. doi:10.3390/rs14102368



Article

Shipborne GNSS-Determined Sea Surface Heights Using Geoid Model and Realistic Dynamic Topography

Sander Varbla ^{1,*}, Aive Liibusk ² and Artu Ellmann ¹

¹ Department of Civil Engineering and Architecture, Tallinn University of Technology, Ehitajate Road 5, 19086 Tallinn, Estonia; artu.ellmann@taltech.ee

² Chair of Forest and Land Management and Wood Processing Technologies, Estonian University of Life Sciences, Kreutzwaldi 1, 51006 Tartu, Estonia; aive.liibusk@emu.ee

* Correspondence: sander.varbla@taltech.ee

Abstract: With an increasing demand for accurate and reliable estimates of sea surface heights (SSH) from coastal and marine applications, approaches based on GNSS positioning have become favored, to bridge the gap between tide gauge (TG) and altimetry measurements in the coastal zone, and to complement offshore altimetry data. This study developed a complete methodology for jointly deriving and validating shipborne GNSS-determined SSH, using a geoid model and realistic dynamic topography estimates. An approach that combines the properties of hydrodynamic models and TG data was developed to obtain the latter. Tide gauge data allow estimating the spatiotemporal bias of a hydrodynamic model and, thus, linking it to the used vertical datums (e.g., a novel geoid-based Baltic Sea Chart Datum 2000). However, TG data may be erroneous and represent different conditions than offshore locations. The qualities of spatiotemporal bias are, hence, used to constrain TG data errors. Furthermore, a rigid system of four GNSS antennas was used to ensure SSH accuracy. Besides eliminating the vessel's attitude effect on measurement data, the rigid system also provides a means for internal validation, suggesting a 4.1 cm height determination accuracy in terms of standard deviation. The methodology also involves eliminating the effect of sea state conditions via a low-pass filter and empirical estimation of vessel sailing-related corrections, such as the squat effect. The different data validation (e.g., examination of residual values and intersection analyses) results, ranging from 1.8 cm to 5.5 cm in terms of standard deviation, indicate an SSH determination accuracy of around 5 cm.

Keywords: Baltic Sea; BSCD2000; dynamic topography; geoid; GNSS; hydrodynamic model; hydrogeodesy; sea surface height



Citation: Varbla, S.; Liibusk, A.; Ellmann, A. Shipborne

GNSS-Determined Sea Surface Heights Using Geoid Model and Realistic Dynamic Topography.

Remote Sens. **2022**, *14*, 2368.

<https://doi.org/10.3390/rs14102368>

Academic Editors: Jong-Hoon Won and Nobuaki Kubo

Received: 22 March 2022

Accepted: 12 May 2022

Published: 13 May 2022

Publisher's Note: MDPI stays neutral with regard to jurisdictional claims in published maps and institutional affiliations.



Copyright: © 2022 by the authors. Licensee MDPI, Basel, Switzerland. This article is an open access article distributed under the terms and conditions of the Creative Commons Attribution (CC BY) license (<https://creativecommons.org/licenses/by/4.0/>).

1. Introduction

Sea surface height (SSH), an imperative parameter for understanding the marine environment, sees an increasing demand for accurate and reliable estimates from coastal and marine applications (e.g., engineering, navigation, research). Historically, tide gauge (TG) stations, some as old as a few centuries, have provided continuous sea level information, which is now essential, for instance, to climate studies [1–3]. Although modern TGs also allow a high accuracy (centimeter-level) and sampling rate (up to seconds), the distribution of TG stations is generally sparse and restricted to land-bound coastal locations. Since the TG-determined sea level information represents only a limited spatial domain, complementary data from space geodetic techniques are invaluable. Satellite altimetry (SA) records now span over three decades, densely covering most of the Earth's marine areas with a reasonable quantification of SSH [4–6]. However, the SA method is often limited by its spatial and temporal resolution characteristics and reliability, which tend to diminish in the coastal zone due to approximations in atmospheric, sea state, and geophysical corrections and waveform distortions caused by coastal inhomogeneities [7–9].

Approaches based on GNSS (global navigation satellite system) positioning have, thus, become favored for bridging the gap between TG and SA measurements in the coastal zone and complementing SA data offshore. These methods are also appropriate for the validation and calibration of SA-based SSH, in addition to commonly used TG-based methods. It has been demonstrated that relatively accurate SSH can be acquired by shipborne GNSS measurements [10–12], airborne laser scanning surveys [13–15], and other alternatives, such as GNSS-equipped buoys [16,17] and uncrewed sea vessels [18,19]. While airborne laser scanning surveys currently require expensive equipment and a survey aircraft, and buoys or uncrewed vessels may first demand watercraft development, the shipborne GNSS approach appears most convenient. Some studies have used transit vessels (e.g., ferries) and their routes for research purposes [20–22], demonstrating that dedicated survey vessels and routes are not necessarily required either.

In the spring and summer of 2021, six marine survey campaigns were conducted with the primary focus on marine condition monitoring of the Baltic Sea. Concurrently, four GNSS devices installed on the research vessel collected SSH data autonomously. In [23] are provided a comprehensive review of the six marine survey campaigns, discussions concerning the problems occurring during autonomous data collection, and a description of the GNSS data post-processing. Following lessons learned in our previous studies [11,24], this paper presents improved data processing approaches and a complete exploration of the methodology for deriving accurate SSH from initial post-processed GNSS measurements (i.e., instantaneous SSH), which, unless further treated, are impractical for use in data applications. Accurate derivation of shipborne GNSS-based SSH requires consideration of a vessel's high-frequency attitude changes (e.g., pitch and roll motions) [11] and sea state conditions (i.e., waves) [24], which contaminate the instantaneous SSH, but also need vessel sailing-related corrections [11]. These corrections account for the squat effect, which causes a moving vessel to sail deeper than its nominal draft, and gradual changes in the static draft (e.g., continuous fuel consumption causes a vessel to float higher).

Aside from deriving SSH, the developed methodology involves a joint validation of the results, demanding comparable data from an independent source. It will be demonstrated that such a joint approach can enhance data accuracy by processing residual values instead of the instantaneous SSH. Thus, the emphasis of the study is also on the structuring of validation datasets. Since SSH is the sum of geoidal height and dynamic topography (DT), a suitable geoid model and DT estimates are required. In the current study, an essential component of the latter is the recently initiated implementation of the Baltic Sea Chart Datum 2000 (BSCD2000), a common height reference for the Baltic Sea region [25,26]. The BSCD2000 will be realized through GNSS and geoid modeling (i.e., BSCD2000 is an equipotential surface) and is compatible with the EVRS (European Vertical Reference System) associated national height system realizations of the Baltic Sea countries. As the Baltic Sea TGs are rigorously connected to the national height systems [27,28], the TG readings refer to the BSCD2000 at the reference epoch, implying that the contemporary TG readings can be expressed directly as DT (cf. Figure 1).

However, because TG stations are generally distributed in sparse land-bound coastal locations, hydrodynamic models (HDMs) providing high spatial and temporal (hourly) resolution DT may appear an appealing offshore data source. Caution should be exercised using these models, since they usually contain a long-wavelength nature [29,30] spatiotemporal dynamic bias (DB) relative to the used height reference [15,30,31] (also refer to Figure 1). Hence, it would be advantageous to employ the method developed by [15,30]: the DB estimated at TG stations is gridded and then removed from an HDM; therefore, linking the model with height references. In these studies, exact interpolators were employed for gridding. Such an approach assumes that a DB estimate at a TG station is errorless and represents all nearby offshore locations, which may not be necessarily true. Utilizing the qualities of DB, an approach was developed for estimating DB uncertainties used during offshore DB prediction by least-squares collocation (i.e., an inexact interpola-

tor); thus, constraining TG data errors. By combining the properties of TG data and HDMs, realistic DT can be derived for shipborne GNSS-determined SSH validation.

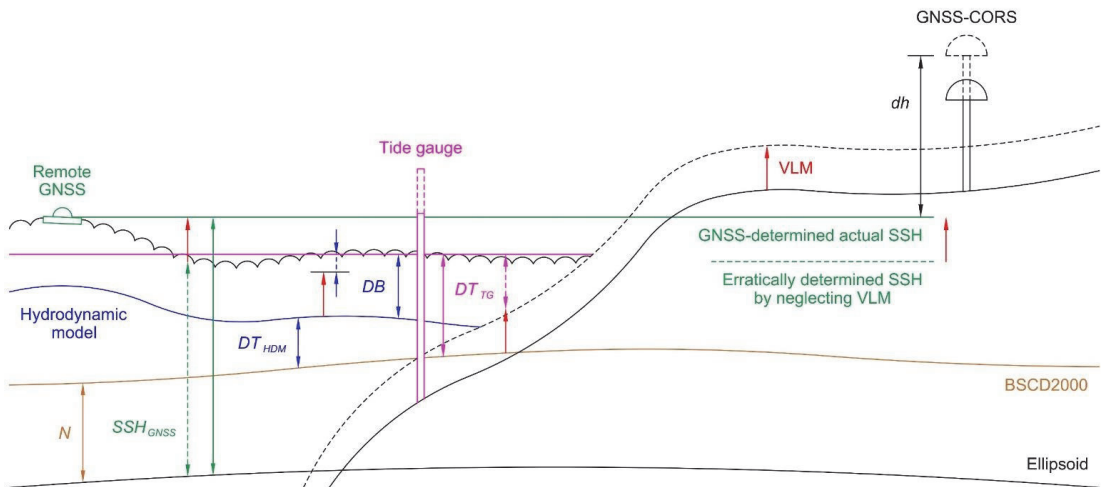


Figure 1. Interrelations between the used datasets. The solid lines denote geometry at a reference epoch, whereby the dashed lines show the vertical land motion (VLM) affected geometry at a GNSS observation epoch. Global sea level rise and geoid change trends are neglected for simplification (i.e., the sea’s surface is assumed to be unchanged). Notice that the depicted dynamic bias (DB) is negative, cf. Equation (3).

This contributions’ outline is as follows. Section 2 reviews the core theoretical principles for deriving and validating shipborne GNSS-determined sea surface heights (note that subsequent sections reveal additional details with data examples, since these reinforce the developed principles). Section 3 provides an overview of the shipborne GNSS surveys and used information. The derivation of offshore DT is examined next in Section 4; whereas, Section 5 is dedicated to shipborne GNSS data processing and validation. The paper continues with a discussion in Section 6 and concludes with a summary in Section 7.

2. Theoretical Principles

With the knowledge of the vertical range (R) between a reference point on a vessel (e.g., GNSS antenna’s reference point) and the sea surface (e.g., determined by a total station survey), instantaneous SSH can be calculated relative to a geodetic reference ellipsoid (e.g., GRS80), using GNSS measured ellipsoidal heights h :

$$iSSH(\varphi, \lambda, t) = h(\varphi, \lambda, t) - R, \tag{1}$$

where φ and λ are the measurement points’ geodetic latitude and longitude at a GNSS observation epoch t , respectively. Instantaneous SSH is only an approximation of the actual SSH, as it contains the vessel’s high-frequency attitude changes (e.g., pitch and roll motions) and the impact of sea state (i.e., waves). In addition, vessel sailing-related squat and static draft corrections must be applied, since these cause the vessel to sail with an offset relative to the reference level at which R is usually determined. Accurate derivation of shipborne GNSS-based SSH requires consideration of all these factors.

During GNSS data sampling, an inertial measurement unit can be deployed for specifying the vessel’s attitude [12,32]. However, utilizing an inertial measurement unit may be costly and require dedicated software for data processing. As an alternative, the vessel’s high-frequency attitude changes can be estimated and eliminated from GNSS measurements by using data from at least three GNSS antennas [11,33]. The elimination of

the vessel's high-frequency attitude changes, by computing a joint height solution from multiple antennas to the vessel's mass center, is further discussed in Section 5.1, with a complementing data example.

Note that such a joint height solution from multiple antennas retains the impact of waves, which manifests itself as heave motion (i.e., vertical movements of the vessel). The required SSH data can be separated from these height estimates by applying a low-pass filter [11,32]. The filtering window (spatial) length can be several kilometers long, depending on the GNSS data sampling rate, implying that the filter may propagate errors to the resulting SSH data; for instance, in steep geoid gradient areas. Therefore, the heights should be reduced to residual values prior to low-pass filtering:

$$r^{UF}(\varphi, \lambda, t) = iSSH(\varphi, \lambda, t) - \hat{DT}(\varphi, \lambda, t) - N(\varphi, \lambda), \quad (2)$$

where r^{UF} denotes unfiltered residual values. The term \hat{DT} denotes the ever-changing DT during a shipborne GNSS survey and N geoidal heights. The latter can be obtained from a suitable geoid model, whereas DT must be estimated.

As already discussed in the Introduction, the combination of TG and HDM datasets allows DT estimation [15,30]. First, the DB values of an HDM are determined at the locations of TG stations:

$$DB(\varphi^{TG}, \lambda^{TG}, t) = DT_{HDM}(\varphi^{TG}, \lambda^{TG}, t) - DT_{TG}(\varphi^{TG}, \lambda^{TG}, t), \quad (3)$$

where DT_{HDM} and DT_{TG} are HDM- and TG-based DT, respectively (see also Figure 1). With a suitable spatial interpolation method, the DB estimates are then gridded with HDM resolution. These predicted offshore DB (\hat{DB}) provide correction to the initial HDM:

$$\hat{DT}(\varphi^{HDM}, \lambda^{HDM}, t) = DT_{HDM}(\varphi^{HDM}, \lambda^{HDM}, t) - \hat{DB}(\varphi^{HDM}, \lambda^{HDM}, t), \quad (4)$$

where \hat{DT} denotes the corrected HDM-based DT. Dynamic topography at the GNSS measurement locations can finally be estimated via bilinear interpolation. Derivation of offshore DT is further discussed in Section 4, with accompanying data processing examples. Similarly, Section 5.2 further examines the low-pass filtering of the residual values.

The above computations result in filtered residual values r^F , which should be corrected for vessel sailing-related effects, such as squat and static draft:

$$r^{F+C}(\varphi, \lambda, t) = r^F(\varphi, \lambda, t) - C(t), \quad (5)$$

where the term C denotes the vessel sailing-related corrections collectively. Section 5.3 presents an example of their empirical derivation. Ideally, the resulting filtered and corrected residuals r^{F+C} should be near-zero, but such results cannot be expected, due to measurement errors and deficiencies in the used models. Thus, the residual values provide means for validation. Assuming that the estimated DT, geoid model, and vessel sailing-related corrections are accurate, the residuals primarily represent errors of the GNSS-determined SSH. Finally, the corrected SSH can be restored from the filtered and corrected residuals:

$$SSH^{F+C}(\varphi, \lambda, t) = r^{F+C}(\varphi, \lambda, t) + \hat{DT}(\varphi, \lambda, t) + N(\varphi, \lambda), \quad (6)$$

whereby these results are now suitable for further SSH data applications.

3. Shipborne GNSS Surveys, Data, and Other Used Information

Six marine survey campaigns were conducted in the Eastern Baltic Sea in the spring and summer of 2021 (Table 1 and Figure 2). Each campaign had a primary objective related to different Tallinn University of Technology marine condition monitoring projects. For instance, some tasks involved collecting water samples (e.g., chlorophyll, turbidity, nutrients, phytoplankton), measuring the vertical profiles of water properties (e.g., temperature, salinity, oxygen, light attenuation), or servicing marine monitoring stations. Concurrently, ellipsoidal heights were measured autonomously by four vessel-installed GNSS devices (the used instrumentation is described in [23]). The multi-frequency GNSS receivers were turned on before the vessel left the harbor, and the stored data were downloaded upon returning. During the campaigns, no dedicated GNSS operator was on-board. The GNSS sampling rates were 15 s for the first C1 campaign and 30 s for subsequent campaigns.

Table 1. General information about the conducted marine survey campaigns.

Campaign Identifier	Month (GPS Week)	Duration of a Campaign (h)	Route Length of a Campaign (km)	Number of HDM Grids/DT Computation Duration (h)	Number of Computed SSH Data Points	Temporal Resolution of SSH (s)
C1	April (2152)	52	544	120	11,908	15
C2	July (2168)	106	1439	168	12,253	30
C3	August (2169)	146	1874	192	16,222	30
C4	August (2172)	40	515	96	4390	30
C5	September (2174)	9	98	96	832	30
C6	September (2175)	40	454	120	4449	30

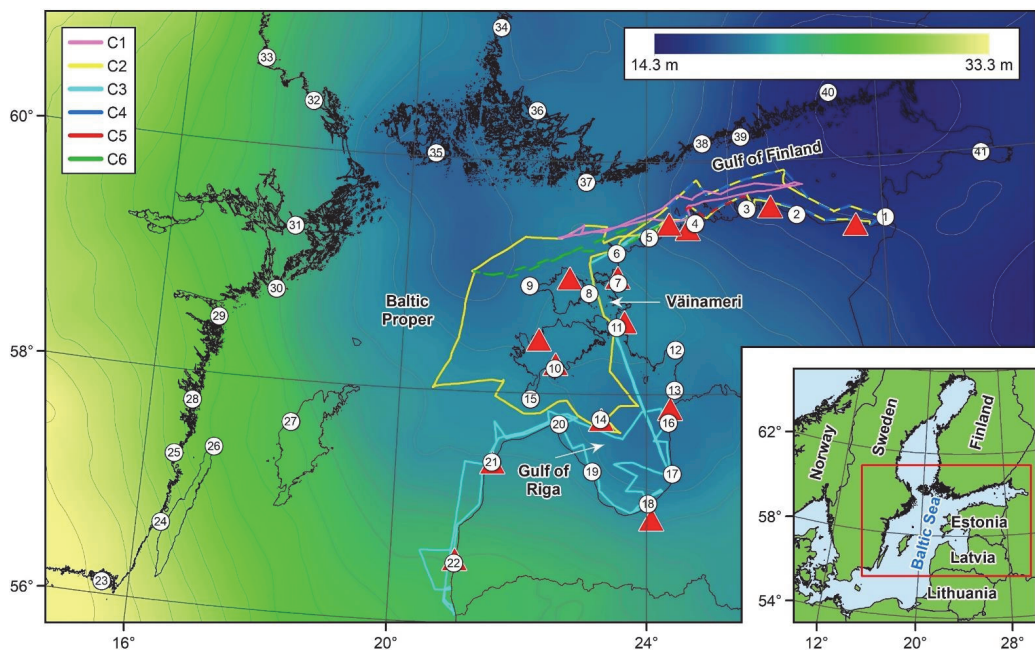


Figure 2. Study area (see the red rectangle) and routes of marine survey campaigns. Numbered circles denote the used TG stations, and red triangles continuously operating reference stations that were employed for GNSS post-processing. Colored background and grey isolines (contour interval is one meter) depict the NKG2015 quasigeoid model.

The collected shipborne GNSS data were post-processed relative to the Estonian [34] and Latvian [35] national GNSS continuously operating reference stations (CORS) with the commercial Trimble Business Centre software (version 5.52; Trimble Inc., Sunnyvale, CA, USA). Precise GNSS ephemerides (final orbits) from the International GNSS Service were incorporated into post-processing. Since Trimble Business Centre allows only one base station at a time for kinematic data post-processing, the closest GNSS-CORS (cf. Figure 2) was always employed for a GNSS data point computation (similarly to [11,24]). The GNSS-CORS coordinates were fixed to the reference epochs of the national reference frames (i.e., the standard data processing scheme was used). However, the Baltic Sea region's geodetic networks are deforming, primarily due to glacial isostatic adjustment induced vertical land motion (VLM). The VLM generates discrepancies between the reference and observation epoch positions of a GNSS-CORS, consequently introducing an offset to the marine GNSS measurements (cf. Figure 1), since sea level trends do not follow the VLM directly (but do contain the glacial isostatic adjustment induced geoid change). The neglected VLM correction may, thus, yield lower than actual SSH in the land uplift regions. By employing the principles outlined in [26], the GNSS measurements were corrected retrospectively for VLM occurring at the GNSS-CORS:

$$h(\varphi, \lambda, t, t_0) = h_0(\varphi^{RS}, \lambda^{RS}, t_0) + dh(t) + [VLM_{geocentric}(\varphi^{RS}, \lambda^{RS}) - GC(\varphi, \lambda)] \cdot (t - t_0), \quad (7)$$

where h_0 is the ellipsoidal height of a reference station at a reference epoch t_0 , and dh represents the estimated height difference between a reference station and remote GNSS measurement at an observation epoch t . The term $VLM_{geocentric}$ denotes the geocentric VLM rate at a GNSS reference station, and GC is the geoid change rate at a GNSS measurement location. The VLM and geoid change rates were obtained from the NKG2016LU VLM model [36].

It became evident during GNSS post-processing that some of the vessel's routes were too distant from the GNSS-CORS (westernmost routes in the Baltic Proper shown in Figure 2), resulting in reduced post-processed data quality. Previous studies [24,37,38] have shown that the Canadian CSRS-PPP online global precise point positioning service [39] can provide reliable post-processing for remote shipborne GNSS measurements. In particular [37], demonstrated that CSRS-PPP is a viable option for post-processing GNSS data, even in a transoceanic scenario for determining SSH. The results in [23] indicate that CSRS-PPP-based data are consistent, regardless of the distance from the coast and, thus, suitable for complementing poor-performing Trimble Business Centre post-processed route sections. Therefore, the poor-performing sections were replaced by CSRS-PPP solutions.

The results of a total station survey and tape measurements (in the harbor) allowed reducing the post-processed and VLM corrected GNSS ellipsoidal heights to the sea surface. The four GNSS antennas' reference points and three benchmarks on the vessel's railing were assigned coordinates in an arbitrary local system, whereby tape measurements (conducted separately for each campaign) determined the vertical distances between benchmarks and the sea surface. The ellipsoidal heights h obtained using Equation (7) were transformed into instantaneous SSH as (Equation (1) modification):

$$iSSH(\varphi, \lambda, t, t_0) = h(\varphi, \lambda, t, t_0) - H_{TS}^{ARP} + H_{TS}^{BM} - H_{tape}^{BM}, \quad (8)$$

where H_{TS}^{ARP} and H_{TS}^{BM} denote the total station determined heights of an antenna's reference point and a benchmark on the railing, respectively, and H_{tape}^{BM} is a distance measured by tape. Additional details about the total station survey and instantaneous SSH calculations can be found in [23].

This contribution now aims to further process the instantaneous SSH data, so that these are suitable for subsequent applications (e.g., validation of SA results, marine geoid models, HDMs' performance). However, Section 4 first examines the derivation of offshore DT, since SSH computations were performed jointly with data validation, which also requires

geoidal heights. The latter were obtained from the high-resolution (0.01×0.02 arc-deg, i.e., approximately 0.6 nautical miles) NKG2015 quasigeoid (over marine areas, the geoid coincides with the quasigeoid; henceforth, the shorter term will be used) model [40] (cf. Figure 2). Note that NKG2015 represents a geoid model using the zero-tide permanent tide concept, to which a correction from zero-tide to the tide-free concept has been applied (see [41,42] for details about permanent tide concepts). The correction provides consistency with GNSS measurements (using the tide-free concept). In other words, by subtracting NKG2015 heights from the GNSS determined ellipsoidal heights, normal heights using the zero-tide concept are obtained.

Hydrodynamic Model and Tide Gauge Data

Previous works [11,15,30,43] have evaluated the ability of the various HDMs available for the Baltic Sea in deriving sea surface dynamics. Based on these assessments, all the models contain a DB relative to the used height reference (i.e., BSCD2000), whereby the bias varies between models. It also appears that, generally, the most accurate representation of sea surface dynamics in the region can be obtained from the high-resolution (hourly data, with a spatial resolution of approximately 1.0 nautical miles) NEMO-Nordic model [44,45], which was, thus, also chosen for DT determination in this study. If TGs are connected (e.g., by geodetic leveling) to the used height system(s), the DB in the NEMO-Nordic-based DT can be estimated using TG readings. This study employed hourly data from 41 TG stations: 15 Estonian, 7 Latvian [46], 11 Swedish [47], 7 Finnish [48], and one Russian [49] (cf. Figure 2). Note that the NEMO-Nordic model and Russian TG data should be first converted from mean-tide to the zero-tide permanent tide concept for compatibility with the Estonian, Latvian, Swedish, and Finnish TG data [26] (and the normal heights discussed at the end of the previous section). Moreover, the Latvian [50] and Finnish [26,51] TG readings are initially given relative to alternative height reference levels. Hence, before utilization, these data must be converted relative to the used height reference (i.e., national height systems compatible with the BSCD2000).

Even though the Estonian, Latvian, Swedish, and Finnish height systems are all EVRS-based and heights refer to the Normaal Amsterdams Peil (NAP), some minor discrepancies exist (an additional discussion can be found in [26]). Thus, the pan-continental EVRF2019 [52] solution-based height system discrepancies can improve TG data compatibility further. Since GNSS post-processing was conducted relative to the Estonian and Latvian GNSS-CORS, the respective height systems were considered the zero level. The EVRF2019 solution yielded a -1 cm correction to the Swedish and Finnish TG readings. On the other hand, the Russian TG data are given relative to the Baltic Height System of 1977 (BHS77), and a $+21$ cm offset had to be added.

Similarly to the geodetic networks, the Baltic Sea TG networks are also deforming due to VLM. Even though the zeros of TGs approximately coincide with the reference level at the (common) reference epoch of the national height systems, in the land uplift regions, the zero separates from the reference, yielding lower than actual sea level readings (i.e., DT relative to the nearby solid Earth; cf. Figure 1). The principles outlined in [26] were, hence, employed to obtain absolute DT (i.e., relative to the height reference):

$$DT_{TG}(\varphi^{TG}, \lambda^{TG}, t^H) = DT_{RSL}(\varphi^{TG}, \lambda^{TG}, t^H, t_0) + VLM_{I_{leveled}}(\varphi^{TG}, \lambda^{TG}) \cdot (t^H - t_0), \quad (9)$$

where DT_{TG} and DT_{RSL} are the TG-based absolute and relative DT at an observation epoch t^H (hourly temporal resolution), respectively, and $VLM_{I_{leveled}}$ denotes leveled VLM rate at a TG station (obtained from the NKG2016LU VLM model). The term t_0 denotes the reference epoch of a height system to which the derived DT_{TG} refers. These TG data, corrected for datum offsets and VLM, were then used for linking the NEMO-Nordic HDM to the used height references for offshore DT derivation.

4. Derivation of Offshore Dynamic Topography

Dynamic topography, defined as the SSH and marine geoid separation, represents one of the most valuable parameters, in terms of marine dynamics. Accurate knowledge of DT can guarantee safe navigation at sea, help understand oceanographic processes, and be combined with a suitable geoid model to validate various SSH measurements. With the method developed by [15,30], TG data and an HDM can be combined using Equation (3) to estimate the HDM-contained DB values at the locations of TG stations (at hourly temporal resolution t^H). Both studies used exact interpolators for DB gridding, which inherently assumes errorless TG data and TGs connections to the height system(s), as well as that the estimated DB at a TG station is an expected value for all nearby offshore locations; although, neither is necessarily true. Errors may always exist, due to instrument malfunctions, natural disasters, human errors, or poor maintenance and documentation [53,54]. Such errors propagate to the derived offshore DT when the gridded DB is used to correct the initial HDM. Thus, a new approach utilizing DB qualities was developed for constraining TG data errors in offshore DB prediction.

4.1. Estimation of Dynamic Bias Uncertainties at the Tide Gauge Locations

Although DB changes temporally, over short timeframes (e.g., daily), the DB should remain relatively stable, as erratic behavior (such as sudden jumps, both spatially and temporally) would suggest a lack of consistency in the HDM-based DT. However, such a hypothesis first assumes a well-performing HDM (i.e., the HDM phases should match TG data). Figure 3 shows correlation coefficients between the NEMO-Nordic HDM and TG readings at the TG locations. It can be noticed that the (uncorrected) HDM-based DT is well correlated with the TG data, with coefficients being generally above 0.95. The only slight exception is TG₃₁ (refer to Figure 2), with a correlation coefficient of 0.87, likely due to its location in relatively confined waters. The NEMO-Nordic HDM phases, thus, appear to adequately match TG readings (also see [30]).

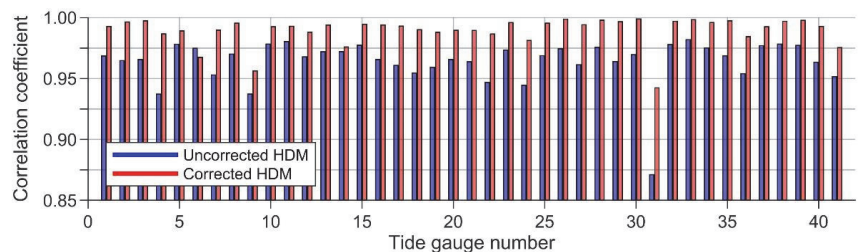


Figure 3. Correlation coefficients between TG and HDM data at the TG locations (based on all 792 h of used data, cf. Table 1). For better readability, only the top of the vertical scale is shown.

High DB standard deviation of NEMO-Nordic HDM may, hence, reveal poorly-performing TGs. For instance, notice in Figure 4b the high DB variability at TG₉ and TG₄₁ (yellow dots; also refer to Figure 2) during the C1 campaign, whereas during the C2 (Figure 4d) and C6 (Figure 4f) campaigns, the DB remained relatively stable. Such behavior may be associated with stormy conditions during the second half of the C1 campaign, since the harbor of TG₉ is relatively vulnerable to extreme weather, and TG₄₁ is affected by westerly winds that rapidly accumulate water during storms. Described variations in a confined harbor may not represent the offshore conditions. Therefore, the first uncertainty component (σ_1) for DB was estimated as a moving standard deviation (centered at an observation epoch t^H) in the DB temporal domain:

$$\sigma_1(t^H) = \sqrt{\frac{1}{T-1} \sum_{m=t^H-\frac{T-1}{2}}^{t^H+\frac{T-1}{2}} \left[DB(\varphi^{TG}, \lambda^{TG}, m) - \frac{1}{T} \sum_{m=t^H-\frac{T-1}{2}}^{t^H+\frac{T-1}{2}} DB(\varphi^{TG}, \lambda^{TG}, m) \right]^2}, \quad (10)$$

where T denotes the time extent considered at a certain time. A 25-h period was determined suitable, whereby a minimum of 12 h of data was included in all DB (and DT) computations, before and after the campaigns. This was done to avoid shorter than 25 h window sizes during the campaigns, which would have introduced inconsistency to the temporal domain uncertainty estimation.

Since DB has a long-wavelength nature, the mean DB estimates at neighboring TG stations should ideally be similar in value. Therefore, discrepancies between mean DB estimates may reveal, for example, errors in TGs connections to height system(s) or near-shore processes. In the Gulf of Riga (cf. Figure 2), the mean DB estimates differ over relatively short spatial scales (Figure 4a,c,e); whereby, the discrepancies appear similar during all the campaigns. For instance, the mean DB at TG₁₇ always appears higher than at TG₁₆ and TG₁₈ (refer to Figure 2). A higher mean DB estimate can similarly be observed at TG₄₀. Such reoccurring discrepancies could indicate errors in the levelings that connect TGs to height system(s).

Alternatively, the mean DB at TG₁₄ (refer to Figure 2) was significantly higher (more than usual) than at the neighboring TG stations during the C2 campaign (Figure 4c). According to the nearby weather station, during the second half of the C2 campaign, relatively strong winds (occasionally over 10 m/s) blew in the general direction of the exit of the harbor in which TG₁₄ resides. The receding water level in the harbor may, thus, have been a cause for a high mean DB estimate. Such behavior, however, does not represent offshore marine processes. Additionally [23], compared TG₄ readings to DT determined at the vessel's harbor, roughly 5 km away. It was demonstrated that the DT could differ by up to 8–9 cm between two nearby sheltered locations. According to the [15] and [30] approach, TG₄ data would represent the DT at the harbor.

In predicting offshore DB, the described potential offsets should be considered. Hence, the second uncertainty component (σ_2) was estimated by first comparing mean DB values at neighboring TG stations. These comparisons yielded N discrepancy estimates dDB for each mean DB value (i.e., mean discrepancies). The second uncertainty component was then estimated in the DB spatial domain as:

$$\sigma_2 = \sqrt{\frac{1}{N-1} \sum_{m=1}^N \left[\overline{dDB}_m(\varphi^{TG}, \lambda^{TG}) - \frac{1}{N} \sum_{m=1}^N \overline{dDB}_m(\varphi^{TG}, \lambda^{TG}) \right]^2}, \quad (11)$$

It was determined that comparisons with mean DB estimates at the nearest three TG stations (by also considering the distribution of TG stations) provided satisfactory results (i.e., $N = 3$). Note that the second uncertainty component was calculated separately for each campaign (e.g., for campaign C1, precisely the values shown in Figure 4a were used), whereby the mean DB values were estimated over an extended period. For example, the 9-h length of campaign C5 may not have been sufficient for calculations, which were therefore performed over a 96-h period instead (cf. Table 1). In studies investigating extensive periods, the second uncertainty component should also be estimated as a moving window (as is done for the first component), because offsets caused by marine processes are not likely to reoccur often (for instance, the TG₁₄ example). Here, this is emulated by a separate estimation for each campaign.

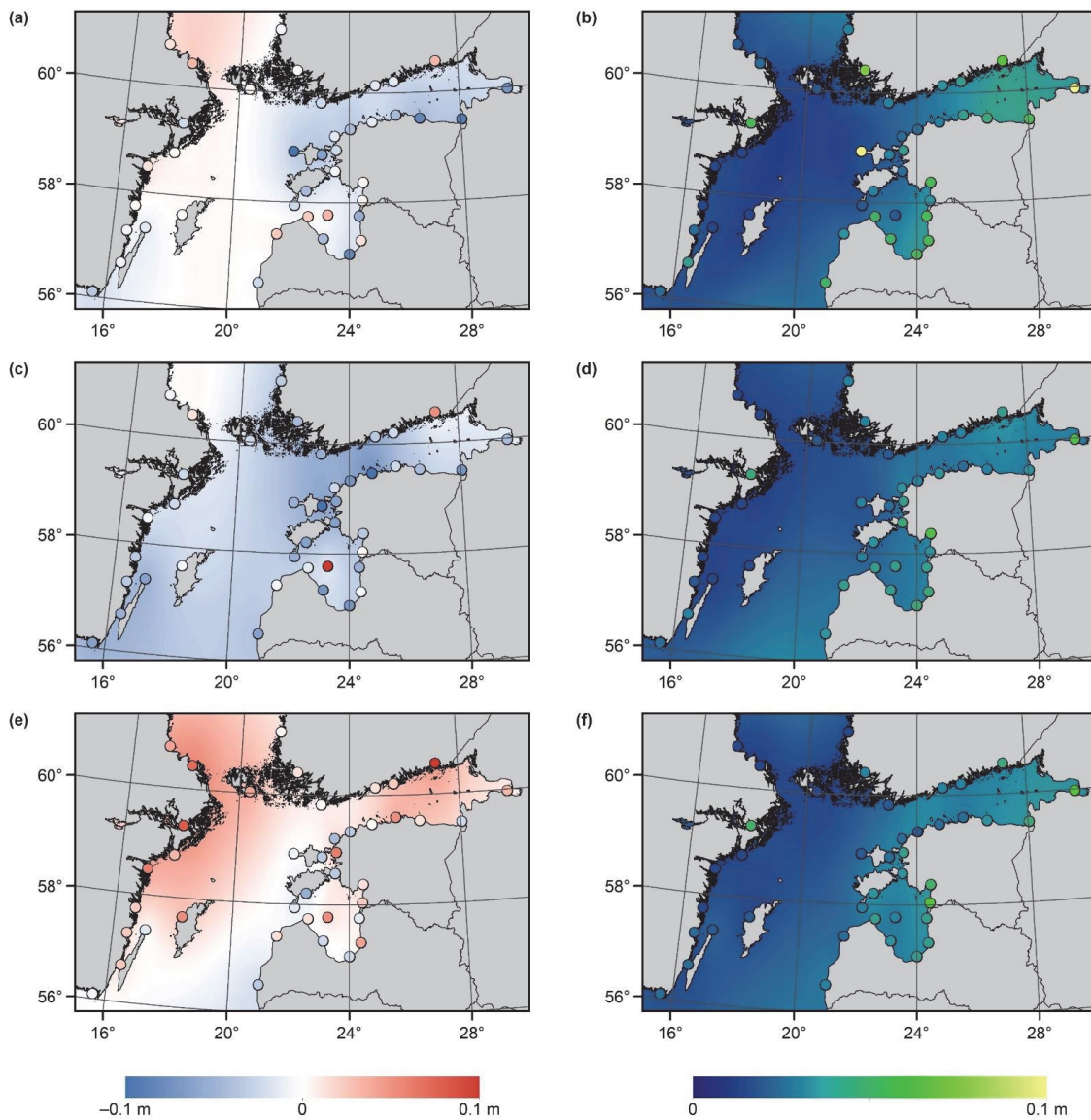


Figure 4. The mean predicted DB (left) and standard deviation estimates of predicted DB (right) for campaigns C1 (a,b), C2 (c,d), and C6 (e,f). The colored circles show, correspondingly, the mean DB values and standard deviation estimates of the DB values determined at the locations of TG stations.

It is assumed that the first (temporal domain) and second (spatial domain) uncertainty components are (generally) independent variables. The final uncertainty estimates for DB were, thus, calculated as:

$$\sigma_{DB}(t^H) = \sqrt{[\sigma_1(t^H)]^2 + [\sigma_2]^2}, \tag{12}$$

where t^H denotes hourly temporal resolution. The resulting DB uncertainties for campaign C1 are shown in Figure 5a. Notice how the estimates at TG₉ increase significantly during

the second half of the campaign, which coincides with the period of strongest storm winds (as discussed earlier). The uncertainty estimates are summarized for all campaigns in Figure 5b by averaging. These (hourly resolution) results were next employed in predicting offshore DB.

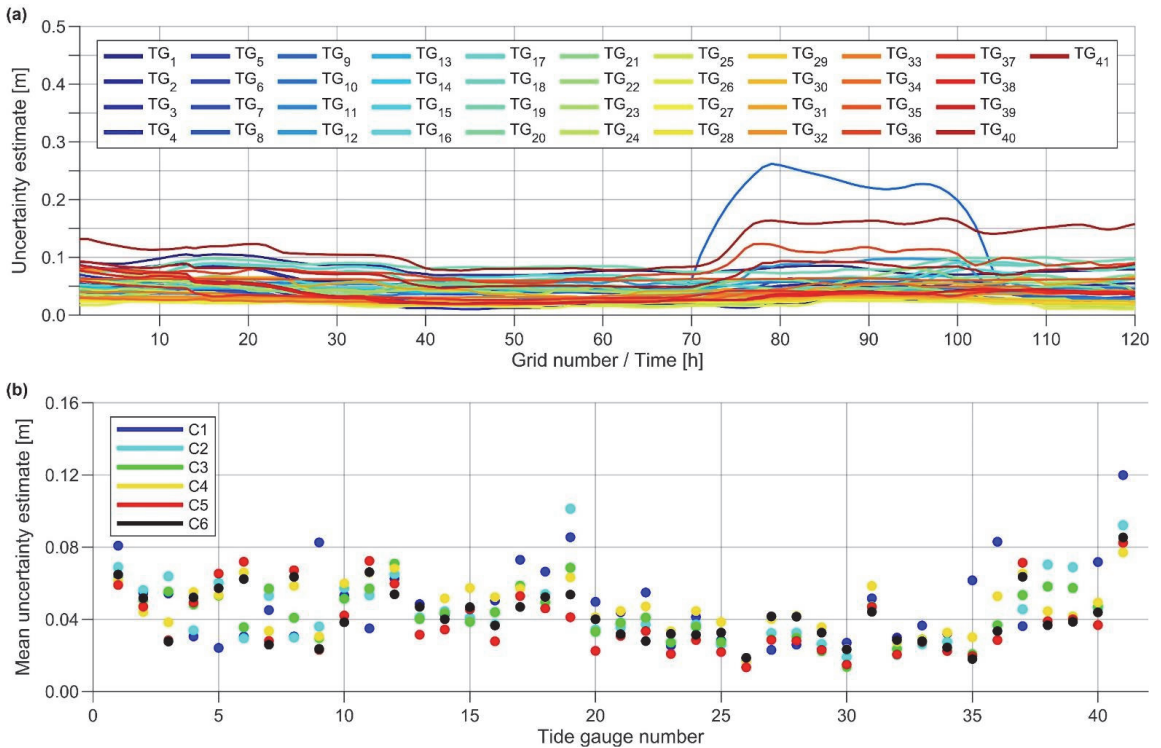


Figure 5. Uncertainty estimates of DB (a) at each TG station (refer to Figure 2) during the C1 campaign (i.e., $\sigma_{DB}(t^H)$; cf. Equation (12)) and (b) averaged for all campaigns.

4.2. Correction of Hydrodynamic Model Based Dynamic Topography

With the inclusion of determined uncertainties, the DB estimates were predicted offshore (with the NEMO-Nordic spatial resolution) by employing least-squares collocation [55] with the second-order Markov model covariance function [56]. In Figure 4, the mean predicted DB and standard deviation estimates of predicted DB for campaigns C1, C2, and C6 are presented. The estimated surfaces smoothly follow the long-wavelength DB trends determined at TG locations, but do not include the erratic behavior and offsets described in Section 4.1. It appears that the primary variations of DB occur in the Gulf of Finland and Gulf of Riga, while DB is more stable in the Baltic Proper (Figure 4b,d,f; refer to Figure 2 for basin locations). Additionally, notice how the mean DB surfaces differ for campaigns C1, C2, and C6 (Figure 4a,c,e). These results demonstrate the spatiotemporal changes of the NEMO-Nordic contained DB well.

The predicted offshore DB was used to correct the initial HDM (at hourly temporal resolution t^H) by employing Equation (4). Notice that the comparisons between the corrected NEMO-Nordic HDM and TG readings now yield improved correlation coefficients, except for TG₆, which shows a slightly reduced correlation (Figure 3). Since this study aimed to derive and validate shipborne GNSS-based SSH, the DT estimates were finally determined at the GNSS measurement locations via bilinear interpolation at observation epochs t (interpolated linearly from the hourly resolution data). These values are shown

in Figure 6b and denoted as $\hat{D}T(\varphi, \lambda, t)$. See also the predicted DB during marine survey campaigns in Figure 6a.

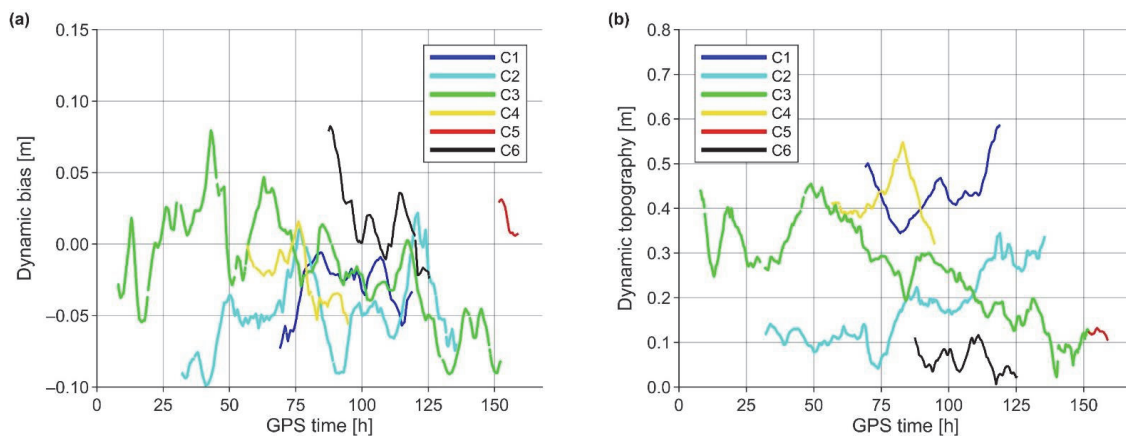


Figure 6. The (a) predicted DB and (b) corrected HDM-based DT during marine survey campaigns.

5. Derivation and Validation of Shipborne GNSS-Based Sea Surface Heights

5.1. Reducing the Effects of Vessel’s High-Frequency Attitude Changes

Determination of accurate SSH requires considering the vessel’s pitch and roll motions (Figure 7), where the yaw motion can be neglected, as the focus is on heights. In this study, the approach developed by [11] was improved using an additional GNSS antenna. By computing instantaneous SSH from multiple antennas jointly to the vessel’s stable mass center, the method eliminates (or, at the very least, significantly reduces) the vessel’s high-frequency attitude changes from the joint SSH solution. The distances between GNSS antennas relative to the vessel’s mass center (Figure 7) were derived from total station measurements (see also [23]).

The GNSS determined instantaneous SSH (cf. Equation (8)) from three antennas were first interpolated linearly to the location of the vessel’s center of mass in two steps:

$$iSSH_{X\alpha}(\varphi, \lambda, t, t_0) = iSSH_{A\gamma}(\varphi, \lambda, t, t_0) + c_1 \left[iSSH_{A(\gamma+1)}(\varphi, \lambda, t, t_0) - iSSH_{A\gamma}(\varphi, \lambda, t, t_0) \right] \tag{13}$$

$$iSSH_{CoM}^{\xi}(\varphi, \lambda, t, t_0) = iSSH_{X\alpha}(\varphi, \lambda, t, t_0) + c_2 \left[iSSH_{A(\{1,2,3,4\}-\{\gamma,\gamma+1,\xi\})}(\varphi, \lambda, t, t_0) - iSSH_{X\alpha}(\varphi, \lambda, t, t_0) \right], \tag{14}$$

where the index α denotes the number of an imaginary intersection point, the index γ number of an antenna and ξ solution numbered according to an excluded fourth antenna (also refer to Figure 7 and Table 2). Coefficients c_1 and c_2 are determined from total station measurement derived distances. The geodetic coordinates (φ, λ) represent the general location of the vessel (e.g., chosen according to the best performing antenna; in this study, coordinates of the antenna A4 were consistently used), and t is an observation epoch of a GNSS measurement. These calculations resulted in four $iSSH_{CoM}^{\xi}$ solutions (i.e., instantaneous SSH at the vessel’s mass center). Unfortunately, such calculations were not possible for the C4 campaign, due to the malfunctioning of two instruments [23]. For the C4 campaign, the instantaneous SSH of antennas A1 and A2 were averaged at observation epochs t .

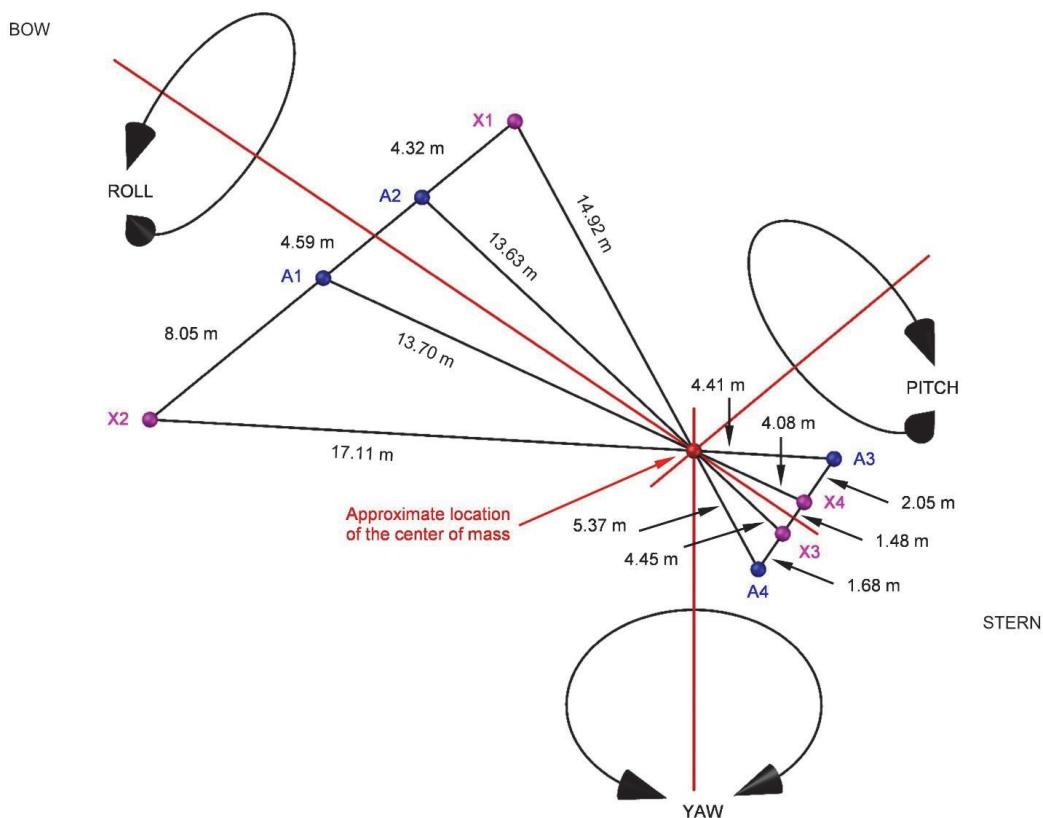


Figure 7. Pitch, roll, and yaw motions of a moving vessel and relative locations of the used GNSS antennas (colored blue). The red lines are the principal axes of the vessel, whereas the black lines denote total station measurement derived distances between antennas and imaginary (magenta colored) intersection points. All points are shown in horizontal projection (i.e., as reduced to the sea surface).

Table 2. The solutions' (ζ) associated indexes (α , β , and γ) and coefficient values (c_1 , c_2 , c_3 , and c_4 ; also see Figure 7).

Index/Coefficient	Solution $\zeta=1$	Solution $\zeta=2$	Solution $\zeta=3$	Solution $\zeta=4$
α	3	4	1	2
β	4	3	2	1
γ	3	3	1	1
c_1	$\frac{2.05 + 1.48}{2.05 + 1.48 + 1.68}$	$\frac{2.05}{2.05 + 1.48 + 1.68}$	$\frac{4.59 + 4.32}{4.59 + 4.32 + 4.41}$	$\frac{8.05}{8.05 + 4.59 + 4.32}$
c_2	$\frac{4.45}{4.45 + 13.63}$	$\frac{4.08 + 13.70}{2.05 + 1.48}$	$\frac{14.92 + 5.37}{8.05}$	$\frac{17.11 + 4.41}{4.59 + 4.32}$
c_3	$\frac{2.05 + 1.48 + 1.68}{4.08 + 13.70}$	$\frac{2.05 + 1.48 + 1.68}{4.45 + 13.63}$	$\frac{-4.59}{17.11 + 4.41}$	$\frac{4.59}{14.92 + 5.37}$
c_4	$\frac{4.08}{4.08}$	$\frac{4.45}{4.45}$	$\frac{17.11}{17.11}$	$\frac{14.92}{14.92}$

Since the four antennas form a rigid system, the instantaneous SSH at the vessel's mass center can be further used for validation purposes. Hence, the instantaneous SSH estimates at the previously excluded fourth antenna location were interpolated similarly:

$$iSSH_{X\beta}(\varphi, \lambda, t, t_0) = iSSH_{A\gamma}(\varphi, \lambda, t, t_0) + c_3 \left[iSSH_{A(\gamma+1)}(\varphi, \lambda, t, t_0) - iSSH_{A\gamma}(\varphi, \lambda, t, t_0) \right] \tag{15}$$

$$i\hat{S}H_{A\bar{\xi}}(\varphi, \lambda, t, t_0) = iSSH_{X\beta}(\varphi, \lambda, t, t_0) + c_4 \left[iSSH_{CoM}^{\bar{\xi}}(\varphi, \lambda, t, t_0) - iSSH_{X\beta}(\varphi, \lambda, t, t_0) \right], \tag{16}$$

where the index β denotes the number of an imaginary intersection point, and coefficients c_3 and c_4 are determined from total station measurement derived distances (Figure 7 and Table 2). The conducted calculations were validated by comparing the estimated ($i\hat{S}H_{A\bar{\xi}}$) and measured ($iSSH_{A\bar{\xi}}$) heights:

$$d_{A\bar{\xi}}(\varphi, \lambda, t) = i\hat{S}H_{A\bar{\xi}}(\varphi, \lambda, t, t_0) - iSSH_{A\bar{\xi}}(\varphi, \lambda, t, t_0), \tag{17}$$

where $d_{A\bar{\xi}}$ denotes discrepancies at the location of the initially excluded fourth antenna. Statistics of discrepancies are summarized in Figure 8, indicating the expected GNSS height determination accuracy. It can be noticed that, generally, the discrepancy mean values are sub-centimeter, suggesting the successful reduction of ellipsoidal heights to the sea surface using Equation (8) (i.e., all four antennas are approximately on the same plane). Note that the weighted mean (according to campaign distances presented in Table 1) standard deviation estimate (by averaging the values shown in Figure 8) of 4.1 cm showed a good performance for height determination.

Ideally, all four $iSSH_{CoM}^{\bar{\xi}}$ solutions should be free of vessel high-frequency attitude changes and have matching results considering the successful reduction of ellipsoidal heights. The performance of $iSSH_{CoM}^{\bar{\xi}}$ was evaluated as:

$$\bar{\sigma}_{CoM} = \frac{1}{I} \sum_{i=1}^I \left\{ \sqrt{\frac{1}{3} \sum_{\bar{\xi}=1}^4 \left[iSSH_{CoM}^{\bar{\xi}}(\varphi, \lambda, i, t_0) - \frac{1}{4} \sum_{\bar{\xi}=1}^4 iSSH_{CoM}^{\bar{\xi}}(\varphi, \lambda, i, t_0) \right]^2} \right\}, \tag{18}$$

where $i = 1, 2, \dots, I$ is the number of a GNSS observation. These evaluation results vary between 0.4 cm (C5 campaign) and 1.1 cm (C1 campaign), indicating excellent agreement between the four solutions for all campaigns. Even though the C2 campaign validation suggests more significant (than usual) discrepancies at the antenna locations (Figure 8), the solutions agree well at the vessel’s mass center ($\bar{\sigma}_{CoM}$ is 0.8 cm). In practical applications use of three GNSS antennas, thus, appears sufficient, and any of the four $iSSH_{CoM}^{\bar{\xi}}$ solutions would be equally suitable for further use. Due to data availability, the final instantaneous SSH solution was calculated as:

$$iSSH_{CoM}^{Final}(\varphi, \lambda, t, t_0) = \frac{1}{4} \sum_{\bar{\xi}=1}^4 iSSH_{CoM}^{\bar{\xi}}(\varphi, \lambda, t, t_0) \tag{19}$$

and used in subsequent data filtering. The temporal resolutions of $iSSH_{CoM}^{Final}$ were 15 s for the first C1 campaign and 30 s for subsequent campaigns. Recall that the $iSSH_{CoM}^{Final}$ of campaign C4 is a simple average of the A1 and A2 antenna heights.

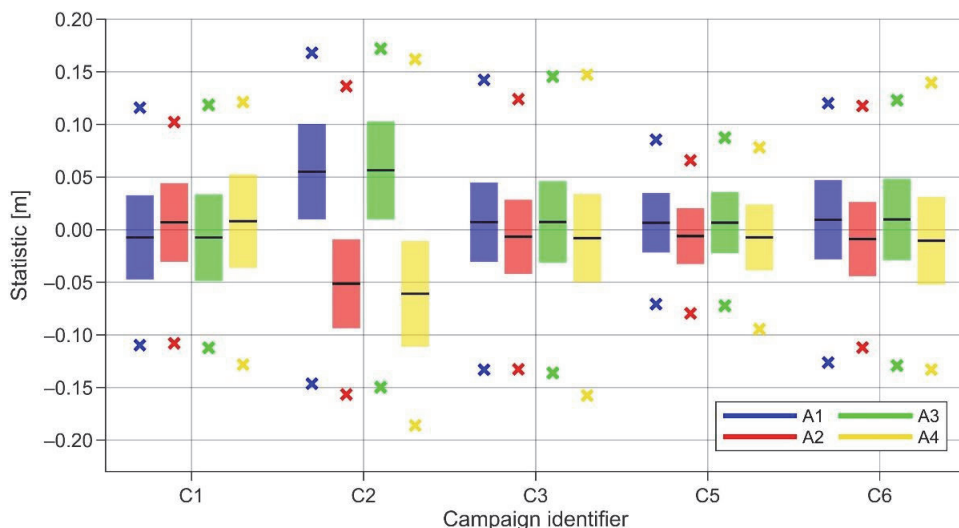


Figure 8. Statistical properties of discrepancies d_{A_g} for antennas A1–A4. The black lines are mean values, and colored bars denote standard deviation estimates. Crosses show 99th percentile minimum and maximum discrepancies.

5.2. Reducing the Effects of Sea State Conditions

The computed instantaneous SSH, now with a substantially reduced impact from the vessel’s high-frequency attitude changes (i.e., pitch and roll motions), still contains some influence from sea state conditions (i.e., waves), which primarily manifest as the vessel’s up–down direction heave motion. As a result, instantaneous SSH contains high-frequency variations that should be eliminated from the expected SSH; for instance, by applying a low-pass filter. This study used the approach developed by [24] and successfully employed by [11]:

$$OUT(i) = \frac{1}{F} \sum_{m_2=m_1-\frac{F-1}{2}}^{m_1+\frac{F-1}{2}} Median_{m_2} \left\{ IN_{m_1}(i) \left| i - \frac{F-1}{2} \leq m_1 \leq i + \frac{F-1}{2} \right. \right\}, \quad (20)$$

where *IN* and *OUT* denote input and output data, respectively, and *F* is the filtering window size (i.e., a certain number of measurements). As in Equation (18), *i* represents a GNSS observation number.

Refs. [11,24] used the low-pass filter directly on SSH data. Recall the temporal data resolution of 15 or 30 s, which at a vessel velocity of around 9 knots results in a filtering window (spatial) length of several kilometers. With such lengthy window sizes, low-pass filtering may contaminate results, due to the gradients of DT and geoid. Thus, (unfiltered) residual estimates were first calculated from $iSSH_{CoM}^{Final}$ using Equation (2) (note that the residuals are not dependent on the reference epoch t_0 , since this dependency disappears using a compatible geoid model NKG2015). A sum of absolute differences (between unfiltered and filtered signals) function was then compiled for each marine survey campaign, by applying the Equation (20) low-pass filter on unfiltered residuals. Only odd filtering window sizes were considered, and the optimal windows were estimated as sizes where the functions became roughly linear. The results are summarized in Figure 9. For comparability, the functions are normalized according to the maximum values.

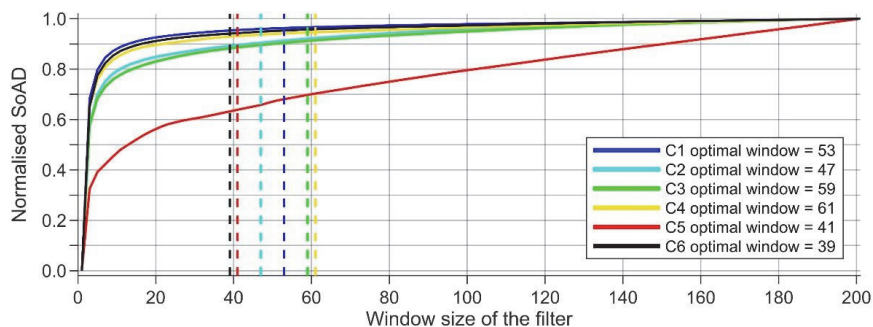


Figure 9. Sum of absolute difference (SoAD) functions for the marine survey campaigns. Optimal filtering window sizes are shown with dashed vertical lines.

Notice that the functions are similar in shape, except for the C5 campaign, which is much shorter than the others (i.e., containing fewer measurements; cf. Table 1). However, the optimal filtering window sizes vary, likely due to approximations assumed during the size determination. For consistency, the final filtering window size (used for all data filtering) was estimated as a weighted mean (according to the campaign distances presented in Table 1) of an individual campaigns’ optimal window sizes. The resulting 53 measurements are almost the same as the window size (51 measurements, at which the filtered data had a similar signal frequency to the geoid) suggested by [11].

Notably, such a filtering approach is independent of temporal data resolution (unless the GNSS sampling rate is very high, i.e., sub-second), since sea state conditions cause random data noise; hence, allowing investigation of the filtering window (spatial) length dependency on the GNSS sampling rate and vessel velocity (Figure 10). Ideally, the filtering window length should approximately match the spatial resolution of the employed model datasets (i.e., geoid model and HDM), to decrease error propagation. At a vessel velocity of 9 knots, this implies a GNSS sampling rate of around 5 s. In this study, the sampling rates were 15 or 30 s, and the filtering window lengths were, correspondingly, roughly 4 and 8 km. Future studies and marine survey campaigns should consider the results in Figure 10.

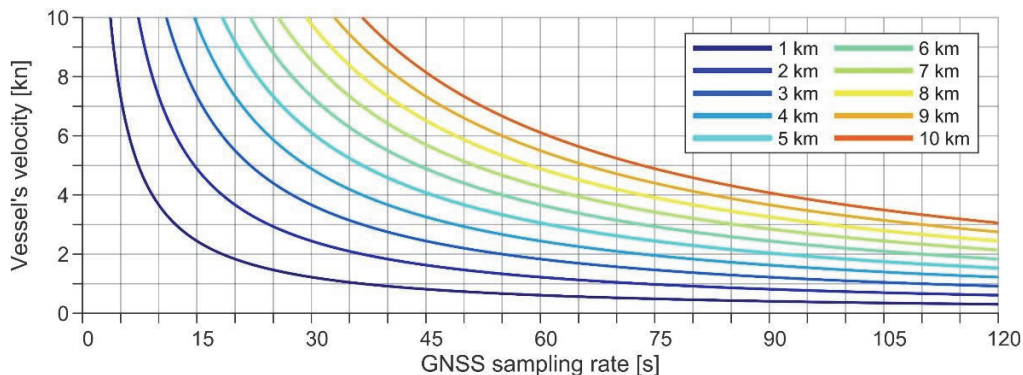


Figure 10. Filtering window length dependency on GNSS sampling rate and vessel velocity, by assuming an optimal filtering window size of 53 measurements.

Low-Pass Filtering Results

The Equation (20) low-pass filter, with the filtering window size of 53 measurements, was applied on the unfiltered residuals, resulting in the filtered residuals denoted as $r_{CoM}^F(\varphi, \lambda, t)$ in the following. For comparison, the low-pass filter was also used on residuals (also estimated using Equation (2)) determined directly from the instantaneous SSH of

individual antennas (i.e., instantaneous SSH from Equation (8)). The results of the C2 campaign before and after data filtering are shown in Figure 11. Notice how the unfiltered residuals of antennas A1 and A2 (at the vessel's bow) are more scattered than antennas A3 and A4 (and the joint solution), suggesting a dominating pitch motion at the vessel's bow and that the vessel is more stable near its mass center (cf. Figure 7). Such a revelation implies inferior results for the C4 campaign (recall that the center of mass solution could not be computed).

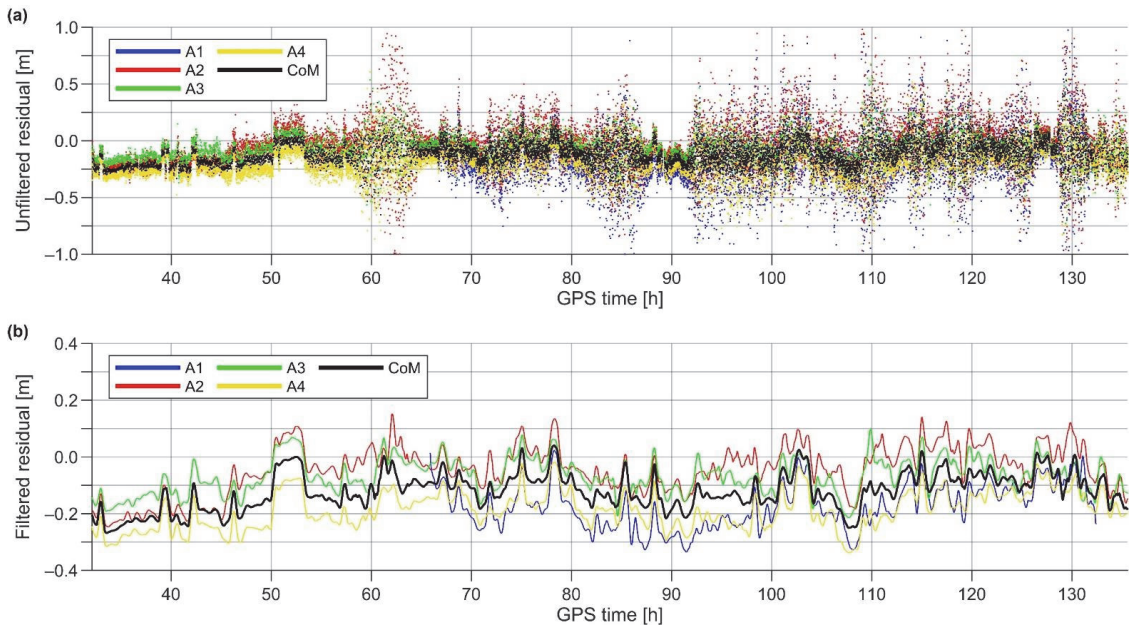


Figure 11. Residuals of the C2 campaign for antennas A1–A4 and the mass center solution (denoted CoM), (a) before and (b) after low-pass filtering.

After filtering, significant discrepancies could be detected between the center of mass and individual antenna solutions (Figure 11b). Residuals of the port side antennas generally appeared lower than starboard antennas' (a similar pattern can be observed for all other campaigns). The likely cause is the change in the vessel's general attitude. During total station and tape measurements in the harbor, the vessel was always tilted slightly to the right [23]. The vessel may correct its general attitude while in motion; thus, resulting in lower and higher than actual heights for port and starboard side antennas, respectively. Since the vessel rotates approximately around its mass center, the joint solution $iSSH_{CoM}^{Final}$ should consider such a motion.

To further analyze the performance of conducted computations, the unfiltered and filtered residuals were compared (i.e., filtered results were subtracted from unfiltered). The statistics of their differences are summarized in Figure 12. The most significant differences were consistently detected for antennas A1 and A2, again suggesting dominating pitch motion at the vessel's bow. A reduced standard deviation was always (except for the C4 campaign, which showed no improvement) produced for the mass center solution. In contrast, the low-pass filter eliminated more noise from individual antenna solutions (i.e., resulting in greater differences between unfiltered and filtered residuals). It, hence, appears that the vessel's high-frequency attitude changes were indeed eliminated (or at the very least significantly reduced) in the $iSSH_{CoM}^{Final}$ (cf. Section 5.1).

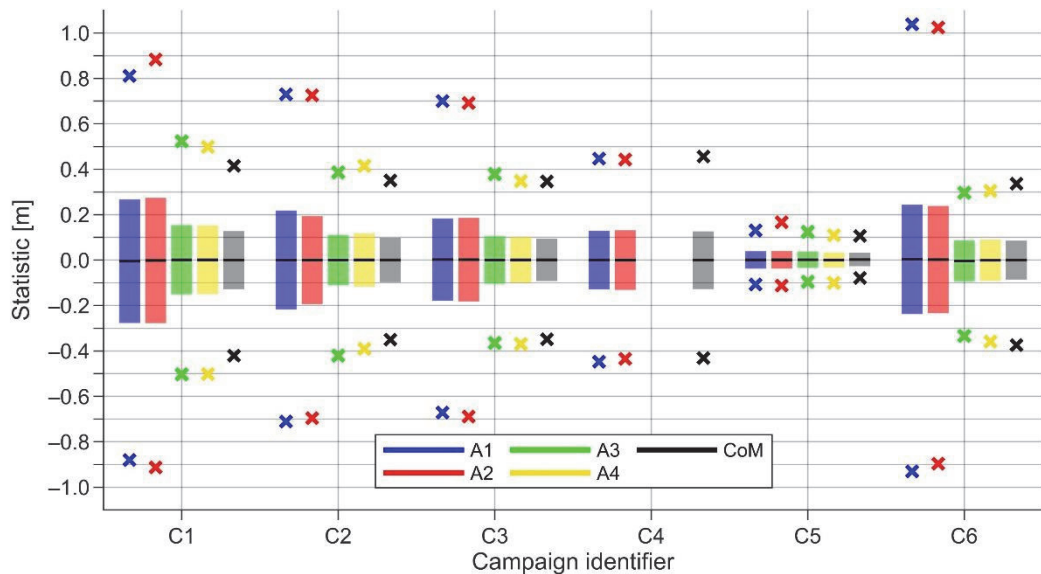


Figure 12. Statistical properties of differences between unfiltered and filtered residuals (filtered results were subtracted from unfiltered) for antennas A1–A4 and the mass center solution (denoted CoM). The black lines are mean values, and colored bars denote standard deviation estimates. Crosses show 99th percentile minimum and maximum differences.

The described outcomes demonstrate the importance of proper planning for such marine GNSS surveys; the location of the antenna has a significant influence on data accuracy. Before validating this study’s results, vessel sailing-related corrections must be estimated and removed from the filtered residuals. The following section describes their empirical derivation.

5.3. Vessel Sailing-Related Corrections

In Figure 11b, abnormal peaks can be detected in the C2 campaign mass center solution. These coincide with the occasions of the vessel’s stopping; for example, to collect water samples. This phenomenon occurs due to the disappearance of the squat effect that causes a vessel to sail deeper than its nominal draft. The squat is a function of a vessel’s velocity and dimensions, but is also influenced by depth in shallower, more confined waters [57]. Since the surveys were generally conducted in relatively deep and open marine areas, it is assumed that depth has a negligible influence on the squat. The only slight exception could be campaign C3, which also surveyed shallower regions of the Baltic Sea (notice the near-shore routes in Figure 2).

Due to occasional stops, the velocity could be related to height changes between a moving and static vessel, by utilizing filtered residuals over distances up to 3 km. These estimates that represent squat values at various velocities are presented in Figure 13a as black dots. Since the vessel’s dimensions are constant, the squat is approximately a quadratic velocity function [37,57]. It was, thus, estimated as a least-squares fit of a quadratic function to the empirical data. A linear squat approximation, also shown in Figure 13a, is further discussed in Section 6.4.

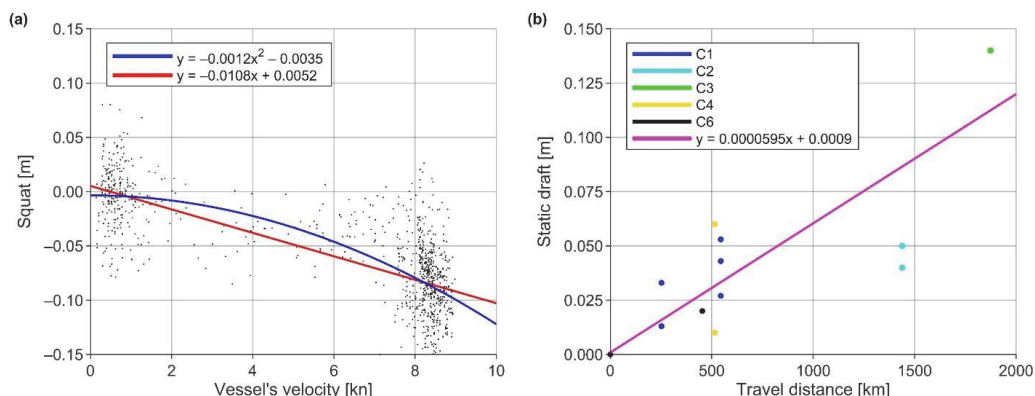


Figure 13. Empirically estimated (a) squat and (b) static draft corrections.

The second vessel sailing-related correction that must be considered is the static draft. Due to fuel consumption, the vessel floats gradually higher. The lowest/highest estimates of the static draft are, correspondingly, at the time of harbor departure/return. Thus, the static draft was approximated from differences in tape measurements conducted before and after marine survey campaigns. Since tape measurements may contain errors in the range of static draft itself (e.g., notice the difference between the campaign C4 estimates in Figure 13b), the empirical data were considered altogether, whereas all negative values were excluded. The static draft was then estimated as a distance-related least-squares fit of a linear trend (Figure 13b).

The empirically derived vessel sailing-related squat (a function of the vessel’s velocity v) and static draft (a function of the total traveled distance s) corrections were subsequently applied to the filtered residuals (Equation (5) modification; also notice the functions presented in Figure 13):

$$\begin{aligned}
 r_{CoM}^{F+C}(\varphi, \lambda, t) &= r_{CoM}^F(\varphi, \lambda, t) - \{squat(v)\} - \{static\ draft t(s)\} \\
 &= r_{CoM}^F(\varphi, \lambda, t) - \left\{ (-0.0012) \cdot [v(t)]^2 \right\} - \left\{ 5.95 \cdot 10^{-5} \cdot s(t) \right\},
 \end{aligned}
 \tag{21}$$

where the first set of curly braces denotes squat correction, and the second set, static draft correction. The values of v and s are given at a GNSS observation epoch t . Note that the vessel’s velocity is considered in knots, and the total traveled distance is in kilometers from the beginning (i.e., home harbor) of the campaign. The term r_{CoM}^{F+C} denotes filtered and corrected residuals, which were validated as described in the following section.

5.4. Validation and Least-Squares Adjustment of the Results

Ideally, the filtered and corrected residuals should be near-zero. However, such idealistic results cannot be expected, due to errors in the total station, tape, GNSS, and TG measurements; estimated corrections’ inaccuracies; and deficiencies in the used VLM, HDM, and geoid models. For instance, an examination of the residuals’ statistical properties (Figure 14a) shows biases between the results of different campaigns (notice mean values). A likely explanation is errors in tape measurements conducted in the harbor, for reducing surveys’ GNSS results to the sea surface (cf. Equation (8)). Since such measurements are subjective (the surveyor had to assess the optimal measure from the moving sea surface) and the vessel swayed slightly during the measurements, the tape-determined values likely induce the most significant errors.

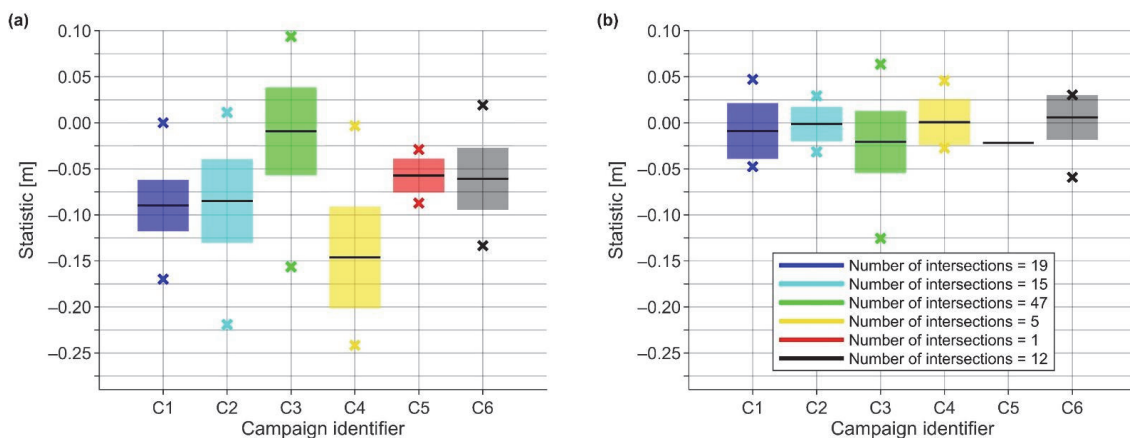


Figure 14. Statistical properties of (a) filtered and corrected residuals and (b) their differences at campaign–internal intersections. The black lines are mean values, and colored bars denote standard deviation estimates. With crosses are shown minimum and maximum residuals and their differences at intersections in (a,b), respectively.

The residuals’ standard deviation estimates vary between 1.8 cm and 5.5 cm (Figure 14a), demonstrating, in general, the satisfactory performance of the results, especially considering the variety of different datasets combined. The highest standard deviation estimate describes the C4 campaign, which is expected, as only two GNSS antennas (instead of four) could be used for the $iSSH_{CoM}^{Final}$ solution (cf. Section 5.1). Thus, the vessel’s high-frequency attitude changes likely contaminated the solution. On the other hand, although the second half of campaign C1 was conducted in windy and wavy conditions (due to a rising storm; recall the discussion in Section 4.1), the resulting standard deviation estimate was only 2.8 cm, suggesting that the approach used could successfully eliminate the vessel’s high-frequency attitude changes and marine conditions’ influence on GNSS measurements.

Another principal measure is the consistency of the residuals, which were, hence, compared at the campaign–internal intersections, by defining two criteria: (i) distance between points less than 250 m, and (ii) time between intersections (also consecutive points) more than 30 min. The two criteria had to be true at the same time. According to the first criterion, nearby parallel routes could also yield an intersection (geoidal heights and DT remain relatively unchanged over short distances), to avoid a lack of detected intersections when no actual route crossings existed. Moreover, if a vessel stopped for more than 30 min (e.g., to collect water samples) and did not drift significantly (more than 250 m), the stopping was counted as an intersection (the low-pass filtering influence disappears with 30 min: $53 \text{ measurements} \times 30 \text{ s} = 26.5 \text{ min}$). The resulting statistics (Figure 14b) indicate a good consistency, with generally near-zero mean differences, and standard deviation estimates varying between 1.8 cm and 3.4 cm. Notably, the NKG2015 geoid model errors do not affect these comparisons, since the model is static (i.e., not a time-dependent variable).

The defined criteria were further employed to compare residuals of different campaigns at their intersections, following the principles described above. Notice in Figure 15 that the absolute values of mean differences (sign difference is due to the subtraction order) and standard deviation estimates differ slightly, for example, if campaign C1 is compared to C2 and vice-versa. Since the algorithm searches intersections by moving along the validated campaign, the two tests may yield different points for comparisons, due to the second intersection search criterion (i.e., the algorithm moves along different routes, detecting different points based on the definitions). Generally, these assessments show a good agreement between the residuals of different campaigns, in terms of standard

deviation. The most significant residual differences were detected between campaigns C2 and C3, resulting in standard deviation estimates of 4.4 cm and 5.0 cm. The compared intersections were primarily detected in the relatively shallow Vänameri (cf. Figure 2), which could imply errors in squat estimation, but Vänameri also has more than 300 islands and islets, which may have influenced the HDM-embedded DT modeling.

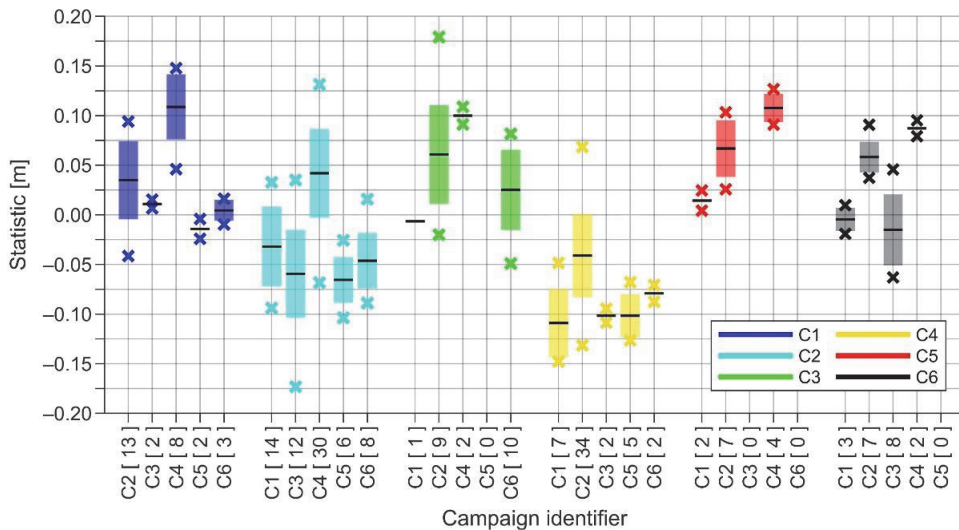


Figure 15. Statistical properties of filtered and corrected residuals’ differences at intersections between campaigns. The black lines are mean values, and colored bars denote standard deviation estimates. Crosses show minimum and maximum differences. Note that color shows the validated campaign and the X-axis validation dataset. In square brackets are the total number of detected intersections for each comparison.

Similarly to Figure 14a, Figure 15 suggests biases in the data (notice mean values). As described earlier, errors in tape measurements likely contributed significantly to these estimates. Hence, to increase the consistency of the residuals (and reduce the potential influence of tape measurement errors), the bias differences between campaigns were estimated by free network least-squares adjustment:

$$\hat{X} = \left(A^T P A \right)^{-1} A^T P L, \tag{22}$$

where vector L denotes the estimated residuals’ mean differences between campaigns at intersections (i.e., the mean values shown in Figure 15) and design matrix A corresponding comparisons. Thus, a system of $[6! / (6 - 2)!] - 4 = 26$ linear equations was compiled (order matters, due to the second intersection search criterion, and for 4 comparisons, no intersections were detected). Weights P were assigned according to the number of detected intersections between campaigns (cf. Figure 15). The estimated bias corrections denoted by vector \hat{X} (consisting of 6 estimates, one for each campaign) were then subtracted from the filtered and corrected residuals. This approach resulted in least-squares adjusted residuals, denoted as $r_{CoM}^{F+C+A}(\varphi, \lambda, t)$ in the following.

Figure 16 presents the comparisons between the initial (filtered and corrected) and least-squares adjusted residuals. Since free network adjustment was used, the average value of the six mean residual estimates (i.e., the average of the 6 values shown in Figure 16a) remained unchanged. It can be noticed that the mean residuals of campaigns agree better after adjustment (Figure 16a) and that the results are more consistent (histograms in Figure 16b combine residuals of all six campaigns). However, since some biases still

exist (which cannot be detected due to lack of intersections), the combined data standard deviation in Figure 16b exceeds that of most individual campaigns in Figure 14a.

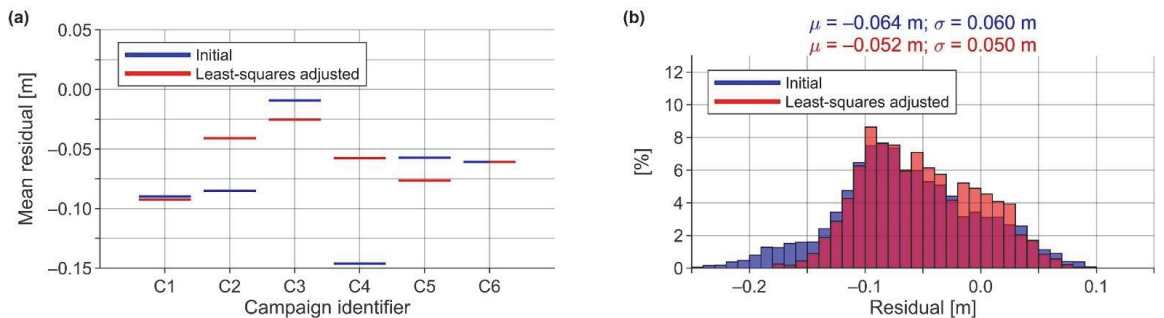


Figure 16. The (a) mean values of residuals (the initial ones coincide with those in Figure 14a) and (b) histograms of residuals (all campaigns combined).

5.4.1. The Final Data Processing Results

The results in Figure 16b suggest that around a 5 cm accuracy can be achieved with the presented methodology, but it is also evident that a data bias of 5.2 cm exists simultaneously. According to Figure 17, the bias primarily originates from areas in the Gulf of Finland and Väinameri (refer to Figure 2) and appears to possess a long-wavelength nature. The bias could likely represent the NKG2015 geoid model errors to some extent. Similarly probable is that there are errors in the estimated DT, since even after correcting the used HDM with TG data, the determination of instantaneous DT with an accuracy of a few centimeters is a difficult task. It could also be that the tape measurements were systematically conducted in a way that resulted in lower than actual SSH. Unfortunately, these are all assumptions, and the origin of the bias currently remains unknown.

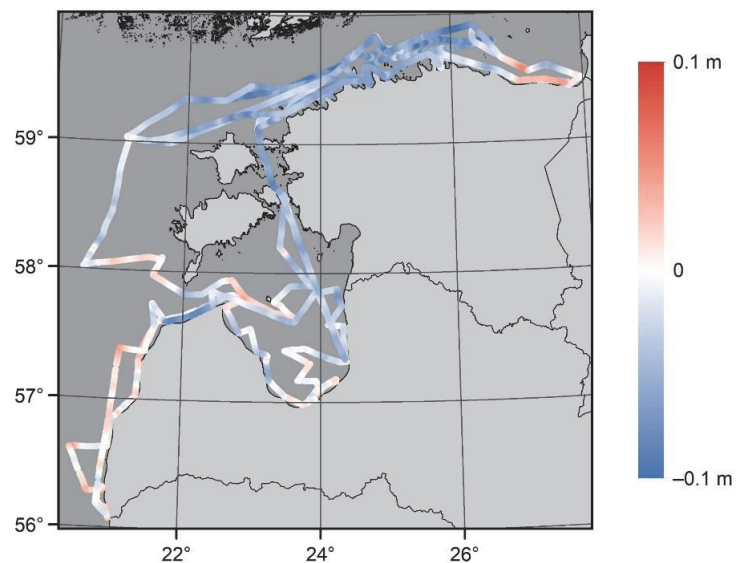


Figure 17. The final filtered, corrected, and least-squares adjusted residuals r_{CoM}^{F+C+A} .

However, recall that this study aimed to derive accurate SSH from shipborne GNSS surveys. As a final step, the SSH was restored from filtered, corrected, and adjusted residuals (Equation (6) modification):

$$SSH_{CoM}^{F+C+A}(\varphi, \lambda, t) = r_{CoM}^{F+C+A}(\varphi, \lambda, t) + \hat{DT}(\varphi, \lambda, t) + [N(\varphi, \lambda, t_0) + GC(\varphi, \lambda) \cdot (t - t_0)], \quad (23)$$

where \hat{DT} and N are correspondingly the DT and NKG2015 geoidal heights initially used to reduce SSH into residuals. The geoid change denoted as GC is restored to obtain the actual SSH (recall that Equation (7) initially eliminated geoid change for data consistency). Assuming minimal error propagation during data filtering, the derived SSH should be mostly free of DT and geoid model errors. It is, thus, plausible that the expected accuracy of the derived SSH exceeds that of the presented and discussed residual values. Therefore, the derived SSH data are suitable for subsequent applications, such as validation of various marine models and measurements (with a limiting factor that measurements must be conducted at the same time as marine survey campaigns). Notably, the presented methodology works under harsh weather conditions (recall that the second half of the C1 campaign was conducted in stormy conditions), which is often the case in real life when marine campaigns are planned long in advance (i.e., the weather becomes unpredictable).

6. Discussion

This paper has described a methodology for deriving accurate SSH from the initial untreated post-processed shipborne GNSS measurements (detailed in [23]). The results indicate a 4.1 cm height determination accuracy, in terms of standard deviation (cf. Section 5.1), for the unfiltered SSH data. Since sea state conditions should not influence this estimate (i.e., the estimate represents a rigid system), it can also describe the final SSH accuracy, assuming sufficiently well-estimated vessel sailing-related corrections (cf. Section 5.3). Note that the application of the low-pass filter may have improved the accuracy by reducing data noise. Further data validation demonstrated standard deviation estimates of 1.8 cm to 5.5 cm for the determined residual values of individual campaigns (cf. Figure 14a), whereby the combination of all campaigns provided an estimate of 5.0 cm (cf. Figure 16b). The standard deviation estimates of campaign–internal intersections varied between 1.8 cm and 3.4 cm (cf. Figure 14b). By comparing the residuals of various campaigns to each other at intersections, the standard deviation estimates also remained within 5 cm (cf. Figure 15).

These results suggest that the developed methodology can provide at least a 5 cm accuracy for the SSH. For comparison, Baltic Sea region geoid validation studies (using NKG2015 model) have indicated the following agreement (in terms of standard deviation) with shipborne GNSS measurements: 3.4 cm [11], 3.8–6.8 cm [12], 4.2–12.0 cm [24], and 1.2–27.9 cm [32]. Other previous studies that investigated shipborne GNSS-determined SSH demonstrated 5–15 cm [10], 4.0–5.3 cm [33], and 7.4–11.9 cm [38] accuracies, in terms of standard deviation. The results of this study are, hence, in good agreement with the previous results, or surpass them.

Another notable result is that all GNSS data collection was autonomous [23], implying that GNSS devices can be installed on various vessels and for extended periods. Here, CORS-based post-processing of GNSS data were primarily used, but distant offshore locations may similarly be of interest for SSH measurements. It has been demonstrated in earlier studies that, for instance, the CSRS-PPP approach can provide reasonable height determination accuracy on such occasions, and even for transoceanic scenarios [24,37,38]. In future studies, it could be interesting to investigate the potential of the developed method exactly in distant offshore locations (using, e.g., CSRS-PPP instead of relying on CORS-based post-processing). This could provide essential SSH datasets with satisfactory accuracy for marine-related studies.

As is evident from the previous analyses and discussions, the presented joint SSH derivation and validation entails several steps and datasets that can influence the results. The following sections now examine the impact of some of these components. For that

purpose, a single step or dataset was exchanged for an alternative, whereby all other data processing was conducted as described above.

6.1. Dynamic Bias Prediction Method

Previously, refs. [15,30] used exact interpolators to predict offshore DB (required for correcting the used HDM for DT determination). Such an approach inherently assumes that there are no errors in the TG data and TGs connections to the height system(s), as well as that the estimated DB at a TG station is an expected value for all nearby offshore locations. In Section 4.1, it was suggested that this might not be the case. Therefore, a new approach was developed for estimating DB uncertainties and predicting offshore DB with an inexact interpolator (least-squares collocation) employing these estimates. The difference between an exact and inexact interpolator is now investigated.

A well-performing inverse distance weighted interpolation method (out of various exact interpolators, this one appears to provide the best results—Jahanmard, V., personal communication, September 2021) was used to predict offshore DB. A comparison with the developed approach is presented in Figure 18a. Notice that the residuals of the inverse distance weighted method are more spread out and biased; thus, highlighting the significant impact of the DB prediction approach on the results. Since the developed approach does not require the predicted DB to follow estimates at the locations of TG stations, the differences between the two histograms are primarily the direct impact of potentially erroneous (or misleading, since DT at TG stations may not represent offshore conditions) TG data.

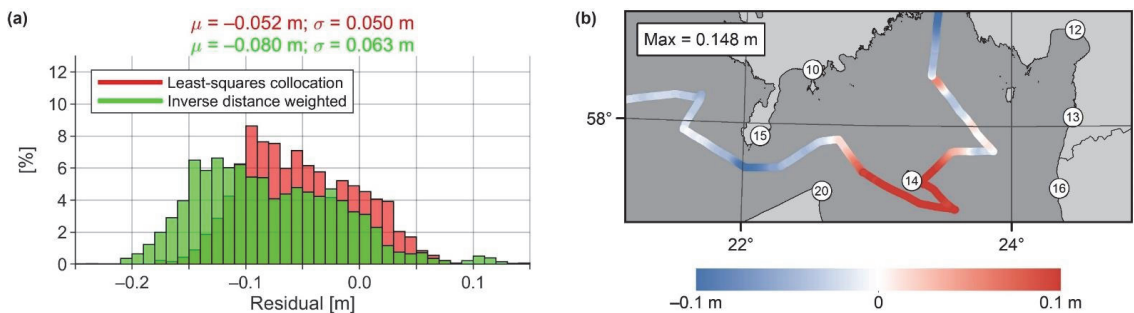


Figure 18. (a) Histograms of residuals (all campaigns combined): the impact of the DB prediction method, and (b) filtered, corrected, and least-squares adjusted residuals, derived using inverse distance weighted interpolation for DB prediction. Numbered circles in (b) denote the used TG stations.

Figure 18b presents residuals of the C2 campaign, derived using inverse distance weighted interpolation to predict offshore DB. Notice the residuals over a decimeter near TG₁₄, whereas no such residuals appeared when the newly developed method was used (cf. Figure 17). This difference is a direct cause of the issue described in Section 4.1, where the estimated DB at TG₁₄ was significantly higher (more than usual) than at the neighboring TG stations, likely due to offshore-directed strong winds, which may have pushed the water away from the harbor (i.e., lower TG readings result in higher DB, cf. Equation (3)).

An alternative example from Section 4.1 can also be further discussed. Namely, a significant contributor to the more negative bias of the inverse distance weighted method in Figure 18a is TG₄. It was demonstrated in [23], how the DT at TG₄ was up to 8–9 cm higher in comparison to the vessel’s nearby harbor (higher DT results in lower residual values, cf. Equation (2)). Relatedly, differences around a decimeter appeared for campaigns C2 and C3 near TG₄, between the inverse distance weighted method and the developed approach. These examples show how near-TG localized phenomena propagate to the estimated offshore DB with exact interpolators and demonstrate the superior performance of the developed approach.

6.2. Data Filtering Approach

In the production of SSH data, it would be convenient to skip the data validation step (as it requires derivation of DT), which means direct filtering of SSH data. However, in Section 2, it was suggested that gradients of DT and geoid might contaminate the low-pass filtering results. The Equation (20) low-pass filter was, hence, applied directly to the SSH data, to test this assumption. Subsequently, the filtered SSH data were reduced to residual values by the Equation (2) principle, and all following data processing was conducted as described in Section 5. The results were then compared to the initially derived residual values (Figure 19a). From this comparison, the directly filtered SSH resulted in slightly less biased residuals, whereby the variation of the residuals appears statistically insignificant. However, Figure 19b shows (an example from campaign C3) the actual impact of gradients on the filtering results (notice the peaks in the results when SSH was filtered directly).

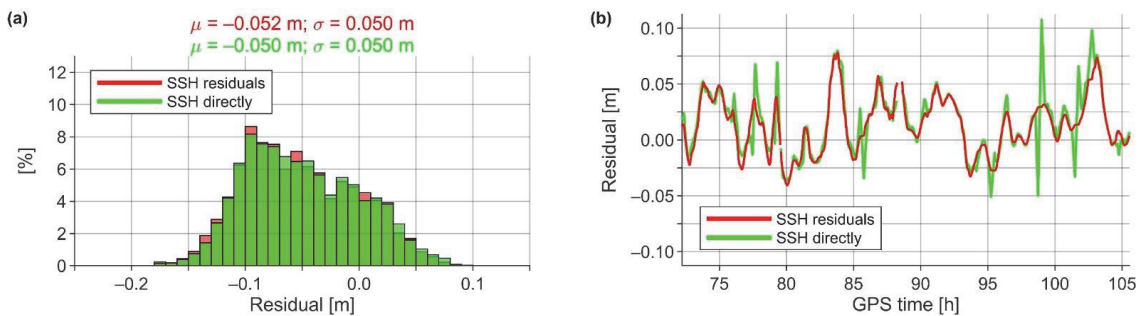


Figure 19. (a) Histograms of residuals (all campaigns combined): the impact of the data filtering approach, and (b) a comparison between residuals (a section of campaign C3) resulting from the two approaches.

The comparison in Figure 19b demonstrates the necessity of reducing the SSH to residual values before data filtering. Otherwise, gradients of DT and geoid may result in avoidable discrepancies of over 5 cm (the primary contributor being the geoid). An alternative could be to increase the GNSS data sampling rate, which would allow a shorter filtering window (spatial) length (cf. Figure 10), since a lengthy window causes such error propagation. Nevertheless, in steeper gradient areas, this may not be sufficient to avoid errors shown in Figure 19b. At the very least, geoidal heights should be reduced from SSH before data filtering, since the gradients of the geoid contribute the most to the described errors. Furthermore, note that the squat estimation was unsuccessful from SSH data directly, resulting in nearly twice as low squat estimates, meaning more negatively biased results (for the experiment in this section, the squat correction was applied as described in Section 5.3).

6.3. Choice of a Geoid Model

The accuracy of marine geoid models is often unknown, as the conventionally used precise GNSS-leveling control points cannot be used for validation purposes over marine areas. It can be assumed that the deficiencies in models may reach up to a few decimeters in the shorter wavelength spectrum. For instance, [11] and [15] showed errors over a decimeter in a marine gravity data void area in the NKG2015 geoid model (in the eastern Gulf of Finland, cf. Figure 2). In contrast, the Estonian national geoid model EST-GEOID2017 [58] appears to perform better, due to additional marine gravity data being included in the model development (see [11], who also provide a comprehensive review of these two models and their differences). The differences between the two models along the vessel's routes are shown in Figure 20b.

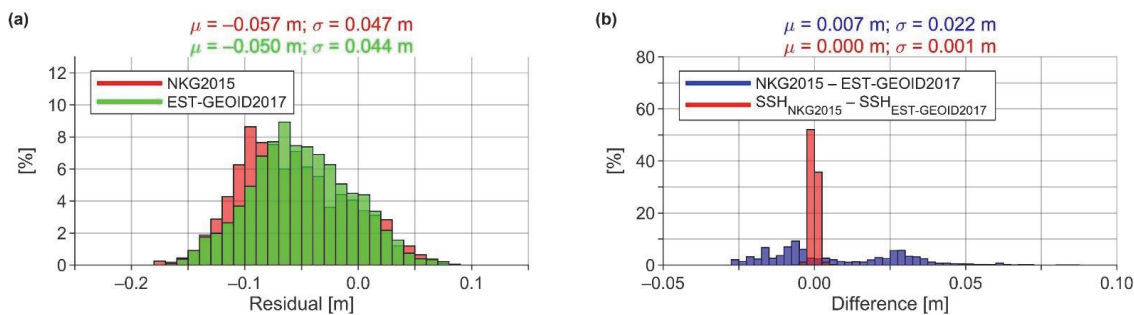


Figure 20. (a) Histograms of residuals (all campaigns combined): the impact of geoid model choice, and (b) histograms showing differences between the NKG2015 and EST-GEOID2017 models (along the vessel’s routes) and the SSH datasets derived using these models during data processing.

For the next experiment, the NKG2015 geoid model was exchanged for the EST-GEOID2017 during data processing. The resulting discrepancies are compared in Figure 20a. Note that the red histogram differs from those in Figure 16b, Figure 18a, and Figure 19a, since the comparison was conducted over a reduced area (EST-GEOID2017 does not extend southward from 57° N). The comparison in Figure 20a demonstrates the slightly better performance of the EST-GEOID2017 model, which is consistent with previous studies’ results.

Since the geoid models contain errors, it would be interesting to know how model errors influence the resulting SSH data. This question can be investigated, as differences exist between the two used geoid models. Figure 20b suggests that the data filtering error propagation is negligible (as assumed in Section 5.4.1), because the two SSH datasets are practically the same. This finding indicates that if a geoid model has reasonable accuracy, the model’s inaccuracies do not influence the derived SSH (by reducing SSH to residuals for data filtering), which also implies that errors in DT do not propagate significantly either. The results would likely be poorer by neglecting geoid and DT information entirely during data processing (recall the example in Section 6.2).

6.4. Squat Estimation Function

Ideally, squat information should be provided by a vessel-specific squat table. Such a table was not available for this study. Thus, the squat correction was estimated empirically as a direct data derivative (cf. Section 5.3). Since the squat is approximately a quadratic velocity function, a quadratic function was fitted to the empirical data in the least-squares sense. As an alternative, a least-squares fit of a linear function was also used to approximate squat correction (cf. Figure 13a). The resulting residuals from using these two functions are compared in Figure 21. Note that the offset term was not considered for the linear function, as was the case with the quadratic function (cf. Equation (21)).

Although the use of the quadratic function is, in theory, more correct, the results in Figure 21 indicate a better performance for the linear function, as the residuals are significantly less biased toward negative. It, thus, appears that the quadratic function underestimates the squat correction. The result also implies that a portion of the 5.2 cm bias in the data originates from inaccurate squat correction.

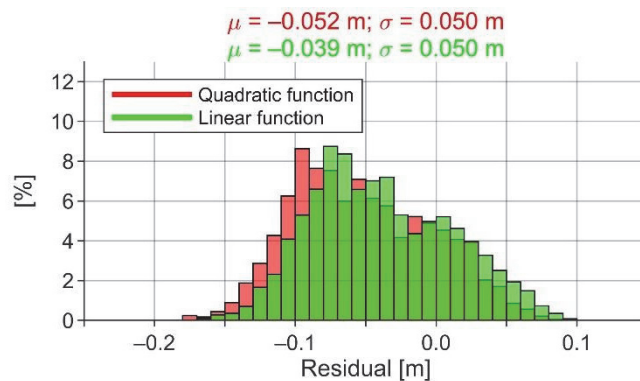


Figure 21. Histograms of residuals (all campaigns combined): the impact of squat estimation function.

7. Conclusions

This contribution presented a methodology for deriving accurate SSH from initial untreated post-processed GNSS data. The methodology involves a joint validation of the results using a geoid model and realistic DT to reduce SSH to residual values. Since GNSS measurements should be low-pass filtered to eliminate the effect of sea state conditions, the approach can also enhance SSH data accuracy, by avoiding error propagation due to DT and geoid gradients, which in this study could have caused larger than 5 cm errors. Furthermore, a rigid system of four GNSS antennas was used to eliminate the vessel's high-frequency attitude changes from the measurement data. Such a system is also beneficial, as it can be validated internally. Accordingly, the results indicated a 4.1 cm height determination accuracy for the whole SSH dataset. Other data validation (e.g., examination of residual values and intersection analyses) results ranged from 1.8 cm to 5.5 cm, in terms of standard deviation; suggesting that SSH can be determined with an accuracy of around 5 cm using the shipborne GNSS method.

As mentioned, the validation requires DT information. A new method was developed that combines the properties of TG data and an HDM. Tide gauge data allow estimating the spatiotemporal bias of an HDM; thus, linking it to used vertical datum (e.g., a novel geoid-based Baltic Sea Chart Datum 2000), whereby the qualities of spatiotemporal bias are used to constrain TG data errors. As a result, realistic DT relative to an equipotential surface can be obtained, which could be beneficial in oceanographic research for studying marine processes accurately (e.g., determination of mean DT relative to an equipotential surface for studying currents). According to the SSH residual value validations, the developed approach was demonstrated to surpass the one used by [15,30], with an improvement in standard deviation estimate from 6.3 cm to 5.0 cm, and mean residual from -8.0 cm to -5.2 cm.

Author Contributions: Conceptualization, S.V., A.L. and A.E.; methodology, S.V.; software, S.V.; validation, S.V.; formal analysis, S.V.; investigation, S.V.; resources, S.V., A.L. and A.E.; data curation, S.V. and A.L.; writing—original draft preparation, S.V.; writing—review and editing, S.V., A.L. and A.E.; visualization, S.V.; supervision, A.E.; project administration, A.L. and A.E.; funding acquisition, A.L. and A.E. All authors have read and agreed to the published version of the manuscript.

Funding: The research was supported by the Estonian Research Council grant “Development of an iterative approach for near-coast marine geoid modelling by using re-tracked satellite altimetry, in-situ and modelled data”, grant number PRG330, and by the Estonian University of Life Sciences baseline funding grant “A 3D model of intraplate deformations combining remote sensing and in-situ measurements with an application to implement a semi-dynamic reference frame in Estonia”, grant number P200188MIGX.

Data Availability Statement: The used hourly TG data can be obtained from the webpages of the Latvian [46,50], Swedish [47], Finnish [48,51], and Russian [49] TG managing authorities. The employed NKG2016LU VLM model is provided by the Lantmäteriet (on behalf of the Nordic Geodetic Commission—NKG): <https://www.lantmateriet.se/en/maps-and-geographic-information/gps-geodesi-och-swepos/reference-systems/posTGlacial-land-uplift/> (accessed on 28 February 2021). The NKG2015 geoid model is provided by the International Service for the Geoid (on behalf of the NKG): https://www.isgeoid.polimi.it/Geoid/Europe/NordicCountries/nordic_baltic_countries_g.html (accessed on 28 February 2021). The derived (GRS80 reference ellipsoid referred) SSH dataset is available from the corresponding author upon reasonable request.

Acknowledgments: Colleagues from the Marine Systems Institute at the Tallinn University of Technology and the crew of the research surveying vessel Salme are thanked for assisting in conducting shipborne GNSS campaigns. A special thanks to OÜ Geosoft, who provided the used GNSS equipment. The Estonian Environment Agency provided the used Estonian TG data. A special thanks to the Swedish Meteorological and Hydrological Institute for their cooperation in obtaining NEMO-Nordic model data. The four anonymous reviewers are thanked for their contribution to the quality of the manuscript.

Conflicts of Interest: The authors declare no conflict of interest.

References

1. Visser, H.; Dangendorf, S.; Petersen, A.C. A review of trend models applied to sea level data with reference to the “acceleration-deceleration debate”. *J. Geophys. Res. Ocean.* **2015**, *120*, 3873–3895. [\[CrossRef\]](#)
2. Breili, K.; Simpson, M.J.R.; Nilsen, J.E.Ø. Observed sea-level changes along the Norwegian coast. *J. Mar. Sci. Eng.* **2017**, *5*, 29. [\[CrossRef\]](#)
3. Madsen, K.S.; Høyer, J.L.; Suursaar, Ü.; She, J.; Knudsen, P. Sea level trends and variability of the Baltic Sea from 2D statistical reconstruction and altimetry. *Front. Earth Sci.* **2019**, *7*, 243. [\[CrossRef\]](#)
4. Vu, P.L.; Frappart, F.; Darrozes, J.; Marieu, V.; Blarel, F.; Ramillien, G.; Bonnefond, P.; Birol, F. Multi-satellite altimeter validation along the French Atlantic coast in the southern Bay of Biscay from ERS-2 to SARAL. *Remote Sens.* **2018**, *10*, 93. [\[CrossRef\]](#)
5. Yang, J.; Zhang, J.; Wang, C. Sentinel-3A SRAL global statistical assessment and cross-calibration with Jason-3. *Remote Sens.* **2019**, *11*, 1573. [\[CrossRef\]](#)
6. Liibusk, A.; Kall, T.; Rikka, S.; Uiboupin, R.; Suursaar, Ü.; Tseng, K.-H. Validation of Copernicus sea level altimetry products in the Baltic Sea and Estonian lakes. *Remote Sens.* **2020**, *12*, 4062. [\[CrossRef\]](#)
7. Passaro, M.; Cipollini, P.; Vignudelli, S.; Quartly, G.D.; Snaith, H.M. ALES: A multi-mission adaptive subwaveform retracker for coastal and open ocean altimetry. *Remote Sens. Environ.* **2014**, *145*, 173–189. [\[CrossRef\]](#)
8. Cipollini, P.; Calafat, F.M.; Jevrejeva, S.; Melet, A.; Prandi, P. Monitoring sea level in the coastal zone with satellite altimetry and tide gauges. *Surv. Geophys.* **2017**, *38*, 33–57. [\[CrossRef\]](#)
9. Vignudelli, S.; Birol, F.; Benveniste, J.; Fu, L.-L.; Picot, N.; Raynal, M.; Roinard, H. Satellite altimetry measurements of sea level in the coastal zone. *Surv. Geophys.* **2019**, *40*, 1319–1349. [\[CrossRef\]](#)
10. Bouin, M.-N.; Ballu, V.; Calmant, S.; Boré, J.-M.; Folcher, E.; Ammann, J. A kinematic GPS methodology for sea surface mapping, Vanuatu. *J. Geod.* **2009**, *83*, 1203. [\[CrossRef\]](#)
11. Varbla, S.; Ellmann, A.; Delpeche-Ellmann, N. Validation of marine geoid models by utilizing hydrodynamic model and shipborne GNSS profiles. *Mar. Geod.* **2020**, *43*, 134–162. [\[CrossRef\]](#)
12. Saari, T.; Bilker-Koivula, M.; Koivula, H.; Nordman, M.; Häkli, P.; Lahtinen, S. Validating geoid models with marine GNSS measurements, sea surface models, and additional gravity observations in the Gulf of Finland. *Mar. Geod.* **2021**, *44*, 196–214. [\[CrossRef\]](#)
13. Gruno, A.; Liibusk, A.; Ellmann, A.; Oja, T.; Vain, A.; Jürgenson, H. Determining sea surface heights using small footprint airborne laser scanning. In Proceedings of the Remote Sensing of the Ocean, Sea Ice, Coastal Waters, and Large Water Regions 2013, Dresden, Germany, 23–26 September 2013. [\[CrossRef\]](#)
14. Zlinszky, A.; Timár, G.; Weber, R.; Székely, B.; Briese, C.; Ressel, C.; Pfeifer, N. Observation of a local gravity potential isosurface by airborne lidar of Lake Balaton, Hungary. *Solid Earth* **2014**, *5*, 355–369. [\[CrossRef\]](#)
15. Varbla, S.; Ellmann, A.; Delpeche-Ellmann, N. Applications of airborne laser scanning for determining marine geoid and surface waves properties. *Eur. J. Remote Sens.* **2021**, *54*, 557–567. [\[CrossRef\]](#)
16. Xu, X.-Y.; Xu, K.; Shen, H.; Liu, Y.-L.; Liu, H.-G. Sea surface height and significant wave height calibration methodology by a GNSS buoy campaign for HY-2A altimeter. *IEEE J. Sel. Top. Appl. Earth Obs. Remote Sens.* **2016**, *9*, 5252–5261. [\[CrossRef\]](#)
17. Zhou, B.; Watson, C.; Legresy, B.; King, M.A.; Beardsley, J.; Deane, A. GNSS/INS-equipped buoys for altimetry validation: Lessons learnt and new directions from the Bass Strait validation facility. *Remote Sens.* **2020**, *12*, 3001. [\[CrossRef\]](#)
18. Penna, N.T.; Morales Maqueda, M.A.; Martin, I.; Guo, J.; Foden, P.R. Sea surface height measurement using a GNSS wave glider. *Geophys. Res. Lett.* **2018**, *45*, 5609–5616. [\[CrossRef\]](#)

19. Chupin, C.; Ballu, V.; Testut, L.; Tranchant, Y.-T.; Calzas, M.; Poirier, E.; Coulombier, T.; Laurain, O.; Bonnefond, P.; Team FOAM Project. Mapping sea surface height using new concepts of kinematic GNSS instruments. *Remote Sens.* **2020**, *12*, 2656. [[CrossRef](#)]
20. Rocken, C.; Johnson, J.; Van Hove, T.; Iwabuchi, T. Atmospheric water vapor and geoid measurements in the open ocean with GPS. *Geophys. Res. Lett.* **2005**, *32*, L12813. [[CrossRef](#)]
21. Jürgenson, H.; Liibusk, A.; Ellmann, A. Geoid profiles in the Baltic Sea determined using GPS and sea level surface. *Geod. Cartogr.* **2008**, *34*, 109–115. [[CrossRef](#)]
22. Ince, E.S.; Förste, C.; Barthelmes, F.; Pflug, H.; Li, M.; Kaminskis, J.; Neumayer, K.-H.; Michalak, G. Gravity measurements along commercial ferry lines in the Baltic Sea and their use for geodetic purposes. *Mar. Geod.* **2020**, *43*, 573–602. [[CrossRef](#)]
23. Liibusk, A.; Varbla, S.; Ellmann, A.; Vahter, K.; Uiboupin, R.; Delpeche-Ellmann, N. Shipborne GNSS acquisition of sea surface heights in the Baltic Sea. *J. Geod. Sci.* **2022**, *in print*. [[CrossRef](#)]
24. Varbla, S.; Ellmann, A.; Märdla, S.; Gruno, A. Assessment of marine geoid models by ship-borne GNSS profiles. *Geod. Cartogr.* **2017**, *43*, 41–49. [[CrossRef](#)]
25. Schwabe, J.; Ågren, J.; Liebsch, G.; Westfeld, P.; Hammarklint, T.; Mononen, J.; Andersen, O.B. The Baltic Sea Chart Datum 2000 (BSCD2000)—Implementation of a common reference level in the Baltic Sea. *Int. Hydrogr. Rev.* **2020**, *23*, 63–83.
26. Varbla, S.; Ågren, J.; Ellmann, A.; Poutanen, M. Treatment of tide gauge time series and marine GNSS measurements for vertical land motion with relevance to the implementation of the Baltic Sea Chart Datum 2000. *Remote Sens.* **2022**, *14*, 920. [[CrossRef](#)]
27. Suursaar, Ü.; Kall, T. Decomposition of relative sea level variations at tide gauges using results from four Estonian precise levelings and uplift models. *IEEE J. Sel. Top. Appl. Earth Obs. Remote Sens.* **2018**, *11*, 1966–1974. [[CrossRef](#)]
28. Kollo, K.; Ellmann, A. Geodetic reconciliation of tide gauge network in Estonia. *Geophysica* **2019**, *54*, 27–38.
29. Lagemaa, P.; Elken, J.; Kõuts, T. Operational sea level forecasting in Estonia. *Est. J. Eng.* **2011**, *17*, 301–331. [[CrossRef](#)]
30. Jahanmard, V.; Delpeche-Ellmann, N.; Ellmann, A. Realistic dynamic topography through coupling geoid and hydrodynamic models of the Baltic Sea. *Cont. Shelf Res.* **2021**, *222*, 104421. [[CrossRef](#)]
31. Slobbe, D.C.; Verlaan, M.; Klees, R.; Gerritsen, H. Obtaining instantaneous water levels relative to a geoid with a 2D storm surge model. *Cont. Shelf Res.* **2013**, *52*, 172–189. [[CrossRef](#)]
32. Nordman, M.; Kuokkanen, J.; Bilker-Koivula, M.; Koivula, H.; Häkli, P.; Lahtinen, S. Geoid validation on the Baltic Sea using ship-borne GNSS data. *Mar. Geod.* **2018**, *41*, 457–476. [[CrossRef](#)]
33. Roggenbuck, O.; Reinking, J. Sea surface heights retrieval from ship-based measurements assisted by GNSS signal reflections. *Mar. Geod.* **2019**, *42*, 1–24. [[CrossRef](#)]
34. Metsar, J.; Kollo, K.; Ellmann, A. Modernization of the Estonian national GNSS reference station network. *Geod. Cartogr.* **2018**, *44*, 55–62. [[CrossRef](#)]
35. Balodis, J.; Morozova, K.; Reiniks, M.; Normand, M. Normal heights for GNSS reference station antennas. In Proceedings of the IOP Conference Series: Materials Science and Engineering, Riga, Latvia, 27–29 September 2017. [[CrossRef](#)]
36. Vestøl, O.; Ågren, J.; Steffen, H.; Kierulf, H.; Tarasov, L. NKG2016LU: A new land uplift model for Fennoscandia and the Baltic region. *J. Geod.* **2019**, *93*, 1759–1779. [[CrossRef](#)]
37. Roggenbuck, O.; Reinking, J.; Härtling, A. Oceanwide precise determination of sea surface height from in-situ measurements on cargo ships. *Mar. Geod.* **2014**, *37*, 77–96. [[CrossRef](#)]
38. Shih, H.-C.; Yeh, T.-K.; Du, Y.; He, K. Accuracy assessment of sea surface height measurement obtained from shipborne PPP positioning. *J. Surv. Eng.* **2021**, *147*, 04021022. [[CrossRef](#)]
39. Natural Resources Canada. Precise Point Positioning. Available online: <https://webapp.geod.nrcan.gc.ca/geod/tools-outils/ppp.php> (accessed on 28 February 2022).
40. Ågren, J.; Strykowski, G.; Bilker-Koivula, M.; Omang, O.; Märdla, S.; Forsberg, R.; Ellmann, A.; Oja, T.; Liepins, I.; Parseliunas, E.; et al. The NKG2015 gravimetric geoid model for the Nordic-Baltic region. In Proceedings of the International Symposium on Gravity, Geoid and Height Systems 2016, Thessaloniki, Greece, 19–23 September 2016. [[CrossRef](#)]
41. Poutanen, M.; Vermeer, M.; Mäkinen, J. The permanent tide in GPS positioning. *J. Geod.* **1996**, *70*, 499–504. [[CrossRef](#)]
42. Ihde, J.; Mäkinen, J.; Sacher, M. *Conventions for the Definition and Realization of a European Vertical Reference System (EVRS)*; Version 5.2; Federal Agency for Cartography and Geodesy (BKG): Frankfurt, Germany, 2019.
43. Varbla, S.; Ellmann, A.; Delpeche-Ellmann, N. Utilizing airborne laser scanning and geoid model for near-coast improvements in sea surface height and marine dynamics. *J. Coast. Res.* **2020**, *95*, 1339–1343. [[CrossRef](#)]
44. Hordoir, R.; Axell, L.; Höglund, A.; Dieterich, C.; Fransner, F.; Gröger, M.; Liu, Y.; Pemberton, P.; Schimanke, S.; Andersson, H.; et al. Nemo-Nordic 1.0: A NEMO-based ocean model for the Baltic and North seas—Research and operational applications. *Geosci. Model Dev.* **2019**, *12*, 363–386. [[CrossRef](#)]
45. Kärnä, T.; Ljungemyr, P.; Falahat, S.; Ringgaard, I.; Axell, L.; Korabel, V.; Murawski, J.; Maljutenko, I.; Lindenthal, A.; JanDT-Scheelke, S.; et al. Nemo-Nordic 2.0: Operational marine forecast model for the Baltic Sea. *Geosci. Model Dev.* **2021**, *14*, 5731–5749. [[CrossRef](#)]
46. LVGMC Hydrological Data Search (in Latvian). Available online: <https://www.meteo.lv/hidrologija-datu-meklesana/?nid=466> (accessed on 28 February 2021).
47. SMHI Oceanographic Observations. Available online: <https://www.smhi.se/data/oceanografi/ladda-ner-oceanografiska-observationer/#param=sealevelrh2000,stations=all> (accessed on 28 February 2021).
48. FMI Observations. Available online: <https://en.ilmatieteenlaitos.fi/download-observations#!/> (accessed on 28 February 2021).

49. EMODnet Data Explorer. Available online: <http://www.emodnet-physics.eu/Map/DefaultMap.aspx> (accessed on 28 February 2021).
50. LVGMC Observation Network (in Latvian). Available online: <https://www.meteo.lv/hidrologijas-staciju-karte/?nid=465> (accessed on 28 February 2021).
51. Theoretical Mean Water and Geodetical Height Systems in Finland. Available online: <https://en.ilmatieteenlaitos.fi/theoretical-mean-sea-level> (accessed on 28 February 2021).
52. EVRS Height Datum Relations. Available online: <https://evrs.bkg.bund.de/Subsites/EVRS/EN/Projects/HeightDatumRel/height-datum-rel.html> (accessed on 28 February 2021).
53. Lan, W.-H.; Kuo, C.-Y.; Kao, H.-C.; Lin, L.-C.; Shum, C.K.; Tseng, K.-H.; Chang, J.-C. Impact of geophysical and datum corrections on absolute sea-level trends from tide gauges around Taiwan, 1993–2015. *Water* **2017**, *9*, 480. [[CrossRef](#)]
54. Denys, P.H.; Beavan, R.J.; Hannah, J.; Pearson, C.F.; Palmer, N.; Denham, M.; Hreinsdottir, S. Sea level rise in New Zealand: The effect of vertical land motion on century-long tide gauge records in a tectonically active region. *J. Geophys. Res. Solid Earth* **2020**, *125*, e2019JB018055. [[CrossRef](#)]
55. Moritz, H. *Advanced Physical Geodesy*; Wichmann: Karlsruhe, Germany, 1980.
56. Kasper, J.F. A second-order Markov gravity anomaly model. *J. Geophys. Res.* **1971**, *76*, 7844–7849. [[CrossRef](#)]
57. Barrass, C.B. *Ship Design and Performance for Masters and Mates*; Elsevier: Oxford, UK, 2004.
58. Ellmann, A.; Märdla, S.; Oja, T. The 5 mm geoid model for Estonia computed by the least squares modified Stokes’s formula. *Surv. Rev.* **2020**, *52*, 352–372. [[CrossRef](#)]

Appendix 6

Publication VI

Varbla, S. (2022). The influence of bathymetry on regional marine geoid modeling in Northern Europe. *Journal of Marine Science and Engineering*, 10(6), #793. doi:10.3390/jmse10060793

Article

The Influence of Bathymetry on Regional Marine Geoid Modeling in Northern Europe

Sander Varbla 

Department of Civil Engineering and Architecture, Tallinn University of Technology, Ehitajate Road 5, 19086 Tallinn, Estonia; sander.varbla@taltech.ee

Abstract: Although Northern Europe has been the target area in many regionwide geoid determination studies, the research has been land-focused, neglecting bathymetry information. With new projects, such as the Baltic Sea Chart Datum 2000, the attention is shifting toward the marine geoid. Hence, consideration for bathymetry has become relevant, the influence of which is studied. In the relatively shallow Baltic Sea, accounting for bathymetry-based residual terrain model reduction during gravity data processing induces marine geoid modeling differences (relative to neglecting bathymetry) mainly within 2 cm. However, the models can deviate up to 3–4 cm in some regions. Rugged Norwegian coastal areas, on the other hand, had modeling improvements around a decimeter. Considering bathymetry may thus help improve geoid modeling outcomes in future Northern Europe geoid determination projects. Besides using the conventional precise GNSS-leveling control points, the paper also demonstrates the usefulness of shipborne GNSS and airborne laser scanning-derived geoidal heights in validating geoid modeling results. A total of 70 gravimetric geoid solutions are presented, for instance, by varying the used reference global geopotential models. According to the comparisons, GOCO05c-based solutions generally perform the best, where modeling agreement with GNSS-leveling control points reached 2.9 cm (standard deviation) from a one-dimensional fit.

Keywords: bathymetry; gravity field; quasigeoid; Stokes's formula; BSCD2000; Baltic Sea



Citation: Varbla, S. The Influence of Bathymetry on Regional Marine Geoid Modeling in Northern Europe. *J. Mar. Sci. Eng.* **2022**, *10*, 793. <https://doi.org/10.3390/jmse10060793>

Academic Editors: Luis Carral, Juan José Cartelle Barros, Rodrigo Carballo Sánchez and María Isabel Lamas Galdo

Received: 30 April 2022
Accepted: 7 June 2022
Published: 9 June 2022

Publisher's Note: MDPI stays neutral with regard to jurisdictional claims in published maps and institutional affiliations.



Copyright: © 2022 by the author. Licensee MDPI, Basel, Switzerland. This article is an open access article distributed under the terms and conditions of the Creative Commons Attribution (CC BY) license (<https://creativecommons.org/licenses/by/4.0/>).

1. Introduction

Determination of accurate marine (quasi)geoid models is essential for geodetic and engineering applications but can also be required in oceanographic research (over marine areas, the geoid coincides with the quasigeoid; henceforth, the shorter term will be primarily used). The advances in satellite gravimetry (e.g., the use of GRACE and GOCE missions' data) allow us to solve the marine geoid with an accuracy of a few centimeters for longer wavelengths [1,2]. Due to omission errors, however, global geopotential models (GGMs) may be insufficient for regional-scale applications. For example, centimeter-level geoid modeling accuracy is required for GNSS (global navigation satellite system)-based height determination in engineering and navigation, especially near coastal areas. Additionally, improving coastal mean dynamic topography estimates [3,4] and detecting significant mean dynamic topography signals on smaller spatial scales [5,6] require more precise marine geoid models than GGMs. Thus, methods for regional geoid determination need to be employed to improve marine geoid models for shorter wavelengths.

Gravimetric geoid models can be computed, for instance, by Stokes's formula [7], which enables the determination of models from globally distributed gravity anomalies. Since such an approach is unfeasible in practice, the integration can be limited to a smaller spatial domain around the computation points. The resulting truncation error (due to neglecting the far zone) can be reduced by modifying Stokes's formula [8], allowing terrestrial gravity anomalies to be combined with a suitable satellite-derived GGM. The latter provides the long-wavelength component of the geoid. Two primary groups of Stokes's formula modifications exist: deterministic and stochastic methods. Deterministic

modification methods aim to reduce the truncation error only. On the other hand, stochastic methods also attempt to reduce errors in terrestrial gravity anomalies and GGMs. For further details and comparisons between these modification methods, see [9–11]. This study employs the least-squares modification of Stokes's formula with additive corrections (LSMSA) [12,13] for geoid modeling, which uses stochastic modification.

The above-described approach is only one possibility for regional geoid determination, and other alternatives exist (e.g., the remove–compute–restore technique and least-squares collocation), whereby various computation methods may result in similar modeling accuracies [14]. Instead, the geoid modeling outcome can be influenced more significantly by the quality and processing of the input gravity data [15]. Although methods for geoid determination from discrete gravity data exist [16,17], a regular grid of gravity anomalies is usually required. Thus, a suitable gravity data gridding approach also needs to be selected. Due to terrain and bathymetry correlated high-frequency gravity field variations, the direct gridding of surface gravity anomalies is usually unreliable since it is difficult for interpolation algorithms to estimate correct gravity values at the grid nodes. The remove–solve–restore procedure can be used instead, meaning that the gravity anomalies are reduced to some smoother alternative (e.g., Bouguer or residual terrain model (RTM) anomalies), gridded and then restored [15]. Such an approach allows a more reliable prediction of gravity values but can also add gravity information to data void areas during the signal restoration. A digital terrain model (DTM) is essential for estimating the high-frequency gravity field component, which needs to be removed from the discrete points and restored on the gridded gravity dataset [18]. Although the initial gravity anomalies are smoother in marine areas, it could be advantageous also to consider bathymetry information besides a DTM for marine geoid modeling.

Several regionwide geoid modeling projects have been conducted in the Baltic Sea region in Northern Europe [15,18–29], with the primary focus on land areas. No bathymetry information was considered in these projects. However, it was shown by [30] that consideration for bathymetry could significantly influence geoid modeling outcomes in the Norwegian fjords. The focus has now shifted from land to the marine geoid. Implementation of the Baltic Sea Chart Datum 2000 (BSCD2000), a common height reference for the Baltic Sea region, has been initiated to effectively use GNSS methods for accurate navigation and real-time offshore surveying [31,32]. The BSCD2000 will be realized through GNSS and geoid modeling. This paper details the Tallinn University of Technology's (one of the BSCD2000 computation centers) geoid modeling efforts toward realizing BSCD2000. Since the focus is now on the marine geoid, it can be of interest how consideration for bathymetry affects the (regular) gravity field estimation and subsequent geoid modeling outcomes. This contribution also aims to investigate these influences in the Baltic Sea region.

An essential component of geoid determination studies is the validation of modeling results. Conventionally, precise GNSS-leveling control points are used, but such validation datasets are limited only to land areas, and no information about the offshore modeling performance is retrieved. The shipborne GNSS [33–35] and airborne laser scanning [36–38] measured sea surface heights may provide valuable knowledge about the marine geoid instead. By removing the ever-changing dynamic topography, for instance, using hydrodynamic models and tide gauge data [35,38,39], the sea surface heights can be reduced to geoidal heights. This study demonstrates how such marine datasets can help evaluate various gravimetric geoid modeling solutions, especially if the aim is to model the marine geoid.

The structure of the paper is as follows. Section 2 describes the gravity data processing and geoid modeling approaches. Note that in this study, quasigeoid is being modeled; thus, in Section 2, the focus is on quasigeoid-associated values. The subsequent Section 3 introduces the study area and gives an overview of the used data. Section 4 then presents the results of the gravity data gridding and geoid modeling. The influence of bathymetry information is investigated, and various geoid modeling solutions are evaluated. The paper continues with a discussion in Section 5 and ends with a summary in Section 6.

2. Methods

2.1. From Discrete Gravity Data to a Gridded Gravity Field Representation

The measured gravity value g_P on or above terrain (or sea surface) at point P (at a normal height H_P^* relative to the quasigeoid) can be reduced to the surface free-air anomaly:

$$\Delta g_P^{FAA} = g_P - \gamma_Q, \tag{1}$$

where γ_Q is the normal gravity at point Q (at height $h_Q = H_P^*$ above the GRS80 reference ellipsoid) on the telluroid. According to [40], the normal gravity γ_Q can be approximated as:

$$\gamma_Q \approx \gamma_0 - \frac{2\gamma_e}{a} \left[1 + f + m + \left(-3f + \frac{5}{2}m \right) \sin^2 \varphi \right] H_P^* + \frac{3\gamma_e}{a^2} H_P^{*2}, \tag{2}$$

where γ_0 and φ are the normal gravity on the reference ellipsoid and the geodetic latitude of point P , respectively. The former is defined as:

$$\gamma_0 = \gamma_e \frac{1 + k \sin^2 \varphi}{\sqrt{1 - e^2 \sin^2 \varphi}}. \tag{3}$$

Terms γ_e (normal gravity at equator), a (equatorial radius), f (flattening), $m \approx \omega^2 a / \gamma_e$ (ω is angular velocity), $k = b\gamma_p / a\gamma_e - 1$ (b and γ_p are polar radius and normal gravity at pole, respectively) and e (first eccentricity) in Equations (2) and (3) are parameters associated with the GRS80 reference ellipsoid [41]. From the obtained surface free-air anomalies Δg_P^{FAA} at discrete locations P , a regular grid needs to be estimated for geoid modeling purposes. However, since surface free-air anomalies contain terrain and bathymetry correlated high-frequency gravity field variations, direct gridding of these data may provide unreliable results. A reduction in these values to a smoother alternative is thus required.

To improve data gridding performance, implementing the concept of a band-pass filter that attenuates gravity signals above and below desired frequency could be beneficial. Such an approach allows the derivation of RTM anomalies:

$$\Delta g_P^{RTMA} = \Delta g_P^{FAA} - \Delta g_P^{GGM} - \delta g_P^{RTM}, \tag{4}$$

where Δg_P^{GGM} represents the long-wavelength component from a GGM evaluated to a suitable degree and order (d/o). The term δg_P^{RTM} , on the other hand, represents the short-wavelength topographic effect of RTM reduction estimated from a DTM (and/or bathymetry model). The RTM reduction can be computed as:

$$\delta g_P^{RTM} = 2\pi G\rho \left(H_P^* - H_P^{ref} \right) - \left(\delta g_P^T \Big|_{z_1=H_P^*}^{z_2=H^*} - \delta g_P^T \Big|_{z_1=H_P^{ref}}^{z_2=H^{ref}} \right), \tag{5}$$

where δg_P^T is the terrain correction estimated by summing the attraction of a finite number of rectangular prisms according to [42,43]:

$$\delta g_P^T = -G \sum \int_{x_1}^{x_2} \int_{y_1}^{y_2} \int_{z_1}^{z_2} \frac{\rho(z - z_P)}{\left[(x - x_P)^2 + (y - y_P)^2 + (z - z_P)^2 \right]^{3/2}} dx dy dz, \tag{6}$$

where x_P, y_P, z_P and x, y, z are the local Cartesian coordinates of the computation point P and the moving integration element, respectively, with $x_1, x_2, y_1, y_2, z_1,$ and z_2 defining the sizes of prisms. In Equations (5) and (6), the term G denotes the gravitational constant and ρ topographic density. The latter can be assumed at 2670 kg/m^3 for terrain and 1640 kg/m^3 for bathymetry (i.e., the difference between terrain and seawater densities). Note that in Equation (5), terms H_P^* and H^* represent normal heights of the computation point P and moving integration element (determined from a DTM), respectively. The

terms H_p^{ref} and H^{ref} are correspondingly normal heights of a smooth reference surface, which can be constructed by low-pass filtering the used DTM. Ideally, the resolution of the reference surface should correspond to the d/o of the used GGM since RTM reduction aims to remove the remaining higher-frequency gravity contribution beyond that d/o. The described RTM reduction is implemented in sub-program TC [43] of the GRAVSOFTE research software package.

Generally, marine gravity is measured along relatively sparse parallel tracks, whereby gaps in data coverage are also common. It has been demonstrated that least-squares collocation (LSC) can provide reliable gridding results for such data [15]. Provided that gravity data have reliable a priori error estimates, LSC using RTM anomalies can also result in high-quality gravity field representation in areas with dense gravity data coverage [15]. With the weighted LSC method, the RTM anomaly values Δg_G^{RTMA} at grid nodes are predicted from discrete values Δg_P^{RTMA} at locations P according to [44] by solving the following matrix equation:

$$\Delta g_G^{RTMA} = C_{st}(C_{tt} + C_{nn})^{-1} \Delta g_P^{RTMA}, \tag{7}$$

where C_{st} is the cross-covariance matrix of the predicted (Δg_G^{RTMA}) and known (Δg_P^{RTMA}) signals and C_{tt} and C_{nn} are the covariance matrixes of known signal and observation errors, respectively. Since $\Delta g_P^{RTMA} = t + n$, the covariance matrix of observed values at discrete locations is $C_{s_p^{RTMA} s_p^{RTMA}} = C_{tt} + C_{nn}$. The LSC method is implemented in the GRAVSOFTE sub-program GEOGRID.

For such a gridding approach, covariance matrixes estimated from survey data describe the data spatial dependence by fitting a theoretical model to the empirical covariance values. In this study, the second-order Markov covariance model [45] was used:

$$C(l) = C_0 \left(1 + \frac{l}{\alpha} \right) e^{-l/\alpha}, \tag{8}$$

where $C(l)$ is the modeled covariance value over the distance l , C_0 is the signal variance and α is a parameter related to the correlation length $X_{1/2}$ as $\alpha \approx 0.595X_{1/2}$. The correlation length is defined as the distance at which the covariance function reaches half the value of C_0 .

To finally obtain the gridded surface free-air anomalies, the previously removed long- and short-wavelength gravity contributions can be restored on the gridded RTM anomalies:

$$\Delta g_G^{FAA} = \Delta g_G^{RTMA} + \Delta g_G^{GGM} + \delta g_G^{RTM}, \tag{9}$$

where Δg_G^{GGM} and δg_G^{RTM} are now computed at the locations of grid nodes. The long- and short-wavelength gravity signals estimated from a GGM and DTM, respectively, can hence also provide information at the locations of previously existing data voids. A high-quality DTM may thus significantly enhance the gravity field estimation, improving the accuracy of subsequent geoid modeling (a bathymetry model may have a similar influence).

2.2. Quasigeoid Determination

Geoidal heights can be approximated using the unbiased LSMSA geoid modeling approach [12,46] with the gridded surface free-air anomalies:

$$\tilde{N} = \frac{R}{4\pi\gamma_0} \iint_{\sigma_0} S^L(\psi) \Delta g_G^{FAA} d\sigma + \frac{R}{2\gamma_0} \sum_{n=2}^M (s_n + Q_n^L) \Delta g_n^{GGM}, \tag{10}$$

where R is the mean Earth radius, $S^L(\psi)$ is the Stokes's function modified up to the degree limit L and ψ denotes a geocentric angle between computation and moving integration

points. Integration is limited to a spherical cap σ_0 (with geocentric angle ψ_0) around a computation point. The modified Stokes's function is:

$$S^L(\psi) = \sum_{n=2}^{\infty} \frac{2n+1}{n-1} P_n(\cos \psi) - \sum_{n=2}^L \frac{2n+1}{2} s_n P_n(\cos \psi), \tag{11}$$

where the first term denotes the original Stokes's function $S(\psi)$ and $P_n(\cos \psi)$ Legendre polynomial of degree n . The modification parameters s_n in Equations (10) and (11) are solved from a linear system of equations in the least-squares sense [12]. These were estimated as described in [47,48]. Since the unbiased LSMSA approach leads to an ill-conditioned system of linear equations, singular value decomposition was used to ensure the solution's stability. The terrestrial gravity data uncertainties were assumed at 2 mGal as the focus is on marine areas where gravity data noise is more significant (due to dynamic measuring conditions) than on land (generally in the range of 0.5–1 mGal).

The modified truncation coefficients Q_n^L in Equation (10) are computed as:

$$Q_n^L = Q_n^L(\psi_0) = Q_n(\psi_0) - \sum_{k=2}^L \frac{2k+1}{2} s_k R_{nk}(\psi_0). \tag{12}$$

Molodenskii's truncation coefficients Q_n and coefficients R_{nk} (both a function of ψ_0) can be evaluated using recursive algorithms given by [49,50]. By employing a suitable GGM up to the degree M , Laplace harmonics Δg_n^{GGM} in Equation (10) can be computed as:

$$\Delta g_n^{GGM} = \frac{GM}{r^2} \left(\frac{a}{r}\right)^n (n-1) \sum_{m=0}^n (\Delta \bar{C}_{nm} \cos m\lambda + \bar{S}_{nm} \sin m\lambda) \bar{P}_{nm}(\cos \theta), \tag{13}$$

where $\Delta \bar{C}_{nm}$ and \bar{S}_{nm} are fully normalized spherical harmonic coefficients of the disturbing potential (relative to the GRS80 reference ellipsoid). Note that modification limits M and L are consistently selected as equal in this study. Term GM is the terrestrial gravitational constant, a is the equatorial radius, r , λ and θ are spherical geocentric radius, longitude and co-latitude, respectively, and $\bar{P}_{nm}(\cos \theta)$ denotes fully normalized Legendre functions.

With the geoid estimator \tilde{N} computed, height anomalies (i.e., quasigeoid heights) can be determined:

$$\zeta = \tilde{N} + \delta\zeta_{DWC} + \delta\zeta_{ATM} + \delta\zeta_{ELL}, \tag{14}$$

where $\delta\zeta_{DWC}$ is the combined downward continuation effect [51], $\delta\zeta_{ATM}$ is the combined atmospheric effect [52–54], and $\delta\zeta_{ELL}$ is the combined ellipsoidal effect [55–57] (i.e., the additive corrections). The equations for these effects are explicitly spelled out in [58] and are thus not repeated here. Importantly, the presented investigations neglect consideration for atmospheric and ellipsoidal effects due to their relatively small magnitude (generally sub-centimeter; see numerical examples in [58–60]). Since these effects are also computed independently of surface free-air anomalies, they do not affect the examination of bathymetry contribution to geoid modeling outcomes (i.e., their influence cancels out in comparisons). The combined downward continuation effect, on the other hand, requires knowledge of the vertical gradients of surface free-air anomalies (estimated using GRAVSOF sub-program GEOFOUR) and has a magnitude up to a few decimeters (in the study area).

3. Study Area and Data

In the BSCD2000 project, the geoid modeling target area extends from 53° N to 66.5° N and 8.5° E to 31° E (cf. Figure 1), whereby the modeling resolution is 0.01° × 0.02°. The defined extents cover the whole Baltic Sea and its surrounding areas. For modeling the BSCD2000 geoid, a dataset of surface free-air anomalies (Figure 2) was provided in the zero-tide permanent tide concept (see [61,62] for details about permanent tide concepts). This study uses the final version 3 of the database release. These gravity data cover the area from 52° N to 67.5° N and 5.5° E to 34° E. Comparison between Figures 1 and 2 shows that

the surface free-air anomalies are highly correlated with rugged terrain (notice Norway and Sweden) and thus ill-suited for gridding.

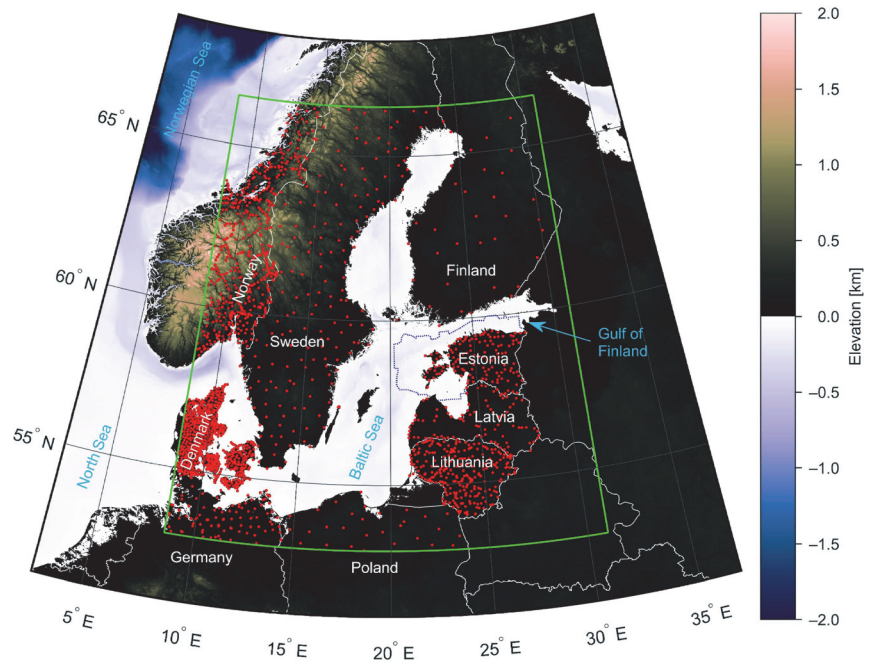


Figure 1. Terrain elevations and bathymetry. The dashed blue line surrounding Estonia shows the boundaries of the Estonian Maritime Administration obtained bathymetry data. Red dots are GNSS-leveling control point locations, and the green rectangle denotes the geoid modeling target area.

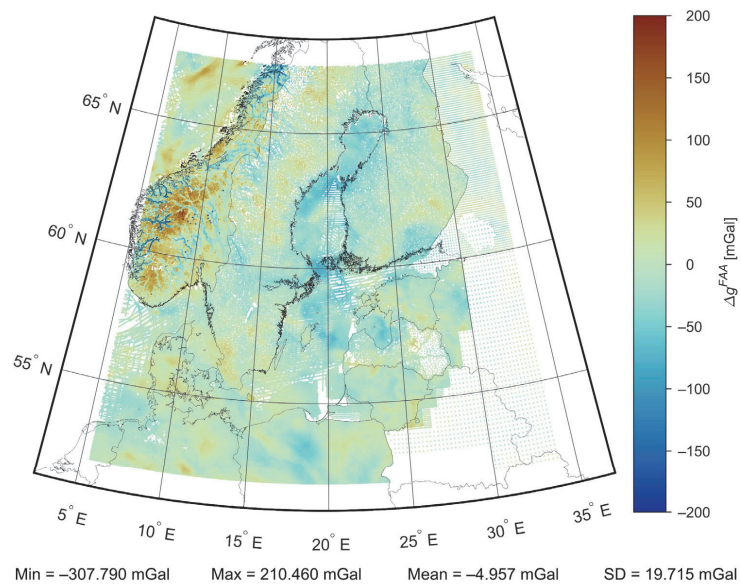


Figure 2. Surface free-air anomalies (final release of BSCD2000 dataset version 3).

To reduce surface free-air anomalies to RTM anomalies, which are more suitable for gridding, a DTM is required. For the BSCD2000 geoid modeling project, a section of the 3" × 3" NKG-DEM2014 was provided. The same model has previously been used in modeling the NKG2015 quasigeoid [15,27,29]. For the current study, the model was averaged to 0.001° × 0.002° (i.e., 3.6" × 7.2") and 0.01° × 0.02° grids covering the area from 51° N to 68.5° N and 2.5° E to 37° E. These datasets were used in geoid modeling solutions that neglected bathymetry information during RTM computations. The coarse grid with elevations above zero is also required for geoid determination using the LSMSA approach.

An alternative elevation model was also constructed since the NKG-DEM2014 does not contain any bathymetry information (i.e., marine areas have zero elevations). As the primary bathymetry data source, the 15" × 15" GEBCO_2021 grid [63] was used. Employing multibeam and single-beam shipborne bathymetry data for validation, ref [64] suggested that the GEBCO_2020 grid (i.e., the previous version) has an accuracy of 58 m (in terms of standard deviation) in the Arctic Ocean (northwest from the study area), where the average depth of the investigated region was around 2500 m. A multibeam bathymetry dataset was used to complement the GEBCO_2021 grid in the Estonian marine areas (notice the dashed blue line surrounding Estonia in Figure 1), obtained from the Estonian Maritime Administration. The dataset is primarily a 3.6" × 3.6" grid but also contains some dense scattered data points. A comparison between the GEBCO_2021 and Estonian Maritime Administration datasets yielded a standard deviation estimate of 1.9 m, indicating adequate accuracy of the GEBCO_2021 grid in the Baltic Sea. However, it should be noted that the differences reach up to 10–30 m range in some regions, generally where depth changes are steep. Such differences are likely due to the lower resolution of the GEBCO_2021 grid (i.e., seabed details are not well-captured). All these bathymetry data were jointly resampled to a 3" × 3" grid and then subtracted from the NKG-DEM2014. The resulting model was then averaged to 0.001° × 0.002° and 0.01° × 0.02° grids (Figure 1 presents the coarse grid). These datasets were used in geoid modeling solutions that considered bathymetry information during RTM computations.

It is evident from Figure 1 that the Baltic Sea is relatively shallow, having a mean depth of only 54 m and a maximum depth of 459 m [65]. On the other hand, the regions in the northwestern section of the study area at the Norwegian Sea are much deeper, with depths exceeding 2000 m. An essential measure for examining bathymetry's influence on gravity data processing and geoid modeling is the ruggedness of bathymetry. The terrain ruggedness index (describes elevation differences between adjacent cells of a DTM) developed by [66] was modified for the current study. The modified index is named the bathymetry ruggedness index and computed as:

$$BRI_P = \frac{1}{I} \sum_{i=1}^I |H_i^* - H_P^*| \cdot \left(1 - \sqrt{d_i/d_{LIM}}\right), \tag{15}$$

where H_P^* is depth at a computation point P , and H_i^* represents depth at a data point i with a distance d_i from the computation point. The term I is the total number of data points within the specified radius d_{LIM} . The parameter d_{LIM} behaves as a low-pass filter, where the increasing value yields smoother bathymetry ruggedness index features.

The bathymetry ruggedness index (Figure 3 shows the computation results) was computed on a 0.01° × 0.02° grid using the GEBCO_2021 and Estonian Maritime Administration bathymetry datasets. The computation radius d_{LIM} was set to 10 km for the resulting index features to be (visually) similar to surface free-air anomalies. Although the bathymetry ruggedness index values are somewhat arbitrary, the relative comparisons indicate the locations of smooth bathymetry (e.g., near-zero values in the North Sea) and rugged bathymetry (e.g., coastal areas of Norway and in the Norwegian Sea) effectively. Rugged bathymetry can also contribute to the high-frequency gravity field variations like rugged terrain. Thus, the most notable influence of bathymetry information on the geoid

modeling results can be expected near the coastal area of Norway, which is described by the study area's most rugged bathymetry (cf. Figure 3).

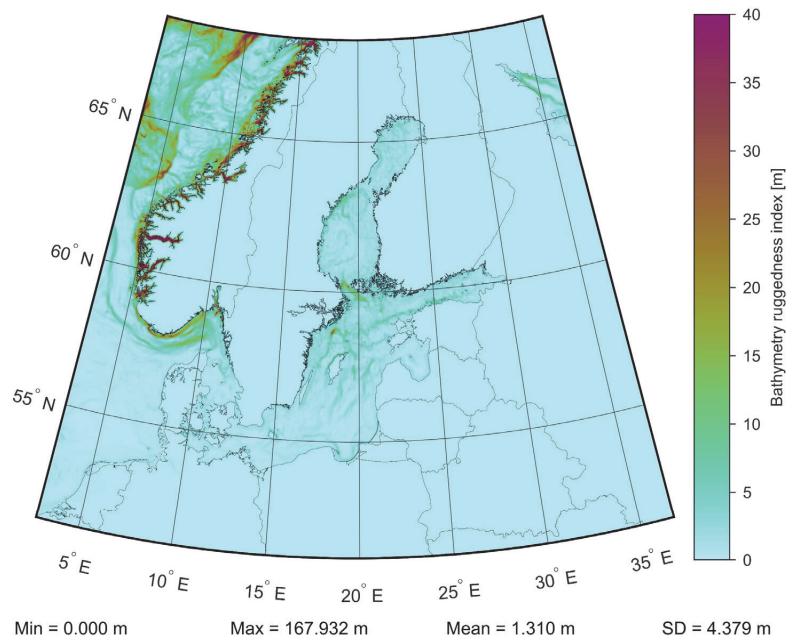


Figure 3. Estimated ruggedness of bathymetry.

Geoid modeling using modified Stokes's formula also requires a suitable GGM. This study tested modeling by employing GOCO05c [67,68], GO_CONS_GCF_2_DIR_R6 [69], GOCO06s [70,71] and XGM2019 [72,73] models. While GO_CONS_GCF_2_DIR_R6 and GOCO06s represent satellite-only gravity field models, GOCO05c and XGM2019 are combined models containing additional terrestrial and altimetry-based gravity data. Note that GO_CONS_GCF_2_DIR_R6 is initially given in the tide-free permanent tide concept (the other three use the zero-tide concept) and was thus converted to the zero-tide concept first.

Validation Datasets

A dataset of 1902 precise GNSS-leveling control points (Figure 1) was provided to evaluate the gravimetric geoid modeling solutions (Estonian data are available from [74]). The employed geodetic coordinates and ellipsoidal heights are in the ITRF2008 reference frame and use the zero-tide permanent tide concept. Temporal changes due to the postglacial land uplift in the Baltic Sea region have been reduced to the epoch 2000.0. Leveled normal heights are in the national (European Vertical Reference System based or compatible) height system realizations and use the zero-tide permanent tide concept with uplift epoch 2000.0. If the provided data used a different tide concept or had a different uplift epoch (Danish and German GNSS-leveling data), a conversion to the zero-tide permanent tide concept (relative to the Normaal Amsterdams Peil) and uplift epoch 2000.0 was conducted. The NKG2016LU model [75] was used to correct for the land uplift.

Besides the conventional GNSS-leveling control points, alternative marine datasets were also used to evaluate the results. These include shipborne GNSS and airborne laser scanning measured sea surface heights, which were reduced into geoidal heights using instantaneous dynamic topography estimates. Dynamic topography was estimated by combining hydrodynamic models and tide gauge data [35,38,39]. The datasets include the Sektori shipborne GNSS-determined profiles [76] (Figure 4 left), airborne laser scanning-derived profiles [38] (Figure 4 left) and six campaigns (denoted from C1 to C6) of the

Salme shipborne GNSS-determined profiles [35,77] (Figure 4 right) of geoidal heights (converted to the zero-tide permanent tide concept). Such marine datasets can be valuable in validating marine geoid models since GNSS-leveling control points cannot be established over marine areas.

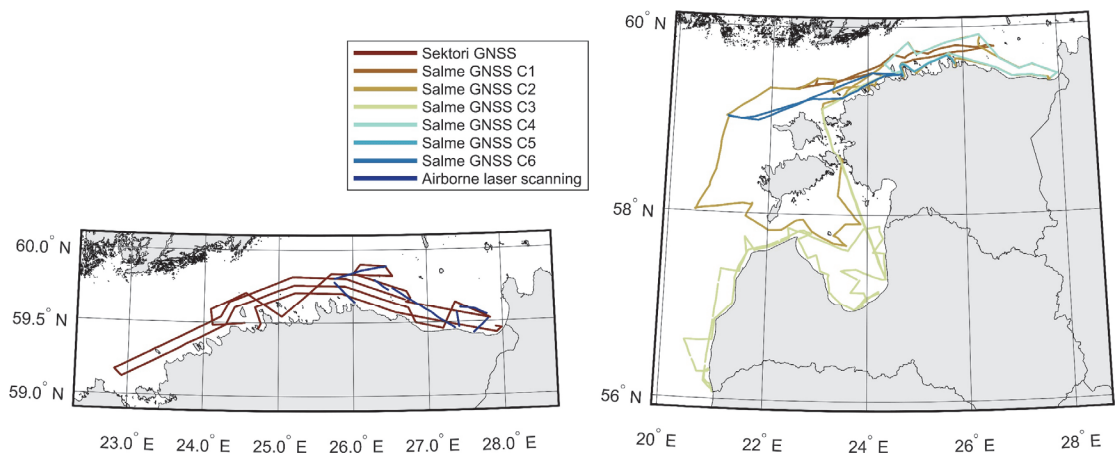


Figure 4. Shipborne GNSS-determined and airborne laser scanning-derived marine profiles of geoidal heights.

4. Gravity Field Estimation and Geoid Modeling

4.1. Preparation of Gravity Data

Before regular gravity field estimation, additional gravity data processing had to be applied to the dataset of surface free-air anomalies (Figure 2). Besides terrestrial and marine gravity data, the dataset also contains some airborne measurements [78]. Since such gravity values are given at the flight altitude, a downward continuation correction must be applied due to signal attenuation. Then, airborne gravity measurements can be treated as terrestrial data. A straightforward method proposed by [79] can be used, where the correction is estimated as a difference between free-air anomaly values at the flight altitude and surface level using a high-resolution GGM (the method has also been tested and found suitable by [15]). Here, EIGEN-6C4 [80] evaluated to its maximum d/o of 2190 was selected. The estimated correction's standard deviation and maximum value were 0.49 mGal and 3.32 mGal, respectively. Note that XGM2019e [72,73] was also tested, but the application of EIGEN-6C4-based downward continuation correction yielded slightly better (although statistically insignificant) agreement with the (actual) terrestrial data.

A few obvious outlier points in the dataset were removed by comparing the initial anomalies to a preliminary grid solution (computed following subsequent steps). Otherwise, no specific outlier detection was implemented. It is assumed that through many years of significant effort by participating countries (especially prior to NKG2015 computations; some details are in [15]) that have submitted gravity data, gross errors have been largely removed and data quality has been ensured (for instance, ref [81] describes the Estonian gravity data).

Additional gravity data were derived from the EIGEN-6C4 GGM to improve gridding quality at the study area edges. The model was evaluated to its maximum d/o of 2190 on a regular $0.025^\circ \times 0.05^\circ$ grid. These points were no closer to the existing data than 0.15° and 0.3° in latitude and longitude, respectively. The error estimates for these points were assumed at 6 mGal to comply with the typical accuracy of GGMs over oceans [80]. Regarding a priori error estimates, note that most Norwegian data were associated with pessimistic estimates of 5 mGal, which may result in unwanted gravity field smoothing using the weighted LSC method. Thus, to improve gridding results, the a priori error

estimates were set to 1 mGal for Norwegian land data exceeding that limit (marine data were left unchanged). The gravity data associated and updated a priori error estimates are shown in Figure 5.

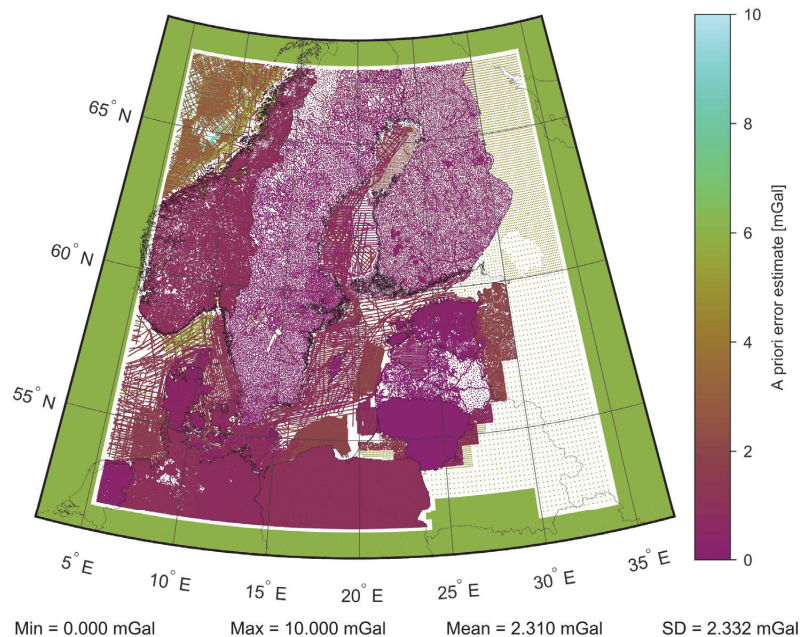


Figure 5. A priori error estimates of gravity data.

4.2. Determination of Residual Terrain Model Anomalies

Residual terrain model reduction was computed to reduce surface free-air anomalies, prepared as described in the previous section, into RTM anomalies. Two sets of computations were conducted—one, where bathymetry information was included, and the second, where it was neglected. Smooth reference surfaces for the RTM reduction computations were determined by applying a moving average low-pass filter on the respective elevation models, averaged roughly to the resolution corresponding to the degree 300. Integration using the $0.001^\circ \times 0.002^\circ$ grids was performed over a 15 km distance from computation points and over a 200 km distance using the $0.01^\circ \times 0.02^\circ$ grids. Elevation models on land were locally spline interpolated to fit heights of gravity observations in computation points (models were left unchanged for marine points).

Figure 6 shows RTM reduction as the grid used in the restoration step, computed by including bathymetry information, and Figure 7 demonstrates bathymetry's contribution to the reduction, obtained as the difference between the two RTM reduction grids. In the Baltic Sea, bathymetry contribution generally remains within 5 mGal, but a more considerable influence can be seen in rougher seabed areas (also refer to Figure 3). Significant bathymetry influence in the 20 mGal range can be observed in the Norwegian Sea and around the Norwegian shoreline, where fjords' depth information can contribute even up to 50 mGal to the RTM reduction. The Norwegian coast is also where marine RTM reduction appears relatively rough, whereas generally, the reduction is rather smooth compared to how it appears in the land areas, especially in Norway (cf. Figure 6). It can be noticed in Figure 7 that bathymetry information also propagates inland from the coast, which is due to the used integration radiuses.

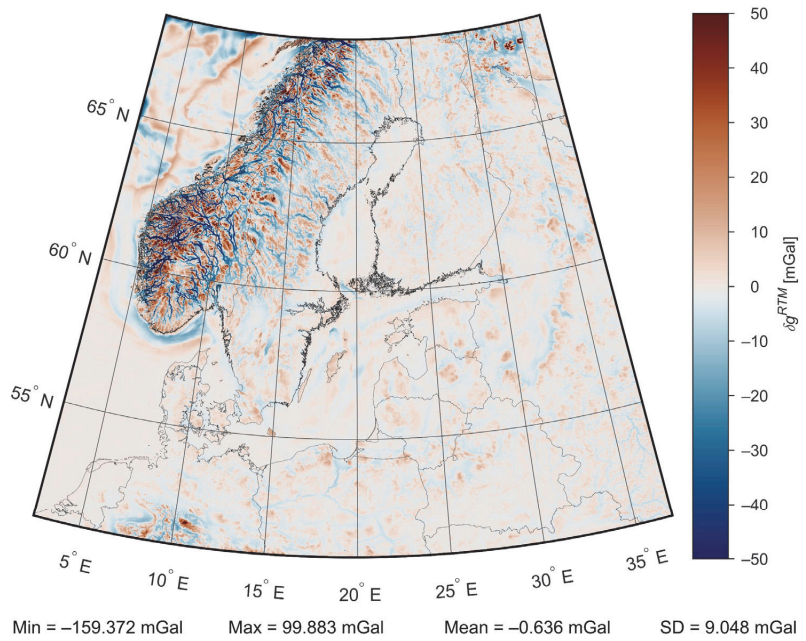


Figure 6. RTM reduction computed by also considering bathymetry information.

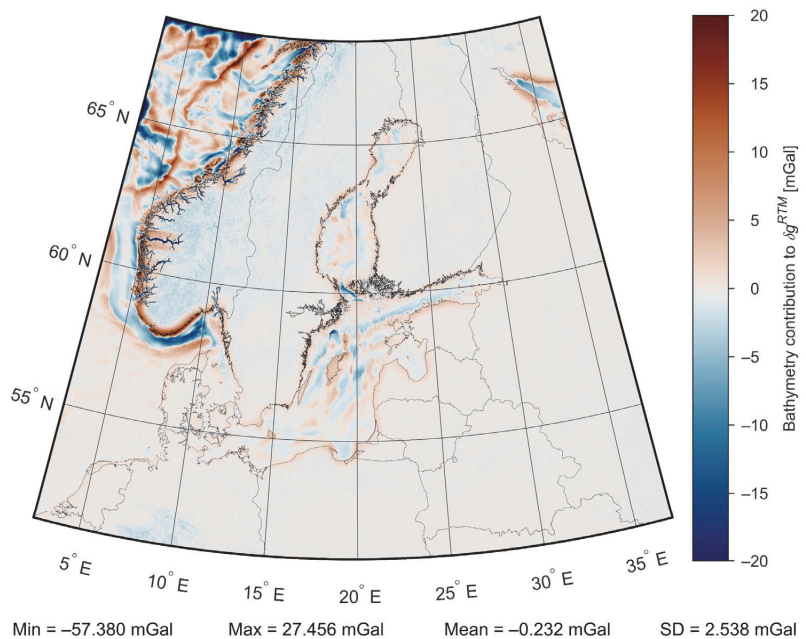


Figure 7. Bathymetry contribution to RTM reduction.

Besides RTM reduction, computation of RTM anomalies also requires the long-wavelength component from a suitable GGM. The GO_CONS_GCF_2_DIR_R6 model evaluated to its maximum d/o of 300 was used here. After RTM anomalies were computed, a single data point with the smallest a priori error estimate was retained within each $0.01^\circ \times 0.02^\circ$ grid

cell to avoid aliasing during gravity gridding. If more than one such point existed, all the potential points were averaged both in value and spatially (note that Figure 5 shows the thinned dataset, whereby Norwegian data were assigned 1 mGal a priori error estimates after thinning).

Figure 8 presents RTM anomalies where bathymetry information was considered during computations. Comparison between Figures 2 and 8 demonstrates that the RTM anomalies are much smoother (notice standard deviation estimates) and less biased (notice mean values) than the initial surface free-air anomalies, and thus better suited for gridding. When bathymetry was neglected during the computation of RTM anomalies, the resulting standard deviation estimate was 10.61 mGal, and the mean value was -0.50 mGal. Therefore, consideration for bathymetry yielded a slightly smoother dataset of RTM anomalies (respective estimates shown in Figure 8 are 10.30 mGal and -0.37 mGal). Note that the GOCO06s model evaluated to its maximum d/o of 300 was also tested in determining RTM anomalies. When bathymetry was considered and neglected in computations, the standard deviation estimates were 10.86 mGal and 11.16 mGal, respectively. The use of GO_CONS_GCF_2_DIR_R6 instead of GOCO06s hence provided considerably smoother datasets of RTM anomalies.

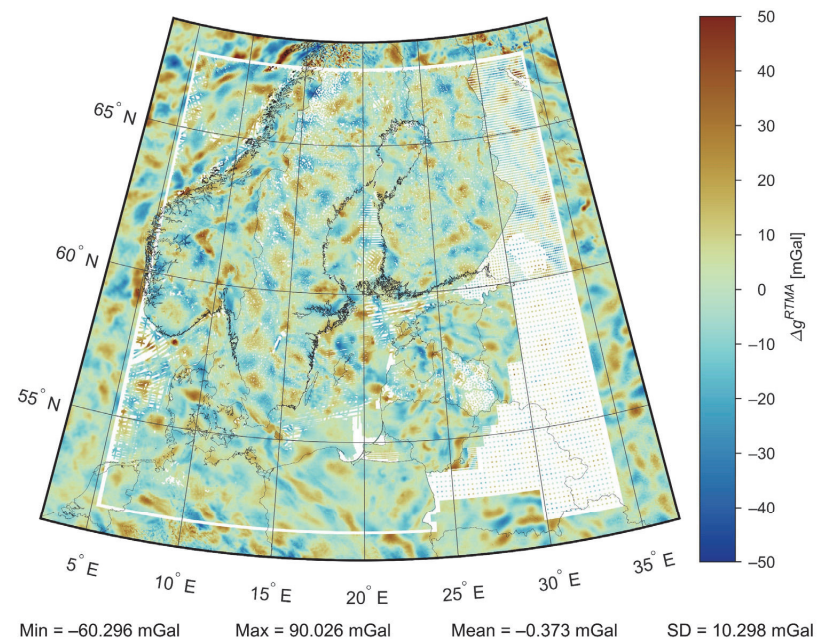


Figure 8. RTM anomalies computed by also considering bathymetry information.

4.3. Gravity Data Gridding

Besides comparing surface free-air and RTM anomalies in Figures 2 and 8, respectively, covariance analysis of these quantities was also conducted (Figure 9). It can be noticed that the autocovariance values of RTM anomalies are smaller, especially at short distances (note the 783.4 mGal² estimate of surface free-air anomalies that describes the first-kilometer distance), indicating that the derived RTM anomalies are smoother than the initial surface free-air anomalies. The relative smoothness of RTM anomalies compared to the surface free-air anomalies (here, the processed and thinned dataset is used, which causes the $19.7 \text{ mGal} \neq \sqrt{544.5} = 23.3 \text{ mGal}$ discrepancy between Figures 2 and 9) is also suggested by the signal variances. Consequently, the smoother RTM anomalies can be spaced sparser to guarantee grid prediction accuracy, whereas the use of surface free-air anomalies would require much denser data. Furthermore, in the case of surface free-air anomalies, the

second-order Markov covariance model does not fit the empirical data well. Notice how the model either overestimates (at shorter distances) or underestimates (at longer distances) the data spatial correlation. On the other hand, the second-order Markov models' better fit for RTM anomalies (i.e., the modeled covariance represents empirical data closely) suggests that good data-gridding performance can be expected. Note that the inclusion/neglect of bathymetry data does not significantly affect the second-order Markov covariance models' estimation, although some parameter differences exist (cf. Figure 9).

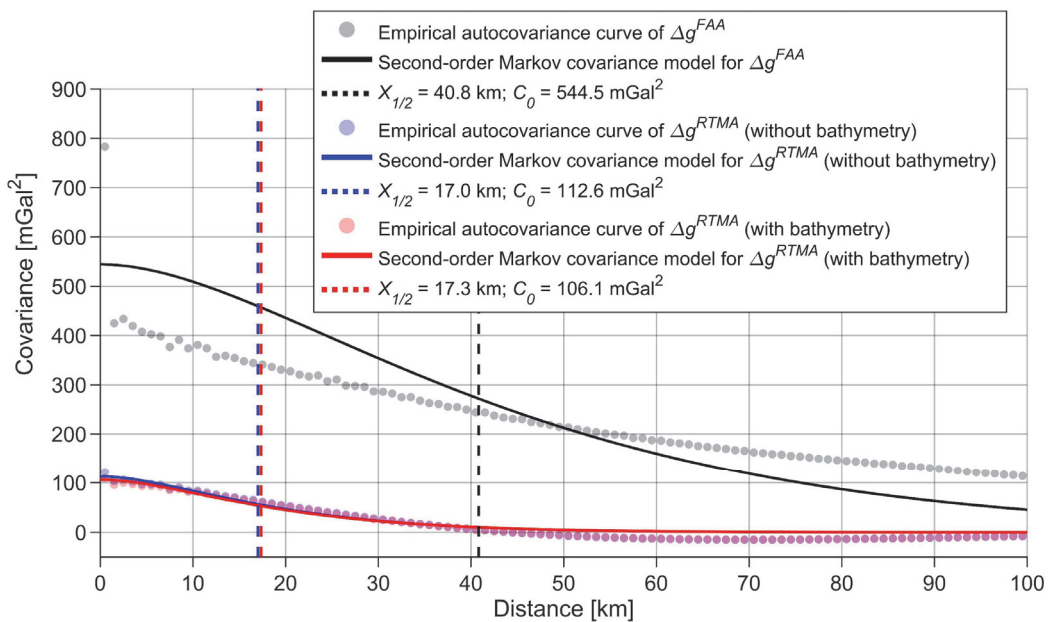


Figure 9. Empirical autocovariance curves and respective least-squares fitted second-order Markov covariance models with the associated correlation lengths $X_{1/2}$ (shown with dashed lines) and signal variances C_0 (see the legend).

Residual terrain model anomalies were gridded using the weighted LSC method. The second-order Markov covariance models, defined by the estimated correlation lengths and determined signal variances (cf. Figure 9), described data spatial dependence. The LSC prediction was set to use the 10 closest data points in each quadrant around a prediction point for computational efficiency. A minimum of 0.5 mGal a priori error estimate was defined, whereas if a data point was associated with a larger error estimate, specific a priori estimates in Figure 5 were used. Such data gridding resulted in two RTM anomaly grids—one with bathymetry information included and the second where it was neglected during previous RTM reduction computations. Finally, the RTM reduction and long-wavelength GGM effects were restored to obtain gridded surface free-air anomalies. Figure 10 shows the grid where bathymetry was considered during computations, and Figure 11 demonstrates the influence of bathymetry on gravity field estimation, obtained as the difference between the two grids of surface free-air anomalies.

In the Baltic Sea, bathymetry contribution to the gridded surface free-air anomalies generally remains within 2 mGal (Figure 11). Around the same magnitude, the contribution propagates to inland areas due to two reasons. The first reason is differences in computed RTM reductions, described in Section 4.2, which also influence gridding results, and the second one is variation in signal properties, which causes differences in the second-order Markov covariance models (cf. Figure 9). The latter induces up to 3 mGal differences in sparse gravity data areas (refer, e.g., to Figure 8).

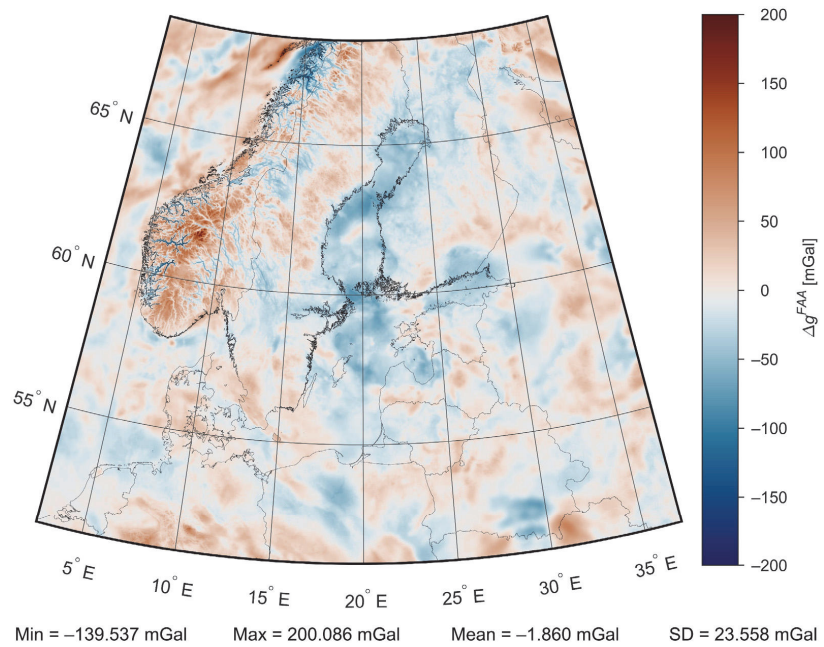


Figure 10. Gridded surface free-air anomalies computed by also considering bathymetry information.

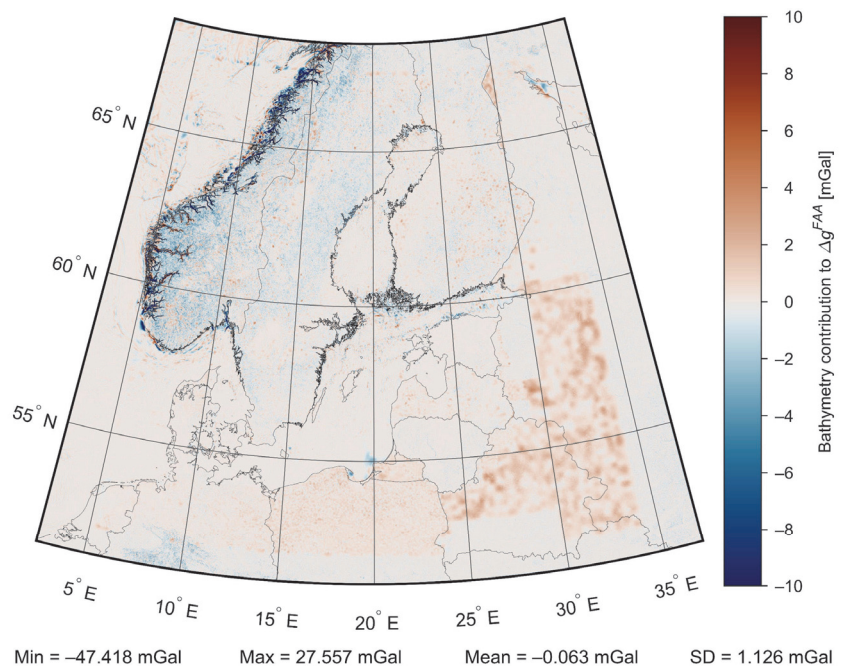


Figure 11. Bathymetry contribution to gridded surface free-air anomalies.

There are also some sparse marine locations where bathymetry contribution has resulted in around 4 mGal differences. These are in the central part of the Baltic Sea and the Gulf of Finland, where increased ruggedness of bathymetry can also be observed (cf.

Figure 3). In the same magnitude, bathymetry has influenced gravity field estimation in the Norwegian Sea. Importantly, a significant impact of bathymetry on the gridding results can be noticed around the shoreline of Norway, where bathymetry contribution is generally within 20 mGal but can reach up to around 40 mGal in some locations. By comparing Figures 3 and 11, it can be noticed that these significant differences coincide with regions of most rugged bathymetry. The bathymetry ruggedness index is also rather well correlated with the bathymetry contribution to the gridded surface free-air anomalies, yielding a correlation coefficient of 0.78 (all marine areas in the geoid modeling target area were considered; absolute values of bathymetry contribution to gravity anomalies were used). It can be concluded that considering bathymetry in gravity field estimation can help retain valuable short-wavelength gravity information.

4.4. Results of Geoid Modeling

The surface free-air anomaly grids were employed in geoid determination using the unbiased LSMSA modeling approach. In all computations, integration was limited to 2° (i.e., the geocentric angle ψ_0). Altogether four GGMs were tested (cf. Section 3), where modification limits (recall that M and L were always set equal) varied between 140 and 300 with an increment of 10. Figure 12 presents validation results based on GNSS-leveling control points (cf. Figure 1), whereby in all these computations, bathymetry information was considered (i.e., the surface free-air anomaly grid where the RTM reduction utilized bathymetry was employed). In the first validation case (upper subplot of Figure 12), a one-dimensional fit was used (i.e., models were directly compared to all GNSS-leveling control points). Since height system biases between countries may exist, in the second validation case (bottom subplot of Figure 12), the control points of each country were first compared with the models separately, and then the residual differences of all countries were considered altogether (i.e., country means were removed).

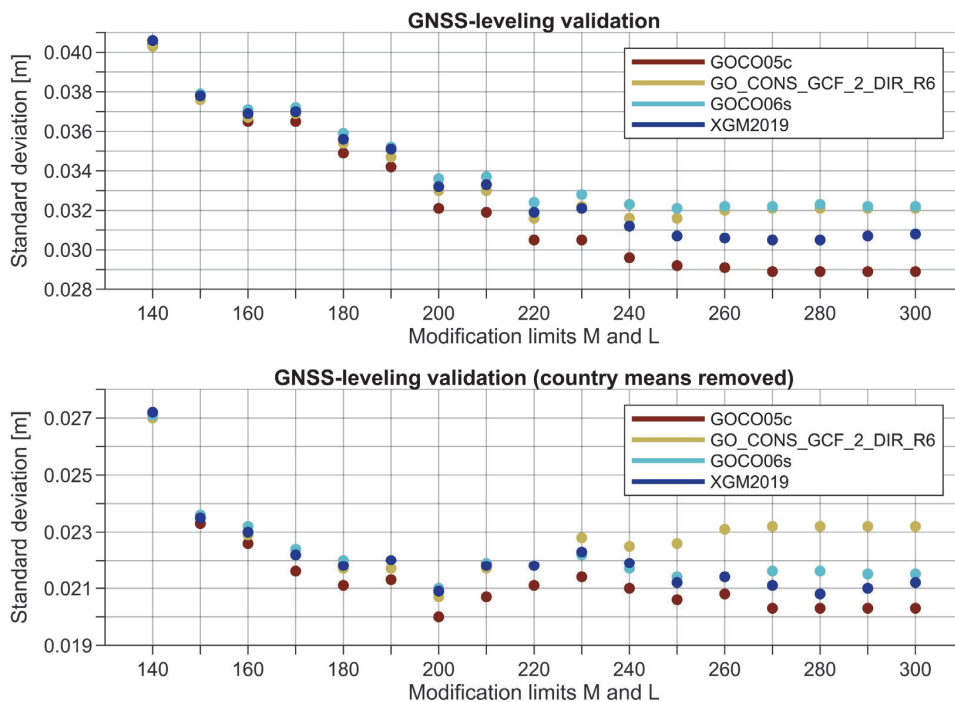


Figure 12. Validation results of gravimetric geoid models using GNSS-leveling control points.

According to the GNSS-leveling control points, the GOCO05c-based solutions outperform models that use the other three tested GGMs regardless of modification limits. The accuracy (in terms of standard deviation) from a one-dimensional fit reached 2.9 cm with modification limits of 280, whereas limits of 200 yielded an estimate of 2.0 cm when country means were removed from the validation. Up to limits of 220, the GO_CONS_GCF_2_DIR_R6-based solutions appear to show the second-best performance. However, the relative (to other models) accuracy degrades with higher modification limits, where XGM2019-based (the other combined GGM besides GOCO05c) solutions agree better with the GNSS-leveling control points.

The above comparisons only provide information about modeling performance on land, whereas the BSCD2000 project aims to model the marine geoid. Knowledge of the marine geoid’s geometry would thus be valuable. Therefore, a set of marine profiles (cf. Figure 4) was also employed to assess the computed geoid solutions. Figure 13 shows the results of these comparisons, whereby bathymetry information was considered during computations of all the validated models.

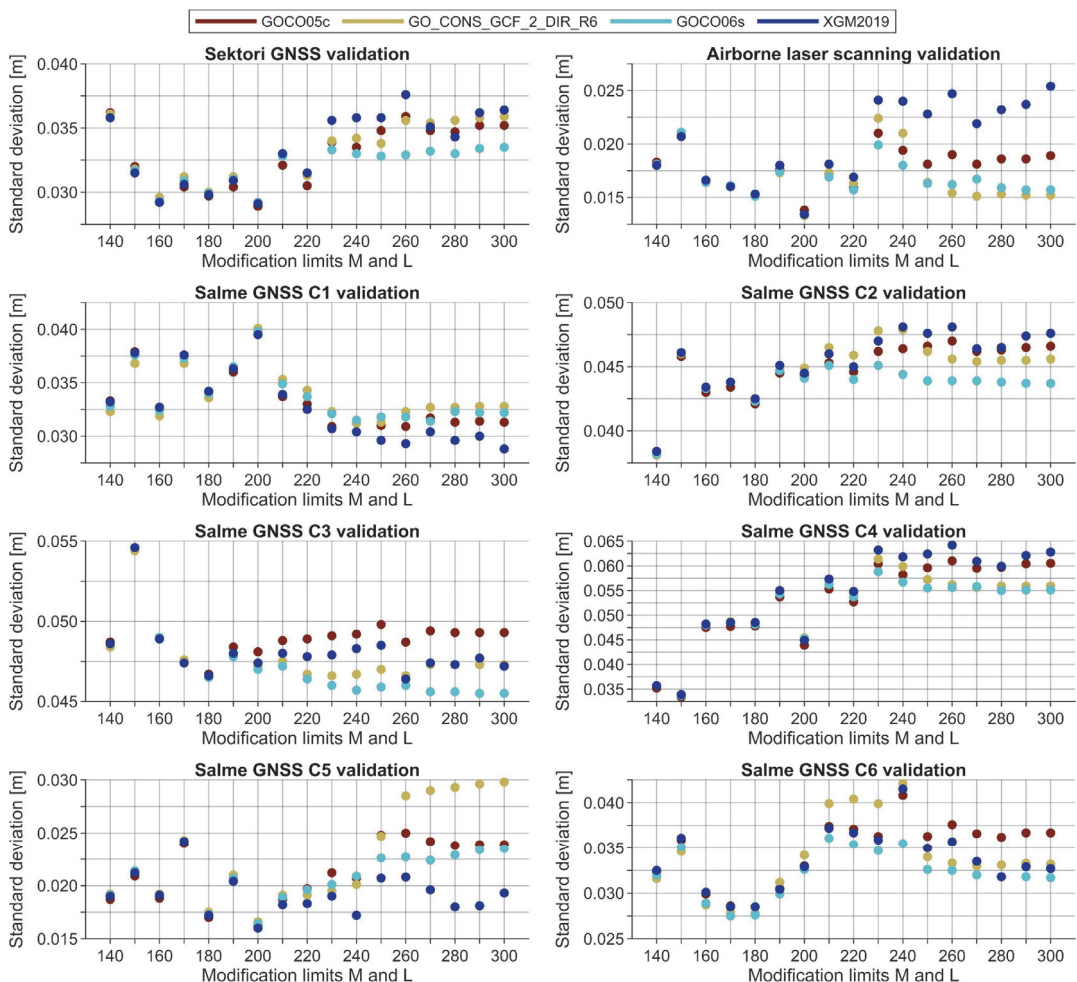


Figure 13. Validation results of gravimetric geoid models using shipborne GNSS-determined and airborne laser scanning-derived marine profiles of geoidal heights.

In contrast to the comparisons using GNSS-leveling control points, the picture is not as clear with profile-based assessments. For instance, the profiles suggest that the accuracy of modeling solutions based on combined GGMs (GOCO05c and XGM2019) generally degrades with higher modification limits. Contrarily, GOCO06s-based solutions seem to perform the best when limits are high. The agreement between solutions is better with lower modification limits (similarly to the GNSS-leveling comparisons), where GOCO05c-based models perform adequately. It seems that the preferable modification limits could be around 180–200. For example, notice how the comparison with airborne laser scanning profiles (with a total length of 184.4 km) yields an excellent 1.3–1.4 cm agreement (in terms of standard deviation) using modification limits of 200. Interestingly, according to the Salme GNSS C1 profiles, limits of 200 yield the worst results.

It is essential to mention that contrary to GNSS-leveling control points, the profile-based comparisons represent a limited area (cf. Figure 4). Additionally, the accuracy of these marine profiles is most certainly not as high as GNSS-leveling control points. The measurements are conducted in dynamic conditions, but the more crucial issue is that dynamic topography must be estimated to derive geoidal heights from the measured sea surface heights. Due to tide gauge data and hydrodynamic models’ inaccuracies, estimation of instantaneous dynamic topography with an accuracy of a few centimeters is a difficult task. However, even then, such marine profiles can provide beneficial geometric information that can help decision-making in choosing a suitable geoid model out of various solutions.

4.5. Bathymetry Influence on Geoid Modeling

Considering both the GNSS-leveling and profile-based comparisons, the GOCO05c-based regional gravimetric geoid solution, where modification limits were set to 200, seems to show good overall accuracy. The model is presented in Figure 14. Similar to the previous bathymetry influence investigations, the contribution to geoid modeling was derived by comparing the model to its counterpart, which used the surface free-air anomaly grid where bathymetry information was neglected during the computation.

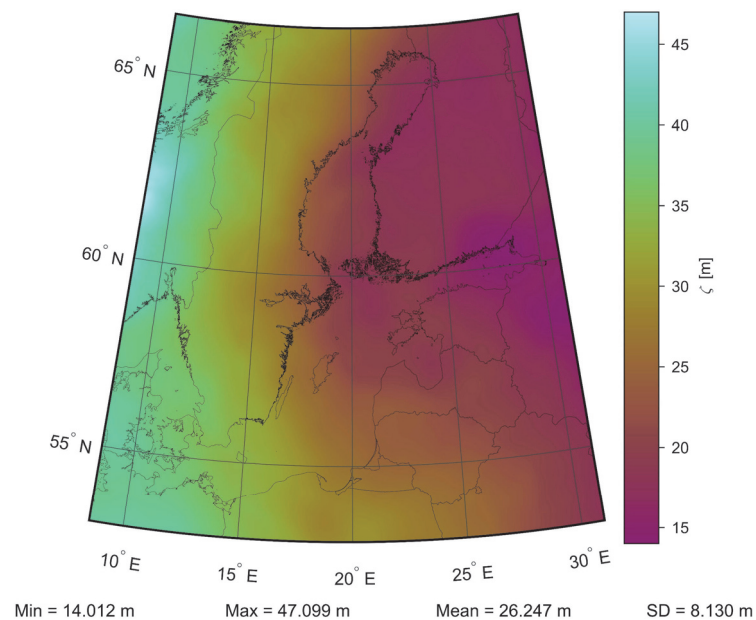


Figure 14. Gravimetric geoid modeling solution of the Baltic Sea region. GGM: GOCO05c, modification limits: 200, bathymetry was considered in computations.

Examination of geoid modeling differences (Figure 15) indicates that most variability in the Baltic Sea remains within 2 cm, being generally around a centimeter. The same magnitude differences can be noticed inland due to causes discussed in Sections 4.2 and 4.3, which also influence geoid modeling results. More considerable area-extensive differences inland and in the southern Baltic Sea are in regions of sparse or no gravity data (refer, e.g., to Figure 8). However, in the central Baltic Sea and the Gulf of Finland, larger detailed differences up to 3–4 cm can be detected. Comparing the bathymetry ruggedness index to the bathymetry influence on the modeling results in Figure 16 shows that these differences appear in more rugged regions of the seabed. Figure 16 also shows more detailed similarities between the bathymetry ruggedness index and the bathymetry contribution to gridded surface free-air anomalies, previously mentioned in Section 4.3.

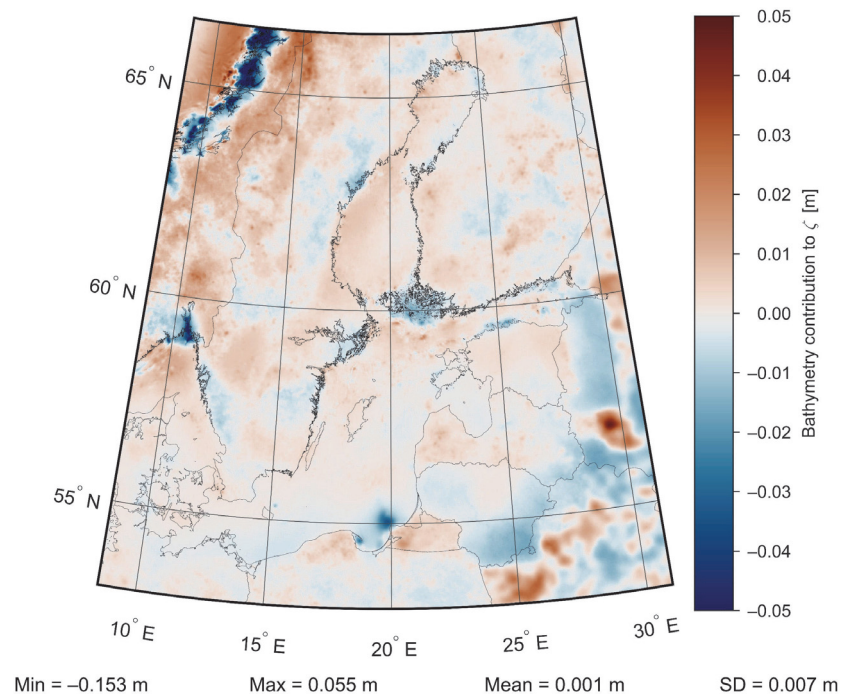


Figure 15. Bathymetry contribution to geoid modeling results. GGM: GOCO05c, modification limits: 200.

The most significant influence of bathymetry consideration can again be seen near the coastal areas of Norway, where bathymetry is most rugged (cf. Figure 3), resulting in differences around a decimeter (but can reach up to 15 cm). Although these differences in geoid features are much smoother than the computed bathymetry ruggedness index, the correlation coefficient between the two datasets is 0.65 (all marine areas in the geoid modeling target area were considered; absolute values of bathymetry contribution to geoid modeling results were used). The discussed results suggest that consideration for bathymetry has allowed the inclusion of short-wavelength details of the marine geoid in the modeling results.

To further examine the influence of bathymetry on geoid modeling, the validation results of GOCO05c-based solutions (by considering/neglecting bathymetry) with modification limits of 200 were compared. Differences between the two sets of comparisons shown in Figure 17 appear to be minor. For demonstration, Figure 18 presents comparisons of another two solutions. Since GOCO06s-based models appeared to perform well over marine areas at higher modification limits (cf. Figure 13), the respective solutions with

limits of 280 were selected for presentation. By comparing Figures 17 and 18, it is clear that the considering/neglecting bathymetry tendencies change. The validation differences in Figures 17 and 18 are primarily caused by the long-wavelength contributions caused by GGM and modification limits' choice and not due to the influence of bathymetry. Additionally, the contribution of bathymetry is too localized, and the accuracy of marine profiles is too low to say with certainty whether bathymetry has contributed positively or not using these validation results. An exception could be the Salme GNSS C5 profiles that largely coincide with the bathymetry-induced localized changes north of Estonia (cf. Figures 4 and 16), suggesting that modeling has benefited slightly from bathymetry (cf. Figures 17 and 18). On a side note, a comparison between difference plots (e.g., Figure 15 compared to GOCO06s-based solutions' differences) would result in discrepancies of long-wavelength nature. The short-wavelength differences between modeling solutions are similar regardless of the selection of GGM and modification limits.

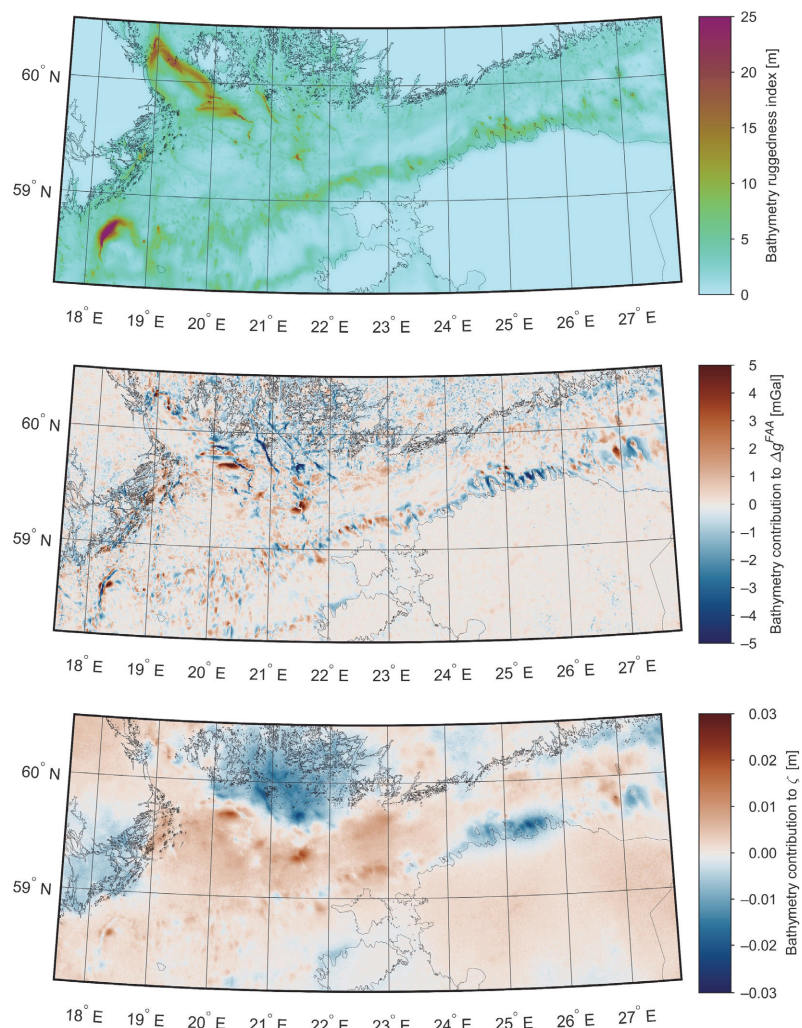


Figure 16. Estimated ruggedness of bathymetry (up), bathymetry contribution to gridded surface free-air anomalies (middle) and bathymetry contribution to geoid modeling results (down; GGM: GOCO05c, modification limits: 200) in the central Baltic Sea and the Gulf of Finland.

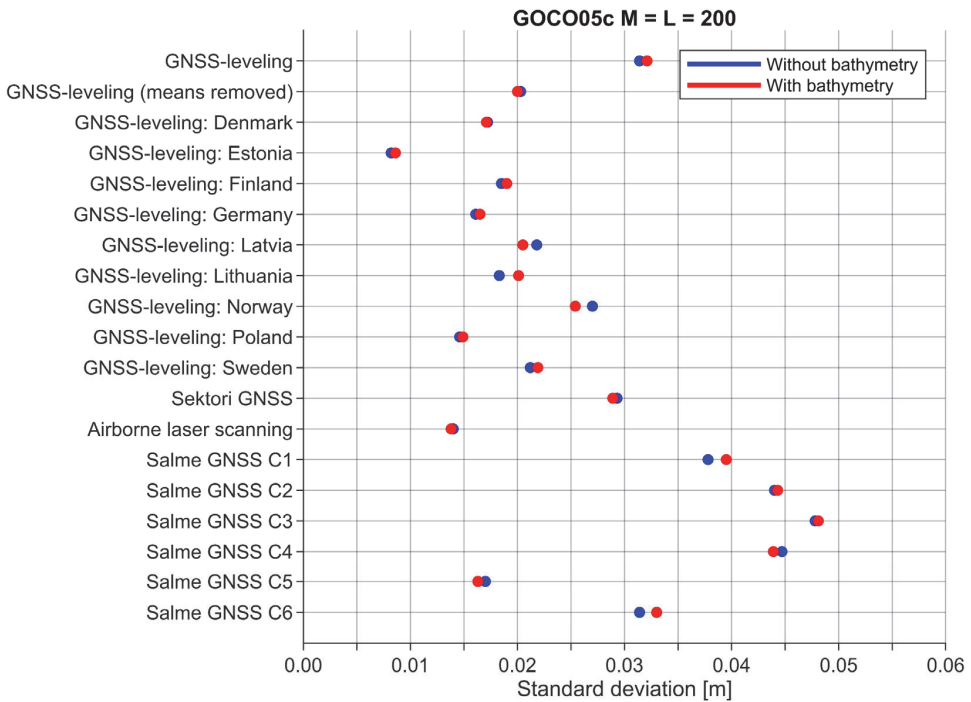


Figure 17. Validation results of gravimetric geoid models. GGM: GOCO05c, modification limits: 200.

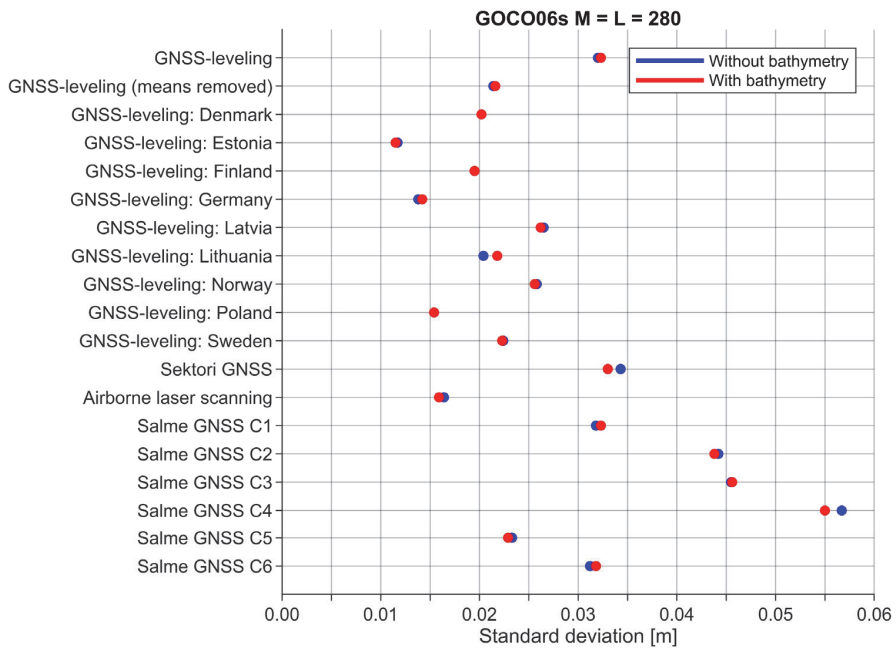


Figure 18. Validation results of gravimetric geoid models. GGM: GOCO06s, modification limits: 280.

A more detailed look was taken at Norway, where geoid modeling differences due to bathymetry were the largest. The residual values relative to GNSS-leveling control points (Figure 19) show significant modeling improvements up to around a decimeter in locations where bathymetry contributed the most (also refer to Figure 15). Therefore, considering high-frequency gravity field variations due to bathymetry during geoid modeling (in this study, within RTM reduction) can significantly increase the resulting model accuracy, especially in regions with the rugged seabed (cf. Figure 3). Based on improvements in Norway, it could be assumed that the localized details of the marine geoid that appear due to consideration for bathymetry have similarly increased the modeling accuracy (e.g., in the central Baltic Sea).

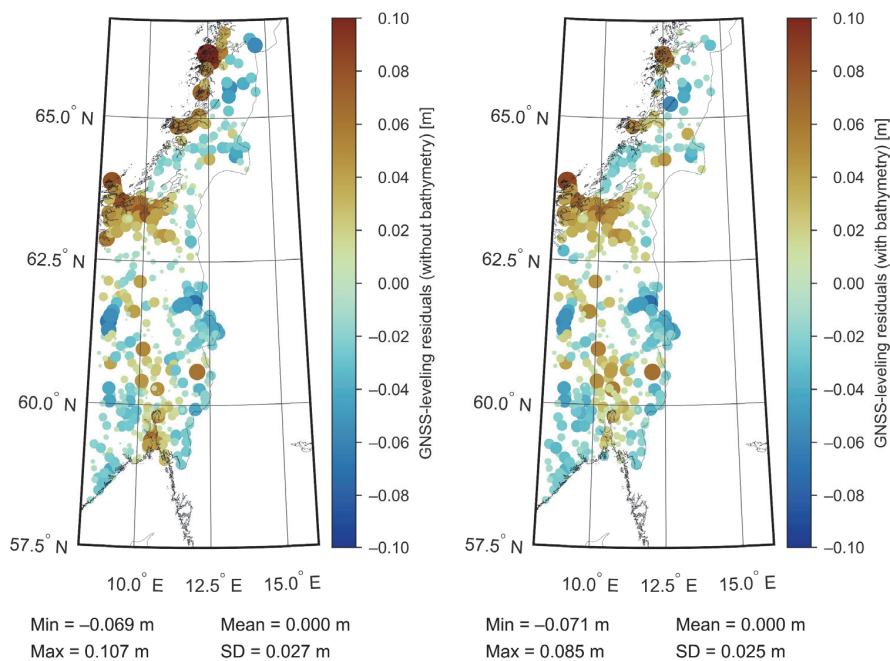


Figure 19. Residuals (mean removed) of gravimetric geoid models relative to the Norwegian GNSS-leveling control points. GGM: GOCO05c, modification limits: 200. The sizes of colored dots are proportional to the residual values.

5. Discussion

This study investigated bathymetry’s influence on gravity field estimation and geoid modeling in the Baltic Sea region in Northern Europe. By accounting for bathymetry-based RTM reduction during gravity data processing, valuable short-wavelength gravity information can be retained in the gridded gravity field (cf. Figure 11). The influence of bathymetry was especially significant in regions of rugged terrain/bathymetry (e.g., Norwegian fjords; also refer to Figure 3), where up to around 40 mGal differences (relative to neglecting bathymetry during gravity field estimation) could be observed. These gravity field refinements propagated further to the determined geoid models. The differences (relative to neglecting bathymetry) were up to 3–4 cm in some sparse regions of the Baltic Sea, being generally around a centimeter (cf. Figures 15 and 16). However, a significant influence of bathymetry on geoid modeling could be seen in the coastal area of Norway, where geoid modeling accuracy improved up to around a decimeter (cf. Figure 19).

Conventionally, precise GNSS-leveling control points are employed to validate geoid modeling results. Unfortunately, such control data are limited to land areas. This study demonstrated that various marine measurements (e.g., shipborne GNSS or airborne laser

scanning) could be beneficial in assessing the performance of various marine geoid modeling solutions. Figure 13 presented such a validation case with a total of 68 geoid models. Although the accuracy of geoidal heights derived from marine measurements is not comparable to GNSS-leveling control points due to dynamic measuring conditions and inaccuracies in dynamic topography estimation (required to determine geoidal heights from the measured sea surface heights), the geometric information these data provide can be invaluable.

In this study, such marine profiles were limited to a small area around Estonia and Latvia (cf. Figure 4). Only the Salme GNSS C5 profiles (north of Estonia) coincided well (considering the whole dataset) with more considerable geoid modeling differences due to bathymetry. These validation results indicated a slight modeling improvement when bathymetry was considered (cf. Figures 17 and 18). In other validation cases using different datasets, differences due to GGM and modification limits' choice dominated. In future studies, it would be interesting to investigate how satellite altimetry, which can provide sea surface heights with worldwide coverage, could benefit the validation of marine geoid models in a similar manner (also see [82]). Importantly, from a statistical point of view, altimetry measurements could also allow a more uniformly distributed dataset of points for validation.

It is essential to address that by using RTM reduction during data processing, the influence of bathymetry is not limited to marine areas but also propagates inland (cf. Figure 7). These influences can then affect subsequent gravity field estimation and geoid modeling. A good quality dataset of depth information is thus required, whereas poor bathymetry data may reduce the modeling accuracy. According to the results of this study, even the $15'' \times 15''$ GEBCO grid can contribute significantly to the improvement of geoid modeling solutions (cf. Figure 19), suggesting the good quality of the GEBCO bathymetry data in the Northern Europe region.

Here, the unbiased LSMSA modeling approach was employed for geoid determination, where the benefits of bathymetry consideration are introduced during gravity field estimation. The remove–compute–restore technique is another widely used geoid modeling method. In that, the terrain and GGM effects are removed from gravity data, and Stokes's formula is applied to the residual gravity values, after which the removed effects are restored. The bathymetry information would then be used in estimating the terrain effects. It is believed that a similar influence of bathymetry to geoid modeling could be expected using that method (also see [30]).

6. Conclusions

Northern Europe has been the target area in many regionwide geoid determination studies. However, the research has been land-focused and bathymetry information has been neglected. This study demonstrated that considering bathymetry through RTM reduction in gravity field estimation could help refine the results by retaining valuable short-wavelength gravity information. These refinements can then help enhance geoid modeling accuracy, whereby significant improvements can be expected in the rugged seabed regions. The geoid modeling accuracy increased up to around a decimeter in the coastal areas of Norway, where bathymetry contributed the most. It is concluded that the inclusion of bathymetry information in computations can improve geoid modeling outcomes in future Northern Europe geoid determination projects. Although the focus was on the Baltic Sea region, it is expected that similar outcomes could be observed in other parts of the world.

Funding: The research was supported by the Estonian Research Council grant “Development of an iterative approach for near-coast marine geoid modelling by using re-tracked satellite altimetry, in-situ and modelled data”, grant number PRG330.

Institutional Review Board Statement: Not applicable.

Informed Consent Statement: Not applicable.

Data Availability Statement: The Estonian GNSS-leveling data are available from [74]. The ship-borne GNSS-determined and airborne laser scanning-derived marine profiles of geoidal heights are available from the corresponding author upon reasonable request.

Acknowledgments: The Nordic Geodetic Commission (NKG) and the Baltic Sea Chart Datum 2000 project partners are thanked for making this study possible. The author is thankful to Artu Ellmann for helpful discussions during the manuscript's compilation and for providing the MATLAB programs for geoid modeling. Jonas Ågren is thanked for providing the GRAVSOFT software package. The three anonymous reviewers are thanked for their valuable comments and contribution to the quality of the manuscript. Estonian Maritime Administration is thanked for bathymetry data of the Estonian marine areas.

Conflicts of Interest: The author declares no conflict of interest.

References

- Gruber, T.; Willberg, M. Signal and error assessment of GOCE-based high resolution gravity field models. *J. Geod. Sci.* **2019**, *9*, 71–86. [[CrossRef](#)]
- Brockmann, J.M.; Schubert, T.; Schuh, W.-D. An improved model of the Earth's static gravity field solely derived from reprocessed GOCE data. *Surv. Geophys.* **2021**, *42*, 277–316. [[CrossRef](#)]
- Huang, J. Determining coastal mean dynamic topography by geodetic methods. *Geophys. Res. Lett.* **2017**, *44*, 11125–11128. [[CrossRef](#)]
- Andersen, O.B.; Nielsen, K.; Knudsen, P.; Hughes, C.W.; Bingham, R.; Fenoglio-Marc, L.; Gravelle, M.; Kern, M.; Polo, S.P. Improving the coastal mean dynamic topography by geodetic combination of tide gauge and satellite altimetry. *Mar. Geod.* **2018**, *41*, 517–545. [[CrossRef](#)]
- Idžanović, M.; Ophaug, V.; Andersen, O.B. The coastal mean dynamic topography in Norway observed by CryoSat-2 and GOCE. *Geophys. Res. Lett.* **2017**, *44*, 5609–5617. [[CrossRef](#)]
- Knudsen, P.; Andersen, O.; Maximenko, N. A new ocean mean dynamic topography model, derived from a combination of gravity, altimetry and drifter velocity data. *Adv. Space Res.* **2021**, *68*, 1090–1102. [[CrossRef](#)]
- Stokes, G.G. On the variation of gravity on the surface of the Earth. *Trans. Cambridge Philos. Soc.* **1849**, *8*, 672–695.
- Molodenskii, M.S.; Eremeev, V.F.; Yurkina, M. *Methods for Study of the External Gravitational Field and Figure of the Earth*; Israel Program for Scientific Translations: Jerusalem, Israel, 1962.
- Sjöberg, L.E.; Hunegnaw, A. Some modifications of Stokes' formula that account for truncation and potential coefficient errors. *J. Geod.* **2000**, *74*, 232–238. [[CrossRef](#)]
- Ellmann, A. Two deterministic and three stochastic modifications of Stokes's formula: A case study for the Baltic countries. *J. Geod.* **2005**, *79*, 11–23. [[CrossRef](#)]
- Goyal, R.; Ågren, J.; Featherstone, W.E.; Sjöberg, L.E.; Dikshit, O.; Balasubramanian, N. Empirical comparison between stochastic and deterministic modifiers over the French Auvergne geoid computation test-bed. *Surv. Rev.* **2022**, *54*, 57–69. [[CrossRef](#)]
- Sjöberg, L.E. A computational scheme to model the geoid by the modified Stokes formula without gravity reductions. *J. Geod.* **2003**, *77*, 423–432. [[CrossRef](#)]
- Sjöberg, L.E.; Bagherbandi, M. (Eds.) Applications and comparisons of LSMSA and RCR. In *Gravity Inversion and Integration*; Springer: Cham, Switzerland, 2017; pp. 181–202. [[CrossRef](#)]
- Wang, Y.M.; Sánchez, L.; Ågren, J.; Huang, J.; Forsberg, R.; Abd-Elmotaal, H.A.; Ahlgren, K.; Barzaghi, R.; Bašić, T.; Carrion, D.; et al. Colorado geoid computation experiment: Overview and summary. *J. Geod.* **2021**, *95*, 127. [[CrossRef](#)]
- Märdla, S.; Ågren, J.; Strykowski, G.; Oja, T.; Ellmann, A.; Forsberg, R.; Bilker-Koivula, M.; Omang, O.; Paršeliūnas, E.; Liepinš, I.; et al. From discrete gravity survey data to a high-resolution gravity field representation in the Nordic-Baltic region. *Mar. Geod.* **2017**, *40*, 416–453. [[CrossRef](#)]
- Sakil, F.F.; Erol, S.; Ellmann, A.; Erol, B. Geoid modeling by the least squares modification of Hotine's and Stokes' formulae using non-gridded gravity data. *Comput. Geosci.* **2021**, *156*, 104909. [[CrossRef](#)]
- dos Santos, N.P.; Escobar, I.P. Discrete evaluation of Stokes's integral by means of Voronoi and Delaunay structures. *J. Geod.* **2004**, *78*, 354–367. [[CrossRef](#)]
- Omang, O.C.D.; Forsberg, R. How to handle topography in practical geoid determination: Three examples. *J. Geod.* **2000**, *74*, 458–466. [[CrossRef](#)]
- Tscherning, C.C.; Forsberg, R. Geoid determination in the Nordic countries from gravity and height data. *Boll. Geod. Sci. Affin.* **1987**, *46*, 21–43.
- Forsberg, R. A new high-resolution geoid of the Nordic area. In *Determination of the Geoid*; Rapp, R.H., Sansò, F., Eds.; Springer: New York, NY, USA, 1991; pp. 241–250. [[CrossRef](#)]
- Forsberg, R.; Kaminskis, J.; Solheim, D. Geoid of the Nordic and Baltic region from gravimetry and satellite altimetry. In *Gravity, Geoid and Marine Geodesy*; Segawa, J., Fujimoto, H., Okubo, S., Eds.; Springer: Berlin, Germany, 1997; pp. 540–547. [[CrossRef](#)]
- Denker, H.; Torge, W. The European gravimetric quasigeoid EGG97—An IAG supported continental enterprise. In *Geodesy on the Move*; Forsberg, R., Feissel, M., Dietrich, R., Eds.; Springer: Berlin, Germany, 1998; pp. 249–254. [[CrossRef](#)]

23. Omang, O.C.D.; Forsberg, R. The Northern European geoid: A case study on long-wavelength geoid errors. *J. Geod.* **2002**, *76*, 369–380. [[CrossRef](#)]
24. Forsberg, R.; Strykowski, G.; Solheim, D. NKG-2004 geoid of the Nordic and Baltic area. In Proceedings of the International Association of Geodesy Symposium on Gravity, Geoid, and Space Missions, Porto, Portugal, 30 August–3 September 2004.
25. Denker, H.; Barriot, J.-P.; Barzaghi, R.; Fairhead, D.; Forsberg, R.; Ihde, J.; Kenyeres, A.; Marti, U.; Sarrailh, M.; Tziavos, I.N. The development of the European gravimetric geoid model EGG07. In *Observing our Changing Earth*; Sideris, M.G., Ed.; Springer: Berlin, Germany, 2009; pp. 177–185. [[CrossRef](#)]
26. Denker, H. Regional gravity field modeling: Theory and practical results. In *Sciences of Geodesy—II*; Xu, G., Ed.; Springer: Berlin, Germany, 2013; pp. 185–291. [[CrossRef](#)]
27. Ågren, J.; Strykowski, G.; Bilker-Koivula, M.; Omang, O.; Mårdla, S.; Oja, T.; Ellmann, A.; Liepins, I.; Parseliunas, E.; Forsberg, R.; et al. On the development of the new Nordic gravimetric geoid model NKG2015. In Proceedings of the 26th International Union of Geodesy and Geophysics General Assembly, Prague, Czech Republic, 22 June–2 July 2015. [[CrossRef](#)]
28. Denker, H. A new European gravimetric (quasi)geoid EGG2015. In Proceedings of the 26th International Union of Geodesy and Geophysics General Assembly, Prague, Czech Republic, 22 June–2 July 2015.
29. Ågren, J.; Strykowski, G.; Bilker-Koivula, M.; Omang, O.; Mårdla, S.; Forsberg, R.; Ellmann, A.; Oja, T.; Liepins, I.; Parseliunas, E.; et al. The NKG2015 gravimetric geoid model for the Nordic-Baltic region. In Proceedings of the International Symposium on Gravity, Geoid and Height Systems 2016, Thessaloniki, Greece, 19–23 September 2016. [[CrossRef](#)]
30. Dahl, O.C.; Forsberg, R. Geoid models around Sognefjord using depth data. *J. Geod.* **1998**, *72*, 547–556. [[CrossRef](#)]
31. Schwabe, J.; Ågren, J.; Liebsch, G.; Westfeld, P.; Hammarklint, T.; Mononen, J.; Andersen, O.B. The Baltic Sea Chart Datum 2000 (BSCD2000)—Implementation of a common reference level in the Baltic Sea. *Int. Hydrogr. Rev.* **2020**, *23*, 63–83.
32. Varbla, S.; Ågren, J.; Ellmann, A.; Poutanen, M. Treatment of tide gauge time series and marine GNSS measurements for vertical land motion with relevance to the implementation of the Baltic Sea Chart Datum 2000. *Remote Sens.* **2022**, *14*, 920. [[CrossRef](#)]
33. Bouin, M.-N.; Ballu, V.; Calmant, S.; Boré, J.-M.; Folcher, E.; Ammann, J. A kinematic GPS methodology for sea surface mapping, Vanuatu. *J. Geod.* **2009**, *83*, 1203. [[CrossRef](#)]
34. Saari, T.; Bilker-Koivula, M.; Koivula, H.; Nordman, M.; Häkli, P.; Lahtinen, S. Validating geoid models with marine GNSS measurements, sea surface models, and additional gravity observations in the Gulf of Finland. *Mar. Geod.* **2021**, *44*, 196–214. [[CrossRef](#)]
35. Varbla, S.; Liibus, A.; Ellmann, A. Shipborne GNSS-determined sea surface heights using geoid model and realistic dynamic topography. *Remote Sens.* **2022**, *14*, 2368. [[CrossRef](#)]
36. Gruno, A.; Liibus, A.; Ellmann, A.; Oja, T.; Vain, A.; Jürgenson, H. Determining sea surface heights using small footprint airborne laser scanning. In Proceedings of the Remote Sensing of the Ocean, Sea Ice, Coastal Waters, and Large Water Regions 2013, Dresden, Germany, 23–26 September 2013. [[CrossRef](#)]
37. Zlinszky, A.; Timár, G.; Weber, R.; Székely, B.; Briese, C.; Ressel, C.; Pfeifer, N. Observation of a local gravity potential isosurface by airborne lidar of Lake Balaton, Hungary. *Solid Earth* **2014**, *5*, 355–369. [[CrossRef](#)]
38. Varbla, S.; Ellmann, A.; Delpêche-Ellmann, N. Applications of airborne laser scanning for determining marine geoid and surface waves properties. *Eur. J. Remote Sens.* **2021**, *54*, 557–567. [[CrossRef](#)]
39. Jahanmard, V.; Delpêche-Ellmann, N.; Ellmann, A. Realistic dynamic topography through coupling geoid and hydrodynamic models of the Baltic Sea. *Cont. Shelf Res.* **2021**, *222*, 104421. [[CrossRef](#)]
40. Heiskanen, W.A.; Moritz, H. *Physical Geodesy*; W. H. Freeman and Company: San Francisco, CA, USA, 1967.
41. Moritz, H. Geodetic Reference System 1980. *J. Geod.* **2000**, *74*, 128–133. [[CrossRef](#)]
42. Forsberg, R.; Tscherning, C.C. The use of height data in gravity field approximation by collocation. *J. Geophys. Res. Solid Earth* **1981**, *86*, 7843–7854. [[CrossRef](#)]
43. Forsberg, R. *A Study of Terrain Reductions, Density Anomalies and Geophysical Inversion Methods in Gravity Field Modelling*; Ohio State University: Columbus, OH, USA, 1984.
44. Moritz, H. *Advanced Physical Geodesy*; Wichmann: Karlsruhe, Germany, 1980.
45. Kasper, J.F. A second-order Markov gravity anomaly model. *J. Geophys. Res.* **1971**, *76*, 7844–7849. [[CrossRef](#)]
46. Sjöberg, L.E. Refined least squares modification of Stokes’ formula. *Manus. Geod.* **1991**, *16*, 367–375.
47. Ellmann, A. Computation of three stochastic modifications of Stokes’s formula for regional geoid determination. *Comput. Geosci.* **2005**, *31*, 742–755. [[CrossRef](#)]
48. Ellmann, A. Using high-resolution spectral models of gravity anomaly for computing stochastic modifications of Stokes’s formula. *Comput. Geosci.* **2012**, *39*, 188–190. [[CrossRef](#)]
49. Paul, M.K. A method of evaluating the truncation error coefficients for geoidal height. *Bull. Géodésique* **1973**, *110*, 413–425. [[CrossRef](#)]
50. Hagiwara, Y. A new formula for evaluating the truncation error coefficient. *Bull. Géodésique* **1976**, *50*, 131–135. [[CrossRef](#)]
51. Sjöberg, L.E. A solution to the downward continuation effect on the geoid determined by Stokes’ formula. *J. Geod.* **2003**, *77*, 94–100. [[CrossRef](#)]
52. Sjöberg, L.E. The IAG approach to the atmospheric geoid correction in Stokes’ formula and a new strategy. *J. Geod.* **1999**, *73*, 362–366. [[CrossRef](#)]
53. Sjöberg, L.E.; Nahavandchi, H. The atmospheric geoid effects in Stokes’ formula. *Geophys. J. Int.* **2000**, *140*, 95–100. [[CrossRef](#)]

54. Sjöberg, L.E. Topographic and atmospheric corrections of gravimetric geoid determination with special emphasis on the effects of harmonics of degrees zero and one. *J. Geod.* **2001**, *75*, 283–290. [[CrossRef](#)]
55. Sjöberg, L.E. Ellipsoidal corrections to order e^2 of geopotential coefficients and Stokes' formula. *J. Geod.* **2003**, *77*, 139–147. [[CrossRef](#)]
56. Ellmann, A.; Sjöberg, L.E. Ellipsoidal correction for the modified Stokes formula. *Boll. Geod. Sci. Affin.* **2004**, *63*, 153–172.
57. Sjöberg, L.E. A spherical harmonic representation of the ellipsoidal correction to the modified Stokes formula. *J. Geod.* **2004**, *78*, 180–186. [[CrossRef](#)]
58. Ågren, J.; Sjöberg, L.E.; Kiamehr, R. The new gravimetric quasigeoid model KTH08 over Sweden. *J. Appl. Geod.* **2009**, *3*, 143–153. [[CrossRef](#)]
59. Ellmann, A. A numerical comparison of different ellipsoidal corrections to Stokes' formula. In *A Window on the Future of Geodesy*; Sansò, F., Ed.; Springer: Berlin, Germany, 2005; pp. 409–414. [[CrossRef](#)]
60. Mårdla, S.; Ellmann, A.; Ågren, J.; Sjöberg, L.E. Regional geoid computation by least squares modified Hotine's formula with additive corrections. *J. Geod.* **2018**, *92*, 253–270. [[CrossRef](#)]
61. Ekman, M. Impacts of geodynamic phenomena on systems for height and gravity. *Bull. Géoésique* **1989**, *63*, 281–296. [[CrossRef](#)]
62. Poutanen, M.; Vermeer, M.; Mäkinen, J. The permanent tide in GPS positioning. *J. Geod.* **1996**, *70*, 499–504. [[CrossRef](#)]
63. GEBCO_2021 Grid. Available online: <https://doi.org/10.5285/c6612cbe-50b3-0cff-e053-6c86abc09f8f> (accessed on 25 March 2022).
64. Hao, R.; Wan, X.; Wang, Y.; Annan, R.F.; Sui, X. Evaluation of four global bathymetry models by shipborne depths data. *J. Surv. Eng.* **2022**, *148*, 04021033. [[CrossRef](#)]
65. Leppäranta, M.; Myrberg, K. *Physical Oceanography of the Baltic Sea*; Springer: Berlin, Germany, 2009. [[CrossRef](#)]
66. Riley, S.J.; DeGloria, S.D.; Elliot, R. A terrain ruggedness index that quantifies topographic heterogeneity. *Intermt. J. Sci.* **1999**, *5*, 23–27.
67. Pail, R.; Gruber, T.; Fecher, T.; GOCO Project Team. The combined gravity model GOCO05c. *GFZ Data Serv.* **2016**. [[CrossRef](#)]
68. Fecher, T.; Pail, R.; Gruber, T.; the GOCO Consortium. GOCO05c: A new combined gravity field model based on full normal equations and regionally varying weighting. *Surv. Geophys.* **2017**, *38*, 571–590. [[CrossRef](#)]
69. Förste, C.; Abrykosov, O.; Bruinsma, S.; Dahle, C.; König, R.; Lemoine, J.-M. ESA's release 6 GOCE gravity field model by means of the direct approach based on improved filtering of the reprocessed gradients of the entire mission (GO_CONS_GCF_2_DIR_R6). *GFZ Data Serv.* **2019**. [[CrossRef](#)]
70. Kvas, A.; Mayer-Gürr, T.; Krauss, S.; Brockmann, J.M.; Schubert, T.; Schuh, W.-D.; Pail, R.; Gruber, T.; Jäggi, A.; Meyer, U. The satellite-only gravity field model GOCO06s. *GFZ Data Serv.* **2019**. [[CrossRef](#)]
71. Kvas, A.; Brockmann, J.M.; Krauss, S.; Schubert, T.; Gruber, T.; Meyer, U.; Mayer-Gürr, T.; Schuh, W.-D.; Jäggi, A.; Pail, R. GOCO06s—A satellite-only global gravity field model. *Earth Syst. Sci. Data* **2021**, *13*, 99–118. [[CrossRef](#)]
72. Zingerle, P.; Pail, R.; Gruber, T.; Oikonomidou, X. The experimental gravity field model XGM2019e. *GFZ Data Serv.* **2019**. [[CrossRef](#)]
73. Zingerle, P.; Pail, R.; Gruber, T.; Oikonomidou, X. The combined global gravity field model XGM2019e. *J. Geod.* **2020**, *94*, 66. [[CrossRef](#)]
74. Rüdja, A.; Varbla, S. Estonian GNSS-leveling dataset with relevance to the implementation of the Baltic Sea Chart Datum 2000. *SEANOE* **2022**. [[CrossRef](#)]
75. Vestøl, O.; Ågren, J.; Steffen, H.; Kierulf, H.; Tarasov, L. NKG2016LU: A new land uplift model for Fennoscandia and the Baltic region. *J. Geod.* **2019**, *93*, 1759–1779. [[CrossRef](#)]
76. Varbla, S.; Ellmann, A.; Delpeche-Ellmann, N. Validation of marine geoid models by utilizing hydrodynamic model and shipborne GNSS profiles. *Mar. Geod.* **2020**, *43*, 134–162. [[CrossRef](#)]
77. Liibus, A.; Varbla, S.; Ellmann, A.; Vahter, K.; Uiboupin, R.; Delpeche-Ellmann, N. Shipborne GNSS acquisition of sea surface heights in the Baltic Sea. *J. Geod. Sci.* **2022**. *in print*. [[CrossRef](#)]
78. Forsberg, R.; Olesen, A.V.; Keller, K.; Møller, M.; Gidskehaug, A.; Solheim, D. Airborne gravity and geoid surveys in the Arctic and Baltic seas. In Proceedings of the International Symposium on Kinematic Systems in Geodesy, Geomatics and Navigation (KIS-2001), Banff, Canada, 5–8 June 2001.
79. Ellmann, A. Downward continuation of airborne gravity data using high-resolution global geopotential models. In Proceedings of the 8th International Conference on Environmental Engineering, Vilnius, Lithuania, 19–20 May 2011.
80. Förste, C.; Bruinsma, S.L.; Abrykosov, O.; Lemoine, J.-M.; Marty, J.C.; Flechtner, F.; Balmino, G.; Barthelmes, F.; Biancale, R. EIGEN-6C4 the latest combined global gravity field model including GOCE data up to degree and order 2190 of GFZ Potsdam and GRGS Toulouse. *GFZ Data Serv.* **2014**. [[CrossRef](#)]
81. Oja, T.; Ellmann, A.; Mårdla, S. Gravity anomaly field over Estonia. *Estonian J. Earth Sci.* **2019**, *68*, 55–75. [[CrossRef](#)]
82. Mostafavi, M.; Delpeche-Ellmann, N.; Ellmann, A. Accurate sea surface heights from Sentinel-3A and Jason-3 retracers by incorporating high-resolution marine geoid and hydrodynamic models. *J. Geod. Sci.* **2021**, *11*, 58–74. [[CrossRef](#)]

Appendix 7

Publication VII

Varbla, S., & Ellmann, A. (2023). Iterative data assimilation approach for the refinement of marine geoid models using sea surface height and dynamic topography datasets. *Journal of Geodesy*, 97(3), #24. doi:10.1007/s00190-023-01711-7



Iterative data assimilation approach for the refinement of marine geoid models using sea surface height and dynamic topography datasets

Sander Varbla¹ · Artu Ellmann¹

Received: 20 September 2022 / Accepted: 1 February 2023
© Springer-Verlag GmbH Germany, part of Springer Nature 2023

Abstract

The modelling errors of marine geoid models may reach up to a few decimetres in the shorter wavelength spectrum due to gravity data void areas and/or inaccurate data. Various data acquisition methods can provide sea surface heights more accurately. Similarly, hydrodynamic model data in conjunction with tide gauge readings allow the derivation of reliable dynamic topography. Geometrical marine geoid heights, independent of the usual gravity-based marine geoid models, can be obtained by removing the estimated dynamic topography from sea surface height measurements. This study exploits such geometry information to refine marine geoid models. A data assimilation approach was developed that iteratively combines sea surface height and dynamic topography datasets with an initial gravimetric geoid model. A case study is presented using sea surface heights from shipborne GNSS campaigns and an airborne laser scanning survey for refining the EIGEN-6C4 global geopotential model. Comparisons with a high-resolution regional marine geoid model reveal that the initial discrepancies of up to around two decimetres reduce to sub-decimetre within the study area. It is concluded that the developed iterative data assimilation approach can significantly improve the accuracy of marine geoid models, especially in regions where gravity data are of poor quality or unavailable.

Keywords Data assimilation · Dynamic topography · Geoid · Hydrogeodesy · Least-squares collocation · Sea surface height

1 Introduction

Although remarkable effort has gone towards developing geoid modelling theory and approaches that support achieving high accuracy (e.g. see the overview of Wang et al. 2021), a significant offshore limitation is in the quality and distribution of marine gravity data. Satellite altimetry, the primary source of offshore gravity data products, provides uniform global coverage with an accuracy of a few mGal (e.g. Andersen and Knudsen 2019; Sandwell et al. 2021). A crucial exception, however, is the coastal region (also regions with complex seabed topography) where data quality degradation can be substantial, for instance, due to inaccuracies in

tidal correction and altimeter range estimation (e.g. Li et al. 2021; Zhang et al. 2021; Kamto et al. 2022). Conventional methods, such as shipborne (e.g. Lu et al. 2019; Ince et al. 2020) and airborne (e.g. Jamil et al. 2017; Wu et al. 2019) gravity surveys and measurements on ice (e.g. Noréus et al. 1997; Märdla et al. 2015), can instead provide high-quality data but are usually costly, laborious, and time-consuming. Additionally, it should be emphasized that historic marine gravity data may be unreliable (e.g. Denker and Roland 2005; Featherstone 2009; Kamto et al. 2022), for example, due to datum inconsistency-related issues. The distribution of high-quality marine gravity observations obtained using conventional methods is thus often sparse.

Determination accuracy of sea surface heights (SSHs) can surpass the modelling accuracy of marine geoid models, especially in the gravity data void areas (e.g. Müller et al. 2019; Varbla et al. 2020a). Accuracy better than a decimetre (and up to a few centimetres with some methods) is possible with satellite altimetry (e.g. Yang et al. 2019; Mostafavi et al. 2021), shipborne GNSS (global navigation satellite system) measurements (e.g. Bouin et al. 2009; Varbla et al. 2022a)

✉ Sander Varbla
sander.varbla@taltech.ee

Artu Ellmann
artu.ellmann@taltech.ee

¹ Department of Civil Engineering and Architecture, Tallinn University of Technology, Ehitajate Road 5, 19086 Tallinn, Estonia

and reflectometry (Roggenbuck and Reinking 2019), GNSS-equipped buoys (e.g. Zhou et al. 2020; Xie et al. 2021) and uncrewed sea vessels/floats (e.g. Penna et al. 2018; Bonnefond et al. 2022), and airborne laser scanning (e.g. Zlinszky et al. 2014; Varbla et al. 2021). High-quality SSH data acquisition does not necessarily require dedicated campaigns. For example, Rocken et al. (2005) and Roggenbuck et al. (2014) used commercial vessels for GNSS-based measurements, whereas Liibusk et al. (2022) mounted GNSS instrumentation on a marine condition monitoring research vessel for autonomous data acquisition. In the case of airborne laser scanning, Varbla et al. (2021) benefitted from the en route data collected during the routine mapping of offshore islands. However, SSH only approximates the geoid shape due to the ever-changing dynamic topography (DT) that separates the two terms.

Sea surface elevations from high-resolution hydrodynamic models (HDMs) are used widely for various practical and research applications. Some examples are operational sea level forecasting (e.g. Lagemaa et al. 2011; Fortunato et al. 2017), climate change influence assessment (e.g. Vousedoukas et al. 2016; Hong et al. 2020), and vertical datum unification (e.g. Slobbe et al. 2014; Filmer et al. 2018), which imply the capability of HDMs to capture realistic marine dynamics. A drawback, however, is that these models usually contain long-wavelength (Lagemaa et al. 2011; Jahanmard et al. 2021) spatiotemporal biases relative to the used vertical datums (e.g. Slobbe et al. 2013; Rulent et al. 2020). Such a dynamic bias (DB) contained in an HDM can be estimated and eliminated using vertical datum referred tide gauge (TG) stations' readings (e.g. Jahanmard et al. 2021; Varbla et al. 2022a). In an idealistic case, if the zeros of TGs also coincide with the geoid (e.g. Kollo and Ellmann 2019; Varbla et al. 2022b), combining HDM and TG data allows the derivation of realistic geoid-referred DT.

Offshore geoid geometry can then be determined by subtracting the derived DT from SSH measurements. So far, such geometry information has been used to validate marine geoid modelling solutions, effectively indicating problematic regions and significant model errors (e.g. Saari et al. 2021; Varbla 2022). This capability could be further exploited in refining the models (also indicated by Mazloff et al. 2014). Hence, this study aims to develop an iterative data assimilation approach that combines gravimetric geoid models with SSH and DT datasets. It will be demonstrated that these data can potentially improve marine geoid models, especially in regions described by poor-quality gravity data and gravity data void areas, where the most significant modelling errors could be expected. Data assimilation using geometry information for refining existing gravimetric marine geoid models can therefore be the follow-on stage to conventional gravimetric geoid modelling, analogously to the usage of GNSS-levelling fitting over dry land.

The remainder of this paper is organized as follows. Section 2 describes the developed methodological aspects, and subsequent Sect. 3 illustrates these with a case study. Note that quasigeoid-associated terminology is used throughout the following since the experiment region has officially adopted height anomalies. Nevertheless, the developed principles are equivalent for geoid/geoid undulations since, over marine areas, the quasigeoid coincides with the geoid. The paper continues with a discussion in Sect. 4 and ends with a brief conclusion in Sect. 5.

2 Method

In this section, the developed principles of the iterative data assimilation approach will be presented. Although an essential component of the method, discussion on the determination of SSHs is neglected for conciseness. It is assumed that a suitable and sufficiently accurate SSH data product exists (see the references to various methods in the Introduction). The developed method is illustrated with a case study (explained in Sect. 3) that employs data from shipborne GNSS campaigns (Varbla et al. 2020a; Liibusk et al. 2022) and an airborne laser scanning survey (Varbla et al. 2021).

Depending on the origin of SSH data, the permanent tide concept (e.g. Ekman 1989; Poutanen et al. 1996) varies. Typically, GNSS-based measurements use the tide-free concept, whereas the mean-tide concept is usual for altimetry products. A common permanent tide concept should be selected for SSH and DT data, and the gravimetric quasigeoid model to be refined. The practical conversion equations used in this study are (Mäkinen 2008; Ihde et al. 2019):

$$\Delta H_{\text{tide-free} \Rightarrow \text{zero-tide}}(\varphi) = 0.0603 - 0.1790 \sin^2 \varphi - 0.0019 \sin^4 \varphi, \quad (1)$$

$$\Delta H_{\text{mean-tide} \Rightarrow \text{zero-tide}}(\varphi) = 0.09940 - 0.29541 \sin^2 \varphi - 0.00042 \sin^4 \varphi, \quad (2)$$

where the tide-related height correction ΔH at a geodetic latitude φ is in meters (i.e. the coefficient values in these equations are in meters). Another consideration when using satellite altimetry data is the selection of a common reference ellipsoid (see the approaches of, for example, Mostafavi et al. 2021; Smith 2022). When relevant, data referred to the TOPEX/Poseidon ellipsoid (e.g. Jason altimeter series) should be converted relative to the GRS80 ellipsoid (or WGS84; the two can be considered equivalent within the frames of the current application). In this study, no such conversions were conducted because all data already referred to the GRS80 ellipsoid.

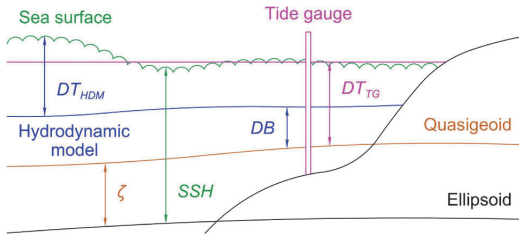


Fig. 1 Interrelations between the used datasets. Notice that the depicted DB (Eq. 3) is negative

2.1 Derivation of dynamic topography

Despite being an appealing source of DT information, HDMs should be utilized cautiously due to spatiotemporal biases relative to the used vertical datums. Since TG stations are nowadays commonly connected to the national height reference systems via precise levelling (e.g. Slobbe et al. 2014; Kollo and Ellmann 2019), the DB values of a HDM can be estimated at TG station locations (with coordinates $\varphi^{TG}, \lambda^{TG}$; also see Fig. 1):

$$DB(\varphi^{TG}, \lambda^{TG}, t) = DT_{HDM}(\varphi^{TG}, \lambda^{TG}, t) - DT_{TG}(\varphi^{TG}, \lambda^{TG}, t), \tag{3}$$

where DT_{HDM} and DT_{TG} are HDM- and TG-based DT, respectively, at an observation epoch t . Note that some essential considerations should be accounted for successful DB estimation:

1. The HDM and TG datasets should use a common permanent tide concept with the SSH data and gravimetric quasigeoid model. Hydrodynamic models and TG data generally utilize the mean-tide concept, but exceptions exist. For instance, the zero-tide concept is primarily used for the Baltic Sea region TG data (Varbla et al. 2022b).

region (Schwabe et al. 2020; Varbla 2022; Varbla et al. 2022b), which is compatible with the European Vertical Reference System associated national height system realizations of the Baltic Sea countries.

4. The relative TG sea level readings, which refer to local solid Earth, should be converted into the absolute frame and desired time epoch in the vertical land motion regions (i.e. movements of the local solid Earth must be considered). In the most common case, where vertical land motion is induced by glacial isostatic adjustment (i.e. vertical land motion is linear), the corresponding conversion is (Varbla et al. 2022b):

$$DT_{TG}(\varphi^{TG}, \lambda^{TG}, t) = DT_{RSL}(\varphi^{TG}, \lambda^{TG}, t, t_0) + VLM_{levelled}(\varphi^{TG}, \lambda^{TG}) \cdot (t - t_0), \tag{4}$$

where DT_{RSL} is TG-based relative DT and $VLM_{levelled}$ is levelled vertical land motion rate (i.e. geoid change rate should not be included) at a TG station. The term t_0 denotes the reference time epoch of a height reference system.

Once the DB values at TG stations are estimated, the offshore DB can be predicted by adapting least-squares collocation principles (Moritz 1980). This first involves estimating the DB uncertainty (following principles in Varbla et al. 2022a), which is based on two assumptions:

1. Over short timeframes (e.g. daily), the DB should remain relatively stable. Erratic behaviour could indicate, for example, poorly performing TGs or extreme weather conditions. Alternatively, DB variability could be due to modelling errors of the used HDM. The temporal domain uncertainty component σ_{db1} can be estimated as a moving standard deviation centred at an observation epoch t (Varbla et al. 2022a):

$$\sigma_{db1}(\varphi^{TG}, \lambda^{TG}, t) = \sqrt{\frac{1}{T_1 - 1} \sum_{i=t-\frac{T_1-1}{2}}^{t+\frac{T_1-1}{2}} \left[DB(\varphi^{TG}, \lambda^{TG}, i) - \frac{1}{T_1} \sum_{i=t-\frac{T_1-1}{2}}^{t+\frac{T_1-1}{2}} DB(\varphi^{TG}, \lambda^{TG}, i) \right]^2}, \tag{5}$$

2. Ocean tides should be treated consistently for the HDM, TG and SSH datasets. It should be emphasized that some, but not all, HDMs contain tidal information.
3. The TG data should refer to a common height reference system. For example, the Baltic Sea Chart Datum 2000 is a common geoid-based height reference for the Baltic Sea

where T_1 denotes the time window (i.e. the number of sequential hours) in which the DB is assumed to remain stable.

2. A long-wavelength signal represents the DB. Significant differences in DB values at nearby TG stations could indicate errors in levelling connections to the height reference system or localized phenomena occurring near a

TG station. Note that TG stations are generally in sheltered locations (e.g. river mouths, harbours), which may cause a difference relative to the offshore marine processes. For the spatial domain uncertainty estimation, the DB values at TG station A are first compared to those at $B = 1, \dots, N$ nearest TG stations, yielding averaged differences:

$$\overline{dDB}_B(\varphi^{TG_A}, \lambda^{TG_A}, t) = \frac{1}{T_2} \sum_{i=t-\frac{T_2-1}{2}}^{t+\frac{T_2-1}{2}} DB(\varphi^{TG_A}, \lambda^{TG_A}, i) - \frac{1}{T_2} \sum_{i=t-\frac{T_2-1}{2}}^{t+\frac{T_2-1}{2}} DB(\varphi^{TG_B}, \lambda^{TG_B}, i), \tag{6}$$

where T_2 denotes the considered time window ($T_2 > T_1$). Such a moving window (centred at an observation epoch t) is used due to infrequent localized phenomena that do not influence temporal domain uncertainty estimation (i.e. changes in sea level occur progressively). The spatial domain uncertainty component σ_{db2} at TG A can then be estimated as Varbla et al. (2022a):

$$\sigma_{db2}(\varphi^{TG}, \lambda^{TG}, t) = \sqrt{\frac{1}{N-1} \sum_{B=1}^N \left[\overline{dDB}_B(\varphi^{TG_A}, \lambda^{TG_A}, t) - \frac{1}{N} \sum_{B=1}^N \overline{dDB}_B(\varphi^{TG_A}, \lambda^{TG_A}, t) \right]^2}. \tag{7}$$

The temporal and spatial domain uncertainty components are assumed to be generally independent. Therefore, the uncertainty propagation law for uncorrelated quantities can be applied. The final DB uncertainty at a TG station is calculated as:

$$\sigma_{DB}(\varphi^{TG}, \lambda^{TG}, t) = \sqrt{[\sigma_{db1}(\varphi^{TG}, \lambda^{TG}, t)]^2 + [\sigma_{db2}(\varphi^{TG}, \lambda^{TG}, t)]^2 + [\sigma_{VLM}(\varphi^{TG}, \lambda^{TG}) \cdot (t - t_0)]^2}, \tag{8}$$

where σ_{VLM} is the uncertainty associated with the vertical land motion rate at a TG station. If the vertical land motion is negligible at the TG station site, the last component of the equation can be neglected.

Employing the DB uncertainty estimates, the offshore DB is predicted (computation points are selected according to the HDM grid nodes with coordinates $\varphi^{HDM}, \lambda^{HDM}$) using least-squares collocation (Moritz 1980):

$$\widehat{DB}(\varphi^{HDM}, \lambda^{HDM}, t) = C_{st}(C_{tt} + C_{nn})^{-1} DB(\varphi^{TG}, \lambda^{TG}, t), \tag{9}$$

where C_{st} is the cross-covariance matrix of the predicted (\widehat{DB}) and known (DB) signals, and C_{tt} and C_{nn} are the covariance matrices of known signal and observation errors

(uncertainties), respectively. Importantly, before prediction, the mean signal should be removed from the vector of the known (DB) signal (i.e. the vector should contain centred random variables), which can later be restored on the pre-

dicted (\widehat{DB}) signal. Note that in practical computations, the C_{st} and C_{tt} matrices are derived using a suitable theoretical model, which is fitted to empirical covariance values.

The DB prediction variance is obtained as Moritz (1980):

$$E_{ss} = C_{ss} - C_{st}(C_{tt} + C_{nn})^{-1} C_{st}^T, \tag{10}$$

where C_{ss} is the covariance matrix of the predicted signal, E_{ss} is its error covariance matrix, and parameter T is the transpose operator. The diagonal elements of matrix E_{ss} represent the DB prediction variance

$[\sigma_{\widehat{DB}}(\varphi^{HDM}, \lambda^{HDM}, t)]^2$ estimates. Since the estimated DB uncertainty (Eq. 8) depends on the agreement between the HDM and TG data (i.e. the two sources of DT data), the DT variance is taken to be equal to the DB prediction variance. The DT uncertainty used in the following is hence:

$$\sigma_{DT}(\varphi^{HDM}, \lambda^{HDM}, t) \equiv \sqrt{[\sigma_{\widehat{DB}}(\varphi^{HDM}, \lambda^{HDM}, t)]^2}. \tag{11}$$

The final DT itself is obtained by subtracting the predicted DB from the initial HDM at all the grid nodes ($\varphi^{HDM}, \lambda^{HDM}$):

$$\widehat{DT}(\varphi^{\text{HDM}}, \lambda^{\text{HDM}}, t) = DT_{\text{HDM}}(\varphi^{\text{HDM}}, \lambda^{\text{HDM}}, t) - \widehat{DB}(\varphi^{\text{HDM}}, \lambda^{\text{HDM}}, t). \tag{12}$$

Then, the estimates of the derived DT and its uncertainty at SSH data locations $(\varphi^{\text{SSH}}, \lambda^{\text{SSH}})$ can be found using bilinear interpolation in-between the corresponding quantities at adjacent locations $(\varphi^{\text{HDM}}, \lambda^{\text{HDM}})$.

2.2 Computation of geometric height anomalies

The derived DT estimates allow reducing the SSH data into geometric height anomalies (also see Fig. 1):

$$\zeta_{\text{geom}}^k(\varphi^{\text{SSH}}, \lambda^{\text{SSH}}, t) = \text{SSH}^k(\varphi^{\text{SSH}}, \lambda^{\text{SSH}}, t) - \widehat{DT}^k(\varphi^{\text{SSH}}, \lambda^{\text{SSH}}, t), \tag{13}$$

where superscript k ($1 \leq k$) is introduced to distinguish between data assimilation iterations. Uncertainty of geometric height anomalies is calculated as in Eq. (8):

$$\sigma_{\text{geom}}^k(\varphi^{\text{SSH}}, \lambda^{\text{SSH}}, t) = \sqrt{[\sigma_{\text{SSH}}^k(\varphi^{\text{SSH}}, \lambda^{\text{SSH}}, t)]^2 + [\sigma_{\widehat{DT}}^k(\varphi^{\text{SSH}}, \lambda^{\text{SSH}}, t)]^2}. \tag{14}$$

Analogously to offshore DB prediction in Sect. 2.1, the aim is to grid the discrete geometric height anomalies for obtaining a continuous surface. These grids of geometric height anomalies and associated uncertainties are needed for adjusting the quasigeoid model between the SSH data point locations. However, the geometric height anomalies are ill-suited for gridding using least-squares collocation. A quasigeoid model ($k = 1$ is the initial gravimetric model; the permanent tide concept should be common with SSH and DT datasets) is therefore used to obtain residual heights:

$$r^k(\varphi^{\text{SSH}}, \lambda^{\text{SSH}}, t) = \zeta_{\text{geom}}^k(\varphi^{\text{SSH}}, \lambda^{\text{SSH}}, t) - \zeta_{\text{model}}^k(\varphi^{\text{SSH}}, \lambda^{\text{SSH}}). \tag{15}$$

As it is likely that the available data does not stretch everywhere (e.g. land areas), data void regions should be padded with near-zero residual signal to avoid extrapolation errors. The minimum padding distance (i.e. more distant regions are padded) from available data points will be denoted l_{ZP} . The residual heights and zero pad are then gridded jointly analogously to offshore DB prediction (refer to Eqs. 9 and 10). Computation points are selected according to the quasigeoid model grid nodes (with coordinates φ, λ). The quasigeoid model uncertainty is not propagated (i.e. σ_{geom}^k is used; see

Eq. 14) since the removed quasigeoid model signal is restored in the post-gridding stage to obtain gridded geometric height anomalies (a similar approach is used, e.g. in gravity data gridding; Mårdla et al. 2017):

$$\widehat{\zeta}_{\text{geom}}^k(\varphi, \lambda) = \widehat{r}^k(\varphi, \lambda) + \zeta_{\text{model}}^k(\varphi, \lambda). \tag{16}$$

Because the uncertainty of geometric height anomalies is used as a gridding input, the variance of gridded geometric height anomalies is equivalent to the computed variance of gridded residual heights. The uncertainty of gridded geometric height anomalies is thus:

$$\sigma_{\widehat{\zeta}_{\text{geom}}}^k(\varphi, \lambda) \equiv \sqrt{[\sigma_{r^k}(\varphi, \lambda)]^2}. \tag{17}$$

Notice that the terms in Eqs. (16) and (17) are considered time-independent. While in offshore DB prediction, a single observation epoch is considered at a time, the data used in computing gridded geometric height anomalies represent various observation epochs (i.e. SSH data does not represent a single observation epoch). It is assumed that such a data combination eliminates the dependence on time (i.e. gridded height anomalies are static).

Before combining gridded geometric height anomalies with a quasigeoid model, it should be mentioned that the uncertainty of gridded geometric height anomalies in distant regions from the available SSH data depends on the selected uncertainty of the zero pad. This uncertainty should be moderate to avoid residual heights' signal leakage during least-squares collocation to the padding region. For the employed assimilation approach (cf. Sect. 2.3), on the other hand, significant uncertainties are essential for limiting the assimilation (primarily, for determining the uncertainty of the best assimilation estimate) to the available data region. The requirement would be fulfilled if $\sigma_{\widehat{\zeta}_{\text{geom}}}^k \gg \sigma_{\text{model}}^k$ in data void regions (i.e. regions represented by the generated zero pad), where σ_{model}^k represents the uncertainty of the quasigeoid model. The uncertainty of gridded geometric height anomalies is hence modified by a location-dependent modification coefficient MOD^k :

$$\sigma_{\text{MOD}}^k(\varphi, \lambda) = \sigma_{\widehat{\zeta}_{\text{geom}}}^k(\varphi, \lambda) \text{MOD}^k(\varphi, \lambda), \tag{18}$$

which aims to increase the uncertainty of gridded geometric height anomalies in distant regions from the available SSH data.

For computing the MOD^k coefficient, a function was constructed that results in smooth σ_{MOD}^k uncertainties in data and zero pad transition zones, whereby the function values after that zone increase rapidly, fulfilling the condition

$\sigma_{MOD}^k \gg \sigma_{model}^k$. The function (representing the MOD^k coefficient values) is defined as:

$$MOD^k(\varphi, \lambda) = 1 + e^{(\ln 10^M / l_{ZP})[l_{MOD}(\varphi, \lambda) - 3l_{ZP}/4]} - e^{-(\ln 10^M / l_{ZP})[l_{MOD}(\varphi, \lambda) + 3l_{ZP}/4]}, \quad (19)$$

where l_{ZP} is the selected minimum zero padding distance, and l_{MOD} is the distance from a computation point (φ, λ) to the closest data point $(\varphi^{SSH}, \lambda^{SSH})$. Parameter M controls the shape of the modification function (Fig. 2). At distance $l_{MOD} = 0$, the function always equals one, and with $M \geq 1$, the function reaches a value of approximately two at a three-quarters distance of l_{ZP} .

2.3 Iterative data assimilation

In this study, the cost function (modified from Reichle 2008) of the assimilation system is defined as:

$$J^k(\varphi, \lambda) = [2 - P(\varphi, \lambda)] \frac{[\zeta_{model}^{k+1}(\varphi, \lambda) - \zeta_{model}^k(\varphi, \lambda)]^2}{[\sigma_{model}^k(\varphi, \lambda)]^2} + P(\varphi, \lambda) \frac{[\zeta_{model}^{k+1}(\varphi, \lambda) - \widehat{\zeta}_{geom}^k(\varphi, \lambda)]^2}{[\sigma_{MOD}^k(\varphi, \lambda)]^2}, \quad (20)$$

where the weight P is:

$$\widehat{\zeta}_{model}^{k+1}(\varphi, \lambda) = \frac{P(\varphi, \lambda)[\sigma_{model}^k(\varphi, \lambda)]^2 \widehat{\zeta}_{geom}^k(\varphi, \lambda) + [2 - P(\varphi, \lambda)][\sigma_{MOD}^k(\varphi, \lambda)]^2 \zeta_{model}^k(\varphi, \lambda)}{P(\varphi, \lambda)[\sigma_{model}^k(\varphi, \lambda)]^2 + [2 - P(\varphi, \lambda)][\sigma_{MOD}^k(\varphi, \lambda)]^2}, \quad (23)$$

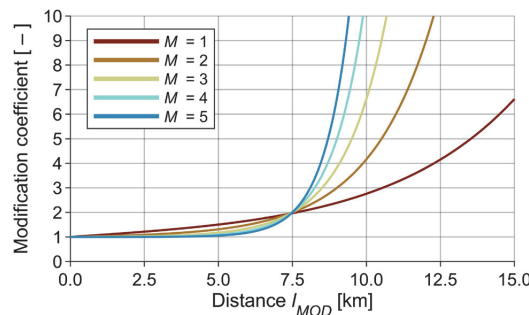


Fig. 2 The dependence of modification function (cf. Eq. 19) on parameter M by assuming a 10 km minimum zero padding distance. Function value at distance l_{MOD} represents the modification coefficient value used for modifying the gridded geometric height anomalies' uncertainty estimates (cf. Eq. 18)

$$P(\varphi, \lambda) = \begin{cases} 1, & |\widehat{r}^k(\varphi, \lambda)| \leq \sigma_{r_SSH}^k \\ \sqrt{\frac{\sigma_{r_SSH}^k}{|\widehat{r}^k(\varphi, \lambda)|}}, & |\widehat{r}^k(\varphi, \lambda)| > \sigma_{r_SSH}^k \end{cases} \quad (21)$$

$$\sigma_{r_SSH}^k = \sqrt{\frac{1}{I-1} \sum_{i=1}^I [\widehat{r}^k(\varphi^{SSH}, \lambda^{SSH}, i) - \frac{1}{I} \sum_{i=1}^I \widehat{r}^k(\varphi^{SSH}, \lambda^{SSH}, i)]^2}, \quad (22)$$

with $\sigma_{r_SSH}^k$ estimated using gridded residual heights at the locations of initial SSH data. Here, $i = 1, \dots, I$ denotes the number of an SSH data point (I being the total number of points). Gridded residual heights are used as the gridding procedure is expected to eliminate some of the data noise. Such a weighting scheme is implemented to reduce the influence of gridded geometric height anomalies in locations of most significant discrepancies relative to the quasigeoid model. In practical application, the discrepancies could be either due to errors in the quasigeoid model or SSH and DT data, with the truth being unknown (i.e. uncertainty estimates may not always be reliable). The weighting reduces the risk of propagating significant errors in SSH and DT data to the quasigeoid model.

The cost function J^k should be minimized relative to the refined quasigeoid model ζ_{model}^{k+1} to obtain the practical assimilation equation. Thus, solving the differential condition $\partial J^k / \partial \zeta_{model}^{k+1} = 0$ yields:

where $\widehat{\zeta}_{model}^{k+1}$ is the best assimilation estimate of ζ_{model}^{k+1} . The uncertainty of the best assimilation estimate is defined as:

$$\sigma_{model}^{k+1}(\varphi, \lambda) = \sqrt{\frac{[2 - P(\varphi, \lambda)][\sigma_{model}^k(\varphi, \lambda)]^2 [\sigma_{MOD}^k(\varphi, \lambda)]^2}{P(\varphi, \lambda)[\sigma_{model}^k(\varphi, \lambda)]^2 + [2 - P(\varphi, \lambda)][\sigma_{MOD}^k(\varphi, \lambda)]^2}}. \quad (24)$$

Due to the modification of the gridded geometric height anomalies' uncertainty (cf. Eq. 18), $\sigma_{MOD}^k \gg \sigma_{model}^k$ and consequently $\sigma_{model}^{k+1} \approx \sigma_{model}^k$ in SSH data void regions where no assimilation occurs.

The above system is solved iteratively, where each new iteration should be based on a new dataset of SSHs (i.e. repeated use of the same data should be avoided). This way, more new information (i.e. refinements) can be introduced to the final combined model as opposed to a case where all available data are combined to conduct a single assimilation

iteration. In other words, available data should be separated into sub-datasets used in consecutive assimilation iterations. Such an approach also allows refining propagated SSH and DT errors in the combined model, besides inaccuracies of the initial gravimetric quasigeoid model. Furthermore, the iterative scheme can always be continued once new data becomes available. Note that for the next assimilation iteration $\zeta_{\text{model}}^k \equiv \widehat{\zeta}_{\text{model}}^{k+1}$ and $\sigma_{\text{model}}^k \equiv \sigma_{\text{model}}^{k+1}$ in Eqs. (23) and (24). Since $\sigma_{\text{model}}^{k+1} < \sigma_{\text{model}}^k$ and $\sigma_{\text{model}}^{k+1} < \sigma_{\text{MOD}}^k$, the iterative solution converges.

The described iterative data assimilation methodology is summarized as a flowchart in Fig. 3. Results of the assimilation iteration $k = 1$ are denoted by red coloured rectangles (also the results of following iterations). These are then employed for the subsequent iterations $k \geq 2$ as the input, making the process iterative. The developed method is next illustrated with a case study.

3 Case study

The case study was conducted in the eastern section of the Baltic Sea, the Gulf of Finland (Fig. 4). The aim was to improve a quasigeoid model derived from a global geopotential model and then validate the results with a recent high-resolution regional quasigeoid model. For iterative refinement, the EIGEN-6C4 global geopotential model (Förste et al. 2014), evaluated to its maximum d/o of 2190 (height anomalies were computed on a $0.01^\circ \times 0.02^\circ$ grid), was selected due to its significant discrepancies north of Estonia (Fig. 5). The primary cause for Fig. 5 discrepancies, especially towards the west, is that the EIGEN-6C4 data does not sufficiently represent the region's significant negative anomalous gravity field. Similar modelling errors can be detected in EGM2008 (Ellmann et al. 2009), the data of which was the basis for the compilation of higher-degree coefficients of EIGEN-6C4 (Pavlis et al. 2012; Förste et al. 2014). These discrepancies also resemble the typical magnitude of errors in regional high-resolution models caused by gravity data void areas. For instance, Varbla et al. (2020a) and Varbla et al. (2021) have proven NKG2015 regional quasigeoid model (Ågren et al. 2016) errors around a decimetre in the eastern part of the Gulf of Finland.

A high-resolution regional gravimetric quasigeoid model (Fig. 4; computational details can be found in Varbla 2022), henceforth denoted as GQM2022, was employed to validate the iterative data assimilation results. Its accuracy over dry land is sub-centimetre, whereas, over marine areas, the accuracy is estimated to be in the sub-decimetre level. The model was computed using the least-squares modification of Stokes' formula with additive corrections (Sjöberg 2003; Sjöberg and Bagherbandi 2017). GOCO05c (Fecher

et al. 2017) was selected as the reference global geopotential model; modification limits were set to degree 200. Bathymetry data were utilized to refine the gravity field model used in quasigeoid determination. The GQM2022 computation also incorporated new shipborne marine gravity data (Varbla et al. 2020a; Saari et al. 2021), which were not included in developing the earlier NKG2015 model.

The SSH data originate from (i) Sektori shipborne GNSS campaign (Varbla et al. 2020a), (ii) six (denoted from C1 to C6) Salme shipborne GNSS campaigns (Liibus et al. 2022), and (iii) an airborne laser scanning survey (Varbla et al. 2021). Note that the Sektori and Salme SSH data were reprocessed similarly, following the principles in Varbla et al. (2022a). Interested readers are encouraged to refer to the papers mentioned above for details regarding SSH determination. The DT data described in these papers were not used here but were reanalysed and recomputed as described in the next section. Since all shipborne GNSS and airborne laser scanning data processing was conducted relative to the Estonian GNSS-CORS (continuously operating reference stations), the EIGEN-6C4-derived height anomalies and GQM2022 were fitted to the Estonian high-precision GNSS-levelling control points (Fig. 4; Rüdja and Varbla 2022) using a one-dimensional fit. Importantly, all the described datasets (including the DT data) use or were converted to the zero-tide permanent tide concept (cf. Equations 1 and 2) for consistency.

3.1 Derivation of dynamic topography

The NEMO-Nordic HDM (Hordoir et al. 2019; Kärnä et al. 2021) was used to derive DT. To estimate the DB (cf. Eq. 3) of NEMO-Nordic HDM, the same set of Estonian, Finnish, Latvian, Russian and Swedish TG stations, a total of 41 (cf. Fig. 4), was employed as in Varbla et al. (2022a). Tide gauge data were corrected for vertical land motion (cf. Eq. 4) using the NKG2016LU model (Vestøl et al. 2019). The pancontinental EVRF2019 (EVRF 2019) solution-based height system discrepancies relative to the Estonian EH2000 were used to improve TG data consistency. Since tides in the Baltic Sea generally remain within a few centimetres at most due to the narrow connection to the Atlantic Ocean via Danish straits (e.g. Medvedev et al. 2013, 2016), no special treatment for ocean tides was considered in this case study. However, it should be mentioned that consistently the tidal effect has not been removed from the used TG and SSH data. The potential influence of tides is therefore present in these datasets. To an extent, this influence cancels out when DT is subtracted from SSH because the modelled DT is tied to TG readings. In other words, minor discrepancies between TG readings and HDM-embedded DT due to different treatments of tides (similarly to TG and SSH data, NEMO-Nordic represents

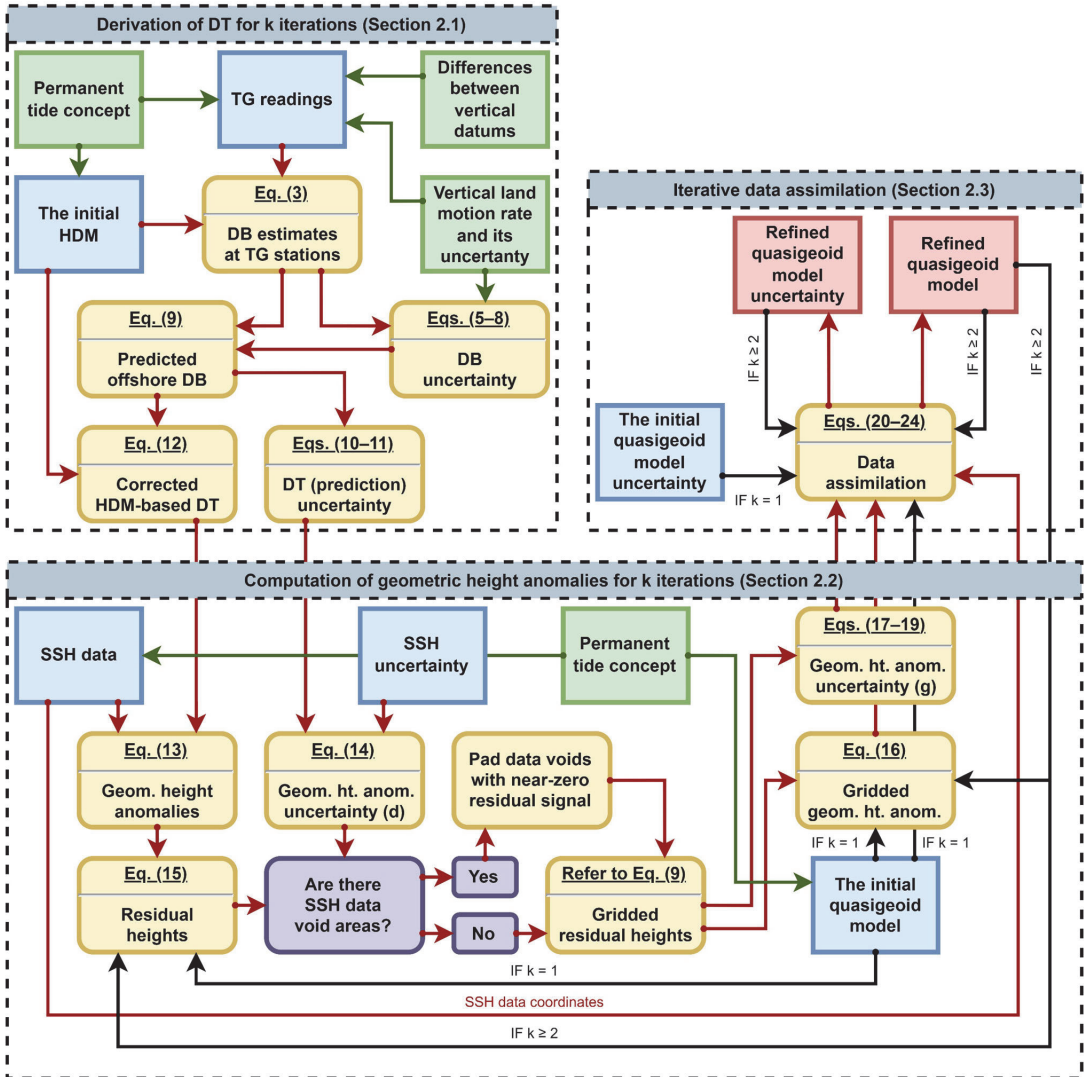


Fig. 3 Flowchart of the iterative data assimilation methodology for determining the refined quasigeoid model using sea surface height and dynamic topography datasets. Equation numbers above derived quantities and data processing steps refer to equations within the text that were employed for that specific procedure. The initial data sources

are denoted by blue (required) and green (optional) coloured rectangles, whereby red rectangles denote the assimilation results. Denotation (d) and (g) associated with the uncertainty of geometric height anomalies means discrete and gridded data, respectively

tides, but in a model instead of the observed form), if there are any, are considered within the DB.

Covariance analysis (for each time instance separately; in total, 1056 hourly time instances were analysed) was conducted to determine a suitable covariance model for

describing DB spatial dependence. Before covariance computations, the mean signal was removed from DB values to centre a dataset (tilt and mean signal reduction was also tested, but this yielded degraded DB prediction performance compared to the mean signal reduction only). Empirical DB autocovariance values were then computed in 25 km

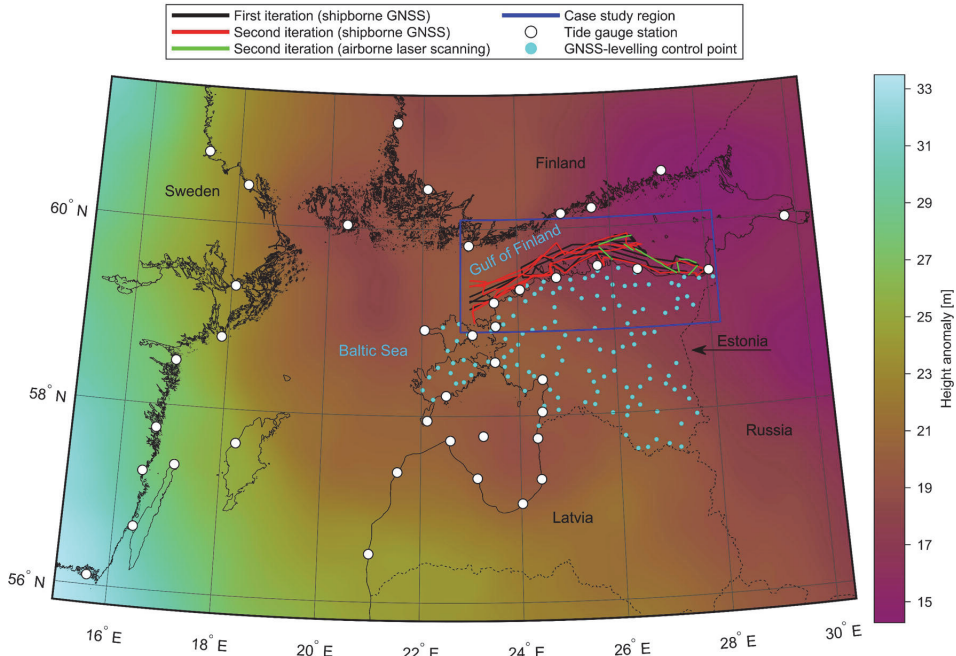


Fig. 4 Study area and the distribution of used data (see the legend). Note that GNSS-levelling control points (cyan-coloured dots) are not needed directly in the assimilation but were employed for dry-land fitting of the

involved quasigeoid models. In the background is the high-resolution GQM2022 quasigeoid model (fitted to the Estonian GNSS-levelling control points), which is used to validate this study's results

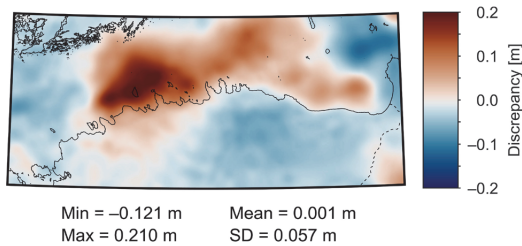


Fig. 5 Spatial distribution and statistics of the initial discrepancies between the EIGEN-6C4 and GQM2022 quasigeoid models. Both models are fitted to the Estonian GNSS-levelling control points

distance groups, whereby groups with less than 15 station pairs (regarding pairs AB and BA as the same, i.e. one) were excluded (also from subsequent evaluations). Autocovariance uncertainty was computed as a standard deviation estimate for each distance group. Note that DB estimates contain both HDM and TG errors, which can be of the same magnitude as DB (an example of DB uncertainty estimation at TG stations is presented in Varbla et al. 2022a). The variability of DB autocovariance values within a distance group can hence be rather significant, sometimes leading to

scattered autocovariance curves (use of 41 TG stations, i.e. including some data outside the case study region, improved covariance analysis).

The estimated empirical autocovariance curves (in total, 1056) were employed to test 11 isotropic covariance models by fitting these to the empirical values in the least-squares sense (signal variance was determined from data, not through the fitting procedure). These were Hirvonen's (Hirvonen 1962), exponential (Shaw et al. 1969), exponential-cosine (both variants in Vyskočil 1970 were tested, henceforth referred to as EQ4 and EQ5), second- and third-order Markov (Kasper 1971; Jordan 1972), Gaussian (Kearsley 1977), Reilly's (Reilly 1979), logarithmic (Forsberg 1987) and triple and quadruple real pole ARMA (Schubert et al. 2021) covariance models. Examples of each model can be seen in Fig. 6 (sub-plots a and b; also notice that the spatial correlation of DB can vary significantly at different time instances). Note that the least-squares fitted exponential-cosine covariance models (both variants) often oscillated unrealistically. On the other hand, three zero crossings generally occurred over the first 1000 km distance (similar to the EQ5 example in Fig. 6a) for successful model fits. Thus, an additional constraint of allowing at most four zero crossings (i.e. one extra crossing

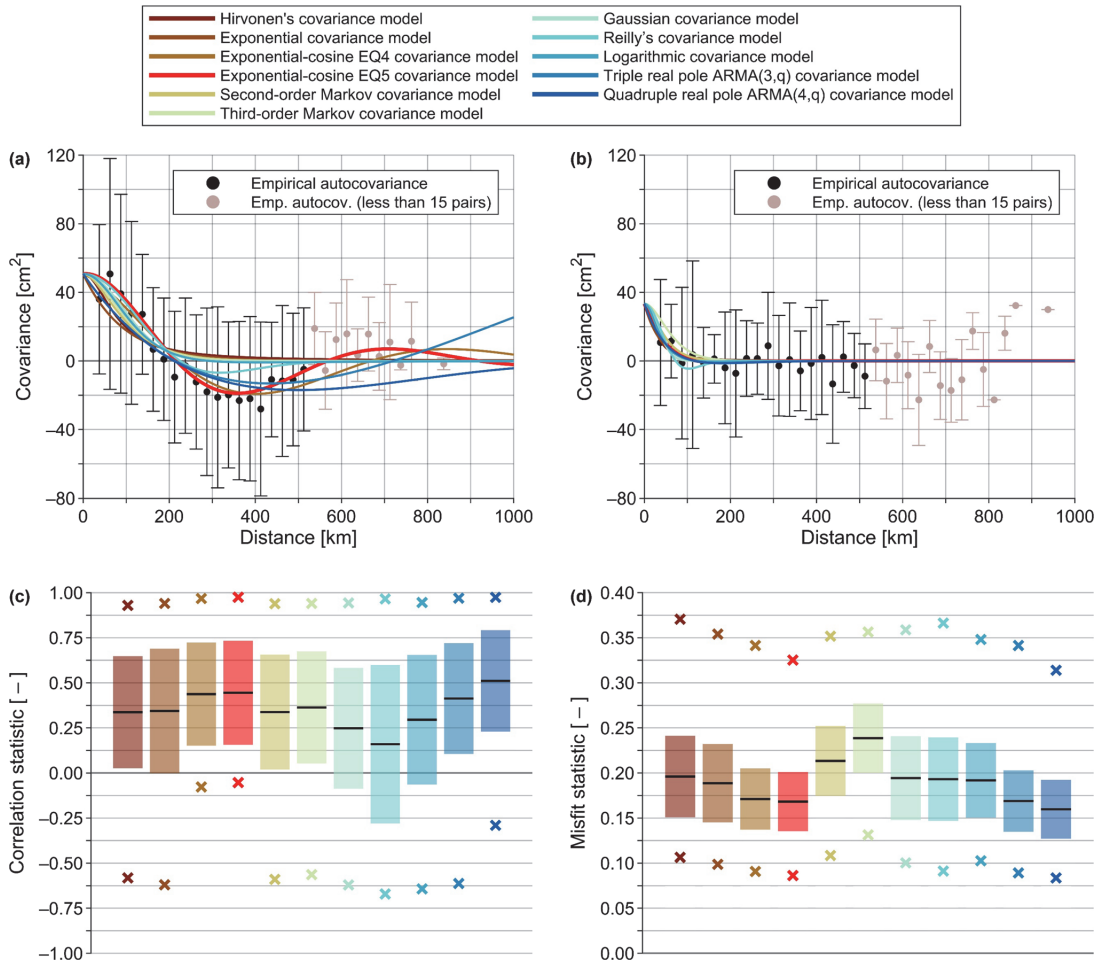


Fig. 6 Empirical DB autocovariance curves (uncertainty is shown with whiskers) corresponding to arbitrary time instances of 04.07.2017 00:00 UTC (a) and 28.07.2021 00:00 UTC (b), and respective least-squares fitted (distance groups with less than 15 station pairs were not considered) covariance models. Sub-plots (c) and (d) show covariance

models' associated statistics of Pearson correlation coefficients and misfits, respectively, based on 1056 h of DB data. Black lines denote mean values, coloured (see the legend) bars standard deviation estimates and coloured crosses minimum and maximum values

relative to the general case) was implemented in estimating the exponential-cosine covariance models' parameters.

The performance of the tested covariance models was evaluated by investigating their correlation with empirical autocovariance curves and misfits (MF_C) between the models and curves. The latter is defined as:

$$MF_C = \frac{1}{C_0} \sqrt{\frac{1}{N} \sum_{i=1}^N [C_{\text{model}}(l_i) - C_{\text{emp}}(l_i)]^2}, \quad (25)$$

where N is the number of distance groups, $C_{\text{model}}(l)$ is the modelled covariance value at a distance l , and $C_{\text{emp}}(l)$ is the empirical autocovariance value at a distance l . Since the magnitude of DB can vary significantly (from millimetres to decimetres), division with signal variance C_0 allows more definite comparisons. Descriptive statistics of Pearson correlation coefficients and misfits are summarized in Fig. 6 (sub-plots c and d, respectively). Better performance is associated with higher correlation (ideally near 1) and smaller misfit (ideally near 0). The decision of the covariance model selection was based on these statistics with the

primary focus on mean values (i.e. a theoretical model was selected according to the agreement with empirically estimated autocovariances).

Notice that the exponential-cosine and the triple and quadruple real pole ARMA covariance models show slightly better performance than the rest of the tested models. The primary reason is the ability of these models to describe, if necessary, the hole effect (e.g. Journel and Froidevaux 1982; Ababou et al. 1994) since distinct negative correlations over some distance typically seem to describe DB (similar to the empirical autocovariance curve example in Fig. 6a). Note that the Reilly’s covariance model and the logarithmic covariance model also allow negative spatial correlation modelling. However, the Reilly’s model always assumes that a negative correlation occurs (e.g. as in Fig. 6b example), and the logarithmic model allows modelling only minor negative correlation. Due to that, these two models perform similarly or worse (notice Pearson correlation-related statistics of the Reilly’s covariance model) than models that do not allow negative spatial correlation modelling (i.e. Hirvonen’s, exponential, second- and third-order Markov, and Gaussian covariance models).

According to Fig. 6 statistics, the best performing model for describing DB spatial dependence is the quadruple real pole ARMA covariance model. Even so, detailed examination revealed that the best fitting triple and quadruple real pole ARMA covariance models occasionally overestimated data spatial correlation (e.g. notice the triple real pole ARMA covariance model example in Fig. 6a) or had an unrealistic model shape (i.e. the models are too sensitive to empirical estimates). Hence, the exponential-cosine EQ5 covariance model (slightly better performing than the EQ4 variant) was chosen instead, which after the four zero crossings constraint, appeared to agree with empirical DB autocovariance curves adequately. The model is defined as:

$$C_{\text{model}}(l) = C_0 e^{-l/\alpha} [\cos(\beta l) + (\alpha/\beta) \sin(\beta l)], \quad (26)$$

where α and β are parameters (determined through nonlinear least-squares fitting) controlling the model shape, estimated through covariance analysis for each time instance separately. Due to the spatiotemporal variations of DB, the model shape (as do empirical autocovariance curves) can vary significantly. Two examples at arbitrary time instances can be seen in Fig. 6 (sub-plots a and b).

The DT was then derived following principles in Sect. 2.1, where the exponential-cosine EQ5 covariance model described the C_{st} and C_{tt} covariance matrices in Eqs. (9) and (10). Parameter T_1 in Eq. (5) was set to 25 h; \overline{dDB}_B computation (Eq. 6) was simplified by calculating mean differences (for each campaign separately) as:

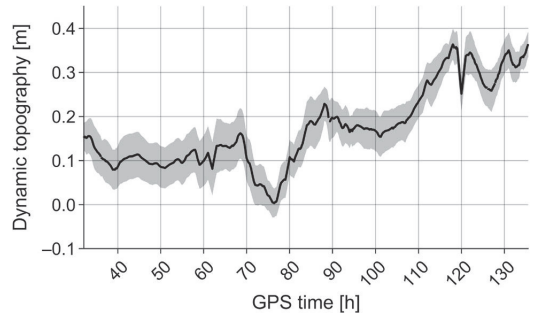


Fig. 7 Dynamic topography along the vessel’s route during the Salmé C2 shipborne GNSS campaign. The shaded area shows the associated 1-sigma uncertainty envelope

$$\begin{aligned} \overline{dDB}_B(\varphi^{\text{TGA}}, \lambda^{\text{TGA}}) &= \frac{1}{T_2} \sum_{i=1}^{T_2} DB(\varphi^{\text{TGA}}, \lambda^{\text{TGA}}, i) \\ &\quad - \frac{1}{T_2} \sum_{i=1}^{T_2} DB(\varphi^{\text{TGB}}, \lambda^{\text{TGB}}, i), \end{aligned} \quad (27)$$

where T_2 (from 96 to 192 h) is the duration over which DT computations were performed; comparisons were conducted with $N = 3$ (Eq. 7) nearest TG stations (i.e. all as was done in Varbla et al. 2022a). The moving window in Eq. (6) was neglected for computational efficiency since this would have required analysis and computation over much lengthier periods. As an example, the estimated DT (Eq. 12) with its associated uncertainty (Eqs. 10 and 11) during the Salmé C2 campaign is shown in Fig. 7.

3.2 Preparation of geometric height anomalies

Geometric height anomalies at discrete locations along the survey routes were calculated by subtracting the DT estimates from SSHs (Eq. 13). Biases between these datasets were then reduced using free network least-squares adjustment (analogously to Varbla et al. 2022a) considering all eight datasets altogether (Sektorí GNSS campaign, six Salmé GNSS campaigns and an airborne laser scanning survey). The geometric height anomalies employed in data assimilation were finally extracted within limits from 59° N to 60° N and from 23° E to 28° E (i.e. the case study region). These data are compared with the EIGEN-6C4-derived height anomalies and the GQM2022 model in Fig. 8. Resulting discrepancies in Fig. 8a are in good agreement with those shown in Fig. 5, whereby standard deviation estimates of 7.6 cm (EIGEN-6C4) and 3.4 cm (GQM2022) demonstrate the better performance of the GQM2022 model. Notice also

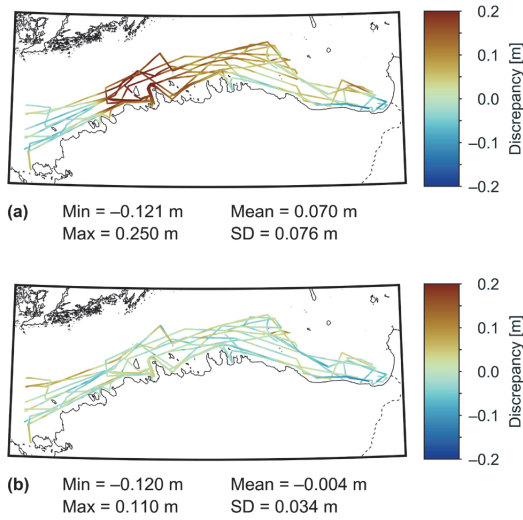


Fig. 8 Discrepancies (and associated statistics) of the EIGEN-6C4-derived height anomalies (a) and GQM2022 model (b) relative to the geometric height anomalies along the survey routes

the 7.0 cm mean discrepancy (i.e. systematic bias) associated with EIGEN-6C4, whereas the mean discrepancy of GQM2022 is near zero. The standard deviation estimates are 2.9 cm and 0.9 cm, respectively, from comparisons with the Estonian GNSS-levelling control points. These evaluations signify the suitability of the GQM2022 model for validating the iterative data assimilation results. Based on the assessment in Fig. 8a, a constant uncertainty of 8 cm was assumed for the EIGEN-6C4 during the data assimilation procedure.

For obtaining the uncertainty of geometric height anomalies, the uncertainty of SSHs was derived first. During Salme shipborne GNSS campaigns, the use of four GNSS antennas formed a rigid system. The heights of three antennas defined a plane that was then employed to estimate the control height of the remaining fourth antenna at each observation epoch. The difference between estimated and measured heights then provided GNSS measurement error estimates $d_{A\xi}(\varphi^{SSH}, \lambda^{SSH}, t)$, where $\xi = 1, \dots, 4$ is the controlled antenna number (cf. Eqs. 13–17 in Varbla et al. 2022a). The uncertainty associated with GNSS measurements was then calculated as:

$$\sigma_{GNSS}(\varphi^{SSH}, \lambda^{SSH}, t) = \frac{1}{4} \sum_{\xi=1}^4 |d_{A\xi}(\varphi^{SSH}, \lambda^{SSH}, t)|. \quad (28)$$

Note that for the Salme C4 campaign, data from only two antennas could be utilized (Liibus et al. 2022). Varbla et al. (2022a) demonstrated poorer SSH determination accuracy for that campaign as reducing vessel’s attitude effects on measurement data requires three GNSS antennas. The uncertainty of GNSS measurements of the C4 campaign was thus set to three times larger than the mean uncertainty of the other five campaigns (estimated mean uncertainty being 3.3 cm). Since three antennas were used during the Sektori shipborne GNSS campaign, such control calculations could not be conducted either. However, because the data processing strategy was the same as for Salme campaigns, the uncertainty of Sektori GNSS measurements was assumed to be equivalent to the mean uncertainty of 3.3 cm.

An additional uncertainty component related to the vertical land motion was included. During GNSS post-processing, the coordinates of GNSS-CORS were fixed to the reference epoch of the national reference frame. Due to the glacial isostatic adjustment occurring in the Baltic Sea region, however, the actual positions of GNSS-CORS (at an observation epoch t) may differ from the reference epoch positions. On land, such an approach facilitates consistency between reference coordinates and results of GNSS measurements (i.e. a height difference between GNSS-CORS and GNSS measurement location is referred to the reference epoch). For marine GNSS surveys, on the other hand, a discrepancy relative to the observation epoch positions is introduced because sea level trends do not directly follow vertical land motion (but contain geoid change induced by glacial isostatic adjustment). The post-processed heights were therefore corrected retrospectively for vertical land motion occurring at the GNSS-CORS following Varbla et al. (2022b); the NKG2016LU model was used. Furthermore, Varbla et al. (2022a) demonstrated inaccuracies in the sailing-related corrections (squat effect and changes in static draft) that also contribute to the errors of determined SSHs. Hence, an additional 3 cm uncertainty component σ_{CORR} related to the inaccuracies of sailing-related corrections was considered. The final SSH uncertainty of shipborne GNSS campaigns was derived as:

$$\sigma_{SSH}(\varphi^{SSH}, \lambda^{SSH}, t) = \sqrt{[\sigma_{GNSS}(\varphi^{SSH}, \lambda^{SSH}, t)]^2 + [\sigma_{VLM}(\varphi^{CORS}, \lambda^{CORS}) \cdot (t - t_0)]^2 + \sigma_{CORR}^2}, \quad (29)$$

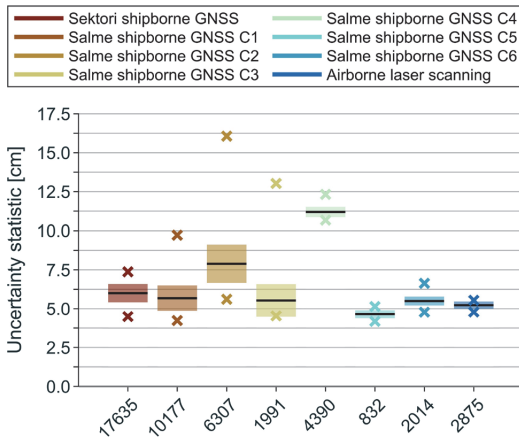


Fig. 9 Descriptive statistics of geometric height anomalies’ uncertainty estimates. Black lines denote mean values, coloured bars standard deviation estimates and coloured crosses minimum and maximum values. The X-axis shows the number of corresponding data points within the case study region

where superscript *CORS* refers to the coordinates of a GNSS-CORS (relative to which GNSS post-processing was conducted) and t_0 is the reference frame’s reference time epoch. Following evaluations in Varbla et al. (2020b, 2021), the SSH uncertainty of airborne laser scanning was assumed to be 3 cm.

Uncertainty of geometric height anomalies was calculated employing Eq. (14). Figure 9 presents the descriptive statistics of these uncertainty estimates for all eight datasets (considering the specified limits of the case study region). Slightly more considerable uncertainty of the Salme C2 campaign compared to the other datasets (excluding the Salme C4 campaign) is due to inaccuracies associated with reducing GNSS antenna heights to the sea surface (Varbla et al. 2022a), which increase the σ_{GNSS} uncertainty component.

3.3 Gridding of geometric height anomalies

The geometric height anomalies were divided between two assimilation iterations considering the data distribution. In the first iteration ($k = 1$), Sektori and Salme C4–C6 shipborne GNSS datasets were used, whereas the second iteration ($k = 2$) included Salme C1–C3 shipborne GNSS and airborne laser scanning datasets (cf. Fig. 4). Since the combined datasets were unnecessarily dense, these were thinned by averaging all points within each $0.01^\circ \times 0.02^\circ$ grid cell both in value and spatially. Such data thinning can also reduce data noise and help avoid aliasing during gridding. The geometric height anomalies used in the first iteration were then reduced to residual heights r^1 (Eq. 15) using the EIGEN-6C4-derived height anomalies. A zero pad was generated on

a $0.01^\circ \times 0.02^\circ$ grid, where the minimum distance to residual heights was set to 10 km (i.e. l_{ZP} in Eq. 19). The uncertainty of the zero pad was defined as the mean uncertainty of used geometric height anomalies, which appeared to provide optimal gridding solutions (based on visual inspection and subsequent assimilation validation results). Note that all subsequent computations were conducted (i.e. the zero pad generation region) considering a slightly larger area than the case study region (an additional 0.5° and 1° in the latitudinal and longitudinal direction, respectively) to avoid artefacts at edges.

The shorter wavelength spectrum errors primarily associated with EIGEN-6C4 dominate the determined residual heights (but also contain inaccuracies of geometric height anomalies), suggesting that the residual heights correlate only over a limited area. Covariance analysis and gridding employing least-squares collocation were thus conducted using a moving window, where data within the radius of 30 km from a computation point was considered at a time. The zero pad values were treated as residual heights in covariance analysis and gridding. A suitable covariance model for describing the spatial dependence of residual heights was determined following the principles described in Sect. 3.1. Before covariance computations, the mean signal was removed from residual heights to centre a dataset (mean signal values at computation points can be seen in Fig. 11a). Empirical autocovariance values were then computed in 2 km distance groups, whereby groups with less than 50 station pairs were excluded. Computations were conducted only if at least 50 data points (not considering the zero pad) could be found within the 30 km radius from the computation point. For the first iteration, a total of 17,721 computation points were determined.

The estimated empirical autocovariance curves (in total, 17,721) were employed to test the previously listed 11 covariance models (cf. Section 3.1). At most, four zero crossings over the first 100 km distance were allowed in estimating the exponential-cosine covariance models’ parameters. An arbitrarily selected example of a residual heights’ autocovariance curve and corresponding least-squares fitted covariance models can be seen in Fig. 10a (note that this example represents only a single computation point out of 17,721 in total). Evaluation results of covariance models are summarized in Fig. 10 sub-plots c and e.

It can be noticed that according to the covariance analysis, the best performance is associated with the ARMA covariance models. However, tests with models allowing negative spatial correlation (e.g. notice quadruple real pole ARMA covariance model in Fig. 10a) provided unsatisfactory gridding results, especially in areas of sparse data or between the data and zero pad, where opposite-signed gridded residual heights tended to appear. Therefore, a covariance model that decays gradually to zero (these are Hirvonen’s, exponential,

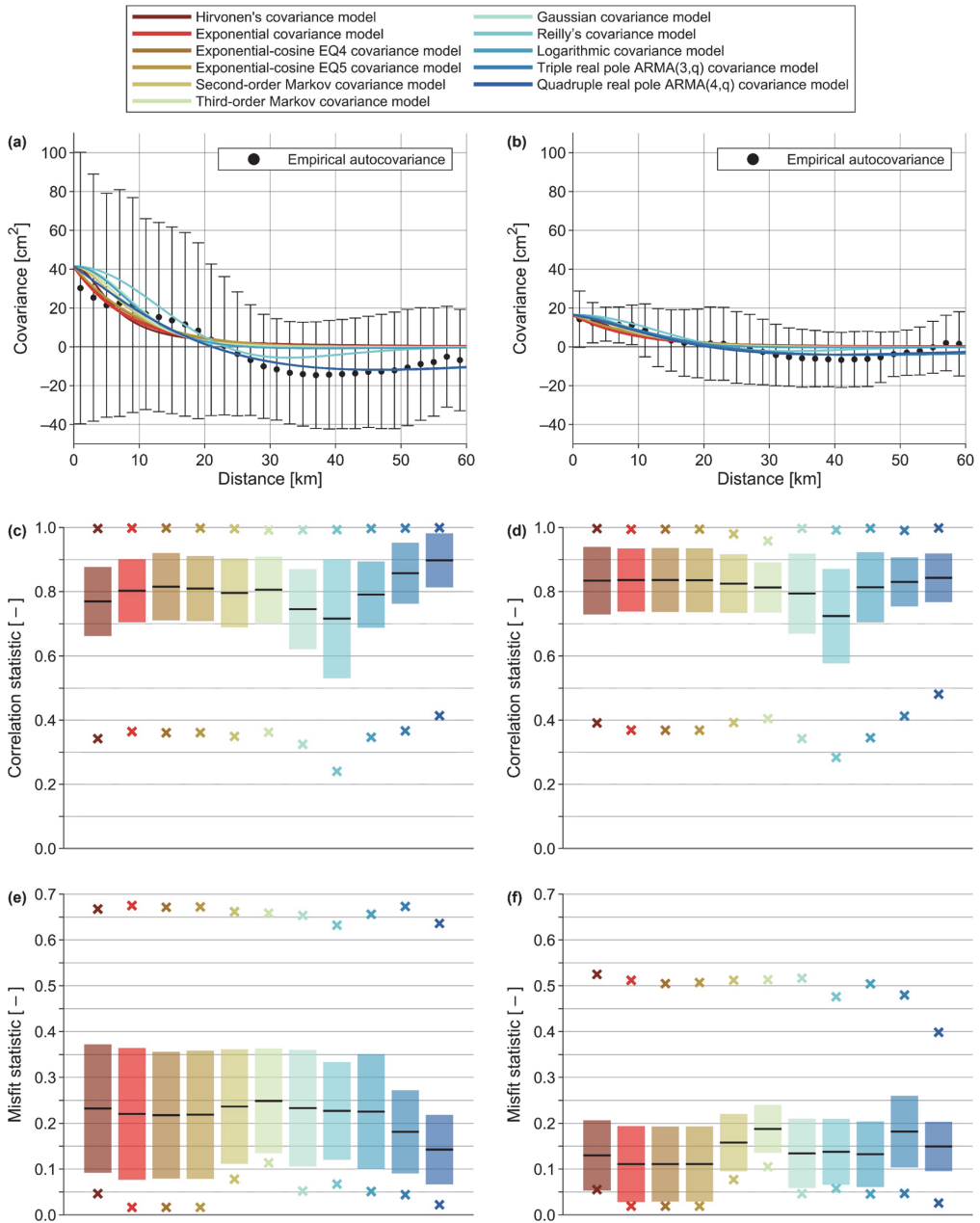


Fig. 10 Empirical residual heights' autocovariance curves (uncertainty is shown with whiskers) corresponding to the first (a) and second (b) iteration at arbitrarily selected computation points, and respective least-squares fitted covariance models. Sub-plots (c, d) and (e, f) show covariance models' associated statistics of Pearson correlation coefficients and misfits, respectively, based on 17,721 computation points of

the first iteration (c, e) and 17,783 computation points of the second iteration (d, f). Black lines denote mean values, coloured (see the legend) bars standard deviation estimates and coloured crosses minimum and maximum values

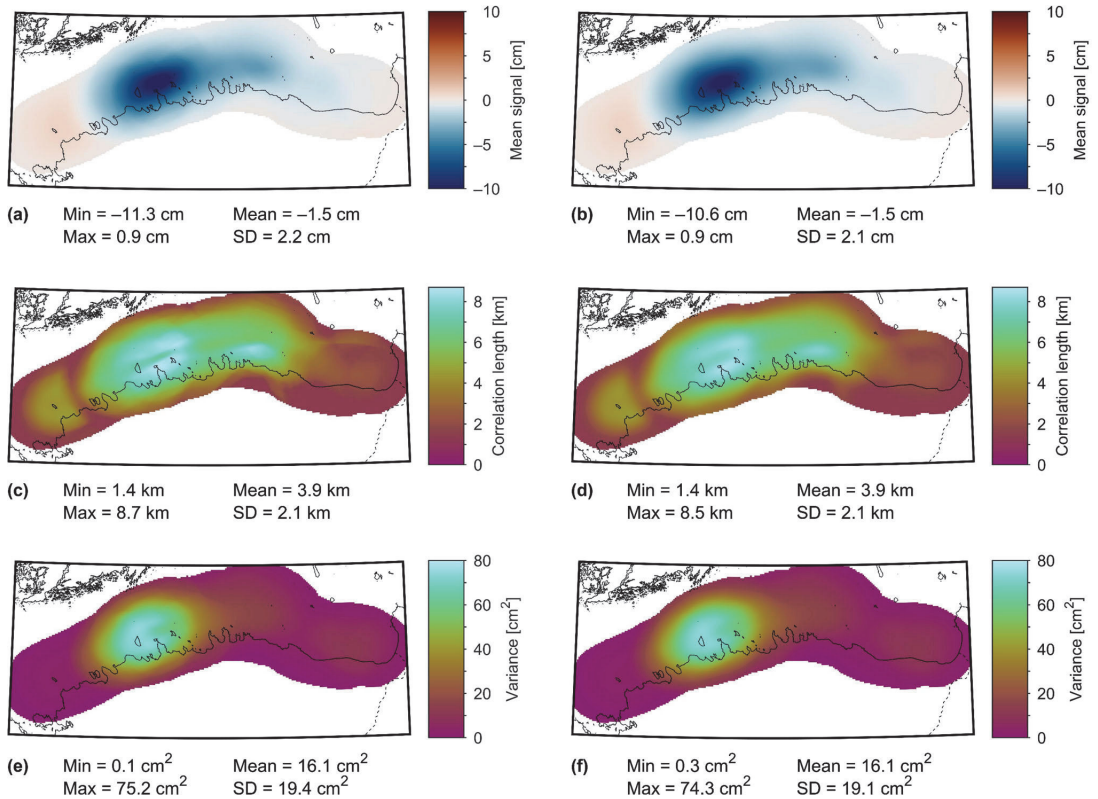
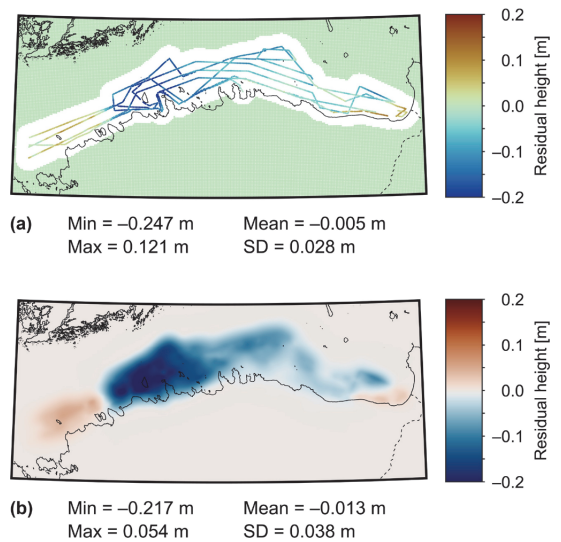


Fig. 11 Estimated mean signals (a, b), correlation lengths (c, d) and signal variances (e, f) of the first iteration residual heights r^1 before (a, c, e) and after (b, d, f) filtering

Fig. 12 Residual heights (including zero pad) of the first iteration (a) before (i.e. r^1) and (b) after (i.e. \hat{r}^1) gridding



second- and third-order Markov, and Gaussian covariance models) was preferred, among which the exponential model showed the best performance (Fig. 10 sub-plots c and e). The model is defined as:

$$C_{\text{model}}(l) = C_0 e^{-l/\alpha}, \tag{30}$$

where parameter α is related to the correlation length $X_{1/2}$ as $\alpha = (-\ln 0.5)^{-1} X_{1/2} \approx 1.443 X_{1/2}$. The correlation length is defined as the distance at which the covariance reaches half the value of signal variance C_0 .

Parameter α and signal variance were estimated for gridding at each computation point using the exponential covariance model. The heterogeneous nature of the residual heights' signal is evident from the estimated values presented in Fig. 11. Occasionally, the change in values of parameter α and signal variance at nearby cells was steep (Fig. 11 sub-plots c and e, respectively; Fig. 11 presents correlation lengths because these are more meaningful quantities than the α parameter), resulting in gridding artefacts. Data were hence filtered spatially. First, a 3 km radius median filter was used to eliminate potential gross estimates; these results were smoothed with a 5 km radius averaging filter. The filtered values are shown in Fig. 11 sub-plots d and f. The mean signal used for centring data for least-squares collocation at each computation point (removed and restored before and after computation, respectively) was also filtered for methodological consistency (Fig. 11b). Residual heights r^1 were then gridded using least-squares collocation, where the exponential covariance model (with filtered parameter α and signal variance) described the C_{st} and C_{tt} covariance matrices (refer to Eqs. 9 and 10). Figure 12 presents the first iteration residual heights before and after gridding. Restoring the initially removed EIGEN-6C4 signal on gridded residual heights \hat{r}^1 provided gridded geometric height anomalies $\hat{\zeta}_{\text{geom}}^1$ (Eq. 16).

The computed uncertainty σ_{geom}^1 of gridded geometric height anomalies (Eq. 17) was modified by setting the modification parameter to $M = 2$ (Eqs. 18 and 19; see also Fig. 2). With a 10 km zero padding distance (i.e. l_{zp} in Eq. 19), $M = 2$ facilitated smooth transition zones from data to the zero pad regions. The large values of uncertainty-associated statistics in Fig. 13 occur due to this uncertainty modification. Note that the uncertainty of gridded geometric height anomalies is correlated with the distance to SSH data locations (also before modifying). Thus, the pattern of vessels' trajectory is clearly visible (Fig. 13a), which means that these patterns also appear in the combined model after uncertainty-dependent data assimilation. The previously described filtering scheme was employed to reduce the appearance of such patterns in the combined model; Fig. 13b shows the filtering results.

Gridding of second iteration geometric height anomalies and derivation of their uncertainty was conducted precisely

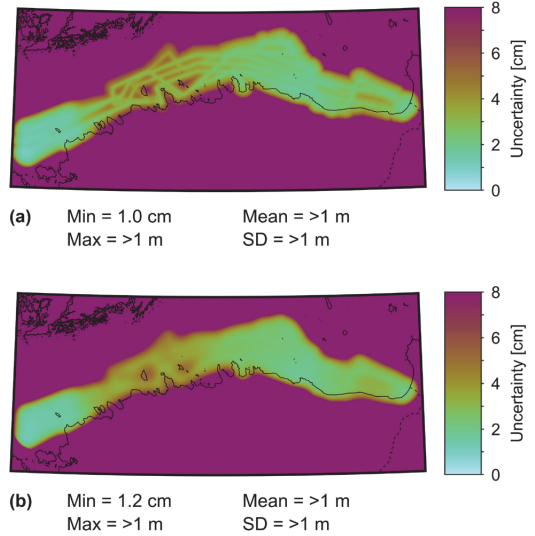


Fig. 13 Modified uncertainty σ_{MOD}^1 of the first iteration gridded geometric height anomalies before (a) and after (b) filtering

as already described. The only difference was that instead of using EIGEN-6C4-derived height anomalies for determining residual heights r^2 , the assimilation result of the first iteration (i.e. EIGEN-6C4-i1; cf. the next section) was used instead. For the second iteration, a total of 17,783 computation points were determined. According to the covariance analysis, the exponential covariance model appeared to perform the best (Fig. 10 sub-plots d and f), as was the case when analysing first iteration data. An arbitrarily selected example of a residual heights' autocovariance curve and corresponding least-squares fitted covariance models can be seen in Fig. 10b (note that this example represents only a single computation point out of 17,783 in total).

3.4 Iterative data assimilation

Iterative data assimilation (Eqs. 21 to 24) was conducted to refine EIGEN-6C4-derived height anomalies using the gridded geometric height anomalies and associated uncertainties. The assimilation results (i.e. combined models) are denoted as EIGEN-6C4-i1 (Fig. 14a) and EIGEN-6C4-i2 (Fig. 14c) according to the first and second iteration, respectively. The associated uncertainties of these combined models are correspondingly shown in Fig. 14b and d. Recall that the EIGEN-6C4-i1 and its uncertainty served as an input dataset for the second assimilation iteration. It can be noticed that outside the area of available SSH data, the combined models

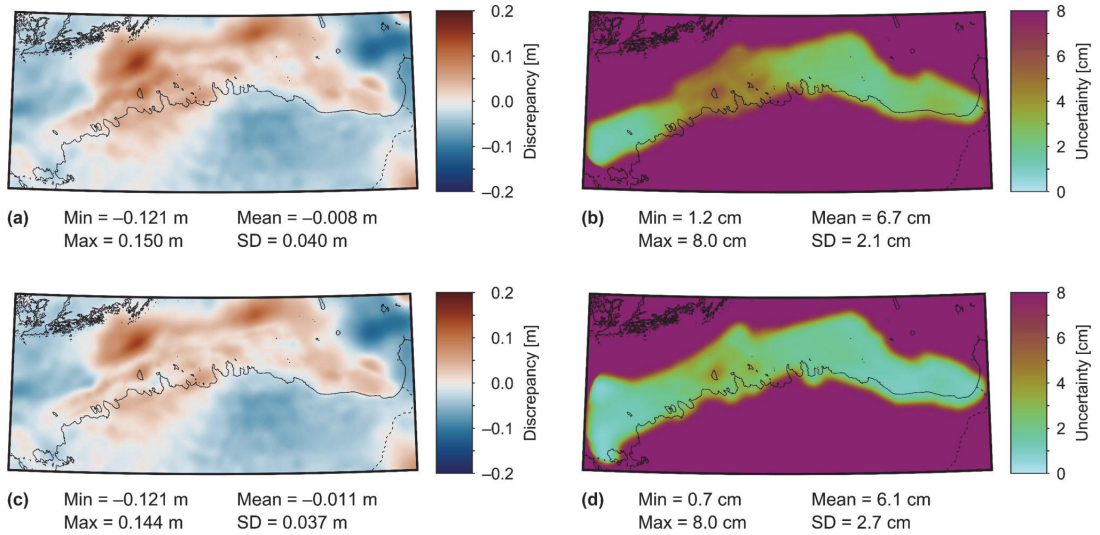


Fig. 14 EIGEN-6C4-i1 (a) and EIGEN-6C4-i2 (c) discrepancies relative to the GQM2022 quasigeoid model and the associated uncertainties of these combined models (b and d, respectively)

retain the initial 8 cm uncertainty assigned to EIGEN-6C4-derived height anomalies, which is due to the uncertainty modification (Eqs. 18 and 19).

The most significant improvements occurred during the first assimilation iteration (compare Figs. 14a and 5). Due to the reduced uncertainty of the first iteration combined model (Fig. 14b), the second iteration contributed less to the improvements. However, the reduction of discrepancies is still noticeable (compare Fig. 14c–a). The contribution of the first and second assimilation iterations is shown in Fig. 15a (i.e. differences between EIGEN-6C4 and EIGEN-6C4-i1) and 15b (i.e. differences between EIGEN-6C4-i1 and EIGEN-6C4-i2), respectively. The total contribution of the assimilation is presented in Fig. 15c (i.e. differences between EIGEN-6C4 and EIGEN-6C4-i2). Such iterative refinement could be continued if more SSH data were available until the combined model uncertainty diminishes to near zero (refer to Eq. 24). In that case, no further refinements can occur. After conducting two refinement iterations in the current case study, the discrepancies in Fig. 14c along the survey routes indicate satisfactory improvements compared to the initial discrepancies in Fig. 5 (cf. Table 1). The reductions of mean discrepancy from 7.4 cm to 1.1 cm and standard deviation estimate from 6.9 cm to 1.9 cm suggest that accuracy in the same order of magnitude as the GQM2022 model can be achieved in regions of available SSH data by refining the EIGEN-6C4.

It should be mentioned that some new discrepancies appeared in the western and eastern extremes of the case study region, but this assumes that the GQM2022 model

used for validation is correct. To an extent, the EIGEN-6C4-i2 discrepancies relative to the GQM2022 (Fig. 14c) in the eastern extreme of the case study region (i.e. the eastern part of the Gulf of Finland) could be explained by utilizing GNSS-levelling control points. If the GQM2022 model were slightly higher in north-eastern Estonia as GNSS-levelling control points suggest it would be correct (notice negative-signed discrepancies in Fig. 16), then the positive-signed discrepancies of EIGEN-6C4-i2 in the eastern Gulf of Finland (Fig. 14c) would reduce closer to zero. Thus, these discrepancies that appeared through data assimilation could also signify improvements instead of propagated errors of SSH and DT datasets.

4 Discussion

With the current technology and methods, it is possible to derive accurate offshore geoid geometry. Thus far, such information has been successfully used in validating marine geoid modelling solutions (analogously to Fig. 8 example). In this study, geometry information was further exploited. It was demonstrated that these data could be used to refine marine geoid models in gravity data void areas and regions where poor data quality does not allow accurate modelling (i.e. regions where decimetre-level modelling errors could be expected). For that purpose, an iterative data assimilation approach was developed. While gravimetric geoid modelling requires previous experience and theoretical knowledge, the developed approach could be a more accessible alternative by

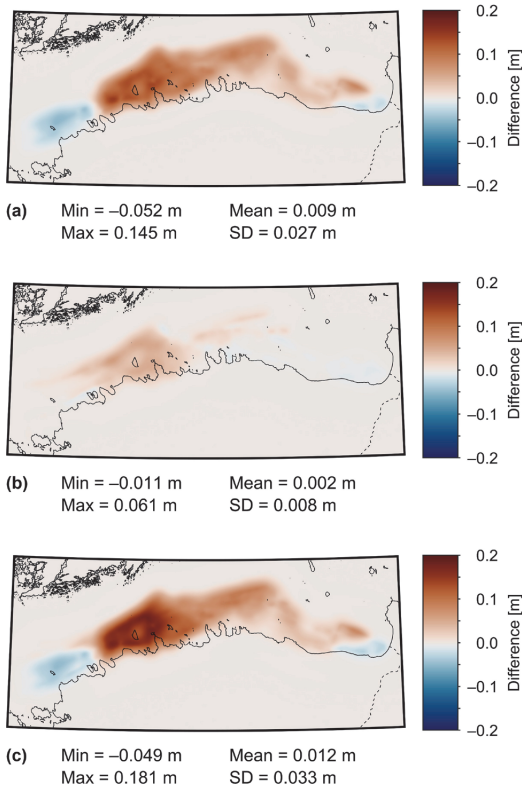


Fig. 15 Differences between EIGEN-6C4 and EIGEN-6C4-i1 (a), and EIGEN-6C4-i1 and EIGEN-6C4-i2 (b). In (c) are shown EIGEN-6C4 differences relative to EIGEN-6C4-i2 (i.e. the sum of a and b sub-plots)

Table 1 Descriptive statistics of EIGEN-6C4-associated models' discrepancies relative to the high-resolution GQM2022 quasigeoid model along the survey routes (considering all eight datasets; refer to Fig. 8). All units are in metres

Model	EIGEN-6C4	EIGEN-6C4-i2	EIGEN-6C4-i2 ($F_{scale} = 10$)
Figure showing the used discrepancies	Figure 5	Figure 14c	Figure 17c
Min	-0.074	-0.075	-0.075
Max	0.209	0.059	0.054
Mean	0.074	0.011	0.007
SD	0.069	0.019	0.019

utilizing existing geoid models (or high-degree global geopotential models as was done here).

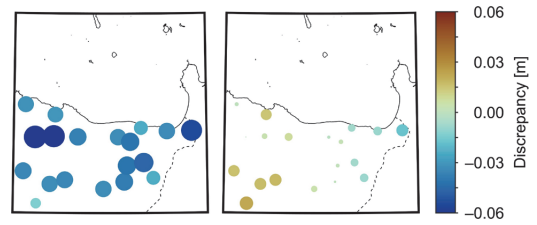


Fig. 16 EIGEN-6C4-i2 (left) and GQM2022 (right) discrepancies relative to the GNSS-levelling control points in north-eastern Estonia. The sizes of coloured dots are proportional to the discrepancies

Because the method relies on uncertainty estimates, location-dependent uncertainties of gravimetric geoid models (e.g. Featherstone et al. 2018; Ellmann et al. 2020) could be beneficial. This way, data assimilation is restricted in regions where the model should already be accurate. In the case of poorly estimated uncertainties, however, potential refinements are neglected, signifying the importance of well-established uncertainties. On the other hand, location-dependent uncertainties of gravimetric geoid models are not mandatory, and the assumption of constant uncertainty is sufficient, as was demonstrated. A drawback of this approach is that errors in SSH and DT datasets may distort already accurate regions of the marine geoid model.

As is evident from Figs. 14 and 15, each additional iteration introduces less information to the new combined model due to the reduced uncertainty of the input combined model. It is possible to increase the impact of subsequent assimilation iterations (and thus extend the process for more iterations) by scaling up the uncertainty of gridded geometric height anomalies in Eq. 24:

$$\sigma_{model}^{k+1}(\varphi, \lambda) = \sqrt{\frac{F_{scale} [2 - P(\varphi, \lambda)] [\sigma_{model}^k(\varphi, \lambda)]^2 [\sigma_{MOD}^k(\varphi, \lambda)]^2}{P(\varphi, \lambda) [\sigma_{model}^k(\varphi, \lambda)]^2 + F_{scale} [2 - P(\varphi, \lambda)] [\sigma_{MOD}^k(\varphi, \lambda)]^2}} \tag{31}$$

where the introduced parameter $F_{scale} > 1$ is the scale factor. The uncertainty of the input model is left unchanged as it would be undesirable for the output model to be associated with increased uncertainties. For meaningful extension of the assimilation process, $F_{scale} [\sigma_{MOD}^k]^2 > [\sigma_{model}^k]^2$, considering either mean or more minor uncertainties (recall that $\sigma_{model}^{k+1} < \sigma_{model}^k$ and $\sigma_{model}^{k+1} < \sigma_{MOD}^k$). Figure 17 shows the assimilation results when F_{scale} is set to an arbitrary value of 10, which fulfils the condition for more minor uncertainties (compare the results to the ones in Fig. 14). It can be noticed that the impact of the second iteration has increased. The discrepancies in Fig. 17c along the survey routes yield a slightly reduced mean discrepancy compared to the one associated with Fig. 14c (cf. Table 1).

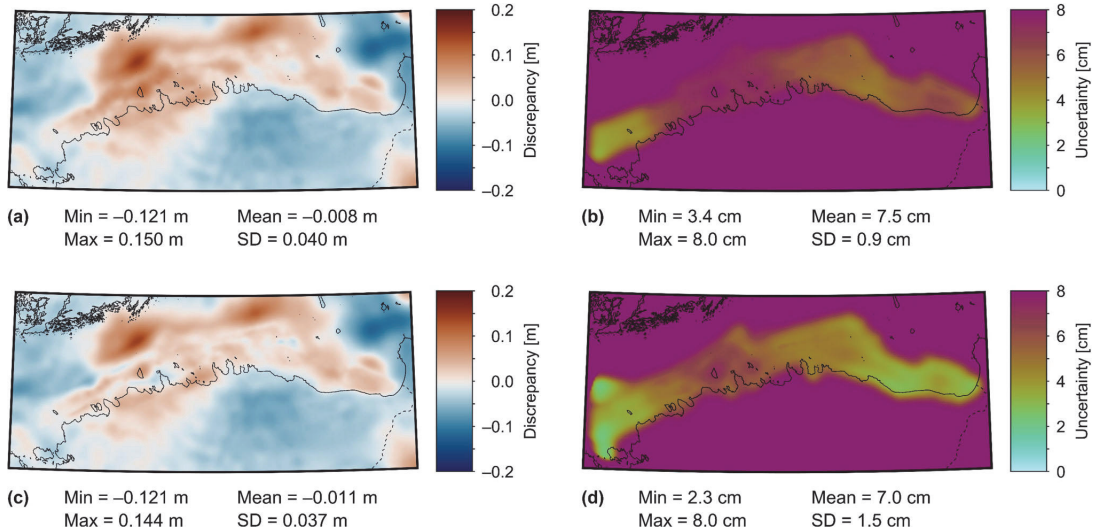


Fig. 17 EIGEN-6C4-i1 (a) and EIGEN-6C4-i2 (c) discrepancies relative to the GQM2022 quasigeoid model and the associated uncertainties of these combined models (b and d, respectively) by setting the scale factor F_{scale} to 10

The SSH data used in this study originated from shipborne GNSS campaigns and an airborne laser scanning survey. Due to the large quantity of available data, it would be interesting to experiment with satellite altimetry measurements over a more extensive study area in a future study (here, the primary objective was to establish the principles and test the method). With the launch of SWOT (Surface Water and Ocean Topography) at the end of 2022, the proposed approach will receive an additional exciting source of SSH data. It should be emphasized that in this case study, all the SSH data represent single-time measurements. Error patterns between different datasets may therefore vary (i.e. a different dataset of geometric height anomalies may reveal a slightly different pattern than the one in Fig. 8). Data reliability, and consequently the assimilation results, can be improved with repeated measurements. For example, multi-year satellite altimetry data can be divided into yearly sub-datasets, where each sub-dataset contains several orbital cycles worth of data. Also, a future study should conduct more than two assimilation iterations to see how well the possibly propagated errors of SSH and DT datasets (besides the initial errors of the gravimetric geoid model) are refined in the combined model.

An important limitation that should be addressed regards the case study region, and the entire Baltic Sea, which are water bodies surrounded by TG stations (cf. Fig. 4). The method developed for DT derivation (cf. Sect. 2.1) benefits significantly from such a situation since the estimated DB is tied to in situ data at all sides. In a case where the coastline stretches along a single side of a water body, the estimated

DB likely suffers from significant extrapolation errors with the increasing distance from the coast. A future study could investigate methods to derive reliable DT in such a situation. Nevertheless, the developed method should still provide satisfactory results in the near-coast region, which are the areas of most interest for accurate geoid modelling.

For practical considerations, the same geoid model should be used over dry land and offshore (e.g. hydrographic surveys, offshore engineering, across-sea infrastructure construction). Hence, merging the regional geoid fitting approaches with data assimilation offshore could be advisable. Over dry land, the GNSS-levelling control points can be used as per convention, whereas, over marine areas, SSH and DT datasets could be employed. A combined seamless solution of the two approaches should be explored in future studies.

5 Conclusion

The modelling errors of marine geoid models can exceed the determination accuracy of SSHs and DT, especially in gravity data void areas and regions of poor-quality gravity data. Such a tendency signifies the potential of SSH and DT datasets in refining marine geoid models. An iterative data assimilation approach was developed to exploit this potential. Sea surface height data from shipborne GNSS campaigns and an airborne laser scanning survey were used to refine errors in the EIGEN-6C4 global geopotential model. It was demonstrated that the combined model agreed significantly

better with a high-resolution regional gravimetric quasigeoid model employed for validation. Using SSH and DT datasets in a data assimilation approach can therefore be the follow-on stage to conventional gravimetric geoid modelling offshore or an alternative to conventional modelling by utilizing, for example, a suitable high-degree global geopotential model.

Acknowledgements The three anonymous reviewers (also another three who worked with an earlier manuscript version) are thanked for their contribution to the quality of the manuscript. The Swedish Meteorological and Hydrological Institute is thanked for their cooperation in obtaining NEMO-Nordic model data. The Estonian Environment Agency is thanked for providing the used Estonian TG data.

Authors' contributions SV and AE designed the research concept; SV developed the iterative data assimilation approach and drafted and visualized the manuscript; SV and AE contributed to the discussion, review, and editing and approved the final manuscript.

Funding The research was supported by the Estonian Research Council grant "Development of an iterative approach for near-coast marine geoid modelling by using re-tracked satellite altimetry, in situ and modelled data" [grant number PRG330].

Data availability The EIGEN-6C4 global geopotential model is available via International Centre for Global Earth Models: http://icgem.gfz-potsdam.de/tom_longtime (accessed 13 September 2022). The used hourly TG data can be obtained from the webpages of Finnish (<https://en.ilmatiiteenlaitos.fi/download-observations#!/>; accessed 13 September 2022), Latvian (<https://www.meteo.lv/hidrologija-datu-meklesana/?nid=466>; accessed 13 September 2022), Russian (<https://www.emodnet-physics.eu/Map/DefaultMap.aspx>; accessed 13 September 2022) and Swedish (<https://www.smhi.se/data/oceanografi/ladda-ner-oceano-grafiska-observationer/#param=sealevelrh2000,stations=all>; accessed 13 September 2022) TG managing authorities. The employed NKG2016LU vertical land motion model is provided by the Lantmäteriet (on behalf of the Nordic Geodetic Commission – NKG): <https://www.lantmateriet.se/en/geodata/gps-geodesi-och-svepos/reference-systems/postglacial-land-uplift> (accessed 13 September 2022). For Estonian GNSS-levelling data, see Rüdja and Varbla (2022). The used airborne laser scanning derived SSHs are available from: <https://doi.org/10.17882/76491>. The shipborne GNSS-determined SSHs are available from the corresponding author upon reasonable request.

Declarations

Conflict of interest The authors have no competing interests to declare that are relevant to the content of this article.

References

Ababou R, Bagtzoglou AC, Wood EF (1994) On the condition number of covariance matrices in kriging, estimation, and simulation of random fields. *Math Geol* 26:99–133. <https://doi.org/10.1007/BF02065878>

Ågren J, Strykowski G, Bilker-Koivula M, Omang O, Märdla S, Forsberg R, Ellmann A, Oja T, Liepins I, Parseliunas E, Kaminskis J, Sjöberg LE, Valssoon G (2016) The NKG2015 gravimetric geoid model for the Nordic-Baltic region. In: Proceedings of the international symposium on gravity, geoid and height systems 2016.

Thessaloniki, Greece, 19–23 September 2016. <https://doi.org/10.13140/RG.2.2.20765.20969>

Andersen OB, Knudsen P (2019) The DTU17 global marine gravity field: first validation results. In: Mertikas SP, Pail R (eds) *Fiducial reference measurements for altimetry*. Springer, Cham, pp 83–87

Bonnefond P, Laurain O, Exertier P, Calzas M, Guinle T, Picot N, FOAM Project Team (2022) Validating a new GNSS-based sea level instrument (CalNaGeo) at Senetosa Cape. *Mar Geod* 45:121–150. <https://doi.org/10.1080/01490419.2021.2013355>

Bouin M-N, Ballu V, Calmant S, Boré J-M, Folcher E, Ammann J (2009) A kinematic GPS methodology for sea surface mapping. *Vanuatu J Geod* 83:1203. <https://doi.org/10.1007/s00190-009-0338-x>

Denker H, Roland M (2005) Compilation and evaluation of a consistent marine gravity data set surrounding Europe. In: Sansò F (ed) *A window on the future of geodesy*. Springer, Heidelberg, pp 248–253. https://doi.org/10.1007/3-540-27432-4_42

Ekman M (1989) Impacts of geodynamic phenomena on systems for height and gravity. *Bull Géodésique* 63:281–296. <https://doi.org/10.1007/BF02520477>

Ellmann A, Kaminskis J, Parseliunas E, Jürgenson H, Oja T (2009) Evaluation results of the Earth Gravitational Model EGM08 over the Baltic countries. *Newton's Bull* 4:110–121

Ellmann A, Märdla S, Oja T (2020) The 5 mm geoid model for Estonia computed by the least squares modified Stokes's formula. *Surv Rev* 52:352–372. <https://doi.org/10.1080/00396265.2019.1583848>

EVRF (2019) Height datum relations. Federal Agency for Cartography and Geodesy (BKG). <https://evrs.bkg.bund.de/Subsites/EVRS/EN/Projects/HeightDatumRel/height-datum-rel.html>. Accessed 10 September 2022.

Featherstone WE (2009) Only use ship-track gravity data with caution: a case-study around Australia. *Aust J Earth Sci* 56:195–199. <https://doi.org/10.1080/08120090802547025>

Featherstone WE, McCubbin JC, Brown NJ, Claessens SJ, Filmer MS, Kirby JF (2018) The first Australian gravimetric quasigeoid model with location-specific uncertainty estimates. *J Geod* 92:149–168. <https://doi.org/10.1007/s00190-017-1053-7>

Fecher T, Pail R, Gruber T, GOCO Consortium (2017) GOCO05c: a new combined gravity field model based on full normal equations and regionally varying weighting. *Surv Geophys* 38:571–590. <https://doi.org/10.1007/s10712-016-9406-y>

Filmer MS, Hughes CW, Woodworth PL, Featherstone WE,ingham RJ (2018) Comparison between geodetic and oceanographic approaches to estimate mean dynamic topography for vertical datum unification: evaluation at Australian tide gauges. *J Geod* 92:1413–1437. <https://doi.org/10.1007/s00190-018-1131-5>

Forsberg R (1987) A new covariance model for inertial gravimetry and gradiometry. *J Geophys Res Solid Earth* 92:1305–1310. <https://doi.org/10.1029/JB092iB02p01305>

Förste C, Bruinsma SL, Abrykosov O, Lemoine J-M, Marty JC, Flechtner F, Balmino G, Barthelmes F, Biancale R (2014) EIGEN-6C4 the latest combined global gravity field model including GOCE data up to degree and order 2190 of GFZ Potsdam and GRGS Toulouse. GFZ Data Serv. <https://doi.org/10.5880/icgem.2015.1>

Fortunato AB, Oliveira A, Rogeiro J, da Costa RT, Gomes JL, Li K, de Jesus G, Freire P, Rilo A, Mendes A, Rodrigues M, Azevedo A (2017) Operational forecast framework applied to extreme sea levels at regional and local scales. *J Oper Oceanogr* 10:1–15. <https://doi.org/10.1080/1755876X.2016.1255471>

Hirvonen RA (1962) On the statistical analysis of gravity anomalies. Ohio State University, Institute of Geodesy, Photogrammetry and Cartography, report #19, 24 pp

Hong B, Liu Z, Shen J, Wu H, Gong W, Xu H, Wang D (2020) Potential physical impacts of sea-level rise on the Pearl River Estuary, China. *J Mar Syst* 201:103245. <https://doi.org/10.1016/j.jmarsys.2019.103245>

- Hordoir R, Axell L, Höglund A, Dieterich C, Fransner F, Gröger M, Liu Y, Pemberton P, Schimanke S, Andersson H, Ljungemyr P, Nygren P, Falahat S, Nord A, Jönsson A, Lake I, Döös K, Hieronymus M, Dietze H, Löptien U, Kuznetsov I, Westerlund A, Tuomi L, Haapala J (2019) Nemo-Nordic 1.0: a NEMO-based ocean model for the Baltic and North seas—research and operational applications. *Geosci Model Dev* 12:363–386. <https://doi.org/10.5194/gmd-12-363-2019>
- Idhe J, Mäkinen J, Sacher M (2019) Conventions for the definition and realization of a European Vertical Reference System (EVRS); version 5.2. Federal Agency for Cartography and Geodesy (BKG). https://evrs.bkg.bund.de/SharedDocs/Downloads/EVRS/EN/Publications/EVRFConventions2007.pdf?__blob=publicationFile&v=3. Accessed 31 August 2022
- Ince ES, Förste C, Barthelmes F, Pflug H, Li M, Kaminskis J, Neumayer K-H, Michalak G (2020) Gravity measurements along commercial ferry lines in the Baltic Sea and their use for geodetic purposes. *Mar Geod* 43:573–602. <https://doi.org/10.1080/01490419.2020.1771486>
- Jahanmard V, Delpeche-Ellmann N, Ellmann A (2021) Realistic dynamic topography through coupling geoid and hydrodynamic models of the Baltic Sea. *Cont Shelf Res* 222:104421. <https://doi.org/10.1016/j.csr.2021.104421>
- Jamil H, Kadir M, Forsberg R, Olesen A, Isa MN, Rasidi S, Mohamed A, Chihat Z, Nielsen E, Majid F, Talib K, Aman S (2017) Airborne geoid mapping of land and sea areas of East Malaysia. *J Geod Sci* 7:84–93. <https://doi.org/10.1515/jogs-2017-0010>
- Jordan SK (1972) Self-consistent statistical models for the gravity anomaly, vertical deflections, and undulation of the geoid. *J Geophys Res* 77:3660–3670. <https://doi.org/10.1029/JB077i020p03660>
- Journel AG, Froidevaux R (1982) Anisotropic hole-effect modeling. *J Int Assoc Math Geol* 14:217–239. <https://doi.org/10.1007/BF01032885>
- Kamto PG, Yap L, Nguiya S, Kandé LH, Kamguia J (2022) Evaluation of latest marine gravity field models derived from satellite altimetry over the Gulf of Guinea (Central Africa) with shipborne gravity data. *Stud Geophys Geod* 66:23–37. <https://doi.org/10.1007/s1200-021-0157-y>
- Kärnä T, Ljungemyr P, Falahat S, Ringgaard I, Axell L, Korabel V, Murawski J, Maljutenko I, Lindenthal A, Jandt-Scheelke S, Verjovkina S, Lorkowski I, Lagema P, She J, Tuomi L, Nord A, Huess V (2021) Nemo-Nordic 2.0: operational marine forecast model for the Baltic Sea. *Geosci Model Dev* 14:5731–5749. <https://doi.org/10.5194/gmd-14-5731-2021>
- Kasper JF (1971) A second-order Markov gravity anomaly model. *J Geophys Res* 76:7844–7849. <https://doi.org/10.1029/JB076i032p07844>
- Kearsley W (1977) Non-stationary estimation in gravity prediction problems. Ohio State University, Department of Geodetic Science, report #256, 63 pp.
- Kollo K, Ellmann A (2019) Geodetic reconciliation of tide gauge network in Estonia. *Geophysica* 54:27–38
- Lagema P, Elken J, Kõuts T (2011) Operational sea level forecasting in Estonia. *Est J Eng* 17:301–331. <https://doi.org/10.3176/eng.2011.4.03>
- Li Q, Bao L, Wang Y (2021) Accuracy evaluation of altimeter-derived gravity field models in offshore and coastal regions of China. *Front Earth Sci* 9:722019. <https://doi.org/10.3389/feart.2021.722019>
- Liibusk A, Varbla S, Ellmann A, Vahter K, Uiboupin R, Delpeche-Ellmann N (2022) Shipborne GNSS acquisition of sea surface heights in the Baltic Sea. *J Geod Sci* 12:1–21. <https://doi.org/10.1515/jogs-2022-0131>
- Lu B, Barthelmes F, Li M, Förste C, Ince ES, Petrovic S, Flechtner F, Schwabe J, Luo Z, Zhong B, He K (2019) Shipborne gravimetry in the Baltic Sea: data processing strategies, crucial findings and preliminary geoid determination tests. *J Geod* 93:1059–1071. <https://doi.org/10.1007/s00190-018-01225-7>
- Mäkinen J (2008) The treatment of the permanent tide in EUREF products. Regional Reference Frame Sub-Commission for Europe (EUREF). http://www.euref.eu/TWG/EUREF%20TWG%20minutes/47-Brussels2008/05-Makinen_tides.pdf. Accessed 31 August 2022.
- Märdla S, Ellmann A, Oja T, Jürgenson H (2015) Improving and validating gravity data over ice-covered marine areas. In: Rizos C, Willis P (eds) IAG 150 years. Springer, Cham, pp 263–270. https://doi.org/10.1007/1345_2015_163
- Märdla S, Ågren J, Strykowski G, Oja T, Ellmann A, Forsberg R, Bilker-Koivula M, Omang O, Paršeliūnas E, Liepiņš I, Kaminskis J (2017) From discrete gravity survey data to a high-resolution gravity field representation in the Nordic-Baltic region. *Mar Geod* 40:416–453. <https://doi.org/10.1080/01490419.2017.1326428>
- Mazloff MR, Gille ST, Cornuelle B (2014) Improving the geoid: combining altimetry and mean dynamic topography in the California coastal ocean. *Geophys Res Lett* 41:8944–8952. <https://doi.org/10.1002/2014GL062402>
- Medvedev IP, Rabinovich AB, Kulikov EA (2013) Tidal oscillations in the Baltic Sea. *Oceanology* 53:526–538. <https://doi.org/10.1134/S0001437013050123>
- Medvedev IP, Rabinovich AB, Kulikov EA (2016) Tides in three enclosed basins: the Baltic, Black, and Caspian Seas. *Front Mar Sci* 3:46. <https://doi.org/10.3389/fmars.2016.00046>
- Moritz H (1980) Advanced physical geodesy. Wichmann, Karlsruhe.
- Mostafavi M, Delpeche-Ellmann N, Ellmann A (2021) Accurate sea surface heights from Sentinel-3A and Jason-3 retracers by incorporating high-resolution marine geoid and hydrodynamic models. *J Geod Sci* 11:58–74. <https://doi.org/10.1515/jogs-2020-0120>
- Müller FL, Wekerle C, Dettmering D, Passaro M, Bosch W, Seitz F (2019) Dynamic ocean topography of the northern Nordic seas: a comparison between satellite altimetry and ocean modelling. *Cryosphere* 13:611–626. <https://doi.org/10.5194/tc-13-611-2019>
- Noréus JP, Nyborg MR, Hayling KL (1997) The gravity anomaly field in the Gulf of Bothnia spatially characterized from satellite altimetry and in situ measurements. *J Appl Geophys* 37:67–84. [https://doi.org/10.1016/S0926-9851\(97\)00007-4](https://doi.org/10.1016/S0926-9851(97)00007-4)
- Pavlis NK, Holmes SA, Kenyon SC, Factor JK (2012) The development and evaluation of the Earth Gravitational Model 2008 (EGM2008). *J Geophys Res Solid Earth* 117:B04406. <https://doi.org/10.1029/2011JB008916>
- Penna NT, Morales Maqueda MA, Martin I, Guo J, Foden PR (2018) Sea surface height measurement using a GNSS wave glider. *Geophys Res Lett* 45:5609–5616. <https://doi.org/10.1029/2018GL077950>
- Poutanen M, Vermeer M, Mäkinen J (1996) The permanent tide in GPS positioning. *J Geod* 70:499–504. <https://doi.org/10.1007/BF00863622>
- Reichle RH (2008) Data assimilation methods in the Earth sciences. *Adv Water Resour* 31:1411–1418. <https://doi.org/10.1016/j.advwatres.2008.01.001>
- Reilly WI (1979) Mapping the local geometry of the Earth's gravity field. Department of Scientific and Industrial Research (New Zealand), Geophysics Division, report #143, 56 pp
- Rocken C, Johnson J, Van Hove T, Iwabuchi T (2005) Atmospheric water vapor and geoid measurements in the open ocean with GPS. *Geophys Res Lett* 32:L12813. <https://doi.org/10.1029/2005GL022573>
- Roggenbuck O, Reinking J (2019) Sea surface heights retrieval from ship-based measurements assisted by GNSS signal reflections. *Mar Geod* 42:1–24. <https://doi.org/10.1080/01490419.2018.1543220>
- Roggenbuck O, Reinking J, Härting A (2014) Oceanwide precise determination of sea surface height from in-situ measurements on

- cargo ships. *Mar Geod* 37:77–96. <https://doi.org/10.1080/01490419.2013.868385>
- Rüdja A, Varbla S (2022) Estonian GNSS-leveling dataset with relevance to the implementation of the Baltic Sea Chart Datum 2000. *SEANO*. <https://doi.org/10.17882/87718>
- Rulent J, Calafat FM, Banks CJ, Bricheno LM, Gommenginger C, Green JAM, Haigh ID, Lewis H, Martin ACH (2020) Comparing water level estimation in coastal and shelf seas from satellite altimetry and numerical models. *Front Mar Sci* 7:549467. <https://doi.org/10.3389/fmars.2020.549467>
- Saari T, Bilker-Koivula M, Koivula H, Nordman M, Häkli P, Lahtinen S (2021) Validating geoid models with marine GNSS measurements, sea surface models, and additional gravity observations in the Gulf of Finland. *Mar Geod* 44:196–214. <https://doi.org/10.1080/01490419.2021.1889727>
- Sandwell DT, Harper H, Tozer B, Smith WHF (2021) Gravity field recovery from geodetic altimeter missions. *Adv Space Res* 68:1059–1072. <https://doi.org/10.1016/j.asr.2019.09.011>
- Schubert T, Brockmann JM, Korte J, Schuh W-D (2021) On the family of covariance functions based on ARMA models. *Eng Proc* 5:37. <https://doi.org/10.3390/engproc2021005037>
- Schwabe J, Ågren J, Liebsch G, Westfeld P, Hammarklint T, Mononen J, Andersen OB (2020) The Baltic Sea Chart Datum 2000 (BSCD2000) – implementation of a common reference level in the Baltic Sea. *Int Hydrogr Rev* 23:63–83
- Shaw L, Paul I, Henriksen P (1969) Statistical models for the vertical deflection from gravity-anomaly models. *J Geophys Res* 74:4259–4265. <https://doi.org/10.1029/JB074i017p04259>
- Sjöberg LE (2003) A computational scheme to model the geoid by the modified Stokes formula without gravity reductions. *J Geod* 77:423–432. <https://doi.org/10.1007/s00190-003-0338-1>
- Sjöberg LE, Bagherbandi M (2017) Applications and comparisons of LSMSA and RCR. In: Sjöberg LE, Bagherbandi M (eds) *Gravity Inversion and Integration*. Springer, Cham, pp 181–202. https://doi.org/10.1007/978-3-319-50298-4_6
- Slobbe DC, Verlaan M, Klees R, Gerritsen H (2013) Obtaining instantaneous water levels relative to a geoid with a 2D storm surge model. *Cont Shelf Res* 52:172–189. <https://doi.org/10.1016/j.csr.2012.10.002>
- Slobbe DC, Klees R, Gunter BC (2014) Realization of a consistent set of vertical reference surfaces in coastal areas. *J Geod* 88:601–615. <https://doi.org/10.1007/s00190-014-0709-9>
- Smith WHF (2022) Direct conversion of latitude and height from one ellipsoid to another. *J Geod* 96:36. <https://doi.org/10.1007/s00190-022-01608-x>
- Varbla S (2022) The influence of bathymetry on regional marine geoid modeling in Northern Europe. *J Mar Sci Eng* 10:793. <https://doi.org/10.3390/jmse10060793>
- Varbla S, Ellmann A, Delpêche-Ellmann N (2020a) Validation of marine geoid models by utilizing hydrodynamic model and shipborne GNSS profiles. *Mar Geod* 43:134–162. <https://doi.org/10.1080/01490419.2019.1701153>
- Varbla S, Ellmann A, Delpêche-Ellmann N (2020b) Utilizing airborne laser scanning and geoid model for near-coast improvements in sea surface height and marine dynamics. *J Coast Res* 95:1339–1343. <https://doi.org/10.2112/S195-257.1>
- Varbla S, Ellmann A, Delpêche-Ellmann N (2021) Applications of airborne laser scanning for determining marine geoid and surface waves properties. *Eur J Remote Sens* 54:558–568. <https://doi.org/10.1080/22797254.2021.1981156>
- Varbla S, Liibuska A, Ellmann A (2022a) Shipborne GNSS-determined sea surface heights using geoid model and realistic dynamic topography. *Remote Sens* 14:2368. <https://doi.org/10.3390/rs14102368>
- Varbla S, Ågren J, Ellmann A, Poutanen M (2022b) Treatment of tide gauge time series and marine GNSS measurements for vertical land motion with relevance to the implementation of the Baltic Sea Chart Datum 2000. *Remote Sens* 14:920. <https://doi.org/10.3390/rs14040920>
- Vestøl O, Ågren J, Steffen H, Kierulf H, Tarasov L (2019) NKG2016LU: a new land uplift model for Fennoscandia and the Baltic Region. *J Geod* 93:1759–1779. <https://doi.org/10.1007/s00190-019-01280-8>
- Vousdoukas MI, Voukouvalas E, Annunziato A, Giardino A, Feyen L (2016) Projections of extreme storm surge levels along Europe. *Clim Dyn* 47:3171–3190. <https://doi.org/10.1007/s00382-016-3019-5>
- Vyskočil V (1970) On the covariance and structure functions of the anomalous gravity field. *Stud Geophys Geod* 14:174–177. <https://doi.org/10.1007/BF02585616>
- Wang YM, Sánchez L, Ågren J, Huang J, Forsberg R, Abd-Elmotaal HA, Ahlgren K, Barzaghi R, Bašić T, Carrion D, Claessens S, Erol B, Erol S, Filmer M, Grigoriadis VN, Isik MS, Jiang T, Koç Ö, Kremaric J, Li X, Liu Q, Matsuo K, Natsiopoulos DA, Novák P, Pail R, Pitoňák M, Schmidt M, Varga M, Vergos GS, Véronneau M, Willberg M, Zingerle P (2021) Colorado geoid computation experiment: overview and summary. *J Geod* 95:127. <https://doi.org/10.1007/s00190-021-01567-9>
- Wu Y, Abulaitijiang A, Featherstone WE, McCubbine JC, Andersen OB (2019) Coastal gravity field refinement by combining airborne and ground-based data. *J Geod* 93:2569–2584. <https://doi.org/10.1007/s00190-019-01320-3>
- Xie S, Chen J, Dixon TH, Weisberg RH, Zumberge MA (2021) Off-shore sea levels measured with an anchored spar-buoy system using GPS interferometric reflectometry. *J Geophys Res Oceans* 126:e2021JC017734. <https://doi.org/10.1029/2021JC017734>
- Yang J, Zhang J, Wang C (2019) Sentinel-3A SRAL global statistical assessment and cross-calibration with Jason-3. *Remote Sens* 11:1573. <https://doi.org/10.3390/rs11131573>
- Zhang S, Abulaitijiang A, Andersen OB, Sandwell DT, Beale JR (2021) Comparison and evaluation of high-resolution marine gravity recovery via sea surface heights or sea surface slopes. *J Geod* 95:66. <https://doi.org/10.1007/s00190-021-01506-8>
- Zhou B, Watson C, Legresy B, King MA, Beardsley J, Deane A (2020) GNSS/INS-equipped buoys for altimetry validation: lessons learnt and new directions from the Bass Strait validation facility. *Remote Sens* 12:3001. <https://doi.org/10.3390/rs12183001>
- Zlinszky A, Timár G, Weber R, Székely B, Briese C, Ressler C, Pfeifer N (2014) Observation of a local gravity potential isosurface by airborne lidar of Lake Balaton, Hungary. *Solid Earth* 5:355–369. <https://doi.org/10.5194/se-5-355-2014>

Springer Nature or its licensor (e.g. a society or other partner) holds exclusive rights to this article under a publishing agreement with the author(s) or other rightsholder(s); author self-archiving of the accepted manuscript version of this article is solely governed by the terms of such publishing agreement and applicable law.

Curriculum vitae

Personal data

Name: Sander Varbla
Date of birth: 21.03.1995
Place of birth: Tallinn, Estonia
Citizenship: Estonian

Contact data

E-mail: sander.varbla@taltech.ee / sander.varbla@gmail.com

Education

2019–2023 Tallinn University of Technology, PhD
2014–2019 Tallinn University of Technology, MSc
2011–2014 Tallinn Secondary School of Science

Language competence

Estonian native
English fluent
Russian poor

Professional employment

2019–2023 Tallinn University of Technology, Early Stage Researcher
2017–2019 Tallinn University of Technology, Technician

R&D related managerial and administrative work

2023–... National contact person of the Nordic Geodetic Commission (NKG) Working Group of Height and Geoid (WGHG)
2021–... The Baltic Sea Hydrographic Commission (BSHC) Chart Datum Working Group (expert)
2021–... EUREF Working Group “European Unified Height Reference” (member)

Supervised MSc theses

Toomsar, U. (2022). Ehituse Mäemaja punktipilve ja digitaalse kaksiku loomine [The development of Ehituse Mäemaja point cloud and digital twin]. Supervised by **Varbla, S.**; Puust, R. Master’s thesis. Tallinn, Estonia: Tallinn University of Technology.

Koobak, J. (2022). Madala hinnaklassi GNSS sensoriga saavutatav 3D asukohamäärangu täpsus [Three-dimensional positioning accuracy achievable by a low-cost GNSS sensor]. Supervised by Ellmann, A.; **Varbla, S.** Master’s thesis. Tallinn, Estonia: Tallinn University of Technology.

Goman, S. (2021). Joonobjekti droon-fotogrammeetrilise mõõdistuse täpsuse sõltuvus kontrollpunktide arvust kasutades integreeritud georefereerimist [Drone-based

photogrammetric corridor survey accuracy dependence on the number of control points by using integrated georeferencing]. Supervised by **Varbla, S.** Master's thesis. Tallinn, Estonia: Tallinn University of Technology.

Haljend, E. (2020). Sildkraanatee laserskanneriga mõõdistamise täpsuse aprobeerimine [Evaluation of Precision of Crane Rails Control Measurements by means of Terrestrial Laser Scanning]. Supervised by Kala, V.; **Varbla, S.** Master's thesis. Tallinn, Estonia: Tallinn University of Technology.

Publications

Articles in peer-reviewed journals indexed in reputable databases (ETIS 1.1):

Varbla, S., & Ellmann, A. (2023). Iterative data assimilation approach for the refinement of marine geoid models using sea surface height and dynamic topography datasets. *Journal of Geodesy*, 97(3), #24. doi:10.1007/s00190-023-01711-7

Jahanmard, V., **Varbla, S.**, Delpeche-Ellmann, N., & Ellmann, A. (2022). Retrieval of directional power spectral density and wave parameters from airborne LiDAR point cloud. *Ocean Engineering*, 266(1), #112694. doi:10.1016/j.oceaneng.2022.112694

Gruber, T., Ågren, J., Angermann, D., Ellmann, A., Engfeldt, A., Gisinger, C., Jaworski, L., Marila, S., Nastula, J., Nilfouroushan, F., Poutanen, M., Saari, T., Schlaak, M., Świątek, A., **Varbla, S.**, & Zdunek, R. (2022). Geodetic SAR for height system unification and sea level research – results in the Baltic Sea test network. *Remote Sensing*, 14(14), #3250. doi:10.3390/rs14143250

Varbla, S. (2022). The influence of bathymetry on regional marine geoid modeling in Northern Europe. *Journal of Marine Science and Engineering*, 10(6), #793. doi:10.3390/jmse10060793

Varbla, S., Liibus, A., & Ellmann, A. (2022). Shipborne GNSS-determined sea surface heights using geoid model and realistic dynamic topography. *Remote Sensing*, 14(10), #2368. doi:10.3390/rs14102368

Liibus, A., **Varbla, S.**, Ellmann, A., Vahter, K., Uiboupin, R., & Delpeche-Ellmann, N. (2022). Shipborne GNSS acquisition of sea surface heights in the Baltic Sea. *Journal of Geodetic Science*, 12(1), 1–21. doi:10.1515/jogs-2022-0131

Varbla, S., Ågren, J., Ellmann, A., & Poutanen, M. (2022). Treatment of tide gauge time series and marine GNSS measurements for vertical land motion with relevance to the implementation of the Baltic Sea Chart Datum 2000. *Remote Sensing*, 14(4), #920. doi:10.3390/rs14040920

Ellmann, A., Kütimets, K., **Varbla, S.**, Väli, E., & Kanter, S. (2022). Advancements in underground mine surveys by using SLAM-enabled handheld laser scanners. *Survey Review*, 54(385), 363–374. doi:10.1080/00396265.2021.1944545

Varbla, S., Ellmann, A., & Delpeche-Ellmann, N. (2021). Applications of airborne laser scanning for determining marine geoid and surface waves properties. *European Journal of Remote Sensing*, 54(1), 558–568. doi:10.1080/22797254.2021.1981156

Varbla, S., Ellmann, A., & Puust, R. (2021). Centimetre-range deformations of built environment revealed by drone-based photogrammetry. *Automation in Construction*, 128, #103787. doi:10.1016/j.autcon.2021.103787

- Varbla, S.,** Puust, R., & Ellmann, A. (2021). Accuracy assessment of RTK-GNSS equipped UAV conducted as-built surveys for construction site modelling. *Survey Review*, 53(381), 477–492. doi:10.1080/00396265.2020.1830544
- Gruber, T., Ågren, J., Angermann, D., Ellmann, A., Engfeldt, A., Gisinger, C., Jaworski, L., Marila, S., Nastula, J., Nilfouroushan, F., Oikonomidou, X., Poutanen, M., Saari, T., Schlaak, M., Świątek, A., **Varbla, S.,** & Zdunek, R. (2020). Geodetic SAR for height system unification and sea level research – observation concept and preliminary results in the Baltic Sea. *Remote Sensing*, 12(22), #3747. doi:10.3390/rs12223747
- Varbla, S.,** Ellmann, A., & Delpeche-Ellmann, N. (2020). Utilizing airborne laser scanning and geoid model for near-coast improvements in sea surface height and marine dynamics. *Journal of Coastal Research*, 95(Sp1), 1339–1343. doi:10.2112/SI95-257.1
- Varbla, S.,** Ellmann, A., & Delpeche-Ellmann, N. (2020). Validation of marine geoid models by utilizing hydrodynamic model and shipborne GNSS profiles. *Marine Geodesy*, 43(2), 134–162. doi:10.1080/01490419.2019.1701153
- Varbla, S.,** Ellmann, A., Märdla, S., & Gruno, A. (2017). Assessment of marine geoid models by ship-borne GNSS profiles. *Geodesy and Cartography*, 43(2), 41–49. doi:10.3846/20296991.2017.1330771

Popular science articles (ETIS 6.3):

- Koobak, J., **Varbla, S.,** & Ellmann, A. (2022). Merevee taseme mõõtmise madala hinnaklassi GNSS-sensoriga [Three-dimensional positioning accuracy achievable by a low-cost GNSS sensor]. *Geodeet*, 51, 19–25.
- Rüdja, A., **Varbla, S.,** Kollo, K., & Metsar, J. (2020). Põhjamaade Geodeesiamisjoni teadusnädal Islandil [Nordic Geodetic Commission Science Week in Iceland]. *Geodeet*, 50, 22–25.
- Haljend, E., Kala, V., & **Varbla, S.** (2020). Sildkraanatee laserskanneriga mõõdistamise täpsuse aprobeerimine [Evaluation of precision of crane rails control measurements by means of terrestrial laser scanning]. *Geodeet*, 50, 26–28.
- Varbla, S.,** & Ellmann, A. (2020). Esimesed kogemused satelliit-tehisavaradari (SAR) aktiivtransponderitega Eestis [First experiences with the synthetic aperture radar active transponders in Estonia]. *Geodeet*, 50, 30–35.
- Varbla, S.** (2019). Meregeoidi mudelite valideerimine GNSS- ja aerolaserskaneerimise profiilidega [Validation of marine geoid models by shipborne GNSS and airborne laser scanning profiles]. *Geodeet*, 49, 19–26.
- Varbla, S.,** & Ellmann, A. (2019). Eesti geodeetid rahvusvahelises teaduses [Estonian geodesists in international research]. *Geodeet*, 49, 56–58.
- Varbla, S.** (2019). Kaugseire sügiskoolist Võrus [An overview of the remote sensing training school in Võru]. *Geodeet*, 49, 59–60.
- Varbla, S.,** & Ellmann, A. (2018). Geodeesiamkonverentsid Põhjamaades 2018. aastal [Geodetic conferences in Nordic countries in 2018]. *Geodeet*, 48, 62–64.

- Varbla, S.,** Ellmann, A., Metsar, J., & Oja, T. (2017). Meregravimeetrilised mõõdistused Soome lahel projekti FAMOS raames [The FAMOS marine gravity survey on the Gulf of Finland]. *Geodeet*, 47, 39–43.
- Varbla, S.** (2017). Ühe geodeesiatudengi kirev konverentsiaasta [An eventful year of a geodesy student]. *Geodeet*, 47, 96–99.

Elulookirjeldus

Isikuandmed

Nimi: Sander Varbla
Sünniaeg: 21.03.1995
Sünnikoht: Tallinn, Eesti
Kodakondsus: Eesti

Kontaktandmed

E-post: sander.varbla@taltech.ee / sander.varbla@gmail.com

Hariduskäik

2019–2023 Tallinna Tehnikaülikool, PhD
2014–2019 Tallinna Tehnikaülikool, MSc
2011–2014 Tallinna Reaalkool

Keelteoskus

Eesti keel emakeel
Inglise keel kõrgtase
Vene keel kasin

Teenistuskäik

2019–2023 Tallinna Tehnikaülikool, doktorant-nooremteadur
2017–2019 Tallinna Tehnikaülikool, tehnik

Teadusorganisatsiooniline ja -administratiivne tegevus

2023–... Põhjamaade Geodeesiakomisjoni (NKG) kõrgussüsteemide ja geoidi töögrupi (WGHG) Eesti kontaktisik
2021–... Läänemere Hüdrograafiakomisjoni (BSHC) vertikaaldaatumi töögrupp (ekspert)
2021–... EUREF töögrupp "European Unified Height Reference" (liige)

Magistritööde juhendamine ja teaduspublikatsioonid

Nimekirjad magistritööde juhendamisest ja teaduspublikatsioonidest on esitatud inglise keelse elulookirjelduse all.

ISSN 2585-6901 (PDF)
ISBN 978-9916-80-013-3 (PDF)